

University of Liège  
Faculty of Applied Sciences  
UEE research unit  
HECE research group

# Contributions to uncertainty analysis of computational models with application to hydrodynamics and physically-based hydrological simulations

Louis GOFFIN

Thesis submitted in partial fulfilment of the requirements for the degree of  
Doctor of Philosophy in Applied Sciences

## Members of the jury

**Frédéric NGUYEN** (chairman), Pr. Dr Ir.  
University of Liège  
*Professor*

**Pierre DUYSINX**, Pr. Dr Ir.  
University of Liège  
*Full Professor*

**Michel PIROTTON** (supervisor), Pr. Dr Ir.  
University of Liège  
*Full Professor*

**Stéphanie ANDRE**, Dr Ir.  
Ecole Polytechnique Fédérale de Lausanne  
*Lecturer*  
STUCKY Ltd.  
*Head of “Water and Environment” dpt.*

**Pierre ARCHAMBEAU** (co-supervisor), Dr Ir.  
University of Liège  
*Associate Lecturer*

**Cédric GOEURY**, Dr Ir.  
Electricité de France R&D  
*Engineer and Research engineer*

January 2021



*A ma tendre épouse, Elsia.*

*A mon grand-père Félix.*



# Acknowledgement – Remerciements

La rédaction d'une thèse de doctorat est le fruit d'un travail personnel mais intimement lié aux rencontres et interactions humaines qui la jalonnent. Il s'agit d'autant de réunions de travail, de recommandations, de moments de détente et de remises en questions qui font d'une thèse un travail qui dépend de bien plus de personnes que de son auteur seul.

L'accompagnement dans le parcours doctoral passe avant tout par les initiateurs du projet. Je remercie Monsieur le Professeur M. Pirotton pour son accueil au sein de son service, ses conseils et son soutien indéfectible durant plus de six années passées à l'ULiège. C'est au travers de son approche qui favorise la liberté de recherche que j'ai pleinement apprécié l'expérience doctorale.

J'ai eu la chance de pouvoir compter sur un second promoteur. Merci à Monsieur P. Archambeau pour son suivi quotidien, les outils mis en place pour les développements informatiques et son approche toujours pragmatique. Merci aussi pour la confiance et la liberté accordées dans le cadre des développements effectués pour le logiciel WOLF.

Outre le soutien quotidien offert par mes promoteurs, je remercie les Professeurs B. Dewals et L. Duchêne pour leur participation aux comités de thèse annuels et leurs conseils toujours pertinents. Merci aussi à Monsieur S. Erpicum pour les échanges stimulants relatifs aux essais sur modèles physiques réalisés dans le cadre de cette thèse.

Je souhaite également remercier les membres du jury qui ont accepté de lire et juger ce travail. Que Madame S. André, Messieurs les Professeurs F. Nguyen et P. Duysinx et Monsieur C. Goeury trouvent ici la marque de ma gratitude.

Bien qu'individuelle, une thèse se réalise aussi accompagnée par des collègues et des amis. Je tiens particulièrement à te remercier, Martin, pour ces nombreuses années passées à partager le même bureau, à faire des compromis quant au degré d'ouverture de la fenêtre, à moduler ton allure lors des séances de running hebdomadaire, à communiquer ta passion pour le sport, la nature et le dépassement de soi. J'ai, sans aucun doute, appris à ton contact et aussi trouvé un partenaire de travail qui m'a fait avancer. Comme tu l'as si bien écrit, nous sommes arrivés au HECE comme « potes », et je termine aussi ma thèse avec un vrai ami.

Merci aussi à tous les autres collègues avec qui j'ai partagé moments de détente et discussions enrichissantes. Hélène, Renaud, Adrien, Anthony, Margaux, Frédéric, Yann, Xuefang, Diana, Thomas, Mohamad, Ismaïl, Velia, Hamid, Christophe, Joris, Laurence, Max, Greg et Claude trouvez ici l'expression de ma profonde sympathie. Merci à toi, Redha, pour ta précieuse aide

fournie au laboratoire. Merci, Vincent, pour ta bonne humeur et ton sourire, qui m'ont été bien utiles dans la dernière ligne droite. Merci aussi à toi, Maurine, pour ton sourire, les échanges et les discussions tout au long de nos thèses.

Arriver à entreprendre des études de troisième cycle est souvent le fruit d'un contexte familial favorisant. Je souhaite exprimer ici ma profonde gratitude à mes parents de m'avoir offert ce terrain fertile pour l'épanouissement intellectuel et de m'avoir enseigné le goût de l'effort et la persévérance. Vous m'avez offert le soutien et les encouragements nécessaires à chaque étape. Merci aussi à mon frère, ma belle-famille et tous mes amis pour leur compréhension et leur soutien lors des moments les plus difficiles.

On dit souvent qu'on garde le meilleur pour la fin et je ne dérogerai pas à l'adage. Elsia, toi qui partages ma vie « pour le meilleur et pour le pire », tu as sans aucun doute été mon soutien le plus fort tout au long de ce travail. Qui d'autre aurait pu supporter mes doutes à répétition, les soirées et week-ends sacrifiés pour une thèse ? C'est bien plus qu'une oreille attentive dont j'ai pu bénéficier auprès de toi, ce sont des encouragements forts et sans relâche que tu as prodigués. Tu m'as aussi poussé et convaincu d'aller jusqu'au bout. J'y suis donc, au bout, grâce à toi. Comme je l'écrivais au début de ces remerciements, une thèse est bien plus qu'un travail individuel. Tu personnalises à merveille cette, désormais, évidence. Trouve ici ma plus profonde gratitude. Merci !

*Louis Goffin, Janvier 2021*

# Abstract

Modelling numerically natural phenomena like river flows, flows on hydraulic structures or groundwater flows, helps engineers quantifying them in order to organise human activities on the one hand and design mitigation measures on the other hand. These models take, as input data, quantities that are uncertain because of their variability in time and space, and because of our lack of knowledge to represent them accurately. Uncertainty analysis aims at quantifying the impact of these uncertain input data on the outputs of the model.

Several uncertainty analysis methods exist, including the well-known Monte Carlo method (MCM). However, it requires to evaluate the numerical model many times, which is not compatible with computationally expensive 2-D hydrodynamic models for instance. Other uncertainty analysis methods (Point Estimates Method (PEM), Perturbance Moment Method (PMM) and Stochastic Response Surface Method (SRSM)), based on simplifying assumptions, allow to decrease significantly the number of model evaluations. Non-hydraulic simple tests performed with these methods showed that they produce very good results compared to MCM. In order to consider testing and challenging these methods on more computationally expensive examples, a fast and robust 1-D steady shallow water model is developed. It includes an original sliding domain strategy used along with the nonlinear Krylov accelerator. After a validation step on academic tests, this new model showed an excellent scalability behaviour. Compared to CasADi, a state-of-the-art optimization tool, the new model produced better performance results.

This new model allows to apply MCM to a real world 1-D shallow water case. The assessment of the flooding risk of a field located on the banks of the Haine River in Belgium is done through MCM, PEM and PMM. PMM showed in this example to produce an excellent compromise between the computation cost and the accuracy. Moreover, results were very close to the ones produced by MCM.

After this successful hydraulic application for PMM, this method is applied to a 2-D horizontal shallow water flow in the Romanche River in the French Alps. Thanks to an uncertainty analysis approach, this emblematic example studies the sediment transport potential after several dam removals. Results reflect an increased sediment movement potential after dam removal even if the uncertainty analysis highlights a relatively wide confidence interval on the amount of sediments transported.

Over the needs for fast computing models for the application to hydrodynamics, the automatic run of an uncertainty analysis requires also robust models. Groundwater partially saturated models can present convergence issues as reported in the scientific literature. In this thesis, a chapter tries to tackle this problem by proposing a promising method. Homotopy is tested and gives encouraging results in terms of convergence rate.



# Résumé

Modéliser numériquement des phénomènes naturels tels que des écoulements en rivière, sur des structures hydrauliques ou dans les sols, aide l'ingénieur à les quantifier afin d'une part, organiser les activités humaines et d'autre part, dimensionner des mesures protectrices en conséquence. Ces modélisations se basent sur des données d'entrée empreintes d'incertitudes de par leur variabilité temporelle et spatiale, et notre capacité limitée à les représenter. L'analyse d'incertitude a pour objectif de quantifier l'impact de ces éléments sur les résultats en sortie de modèle.

Plusieurs méthodes d'analyse d'incertitudes existent dont la réputée méthode de Monte Carlo (MCM). Elle nécessite cependant d'évaluer de nombreuses fois le modèle numérique, ce qui est peu compatible avec des calculs chers en terme de temps de calcul comme par exemple des calculs hydrodynamiques bi-dimensionnels. D'autres méthodes (méthode d'estimations ponctuelles (PEM), méthode des moments par perturbation (PMM) et méthode de surface de réponse stochastique (SRSM)), basées sur des hypothèses simplificatrices, permettent de réduire drastiquement le nombre d'évaluations. Les tests non-hydrauliques simples menés sur ces méthodes montrent qu'elles produisent de très bons résultats comparativement à la MCM.

Pour envisager de tester ces méthodes sur des cas plus contraignants en terme de temps de calcul, un modèle stationnaire 1-D à surface libre rapide et robuste est développé. Il fait intervenir une méthode originale d'évolution du domaine de calcul couplée à l'utilisation de l'accélérateur non-linéaire de Krylov. En plus d'être validé sur des cas hydrauliques académiques, ce nouveau modèle montre d'excellentes caractéristiques, notamment lorsqu'il est déployé pour un nombre de nœuds croissant. Ses performances sont aussi comparées à CasADi, un outil d'optimisation, vis-à-vis duquel il montre des temps de calcul bien plus faibles.

Ce nouveau modèle permet l'application à un cas réel 1-D d'écoulement à surface libre avec la MCM. L'évaluation du risque d'inondation d'un terrain bordant la Haine en Belgique a été menée à l'aide des MCM, PEM et PMM. La PMM a montré sur cet exemple son excellent rapport coût de calcul/précision, tout en produisant des résultats très proches de ceux obtenus par la MCM.

Suite à cette application prometteuse pour la PMM, elle est appliquée à un cas d'écoulement bi-dimensionnel dans la Romanche dans les Alpes françaises. Cette application emblématique permet d'étudier sous l'angle d'une analyse d'incertitude le potentiel de mise en mouvement de sédiments récemment déposés en amont de barrages à déconstruire. Les résultats reflètent un potentiel de mise en mouvement accru après le retrait du barrage mais emprunts d'une marge d'incertitude relativement élevée.

Outre les besoins de rapidité d'exécution liés aux applications hydrodynamiques, l'application automatique d'une analyse d'incertitudes requiert des modèles d'une robustesse irréprochable.

Les modèles d'écoulements souterrains non saturés peuvent présenter des problèmes de convergence comme cela est largement rapporté dans la littérature scientifique. Cette thèse vise dans son dernier chapitre à proposer des pistes de solution pour résoudre ces problèmes de convergence. A cet effet, la méthode d'homotopie a été largement testée et fournit des résultats encourageants en terme de taux de convergence.

# Table of contents

<b>ACKNOWLEDGEMENT – REMERCIEMENTS .....</b>	<b>I</b>
<b>ABSTRACT .....</b>	<b>III</b>
<b>RÉSUMÉ.....</b>	<b>V</b>
<b>TABLE OF CONTENTS.....</b>	<b>VII</b>
<b>CHAPTER 1: GENERAL INTRODUCTION.....</b>	<b>1</b>
<b>1.1 CONTEXT.....</b>	<b>1</b>
1.1.1 ON THE IMPORTANCE TO CONSIDER UNCERTAINTIES IN HYDRAULICS.....	1
1.1.2 NUMERICAL MODELS FOR HYDRODYNAMICS AND GROUNDWATER FLOWS .....	3
1.1.3 UNCERTAINTIES AND HYDRAULICS .....	4
<b>1.2 OBJECTIVES OF THE THESIS .....</b>	<b>5</b>
<b>1.3 WOLF SOFTWARE .....</b>	<b>6</b>
1.3.1 BACKGROUND .....	6
1.3.2 CONTRIBUTION TO THE DEVELOPMENT OF WOLF.....	7
<b>1.4 STRUCTURE OF THE MANUSCRIPT.....</b>	<b>7</b>
<b>CHAPTER 2: INTRODUCTION TO UNCERTAINTY ANALYSIS .....</b>	<b>9</b>
<b>2.1 INTRODUCTION.....</b>	<b>9</b>
<b>2.2 PROBABILITY AND STATISTICS FUNDAMENTALS.....</b>	<b>11</b>
2.2.1 UNIVARIATE CASES .....	12
2.2.2 MULTIVARIATE CASES.....	13
2.2.3 COMMON FORMS OF PROBABILITY DENSITY FUNCTIONS.....	18
2.2.4 FUNCTIONS OF RANDOM VARIABLES.....	21
<b>2.3 DISCRETE EVALUATIONS FOR UNCERTAINTY ANALYSIS .....</b>	<b>21</b>
2.3.1 MONTE CARLO SIMULATION .....	22
2.3.2 POINT ESTIMATES METHODS .....	24
2.3.2.1 Original Rosenblueth’s method .....	24

2.3.2.2	Improved methods.....	27
2.3.2.3	Summary.....	30
2.3.3	STOCHASTIC RESPONSE SURFACE METHOD .....	31
2.3.4	SUMMARY .....	32
<b>2.4</b>	<b>CHARACTERIZATION OF THE OUTPUT UNCERTAINTY.....</b>	<b>33</b>
2.4.1	TAYLOR SERIES EXPANSION OF STATISTICAL MOMENTS .....	34
2.4.2	POINT ESTIMATES METHOD.....	36
2.4.3	PERTURBANCE MOMENT METHOD.....	37
2.4.3.1	PMM for symmetrical distributions.....	38
2.4.3.2	Extension of PMM to skewed distributions.....	43
2.4.4	STOCHASTIC RESPONSE SURFACE METHOD .....	45
2.4.5	SUMMARY .....	46
<b>2.5</b>	<b>UNCERTAINTY ANALYSIS METHODS COMPARISON.....</b>	<b>46</b>
2.5.1	POLYNOMIAL EXAMPLES .....	47
2.5.2	THE BUNGEE JUMP EXAMPLE .....	56
2.5.3	PRELIMINARY CONCLUSIONS .....	61
<b>2.6</b>	<b>SOURCES OF UNCERTAINTY .....</b>	<b>62</b>
2.6.1	DISCHARGE (HYDROLOGICAL INPUT).....	64
2.6.2	RATING CURVE UNCERTAINTY .....	65
2.6.3	ROUGHNESS COEFFICIENT UNCERTAINTY.....	67
<b>2.7</b>	<b>SOFTWARE ARCHITECTURE.....</b>	<b>69</b>
2.7.1	MULTI-VARIATE SAMPLES IMPLEMENTATION .....	70
2.7.2	SIMULATION LAUNCHER IMPLEMENTATION .....	72
2.7.3	UNCERTAIN RESULTS IMPLEMENTATION .....	73
<b>2.8</b>	<b>CONCLUSION.....</b>	<b>74</b>
 <b>CHAPTER 3: FAST CONVERGENCE OF A STEADY 1-D OPEN-CHANNEL FLOW ..</b>		<b>77</b>
<b>3.1</b>	<b>INTRODUCTION.....</b>	<b>77</b>
<b>3.2</b>	<b>GENERAL 1-D MODEL.....</b>	<b>79</b>
3.2.1	SET OF EQUATIONS .....	79
3.2.2	DISCRETIZATION AND NUMERICAL SCHEME.....	82
<b>3.3</b>	<b>MODIFIED 1-D MODEL FOR FAST WATER PROFILE COMPUTATION.....</b>	<b>84</b>
3.3.1	EQUATION.....	84
3.3.2	ORIGINAL SOLVING STRATEGY .....	86

3.3.2.1	Anderson acceleration .....	86
3.3.2.2	Sliding domain .....	90
3.3.2.3	Combination of solving strategies.....	94
<b>3.4</b>	<b>VALIDATION .....</b>	<b>95</b>
3.4.1	GEOMETRY AND TEST CASES DESCRIPTIONS .....	95
3.4.2	GENERAL SUBCRITICAL FLOW (A).....	96
3.4.3	FLOW WITH A HYDRAULIC JUMP (B) .....	100
3.4.4	SUBCRITICAL TO SUPERCRITICAL FLOW (C).....	104
3.4.5	SUMMARY .....	109
<b>3.5</b>	<b>PARAMETERS OPTIMIZATION AND SPEEDUP EVALUATION.....</b>	<b>109</b>
3.5.1	TEST CASES DESCRIPTION .....	109
3.5.2	RESULTS AND ANALYSIS .....	113
<b>3.6</b>	<b>OPTIMIZED ALGORITHM FOR THE EVOLUTION OF THE DOMAIN SPAN .....</b>	<b>134</b>
3.6.1	ALGORITHM STRUCTURE.....	135
3.6.2	COMPARISON TO THE PREVIOUS ALGORITHM .....	139
3.6.3	SCALABILITY TESTS .....	142
<b>3.7</b>	<b>COMPARISON OF OUR OPTIMIZED ALGORITHM AGAINST CASADI .....</b>	<b>145</b>
3.7.1	CASADI: FEATURES AND LIMITATIONS .....	145
3.7.2	IMPLEMENTATION FOR CASADI.....	146
3.7.3	VALIDATION OF CASADI.....	148
3.7.3.1	Case study description: a flow in a tunnel spillway .....	148
3.7.3.2	Measurements on the physical model .....	153
3.7.3.3	Comparison between numerical and physical results .....	155
3.7.4	CASADI VS. OUR OPTIMIZED ALGORITHM.....	157
3.7.4.1	Test description .....	157
3.7.4.2	Performances comparison .....	158
<b>3.8</b>	<b>CONCLUSION.....</b>	<b>159</b>

## CHAPTER 4: UNCERTAINTY ANALYSIS APPLIED TO 1-D HYDRAULIC MODELS

161

<b>4.1</b>	<b>INTRODUCTION.....</b>	<b>161</b>
<b>4.2</b>	<b>FIRST HYDRAULIC APPLICATION TO A FLOW OVER A BUMP .....</b>	<b>162</b>
4.2.1	CASE STUDY DESCRIPTION .....	162
4.2.2	RESULTS AND DISCUSSION .....	166

4.2.2.1	General considerations about computation feasibility.....	166
4.2.2.2	Tests A: avoiding flow regime changes as much as possible.....	167
4.2.2.3	Tests B: effect of hydraulic discontinuities .....	173
4.2.2.4	Summary.....	181
<b>4.3</b>	<b>SECOND HYDRAULIC APPLICATION TO A REAL WORLD EXAMPLE .....</b>	<b>181</b>
4.3.1	CASE STUDY DESCRIPTION .....	181
4.3.2	UNCERTAINTY SOURCES.....	195
4.3.2.1	Uncertainty on the upstream discharge.....	195
4.3.2.2	Uncertainty on the downstream rating curve .....	196
4.3.3	RESULTS AND DISCUSSION .....	201
<b>4.4</b>	<b>CONCLUSION.....</b>	<b>210</b>

**CHAPTER 5: UNCERTAINTY ANALYSIS APPLIED TO 2-D HYDRAULIC SIMULATIONS ..... 211**

<b>5.1</b>	<b>INTRODUCTION.....</b>	<b>211</b>
5.1.1	2-D HYDRODYNAMIC MODELLING .....	211
5.1.2	WOLF 2-D MODEL.....	211
5.1.3	A 2-D APPLICATION .....	213
<b>5.2</b>	<b>CASE STUDY DESCRIPTION.....</b>	<b>214</b>
<b>5.3</b>	<b>RIVERBED STABILITY.....</b>	<b>221</b>
<b>5.4</b>	<b>UNCERTAINTY SOURCES .....</b>	<b>225</b>
<b>5.5</b>	<b>RESULTS AND DISCUSSION .....</b>	<b>228</b>
5.5.1	HYDRAULIC RESULTS .....	228
5.5.2	INDICATOR ON THE RIVER BED STABILITY.....	239
<b>5.6</b>	<b>CONCLUSION.....</b>	<b>251</b>

**CHAPTER 6: INVESTIGATIONS FOR BETTER CONVERGENCE OF THE 1-D RICHARDS EQUATION..... 253**

<b>6.1</b>	<b>INTRODUCTION.....</b>	<b>253</b>
<b>6.2</b>	<b>RICHARDS EQUATION .....</b>	<b>254</b>
6.2.1	CONSERVATION EQUATIONS .....	254
6.2.2	CONSTITUTIVE SOIL LAWS.....	255
<b>6.3</b>	<b>NUMERICAL MODEL .....</b>	<b>264</b>

6.3.1	DISCRETIZED EQUATIONS .....	264
6.3.2	BOUNDARY CONDITIONS.....	265
6.3.3	HYDRAULIC CONDUCTIVITY AT THE BORDERS.....	265
6.3.4	ITERATIVE SOLVING .....	266
6.3.4.1	Matrix formulation.....	266
6.3.4.2	Modified Picard iteration scheme .....	267
6.3.4.3	Anderson accelerator.....	268
6.3.4.4	Evolution limiter .....	268
6.3.4.5	Other techniques facilitating convergence.....	269
<b>6.4</b>	<b>VALIDATION .....</b>	<b>270</b>
<b>6.5</b>	<b>SCENARIOS .....</b>	<b>274</b>
6.5.1	DESCRIPTION OF THE SCENARIOS.....	274
6.5.2	CONVERGENCE SUCCESS WITH THE VAN GENUCHTEN – MUALEM LAW.....	280
<b>6.6</b>	<b>HOMOTOPY TO IMPROVE THE CONVERGENCE .....</b>	<b>284</b>
6.6.1	INTRODUCTION TO HOMOTOPY .....	284
6.6.2	HOMOTOPY APPLIED TO THE SOIL LAW.....	284
6.6.3	HOMOTOPY METHOD APPLIED TO SCENARIOS .....	286
<b>6.7</b>	<b>CONCLUSIONS AND PERSPECTIVES .....</b>	<b>290</b>
 <b>CHAPTER 7: GENERAL CONCLUSIONS.....</b>		<b>291</b>
 <b>7.1 CONTRIBUTIONS.....</b>		<b>291</b>
<b>7.2 PERSPECTIVES .....</b>		<b>293</b>
 <b>BIBLIOGRAPHY .....</b>		<b>297</b>
 <b>APPENDICES .....</b>		<b>311</b>
 <b>A UNCERTAINTY ANALYSIS APPENDIX .....</b>		<b>311</b>
 <b>A.1 COSKEWNESS AND COKURTOSIS FOR NORMALLY DISTRIBUTED AND INDEPENDENT RANDOM VARIABLES .....</b>		<b>311</b>
<b>A.2 MATHEMATICAL DEVELOPMENTS OF TAYLOR SERIES EXPANSION OF STATISTICAL MOMENTS .....</b>		<b>312</b>

<b>A.3</b>	<b>COMPARISON OF FRANCESCHINI’S APPROACH TO THE GENERALIZED BOLLE’S APPROACH.....</b>	<b>318</b>
<b>A.4</b>	<b>PROPOSAL FOR THE EXTENSION OF SRSM TO SKEWED DISTRIBUTIONS .....</b>	<b>319</b>
<b>B</b>	<b>FAST 1-D CONVERGENCE OF A 1-D STEADY FLOW.....</b>	<b>322</b>
<b>B.1</b>	<b>BOXPLOTS FOR PARAMETERS OPTIMIZATION TESTS 3 AND 4.....</b>	<b>322</b>
<b>C</b>	<b>2-D UNCERTAINTY ANALYSIS APPENDIX.....</b>	<b>326</b>
<b>C.1</b>	<b>FULL VIEW OF THE EXTRACTION VECTOR .....</b>	<b>326</b>
<b>C.2</b>	<b>SUPPLEMENTARY MAPS FOR HYDRAULIC VARIABLES .....</b>	<b>327</b>
<b>C.3</b>	<b>SUPPLEMENTARY MAPS FOR UNCERTAINTY CHARACTERIZATION .....</b>	<b>333</b>
<b>D</b>	<b>POROUS MEDIA FLOW APPENDIX.....</b>	<b>334</b>
<b>D.1</b>	<b>LINEAR SOIL LAW.....</b>	<b>334</b>
<b>D.2</b>	<b>INFLUENCE OF THE SPATIAL AND TIME STEPS ON THE VALIDATION TEST .....</b>	<b>339</b>
<b>D.3</b>	<b>MOST FAVORABLE PARAMETERS FOR CONVERGENCE .....</b>	<b>342</b>

# Chapter 1: General introduction

## 1.1 Context

### 1.1.1 On the importance to consider uncertainties in hydraulics

Nowadays, engineers everyday work relies heavily on numerical models. These models help them to design, check and optimize solutions to be implemented in real life conditions. Models are views of reality expressed thanks to mathematical equations. In order to solve these equations, numerical methods and algorithms are deployed on computers. Increasing computing power allows to decrease the overall computation time or to refine meshes and keep a steady computation time. These technological advances open new prospects. Even if equally defined problems can be solved faster today, we should still design very efficient algorithms to take full advantages of increasing computation power.

This increasing computational power can lead to advances in environmental engineering. In this area, and hydraulics in particular, practitioners and scientists deal with natural elements. Field survey campaigns (e.g. Figure 1 and Figure 2), gauging stations (e.g. Figure 3), etc. intend to improve our knowledge of these natural sites and events. Nevertheless, our knowledge is still limited and natural sites and events are fluctuating (Merz & Thielen 2005; Domeneghetti et al. 2013; Apel et al. 2004) (e.g. a river bed can change after a flood or depending on the sediment supply (Goffin et al. 2018)). Engineers and scientists are also aware that their knowledge of natural events is limited and the evaluation of some quantities (e.g. peak discharge for a given return period, roughness coefficient, etc.) is prone to errors. These are sources of uncertainty for the modelers. Being aware of this, one may ask how to quantify the impact of these uncertainties on the final result of a hydraulic model taking advantage of the increasing computational power.

Uncertainties on the output of a model can be evaluated thanks to a so-called uncertainty analysis. As developed further, several uncertainty analysis methods exist. Some require a model to be evaluated more than a thousand times (Metropolis & Ulam 1949) while others limit the number of evaluations to only a few points (Rosenblueth 1975; Bolle 1988; Harr 1989; Hong 1996). Since the evaluation of a complete hydraulic model can be long, the use of algorithms for solving quickly hydraulic problems is of main interest.

In order to target uncertainties to consider, a global sensitivity analysis (Saltelli et al. 2008) can be performed prior to an uncertainty analysis. A global sensitivity analysis quantifies how much an uncertain input influences the output compared to other uncertainty sources. This

*General introduction*

thesis is focused on uncertainty analysis even if a sensitivity analysis can be a prerequisite in some cases.



*Figure 1: Cross section measurement (source: [www.nuterinc.com](http://www.nuterinc.com))*



*Figure 2: Velocity measurement using ADCP (source: Tim Merrick, USGS)*



Figure 3: Brant Broughton gauging station (source: wikimedia commons)

### 1.1.2 Numerical models for hydrodynamics and groundwater flows

The evaluation of uncertainties is closely linked to the use of numerical models. In this thesis, two areas of hydraulics are investigated: hydrodynamics and groundwater flows.

In the hydrodynamic area, and more specifically open channel flow computation, a series of models and meshes exist. 1-D models are used when a main direction is imposed to the flow. For instance, this is the case of channelized flows (Goffin, Dewals, et al. 2016). When the flooding of a plain occurs and that the flow patterns in the flooded area affect the entire flow, one may use a 2-D horizontal model (Horritt & Bates 2002; Wilson et al. 2007). When more complex flow patterns exist, the use of 3-D model can bring much more details and precision (Teng et al. 2017). Usually, when the use of a 1-D model is licit, it leads to a computation time much lower for a given spatial step than 2-D or 3-D models. Having a low computation time can be useful for various purposes, including uncertainty analysis and real-time control of river facilities (Schwanenberg et al. 2015).

In environmental engineering, one of the subjects of major interest is hydrology. Currently, most models are based on conceptual laws which are not linked to physical equation but rather stick to observations (Tran et al. 2018). Besides conceptual models, physically based models exist (Paulus et al. 2013). They use physical equations to reproduce flows in streams and rivers, the water exchange between surface and ground waters and underground flows. Vertical 1-D soil columns are used to convey water from the surface to the fully saturated zone and vice versa. These elements might present convergence issues and will be a focus of this thesis.

These two families of models in hydraulics are used as computation bases for the uncertainty approaches that are developed in this thesis.

### **1.1.3 Uncertainties and hydraulics**

In hydraulics, uncertainty analysis can be applied to various areas: river hydraulics (Teng et al. 2017; Bessar et al. 2020), sewage systems (Van Bijnen et al. 2012), groundwater flows (Refsgaard et al. 2012), etc. In order to approach uncertainty analysis with physically based hydraulic models, since they are computationally more expensive than conceptual models, two strategies can be adopted:

1. Design efficient and fast algorithms to use them in uncertainty analysis that require a large number of runs. One possibility is to rely on material acceleration, such as GPU cards (Brodtkorb et al. 2012). The other possibility is to rethink the way a hydraulic model is solved in order to decrease the time required for solving a problem.
2. Use uncertainty analysis methods that require less model evaluations. This allows the use of standard hydraulic models that can be computationally expensive in practical situations. These uncertainty analysis methods should first prove their accuracy when applied to hydraulic models.

Since uncertainty analysis methods run models with several parameters, a common prerequisite is to ensure a reliable computation independently from the choice of the parameters. This is particularly important for groundwater flow models which might present convergence issues (Farthing & Ogden 2017).

The application of uncertainty analysis in the domains of hydrology, hydrodynamics or groundwater flows is addressed in the literature in several studies with various approaches, including approaches that rely on less model evaluations. For instance, Altarejos Garcia et al. (2012) apply uncertainty analysis to 1-D and 2-D shallow water models using two different approaches and compare them. Bessar et al. (2020) makes also use of uncertainty analysis for hydrodynamic modeling with adaptative roughness coefficients. In hydrology, Franceschini, Marani, et al. (2012) apply an uncertainty analysis method that requires less model evaluations to a conceptual hydrological model. For partially saturated groundwater flows, estimating the output uncertainty is currently difficult due to convergence issues that might be encountered.

The wish of this thesis is to contribute to the extensive use of uncertainty analysis in the hydraulic domain. More precisely, given the lack of experience in using uncertainty methods with less model evaluations for physically-based hydrodynamic and hydrologic modelling, this thesis goal is to bridge this gap.

## **1.2 Objectives of the thesis**

Several challenges and two strategies were identified in section 1.1 linked to uncertainty analysis in hydraulics. The main objective of this thesis is to apply efficiently uncertainty analysis to 1-D and 2-D shallow water models as well as to pave the way to a reliable application of uncertainty analysis to groundwater unsaturated flows.

To do so, as suggested in section 1.1, several strategies can be adopted. One of these consists in relying on uncertainty analysis methods that require less model evaluations. The first objective of the thesis is to review the methods available for uncertainty analysis, including methods designed to decrease the number of model evaluations.

Since hydrodynamic models are nonlinear and can present flow discontinuities, it should be evaluated if the application of uncertainty analysis methods that rely on less model evaluations is relevant compared to methods that use much more evaluation points. To do so, a comparison between analysis methods is needed. Since hydrodynamic models can be computationally expensive, the second objective of this thesis is to develop a 1-D steady state shallow water model able to return a solution in a very short amount of time, shorter than standard 1-D shallow water models.

This new algorithm should be challenged against other solving methods to prove its efficiency. To do so, we chose to develop an innovative solving technique. It relies on CasADi, a toolbox designed for optimization purposes (Andersson et al. 2018). The strategy used to take advantage of the computation core of CasADi is to impose objectives and constraints as the discretized form of steady-state shallow water equations at each node of the discretized domain.

Thanks to the newly developed 1-D steady state shallow water model, we will be able to assess the validity of some uncertainty analysis methods against others in the frame of hydrodynamic modeling. Moreover, a fast solving steady state 1-D model is useful in other areas. For instance, this kind of model can be valuable for the computation of a steady state initial condition or for optimization problems. In order to demonstrate the applicability of this new 1-D model for uncertainty analysis, both academic and real-world cases should be tested.

Based on the knowledge acquired with previous objectives, uncertainty analysis is applied to a real-world 2-D example. The objective of this application is to demonstrate the ability of an uncertainty analysis method that requires less evaluation points to provide useful information to guide decision makers.

The final objective of this thesis is to pave the way to effective uncertainty analysis for unsaturated groundwater flow models. As introduced earlier, convergence issues are observed in some cases when this kind of numerical model is solved. The goal of the final part is to investigate techniques that might improve the convergence stability.

## **1.3 WOLF software**

### **1.3.1 Background**

The WOLF software has been developed in the HECE research group (University of Liège) since more than 20 years. Many PhD theses built the code as it is known today (Dewals 2006; Archambeau 2006; Bruwier 2017; Erpicum 2006). Thanks to this software, researchers from HECE published many research papers (Erpicum, Dewals, Archambeau & Piroton 2010; Kerger et al. 2011; Erpicum, Dewals, Archambeau, Detrembleur, et al. 2010; Bruwier et al. 2018; Paulus et al. 2013). Moreover, WOLF supported the realization of industrial projects and laboratory experiments. Less than 10 years ago, WOLF was rewritten in modern Fortran (Fortran 2008 while the first version was written in FORTRAN 95). Modern language formalism is also used for optimal readability and efficiency. Indeed, an object-oriented approach is adopted and OpenMP is used in many parts of the code to parallelize loops.

WOLF includes several hydraulic and hydrological models. The main modules are listed hereunder:

- WOLF HYDRO for hydrological modelling,
- WOLF 1D for the computation of networks of channels,
- WOLF 2D for quasi 3-D hydraulic modelling and,

A more complete view of the components of WOLF is given in Figure 4. Moreover, WOLF includes several tools for the pre-processing and post-processing of the simulations.

The 1-D model is able to initialize from different types of data. The cross-sections tabular relations can either be an input of the model or they can be generated by WOLF itself from 2-D Digital Elevation Models (DEM). The software solves Saint-Venant equations thanks to a finite volume spatial discretization and an explicit time scheme.

The 2-D model solves the two-dimensional shallow water equations. They are discretized according to a finite volume spatial scheme and an explicit time scheme. This model is able to deal with raster and vector data. Several add-ons are available. They include a turbulence model and a porosity model.

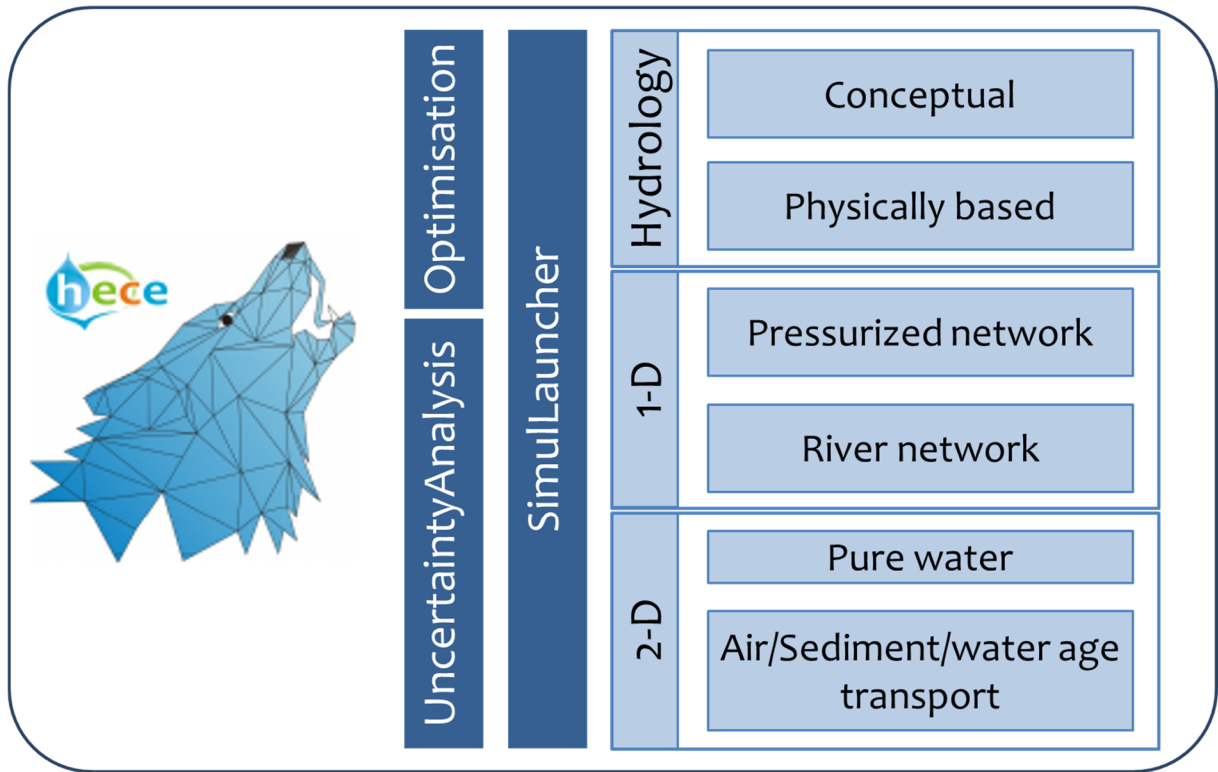


Figure 4: Structure of the WOLF software including the developed modules

### 1.3.2 Contribution to the development of WOLF

In order to reach the objectives of the thesis, several developments were added to the WOLF suite by the author of this thesis. These improvements include, amongst others:

- The development of an add-on to the 1-D model in order to solve quickly steady state solutions
- The development of a module able to launch several simulations in parallel
- The development of an uncertainty analysis module able to make use of the previous module and to compute uncertainty indicators
- The development of an optimization module able to find optimal parameters thanks to a systematic scan or simulated annealing (Kirkpatrick et al. 1983)
- The development of convergence techniques for unsaturated underground flows

## 1.4 Structure of the manuscript

In order to achieve the objectives cited in section 1.2, the thesis is divided in several chapters. First, the fundamentals of uncertainty analysis are introduced in chapter 2. In this chapter, we recall some useful probability and statistics bases, present several uncertainty analysis methods, compare them on a theoretical point of view and on academic tests, introduce some uncertainty sources and present the architecture of the software created specifically for this thesis.

In chapter 3, the development of a fast-solving algorithm for steady 1-D open channel flows is presented. This new model is validated and compared against an implementation that takes advantage of CasADi. The “CasADi implementation” is validated thanks to a comparison with a practical test performed in HECE laboratory.

Chapters 4 and 5 present original practical applications for uncertainty analysis. Chapter 4 uses the 1-D model developed in chapter 3 and chapter 5 deals with 2-D simulations. More than just testing hydraulic models and uncertainty analysis methods, these two chapters bring a fresh insight on practical applications that engineers can meet in their everyday practice.

The last content chapter (chapter 6) deals with the 1-D vertical unsaturated soil column model. First, the equations and constitutive laws are introduced in order to highlight high nonlinearity characteristics of this kind of problem. The numerical model as well as additional techniques to favorize convergence are presented. Convergence issues are identified and a novel method to facilitate convergence is presented and tested.

Finally, a summary of the thesis, main outcomes and perspectives are given in chapter 7.

# Chapter 2: Introduction to uncertainty analysis

## 2.1 Introduction

Water flow in rivers and streams is a natural process which is influenced by many parameters. They can be either natural or human. Concerning natural influences, we can cite hydrologic inputs (e.g. rain falls and snow melts) and the natural state of the channel (vegetation growth (e.g. Figure 5) and sediment deposition and supply (e.g. Figure 6) can influence flow patterns and resistance to the flow). On the human side, many rivers dispose of anthropogenic structures such as dams and weirs. The way humans use these structures influence, the discharge and water levels of the rivers and streams. These natural and anthropogenic inputs influence the values taken by the parameters of a numerical model (e.g. roughness coefficient, upstream hydrograph, digital elevation model (DEM), etc.). Even if empirical approaches and measurement techniques exist to estimate these parameters, their exact values are only known with some level of confidence.



*Figure 5: Growth of the vegetation on the banks of the Haine River (Belgium) can be seasonal*



*Figure 6: The “cône de l’Infernet” provides sediments to the river Romanche in the French Alps (aerial view). The supply quantity and period depend on the winter season. This heavy sediment supply is prone to induce changes to the river morphology.*

Other uncertainties affect hydraulic modelling. Besides the hydraulic model itself, our knowledge is limited and we can introduce errors due to our poor ability to represent phenomenon (e.g. rating curves) or measure physical quantities correctly (water levels and/or discharges can be badly measured in natural environments) (Merz & Thielen 2005). Taking all this into consideration, it appears logical that the output of a hydraulic study cannot be reasonably considered as absolute. In order to quantify the uncertainty on the final result, uncertainty analysis can be performed (Apel et al. 2004).

Since hydraulic computations may require some time to run<sup>1</sup>, the uncertainty analysis methods used should consider this point. This is why a traditional Monte Carlo simulation method

---

<sup>1</sup> Depending on the type of model, the spatial discretization, the total duration and the computers used, the computation time can reach up to several days.

(Metropolis & Ulam 1949), which requires more than a thousand runs, is not suited for many practical hydraulic cases. In order to assess the uncertainty of the output of model, different techniques can be used, including the Monte Carlo simulation (MCS) method<sup>2</sup>, point estimate methods (PEM, (Rosenblueth 1975)), the perturbation moment method (PMM, (Bolle 1988; Franceschini, Marani, et al. 2012)) and the stochastic response surface method (SRSM, (Isukapalli et al. 1998)). This chapter will focus on techniques included in these four groups. For the sake of conciseness, other existing methods will not be investigated in this chapter. These techniques will be introduced and compared. First, this will be done in a general framework. In following chapters, some of these techniques will be applied to hydraulic specific cases.

In the following sections, methods will be presented first with only one random variable then with several random variables (multivariate problems). Random variables  $X_j, j = 1, \dots, N$ ,  $N$  being the number of random variables, are the parameters of the problem which are known with some degree of uncertainty.  $x_j$  is a particular value of  $X_j$ .

First, some probability, statistics and stochastics fundamentals useful for this chapter are recalled to the reader. Then, these principles are used to introduce different methods that can be used for sampling uncertain variables. When these samples are used in a model<sup>3</sup>, some output are generated. The third part of this chapter introduces several techniques to characterize the uncertainty on the output values. A comparison of the methods is then made on simple, non-hydraulic cases. Before applying uncertainty analysis to hydraulic cases, a literature review of possible uncertainty sources is made. The architecture of our software is finally described.

## **2.2 Probability and statistics fundamentals**

In this section, we introduce some fundamentals of probability, statistics and stochastics. These basic notions will be useful later in order to understand the developments and limits of uncertainty analysis methods.

In the theory of probability, three fundamental axioms (also known as Kolmogorov axioms) can be stated:

---

<sup>2</sup> This method is indifferently referred as the Monte Carlo simulation method and the Monte Carlo method in this thesis.

<sup>3</sup> At this point, the term “model” refers to any kind of “black box” that returns an output for a given input.

1. The probability of an event  $A$  is a real number ranging from 0 to 1:

$$0 \leq P(A) \leq 1, P(A) \in \mathbb{R} \quad (1)$$

2. The probability that at least one event from the space  $\Omega$  occurs is 1:

$$P(\Omega) = 1 \quad (2)$$

3. The probability of a disjoint events sequence  $A_1, A_2, \dots, A_n$  is the sum of the probability of each event:

$$P(A_1 \cup A_2 \cup \dots \cup A_n) = \sum_{i=1}^n P(A_i) \quad (3)$$

Another rule that will be useful later in this work is the one that states that the probability of occurrence of several independent events is the product of the probabilities of each event:

$$P(A_1 \cap A_2 \cap \dots \cap A_n) = \prod_{i=1}^n P(A_i) \quad (4)$$

Two events are independent if the occurrence of a first event does not affect the probability of occurrence of the second one. Two events are disjoint if they cannot occur at the same time. These two notions are different.

### 2.2.1 Univariate cases

The occurrence probability of a random variable  $X$  is defined by a probability density function (pdf)  $p_X$ . The  $i$ -th statistical moment of  $X$  is defined as:

$$E[X^i] = \int_{-\infty}^{+\infty} x^i p_X(x) dx \quad (5)$$

where  $x$  is a particular value taken from  $X$ .

$E[X^0]$  is always 1 since it defines the area under  $p_X$ .  $E[X^1] = \bar{X}$  is known as the mean or the expectation of  $X$ . Higher order moments ( $i \geq 2$ ) are commonly defined as centered around the mean:

$$\begin{aligned} E[d^i] &= \int_{-\infty}^{+\infty} d^i p_X(x) dx \\ &= \int_{-\infty}^{+\infty} (x - \bar{X})^i p_X(x) dx \end{aligned} \quad (6)$$

$E[d^2] = E[(X - \bar{X})^2] = \sigma_X^2 = \sigma_{XX} = Var[X]$  is the variance of  $X$ ,  $\sigma_X$  is the standard deviation.

The variance expresses the dispersion of the pdf. Other higher order moments ( $i \geq 3$ ) are

usually normalized by an exponent of the standard deviation. The  $i$ -th normalized moment is expressed as:

$$\frac{E[d^i]}{\sigma_X^i} \quad (7)$$

The skewness is the third ( $i = 3$ ) normalized centered moment and is denoted  $\gamma_X$ . When  $\gamma_X < 0$ , the distribution is skewed to the left, when  $\gamma_X > 0$ , the distribution is skewed to the right and it is symmetric when  $\gamma_X = 0$ . The fourth normalized centered moment ( $i = 4$ ) is the image of the heaviness of the tail of the distribution. Since it is an even order moment, the value is  $\geq 0$ . Higher values of this normalized moment depicts heavy tails. The kurtosis  $\kappa_X$  is defined as:

$$\kappa_X = \frac{E[d^4]}{\sigma_X^4} \quad (8)$$

$\kappa_X = 3$  for a normal distribution.

## 2.2.2 Multivariate cases

Since several sources of uncertainty can affect hydraulic simulations, multivariate cases should be considered and additional notions should be introduced. If we consider a problem with  $N > 1$  random variables  $X_i, i = 1, \dots, N$ , which can also be denoted as a  $N \times 1$  vector  $\mathbf{X}$ , the **joint probability density function**  $p_{\mathbf{X}}$  describes the probability to fall in some point of the random variables space. If integrated over the space of random variables, we obtain one, according to the second probability axiom:

$$\int_{-\infty}^{+\infty} \dots \int_{-\infty}^{+\infty} p_{\mathbf{X}}(x_1, \dots, x_N) dx_1 \dots dx_N = 1 \quad (9)$$

If we look at each random variable separately, we can define the marginal probability density function  $p_{X_i}$  for the random variable  $X_i$  as the integral of the joint probability over random variables  $X_j, j \neq i$ . For three random variables  $X_1, X_2, X_3$ , the **marginal probability density function** of  $X_1$  is:

$$p_{X_1}(x_1) = \int_{-\infty}^{+\infty} \int_{-\infty}^{+\infty} p_{X_1 X_2 X_3}(x_1, x_2, x_3) dx_2 dx_3 \quad (10)$$

Using equations (9) and (10), we can show that the integral of the marginal density function  $p_{X_i}$  gives also one:

$$\int_{-\infty}^{+\infty} p_{X_i}(x_i) dx_i = \int_{-\infty}^{+\infty} \int_{-\infty}^{+\infty} \cdots \int_{-\infty}^{+\infty} p_{X_1 X_2 \cdots X_N}(x_1, x_2, \cdots, x_N) dx_1 dx_2 \cdots dx_N = 1 \quad (11)$$

The moments introduced in the previous section can be defined for each random variable independently. In other words, vectors of  $N$  elements can be introduced to define the mean, the variance, the skewness and the kurtosis of each random variable. For a bivariate case with variables  $X_1$  and  $X_2$ , these vectors are:

$$\bar{\mathbf{X}} = \begin{pmatrix} \bar{X}_1 \\ \bar{X}_2 \end{pmatrix}; \sigma_{\mathbf{XX}} = \begin{pmatrix} \sigma_{X_1}^2 \\ \sigma_{X_2}^2 \end{pmatrix}; \gamma_{\mathbf{X}} = \begin{pmatrix} \gamma_{X_1} \\ \gamma_{X_2} \end{pmatrix}; \kappa_{\mathbf{X}} = \begin{pmatrix} \kappa_{X_1} \\ \kappa_{X_2} \end{pmatrix} \quad (12)$$

However, for the variance, it is not the most common notation. The covariance can be defined between two random variables:

$$\sigma_{X_i X_j} = \int_{-\infty}^{+\infty} \cdots \int_{-\infty}^{+\infty} (x_i - \bar{X}_i)(x_j - \bar{X}_j) p_{\mathbf{X}}(\mathbf{x}) dx_1 \cdots dx_N \quad (13)$$

For a  $N$  random variable problem, a covariance matrix can be defined in place of the vector introduced in (12). Each element  $i, j$  of the matrix is the covariance  $\sigma_{X_i X_j}$ . This means that the elements on the diagonal are the variances and the matrix is symmetric since  $\sigma_{X_i X_j} = \sigma_{X_j X_i}$ .

An example is given for  $N = 3$  :

$$\Sigma = \begin{pmatrix} \sigma_{X_1 X_1} & \sigma_{X_1 X_2} & \sigma_{X_1 X_3} \\ \sigma_{X_1 X_2} & \sigma_{X_2 X_2} & \sigma_{X_2 X_3} \\ \sigma_{X_1 X_3} & \sigma_{X_2 X_3} & \sigma_{X_3 X_3} \end{pmatrix} = \begin{pmatrix} \sigma_{X_1}^2 & \sigma_{X_1 X_2} & \sigma_{X_1 X_3} \\ \sigma_{X_1 X_2} & \sigma_{X_2}^2 & \sigma_{X_2 X_3} \\ \sigma_{X_1 X_3} & \sigma_{X_2 X_3} & \sigma_{X_3}^2 \end{pmatrix} \quad (14)$$

The correlation coefficient  $\rho_{X_i X_j}$  between two random variables,  $X_i$  and  $X_j$ , is defined as:

$$\rho_{X_i X_j} = \frac{\sigma_{X_i X_j}}{\sigma_{X_i} \sigma_{X_j}} \quad (15)$$

It ranges between  $-1$  et  $+1$ . Uncorrelated variables are categorized by  $\rho_{X_i X_j} = 0$  while points drawn from variables that align along a positive, respectively negative, slope show a correlated behavior with  $\rho_{X_i X_j} = 1$ , respectively  $\rho_{X_i X_j} = -1$ . This concept can be understood through the observation of Figure 7. On the left, the positions of discrete points lead to the equality

$$(x_1 - \bar{X}_1) = \alpha(x_2 - \bar{X}_2) \quad (16)$$

which is only possible when a unique linear relationship exists between  $X_1$  and  $X_2$ . When equation (15) is developed considering (16) and  $\alpha \neq 0$ , one gets:

$$\begin{aligned}
 \rho_{X_1, X_2} &= \frac{\int_{-\infty}^{+\infty} \int_{-\infty}^{+\infty} (x_1 - \bar{X}_1)(x_2 - \bar{X}_2) p_{\mathbf{X}}(\mathbf{x}) dx_1 dx_2}{\sqrt{\int_{-\infty}^{+\infty} \int_{-\infty}^{+\infty} (x_1 - \bar{X}_1)^2 p_{\mathbf{X}}(\mathbf{x}) dx_1 dx_2} \sqrt{\int_{-\infty}^{+\infty} \int_{-\infty}^{+\infty} (x_2 - \bar{X}_2)^2 p_{\mathbf{X}}(\mathbf{x}) dx_1 dx_2}} \\
 &= \frac{|\alpha| \int_{-\infty}^{+\infty} \int_{-\infty}^{+\infty} (x_1 - \bar{X}_1)^2 p_{\mathbf{X}}(\mathbf{x}) dx_1 dx_2}{\alpha \int_{-\infty}^{+\infty} \int_{-\infty}^{+\infty} (x_1 - \bar{X}_1)^2 p_{\mathbf{X}}(\mathbf{x}) dx_1 dx_2} = \frac{|\alpha|}{\alpha} = \text{sign}(\alpha)
 \end{aligned} \tag{17}$$

It appears that random variables linearly dependent lead to  $\rho_{X_i, X_j} = \pm 1$ , where the sign depends on the slope of the linear correlation. These variables are referred as correlated. Correlation corresponds to a linear dependency between variables. Random variables are uncorrelated ( $\rho_{X_i, X_j} = 0$ ) if the covariance  $\sigma_{X_i, X_j} = 0$ . This condition is met

- when random variables are aligned along a horizontal or vertical line (Modelling numerically or  $x_1 = \bar{X}_1$ ) or,
- when the integral of the product  $(x_1 - \bar{X}_1)(x_2 - \bar{X}_2) p_{\mathbf{X}}(\mathbf{x})$  gives 0.

Independent variables meet the latter condition. Indeed, in a discrete vision, independent variables are visualized as randomly scattered points (Figure 8 left). The reciprocal which would state that dependent variables are not uncorrelated ( $\rho_{X_i, X_j} \neq 0$ ) is not true. Indeed, the example displayed on the right hand side of Figure 8 shows an obvious sine dependence between variables. However, the application of (15) would return 0.

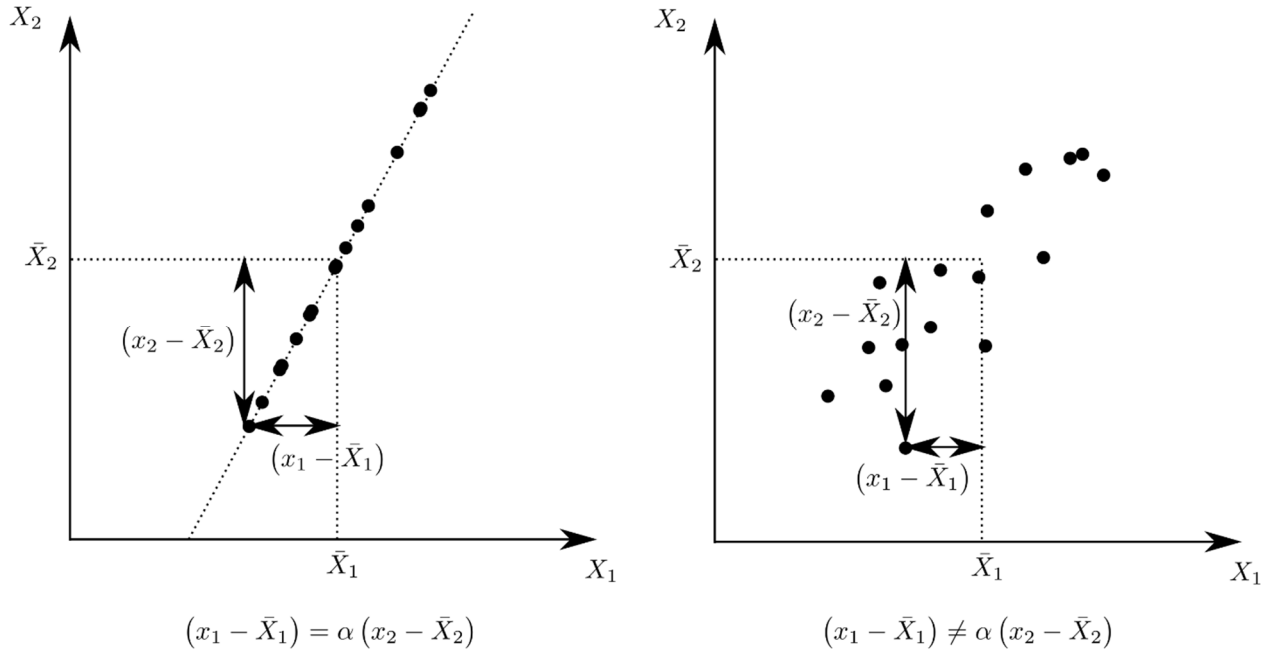


Figure 7: Illustration of the correlation concept with discrete values

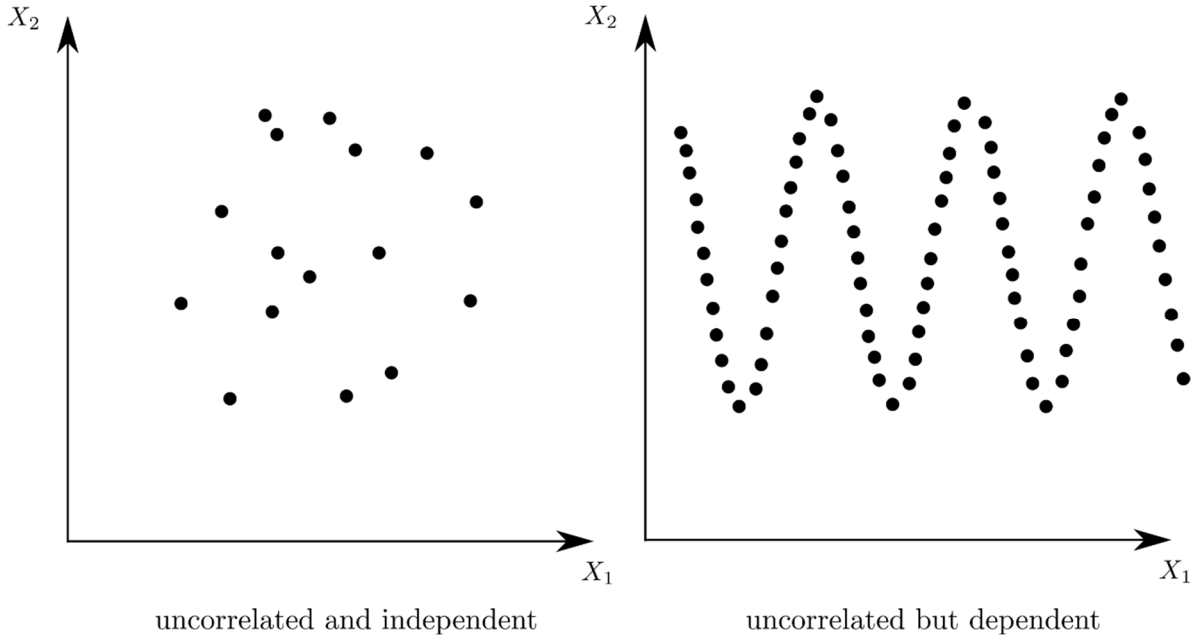


Figure 8: Correlation and independence

The correlation introduced hereabove, known as the Pearson correlation coefficient (Pearson 1895), depicts the linear dependency between two random variables. Another well-known correlation coefficient is the Spearman's correlation coefficient (Spearman 1904). It depicts how well two random variables can be linked by a monotonic function (which can be nonlinear). To the author knowledge, no correlation coefficient exists to depict the cyclic or non-monotonic dependence between two random variables.

Relying on rule (4), when variables are all independent, the joint probability density function is the product of the marginal probability density functions:

$$p_{\mathbf{x}}(x_1, \dots, x_N) = \prod_{i=1}^N p_{X_i}(x_i) \quad (18)$$

Correlated random variables can be uncorrelated through a principal components analysis. This method is exposed in (Bolle 1988). The method's steps are the following:

1. Random variables are centered around the mean and normalized by the standard deviation:

$$T_i = \frac{X_i - \bar{X}_i}{\sigma_{X_i}} \quad (19)$$

2. Uncorrelated variables are obtained by a rotation of  $45^\circ$  of these new centered and normalized  $T_i$  axes. Indeed, since axes are standardized, any correlation should appear along a  $45^\circ$  line. In two dimensions, this can be written in the following matrix form:

$$\begin{pmatrix} U_1 \\ U_2 \end{pmatrix} = \frac{1}{\sqrt{2}} \begin{pmatrix} 1 & 1 \\ -1 & 1 \end{pmatrix} \begin{pmatrix} T_1 \\ T_2 \end{pmatrix} \quad (20)$$

Finding the eigenvectors of the covariance matrix of  $\mathbf{X}$  and using them as a new referential is equivalent to previous method. This approach is further detailed in (Harr 1989). The eigenvectors of a  $N \times N$  matrix are an orthogonal basis in the  $N$ -dimension space. These vectors depict principal directions of the matrix. A matrix  $\mathbf{A}$  can be diagonalized thanks to its eigenvectors ordered in a  $\mathbf{V}$  matrix (Kreyszig 2006):

$$\mathbf{D} = \mathbf{V}^{-1}\mathbf{A}\mathbf{V} \quad (21)$$

The elements along the diagonal of  $\mathbf{D}$  are the variances in the new uncorrelated basis. Going from the correlated referential to the uncorrelated basis can be done through a rotation operation, defined by the matrix of eigenvectors:

$$\mathbf{U} = \mathbf{V}^{-1}\mathbf{X} \quad (22)$$

An example of principal components analysis (as described by Bolle) is made for a 2-D discrete case (Figure 9). The covariance matrix within  $X$  coordinates is

$$\Sigma_x = \begin{pmatrix} 1.7 & 4.2 \\ 4.2 & 11.2 \end{pmatrix} \quad (23)$$

After changing coordinates to  $U$ , the covariance matrix is

$$\Sigma_U = \begin{pmatrix} 1.963 & 0 \\ 0 & 0.037 \end{pmatrix} \quad (24)$$

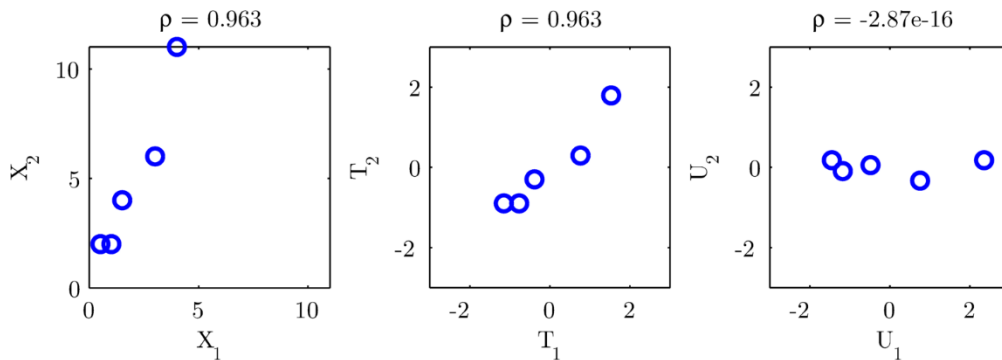


Figure 9: Example to decorrelate random variables with the principal component analysis described by Bolle

The approach that uses eigenvectors (22) is illustrated in Figure 10 for the same example as above. Coordinates in the  $U_i$  referential are different because variables were not standardized

before rotation. This difference is not problematic since the approach aims at reaching  $\rho = 0$ . The transformation from  $U$  to  $X$  should be done according to the technique and conventions used in the earlier step.

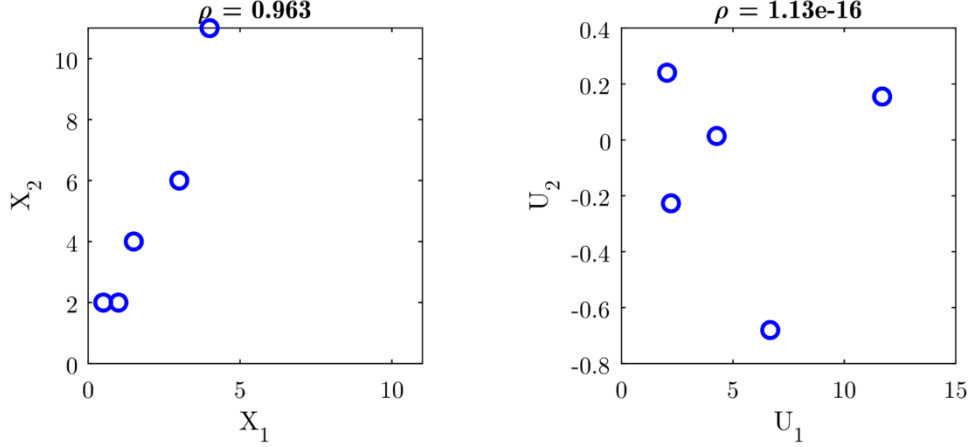


Figure 10: Example to decorrelate random variables with an eigenvectors analysis

Such as covariance describes a “crossed” variance between random variables, coskewness (25) and cokurtosis (26) can be defined and describe how skewness and kurtosis evolve with each variable:

$$S(X_1, X_2, X_3) = \frac{E[(X_1 - \bar{X}_1)(X_2 - \bar{X}_2)(X_3 - \bar{X}_3)]}{\sigma_{X_1} \sigma_{X_2} \sigma_{X_3}} \quad (25)$$

$$K(X_1, X_2, X_3, X_4) = \frac{E[(X_1 - \bar{X}_1)(X_2 - \bar{X}_2)(X_3 - \bar{X}_3)(X_4 - \bar{X}_4)]}{\sigma_{X_1} \sigma_{X_2} \sigma_{X_3} \sigma_{X_4}} \quad (26)$$

For normally distributed and uncorrelated random variables:

- coskewness is nil for any combination of random variables
- cokurtosis is nil for  $K(X_1, X_2, X_3, X_4) = 0$ ,  $K(X_1, X_1, X_2, X_3) = 0$  and  $K(X_1, X_1, X_1, X_2) = 0$  but is not nil for  $K(X_1, X_1, X_1, X_1) = \kappa_{X_1} = 3$  and  $K(X_1, X_1, X_2, X_2) = 1$

These results are proven in appendix A.1.

### 2.2.3 Common forms of probability density functions

In order to depict the probability distribution of uncertainty sources or of the output of a model, we have to introduce what is a probability density function and some typical analytical functions.

A probability density function (pdf) of a continuous random variable defines the relative likelihood that some value can be found in the sample. A probability density function can be modeled thanks to an analytical expression. Three widely used pdf are presented here.

First, the well-known normal distribution (Gaussian distribution, Figure 11 (a)) is defined as

$$f_x(x) = \frac{1}{\sigma_x \sqrt{2\pi}} \exp\left(-\frac{1}{2} \left(\frac{x - \bar{X}}{\sigma_x}\right)^2\right) \quad (27)$$

This bell-shaped distribution is defined with only 2 parameters: the mean  $\bar{X}$  and the standard deviation  $\sigma_x$ . The skewness and the kurtosis are constant and take respectively the values  $\gamma_x = 0$  and  $\kappa_x = 3$ . It should be noticed that the expression (27) is defined for  $x \in \mathbb{R}$ , which means that it is unbounded. Bolle (1988) explains that this function is the most suitable one to model a random variable with few information available about its distribution.

The second expression, which introduces a third parameter, is the gamma distribution (Figure 11 (b)):

$$f_x(x) = \frac{(x-a)^\alpha}{\beta^{\alpha+1} \Gamma(\alpha+1)} \exp(-(x-a)/\beta) \quad (28)$$

with  $\Gamma$  the Gamma function, which can be seen as an extension of the factorial to real and complex numbers. The parameters are  $\alpha$ ,  $\beta$  and  $a$ . They can be determined from the three first moments or from a maximum likelihood fitting if a discrete sample is available. The parameters take the following values from the statistical moments:

$$\begin{aligned} a &= \bar{X} - 2 \frac{\sigma_x}{\gamma_x} \\ \alpha &= \frac{4}{\gamma_x^2} - 1 \\ \beta &= \frac{\sigma_x \gamma_x}{2} \end{aligned} \quad (29)$$

The gamma distribution (28) is defined for  $x \in [a; +\infty[$ .

The last distribution presented in this non-exhaustive section is the beta distribution (Figure 11 (c)). It can be defined with four parameters on a bounded domain. The beta distribution is usually expressed for a standardized random variable  $T$ ,  $t \in [0; 1]$ :

$$f_T(t) = \frac{t^\alpha (1-t)^\beta}{B(\alpha+1, \beta+1)} \quad (30)$$

with  $B$  the Beta function defined from the Gamma function:

$$B(\alpha + 1, \beta + 1) = \frac{\Gamma(\alpha + 1)\Gamma(\beta + 1)}{\Gamma(\alpha + \beta + 2)} \quad (31)$$

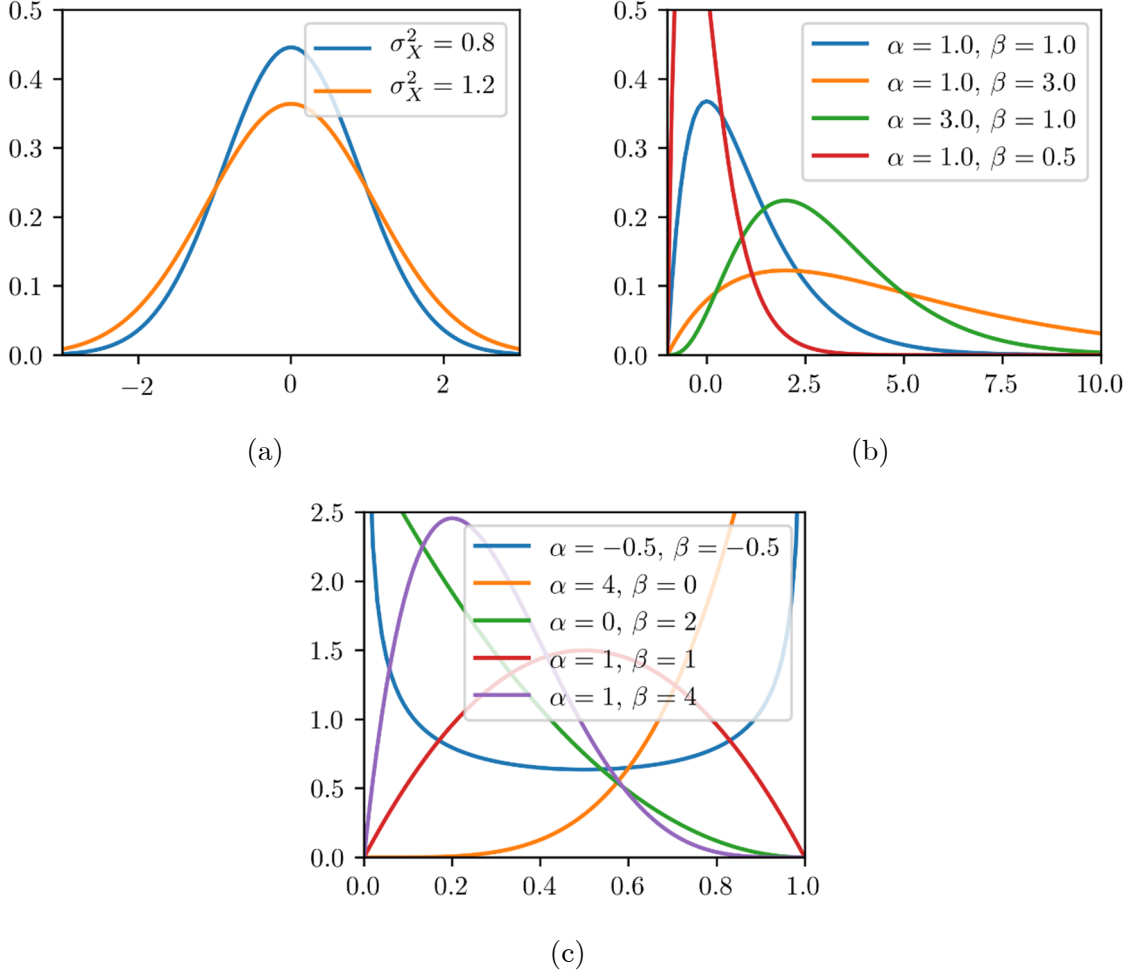


Figure 11: 3 common probability density functions

For a random variable  $X$ ,  $x \in [a; b]$ , equation (30) becomes

$$f_X(x) = \frac{(x-a)^\alpha (b-x)^\beta}{B(\alpha + 1, \beta + 1)(b-a)^{\alpha+\beta+1}} \quad (32)$$

Relationship (32) is a function of four parameters:  $a$ ,  $b$ ,  $\alpha$  and  $\beta$ . One can express the first two statistical moments according to these four parameters:

$$\begin{aligned} \bar{X} &= \frac{(\alpha + 1)b + (\beta + 1)a}{\alpha + \beta + 2} \\ \sigma_X^2 &= \frac{(\alpha + 1)(\beta + 1)(b - a)^2}{(\alpha + \beta + 2)^2 (\alpha + \beta + 3)} \end{aligned} \quad (33)$$

If  $a$  and  $b$  are known, the parameters  $\alpha$  and  $\beta$  can be determined by solving the non-linear system of equations (33). According to the values taken by  $\alpha$  and  $\beta$ , the shape of the distribution changes and can even degenerate to a uniform distribution when  $\alpha = \beta = 0$  (Bolstad 2007).

Three continuous pdf were presented in this section. They are able to reproduce unbounded, semi-bounded or bounded distributions. Other theoretical distributions exist but are not detailed in this thesis.

#### 2.2.4 Functions of random variables

The goal of an uncertainty analysis is to determine the pdf of an unknown  $Y$  which is a function of  $\mathbf{X}$ , a vector of  $N$  random variables:  $Y = f(\mathbf{X}) = f(X_1, \dots, X_N)$ . When applied to hydraulics, for example, the unknown  $Y$  may be the water depth, the velocity field or the flood extent and  $\mathbf{X}$  the roughness coefficient and the downstream boundary condition.

A pdf can be associated to  $Y$  according to the occurrence of the values taken by the function  $f(\mathbf{X})$ . Further, the study of the output will be “*disconnected*” from the position where the values are taken. Indeed, only the values of  $Y$  and their occurrence probability will be considered in order to assess the probabilistic behavior of  $Y$ .

The methodologies presented in the following sections are strategies aiming to determine the  $Y$  pdf with punctual evaluations of  $Y = f(x_1, \dots, x_N)$ . Methodologies differ in the number of  $x$  values chosen, the position of the  $x$  values chosen in  $X$ , how they deal with multivariate problems as well as how the pdf of  $Y$  is generated. These differences lead to computational costs and results accuracy specific to each method.

For completeness, the output of  $f$  can be a vector:  $\mathbf{Y} = f(\mathbf{X})$ . In this frame, statistical moments can be computed for each element of  $\mathbf{Y}$  as well as a covariance matrix. For instance, in hydrodynamics, the  $f$  function can be the hydrodynamic model,  $\mathbf{X}$  the uncertain parameters (e.g. the roughness coefficient, the peak discharge, a weir elevation, etc.) and  $\mathbf{Y}$  the resulting uncertain output (e.g. water depths, velocity fields, downstream hydrograph, etc.).

### 2.3 Discrete evaluations for uncertainty analysis

The goal of an *uncertainty analysis* is to characterize the probabilistic behavior of  $Y$  according to some defined uncertainty of  $\mathbf{X}$ . A *global sensitivity analysis* (Saltelli et al. 2008) aims at quantifying the amount of uncertainty of an output  $Y$  due to different sources of uncertainty  $\mathbf{X}$ . It goes a step further than uncertainty analysis since it quantifies the contribution of each input to the final output uncertainty.

In order to assess the output uncertainty of a function of random variables, a discretization of the input random variables has to be done for functions  $f$  that cannot be treated analytically. This discretization leads to punctual evaluations of  $f$  and thence punctual values of the output  $Y$ . Then, the characteristics (mean, standard deviation, ...) of the random variable  $Y$  can be deduced from these punctual evaluations.

Discrete evaluations of  $f$  can be performed using different techniques. The first one is to use a high number of points randomly distributed in the random variables space (Monte Carlo Simulations (MCS)). Another technique, which goal is to reduce the number of function evaluations, is to use a limited number of points positioned at specific locations with specific weights. This method is referred as point estimates method (PEM). The stochastic response surface method (SRSM) can be classified in the middle of the previous.

### **2.3.1 Monte Carlo Simulation**

MCS is a group of methods based on the principle of random sampling. It is used for a wide range of purposes and is still massively used nowadays (Kroese et al. 2014). It was first proposed in (Metropolis & Ulam 1949). The method is based on the strong law of large numbers (Graham & Talay 2013) which states that the sample mean converges almost surely towards the expected mean when the sample size tends to infinity.

First, a single random variable problem is considered. The probability density function  $p_X$  and the cumulative distribution function (cdf)  $F_X$  (34) are considered as known for the random variable  $X$ .

$$F_X(x) = \int_{-\infty}^x p_X(x) dx \quad (34)$$

Thanks to a uniform pseudo-random number generator (PRNG, (Gentle 2003)), random values  $a \in [0,1]$  are drawn and used with an invert cdf to identify random values  $x_a$  distributed according to the desired pdf (see Figure 12). This method, known as “inverse transform sampling” (Devroye 1986), can be understood intuitively thanks to Figure 13. In this figure, we understand that uniformly distributed values can be transformed to a given distribution (e.g. normal law, gamma law, etc.) thanks to the invert of the corresponding cdf. This transformation allows to get the density of points described by the desired pdf. It should be noticed that the invert of the cdf might not be defined analytically. The use of a numerical approximation is required in such cases.

For this thesis, this method is not directly used. The use of built-in functions in Intel MKL for several theoretical distributions is rather preferred.

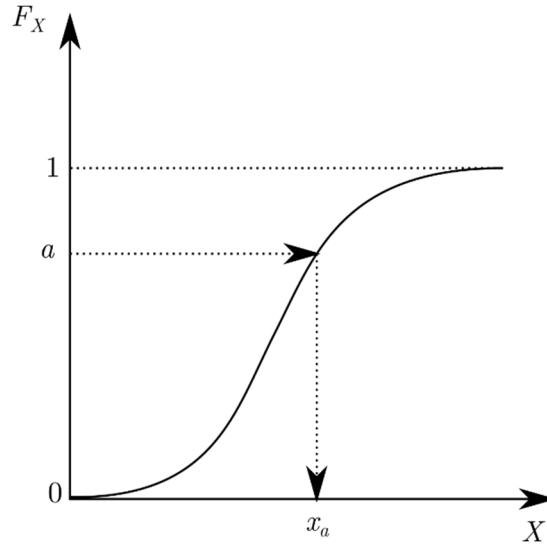


Figure 12: Generation of  $x$  values from a PRNG

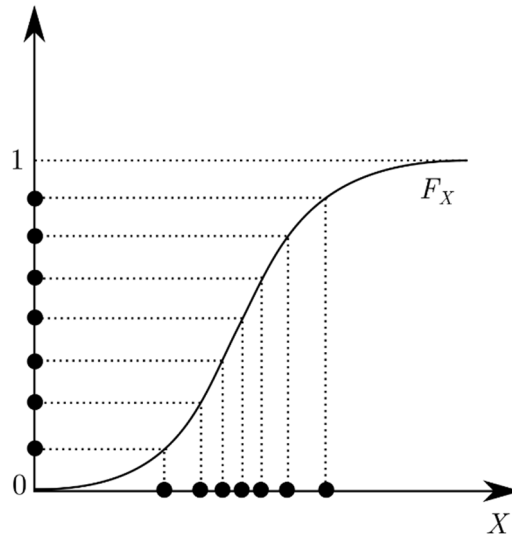


Figure 13: Principle of the inverse transform sampling method

The number  $n$  of values drawn randomly should be large enough in order to capture the essence of the pdf of  $X$ . According to literature and practical cases,  $n$  should be at least of the order  $10^3$ - $10^4$  in order to approach the pdf of  $X$ . An equal probability of  $1/n$  is assigned to each value  $x$ . Then, the function  $f$  is evaluated for each  $x$ :  $y = f(x)$ . Each function result  $y$  is given an equal probability  $1/n$ , which is the probability associated to  $x$ .

For multivariate problems, the approach depends on the correlation between random variables. For this thesis, only uncorrelated  $X_i$  will be considered since decorrelation techniques were presented previously. For each random variables  $X_i$ , a sample of  $N$  values is drawn:  $x_{i,1} \dots x_{i,N}$ . The function  $f$  is evaluated  $N$  times and a sample of  $N$  values of  $Y$  is obtained. For  $M$  random variables  $X_i, i \in [1, M]$ :

$$\begin{aligned} y_1 &= f(x_{1,1}, \dots, x_{M,1}) \\ &\vdots \\ y_N &= f(x_{1,N}, \dots, x_{M,N}) \end{aligned} \quad (35)$$

Other sampling methods exist and allow reducing the number of sampling points. These techniques include Latin Hypercube sampling (McKay et al. 1979), such as used in (Camacho & Martin 2013; Papaioannou et al. 2017), importance sampling (Glynn & Iglehart 1989), such as used in (Zhong et al. 2013), and others (see (Singh et al. 2007)). For further details and explanations, the reader is invited to refer to (Singh et al. 2007). This thesis will not use these techniques and rather stick to the original Monte Carlo method.

## 2.3.2 Point estimates methods

### 2.3.2.1 Original Rosenblueth's method

The large number of evaluations of  $f$  can be cumbersome when it is computationally expensive. Rosenblueth addressed this problem by proposing a two-point estimate method (Rosenblueth 1975; Rosenblueth 1981). The will of the method is to reproduce accurately the few first moments of a statistical distribution.

Rosenblueth was interested in conserving the moments of order 0 to 3. For a single random variable problem, this corresponds to 4 equations. Thus, the probability density function should be expressed with 4 parameters:

$$p_X(x) = P_1 \delta(x - x_1) + P_2 \delta(x - x_2) \quad (36)$$

Where  $\delta(a) = 1$  when  $a = 0$ , otherwise  $\delta(a) = 0$ .  $P_1$ ,  $P_2$ ,  $x_1$  and  $x_2$  are the 4 parameters. Expressing moments up to the 3<sup>rd</sup> order for (36) yields:

$$\begin{aligned} 1 &= \int_{-\infty}^{+\infty} p_X(x) dx = P_1 + P_2 \\ \bar{X} &= \int_{-\infty}^{+\infty} x p_X(x) dx = P_1 x_1 + P_2 x_2 \\ \sigma_X^2 &= \int_{-\infty}^{+\infty} (x - \bar{X})^2 p_X(x) dx = P_1 (x_1 - \bar{X})^2 + P_2 (x_2 - \bar{X})^2 \\ E[d^3] &= \int_{-\infty}^{+\infty} (x - \bar{X})^3 p_X(x) dx = P_1 (x_1 - \bar{X})^3 + P_2 (x_2 - \bar{X})^3 \end{aligned} \quad (37)$$

If  $\xi_i = (x_i - \bar{X}) / \sigma_X$ ,  $i = 1, 2$ , set of equations (37) becomes:

$$\begin{aligned} 1 &= P_1 + P_2 \\ 0 &= P_1 \xi_1 + P_2 \xi_2 \\ 1 &= P_1 \xi_1^2 + P_2 \xi_2^2 \\ \gamma_X &= P_1 \xi_1^3 + P_2 \xi_2^3 \end{aligned} \quad (38)$$

Two symmetrical solutions can be obtained. One of these is:

$$\begin{aligned}
 \xi_1 &= \frac{\gamma_X}{2} + \sqrt{1 + \left(\frac{\gamma_X}{2}\right)^2} \\
 \xi_2 &= \frac{\gamma_X}{2} - \sqrt{1 + \left(\frac{\gamma_X}{2}\right)^2} \\
 P_1 &= \frac{1 - \gamma_X \sqrt{\frac{1}{4 + \gamma_X^2}}}{2} \\
 P_2 &= \frac{1 + \gamma_X \sqrt{\frac{1}{4 + \gamma_X^2}}}{2}
 \end{aligned} \tag{39}$$

When  $p_X$  is symmetrical,  $\gamma_X = 0$ , and the discretization points are:

$$x_1 = \bar{X} + \sigma; x_2 = \bar{X} - \sigma; P_1 = \frac{1}{2}; P_2 = \frac{1}{2} \tag{40}$$

To extend the method to  $N$  random variables, Rosenblueth chose to limit the number of discretization points to  $2^N$ , distributed to form a rectangle ( $N = 2$ ), prism ( $N = 3$ ) or hyperprism<sup>4</sup> ( $N > 3$ ). Unknowns are probabilities at all points ( $2^N$ ) and coordinates of two of them opposite to each other ( $2N$ ) in order to force the points to be arranged as a rectangle, prism or hyperprism. In order to determine unknown values, several equations can be written. These include:

1. 1 equation expressing the total probability
2.  $N$  equations expressing the first order marginal moments (means) for each random variable
3.  $N(N + 1)/2$  equations for each unique element in the covariance matrix (i.e. symmetric elements are not taken into account twice)
4.  $C_{N+2}^3 = (N + 2)!/3!(N - 1)!$  equations for marginal third order moments and “crossed” third order moments.

Table 1 summarizes the number of equations available and the number of unknowns according to the number of random variables involved. It shows that for  $N = 1$  the number of equations is equal to the number of unknowns, while these numbers do not correspond when  $N \geq 2$ . When  $N \in [2, 6]$  the number of equations is too high and some arbitrary choice must be done

---

<sup>4</sup> A hyperprism is the generalization of a prism to more than 3 dimensions.

in the equations to solve. When  $N \geq 7$  and only considering moments up to third order, too few equations are available.

$N$	Nb unknowns	Nb equations
1	4	4
2	8	10
3	14	20
4	24	35
5	42	56
6	76	84
7	142	120

Table 1: Number of unknowns vs. number of equations available in Rosenblueth method

Let us consider an example (inspired from (Rosenblueth 1981)) with  $N = 2$ ,  $\bar{X}_1 = 1$ ,  $\bar{X}_2 = 2$  and symmetrical distributions ( $\gamma_{X_1} = \gamma_{X_2} = 0$ ). Two cases will be considered. The first one (a) involves the covariance matrix  $\Sigma_a$  while for the second one (b) it is  $\Sigma_b$  :

$$\begin{aligned} \Sigma_a &= \begin{pmatrix} 0.04 & 0 \\ 0 & 0.25 \end{pmatrix} \\ \Sigma_b &= \begin{pmatrix} 0.04 & 0.07 \\ 0.07 & 0.25 \end{pmatrix} \end{aligned} \tag{41}$$

Random variables from case (a) are uncorrelated ( $\rho_a = 0$ ) and are correlated ( $\rho_b = 0.7$ ) for case (b). When the equations described above are solved (total probability, 2 means, 2 variances, 1 covariance and 2 symmetries = 8 equations), one obtains the positions and weights depicted in Figure 14 and numerically reproduced in Table 2. It appears that positions are identical while weights vary. This can be easily understood through the principle of correlation. Correlated variables ( $\rho = 1$ ) align along a line passing by the means. It means that outside that line no values can be found, which yields  $P = 0$  at these positions and all probabilities are concentrated along the correlation line.

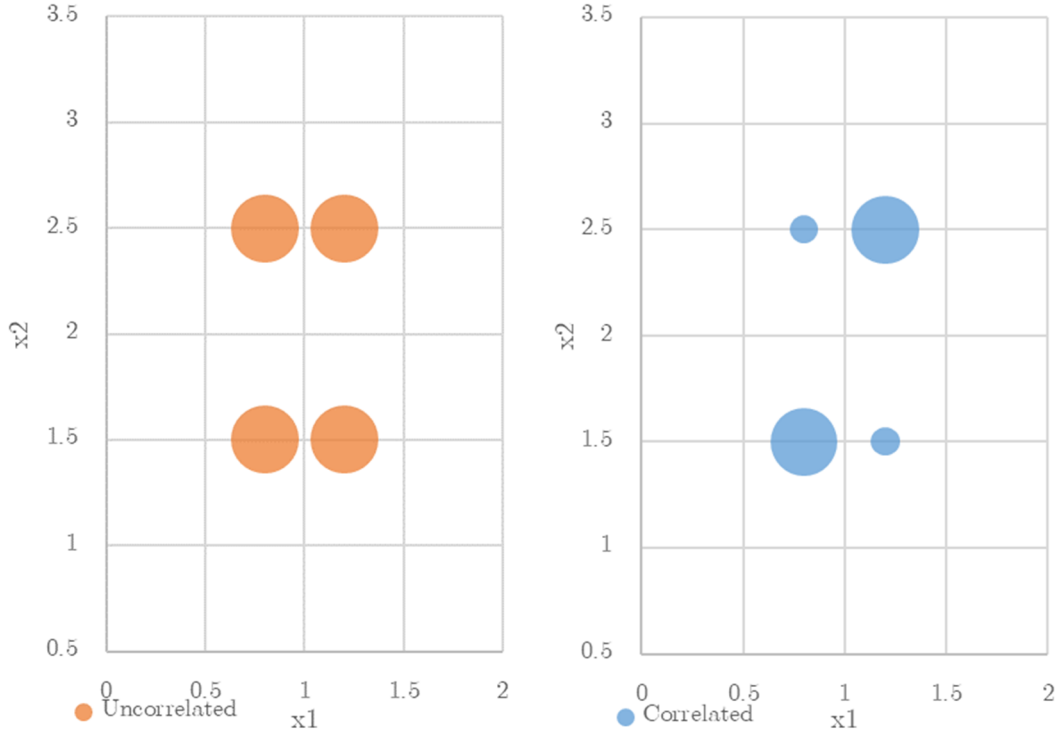


Figure 14: Positions and weights (bullet area) of concentration points

Uncorrelated			Correlated		
$x_1$	$x_2$	$P$	$x_1$	$x_2$	$P$
0.8	1.5	0.25	0.8	1.5	0.425
1.2	1.5	0.25	1.2	1.5	0.075
0.8	2.5	0.25	0.8	2.5	0.075
1.2	2.5	0.25	1.2	2.5	0.425

Table 2: Positions and weights of concentration points

Various drawbacks affect Rosenblueth's method, including:

- the high number of evaluation points ( $2^N$ ) when  $N$  becomes high, and
- the difficulties to generalize the method for  $N > 3$  without additional assumptions.

### 2.3.2.2 Improved methods

Several authors (Bolle 1988; Harr 1989; Hong 1996) proposed new methods to avoid the estimation of function  $f$  too many times. For all of these alternative methods, points are defined only along axes. To do so, variables must be uncorrelated since correlation cannot be expressed in such a framework. To uncorrelate variables, the technique explained previously in section 2.2.2 is applied. Uncorrelation is supposed to be applied previously to the methods described below. For the sake of clarity, the notation  $X$  will be kept for uncorrelated variables.

After having uncorrelated and normalized random variables, Harr (Harr 1989) circumscribes an hypersphere to the hypercube of  $2\sigma_X$  borders. The intersection between the hypersphere and the newly defined coordinate axes give the evaluation points:

$$\begin{aligned} x_{i,1} &= \bar{X}_i - \sqrt{N}\sigma_X \\ x_{i,2} &= \bar{X}_i + \sqrt{N}\sigma_X \end{aligned} \quad (42)$$

Each evaluation point is weighted with  $1/(2N)$ . Christian & Baecher (2002) points out that, when  $N$  becomes high, evaluation points are taken further from the mean value. This may result in unphysical values in some specific cases.

Bolle (Bolle 1988; Bolle 1994) developed a method which goals were to limit the number of evaluations of function  $f$  and to represent moments up to fourth. Bolle developed his method for symmetrical and uncorrelated random variables.

In order to represent moments up to fourth order for each random variables, three concentration points are used per random variable. Bolle chose to position one of these at the mean (denoted by subscript  $c$ ) and to perturb this position for the two others (subscripts  $1$  and  $2$ ). This results in a total of  $2N + 1$  evaluation points:

$$\begin{aligned} x_{i,1} &= \bar{X}_i - \sigma_{X_i} \sqrt{\kappa_{X_i}} \\ x_{i,c} &= \bar{X}_i \\ x_{i,2} &= \bar{X}_i + \sigma_{X_i} \sqrt{\kappa_{X_i}} \\ P_{i,1} &= P_{i,2} = \frac{1}{2\kappa_{X_i}} \\ P_c &= 1 - \sum_{i=1}^N (P_{i,1} + P_{i,2}) \end{aligned} \quad (43)$$

This is the solution of  $4N + 1$  equations (1 total probability,  $N$  means,  $N$  variances,  $N$  skewness and  $N$  kurtosis) for  $4N + 1$  unknowns ( $2N + 1$  weights and  $2N$  perturbations from the central point).

If we consider  $\kappa_{X_1} = \kappa_{X_2} = \dots = \kappa_{X_N} = \kappa$ ,  $P_c$  in (43) becomes

$$P_c = 1 - \frac{N}{\kappa} \quad (44)$$

If  $N > \kappa$ , then  $P_c$  becomes negative which contradicts the first fundamental probability axiom. The user should take care to keep  $\kappa \geq N$ . This constraint is in contradiction with the will to represent a fourth order moment.

Hong's approach (Hong 1996; Hong 1998) is similar to Harr method except that it deals with skewed and uncorrelated variables. He solves  $4N$  equations ( $N$  equations to express that the sum of the weights is  $1/N$  along each variable axis,  $N$  means,  $N$  variances and  $N$  skewness) for  $4N$  unknowns ( $2N$  weights and  $2N$  positions). For 2 concentration points per variable, his developments degenerate to Harr method when  $\gamma_{X_i} = 0$ :

$$\begin{aligned} x_i &= \bar{X}_i + \sigma_{X_i} \left( \frac{\gamma_{X_i}}{2} \pm \sqrt{N + \left( \frac{\gamma_{X_i}}{2} \right)^2} \right) \\ P_i &= \frac{1}{2N} \left( 1 \mp \frac{\gamma_{X_i}}{2} \frac{1}{\sqrt{N + \left( \gamma_{X_i} / 2 \right)^2}} \right) \end{aligned} \quad (45)$$

This approach leads to  $2N$  evaluation points. Hong also developed a method with three concentration points per variable, enabling the representation of the kurtosis. One of these points is common for all variables (same approach as Bolle), which leads to  $2N + 1$  estimation points:

$$\begin{aligned} \xi_{i,1} &= \frac{\gamma_{X_i}}{2} + \sqrt{\kappa_{X_i} - 3 \left( \frac{\gamma_{X_i}}{2} \right)^2} \\ \xi_{i,2} &= \frac{\gamma_{X_i}}{2} - \sqrt{\kappa_{X_i} - 3 \left( \frac{\gamma_{X_i}}{2} \right)^2} \\ x_{i,1} &= \bar{X}_i + \sigma_{X_i} \xi_{i,1} \\ x_{i,c} &= \bar{X}_i \\ x_{i,2} &= \bar{X}_i + \sigma_{X_i} \xi_{i,2} \\ P_{i,1} &= \frac{1}{\xi_{i,1} (\xi_{i,1} - \xi_{i,2})} \\ P_{i,c} &= \frac{1}{N} - \frac{1}{\kappa_{X_i} - \gamma_{X_i}^2} \\ P_{i,2} &= \frac{-1}{\xi_{i,2} (\xi_{i,1} - \xi_{i,2})} \end{aligned} \quad (46)$$

The probability of the central concentration point is

$$P_c = \sum_{i=1}^N P_{i,c} \quad (47)$$

Negative probabilities can be obtained in specific cases, which is opposed to one of the fundamental probability axioms.

### 2.3.2.3 Summary

Table 3 summarizes point estimates methods presented in this thesis. Figure 15 illustrates the position of concentration points for PEM when  $N = 2$  and random variables distributions are symmetric and uncorrelated. Axes in Figure 15 define a centered and normalized space.

Method	Ref.	Variables need to be uncorr.	Skewness	Kurtosis	Nb pts	Comments
Rosenblueth	(Rosenblueth 1975; Rosenblueth 1981)	No	Any	Depends on $N$	$2^N$	Not a general approach when $N > 2$
Harr	(Harr 1989)	Yes	$\gamma = 0$	Not defined	$2N$	Points are moving away when $N$ increases
Bolle	(Bolle 1988; Bolle 1994)	Yes	$\gamma = 0$	Any	$2N + 1$	$P < 0$ in some cases
Hong 2 pts	(Hong 1996; Hong 1998)	Yes	Any	Not defined	$2N$	Points are moving away when $N$ increases
Hong 3 pts	(Hong 1998)	Yes	Any	Any	$2N + 1$	$P < 0$ in some cases

Table 3: Point estimate methods summary

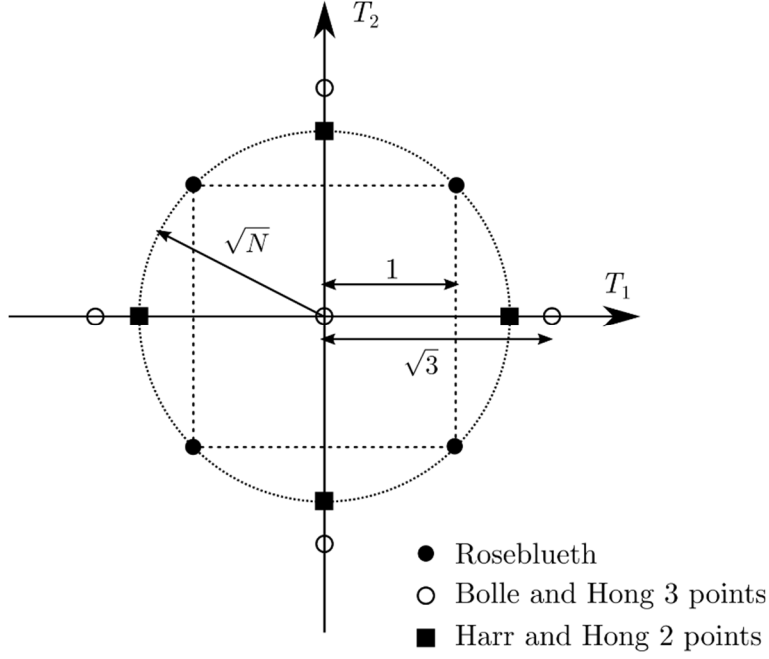


Figure 15: Position of concentration points in 2-D with skewness and kurtosis of a normal distribution

### 2.3.3 Stochastic Response Surface method

The SRS method was originally developed in (Isukapalli et al. 1998). It is presented and tested in this thesis after first approaches by the HECE research group with a master thesis (Kyabu 2011) and a book chapter (Dewals et al. 2014). The method relies on the calibration of a multivariate Hermite polynomial for the output random variable  $Y$ :

$$Y = a_0 + \sum_{i_1=1}^N a_{i_1} \Gamma_1(T_{i_1}) + \sum_{i_1=1}^N \sum_{i_2=1}^{i_1} a_{i_1 i_2} \Gamma_2(T_{i_1}, T_{i_2}) + \sum_{i_1=1}^N \sum_{i_2=1}^{i_1} \sum_{i_3=1}^{i_2} a_{i_1 i_2 i_3} \Gamma_3(T_{i_1}, T_{i_2}, T_{i_3}) + \dots \quad (48)$$

with

$$\Gamma_p(T_{i_1}, \dots, T_{i_p}) = (-1)^p e^{\frac{1}{2}T^T T} \frac{\partial^p}{\partial T_{i_1} \dots \partial T_{i_p}} e^{-\frac{1}{2}T^T T} \quad (49)$$

where  $T$  is a vector of  $p$  standardized random variables  $T_1, \dots, T_p$  and  $a_i$  are constants that have to be determined by calibration. The number of unknowns  $a_i$  to determine in equation (48) for second ( $n_2$ ) and third ( $n_3$ ) order approximations are:

$$\begin{aligned} n_2 &= 1 + 2N + \frac{N(N-1)}{2} \\ n_3 &= 1 + 3N + \frac{3N(N-1)}{2} + \frac{N(N-1)(N-2)}{6} \end{aligned} \quad (50)$$

Isukapalli et al. recommend to use  $2n_i$  to  $4n_i$  points,  $i = 2, 3$ , to estimate coefficients  $a_i$ . This empirical definition of the number of points to use lead to an overdetermination of the system

of equations used to compute  $a_i$  coefficients. This requires the use, for instance, of a least squares method to compute  $a_i$  coefficients. From a general point of view, using an overdetermined system may lead to different solutions for  $a_i$  coefficients since various methods might be used to solve it.

The selection of sampling points is performed through a heuristic algorithm exposed in (Isukapalli et al. 1998):

- The algorithm selects points in the region of high probability
- For each term of (48), a corresponding point is chosen:
  - For the constant term, all variables are taken at their mean value, i.e. 0.
  - For terms involving a single variable, only the concerned coordinate is set to the roots of the next order Hermite polynomial while others are set to 0.
  - For terms involving several variables, roots of the next order Hermite polynomial are taken for those variables while the remaining variables are set to 0.

If  $N = 2$ , the second order Hermite polynomial (48) has the form:

$$Y = a_0 + a_1 T_1 + a_2 T_2 + a_{1,2} T_1 T_2 + a_{1,1} (T_1^2 - 1) + a_{2,2} (T_2^2 - 1) \quad (51)$$

Then, the number of coefficients  $a_i$  to determine is  $n_2 = 1 + 4 + 1 = 6$ . To do so, Isukapalli recommends using ideally 12 estimation points ( $2n_2 = 2 \times 6 = 12$ ). According to his heuristic algorithm, these points are:

- (0,0), for the constant term
- (1,0), (-1,0), (0,1), (0,-1), for the terms of first order
- (1,1), (1,-1), (-1,1), (-1,-1), for the cross product  $T_1 T_2$
- $(\sqrt{3}, 0)$ ,  $(-\sqrt{3}, 0)$ ,  $(0, \sqrt{3})$ ,  $(0, -\sqrt{3})$ , for second order terms

It can be noticed that some of these points correspond to those used in Rosenblueth and Bolle methods when variables are symmetric. It is also interesting to notice that SRSM, as proposed by Isukapalli et al. (1998), does not take into account the skewness and kurtosis in the choice of evaluation points. An alternative approach is proposed in appendix A.4 in order to extend SRSM to skewed uncertain variables.

### **2.3.4 Summary**

Every sampling methods presented in this section are summarized in Table 4.

Method	Statistical moments taken into account to define evaluation points	Nb pts	Comments
Monte Carlo	All	$\sim 10^3\text{-}10^4$	Most general discrete approach but requires a large number of points
Rosenblueth	$\bar{X}, \sigma_X^2, \gamma$ and further moments (depends on $N$ )	$2^N$	Not a general approach when $N > 2$
Harr	$\bar{X}, \sigma_X^2, \gamma = 0$	$2N$	Points are moving away from the mean when $N$ increases
Bolle	$\bar{X}, \sigma_X^2, \gamma = 0, \kappa$	$2N + 1$	$P < 0$ in some cases
Hong 2 pts	$\bar{X}, \sigma_X^2, \gamma$	$2N$	Points are moving away when $N$ increases
Hong 3 pts	$\bar{X}, \sigma_X^2, \gamma, \kappa$	$2N + 1$	$P < 0$ in some cases
SRSM	$\bar{X}, \sigma_X^2$	Depends on the polynomial used	Empirical number of points and method to define them which leads to an overdetermined system of equations.

Table 4: Summary of all discrete evaluation methods included in this thesis

## 2.4 Characterization of the output uncertainty

A model that takes uncertain variables as input returns data with some level of uncertainty. In order to assess the uncertainty of the output of a model, several techniques exist and are presented in this section. First, some Taylor series expansion developments are presented. These developments are useful for next subsections in order to evaluate the order of precision of the methods. The principle of the perturbation moment method is also based on the Taylor series developments shown in section 2.4.1.

### 2.4.1 Taylor series expansion of statistical moments

The Taylor series expansion for statistical moments of a function is developed in (Hahn & Shapiro 1967; Anderson & Mattson 2012). The output of a function of  $\mathbf{X}$  can be approximated by a first-order Taylor series expansion around a central point  $\mathbf{X}_c$ :

$$Y = f(\mathbf{X}) \approx f(\mathbf{X}_c) + \sum_{i=1}^N \left( \frac{\partial f}{\partial x_i} \Big|_{\mathbf{X}_c} (x_i - x_{i,c}) \right) \quad (52)$$

where  $x_{i,c}$  is the  $i^{\text{th}}$  component of the central point  $\mathbf{X}_c$ . It can also be written in a vector notation:

$$Y = f(\mathbf{X}) \approx f(\mathbf{X}_c) + \nabla f(\mathbf{X}_c)(\mathbf{X} - \mathbf{X}_c) \quad (53)$$

where  $\nabla f(\mathbf{X}_c)$  is a  $N$ -dimensional row vector and  $(\mathbf{X} - \mathbf{X}_c)$  a  $N$ -dimensional column vector.

The second-order Taylor series expansion is expressed in vector notation as:

$$Y = f(\mathbf{X}) \approx f(\mathbf{X}_c) + \nabla f(\mathbf{X}_c)(\mathbf{X} - \mathbf{X}_c) + \frac{1}{2}(\mathbf{X} - \mathbf{X}_c)^T \mathbf{H}f(\mathbf{X}_c)(\mathbf{X} - \mathbf{X}_c) \quad (54)$$

with  $\mathbf{H}f(\mathbf{X}_c)$  the Hessian matrix of  $f$  at  $\mathbf{X}_c$ :

$$\mathbf{H}f = \begin{pmatrix} \frac{\partial^2 f}{\partial x_1^2} & \frac{\partial^2 f}{\partial x_1 \partial x_2} & \dots & \frac{\partial^2 f}{\partial x_1 \partial x_N} \\ \frac{\partial^2 f}{\partial x_2 \partial x_1} & \frac{\partial^2 f}{\partial x_2^2} & \dots & \frac{\partial^2 f}{\partial x_2 \partial x_N} \\ \vdots & \vdots & \ddots & \vdots \\ \frac{\partial^2 f}{\partial x_N \partial x_1} & \frac{\partial^2 f}{\partial x_N \partial x_2} & \dots & \frac{\partial^2 f}{\partial x_N^2} \end{pmatrix} \quad (55)$$

The statistical moments of  $Y$  can be evaluated thanks to Taylor series expansion. Extended developments are presented in appendix A.2.

The mean of  $Y$  is evaluated with a second-order Taylor series expansion:

$$\bar{Y} = E[Y] \approx Y_c + \frac{1}{2} \text{Tr}(\Sigma \mathbf{H}f(\mathbf{X}_c)) \quad (56)$$

where  $\text{Tr}$  is the trace operator (sum over the diagonal elements) and  $\Sigma$  the covariance matrix (14). In the frame of uncorrelated random variables, non-diagonal terms in  $\Sigma$  are nil and (56) can be transformed into a more convenient indicial notation:

$$\bar{Y} = E[Y] \approx Y_c + \frac{1}{2} \sum_{i=1}^N \left. \frac{\partial^2 f}{\partial x_i^2} \right|_{X_c} \sigma_{X_i}^2 \quad (57)$$

The first-order approximation of the mean can be deduced from (57):  $\bar{Y} = Y_c$ .

For the variance of  $Y$ , the first-order Taylor series expansion is used:

$$\sigma_Y^2 = E[(Y - \bar{Y})^2] \approx \sum_{i=1}^N \left[ \left( \left. \frac{\partial f}{\partial x_i} \right|_{X_c} \right)^2 \sigma_{X_i}^2 + \sum_{j=i+1}^N \left. \frac{\partial f}{\partial x_i} \right|_{X_c} \left. \frac{\partial f}{\partial x_j} \right|_{X_c} \sigma_{X_i X_j} \right] \quad (58)$$

For uncorrelated random variables, equation (58) becomes:

$$\sigma_Y^2 = \sum_{i=1}^N \left( \left. \frac{\partial f(x_{i,c})}{\partial x_i} \right|_{X_c} \right)^2 \sigma_{X_i}^2 \quad (59)$$

The variance can also be developed with a second-order Taylor series expansion of  $Y$  and  $\bar{Y}$ . As a first step, this thesis considers a general development for  $Y$ . It will be simplified further for uncorrelated variables and normally distributed variables. This original development, due to its length, can be read in appendix A.2. Starting from the general development presented in appendix and simplifying it for a single variable yields:

$$\begin{aligned} \sigma_Y^2 &\approx \overbrace{\left( \left. \frac{\partial f}{\partial x} \right|_{X_c} \right)^2}^{A_1} \sigma_X^2 + \overbrace{\frac{1}{4} \left( \left. \frac{\partial^2 f}{\partial x^2} \right|_{X_c} \right)^2 E[d^4]}^{A_2} + \overbrace{\frac{1}{4} \left( \left. \frac{\partial^2 f}{\partial x^2} \right|_{X_c} \right)^2 \sigma_X^4}^{A_3} + \overbrace{\frac{\partial f}{\partial x} \left. \frac{\partial^2 f}{\partial x^2} \right|_{X_c} E[d^3]}^{A_4} - \overbrace{\frac{1}{2} \left( \left. \frac{\partial^2 f}{\partial x^2} \right|_{X_c} \right)^2 \sigma_X^4}^{A_5} \\ &\approx \left( \left. \frac{\partial f}{\partial x} \right|_{X_c} \right)^2 \sigma_X^2 + \frac{1}{4} \left( \left. \frac{\partial^2 f}{\partial x^2} \right|_{X_c} \right)^2 E[d^4] - \frac{1}{4} \left( \left. \frac{\partial^2 f}{\partial x^2} \right|_{X_c} \right)^2 \sigma_X^4 + \frac{\partial f}{\partial x} \left. \frac{\partial^2 f}{\partial x^2} \right|_{X_c} E[d^3] \\ &\approx \left( \left. \frac{\partial f}{\partial x} \right|_{X_c} \right)^2 \sigma_X^2 + \frac{\partial f}{\partial x} \left. \frac{\partial^2 f}{\partial x^2} \right|_{X_c} E[d^3] + \frac{1}{4} \left( \left. \frac{\partial^2 f}{\partial x^2} \right|_{X_c} \right)^2 (E[d^4] - \sigma_X^4) \end{aligned} \quad (60)$$

Equation (60) is equivalent to the formula presented in (Anderson & Mattson 2012).

For higher order moments, the developments are made with first-order Taylor series expansion.

For the third centered moment, this yields:

$$\gamma_Y \sigma_Y^3 = E[(Y - \bar{Y})^3] \approx \sum_{i=1}^N \left( \left. \frac{\partial f}{\partial x_i} \right|_{X_c} \right)^3 E[(X_i - \bar{X})^3] \quad (61)$$

For the fourth centered moment, one obtains:

$$\begin{aligned} \kappa_Y \sigma_Y^4 &= E\left[(Y - \bar{Y})^4\right] \\ &\approx \sum_{i=1}^N \left( \frac{\partial f}{\partial x_i} \Big|_{X_c} \right)^4 E\left[(X_i - \bar{X})^4\right] + 6 \sum_{i=1}^N \sum_{j=1}^N \left( \frac{\partial f}{\partial x_i} \Big|_{X_c} \frac{\partial f}{\partial x_j} \Big|_{X_c} \right)^2 E\left[(X_i - \bar{X})^2\right] E\left[(X_j - \bar{X})^2\right] \end{aligned} \quad (62)$$

Results presented in this section, whose developments are available in appendix A.2, will be useful for later comparisons.

### 2.4.2 Point estimates method

After some theoretical developments useful for later comparisons, a first method for the evaluation of the output uncertainty is presented: the point estimate method.

When evaluation (concentration) points are chosen, it is possible to compute the output value  $Y$  at these locations. Then, depending on the technique, the output uncertainty parameters (mean, variance, skewness, etc.) can be computed.

For all methods presented in section 2.3, except for SRSM, a weight is associated to each evaluation point. For MCS, this weight is unique for all points ( $1/n$ ,  $n$  being the number of estimation points), while it varies for other methods.

A pdf can be associated to  $Y$  by different ways. Various techniques can be used, depending on the number of evaluation points available:

1. The moments method. It consists in calibrating the parameters of a pdf from the moments computed from  $Y$
2. The L-moments method. It is similar to the previous approach but is renowned to be more robust when dealing with extreme values
3. Maximum likelihood method. It is better suited when a large number of points are available.

The latter two techniques are more suitable for Monte-Carlo simulations.

For each concentration point  $(x_{i,1}, \dots, x_{i,N})$  an output  $y_i$  can be computed. The moments method gives:

$$\begin{aligned}
 \bar{Y} &= \sum_{i=1}^n P_i y_i \\
 \sigma_Y^2 &= \sum_{i=1}^n P_i (y_i - \bar{Y})^2 \\
 \gamma_Y \sigma_Y^3 &= \sum_{i=1}^n P_i (y_i - \bar{Y})^3
 \end{aligned} \tag{63}$$

Rosenblueth (Rosenblueth 1981) shows, with Taylor series developments (similar to what is presented in section 2.4.1), for his technique that  $\bar{Y}$  in (63) is a third-order approximation while  $\sigma_Y^2$  and  $\gamma_Y$  in (63) are respectively second-order and first-order.

When moments are computed, a probability density function can be fitted. For instance, this law can be a gamma law (28) and the parameters can be fitted thanks to (29). From this pdf, various information can be extracted, including confidence intervals. Other statistical laws (e.g. normal law, beta law, ...) could also be used.

### 2.4.3 Perturbance moment method

While the point estimate method shown in previous section can be applied to many points or only a limited amount of points, the method presented in this section is specifically designed to deal with a limited number of evaluation points.

The perturbance moment method (PMM), so called by Franceschini, Tsai, et al. (2012), was initially developed by Bolle in his PhD thesis (Bolle 1988). The method aims to determine the first statistical moments of a function output  $Y = f(\mathbf{X})$ , where  $\mathbf{X}$  is a vector of  $N$  random variables. Estimations of  $f(\mathbf{X})$  are performed at several concentration points aligned along the axis centered at the means of  $\mathbf{X}$ . One of these points is the intersection of the axis. The other points are considered as perturbation of the central one.

PMM is inspired from the form of the Taylor series expansion of statistical moments. The method was initially developed for symmetrical random variables distributions. Franceschini, Tsai, et al. (2012) attempted a generalization for non-symmetrical distributions. Taylor series expansions of moments of  $Y$  ((57), (59), (61) and (62)) show that they can be computed as a sum of perturbations. The central idea is to evaluate the moments of  $Y$  from a central value plus a sum of perturbations.

The technique will be detailed hereafter for symmetrically distributed random variables and then extended to distributions that can be skewed.

The perturbation moment method was already applied in various domains, including soil mechanics (Bolle 1994), hydrology (Franceschini, Marani, et al. 2012) and water quality (Tsai & Li 2014).

### 2.4.3.1 PMM for symmetrical distributions

#### *Method description*

The main assumption made to establish PMM is that perturbations along each axis can be added since random variables are independent. Bolle justifies that independent variables lead to independent effects and consequently, these effects can be added. To ensure the independence of variables, they can be uncorrelated following the technique described earlier.

Some inaccuracy is present in this idea. Indeed, the assumption that uncorrelated variables are independent is not true in a general point of view. It has been shown in section 2.2.2 that uncorrelated variables can be dependent in some cases (e.g. random variables linked with a cyclic law will be uncorrelated while they are obviously dependent). This point is the main weakness of the method. The user should be aware of this and take all precautions when applying it. However, to the author knowledge, this kind of behavior (observing uncorrelated random variables which are actually dependent) is unlikely to occur in hydraulic practical cases.

In the original approach, perturbed concentration points ( $x_{i,1}$  and  $x_{i,2}$ ) are arranged symmetrically and have the same weight  $P_i$ . According to the original main assumption, each random variable is treated separately by maintaining other variables at their mean value. In such a frame, concentration points are chosen according to point estimates method (43) applied to a single variable (see Figure 16). With this method,  $x_{i,1}$  and  $x_{i,2}$  are located the same distance from  $x_{i,c}$ :

$$\begin{aligned}
 x_{i,1} &= \bar{X}_i - \sigma_{X_i} \sqrt{\kappa_{X_i}} \\
 x_{i,c} &= \bar{X}_i \\
 x_{i,2} &= \bar{X}_i + \sigma_{X_i} \sqrt{\kappa_{X_i}} \\
 P_i &= \frac{1}{2\kappa_{X_i}} \\
 P_c &= 1 - \frac{1}{\kappa_{X_i}}
 \end{aligned} \tag{64}$$

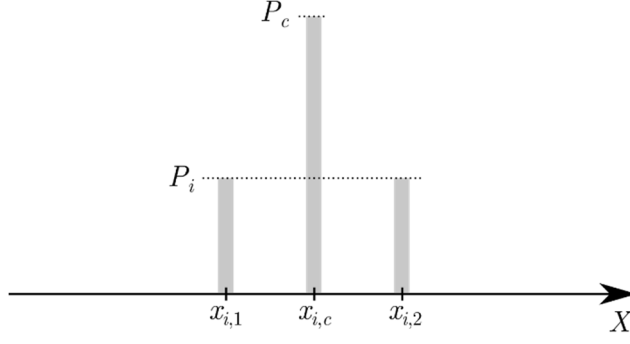


Figure 16: Concentration points positions and weights for PMM (symmetrical variables)

As stated above, the goal of this approach is to compute moments from a central value,  $Y_c$  (see Figure 17), perturbed by non-centered points ( $y_{i,1}$  and  $y_{i,2}$ ). This eccentricity in  $y$  values can be expressed through  $d_{i,k}, i \in [1, N], k = 1, 2$ :

$$\begin{aligned} d_{i,1} &= y_{i,1} - Y_c \\ d_{i,2} &= y_{i,2} - Y_c \end{aligned} \quad (65)$$

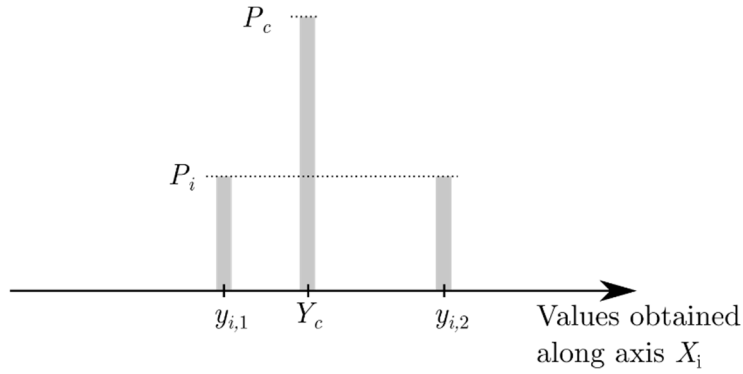


Figure 17: Schematic view of PMM (symmetrical variables)

The mean is computed as the central value  $Y_c$  plus the perturbations along each random variable axis:

$$E[Y] = \bar{Y} = Y_c + \sum_{i=1}^N P_i (d_{i,1} + d_{i,2}) \quad (66)$$

Formula (66) is comparable in its form to the Taylor series version (57): a central estimation plus a sum of perturbations. When equation (66) is developed, the usual formula for computing the mean is obtained:

$$\begin{aligned}
 \bar{Y} &= Y_c + \sum_{i=1}^N P_i (d_{i,1} + d_{i,2}) \\
 &= Y_c + \sum_{i=1}^N P_i (y_{i,1} + y_{i,2} - 2Y_c) \\
 &= Y_c - \sum_{i=1}^N 2P_i Y_c + \sum_{i=1}^N P_i (y_{i,1} + y_{i,2}) \\
 &= Y_c \left(1 - 2 \sum_{i=1}^N P_i\right) + \sum_{i=1}^N P_i (y_{i,1} + y_{i,2}) \\
 &= P_c Y_c + \sum_{i=1}^N P_i (y_{i,1} + y_{i,2})
 \end{aligned} \tag{67}$$

The second and third-order centered moments<sup>5</sup> are given as a sum of perturbation moments  $E[d\mu_i^m]$  :

$$\begin{aligned}
 \sigma_Y^2 &= \sum_{i=1}^N E[d\mu_i^2] \\
 \gamma_Y \sigma_Y^3 &= \sum_{i=1}^N E[d\mu_i^3]
 \end{aligned} \tag{68}$$

Perturbation moments are defined as the sum on an axis of the weights of each concentration point multiplied by a power of the distance of this point to the local mean  $\bar{y}_i$  :

$$E[d\mu_i^m] = P_i \left( (y_{i,1} - \bar{y}_i)^m + (y_{i,2} - \bar{y}_i)^m \right) + P_c (Y_c - \bar{y}_i)^m \quad m = 2, 3 \tag{69}$$

The local mean is computed as

$$\bar{y}_i = P_c Y_c + P_i (y_{i,1} + y_{i,2}) \tag{70}$$

It is useful to notice that the distance between the local mean  $\bar{y}_i$  and the central result  $Y_c$  simplifies into:

$$e_i = \bar{y}_i - Y_c = P_i (d_{i,1} + d_{i,2}) \tag{71}$$

Distances between the local mean and results at evaluation points can also be expressed as a function of  $d_{i,1}$  and  $d_{i,2}$  :

$$\begin{aligned}
 \delta_{i,1} &= y_{i,1} - \bar{y}_i = (1 - P_i) d_{i,1} - P_i d_{i,2} \\
 \delta_{i,2} &= y_{i,2} - \bar{y}_i = (1 - P_i) d_{i,2} - P_i d_{i,1}
 \end{aligned} \tag{72}$$

---

<sup>5</sup> It should be noticed at this point that Bolle's developments differ in his thesis and in his lecture notes. Developments in the lecture notes will be reproduced here because they are more recent.

*Comparison with Taylor series expansion*

To compare PMM with Taylor series, derivatives in Taylor series should be discretized according to concentration points used in PMM. The second derivative in (57) can be discretized by a second-order finite difference approximation:

$$\dots \tag{73}$$

Where  $h = (x_{i,c} - x_{i,1}) = (x_{i,2} - x_{i,c})$  is the spacing between concentration points. In the current approach, as stated earlier,  $h$  is the same at the left and at the right of  $x_{i,c}$ . Considering concentration points positions in (64), (73) becomes

$$\left. \frac{\partial^2 f}{\partial x^2} \right|_{X_c} \approx \frac{y_{i,2} - 2Y_c + y_{i,1}}{(\sigma_{X_i} \sqrt{\kappa_{X_i}})^2} = \frac{y_{i,2} - 2Y_c + y_{i,1}}{\sigma_{X_i}^2 \kappa_{X_i}} \tag{74}$$

When (74) is injected in (57), one obtains

$$\begin{aligned} \bar{Y} &= Y_c + \frac{1}{2} \sum_{i=1}^N \frac{y_{i,2} - 2Y_c + y_{i,1}}{\sigma_{X_i}^2 \kappa_{X_i}} \sigma_{X_i}^2 \\ &= Y_c + \frac{1}{2} \sum_{i=1}^N \frac{y_{i,2} - 2Y_c + y_{i,1}}{\kappa_{X_i}} \\ &= Y_c + \frac{1}{2} \sum_{i=1}^N \frac{1}{\kappa_{X_i}} (d_{i,1} + d_{i,2}) \end{aligned} \tag{75}$$

Equation (75) is strictly equal to the PMM formula (66).

For the variance, the first derivative in (59) can be approximated with second-order finite differences:

$$\left. \frac{\partial f}{\partial x} \right|_{X_c} \approx \frac{f(x_{i,2}) - f(x_{i,1})}{2h} = \frac{y_{i,2} - y_{i,1}}{2\sigma_{X_i} \sqrt{\kappa_{X_i}}} \tag{76}$$

Injecting (76) in the first-order Taylor series expression of the variance (59) yields

$$\begin{aligned}
 \sigma_Y^2 &\approx \sum_{i=1}^N \left( \frac{y_{i,2} - y_{i,1}}{2\sigma_{X_i} \sqrt{\kappa_{X_i}}} \right)^2 \sigma_{X_i}^2 \\
 &\approx \sum_{i=1}^N \frac{(d_{i,2} - d_{i,1})^2}{4\kappa_{X_i}} \\
 &\approx \sum_{i=1}^N \frac{d_{i,2}^2 - 2d_{i,1}d_{i,2} + d_{i,1}^2}{4\kappa_{X_i}} \\
 &\approx \sum_{i=1}^N \left[ \frac{P_i}{2} (d_{i,1}^2 + d_{i,2}^2) - P_i d_{i,1} d_{i,2} \right]
 \end{aligned} \tag{77}$$

Which has to be compared to (68)-(72).

$$\begin{aligned}
 \sigma_Y^2 &= \sum_{i=1}^N E[d\mu_i^2] \\
 &= \sum_{i=1}^N \left[ P_i \left( (y_{i,1} - \bar{y}_i)^2 + (y_{i,2} - \bar{y}_i)^2 \right) + P_c (Y_c - \bar{y}_i)^2 \right] \\
 &= \sum_{i=1}^N \left[ P_i \left( (1 - P_i) d_{i,1} - P_i d_{i,2} \right)^2 + P_i \left( (1 - P_i) d_{i,2} - P_i d_{i,1} \right)^2 + P_c \left( P_i (d_{i,1} + d_{i,2}) \right)^2 \right] \\
 &= \sum_{i=1}^N \left[ P_i (1 - P_i) (d_{i,1}^2 + d_{i,2}^2) - 2P_i^2 d_{i,1} d_{i,2} \right]
 \end{aligned} \tag{78}$$

It appears that expressions (77) and (78) are similar but not identical. Bolle justifies this difference by the fact that (77) does not take into account non-linear effects. This statement can be verified by developing the second-order Taylor series expansion of the variance. To avoid too long mathematical developments, the comparison will be based on the simplification that considers only a single random variable (60). In this expression, the second and first derivatives have already been approximated in (74) and (76) respectively. Injecting (74) and (76) into (60) and remembering that  $E[d^3] = \gamma_X \sigma_X^3 = 0$  yields:

$$\begin{aligned}
 \sigma_Y^2 &= \left( \frac{\partial f(x_c)}{\partial x} \right)^2 \sigma_X^2 + \frac{1}{4} \left( \frac{\partial^2 f(x_c)}{\partial x^2} \right)^2 (E[d^4] - \sigma_X^4) \\
 &\approx \left( \frac{y_2 - y_1}{2\sigma_X \sqrt{\kappa_X}} \right)^2 \sigma_X^2 + \frac{1}{4} \left( \frac{y_2 - 2Y_c + y_1}{\sigma_X^2 \kappa_X} \right)^2 (\kappa_X - 1) \sigma_X^4 \\
 &\approx \frac{P_i}{2} (y_2 - y_1)^2 + \frac{P_i}{2} (1 - 2P_i) (y_2 - 2Y_c + y_1)^2 \\
 &\approx \frac{P_i}{2} (d_1^2 + d_2^2) - P_i d_1 d_2 + \frac{P_i}{2} (1 - 2P_i) (d_1 + d_2)^2 \\
 &\approx P_i (1 - P_i) (d_1^2 + d_2^2) - P_i d_1 d_2
 \end{aligned} \tag{79}$$

Now, comparing (79) to (78) for a single variable shows that the coefficient multiplying  $(d_1^2 + d_2^2)$  in both formulations is identical. It means that this approach is closer to a second-

order Taylor series approximation than a first-order. Bolle's statement claiming that his method is able to better capture non-linear effects is only partly verified. Indeed, the coefficient multiplying  $d_1 d_2$  is still not the same in both formulations.

For the third-order centered moment, the Taylor series expansion (61) can be developed using the finite difference approximation of the first derivative (76):

$$\begin{aligned}
 \gamma_Y \sigma_Y^3 &\approx \sum_{i=1}^N \left( \frac{\partial f(x_{i,c})}{\partial x_i} \right)^3 E \left[ (X_i - \bar{X})^3 \right] \\
 &\approx \sum_{i=1}^N \left( \frac{y_{i,2} - y_{i,1}}{2\sigma_{X_i} \sqrt{\kappa_{X_i}}} \right)^3 \gamma_{X_i} \sigma_{X_i}^3 \\
 &\approx \sum_{i=1}^N \frac{\gamma_{X_i}}{8\kappa_{X_i}^{3/2}} (y_{i,2} - y_{i,1})^3 \\
 &\approx \sum_{i=1}^N \frac{\gamma_{X_i}}{\sqrt{\kappa_{X_i}}} \frac{1}{4P_i} (d_{i,2} - d_{i,1})^3 \\
 &\approx \sum_{i=1}^N \frac{\gamma_{X_i}}{\sqrt{\kappa_{X_i}}} \frac{1}{4P_i} (d_{i,2}^3 - d_{i,1}^3 + 3d_{i,2}d_{i,1}^2 - 3d_{i,2}^2d_{i,1})
 \end{aligned} \tag{80}$$

Formula (80) has to be compared to the PMM formula (68) which can be expanded as:

$$\begin{aligned}
 \gamma_Y \sigma_Y^3 &= \sum_{i=1}^N E \left[ d\mu_i^3 \right] \\
 &= \sum_{i=1}^N P_i \left( (y_{i,1} - \bar{y}_i)^3 + (y_{i,2} - \bar{y}_i)^3 \right) + P_c (Y_c - \bar{y}_i)^3 \\
 &= \sum_{i=1}^N P_i \left( \left( (1 - P_i)d_{i,1} - P_i d_{i,2} \right)^3 + \left( (1 - P_i)d_{i,2} - P_i d_{i,1} \right)^3 \right) + P_c \left( -P_i (d_{i,1} + d_{i,2}) \right)^3 \\
 &= \sum_{i=1}^N P_i \left( \left( (1 - P_i)^3 - P_i^3 \right) (d_{i,1}^3 + d_{i,2}^3) + 3P_i (-2P_i^2 + 3P_i - 1) (d_{i,1}d_{i,2}^2 + d_{i,1}^2d_{i,2}) \right) - P_c P_i (d_{i,1} + d_{i,2})^3 \\
 &= \sum_{i=1}^N P_i \left( (1 - P_i)^3 - P_i^3 - P_c \right) (d_{i,1}^3 + d_{i,2}^3) - 3P_i (2P_i^3 - 3P_i^2 + P_i + P_c) (d_{i,1}d_{i,2}^2 + d_{i,1}^2d_{i,2})
 \end{aligned} \tag{81}$$

It appears that both methods ((80) and (81)) do not lead to similar results. A higher-order analysis could be an interesting alternative study but it is a cumbersome analytical task which is not lead in this thesis.

#### 2.4.3.2 Extension of PMM to skewed distributions

The approach developed in previous section was generalized for skewed random variables (Franceschini, Tsai, et al. 2012). The evaluations of the function  $f(\mathbf{X})$  is done at concentration

points defined by Hong three-point method (46) (see Figure 18).  $Y$  moments are then computed according to the perturbation moment method. A few changes should be done to the original method to take into account the asymmetry in the evaluation points and weights (see Figure 19).

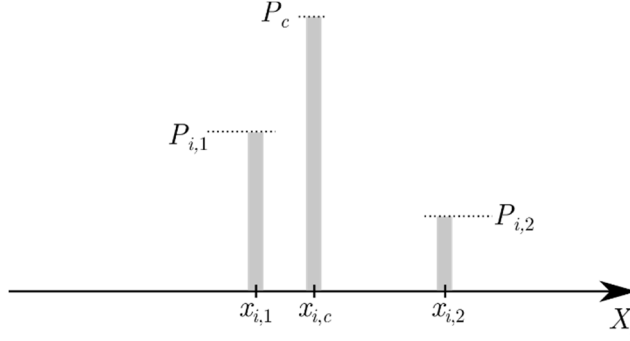


Figure 18: Concentration points positions and weights for PMM (skewed variables)

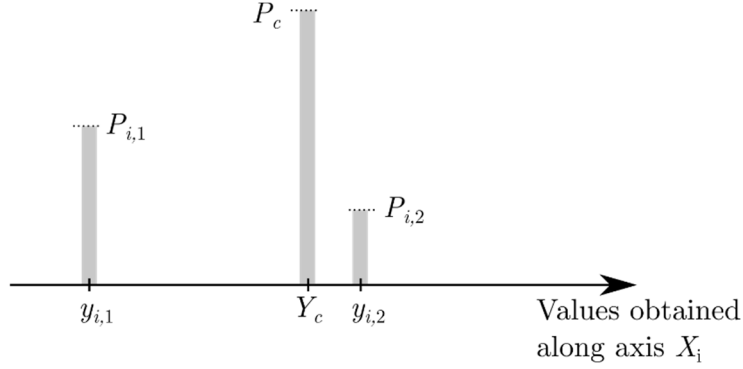


Figure 19: Schematic view of PMM (skewed variables)

The mean is computed from the central value plus the perturbations for each axis:

$$\bar{Y} = Y_c + \sum_{i=1}^N (P_{i,1} d_{i,1} + P_{i,2} d_{i,2}) \quad (82)$$

Equation (82) can be developed in the same way as (67) to show that the computation of the mean is equivalent to a point estimate method.

For second-order and third-order moments, only the computation of perturbation moments changes:

$$E[d\mu_i^m] = P_{i,1} (y_{i,1} - \bar{y}_i)^m + P_{i,2} (y_{i,2} - \bar{y}_i)^m + P_c (Y_c - \bar{y}_i)^m \quad m = 2, 3 \quad (83)$$

Where the local mean is now computed as:

$$\bar{y}_i = P_{i,1} y_{i,1} + P_{i,2} y_{i,2} + P_c Y_c \quad (84)$$

The variance can be computed as

$$\sigma_Y^2 = \sum_{i=1}^N P_{i,1} (y_{i,1} - \bar{y}_i)^2 + P_{i,2} (y_{i,2} - \bar{y}_i)^2 + P_c (Y_c - \bar{y}_i)^2 \quad (85)$$

The third-order moment can be computed as

$$E\left[\left(Y - \bar{Y}\right)^3\right] = \sum_{i=1}^N P_{i,1} (y_{i,1} - \bar{y}_i)^3 + P_{i,2} (y_{i,2} - \bar{y}_i)^3 + P_c (Y_c - \bar{y}_i)^3 \quad (86)$$

In the paper (Franceschini, Tsai, et al. 2012), the variance is computed as<sup>6</sup>

$$\begin{aligned} \sigma_Y^2 &= \sum_{i=1}^N E\left[d\mu_i^2\right] \\ &= \sum_{i=1}^N P_{i,1} (y_{i,1} - Y_c)^2 + P_{i,2} (y_{i,2} - Y_c)^2 - (P_c + P_{i,1} + P_{i,2}) e_i^2 \end{aligned} \quad (87)$$

where  $e_i$  is the generalization of (71):

$$e_i = \bar{y}_i - Y_c = (P_{i,1} y_{i,1} + P_{i,2} y_{i,2} + P_c Y_c) - Y_c \quad (88)$$

Franceschini et al. compare equation (87) to the parallel axis theorem used in mechanics. They state that the second-order moment is first computed centered on  $Y_c$  and then corrected according to weight and the distance between  $Y_c$  and the local mean  $\bar{y}_i$  (i.e.  $e_i$ ). Franceschini et al. do not develop further for higher order moments.

Developing analytically equation (87) yields to formula (85). The mathematical development is reproduced in appendix A.3. If one attempts to generalize (87) for third-order moment by replacing exponents <sup>2</sup> by exponents <sup>3</sup>, it does not correspond to (86).

In following developments and results presented in this thesis, the generalized formulae (82)-(86) are preferred.

## 2.4.4 Stochastic Response Surface Method

The last uncertainty analysis method presented in this section is the one that results from the discrete evaluation method presented in section 2.3.3. Once the unknowns  $a_i$  are determined for equation (48), Monte-Carlo simulations are performed on this equation (Isukapalli et al. 2000). Results can be used to determine statistical moments of the output random variable through moments method, L-moments method or maximum likelihood estimation.

---

<sup>6</sup> In Franceschini's papers, the proposed formula is not the one reproduced in (87). It misses  $P_c$  in the coefficient that multiplies  $e_i^2$ . When  $P_c$  is added (as in (87)) it degenerates correctly to Bolle's approach for symmetrical random variables.

### 2.4.5 Summary

In order to summarize uncertainty analysis methods, Figure 20 is produced. It shows that several methods exist to generate discrete points. The model is evaluated for all of these points. Then, depending on the chosen method, the model results are processed in order to output moments and/or a full discrete distribution.

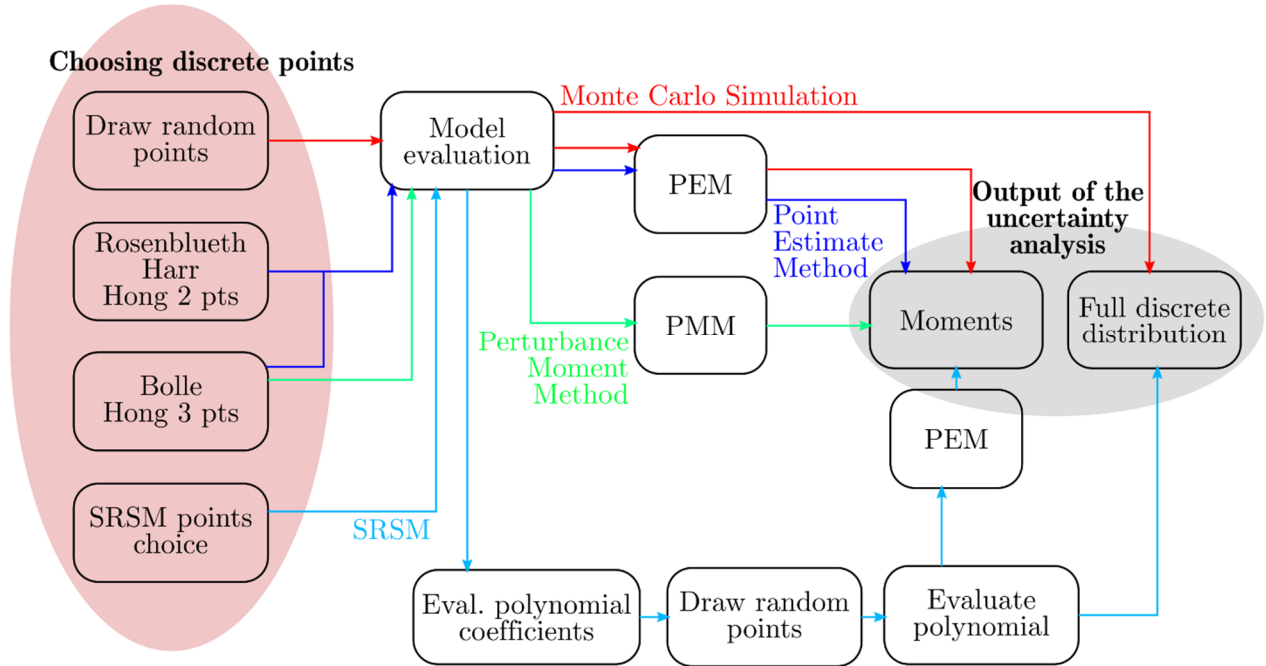


Figure 20: Usage of uncertainty analysis methods summarized in a flowchart

## 2.5 Uncertainty analysis methods comparison

Uncertainty analysis methods exposed in this thesis rely, among other things, on the discretization of the random variable space. Monte Carlo method uses a large number of estimation points based on pseudo-random number generators while Rosenblueth, Harr, Bolle and Hong methods use only a limited amount of points positioned and weighted to respect the first moments of the input random variables. SRSM is similar to the latter methods except that estimation points are used to determine coefficients of a sum of Hermite polynomials.

Once estimation points are chosen, the value of the output can be computed at these locations. For Monte Carlo estimations, each point has the same weight and the output pdf can be determined through various techniques (e.g. moments method or maximum likelihood estimation). Point estimates method and perturbation moment method determine directly first statistical moments of the output based on weighted point estimations. These two methods however differ in the way they compute statistical moments, except for the mean. For SRSM,

a large number of evaluations of the polynomial is performed. Each evaluation has the same weight. A comparison between methods is provided at Table 5.

All the methods presented earlier are tested in subsections 2.5.1 and 2.5.2. First, academic tests are performed on polynomials. This very simple kind of model allows to compare results with analytical solutions. The second test concerns a bungee jump. Since uncertainties arise from various sources, this case exemplifies multivariate uncertainty analysis. Thanks to a simplified equation, we compare the results obtained with all the techniques presented in this thesis.

<b>Methods</b>	<b>Result of the analysis</b>	<b>Comments</b>
MCS	Moments and/or pdf	Requires a large number of evaluations of the full model. Same weight for each evaluation point.
PEM	Moments	Limited number of evaluations of the full model located at concentration points. For some cases, weights and positions of concentration points can be judged as unphysical (negative weights or points far from the mean).
PMM	Moments	Limited number of evaluations of the full model located at concentration points. Weights and positions of each concentration point are computed according to the first four statistical moments. Weights can be negative. Works only for <b><u>independent</u></b> random variables.
SRSSM	Moments and/or pdf	Limited number of evaluations of the full model located at concentration points. This step allows to fit coefficients of a polynomial that is evaluated thanks to the Monte Carlo method.

*Table 5: Comparison between uncertainty analysis methods*

### 2.5.1 Polynomial examples

For the polynomial examples, three univariate and a multivariate cases are developed.

A single random variable problem will be considered first. Polynomials of degrees 1 to 3 will be tested. The mean, the variance and the skewness coefficient will be computed analytically (if possible), by a Taylor series expansion (first and second order), by Monte Carlo simulations (with up to  $10^6$  draws), by PEM, by PMM and by SRSSM (with a second degree polynomial).

The code used for this section is freely available at <https://gitlab.uliege.be/HECE/uncertanex> .

The degree 1 polynomial

$$Y = aX + b \quad (89)$$

links linearly the random variable  $X$  to the output  $Y$ . The random variable  $X$  is characterized by a normal distribution with a mean  $\bar{X} = 2$ , a variance  $\sigma_X^2 = 0.5$  and a skewness coefficient  $\gamma_X = 0$ . The mean, the variance and the skewness coefficient can be computed analytically:

$$\begin{aligned} \bar{Y} &= \int (aX + b) p_X(x) dx \\ &= a\bar{X} + b \end{aligned} \quad (90)$$

$$\begin{aligned} \sigma_Y^2 &= \int [(aX + b) - (a\bar{X} + b)]^2 p_X(x) dx \\ &= \int [aX - a\bar{X}]^2 dx \\ &= a^2 \sigma_X^2 \end{aligned} \quad (91)$$

$$\begin{aligned} \gamma_Y \sigma_Y^3 &= \int [(aX + b) - (a\bar{X} + b)]^3 p_X(x) dx \\ &= \int a^3 [X - \bar{X}]^3 dx \\ &= a^3 \gamma_X \sigma_X^3 \end{aligned} \quad (92)$$

Thanks to the analytical derivation of (89), an analytical expression of the Taylor series expansion for the mean (first (93) and second (94) order), the variance (first (95) and second (96) order) and the skewness coefficient (first order (97)) can be developed:

$$\bar{Y} = Y_c = a\bar{X} + b \quad (93)$$

$$\begin{aligned} \bar{Y} &= Y_c + \frac{1}{2} \frac{d^2 Y}{dX^2} \sigma_X^2 \\ &= a\bar{X} + b \end{aligned} \quad (94)$$

$$\sigma_Y^2 = \left( \frac{dY}{dX} \Big|_{\bar{X}} \right)^2 \sigma_X^2 = a^2 \sigma_X^2 \quad (95)$$

$$\begin{aligned} \sigma_Y^2 &= \left( \frac{dY}{dX} \Big|_{\bar{X}} \right)^2 \sigma_X^2 + \frac{dY}{dX} \Big|_{\bar{X}} \frac{d^2 Y}{dX^2} \Big|_{\bar{X}} E[d^3] + \frac{1}{4} \left( \frac{d^2 Y}{dX^2} \Big|_{\bar{X}} \right)^2 (E[d^4] - \sigma_X^4) \\ &= a^2 \sigma_X^2 \end{aligned} \quad (96)$$

$$\gamma_Y \sigma_Y^3 = \left( \frac{dY}{dX} \Big|_{\bar{X}} \right)^3 \gamma_X \sigma_X^3 = a^3 \gamma_X \sigma_X^3 \quad (97)$$

Equations (93)-(97) are identical to analytical solutions (90)-(92). Monte Carlo, Point Estimate Method, Perturbance Moment Method and Stochastic Response Surface Method are applied according to the descriptions in sections 2.3 and 2.4. Results (for  $a = b = 2$ ) of the mean,

variance and skewness coefficient (Table 6 and Figure 21) show that all methods give the analytical values. A small difference is observed for Monte-Carlo and SRSM. However they converge toward the analytical value.

	nb eval.	$\bar{Y}$	$\sigma_Y^2$	$\gamma_Y$
Analytical	-	6	2	0
Taylor 1 <sup>st</sup> order	1 pt	6	2	0
Taylor 2 <sup>nd</sup> order	1 pt	6	2	-
Monte Carlo	10 <sup>6</sup> pts	6.0006	1.9994	0.0028
PEM	3 pts	6	2	0
PMM	3 pts	6	2	0
SRSM	5 (+ 10 <sup>6</sup> pts*)	5.9997	1.9962	0.0025

*Table 6: Numerical values of the moments of the output with various uncertainty analysis methods (degree 1 polynomial) - \*: 10<sup>6</sup> evaluations of the polynomial for Monte Carlo simulation*

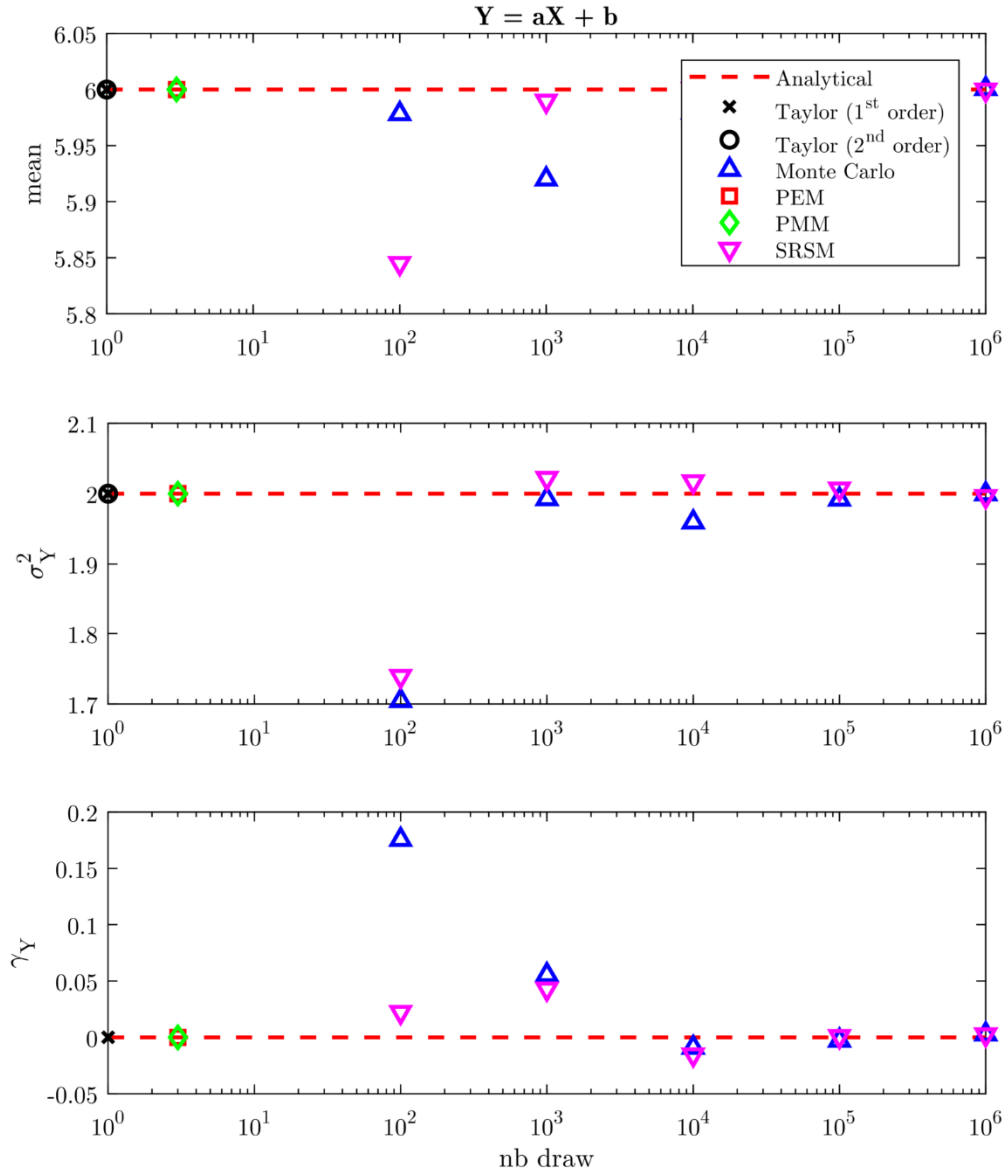


Figure 21: Values of the mean, variance and skewness coefficient for degree 1 polynomial and for different uncertainty analysis methods

When a degree 2 polynomial is considered

$$Y = aX^2 + bX + c \quad (98)$$

with the same characteristics for  $X$  as previously, an analytical solution can be developed for the mean:

$$\begin{aligned} \bar{Y} &= \int (aX^2 + bX + c) p_X(x) dx \\ &= E[X^2] + b\bar{X} + c \\ &= a\sigma_X^2 + a\bar{X}^2 + b\bar{X} + c \end{aligned} \quad (99)$$

Analytical expressions of Taylor series can be developed:

$$\bar{Y} = a\bar{X}^2 + b\bar{X} + c \quad (1^{\text{st}} \text{ order}) \quad (100)$$

$$\bar{Y} = a\bar{X}^2 + b\bar{X} + c + a\sigma_X^2 \quad (2^{\text{nd}} \text{ order}) \quad (101)$$

$$\sigma_Y^2 = (2a\bar{X} + b)^2 \sigma_X^2 \quad (1^{\text{st}} \text{ order}) \quad (102)$$

$$\begin{aligned} \sigma_Y^2 &= (2a\bar{X} + b)^2 \sigma_X^2 + a^2 (3\sigma_X^4 - \sigma_X^4) \quad (2^{\text{nd}} \text{ order}) \\ &= (2a\bar{X} + b)^2 \sigma_X^2 + 2a^2 \sigma_X^4 \end{aligned} \quad (103)$$

$$\gamma_Y \sigma_Y^3 = (2a\bar{X} + b)^3 \sigma_X^3 \gamma_X \quad (1^{\text{st}} \text{ order}) \quad (104)$$

Results for  $a = b = c = 2$  are given in Table 7 and Figure 22 for various analysis methods. It appears that all methods, except first order Taylor series, reach the analytical value for the mean. Concerning the variance, second order Taylor series, MC, PEM, PMM and SRSM converge toward 52. Finally, MC, PEM, PMM and SRSM produce similar values.

Since a second degree polynomial is used in the SRSM method (same degree as polynomial (98) ), it is normal to observe a convergence between MC and SRSM. This means that the fitting of the SRSM polynomial corresponds to equation (98).

	nb eval.	$\bar{Y}$	$\sigma_Y^2$	$\gamma_Y$
Analytical	-	15	-	-
Taylor 1 <sup>st</sup> order	1 pt	14	50	0
Taylor 2 <sup>nd</sup> order	1 pt	15	52	-
Monte Carlo	10 <sup>6</sup> pts	15.0026	52.0368	0.8244
PEM	3 pts	15	52	0.8054
PMM	3 pts	15	52	0.8054
SRSM	5 (+ 10 <sup>6</sup> pts*)	14.9963	51.9890	0.8224

*Table 7: Numerical values of the moments of the output with various uncertainty analysis methods (degree 2 polynomial) - \*: 10<sup>6</sup> evaluations of the polynomial for Monte Carlo simulation*

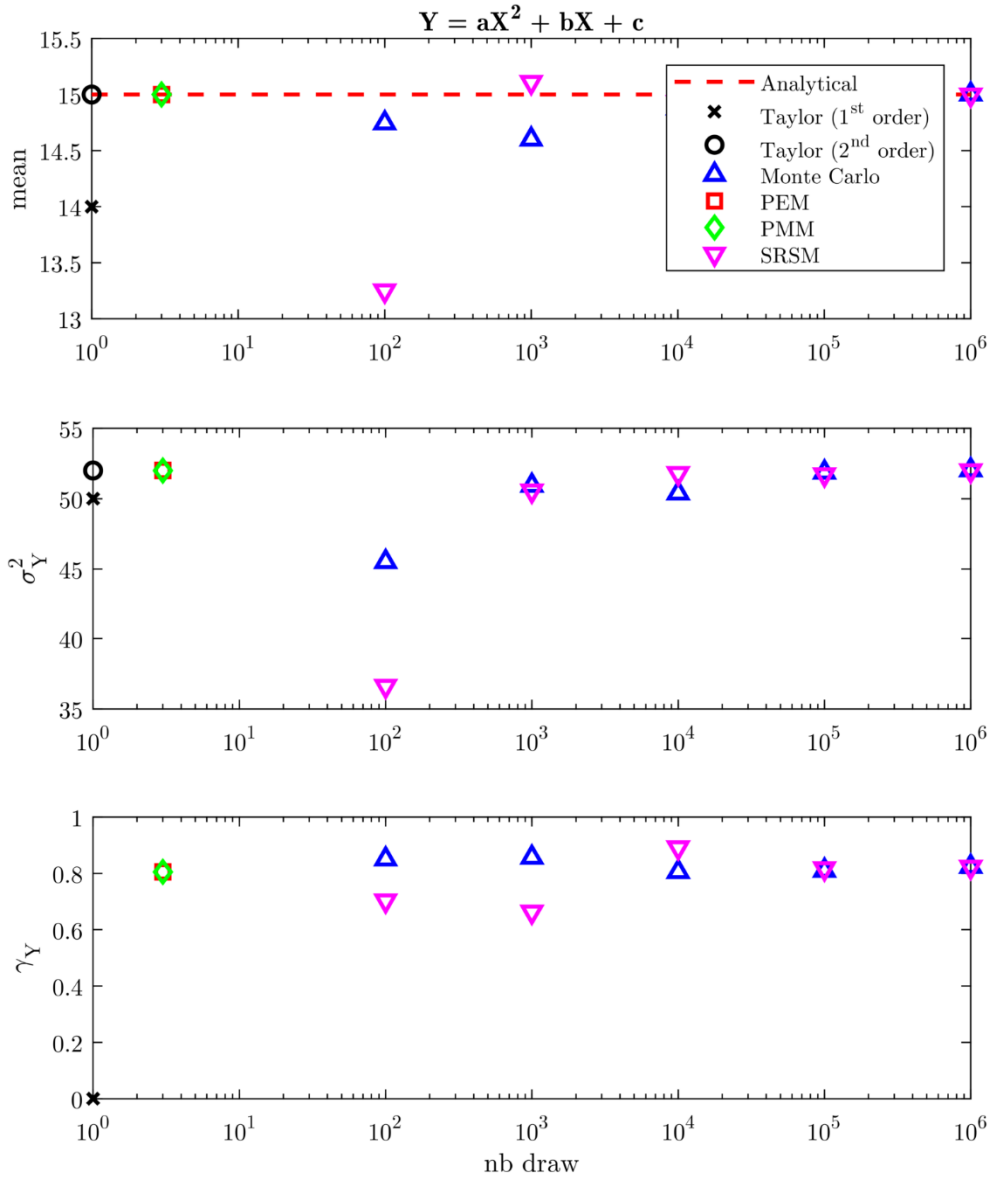


Figure 22: Values of the mean, variance and skewness coefficient for degree 2 polynomial and for different uncertainty analysis methods

For the degree 3 polynomial

$$Y = aX^3 + bX^2 + cX + d \quad (105)$$

no analytical expression for the mean, the variance or the skewness coefficient could be developed. The analytical expressions for the Taylor series expansions are:

$$\bar{Y} = a\bar{X}^3 + b\bar{X}^2 + c\bar{X} + d \quad (1^{\text{st}} \text{ order}) \quad (106)$$

$$\bar{Y} = a\bar{X}^3 + b\bar{X}^2 + c\bar{X} + d + (3a\bar{X} + b)\sigma_X^2 \quad (2^{\text{nd}} \text{ order}) \quad (107)$$

$$\sigma_Y^2 = (3a\bar{X}^2 + 2b\bar{X} + c)^2 \sigma_X^2 \quad (1^{\text{st}} \text{ order}) \quad (108)$$

$$\sigma_Y^2 = (3a\bar{X}^2 + 2b\bar{X} + c)^2 \sigma_X^2 + (3a\bar{X} + b)^2 \sigma_X^4 \quad (2^{\text{nd}} \text{ order}) \quad (109)$$

$$\gamma_Y \sigma_Y^3 = (3a\bar{X}^2 + 2b\bar{X} + c)^3 \gamma_Y \sigma_Y^3 \quad (1^{\text{st}} \text{ order}) \quad (110)$$

Results for  $a = b = c = d = 2$  are given in Table 8 and Figure 23 for various analysis methods. Considering that Monte-Carlo is the reference solution, PEM and PMM are very close to reference for the mean and the variance but their skewness estimation is slightly further. Unlike previous polynomials, SRSM does not converge toward the MC results since the SRSM polynomial degree is too low (degree 2) to capture the polynomial degree of equation (105).

	nb eval.	$\bar{Y}$	$\sigma_Y^2$	$\gamma_Y$
Analytical	-	-	-	-
Taylor 1 <sup>st</sup> order	1 pt	30	578	0
Taylor 2 <sup>nd</sup> order	1 pt	37	676	-
Monte Carlo	10 <sup>6</sup> pts	37.0106	786.79905	1.6675
PEM	3 pts	37	782.5	1.3447
PMM	3 pts	37	782.5	1.3447
SRSM	5 (+ 10 <sup>6</sup> pts*)	37.0019	765.2092	1.4514

Table 8: Numerical values of the moments of the output with various uncertainty analysis methods (degree 3 polynomial) - \*: 10<sup>6</sup> evaluations of the polynomial for Monte Carlo simulation

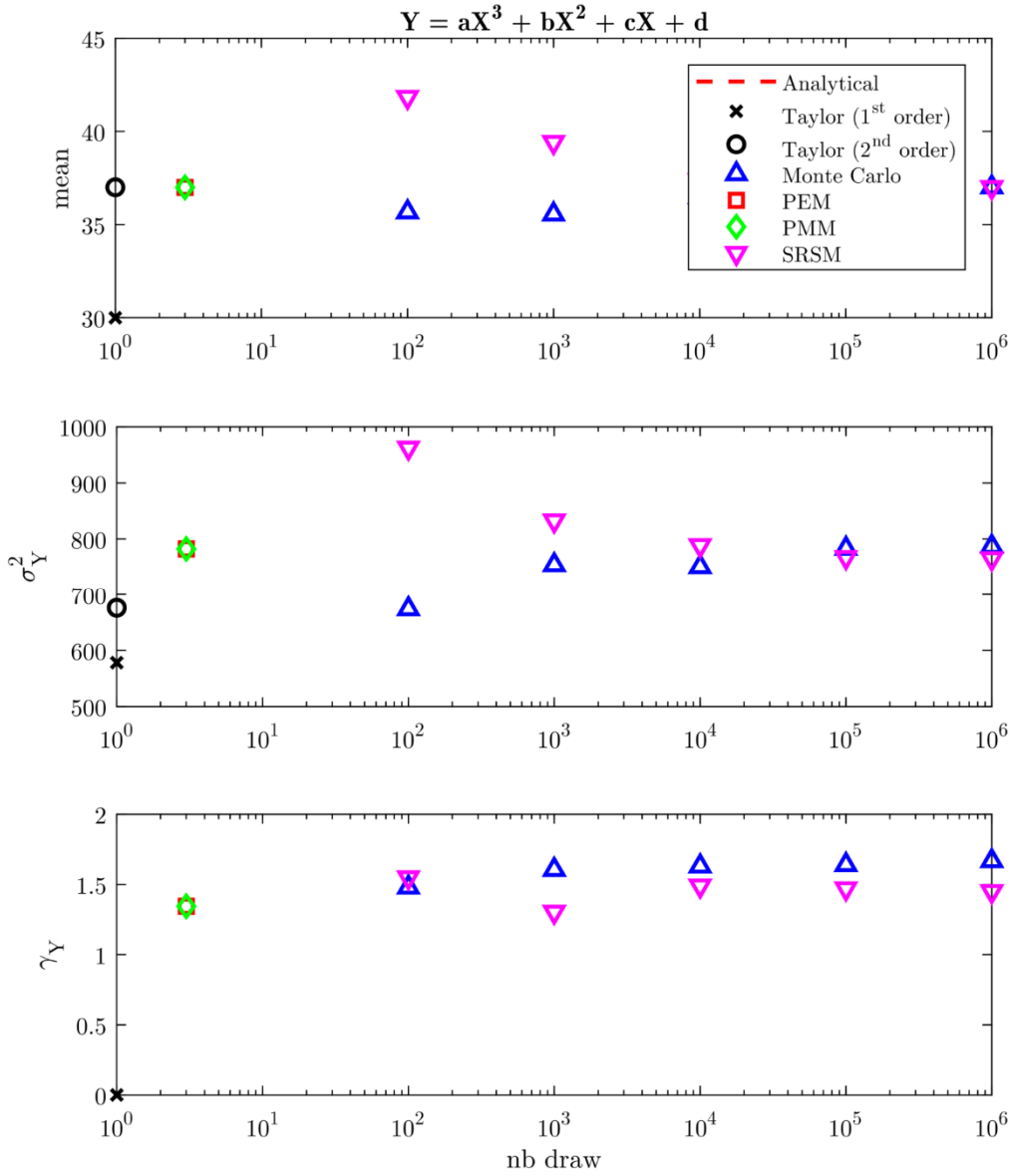


Figure 23: Values of the mean, variance and skewness coefficient for degree 3 polynomial and for different uncertainty analysis methods

Globally, PEM and PMM give good estimations of the mean, variance and skewness coefficients for the tested polynomials. When the degree of the polynomial increases, PEM and PMM give better results than Taylor series expansions. It can be also noticed that PEM and PMM are equivalent for the tested polynomials.

To analyze why PEM and PMM give equivalent results, a degree 2 polynomial with two random variables is tested:

$$Z = aX^2 + bY^2 + cXY + dX + eY + f \quad (111)$$

With  $\bar{X} = 2$ ,  $\bar{Y} = 0$ ,  $\sigma_X^2 = 0.5$ ,  $\sigma_Y^2 = 2$  and  $X$  and  $Y$  have a normal distribution and are not correlated. Results are given in Table 9 and Figure 24.

It appears that PEM and PMM now differ for the variance and the skewness coefficient. Considering Monte Carlo as the reference, PMM is the method that produces the best estimation of the variance and the skewness coefficient.

	nb eval.	$\bar{Z}$	$\sigma_Z^2$	$\gamma_Z$
Taylor 1 <sup>st</sup> order	1 pt	14	122	0
Taylor 2 <sup>nd</sup> order	1 pt	19	-	-
Monte Carlo	10 <sup>6</sup> pts	18.9956	160.1692	1.6840
PEM	5 pts	19	148	0.7120
PMM	5 pts	19	156	1.1076
SRSM	13 (+ 10 <sup>6</sup> pts)	18.9901	159.6819	1.6783

*Table 9: Numerical values of the moments of the output with various uncertainty analysis methods (degree 2 bivariate polynomial) - \*: 10<sup>6</sup> evaluations of the polynomial for Monte Carlo simulation*

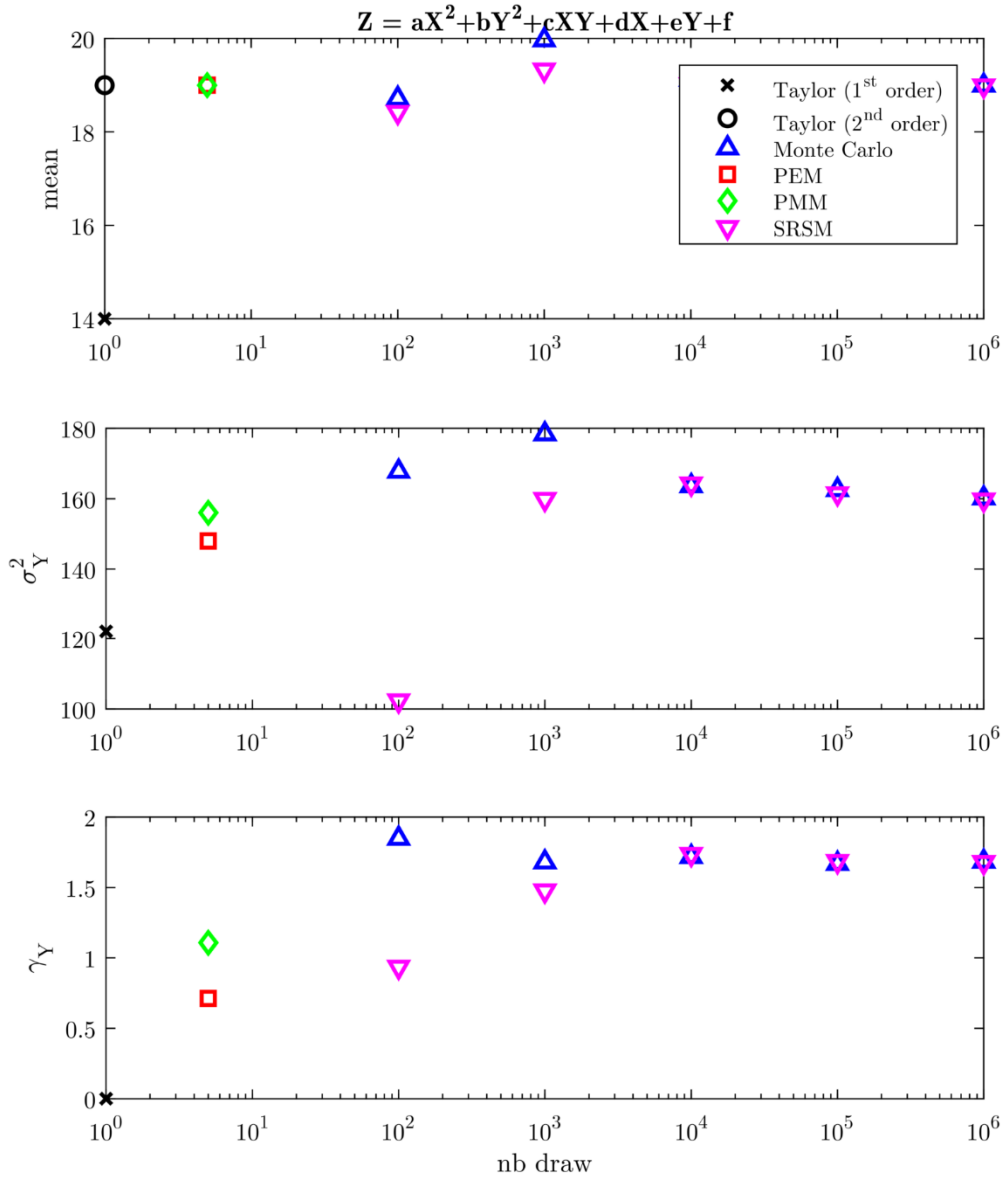


Figure 24: Values of the mean, variance and skewness coefficient for degree 2 polynomial (bivariate) and for different uncertainty analysis methods

### 2.5.2 The bungee jump example

The example of a bungee jump is used to illustrate each method and how they perform when several sources of uncertainties are considered. It is inspired from (Saltelli et al. 2004) and from the workshop on “Uncertainty analysis and global sensitivity analysis” given by Prof. Muñoz-Carpena at Université Catholique de Louvain (6/11/2017). The code used for this section is freely available at <https://gitlab.uliege.be/HECE/uncertanex>.

The minimum distance between the jumper and the ground can be described as<sup>7</sup>:

$$h_{min} = H - \frac{2 M g}{k n} \quad (112)$$

Where  $H$  is the distance between the soil and the jumping point [m],  $M$  is the mass of the jumper [kg],  $g$  is the acceleration of gravity [m/s<sup>2</sup>],  $k$  is the stiffness of the rope [N/m] and  $n$  is the number of strands in the rope [-]. The four unknowns ( $H$ ,  $M$ ,  $k$  and  $n$ , also denoted  $\mathbf{X}$  in vector notation) are considered to be uncorrelated random variables with symmetrical distribution:

$$\begin{aligned} \bar{H} &= 50 & \sigma_H &= 5 \\ \bar{M} &= 70 & \sigma_M &= 3 \\ \bar{k} &= 1.5 & \sigma_k &= 0.01 \\ \bar{n} &= 30 & \sigma_n &= 5 \end{aligned} \quad (113)$$

Monte-Carlo simulations require to draw random values of  $H$ ,  $M$ ,  $k$  and  $n$ . For each point  $\mathbf{x} = (H \ M \ k \ n)^T$ ,  $h_{min}$  can be computed. This was done for 100 up to  $10^7$  evaluation points. Then, moments of  $h_{min}$  are computed. Results for Monte Carlo are shown with blue dots in Figure 25 and numerical values are reproduced in Table 10. In Figure 25, it appears that the moments converge to steady values when the number of points increases. Figure 26 shows in blue the pdf obtained with a gamma law fitted with the moments computed previously.

	nb eval.	$\bar{h}_{min}$ [m]	$\sigma_{h_{min}}$ [m]	$\gamma_{h_{min}}$ [-]
Monte Carlo	$10^7$ pts	18.5480	7.7803	-0.5927
Taylor series	1 pt	18.6309	7.2544	1.9990
PEM	9 pts	18.5538	7.6976	-0.2148
PMM	9 pts	18.5538	7.6978	-0.3781
SRSM	41 (+ $10^7$ pts*)	18.5655	7.5413	-0.3656

Table 10: Numerical values of the moments of the output with various uncertainty analysis methods - \*:  $10^7$  evaluations of the polynomial for Monte Carlo simulation

<sup>7</sup> Considering an initial rope length of 0 m.

The Taylor series expansion is applied to this example. Derivatives in (57), (59) and (61) are computed analytically:

$$\begin{aligned}
 \frac{\partial h_{min}}{\partial H} &= 1 & ; & \frac{\partial^2 h_{min}}{\partial H^2} = 0 \\
 \frac{\partial h_{min}}{\partial M} &= -\frac{2g}{kn} & ; & \frac{\partial^2 h_{min}}{\partial M^2} = 0 \\
 \frac{\partial h_{min}}{\partial k} &= \frac{2Mg}{k^2 n} & ; & \frac{\partial^2 h_{min}}{\partial k^2} = -\frac{4Mg}{k^3 n} \\
 \frac{\partial h_{min}}{\partial n} &= \frac{2Mg}{kn^2} & ; & \frac{\partial^2 h_{min}}{\partial n^2} = -\frac{4Mg}{kn^3}
 \end{aligned} \tag{114}$$

These derivatives are evaluated at the central point whose coordinates are given in (113). Results are available in Table 10 and Figure 25.

To illustrate the point estimate method, Bolle's approach (43) is chosen. As described in this document, moments are computed from the  $2N+1=9$  evaluation points. The three first statistical moments are depicted with red dots in Figure 25. The pdf in Figure 26 is a gamma law fitted in order to reproduce the statistical moments obtained with PEM.

For the perturbation moment method, the same evaluation points as PEM are chosen. One can observe an exact same mean as obtained with PEM. This was already proven mathematically with (67). Standard deviation is close but not identical while the skewness coefficient is closer to Monte Carlo simulations (our reference method) with PMM than PEM. The pdf in Figure 26 is fitted according to the same method as for PEM.

For SRSM and  $N = 4$ , 15 parameters need to be determined:

$$\begin{aligned}
 h_{min} &= a_0 + a_1 T_1 + a_2 T_2 + a_3 T_3 + a_4 T_4 \\
 &+ a_5 T_1 T_2 + a_6 T_1 T_3 + a_7 T_1 T_4 + a_8 T_2 T_3 + a_9 T_2 T_4 + a_{10} T_3 T_4 \\
 &+ a_{11} (T_1^2 - 1) + a_{12} (T_2^2 - 1) + a_{13} (T_3^2 - 1) + a_{14} (T_4^2 - 1)
 \end{aligned} \tag{115}$$

To do so, 41 evaluations points are chosen according to the algorithm described above. These points are:

$$\begin{aligned}
 &(0 \ 0 \ 0 \ 0) \\
 &(-1 \ 0 \ 0 \ 0), (1 \ 0 \ 0 \ 0), (0 \ -1 \ 0 \ 0), (0 \ 1 \ 0 \ 0), \dots \\
 &(-1 \ -1 \ 0 \ 0), (-1 \ 1 \ 0 \ 0), (1 \ -1 \ 0 \ 0), (1 \ 1 \ 0 \ 0), (-1 \ 0 \ -1 \ 0), \dots \\
 &(-\sqrt{3} \ 0 \ 0 \ 0), (\sqrt{3} \ 0 \ 0 \ 0), (0 \ -\sqrt{3} \ 0 \ 0), (0 \ \sqrt{3} \ 0 \ 0), \dots
 \end{aligned} \tag{116}$$

With a least square method, the system

$$\mathbf{a} = \left(\mathbf{T}^T \mathbf{T}\right)^{-1} \mathbf{T}^T \mathbf{h}_{min} \quad (117)$$

is solved, with  $\mathbf{a}$  the vector of polynomial coefficients in (115),  $\mathbf{h}_{min}$  the vector of 41  $h_{min}$  values computed at the evaluation points and  $\mathbf{T}$  a matrix that contains the Hermite polynomial values at the evaluation points such that:

$$\mathbf{h}_{min} = \mathbf{T} \mathbf{a}$$

$$\begin{pmatrix} h_{min,0} \\ h_{min,1} \\ \vdots \\ h_{min,40} \end{pmatrix} = \begin{pmatrix} 1 & T_{1,0} & \cdots & (T_{4,0}^2 - 1) \\ 1 & T_{1,1} & \cdots & (T_{4,2}^2 - 1) \\ \vdots & \vdots & \ddots & \vdots \\ 1 & T_{1,40} & \cdots & (T_{4,40}^2 - 1) \end{pmatrix} \begin{pmatrix} a_0 \\ a_1 \\ \vdots \\ a_{14} \end{pmatrix} \quad (118)$$

Solving (117) yields to these polynomial coefficients:

$$\mathbf{a} = \begin{pmatrix} 18.5647 \\ 5.0000 \\ -1.3155 \\ 0.2046 \\ 5.3272 \\ 0 \\ 0 \\ 0 \\ 0.0087 \\ 0.2242 \\ -0.0349 \\ -0.0082 \\ -0.0082 \\ -0.0096 \\ -0.9142 \end{pmatrix} \quad (119)$$

It appears that the coefficients multiplying  $T_1 T_2$ ,  $T_1 T_3$  and  $T_1 T_4$  are strictly equal to 0 but the coefficients in front of the other crossed terms are not 0. This shows that cross terms should be kept even if uncorrelated problems are considered. The pdf for SRSM is also fitted with the moment method (Figure 26).

This example shows that all methods give similar results. Monte Carlo is considered as the reference solution since it relies on a high number of evaluations of the model. Compared to this reference PMM is the closest approach. SRSM comes second and gives results very close to PMM. PEM gives good estimations of the two first moments but is behind for the skewness coefficient. Finally, Taylor series expansion gives good approximation for the mean and the

standard deviation. However, its estimation of the skewness is completely different from previous methods.

Considering the number of evaluations compared to the accuracy of the results, PMM is the best method for this example. Indeed, it requires only 9 evaluations while SRSM requires 41 evaluations of the full model and approximately  $10^4$  evaluations (at least) of the polynomial.

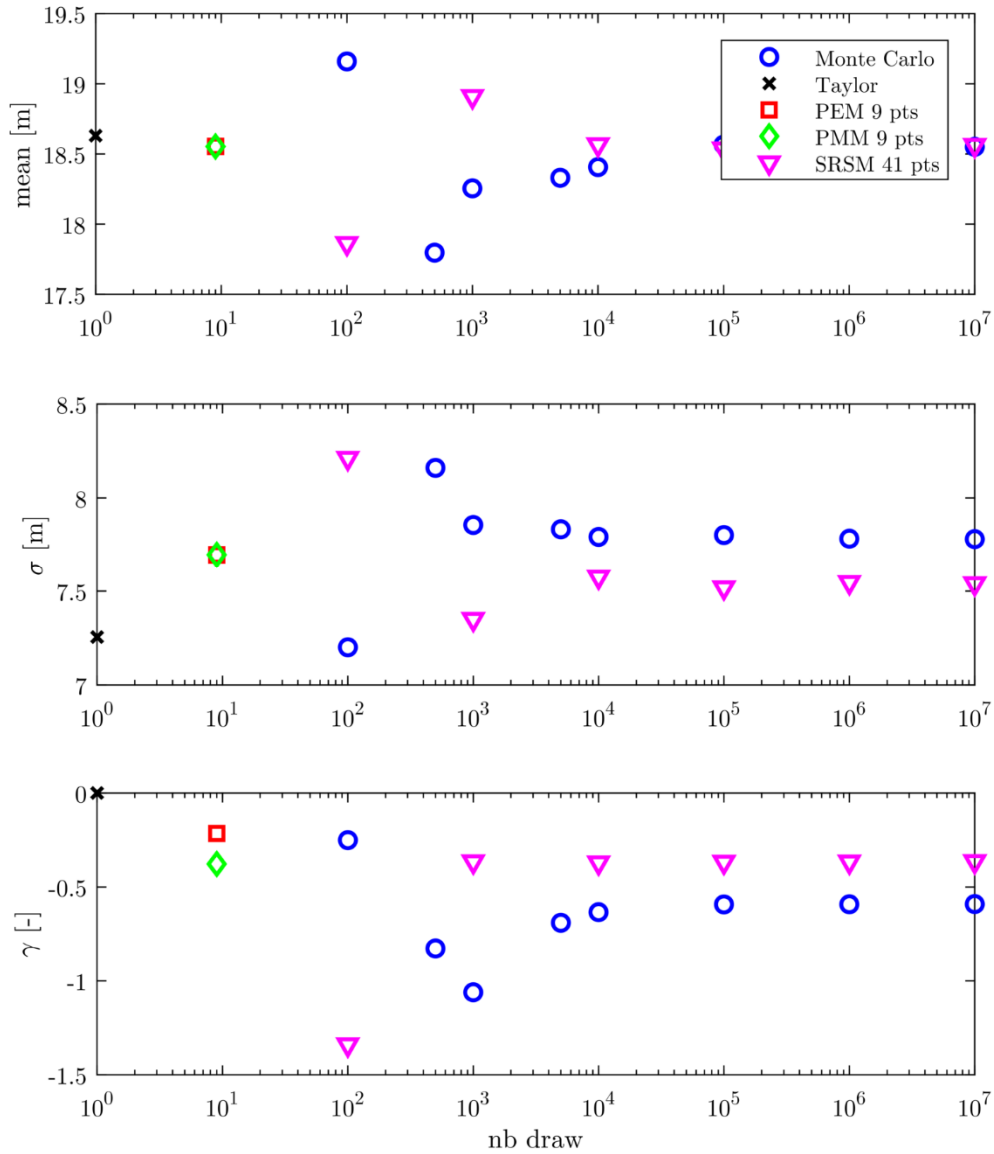


Figure 25: Values of the mean, standard deviation and skewness coefficient for the bungee jump example and for different uncertainty analysis methods

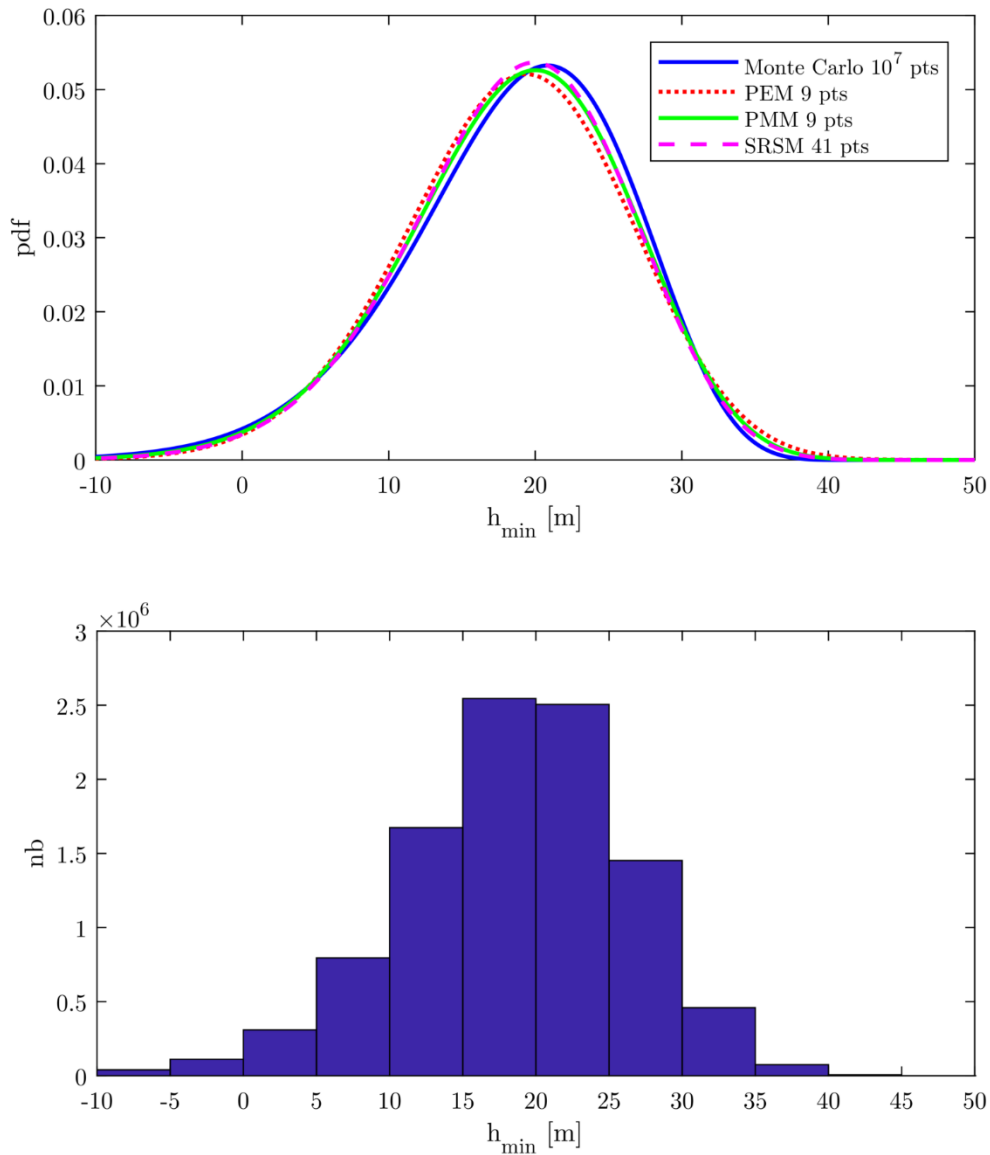


Figure 26: Probability density functions (upper) for the bungee jump example and for different uncertainty analysis methods and histogram obtained with the MC method with  $10^7$  evaluation points (lower)

### 2.5.3 Preliminary conclusions

Based on the polynomial and the bungee jump examples, a few preliminary conclusions can be drawn:

1. With much less estimations than MC simulations, PEM and PMM are able to get satisfactory estimations of the mean, variance and skewness coefficient.
2. SRSM requires more complete model estimations than PEM and PMM for comparable results.

3. PMM performed better than PEM for the variance and the skewness coefficient when a multivariate case was considered.

These preliminary conclusions apply only to the simplified cases tested above. Further investigations will be performed on complete hydraulic models in chapters 4 and 5.

## **2.6 Sources of uncertainty**

After having presented uncertainty analysis methods and having tested them on simple examples, it is now important to focus on the uncertainties that can affect hydraulic models.

The interest of researchers in uncertainty analysis for hydrology and hydraulics is rising since the late 2000's (Di Baldassarre et al. 2010; Montanari 2007). Di Baldassarre (2012) lists some reasons for this. Firstly, hydraulic and hydrological simulations are always affected with uncertainties that, often, cannot be neglected. Then, a fair presentation of hydraulic or hydrological results should be accompanied with confidence intervals. Such approach can support and guide stakeholders to better identify the need and the location of mitigation strategies.

Uncertainties can be classified into two categories (Merz & Thielen 2005): natural and epistemic. Natural uncertainties are inherent to the variability of a quantity over time, space or population of individuals. For example, the discharge in a river over a year is a natural uncertainty. Epistemic uncertainties are related to the representation of the system studied. For instance, the choice of a probabilistic law can lead to some epistemic uncertainty. As reported by Merz & Thielen (2005), many researchers consider that these two kinds of uncertainties should be treated separately.

Apel et al. (2004) list some sources of uncertainties in flood risk assessment. This list is adapted in (Domeneghetti et al. 2013). We sum up these two contributions and adapt it for the more general purpose of river hydraulics (Table 11).

Studying a hydraulic system under all possible sources of uncertainty is cumbersome. Indeed, for each source of uncertainty, statistical moments or a probabilistic law should be defined. It is not always possible according to the data available. Moreover, the resulting uncertainty of a model should always be interpreted with respect to the sources of uncertainty considered. In any situation, the resulting uncertainty should be considered as absolute.

Table 12 lists some papers dealing with uncertainties in the frame of hydrology or hydraulics. For each of them, the sources of uncertainty considered are identified. In this section, four

uncertainty sources will be exposed (discharge (upstream and tributaries), rating curve and roughness coefficient).

Domains	Natural uncertainty	Epistemic uncertainty
Hydrological input	<ul style="list-style-type: none"> <li>- annual maximum discharge</li> <li>- flow hydrograph shape</li> <li>- correlation main river-tributaries</li> </ul>	<ul style="list-style-type: none"> <li>- measurement error</li> <li>- statistical inference</li> <li>- choice of a statistical law</li> <li>- estimation of the parameters of a statistical law</li> <li>- number of considered tributaries</li> </ul>
Hydrodynamics	<ul style="list-style-type: none"> <li>- changes of the river geometry over time</li> <li>- spatial and temporal variability of the roughness</li> </ul>	<ul style="list-style-type: none"> <li>- physical representativeness of a numerical model</li> <li>- grid size</li> <li>- model type</li> <li>- DEM inaccuracy</li> <li>- choice and calibration of a friction law</li> <li>- various parameters estimation/calibration</li> </ul>
Rating curve	<ul style="list-style-type: none"> <li>- variation of river geometry in time</li> </ul>	<ul style="list-style-type: none"> <li>- discharge measurement error</li> <li>- mathematical expression calibration</li> <li>- interpolation/extrapolation errors</li> <li>- hysteresis during flooding</li> </ul>
Dike failure	<ul style="list-style-type: none"> <li>- spatial variability of the dike geometry</li> <li>- spatial variability of geotechnical parameters</li> </ul>	<ul style="list-style-type: none"> <li>- formalism of dike breach process</li> <li>- measurement errors of dike geometry and composition</li> </ul>
Hydraulic structures	<ul style="list-style-type: none"> <li>- obstruction of the river due to debris stuck on built structures</li> <li>- weir gate failure</li> </ul>	<ul style="list-style-type: none"> <li>- measurement errors of turbine flow</li> <li>- water level BC at weir gates</li> </ul>

*Table 11: Natural and epistemic uncertainties in river hydraulics, adapted from (Domeneghetti et al. 2013; Apel et al. 2004)*

	DF	HI	DE	TS	R	RC
(Apel et al. 2004)						
(Camacho & Martin 2013)						
(Dimitriadis et al. 2016)						
(Domeneghetti et al. 2012)						
(Domeneghetti et al. 2013)						
(Kottegoda et al. 2014)						
(Papaioannou et al. 2017)						
(Pappenberger et al. 2005)						
(Tung 2017)						
(Van Bijnen et al. 2012)						
(Zhong et al. 2013)						
(Zhong et al. 2016)						
(Di Baldassarre et al. 2010)						

Table 12: Uncertainty sources considered in various references (DF = Dike failure, HI = Hydrological input, DE = Damage estimation, TS = Tide and surge levels, R = Roughness, RC = Rating curve)

### 2.6.1 Discharge (hydrological input)

The hydrological load (discharge) of a river can be decomposed into several components. The first component is the discharge flowing through the upstream boundary condition while the next contributions are due to tributaries. In this section, uncertainties will be classified according to this approach.

According to the phenomenon that one wishes to simulate, the upstream boundary condition can be steady or unsteady. For unsteady boundary conditions, a hydrograph has to be imposed. This hydrograph has physical properties such as the number of peaks, the rising time, the peak discharge, etc. These parameters vary for each flood event. They constitute a natural uncertainty. Some authors assess the uncertainty of these parameters by comparing several hydrograph of historical events (Domeneghetti et al. 2013; Apel et al. 2004). A similar approach is adopted by Kottegoda et al. (2014) for hyetographs.

When steady upstream boundary conditions are considered, only the discharge is an uncertain variable. For a given return period, the uncertainty on the value of the discharge is epistemic and is a result of the lack of recorded data over time, among other sources. To quantify the uncertainty, Di Baldassarre et al. (2010) consider a uniform distribution around the mean discharge  $\pm 15\%$ . Another approach is to apply bootstrap method on the historical records of the peak discharges and to fit a statistical law (Zhong et al. 2016; Zhong et al. 2013).

The other contribution to the total discharge in a river is the discharge coming from tributaries. These tributaries are gauged or not, according to their importance. In many situations, a modeler will have to deal with ungauged streams. As discussed by Apel et al. (2004) for the Rhine River and Ruhr and Lippe tributaries, a correlation between the discharge upstream and the discharge at the tributaries can be found. However, given the fact that the rainfall is not uniformly distributed over time and space, the coefficients of the linear relationship are uncertain. In order to quantify this uncertainty, a mass balance can be made for several flood events in order to calibrate a statistical law for these coefficients.

## **2.6.2 Rating curve uncertainty**

A rating curve describes the relationship between the water level  $h$  and the discharge  $Q$  at a given cross-section in a river. The most common formulation is a power law (Petersen-Overleir 2004; Schmidt & Yen 2008):

$$Q = \alpha (h + \gamma)^\beta \quad (120)$$

where  $\alpha$ ,  $\beta$  and  $\gamma$  are the parameters to fit. The theoretical justification of this relationship can be found using two approaches (Schmidt & Yen 2008):

1. If a steady and uniform flow is considered, the Manning formula allows to link the discharge to the water depth with a power law.
2. On a weir, the relationship between the discharge and the water depth can be expressed using a power law as well.

The use of a rating curve at gauging stations is preferred in many countries in order to estimate the discharge at a given cross section (Petersen-Overleir 2004). This method is relatively inexpensive compared to techniques that use ultrasonic or electromagnetic instruments. The objective of rating curve is to derive a discharge from a water depth measurement thanks to a unique formula.

The parameters of a rating curve are fitted with respect to several measurements of water depth and discharge. As pointed by Domeneghetti et al. (2012), a European standard (ISO1100-

2:2010 2010) provides guidelines to construct correctly a rating curve. This standard recommends to use at least 15  $(h, Q)$  points to properly fit equation (120). Rantz (1982) suggests to use at least 10 points to fit the rating curve. He gives also the parameters  $\alpha$ ,  $\beta$  and  $\gamma$  for some particular control sections (e.g. thin plate weir, triangular V-notch weir).

The establishment and the use of a rating curve is subject to many sources of uncertainties and errors. Di Baldassarre & Montanari (2009) and Domeneghetti et al. (2012) list some of the uncertainty sources in rating curve:

- measurement errors (for the water depth, the velocity and the cross section area),
- hysteresis of the natural process due to unsteady flow conditions are not taken into account,
- the seasonal variation of the river roughness is neglected and,
- interpolation and extrapolation.

Di Baldassarre & Montanari (2009) evaluate the errors on the discharge measurement as a normal law with mean of 0 and a standard deviation of 2.7 % which is confirmed in (Domeneghetti et al. 2012). These values come from the European standard EN ISO 748 (ISO748:2007 2007). Di Baldassarre & Montanari (2009) investigate in their study interpolation and extrapolation errors, the presence of unsteady flow conditions and seasonal changes of the roughness are evaluated for a reach of the Po River. They conclude, for that particular application, that the error on the discharge for these three sources of uncertainty is about 21 %. In (Domeneghetti et al. 2012), measurement errors of the discharge as well as the rating curve construction approach are considered in the analysis. They show how these factors affect the calibration of a Manning coefficient. These uncertainties are also applied to flood mapping in (Domeneghetti et al. 2013).

Clarke (1999) addresses the problem of poor fitting and its consequences on discharge determination. He gives a general procedure to compute the error made on the discharge for the maximum water level measured. He shows in an example that the 95 % confidence interval of the corresponding discharge can be wide.

In this thesis, the uncertainty on the rating curve will be addressed by two methods: a bootstrap analysis and the use of a third-party software.

For the bootstrap analysis, we consider the calibration of (120) with  $N(h, Q)$  points and a given criterion for the goodness-of-fit. The magnitude of  $N$  influences the confidence in the fitting of the parameters of the rating curve. A bootstrap analysis consists in drawing randomly  $M$  times  $N$  couples  $(h, Q)$  from the original set  $(h, Q)$ , with  $M$  large enough. For each of the  $M$  sets, the

parameters can be calibrated. From the  $M$  values of  $\alpha$ ,  $\beta$  and  $\gamma$  statistical moments can be computed.

In order to quantify the uncertainty linked to the rating curve, the Baratin method can be used through the Baratinage software (Mansanarez et al. 2016; Le Coz et al. 2014; Le Coz et al. 2013). The typical workflow for using Baratin is the following one:

1. Define the hydraulic control section (which may be composed of several segments). This estimation of the control section defines a priori values of the coefficients of the rating curve, each with a confidence interval.
2. Import gauging values and possible measurement error.
3. Define a remaining error (which may be constant or depends on the discharge linearly)
4. Launch the computation in order to get a posteriori values of the rating curve coefficients.

Baratin computation relies on an MCMC (Markov Chain Monte Carlo) approach. For further details, the reader may refer to Baratin scientific publications. The MCMC method generates several  $(\alpha, \beta, \gamma)$  tuples. From these tuples, mean values of the coefficients and a covariance matrix can be computed.

### **2.6.3 Roughness coefficient uncertainty**

Physical hydraulic models require the use of a friction law which links the velocity to head losses in the river. This is done through the use of a friction slope  $S_f$ . Two approaches give a mathematical expression to the friction slope (Machiels et al. 2011). A first approach is the so-called “energy slope based” formulation:

$$S_f = \left( \frac{U}{\alpha R_h^\chi} \right)^2 \quad (121)$$

where  $U$  is the mean flow velocity,  $\alpha$  a friction coefficient and  $R_h$  the hydraulic radius. One the most widely used friction law is the one from Manning where  $\alpha = 1/n$  and  $\chi = 2/3$  in equation (121).

The second approach is called the turbulent regime school. The Darcy-Weisbach formula (122) links the friction slope to a friction coefficient  $\lambda$  that is determined with regard to the flow regime (e.g. Colebrook, Barr-Bathurst).

$$S_f = \frac{\lambda}{4R_h} \frac{U^2}{2g} \quad (122)$$

For instance, the Barr-Bathurst formulation (Machiels et al. 2011) expresses  $\lambda$  as follows:

$$\begin{aligned}
 & \text{pour } \frac{k_s}{h} \leq 0,05 : \\
 & \frac{1}{\sqrt{\lambda}} = -2 \log \left( \frac{1.1295 \log \left( \frac{\text{Re}^*}{1,75} \right)}{\text{Re}^* \left( 1 + \frac{\text{Re}^{*0.52} \left( \frac{k_s}{h} \right)^{0.7}}{37,22} \right)} + \frac{k_s}{14,8h} \right) \\
 & \text{pour } 0,05 \leq \frac{k_s}{h} \leq 0,15 : \tag{123} \\
 & \frac{1}{\sqrt{\lambda}} = 1469,76 \left( \frac{k_s}{h} \right)^3 - 382,83 \left( \frac{k_s}{h} \right)^2 + 9,89 \left( \frac{k_s}{h} \right) + 5,22 \\
 & \text{pour } \frac{k_s}{h} \geq 0,15 : \\
 & \frac{1}{\sqrt{\lambda}} = -1,987 \log \left( \frac{1}{5,15} \min \left( \frac{k_s}{h}, 1 \right) \right)
 \end{aligned}$$

with  $k_s$  a characteristic roughness size,  $h$  the water depth,  $\text{Re}^* = hU / \nu$  and  $\nu$  the kinematic viscosity of the fluid.

The calibration of a hydraulic model consists in finding the best value for the roughness coefficient/parameter (e.g.  $n$ ,  $k_s$ ). This calibration process is based on historical events for which water levels and discharges are recorded over time (Goffin, Dewals, et al. 2016).

A link between the calibrated roughness coefficient and other uncertain variables can be easily conceived. For instance, if the upstream discharge is considered as uncertain, the calibration process should take into account this fact in order to associate a distribution of roughness coefficients to an uncertain input. However, such a dependency is difficult to manage, especially when a large number of values (of upstream discharge for example) should be tested. Further, if a roughness coefficient have to be calibrated, it will be done at the mean values of the uncertain variables. Proceeding in such a way considers that the roughness coefficient is not considered as an uncertain variable.

Another approach to determine these roughness coefficients consists in analyzing the grain size distribution of a riverbed or floodplain. Based on empirical formulae, a Manning coefficient can be determined from this physical information (Papaioannou et al. 2017). Van Bijnen et al. (2012) determine the roughness coefficient based on their expert judgment. When possible, this latter technique should be avoided in order to promote reproducibility and objectivity. Uncertainty on the Manning roughness coefficient was also investigated by Pappenberger et al. (2005). They considered a uniform distribution of the Manning coefficient in the channel and

floodplain is order to assess the performance of the model according to these uncertain parameters. No framework to establish a probabilistic distribution of the Manning coefficient is suggested in this paper.

## 2.7 Software architecture

Performing uncertainty analysis requires an efficient chain of actions. First, the position of evaluation points needs to be determined. Then, the hydraulic model must be run at these different locations. Finally, the results should be collected in order to assess the uncertainty associated, according to the relevant technique. All these actions are gathered in a single software in order to facilitate the job of the modeler.

A framework was designed to enable efficient uncertainty analysis in the WOLF software. Several goals were pursued:

1. Enable uncertainty analysis on all types of models implemented in WOLF
2. Enable efficient parallel computing
3. Compare uncertainty analysis methods among them
4. Provide the possibility to decorrelate variables

To do so, the designed framework relies on a main object that dispatches tasks to secondary objects. This is represented schematically in Figure 27. The “Uncertainty analyzer” is the master object that controls several multivariate samples, the simulation launcher and the uncertain results. Each of these will be developed further on.

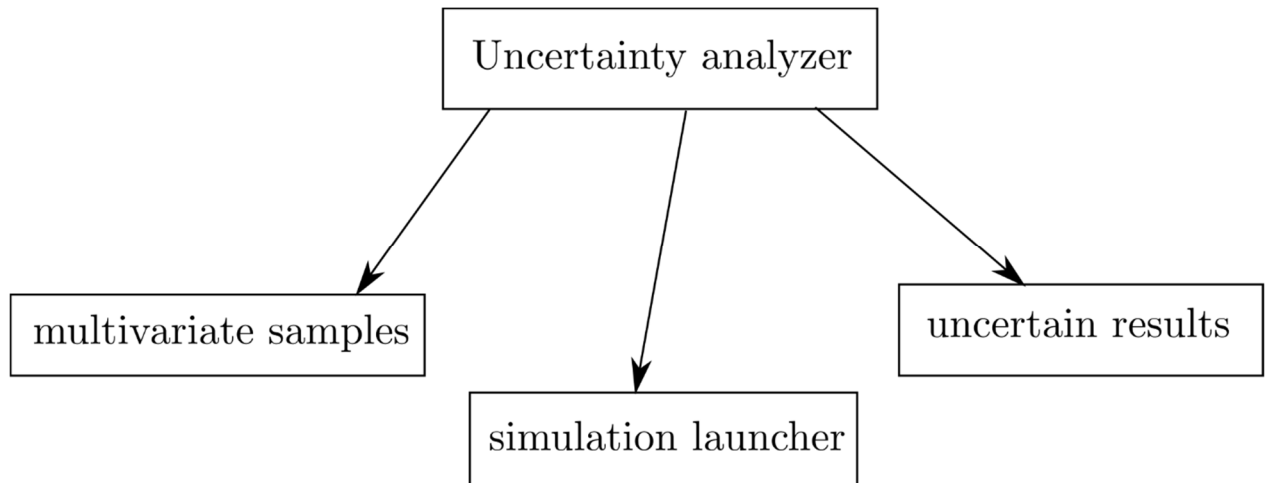


*Figure 27: Main structure of the uncertainty analysis software*

The uncertainty analysis for a same model can be performed using several methods. Each requires specific points to evaluate the outputs of a model. In order to allow this, several “multi-

variate sample” objects are available in the uncertainty analyzer. Since some methods share common points, redundant points are only computed once.

The computation is managed by the simulation launcher that relies on several meshes, which are allocated according to the needs of the analysis. Several evaluation points can be computed in parallel, using the OpenMP API, in order to decrease the overall uncertainty analysis time. Results are sent to the “uncertain results” object. It computes the statistical moments of the uncertain results according to methods chosen by the user.

This architecture allows to evaluate efficiently a model and to compare several techniques between them. Each object is detailed hereafter.

### **2.7.1 Multi-variate samples implementation**

A multivariate sample (Figure 28) is a set of points generated from stochastic properties and according to a given method. Stochastic properties are available in an object of class `stochastic_properties`. It includes the number of variables (`nb_dimensions`) and the statistical moments for each dimension (`m1`, `gamma_3`, `kappa_4`), as well as the covariance matrix (`sigma_2`). From the covariance matrix, the routine `check_if_correlated` determines if the variables are correlated by checking the value of the non-diagonal elements of `sigma_2`. If variables are correlated, the sampling points are generated accordingly (see further). In order to prepare this step, the eigenvectors and eigenvalues are computed when variables are correlated. Eigenvalues are the covariances in the uncorrelated space (`sigma_2_eigen`) and the eigenvectors (`v`) are used for the change of referential.

The multivariate sample is generated from the stochastic properties according to a chosen method. A Monte Carlo sampling (`sampling_MC`) gives the same weight to the points that are drawn randomly. The `sampling_2pts` routine is used when only 2 points are drawn per dimension. The weights are computed according to the developments shown in section 2.3.2. A similar approach is used when 3 points per direction are needed (`sampling_3pts`). The sampling in the SRSM method relies on a heuristic algorithm which is described in section 2.3.3. It is implemented in `sampling_SRSM` for second and third order polynomials.

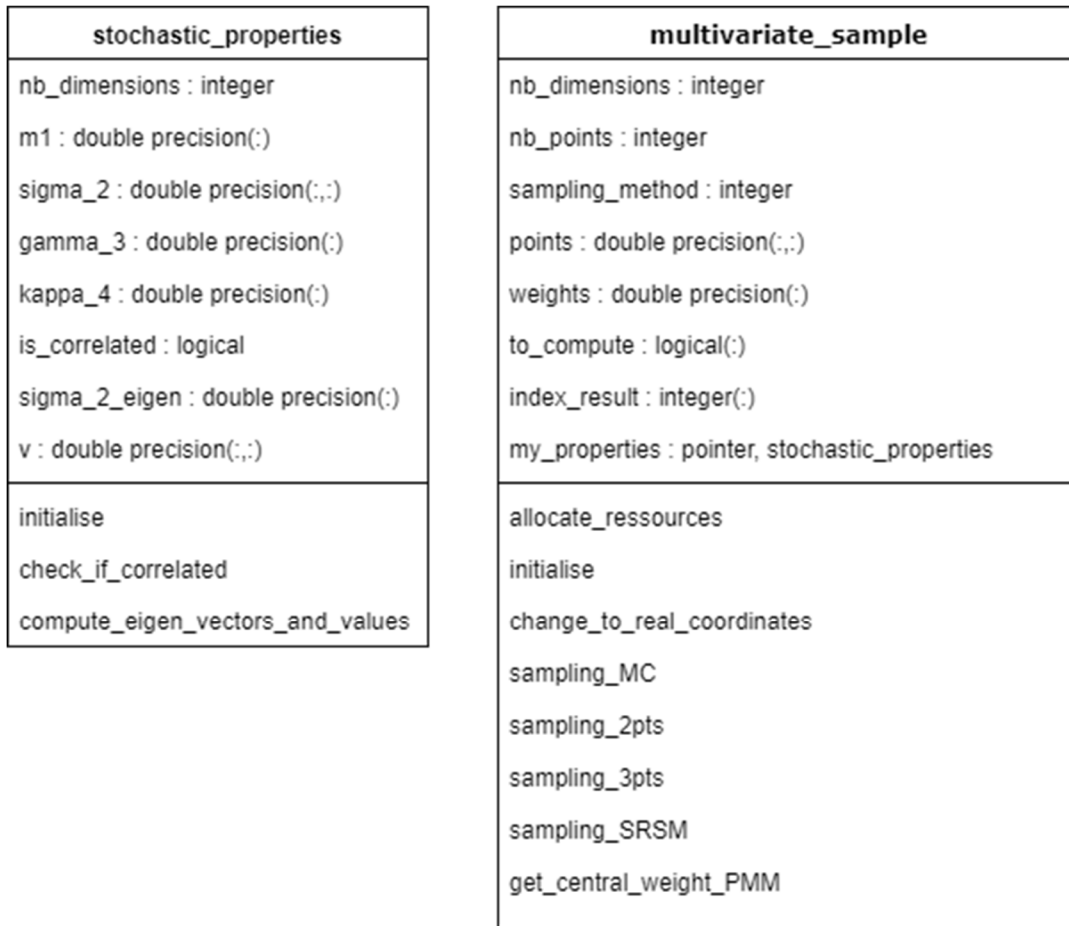


Figure 28: UML diagram for the multivariate sample object

All these sampling techniques are implemented for uncorrelated variables centered on 0 and with a variance of 1. In order to fit with the coordinate system used in the models, a change to real coordinates is performed (**change\_to\_real\_coordinates**). This routine acts differently according to the correlation of variables. If variables are correlated, the points that are drawn in an uncorrelated referential are:

1. scaled according to the square root of the eigenvalues (standard deviation in the uncorrelated referential), then
2. rotated to the correlated referential thanks to the eigenvectors matrix, and finally
3. centered on the mean.

For uncorrelated variables, the transformation consists in scaling the variables according to their standard deviation and then center them on the mean.

If several multivariate samples are used in the uncertainty analyzer, some sampling points may be in common. For instance, the SRSM method shares points with Bolle's method. In order to avoid redundant computations, a system of index for the results is implemented

(`index_result`). The indexes stored in `index_result` correspond to the index of the result in a vector contained in the uncertainty analyzer.

## **2.7.2 Simulation launcher implementation**

The goal of the simulation launcher is to run the same model with different pre-defined parameters. These parameters can include boundary conditions, roughness coefficients, infiltration discharge, etc. The simulation launcher was implemented in such a way that it can be used for other purposes than just an uncertainty analysis.

The simulation launcher object relies on several auxiliary objects (Figure 29). Parameters that vary are defined by several parameter zones. A parameter zone is an area of the mesh where a given parameter value changes. It is geometrically defined by vertices, an array or a vector outline. A parameter zone includes also the values of the parameter to be tested as well as the information concerning the nature of the parameter. This approach allows to define easily several zones impacted by parameters changes but also to define multiple parameter changes for a same geometrical zone.

The launcher can include several meshes for parallel computation. They are first initialized at the same state. Then, the parameters that should be tested are sent to a mesh for computation. Using OpenMP allows computing several meshes at the same time on a multi-core machine. This allows a substantial gain of time. Results of interest are extracted after each computation and stored thanks to a dedicated object.

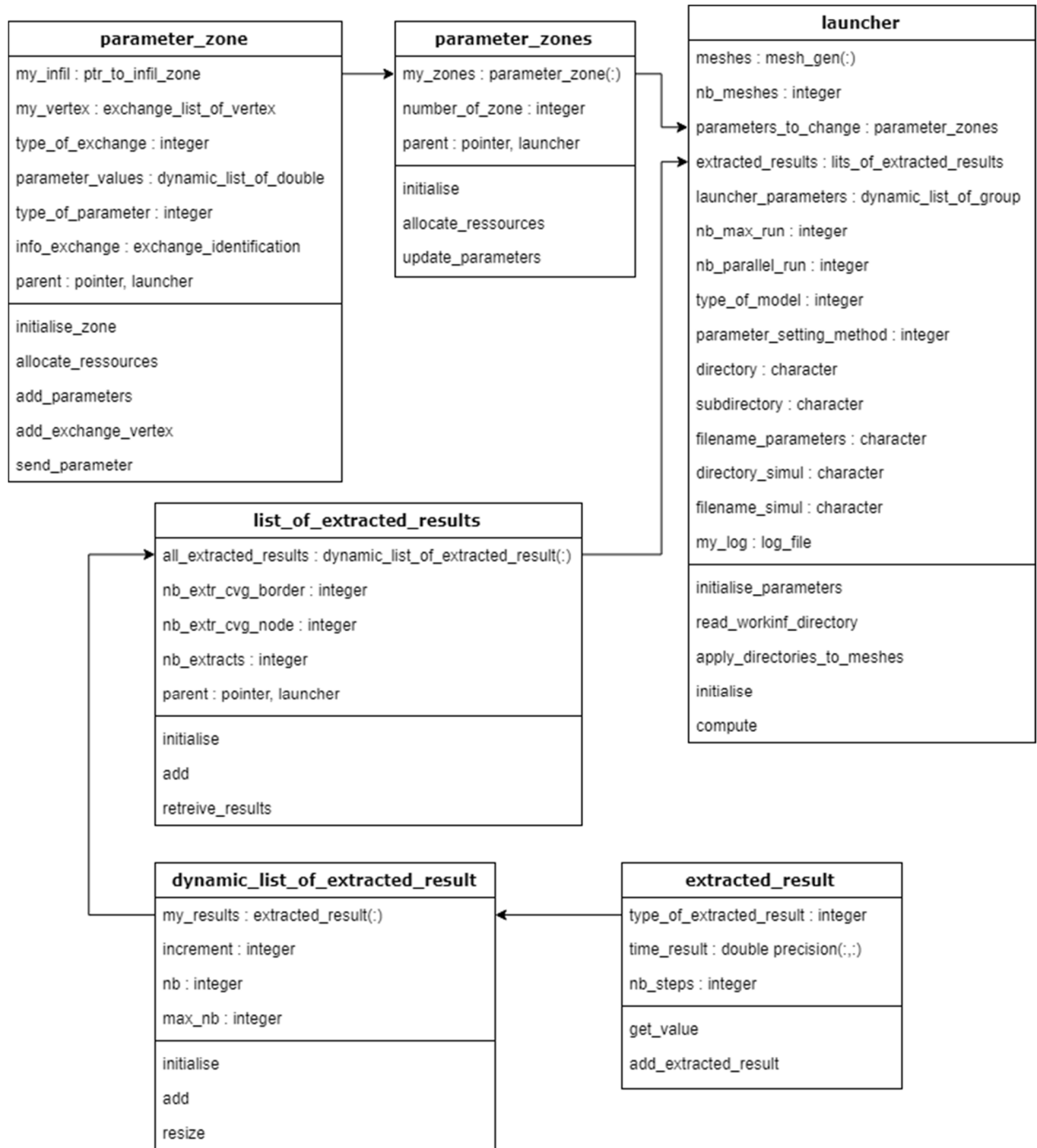


Figure 29: UML diagram for the simulation launcher

### 2.7.3 Uncertain results implementation

The results extracted from the launcher are sent to an object which goal is to compute uncertainty indicators (Figure 30). When data are loaded, the moments (the mean and centered second and third order moments) are computed for each uncertain result according to a desired method (PEM, PMM or SRSM, see section 2.4).

For the SRSM method, polynomials are fitted first. Then, a sampling is performed according to the Monte-Carlo method. Polynomials are evaluated for this new sample and moments are computed.

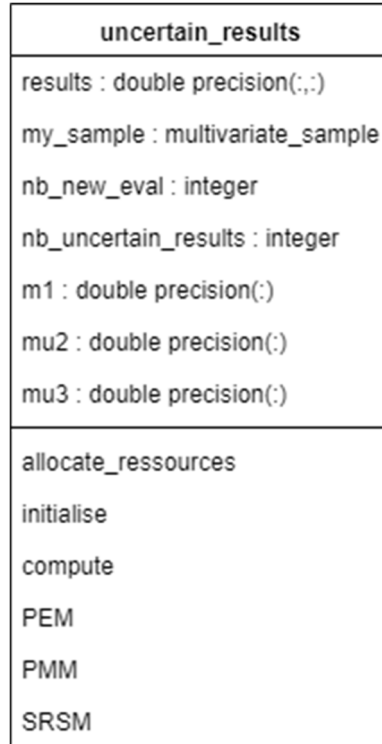


Figure 30: UML diagram for the uncertainty indicator computation

## 2.8 Conclusion

In this chapter, we first introduced some probability fundamentals required for the developments of uncertainty analysis methods. In order to deal with correlated variables correctly, uncorrelation techniques were explained and compared.

Uncertainty analysis relies on two main steps:

- producing evaluation points and,
- computing the statistical characteristics of the output.

For the first step, three main methods were introduced. For the second step, four methods were explained. We brought PMM to reader's attention. We justified its level of accuracy against Taylor series expansions, compared it analytically to PEM and generalized the original formulation to skewed variables.

From these theoretical considerations, first tests were performed. They concerned simple analytical functions: polynomials and a more playful function that represents the distance covered by a bungee jumper. The comparison between techniques showed that PMM performed

well in comparison to more computationally expensive methods (MC and SRSM). PMM also showed to produce better results than PEM.

In order to apply uncertainty analysis to hydraulics, some sources of uncertainty were presented through a literature review. We chose to focus the discussion of 3 uncertainty sources: discharge, rating curve and roughness coefficient.

Finally, the software architecture was briefly introduced. It is designed to be able to compare techniques and compute efficiently concentration points. To do so, redundant points are skipped and OpenMP is used for best performances on multi-core CPUs.

This chapter paves the way for efficient application of uncertainty analysis to hydraulic models.



# Chapter 3: Fast convergence of a steady 1-D open-channel flow

## 3.1 Introduction

Channelized flows can be simulated using 1-D, 2-D or 3-D models depending on the level of flow details that is required (Proust et al. 2016). Results from hydrodynamic numerical models are used in multiple domains including flood risk analysis (Drab & Riha 2010) or real-time control of river facilities (Schwanenberg et al. 2015), for instance.

One-dimensional models are used when a dominant direction can be assumed in the velocity field. This may be the case when the flow is restricted to the main riverbed. A 1-D model can still be used in the case of out-of-bank flooding, although they are unable to represent complex 2-D flow patterns in the floodplain (Tayefi et al. 2007). Several practical cases have shown that flood mapping can be performed using 1-D models (Horritt & Bates 2002; Cook & Merwade 2009) and they can also be used in other fields, such as flood routing for hydropower plant operations (Goffin, Dewals, et al. 2016) and mixed flows in pipes (Bourdarias et al. 2008).

2-D horizontal models enable to represent flow patterns in a horizontal plane. This can be interesting in flood mapping when the flow in the floodplain is complex and/or have an impact on the main flow. 2-D models are widely used for hydraulic simulations in rivers for flood mapping (Ercicum, Dewals, Archambeau, Detrembleur, et al. 2010), dam break flows (Ercicum, Dewals, Archambeau & Piroton 2010), warning wave design (Stilmant et al. 2017), etc. 2-D models are also used for urban flooding, where the geometry of the streets naturally induces 2-D flow patterns (Arrault et al. 2016; Bruwier et al. 2017; Bruwier et al. 2018).

3-D models are used when complex geometries are present and/or when velocities in the horizontal and vertical planes can be observed (Teng et al. 2017). Some examples of their use in the case of bends in rivers can be found in the literature (Han et al. 2011; Xiao et al. 2017). These complex models are computationally more expansive than the less detailed 1-D and 2-D models. However, the latter produce satisfactory results when their assumptions are respected.

1-D models are still used extensively even though 2-D and 3-D models are currently widely available. There are various reasons for their use, for example, digital elevation models (DEM) and bathymetry data are not available in some regions of the world. When only cross-section profiles are available to represent the geometry of a riverbed, 1-D models can make direct use of such profiles whereas they have to be interpolated to be used in 2-D or 3-D models. Besides,

many applications do not require a detailed description of the flow features in the floodplain, and thus, a 1-D modeling approach is sufficient.

Large-scale hydraulic modeling of river networks (Paiva et al. 2011; Paz et al. 2010; Lai et al. 2013; Remo & Pinter 2007; Biancamaria et al. 2009) makes heavy use of 1-D models because of their ability to compute long stretches of a river at a reasonable cost. To initiate a computation, one needs boundary conditions as well as an initial condition. This initial condition is often a steady water profile, which can be obtained by performing a time-dependent simulation with steady boundary conditions over a period of time that is long enough to reach a steady solution (Kerger et al. 2011). This step may consume a considerable amount of time before the main problem can be addressed. The initial condition should be computed with the same numerical scheme as the one used in the unsteady model in order to ensure the steadiness of the first step of the unsteady model. The ability of these models to quickly obtain a steady initial solution is also of great importance.

Optimization is another field where obtaining a steady result as quickly as possible is important. Indeed, most optimization techniques require a large number of runs in order to figure out the optimal solution. In order to ensure that the overall computation time is as short as possible, techniques that are quick should be utilized including parallelization (Sandric et al. 2019) or the use of fast computing models.

Uncertainty analysis, the focus of this thesis, may also require fast solving hydrodynamic models. Indeed, as presented in Chapter 2, a large number of simulations are needed for Monte Carlo method. In order to keep an overall low computation time, fast models should be used. Since one of the purposes of this thesis is to compare the Monte Carlo method to less computationally intensive methods, using a fast model is essential.

Although 1-D simulations are known to provide results in a short period of time, accelerating the computation of the 1-D steady solution is of great interest in the fields mentioned above. This can be achieved by using two main strategies. The first one consists of exploiting the resources of modern computers more efficiently. Such techniques are more frequently applied to 2-D cases, which naturally require more computing resources. Common hardware acceleration strategies include parallelizing codes on several CPU cores (Neal et al. 2010; Lacasta et al. 2013) or on a GPU (Brodtkorb et al. 2012; Petaccia et al. 2016; Smith & Liang 2013). The second method consists of designing algorithms in order to converge with less effort toward the solution. To the authors' knowledge, there is no such work available in the literature. Both strategies can be combined in order to obtain the best performance.

The fast computation of a steady solution in 1-D open-channel flows is the focus of this chapter. Developments presented in this chapter will be used in next chapters in order to apply uncertainty analysis to hydrodynamics. First, the general hydraulic equations for 1-D open channel flows will be detailed and the numerical discretization implemented in WOLF will be developed. This time-dependent model will be used for comparisons later in the chapter. Then, the equation of a modified model for fast convergence of a water profile will be developed. The numerical scheme as well as the implementation details will be explained. This new model will be validated against an academic test case. The optimization of this new method will be performed with various situations. Based on the observations made up to this point, another algorithm, even more optimized, is proposed. Finally, CasADi, a optimization tool, is introduced and its performances are compared to our algorithm. A physical case simulated in the HECE laboratory is also used to validate the use of CasADi for hydrodynamic problems.

A large part of the content of this chapter has been published in (Goffin et al. 2020) although more details are available in this thesis. These supplementary details include a longer discussion about the process of implementation that led to the final algorithm and the application of CasADi to a physical laboratory test.

## **3.2 General 1-D model**

The development of our fast 1-D model relies on the standard Saint-Venant equations. These equations and the discretization method are presented in this section 3.2. This first content is useful for the next development in section 3.3 where the equations are modified in order to provide better computation behaviors for steady state problems.

### **3.2.1 Set of equations**

Starting from the Navier-Stokes equations for the conservation of mass and momentum, one can derive them in an area-integrated form. These equations are commonly known as Saint-Venant equations:

$$\begin{aligned} \frac{\partial A}{\partial t} + \frac{\partial Q}{\partial x} &= q_l \\ \frac{\partial Q}{\partial t} + \frac{\partial}{\partial x} \left( \frac{Q^2}{A} + gI_1 \right) &= gA(S_o - S_f) + gI_2 + gI_3 + u_x q_l \end{aligned} \quad (124)$$

Where  $A$  is the cross-section area,  $Q$  the discharge,  $q_l$  a lateral discharge per unit length,  $g$  the gravity acceleration,  $S_o$  the bed slope,  $S_f$  the friction slope,  $u_x$  the injection velocity according to  $x$  of the lateral discharge,  $I_1$  the pressure integrated on the cross-section and  $I_2$  the force

resulting from the pressure on the banks.  $h$  is the water depth,  $h_b$  and  $h_s$  are the distances between the axis  $x$  and, respectively, the riverbed and the free surface.

$$I_1 = \int_{-h_b}^{h_s} (h_s - \xi) l(x, \xi) d\xi \quad \text{and} \quad I_2 = \int_{-h_b}^{h_s} (h_s - \xi) \frac{\partial l(x, \xi)}{\partial x} d\xi \quad (125)$$

The  $I_3$  term is added to take into account the fact that a cross-section may present a flat bottom (in the transversal direction). In such a case, the reaction of the pressure on the flat bottom creates a force that acts on the fluid. This reaction occurs when the riverbed presents a longitudinal slope:  $\partial h_b / \partial x \neq 0$ .

$$I_3 = h l_b \frac{\partial h_b}{\partial x} \quad (126)$$

One can notice that if the cross-section bottom is not flat transversally ( $l_b = 0$ ), the  $I_3$  term vanishes.

In the set of equations (124), the first one rules the evolution of the cross-section area according to the discharge spatial evolution and the presence of infiltration/exfiltration. The second equation in (124) states that the temporal evolution of the discharge is linked to:

- the spatial change of momentum,
- the spatial change of hydrostatic pressure,
- the bed slope and friction slope,
- the force of reaction coming from the pressure acting on the bed and the banks and,
- a source term to potentially take into account the change of momentum due to the infiltration/exfiltration.

This set of equations, once discretized for numerical solving, is able to reproduce the temporal and spatial evolution of the discharge and cross-section area along a channel according to the major assumption of shallow water equations (SWE): the pressure is considered hydrostatic perpendicular to the flow axis. This assumption can be considered valid in many channel flows when the velocity is mostly directed along the river axis. If 3-D flow patterns exist, the assumption of the SWE are not licit.

For an easier numerical handling of complex cross-sections, the momentum equation in (124) can be written in a non-conservative form<sup>8</sup> (Archanbeau 2006). The pressure derivative can be expanded:

$$\begin{aligned}
 \frac{\partial}{\partial x}(gI_1) &= g \frac{\partial}{\partial x} \left( \int_{-h_b}^{h_s} (h_s - \xi) l(x, \xi) d\xi \right) \\
 &= g \int_{-h_b}^{h_s} \frac{\partial}{\partial x} [(h_s - \xi) l(x, \xi)] d\xi \\
 &\quad + g(h_s - h_s) l(x, h_s) \frac{\partial h_s}{\partial x} - g(h_s + h_b) l(x, -h_b) \frac{\partial(-h_b)}{\partial x} \\
 &= g \int_{-h_b}^{h_s} \frac{\partial(h_s - \xi)}{\partial x} l(x, \xi) d\xi + g \int_{-h_b}^{h_s} (h_s - \xi) \frac{\partial l(x, \xi)}{\partial x} d\xi - gh l_b \frac{\partial(-h_b)}{\partial x} \\
 &= gA \frac{\partial h_s}{\partial x} + gI_2 + gI_3
 \end{aligned} \tag{127}$$

Adding up (with their respective signs) the pressure term in its non-conservative form (127), the forces resulting from the pressure on the banks, the pressure on the bottom of cross-sections and the bed slope results in a single term:

$$\begin{aligned}
 \frac{\partial}{\partial x}(gI_1) - gI_2 - gI_3 - gAS_o &= gA \frac{\partial h_s}{\partial x} + gI_2 + gh l_b \frac{\partial h_b}{\partial x} \\
 &\quad - gI_2 - gI_3 - gAS_o \\
 &= gA \frac{\partial h_s}{\partial x} - gAS_o \\
 &= gA \frac{\partial z_s}{\partial x}
 \end{aligned} \tag{128}$$

The St-Venant equations (124) in their non-conservative form are:

$$\begin{aligned}
 \frac{\partial A}{\partial t} + \frac{\partial Q}{\partial x} &= q_l \\
 \frac{\partial Q}{\partial t} + \frac{\partial}{\partial x} \left( \frac{Q^2}{A} \right) + gA \frac{\partial z_s}{\partial x} &= -gAS_f + u_x q_l
 \end{aligned} \tag{129}$$

The non-conservative form of shallow water equations is interesting for a particular reason: the source of movement of the water in a channel naturally appears. Indeed,  $\partial z_s / \partial x$ , the water surface slope, is explicitly present in (129) while it is not in (124). Moreover, the non-conservative form of shallow water equations showed to perform well in many practical cases, including in the presence of discontinuities (Erpicum, Dewals, Archanbeau & Piroton 2010;

---

<sup>8</sup> The non-conservative form, compared to the conservative form, splits the divergence term into several terms. While on a mathematical basis these forms are exactly the same, the difference appears when the equations are discretized.

Bruwier et al. 2016; Franzini & Soares-Frazão 2016). Further details about the reasons for the good handling of discontinuities by the non-conservative form can be found in (Toro 2000).

The characteristic velocities of equation (129) are obtained from the velocity of the flow  $u$  and the gravity wave speed :

$$\begin{aligned}\lambda_1 &= u - c = c(\text{Fr} - 1) \\ \lambda_2 &= u + c = c(\text{Fr} + 1)\end{aligned}\tag{130}$$

For subcritical flows ( $\text{Fr} < 1$ ),  $\lambda_1 < 0$  and  $\lambda_2 > 0$ , meaning that an upstream boundary condition and a downstream boundary condition must be set for solving equations (129). When the flow is supercritical ( $\text{Fr} > 1$ ), both characteristic velocities are positive, meaning that two upstream boundary conditions are required.

### **3.2.2 Discretization and numerical scheme**

The resolution of equations (129) is implemented in the WOLF software. They are spatially discretized according to the finite volume method. The unknowns  $A$  and  $Q$  are associated to the nodes. Properties (such as the water depth) and unknowns are then reconstructed on the borders in order to operate the derivation. This is achieved through the flux vector splitting method (Epicum, Dewals, Archambeau & Piroton 2010) which is illustrated in Figure 31.

The method is based on the sign and value of the discharges  $Q_i$  and  $Q_{i+1}$  on the neighboring nodes  $i$  and  $i + 1$ . It is independent from the Froude number. In Figure 31, the position of the points represents the direction of the splitting. Basically, the upwinding direction of the discharge  $Q$  and the cross-section area used for computing the velocity in the momentum flux term in (124),  $A_{vel}$ , is upstream. For the bottom elevation  $z_b$ , the wet perimeter  $\chi$  and the water depth  $h$ , the upwinding direction is downstream. If the discharges  $Q_i$  and  $Q_{i+1}$  are directed toward the border, the upwinding direction is chosen according to the direction of the mean discharge. If both discharges are of the same magnitude, the values are averaged from the two neighboring nodes (this is depicted by a centered point). An averaging is also performed if both discharges go away from the border or if one is directed away from the border and the other is nil. If the discharge is nil in a node and the discharge directed toward the border in the other one, then the upwinding direction is consistent with the classical cases (2 upper schemes in Figure 31).

At boundary conditions, special values for the discharge and/or water depth are imposed. All other unknowns/properties are reconstructed from the inner node.

Concerning the time discretization, an explicit Runge-Kutta method is used. The number of steps and the coefficients can be parametrized (Dewals 2006).

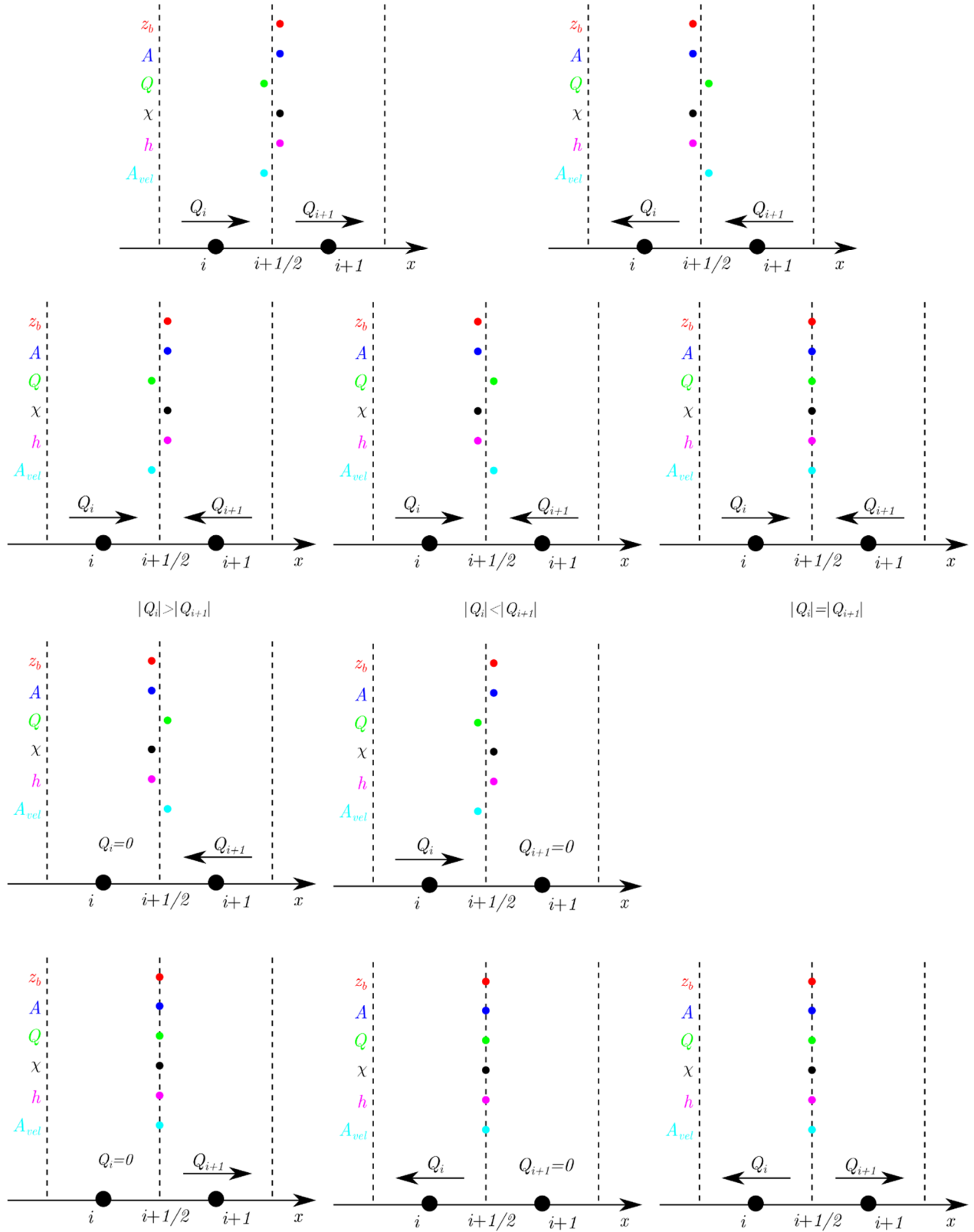


Figure 31: Flux vector splitting method

### 3.3 Modified 1-D model for fast water profile computation

The use of an initial condition is a prerequisite for an unsteady simulation. In many situations, this initial situation is a converged steady flow. For other applications, only a steady solution is the desired output.

The computation of a steady flow is of main importance in the hydraulic field. A fast computation is the key in order to be able to perform a large number of simulations in a reasonable amount of time.

#### 3.3.1 Equation

Assuming a steady flow leads to temporal derivatives equal to 0 in (124):

$$\begin{aligned} \frac{\partial Q}{\partial x} &= q_l \\ \frac{\partial}{\partial x} \left( \frac{Q^2}{A} + gI_1 \right) &= gA(S_o - S_f) + gI_2 + u_x q_l \end{aligned} \quad (131)$$

The first expression means that the discharge is known along the channel thanks to the boundary conditions and lateral discharge injections. It means that a single equation remains with a single unknown  $A$ . In order to keep the same numerical scheme as the one used for the unsteady system, Kerger et al. (2011) add a pseudo-temporal term to equation (131):

$$\beta \frac{\partial A}{\partial \tau} + \frac{\partial}{\partial x} \left( \frac{Q^2}{A} + gI_1 \right) = gA(S_o - S_f) + gI_2 + u_x q_l \quad (132)$$

where  $\tau$  is a pseudo-time and  $\beta = -\text{sign}(Q)$  as explained in (Kerger et al. 2011). This is chosen by analyzing the characteristic velocity of equation (132):

$$\lambda = \frac{c^2 - u^2}{\beta} = \frac{c^2(1 - \text{Fr}^2)}{\beta} \quad (133)$$

where  $c$  is the wave celerity. In subcritical flows ( $\text{Fr} < 1$ ), and the sign of  $\lambda$  is the sign of  $\beta$ . If  $\text{Fr} > 1$ , then  $\text{sign}(\lambda) = -\text{sign}(\beta)$ . For critical flows ( $\text{Fr} = 1$ ), the characteristic velocity is 0, independently from  $\beta$ . In order to keep some form of consistency with the general model, if we choose  $\beta = -\text{sign}(Q)$ , an upstream boundary condition is required when  $\text{Fr} > 1$  and a downstream boundary condition is required when  $\text{Fr} < 1$ . This is equivalent to the position of the water depth boundary condition for the numerical resolution of the general 1-D set of equations (see section 3.2).

Such as the transformation operated on equations (124) to get equations (129), equation (132) can be written in its non-conservative form:

$$\beta \frac{\partial A}{\partial \tau} + \frac{\partial}{\partial x} \left( \frac{Q^2}{A} \right) + gA \frac{\partial z_s}{\partial x} = -gAS_f + u_x q_l \quad (134)$$

With a single boundary condition and a discharge distributed in the river stretch, by solving equation (134) we are able to determine the cross-section area (and subsequently water depth) all along the river. The solving is performed according to the same numerical scheme as the one used for the general unsteady model which was shown to be unconditionally stable (Kerger et al. 2011).

For a node  $i$ , equation (134) is discretized in finite volumes as:

$$\frac{Q_{i+1/2}^2 / A_{i+1/2} - Q_{i-1/2}^2 / A_{i-1/2}}{\Delta x} + gA_i \left( \frac{z_{s,i+1/2} - z_{s,i-1/2}}{\Delta x} + S_{f,i} \right) - u_{x,i} q_{l,i} \approx -\beta \frac{\partial A}{\partial \tau} \quad (135)$$

where  $\Delta x$  is the spatial discretization step and subscripts refer to the position of variables values.

For the sake of clarity, we consider  $Q > 0$  and a constant reconstruction of the flux at finite volume boundaries to explicate the numerical scheme. When applying the considered upwinding directions (see Figure 31) for a node  $i$  not located next to a boundary, equation (135) is equivalent to:

$$\frac{Q_i^2 / A_i - Q_{i-1}^2 / A_{i-1}}{\Delta x} + gA_i \left( \frac{z_{s,i+1} - z_{s,i}}{\Delta x} + S_{f,i} \right) - u_{x,i} q_{l,i} = \frac{\partial A}{\partial \tau} \quad (136)$$

For the node located at the downstream boundary ( $i = N - 1$ ), if a weak water level boundary condition  $z_{s,BC}$  is imposed at the border, equation (135) becomes:

$$\frac{Q_{N-1}^2 / A_{N-1} - Q_{N-2}^2 / A_{N-2}}{\Delta x} + gA_{N-1} \left( \frac{z_{s,BC} - z_{s,N-1}}{\Delta x} + S_{f,N-1} \right) - u_{x,N-1} q_{l,N-1} = \frac{\partial A}{\partial \tau} \quad (137)$$

Without a boundary condition imposed on the value of  $z_s$  at the external border, a nil  $z_s$  gradient is imposed and equation (135) becomes:

$$\frac{Q_{N-1}^2 / A_{N-1} - Q_{N-2}^2 / A_{N-2}}{\Delta x} + gA_{N-1} S_{f,N-1} - u_{x,N-1} q_{l,N-1} = \frac{\partial A}{\partial \tau} \quad (138)$$

At the upstream node ( $i = 0$ ), if a weak boundary condition of the water level is imposed at the border, equation (135) becomes:

$$gA_0 \left( \frac{z_{s,1} - z_{s,BC}}{\Delta x} + S_{f,0} \right) - u_{x,0} q_{t,0} = \frac{\partial A}{\partial \tau} \quad (139)$$

Without a boundary condition at the upstream border, equation (135) becomes:

$$gA_0 \left( \frac{z_{s,1} - z_{s,0}}{\Delta x} + S_{f,0} \right) - u_{x,0} q_{t,0} = \frac{\partial A}{\partial \tau} \quad (140)$$

### 3.3.2 Original solving strategy

Solving equation (134) instead of equation (129) allows time saving in computation since the number of equations and unknowns is reduced.

In order to gain more time, two additional strategies are implemented:

- An Anderson accelerator is used in order to promote fast convergence.
- The computation is performed only on a sliding part of the full domain.

#### 3.3.2.1 Anderson acceleration

Numerically solving a non-linear system can be performed by different means, including Newton's method and Broyden's method (Broyden 1965). Newton's method consists in computing a Jacobian matrix (numerically when an analytical evaluation is not possible) at each iteration in order to converge to a local optimum. Broyden's method is similar to Newton's method except that it computes the entire Jacobian matrix only at the first iteration and then updates it for the following steps.

More sophisticated methods exist in order to solve non-linear systems faster, such as the Jacobian-free Newton-Krylov method (Knoll & Keyes 2004) and Anderson acceleration (Anderson 1965). The Anderson acceleration method uses the results from successive iterations in order to adapt the new approximation. Walker & Ni (2011) showed that this method can be considered equivalent to the well-known GMRES method (Saad & Schultz 1986) when applied to linear systems. The nonlinear Krylov acceleration (NKA) (Carlson & Miller 1998a; Carlson & Miller 1998b), which is similar to Anderson acceleration, showed to be more efficient in some applications than more recent methods such as the Jacobian-Free Newton-Krylov method (Calef et al. 2013). NKA is used for a faster convergence of our pseudo-time model.

Since NKA only relies on the results directly produced by the hydraulic model, it can be easily applied to other algorithms or other domains. Indeed, no gradient evaluation (nor other prerequisite) is required before calling on the NKA algorithm.

The NKA algorithm records  $M$  ( $M \in \mathbb{N}_{>0}$ ) previous moves of the root finding process. Based on these previous moves, NKA adapts its guess for the new root. One of the main assumptions is that the Jacobian matrix remains constant within the scope of  $M$  moves. The details of the method are given hereafter.

The general iterative process to find the root of a nonlinear function  $f(\mathbf{x})$  consists in iteratively changing  $\mathbf{x}$  in order to converge  $f(\mathbf{x})$  toward 0. This iterative process, as explained above, can be performed using different techniques. A well-known method is the Newton-Raphson iterative method. It consists in finding a new evaluation point  $\mathbf{x}_{k+1}$  from a current point  $\mathbf{x}_k$ , the values of the nonlinear functions at the current point  $f(\mathbf{x}_k)$  and the inverse of the Jacobian matrix  $J^{-1}$ :

$$\mathbf{x}_{k+1} = \mathbf{x}_k - J^{-1}f(\mathbf{x}_k) \quad (141)$$

Picard iterations, also known as fixed-point iterations, is an iterative method designed to solve a non-linear equation of the type  $\mathbf{x} = g(\mathbf{x})$ . Successive values of  $\mathbf{x}$  are computed as follows, starting from an arbitrary point  $\mathbf{x}_0$  :

$$\begin{aligned} \mathbf{x}_1 &= g(\mathbf{x}_0) \\ \mathbf{x}_2 &= g(\mathbf{x}_1) \\ &\vdots \\ \mathbf{x}_{k+1} &= g(\mathbf{x}_k) \end{aligned} \quad (142)$$

Denoting  $g(\mathbf{x}) = \mathbf{x} - f(\mathbf{x})$ , the problem is equivalent to a root-finding problem  $f(\mathbf{x}) = 0$  and the iterative process becomes:

$$\mathbf{x}_{k+1} = \mathbf{x}_k - f(\mathbf{x}_k) \quad (143)$$

Equation (143) can be seen as a degenerated Newton-Raphson method where the invert of the Jacobian matrix is considered as the identity matrix ( $J^{-1} = I$ ). This method converges linearly if a solution exists and if the initial point  $\mathbf{x}_0$  is good enough (Kelley 1995).

The method developed by Carlson & Miller (1998a; 1998b), and applied later by Calef et al. (2013) and Wang et al. (2018), for instance, takes advantage of a history of  $M$  corrections of  $\mathbf{x}$  (denoted  $\mathbf{v}$ ) and  $M$  evolutions of  $f(\mathbf{x})$  (denoted  $\mathbf{w}$ ) at iterate  $k$ :

$$\begin{aligned} \mathbf{v}_i &= \mathbf{x}_i - \mathbf{x}_{i-1} \\ \mathbf{w}_i &= f(\mathbf{x}_i) - f(\mathbf{x}_{i-1}), i = k - M + 1, \dots, k \end{aligned} \quad (144)$$

Since the function  $f$  is nonlinear and requires several iterations for finding its root, vectors  $\mathbf{w}_i$  are not aligned and can be considered as linearly independent. It is possible to define a subspace which is a set of vectors  $\mathbf{w}_i$ :  $\mathcal{W}_k = \{\mathbf{w}_{k-M+1}, \dots, \mathbf{w}_k\}$ . An operator to project any vector onto this subspace can also be defined:  $\mathcal{P}_{\mathcal{W}_k}$ .

The NKA method assumes that the Jacobian matrix  $J$  is constant and invertible within the scope of the  $M$  previous iterations, which allows to write:

$$\begin{aligned} J\mathbf{v}_i &= \mathbf{w}_i \\ \mathbf{v}_i &= J^{-1}\mathbf{w}_i \end{aligned} \quad (145)$$

Starting from the Newton-Raphson method, the value of function  $f$  at the next iterate is

$$f(\mathbf{x}_{k+1}) \approx f(\mathbf{x}_k) - J_k \mathbf{v}_{k+1} = 0 \quad (146)$$

with  $J_k$ , the Jacobian matrix evaluated at  $\mathbf{x}_k$ . Equation (146) can also be written as

$$\mathbf{v}_{k+1} = J_k^{-1} f(\mathbf{x}_k) \quad (147)$$

In order to consider previous moves of the function values,  $\mathbf{w}_i$ , the function evaluated at point  $\mathbf{x}_k$  is expressed using a projection in the subspace  $\mathcal{W}_k$ :

$$f(\mathbf{x}_k) = \mathcal{P}_{\mathcal{W}_k} f(\mathbf{x}_k) + (f(\mathbf{x}_k) - \mathcal{P}_{\mathcal{W}_k} f(\mathbf{x}_k)) \quad (148)$$

The first term  $\mathcal{P}_{\mathcal{W}_k} f(\mathbf{x}_k)$  is in the subspace  $\mathcal{W}_k$ , while the second term  $f(\mathbf{x}_k) - \mathcal{P}_{\mathcal{W}_k} f(\mathbf{x}_k)$  is orthogonal to  $\mathcal{W}_k$  since it represents the residual of the projection of  $f(\mathbf{x}_k)$  in  $\mathcal{W}_k$ .

Since the vectors in  $\mathcal{W}_k$  are linearly independent, the projection  $\mathcal{P}_{\mathcal{W}_k} f(\mathbf{x}_k)$  can be expressed as:

$$\mathcal{P}_{\mathcal{W}_k} f(\mathbf{x}_k) = \sum_{i=k-M+1}^k z_i \mathbf{w}_i \quad (149)$$

where  $\mathbf{z}$  is a set of coefficients that has to be optimized (see later).

From equations (147), (148) and (149), one gets:

$$\begin{aligned} \mathbf{v}_{k+1} &= J_k^{-1} f(\mathbf{x}_k) \\ &= J_k^{-1} \mathcal{P}_{\mathcal{W}_k} f(\mathbf{x}_k) + J_k^{-1} (f(\mathbf{x}_k) - \mathcal{P}_{\mathcal{W}_k} f(\mathbf{x}_k)) \\ &= J_k^{-1} \sum_{i=k-M+1}^k z_i \mathbf{w}_i + J_k^{-1} (f(\mathbf{x}_k) - \mathcal{P}_{\mathcal{W}_k} f(\mathbf{x}_k)) \end{aligned} \quad (150)$$

Substituting (145) in (150), gives:

$$\mathbf{v}_{k+1} = \sum_{i=k-M+1}^k z_i \mathbf{v}_i + J_k^{-1} \left( f(\mathbf{x}_k) - \mathcal{P}_{\mathcal{W}_k} f(\mathbf{x}_k) \right) \quad (151)$$

The Jacobian matrix of the second term is unknown. Carlson & Miller chose to substitute  $J_k^{-1}$  by the identity matrix, in the same way as the fixed-point method can be seen in comparison to the Newton-Raphson method:

$$\mathbf{v}_{k+1} = \sum_{i=k-M+1}^k z_i \mathbf{v}_i + \left( f(\mathbf{x}_k) - \sum_{i=k-M+1}^k z_i \mathbf{w}_i \right) \quad (152)$$

where the coefficients  $z_i$  can be optimized by minimizing the difference between the function  $f$  at iterate  $k$  and its projection onto the  $\mathcal{W}_k$  subspace (149):

$$\mathbf{z} = \arg \min_{a \in \mathbb{R}_0} \left\| f(\mathbf{x}_k) - \sum_{i=k-M+1}^k a_i \mathbf{w}_i \right\| \quad (153)$$

Equation (152) shows that the correction of the variable  $\mathbf{x}$  is decomposed into two components:

1. The first term depicts the correction as a linear combination of previous corrections.
2. The second term is similar to the second term of a fixed-point iteration (143) that takes into account previous evolutions of the function  $f$ .

The update of the variable  $\mathbf{x}$  is given by:

$$\mathbf{x}_{k+1} = \mathbf{x}_k + \mathbf{v}_{k+1} \quad (154)$$

It should be noticed here that the assumption that the Jacobian remains constant may not be valid if the record size  $M$  is too large. Wang et al. (2018) suggest that  $M$  should be around 10. The value  $M = 10$  is chosen for our model. They also raise attention about abrupt changes in the function values that may lead to inconsistencies.

In our model, the NKA method is applied to the function that describes the evolution of the cross-section area. In other words, the root of the following nonlinear equations are computed:

$$f(\mathbf{x}) = \left( \frac{\partial A_1}{\partial \tau} \quad \frac{\partial A_2}{\partial \tau} \quad \dots \quad \frac{\partial A_n}{\partial \tau} \right)^T = 0 \quad (155)$$

where  $n$  is the number of nodes in the computation domain and  $\partial A_i / \partial \tau, i \in [1, n]$ , are computed from the discretized form of equation (134) at a given pseudo-time  $\tau$ .

### 3.3.2.2 Sliding domain

In order to decrease the computational cost, a second strategy was designed. It consists in reducing the size of the computation domain and slide it along the river stretch in order to converge the cross-section areas from downstream to upstream. The main principle is explained graphically in Figure 32. Starting from the downstream limit, a partial computation domain slides gradually toward the upstream limit. When the most upstream node is converged, a final computation of the entire domain is performed.

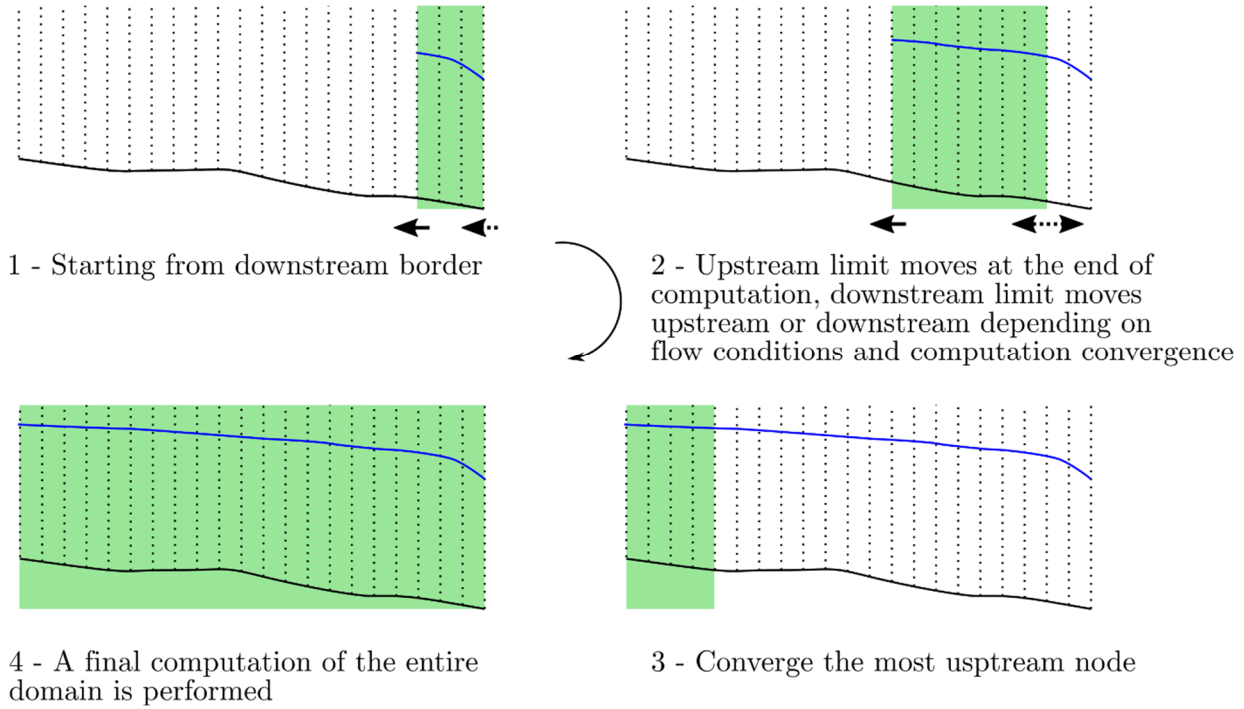


Figure 32: Principle of the sliding domain (green area). It starts from the downstream border et slides gradually toward the upstream limit.

The development of this strategy has arisen from the long history of numerical hydrodynamics in various flow regimes. Indeed, many flows that are solved for rivers are subcritical ( $Fr < 1$ ) at downstream and upstream boundary conditions. In such a situation, the cross-section area information is propagated from downstream to upstream. For a fixed flow direction, the upwinding direction of the numerical scheme takes all unknowns and properties (except those linked to the discharge and velocity) downstream. This means that when a new node is computed, it depends only on the downstream nodes (see Figure 33). It should be noticed that when a node  $i$  is added, the upstream border of node  $i + 1$  produces a change in the upwinding direction of property  $Q$  and the unknown  $A_{vel}$  (cross-section area used to compute the velocity). The node  $i + 1$ , which was supposed to be converged, undergoes a new convergence process that indirectly affects nodes  $i + 2, i + 3, \dots$ . Theoretically, all the nodes located downstream of node  $i$  should be kept in the computational domain. However, for better computation

efficiency, it was chosen to remove a node from the computation domain if the rate of change of the cross-section area was lower than some threshold. When the most upstream node is converged, a last convergence process is performed for the whole domain, ensuring that all nodes have reached a stable value. Indeed, as stated earlier, all nodes should be theoretically kept in the computation domain since newly added upstream nodes affect downstream nodes. This final step ensures that all nodes are converged with a residual  $|\partial A / \partial \tau|$ , denoted  $\xi$ , low enough.

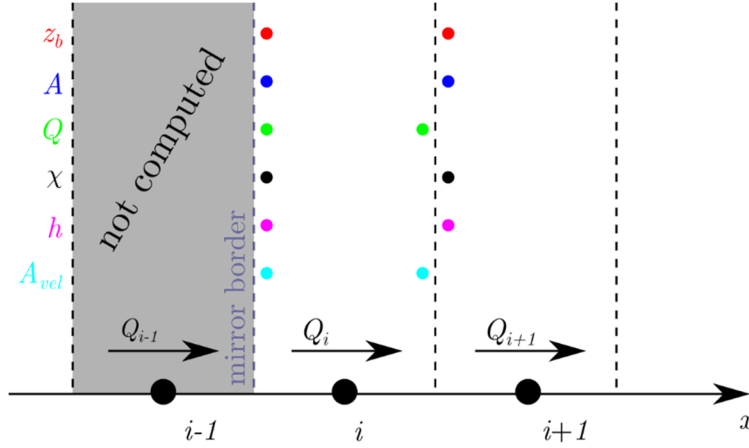


Figure 33: Numerical scheme used at the boundary of the sliding domain

The boundary condition on the border between the node  $i$  and node  $i - 1$  (see Figure 33) is called a “*mirror border*”. On this border, all the unknowns and properties are reconstructed from the computed inner node. It is not considered as a boundary border since no discharge nor water depth are imposed. This method is equivalent to reproducing the node  $i$  in  $i - 1$ , like a mirror.

When a new node is added to the computation domain, a first estimation of the cross section area is performed in order to get an overall faster convergence. The technique used consists in estimating the cross section area of node  $i$  in order to verify the pseudo-time momentum equation for node  $i$ . If the source term is nil, then we should have

$$\begin{aligned} \frac{\partial}{\partial x} \left( \frac{Q^2}{A} + z_s \right) &= 0 \\ \Leftrightarrow \frac{\partial}{\partial x} \left( \frac{Q^2}{A} \right) + \frac{\partial z_s}{\partial x} &= 0 \end{aligned} \tag{156}$$

Since the discharge  $Q$  and the cross section area used for the velocity computation,  $A_{vel}$ , are reconstructed from node  $i$  for both borders, the only solution is to equal the water levels  $z_s$ :

$$\begin{aligned}\frac{\partial}{\partial x} \left( \frac{Q^2}{A} \right) + \frac{\partial z_s}{\partial x} &= 0 \\ \Leftrightarrow \frac{\partial z_s}{\partial x} &= 0\end{aligned}\tag{157}$$

This solution may lead to inconsistency for steep slopes and low water levels. This is why, when the friction source term is nil, the water depth is simply copied to the newly added node.

When this source term is not nil, a Newton-Raphson iteration process is implemented in order to reach an equilibrium between the spatial derivative and the source term. The first estimation of the cross section area of node  $i$  is the cross section area of node  $i+1$ . Then, the cross section area is slightly perturbed by  $\Delta A$ . Two values

$$\begin{aligned}f_1 &= \frac{\partial}{\partial x} \left( \frac{Q^2}{A} + z_s \right) + gAS_f \\ f_2 &= \frac{\partial}{\partial x} \left( \frac{Q^2}{(A + \Delta A)} + z_s \right) + g(A + \Delta A)S_f\end{aligned}\tag{158}$$

are computed. The new trial value of  $A_{new}$  is based on the previous results:

$$A_{new} = A - \frac{f_1}{\frac{f_2 - f_1}{\Delta A}}\tag{159}$$

This procedure is performed until  $f_i$  is lower than some threshold.

As stated earlier, the method described here was designed in the frame of subcritical flows. In order to be able to deal with a larger range of flow regimes, some adaptations were made. When a supercritical node is detected downstream (let say at position  $m$ ), it is not computed and the computation domain is extended until a subcritical node is found upstream (let say at position  $n$ ). Then, the domain starting from  $m$  to  $n$  is computed and converged. If this technique was not used a boundary condition problem would occur. Indeed, a supercritical flow requires an upstream BC since the characteristic velocity is directed downstream.

A general view of the algorithm is given in Figure 34. It shows that after initialization, a main loop is started. It consists in computing only a part of the entire domain, using the evolutionary domain concept explained before. The computation domain span evolves in the ‘‘Vary domain span’’ box. A detailed flowchart of the algorithm of this box is given in Figure 35.

First, a check is made to know if some nodes still not computed. Indeed, when all the nodes are computed at least once, a final computation is done on the entire domain in order to ensure

a final convergence. If some nodes still have to be added to the computation domain, several checks are made in order to identify the status of the computation:

- If the computation is identified as not converged, the computation domain is increased by adding the downstream and upstream nodes (+ 2 nodes)
- If the flow upstream is supercritical, then the downstream limit is not modified but a node is added upstream (+ 1 node)
- If the most downstream node of the computation domain changed more than some threshold, then the domain is extended downstream as well as upstream (+ 2 nodes), otherwise a node is removed from the domain (- 1 node)

When the number of nodes to keep is known (and adjusted to agree with the minimum number of nodes to keep in the list), the upstream and downstream nodes of the computation domain are pointed and a new iteration of the main loop can begin.

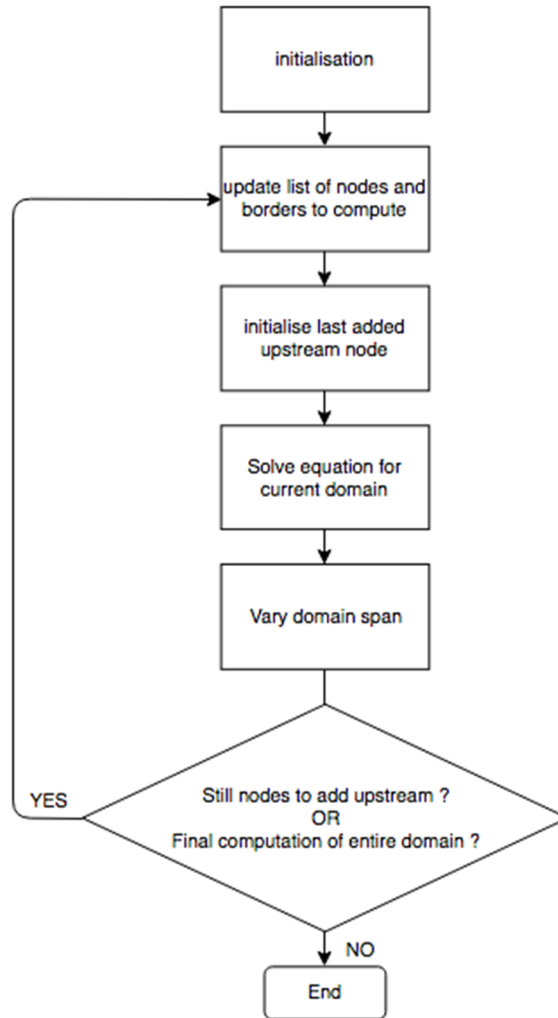


*Figure 34: Flowchart of the general algorithm*

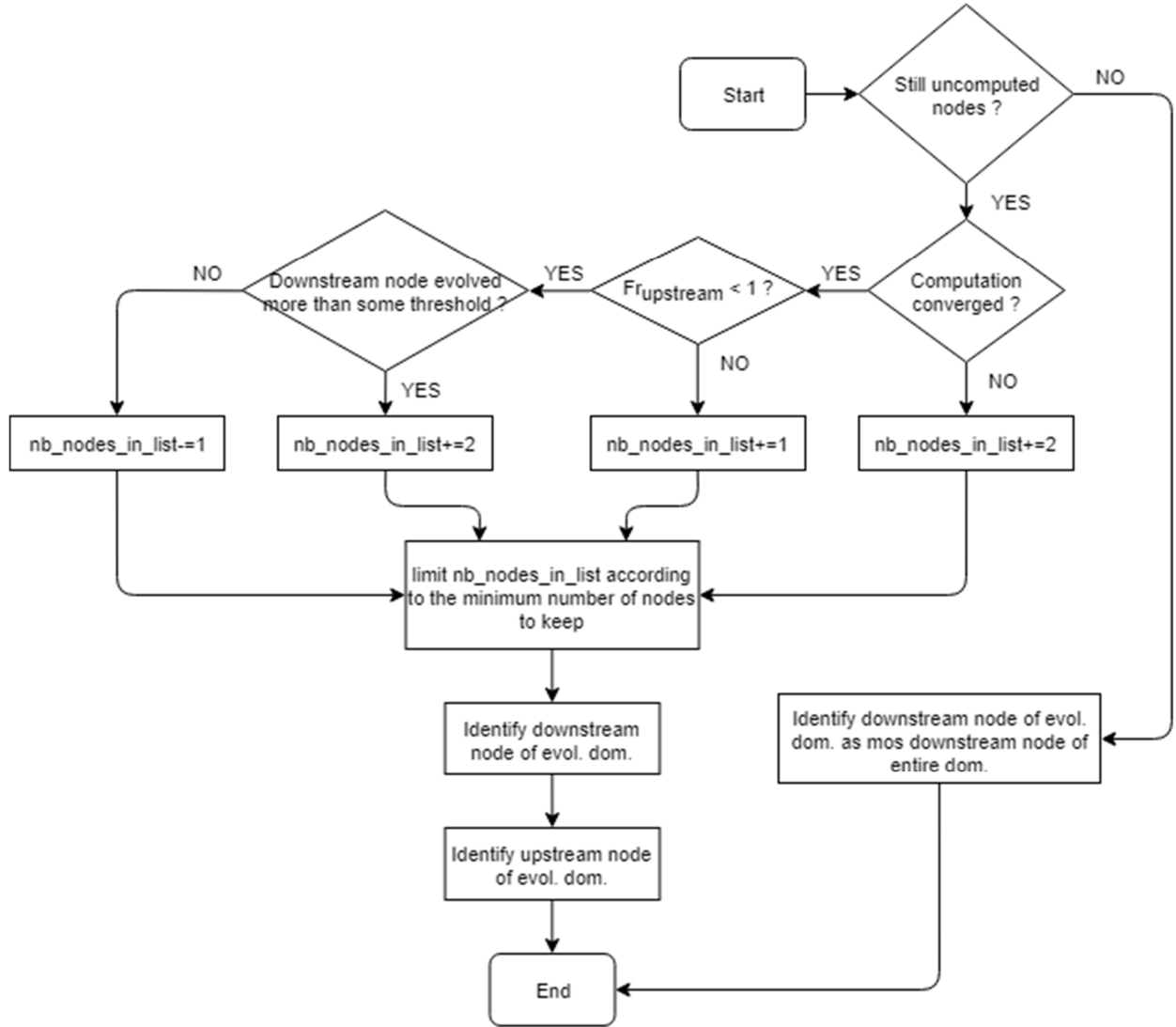


Figure 35: Flowchart for the algorithm that manages the variation of the domain span

### 3.3.2.3 Combination of solving strategies

The combined use of the sliding domain and NKA involves several specific considerations. The use of NKA is implemented in the code with a safety coefficient that deactivates this optimizing technique in some cases. Indeed, it was experienced that NKA could lead to some instabilities when there was a sudden change in the cross-section area. This behavior is due to the assumption in NKA that the Jacobian matrix is constant and invertible locally (Calef et al. 2013; Wang et al. 2018). Problems with this assumption were encountered in several situations. We found that the main one is when cross section areas of the two most upstream nodes are too different. Our experience showed that the accelerator should be deactivated when:

$$|A_{i+1} - A_i| > \eta A_{i+1} \quad (160)$$

where  $A_i$  and  $A_{i+1}$  refer to the cross-section area of the nodes  $i$  and  $i+1$  as depicted in Figure 33,  $0 < \eta \leq 1$  is the safety coefficient. It has to be defined in order to reach optimal computation times. This will be discussed in section 3.5.

### 3.4 Validation

The validation of the model will be performed on a bump in three different flow conditions. The geometry will be detailed later. For each flow condition, various computations will be performed in order to extract the water profile and the computation time. The validity of the result will be assessed against an analytical solution. The computation times for the full model, the pseudo-time model and three versions of the optimized pseudo-time model will be confronted. These three versions are:

- the pseudo-time model with the Anderson accelerator available,
- the pseudo-time model with the evolutionary domain activated and,
- the pseudo-time model with both of these options.

The computation times evaluated here give a first insight to the performance of each model. A deeper and more rigorous analysis will be performed in the parameter optimization section (section 3.5).

#### 3.4.1 Geometry and test cases descriptions

The bump that is studied here is described in (Aureli et al. 2008). The whole domain ranges from 0 to 20 m with the following bed elevation:

$$z_b(x) = \begin{cases} 0.8 \left( 1 - \frac{(x-10)^2}{4} \right) & 8\text{m} \leq x \leq 12\text{m} \\ 0 & \text{elsewhere} \end{cases} \quad (161)$$

The channel is considered rectangular and frictionless. The discretization is chosen at 0.1 m and depicted in Figure 36, Figure 41 and Figure 45. The different flow conditions are described in Table 13.

Test	Upstream BC	Downstream BC
A	$q = 1 \text{ m}^2/\text{s}$	$h = 1.7 \text{ m}$
B	$q = 0.4 \text{ m}^2/\text{s}$	$h = 0.75 \text{ m}$
C	$q = 0.4 \text{ m}^2/\text{s}$	Transmissive

Table 13: Boundary conditions for three test cases

The objective is to show that the models are able to deal accurately with various flow regimes and transitions. Test A intends to simulate a fully subcritical flow with no transitions. Test B is for a subcritical flow upstream, a subcritical flow downstream and a hydraulic jump in between. Finally, the goal of test C is to show the robustness of our method for a downstream supercritical flow and an upstream subcritical flow.

The analytical solutions for tests A, B and C can be computed from the Bernoulli principle (head conservation) and the conjugate water depths formula for test B. The results obtained with the original model presented hereabove are also compared to the standard unsteady 1-D model available in WOLF. This model, which is called “full model”, uses the same upwinding scheme as the one used for the newly developed 1-D steady model. It is based on a finite volume scheme that uses a constant reconstruction at the borders for this application.

### 3.4.2 General subcritical flow (A)

In test A, the water depth is imposed downstream (1.7 m) and the discharge is known in the whole domain ( $q = 1 \text{ m}^2/\text{s}$ ). A head can be computed at the downstream boundary condition and it has to be conserved in the entire domain since the flow does not encounter any head loss:

$$z_b(x) + h(x) + \frac{q^2}{2g} \frac{1}{h^2(x)} = 0 + 1.7 + \frac{1^2}{2g} \frac{1}{1.7^2} \approx 1.718 \text{ m} \quad (162)$$

The solution of (162) is represented in Figure 36.

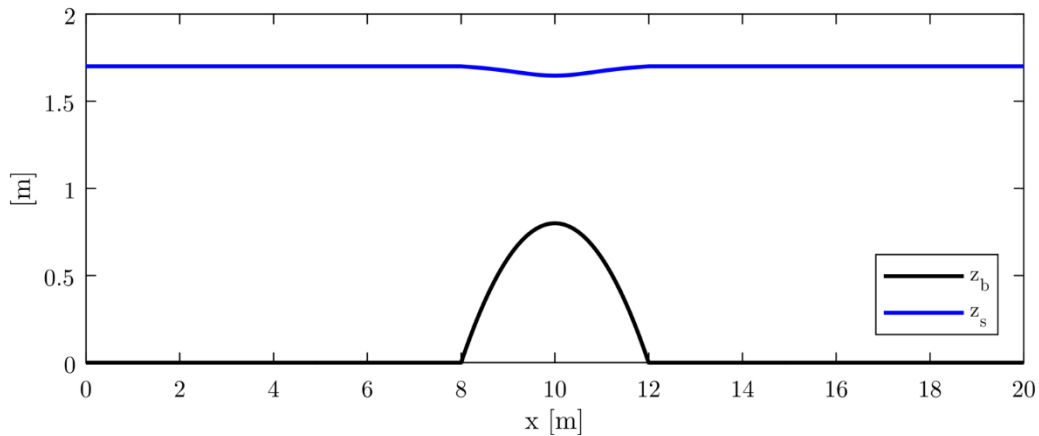


Figure 36: Analytical solution for test A

The numerical solutions with the different versions of the hydraulic model are given in Figure 37. We can observe that all the versions of the numerical model approximate the analytical solution for the water depth with very small errors. This can be quantified through a head

conservation analysis on the bump (Figure 38). The head is computed at the borders in order to be consistent with the flux-splitting scheme. It appears that the head varies on the bump and eventually stabilizes at a higher level upstream of the bump. The error on the head reaches up to 0.22 %. This phenomenon, which is linked to the discretization of the divergence of bottom slope term, is explained and quantified by Bruwier et al. (2016).

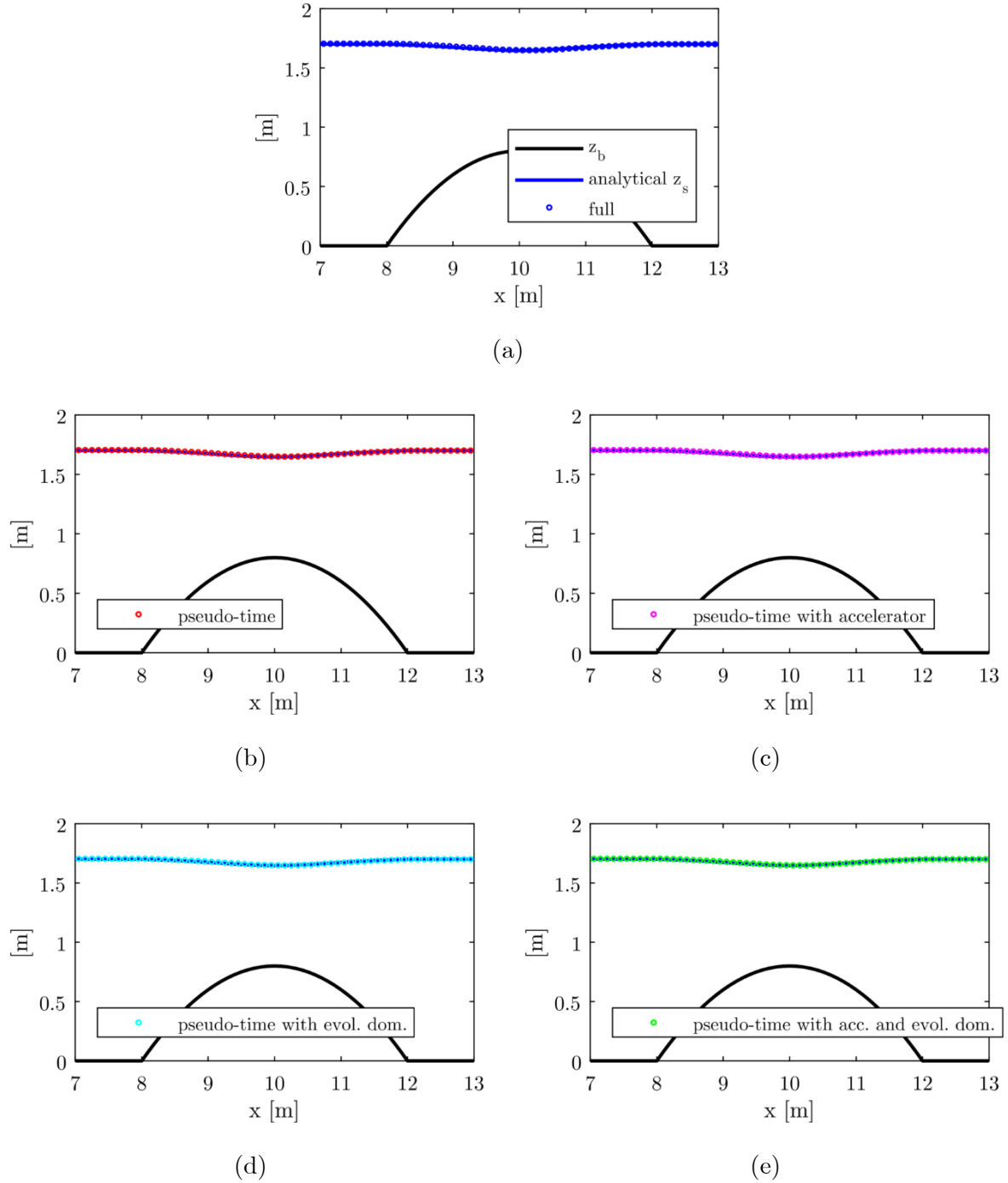


Figure 37: Comparison between the analytical and the numerical solutions for Test A using different models

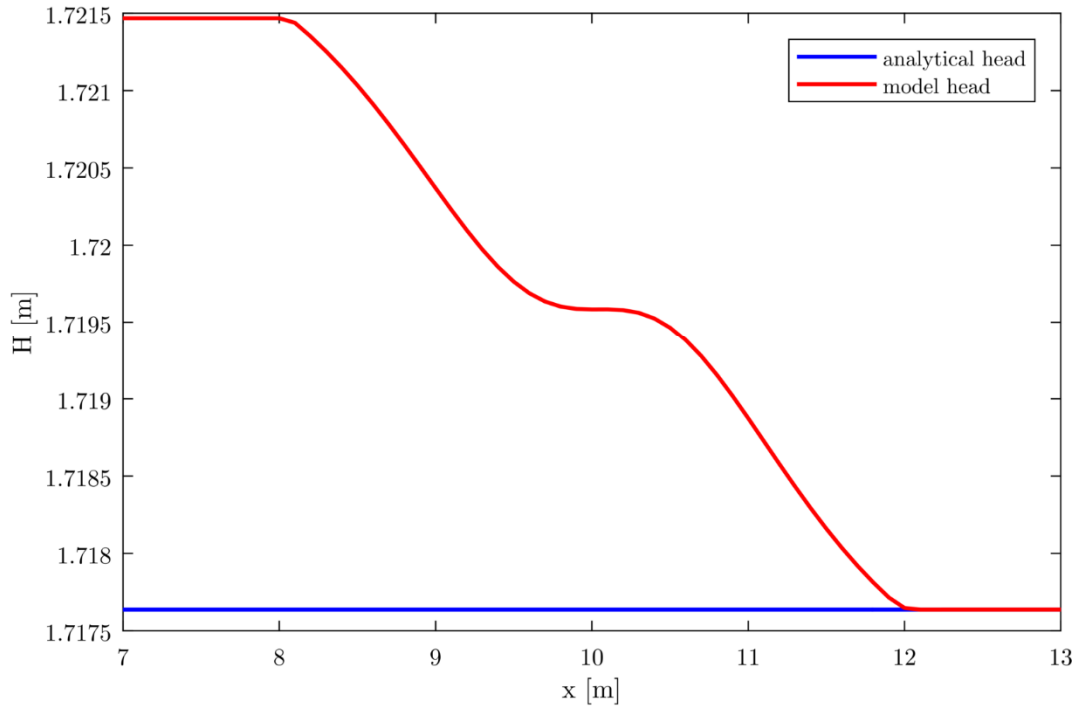


Figure 38: Head conservation on the bump

The computational cost of each technique is also evaluated. The computational cost is standardized according to the cost of the pseudo-time model:  $\bar{T} = T / T_{pt}$ . These times are CPU times, meaning that the other processes running on a machine do not interfere in the measurement. The dimensionless times are given in Table 14. For the full model, the time is highly dependent on the initial condition. The absolute value should be taken with care. However, it appears that this model requires more time (with an order of magnitude 10 to 100) than the optimized models. Concerning, the pseudo-time models, the accelerator alone allows a gain of time of about 20 %. In this specific situation, the evolutionary domain leads to an increased computation time.

Model	Computation time $\bar{T}$ [-]
Full	75.176
Pseudo-time	1.000
Pseudo-time with accelerator	0.782
Pseudo-time with evol. dom.	1.404
Pseudo-time with both	0.883

Table 14: Computational cost for each model

We can also analyze the behavior of the sliding domain from this academic test case. During the first steps, the domain extends until it reaches the minimum number of nodes (here it was set at 25 nodes). When this amount of nodes is reached, the domain begins to slide upstream. In this case, no specificity in the flow or the domain geometry requires the sliding domain to extend. When the upstream node is reached, a final convergence procedure is performed on the entire domain (200 nodes). This process is depicted in Figure 39 and Figure 40.

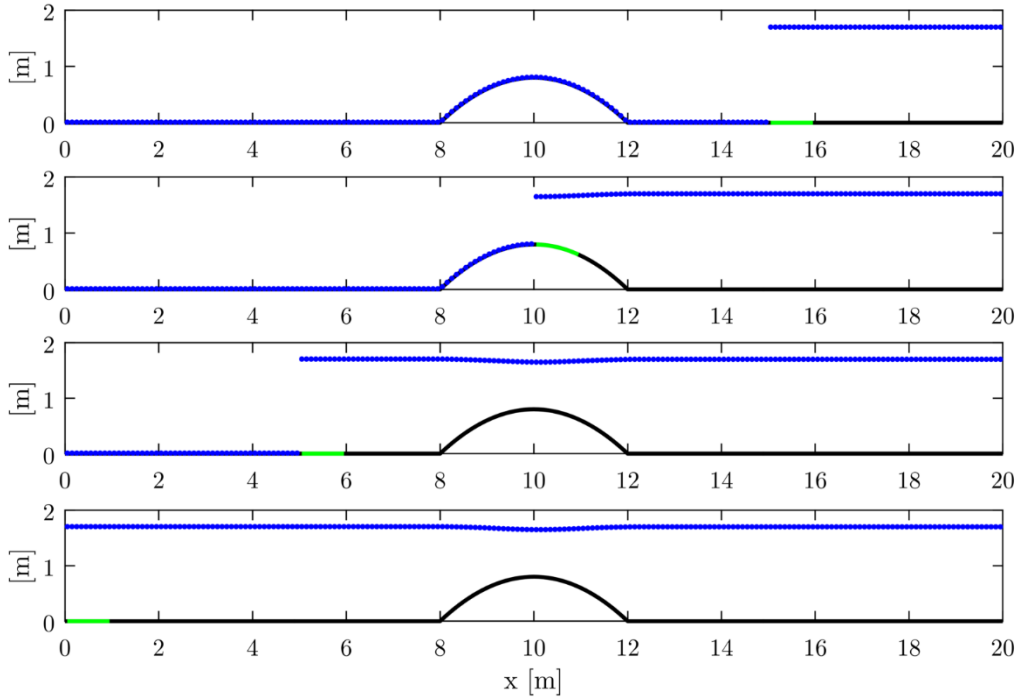


*Figure 39: Sliding of the computation domain (green) for iterates 50, 100, 150 and 200*

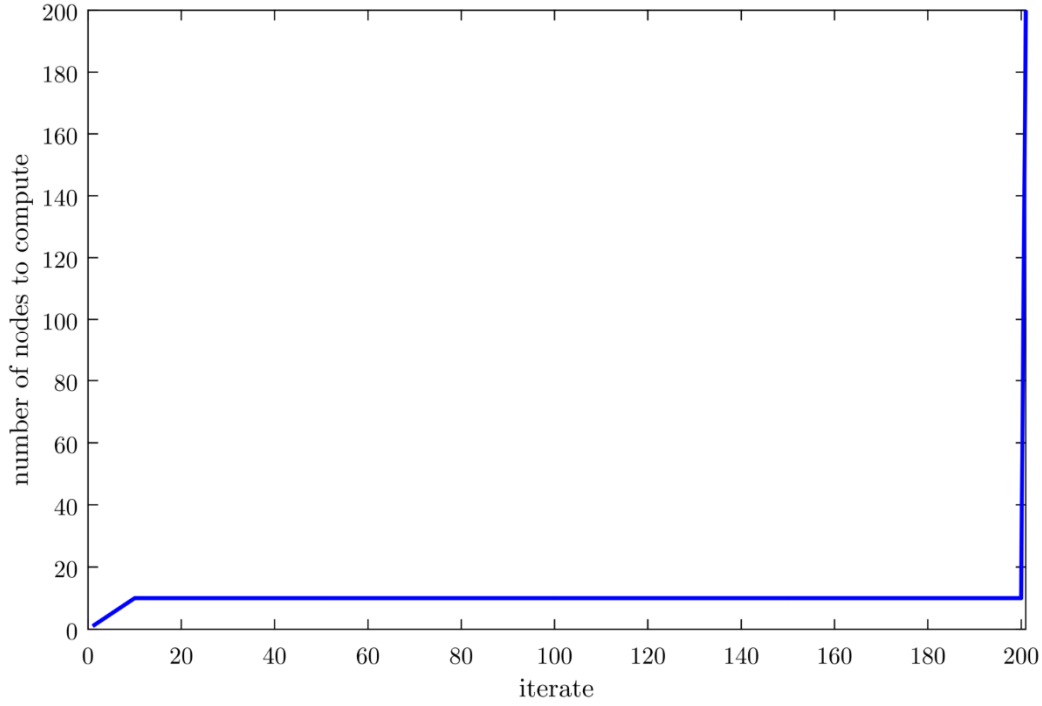


Figure 40: Evolution of the number of computed nodes for test A

### 3.4.3 Flow with a hydraulic jump (B)

For test B, the dimensionless Froude number  $Fr = q / \sqrt{gh^3}$  computed downstream is 0.1966, which means that the flow is subcritical. The water elevation is not sufficient to go over the bump in a subcritical regime. This results in a supercritical flow following the bump crest and a hydraulic jump in order to get a subcritical flow regime back downstream.

The upstream flow can be determined from the critical section at the crest of the bump. The critical water depth is obtained by assuming  $Fr = 1$  at the crest, resulting in  $h_{cr} = 0.2536$  m. From this water depth and since the head is conserved as far as no hydraulic jump is met, the water level can be computed following a similar approach as is equation (162):

$$z_b(x) + h(x) + \frac{q^2}{2g} \frac{1}{h^2(x)} = 0.8 + h_{cr} + \frac{0.4^2}{2g} \frac{1}{h_{cr}^2} \approx 1.1804 \text{ m} \quad (163)$$

For the downstream water level, the same approach is used:

$$z_b(x) + h(x) + \frac{q^2}{2g} \frac{1}{h^2(x)} = 0 + 0.75 + \frac{0.4^2}{2g} \frac{1}{0.75^2} \approx 0.7645 \text{ m} \quad (164)$$

When comparing equations (163) and (164), it appears clearly that the hydraulic jump creates a head loss where it occurs. The position of the hydraulic jump can be computed from the conjugate depths relationship:

$$\frac{h_2}{h_1} = \frac{1}{2} \left( \sqrt{1 + 8Fr^2} - 1 \right) \quad (165)$$

The hydraulic jump occurs at the position that verifies equation (165). In other words, a conjugate water depth  $h_2$  can be computed for every  $h_1$  computed by (163). Once the conjugate water level crosses the water level coming from downstream, the position of the hydraulic jump is found. In our case, this position is around 11.735 m.

The analytical solution computed from the explanations above is given in Figure 41. Blue lines are obtained from the head conservation and the position of the hydraulic jump is found thanks to the crossing of the red line (conjugate depths) and the downstream water profile.

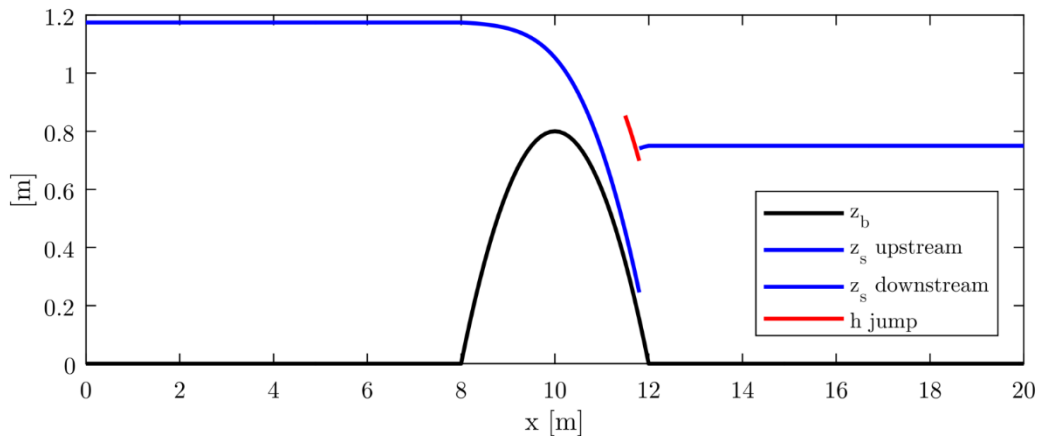
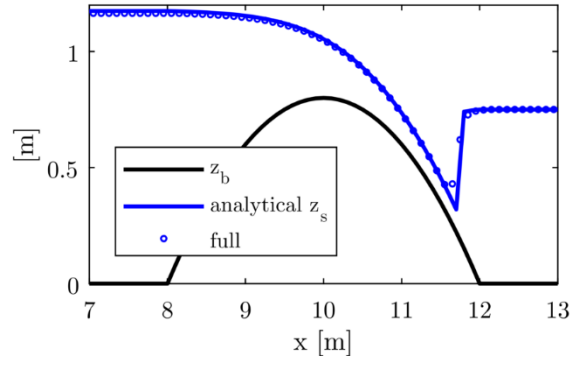


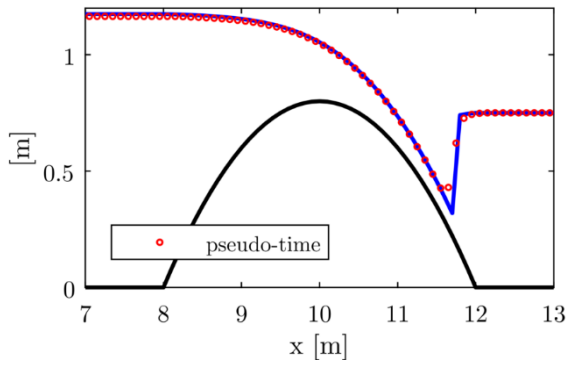
Figure 41: Analytical solution for test B

The numerical results compared with the analytical solution are given at Figure 42 for the 5 different versions of the hydraulic model.

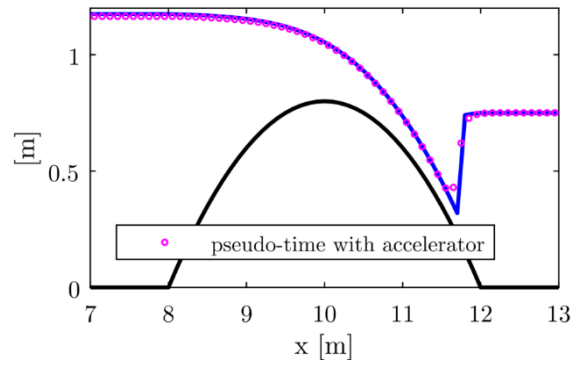
All models approximate the analytical solution (both the water depths and the hydraulic jump position) with satisfactory accuracy. This shows that the non-conservative form of the equations are able to reproduce reliably this kind of discontinuities in the flow. The computational cost (Table 15) decreases by an order of magnitude of 10 between the full model and the pseudo-time model. This number might be lower when a better initial condition is used. When the accelerator and the evolutionary domain options are enabled, the speed-up factor (compared to the pseudo-time model) can reach almost 2. It can be observed from Table 15 that the evolutionary domain provides benefits when coupled with the accelerator while it is neutral when it is used as the only acceleration technique.



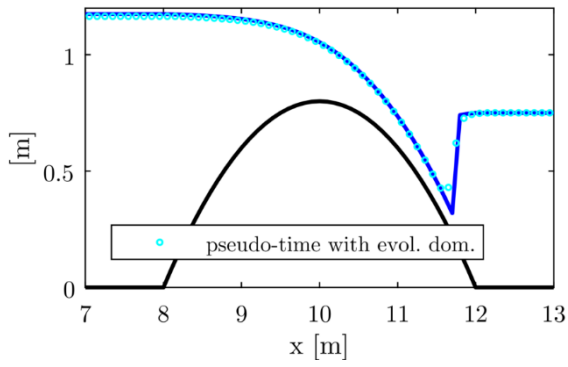
(a)



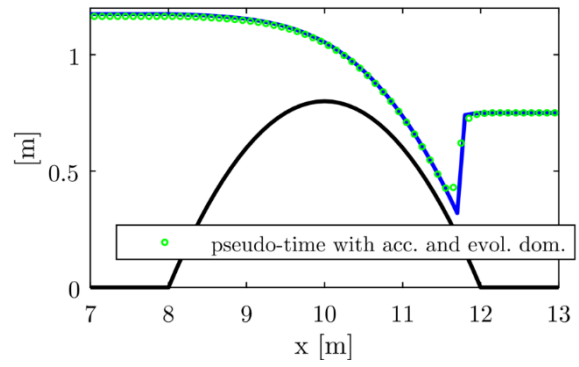
(b)



(c)



(d)



(e)

Figure 42: Comparison between the analytical and the numerical solutions for Test B using different models

Model	Computational time $\bar{T}$ [-]
Full	16.407
Pseudo-time	1.000
Pseudo-time with accelerator	0.686
Pseudo-time with evol. dom.	1.043
Pseudo-time with both	0.497

Table 15: Computational cost for each model

When we look at the domain evolution for this test, it appears that the sliding domain increases its number of computed nodes when it arrives around the hydraulic jump. This increase is due to the super critical flow that occurs upstream of the hydraulic jump. The domain expands until it reaches subcritical flow conditions. After this particularity, the number of nodes decreases down to the minimum number of nodes to keep in the domain. For the last iterate, the entire domain is computed.

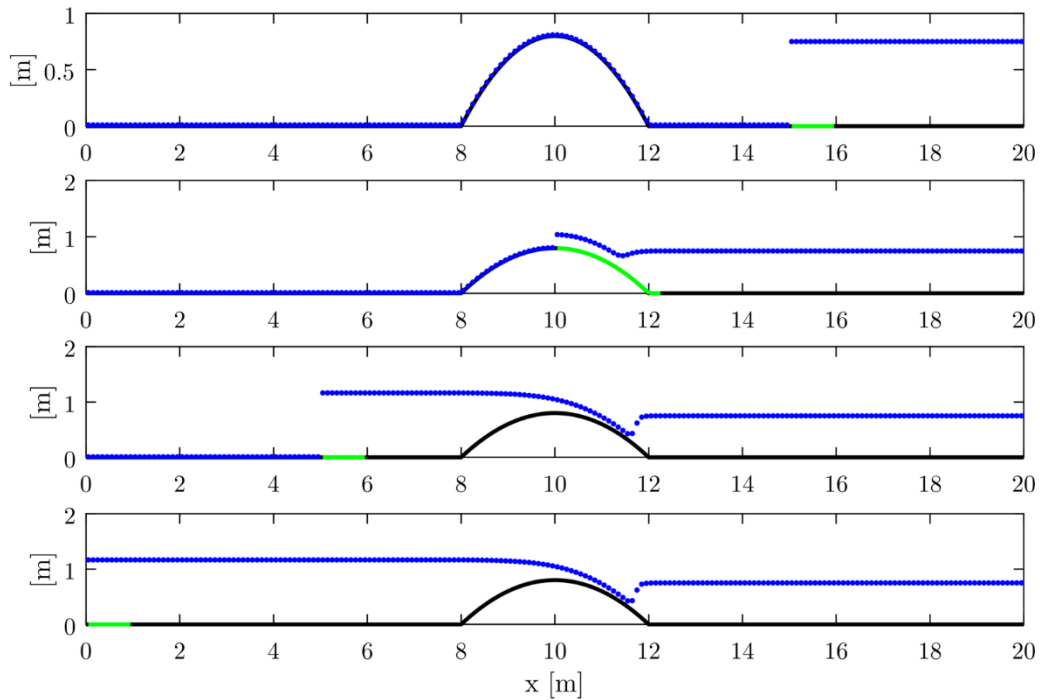


Figure 43: Sliding of the computation domain (green) for iterates 50, 100, 150 and 200

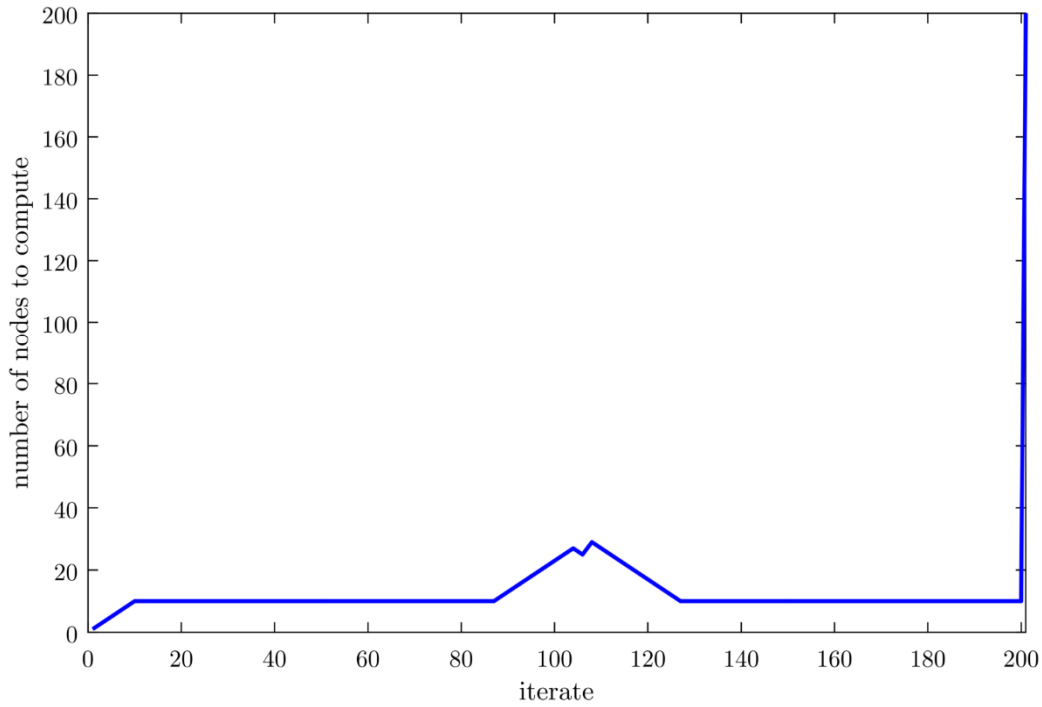


Figure 44: Evolution of the number of computed nodes for test B

### 3.4.4 Subcritical to supercritical flow (C)

For test C, the head is conserved in the entire domain. The head is defined at the critical section (the crest of the bump). At this position,  $h_{cr} = 0.2536$  m. The head in the entire domain is defined by equation (163). Upstream the critical section, the flow is subcritical and downstream it is supercritical. This allows choosing the adequate solution when one solves (163). The analytical solution is given in Figure 45.

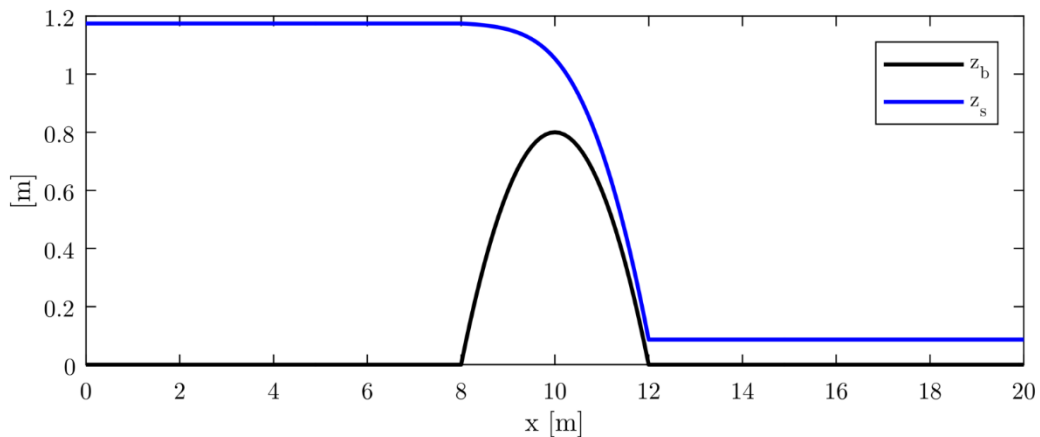


Figure 45: Analytical solution for test C

As explained in section 3.3.2.2, when the evolutionary domain is used, the initialization of a new node depends on the downstream node. For the most downstream node, the initial value

is taken from the water depth boundary condition. For supercritical flows, no downstream boundary conditions is required. In such a situation, the first node would not be able to initialize. In order to trick the model, a downstream boundary condition is imposed in a supercritical state, allowing the first node to initialize. Physically, the water depth propagates from the critical section. Only the last downstream nodes will be affected by this approximation. For the sake of consistency, the same downstream boundary condition is imposed for every model.

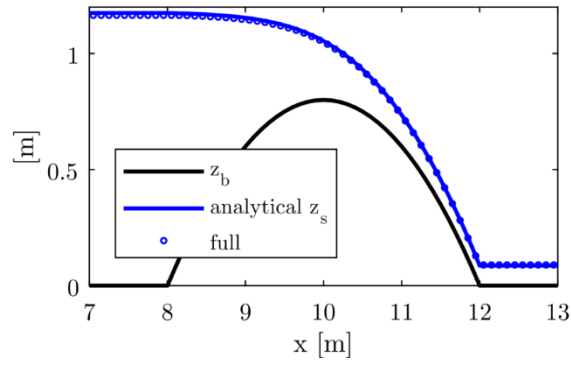
Numerical results are presented in Figure 46. It appears that all the models return results with the same level of accuracy. Differences with the analytical solution can be noticed. They are justified by the discretization scheme used for the bed slope term (Bruwier et al. 2016).

Concerning the computational cost (Table 16), pseudo time models are about 4 times faster than the full hydrodynamic model (the magnitude of the speedup factor might depend on the initial condition used in the full model). Adding the accelerator does not improve the computational time (it even degrades it slightly in this case). Using an evolutionary domain can decrease up to 87 % the computational time.

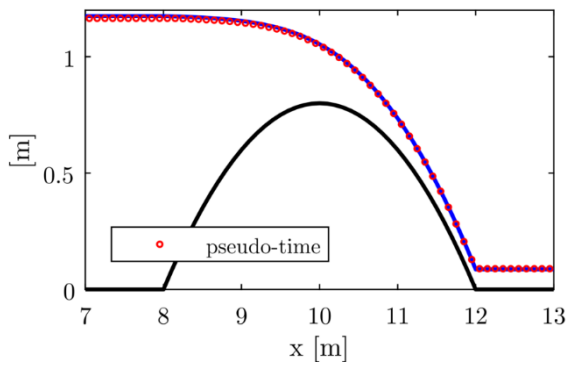
For this test (Figure 47 and Figure 48), the downstream boundary condition is imposed in order to mimic a supercritical flow. In such flow conditions, the computation domain expands until a subcritical flow condition is met. Then, the downstream domain is computed and the sliding domain moves upstream and the number of computed nodes decreases.

Since the flow is supercritical downstream, the downstream boundary condition should be transmissive. However, the model was initially designed to deal with fluvial flows and a downstream boundary condition is required in the computation process. For test C, we show hereafter (Figure 49) that the value of the water depth imposed at the downstream boundary condition has only a limited effect.

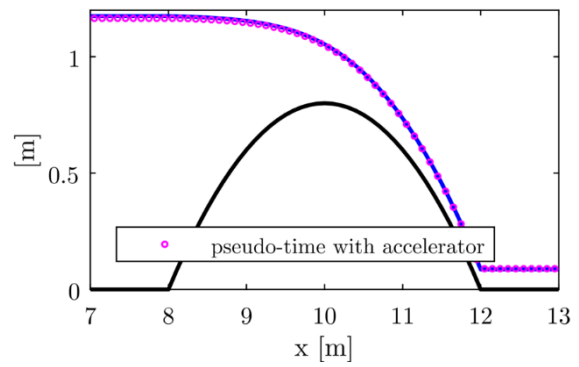
Fast convergence of a steady 1-D open-channel flow



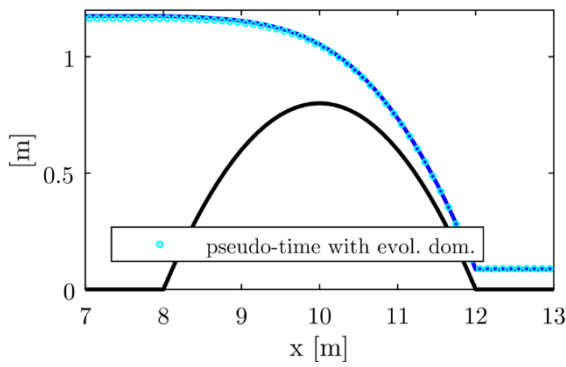
(a)



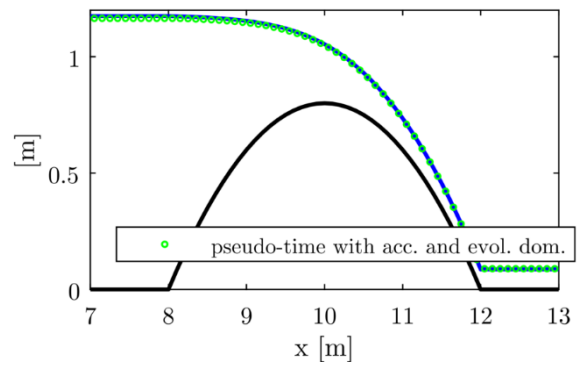
(b)



(c)



(d)



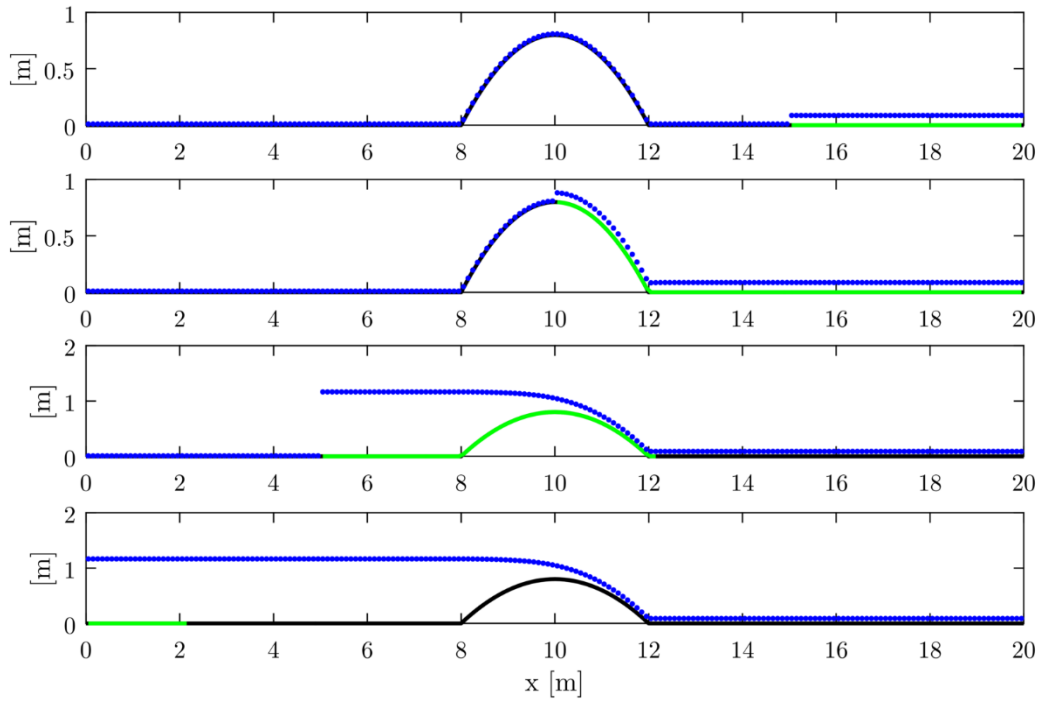
(e)

Figure 46: Comparison between the analytical and the numerical solutions for Test C using different models

*Fast convergence of a steady 1-D open-channel flow*

Model	Computational time $\bar{T}$ [-]
Full	4.967
Pseudo-time	1.000
Pseudo-time with accelerator	1.223
Pseudo-time with evol. dom.	1.878
Pseudo-time with both	1.268

*Table 16: Computational cost for each model*



*Figure 47: Sliding of the computation domain (green) for iterates 50, 100, 150 and 200*

*Fast convergence of a steady 1-D open-channel flow*

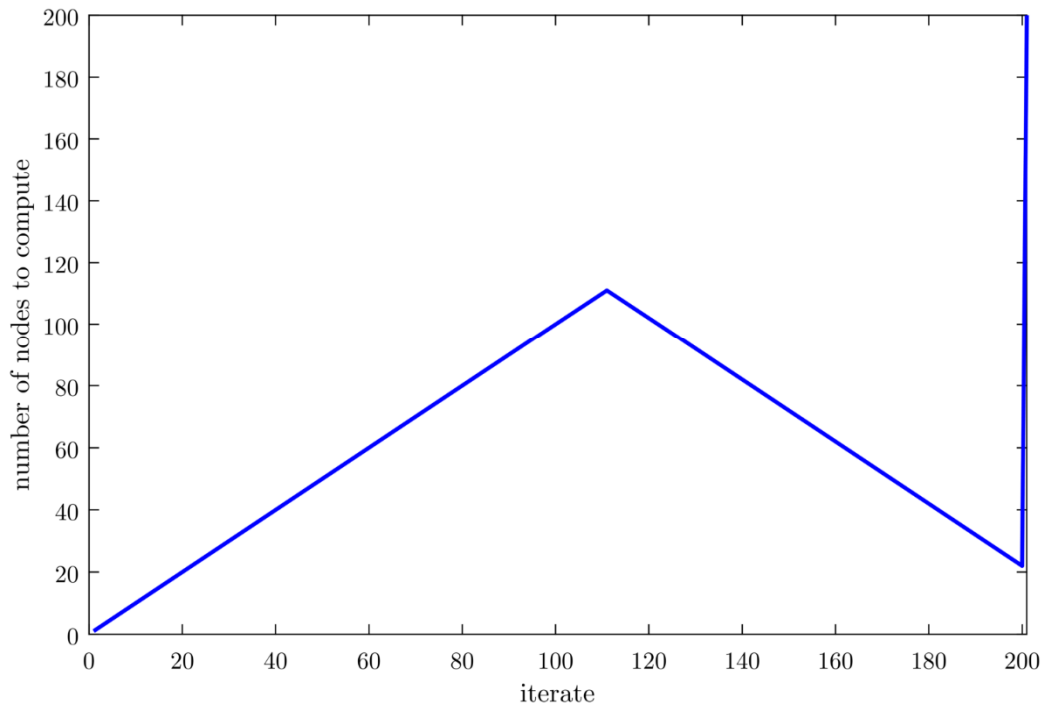


*Figure 48: Evolution of the number of computed nodes for test C*

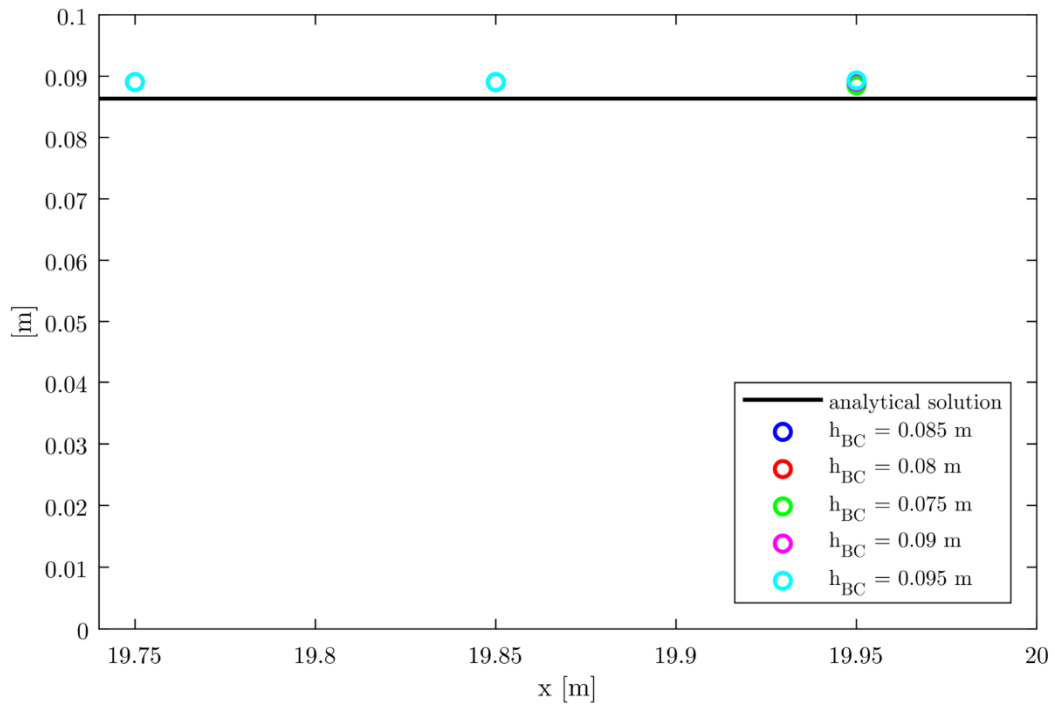


*Figure 49: The value of the downstream boundary condition has a limited impact on the results*

### 3.4.5 Summary

In this section, the models were validated on three academic test cases. The flow conditions were different for each. Test A is a subcritical flow over a bump without any flow regime change. Test B includes a hydraulic jump and test C is supercritical downstream of a bump and subcritical upstream. These test cases allow to evaluate the ability of our models to deal with flow regimes changes.

It appeared that all models (full, pseudo-time and pseudo-time with accelerator and/or sliding domain) gave identical results. These results were close to the analytical solutions. The small differences can be explained by the method used for the discretization of the equation.

Concerning the computation time, the use of the accelerator and/or the sliding domain in the pseudo-time model showed to decrease the computation time in comparison to the full model.

## 3.5 Parameters optimization and speedup evaluation

The model and the solving strategies presented in section 3.3 depend on various parameters:

- The minimum number of nodes to keep in the computation list
- The intermediate allowed residual  $|\partial A / \partial \tau|$ , denoted  $\xi_p$  and also referred as partial residual
- The coefficient used to relax the evolution imposed by the accelerator
- The temporal scheme

In order to reach low computation times for a steady solution, the current section will cope with the definition of optimal parameters.

To do so, a group of test cases is defined. They include various properties that are supposed to test the behavior of our model (changes in the bed shape, changes in the cross-section, etc.).

### 3.5.1 Test cases description

Six test cases are used in this section. The first four tests (1 to 4) concern a channel with a rectangular cross section and a channel bed that follows a sine function:

$$z(x) = \alpha \sin(\beta\pi x) + \gamma \tag{166}$$

With  $x \in [0; 20]$ ,  $\alpha = 0.05$ ,  $\gamma = 0.05$ ,  $\beta = 1/2$  (for tests 1 to 3) and  $\beta = 2$  for test 4. 200 nodes are used to discretize the 20 m long channel, resulting in a 10 cm spatial step. For test 1, the downstream boundary condition is a free surface imposed at 1.2 m. For tests 2 to 4, the same type of boundary condition is imposed at 0.55 m, which results in a higher Froude number

downstream. The specific discharge is imposed upstream at  $1 \text{ m}^3/\text{s}^2$  for test 1 to 4. The Manning law is used for friction in tests 1, 2 and 4, with the Manning coefficient  $n = 0.04 \text{ s}/\text{m}^{1/3}$ . The Barr-Bathurst friction law (Machiels et al. 2011; Goffin, Dewals, et al. 2016) is used for test 3 with a characteristic size of the bottom roughness  $k_s = 0.0963 \text{ m}$ .  $k_s$  was computed in order to generate a loss equivalent the one obtained at the downstream border of test 2.

The topography and the hydraulic solutions are given in Figure 50 for tests 1 to 4. Table 17 summarizes the characteristics of each test. The objectives of tests 1 to 4 are to analyze the influence of a variation of the bed topography on the behavior of the sliding domain. For test 1, the irregularity of the bed has only little influence on the water level. For the other tests, the higher Froude number and shorter wave lengths were meant to investigate the possibility of an influence of oscillations of the water level on the sliding domain performances. Finally, in test 3, a Barr-Bathurst law was used in order to cope with a change in the friction law formulation.

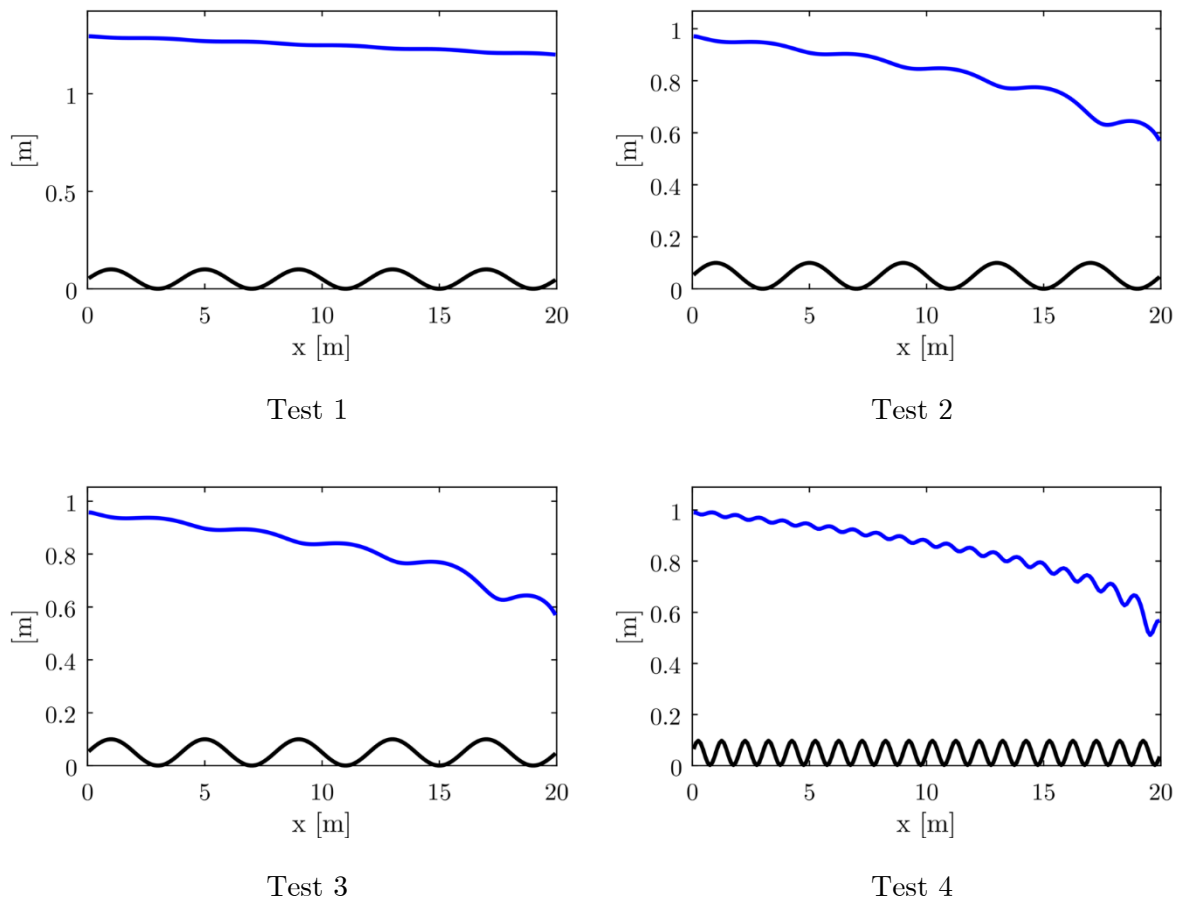


*Figure 50: Topography and free surface results for tests 1 to 4*

Tests 5 and 6 are performed on regular bottoms. The discontinuities that we want to explore here are linked to a change in the flow regime, due to the presence of a weir (test 5) or a severe

change in the cross-section (test 6). For test 5, the topography is set at  $z = 0$  m for all nodes except 3 of them:  $z = 0.5$  m at  $x = 9.85$  m and  $x = 10.05$  m, and  $z = 1$  m at  $x = 9.95$  m. Friction is computed with the Manning formula and a coefficient  $n = 0.04$  s/m<sup>1/3</sup>. The cross-section is uniform along the channel and is rectangular with a width of 1 m. A discharge of 1 m<sup>2</sup>/s is injected upstream and a water level at 0.7 m is imposed downstream.

Test 6 deals with a severe change of the cross-section on an inclined bottom. The channel extends on 100 m, discretized with 200 nodes. The slope is 0.2 %. The cross-section is trapezoidal upstream ( $x \leq 47.5$  m), then suddenly becomes rectangular in the middle of the channel ( $47.5 \text{ m} < x < 52.5 \text{ m}$ ), and finally gets back to a trapezoidal shape in the downstream part ( $x \geq 52.5$  m). Trapezoidal sections have a width at the bottom of 2 m and the banks are inclined with an angle of 45°. The rectangular cross-sections are 1 m wide. Friction and boundary conditions are shared with test 5.

Topography and final water levels for tests 5 and 6 are depicted in Figure 51. A summary of these tests is given in Table 17.

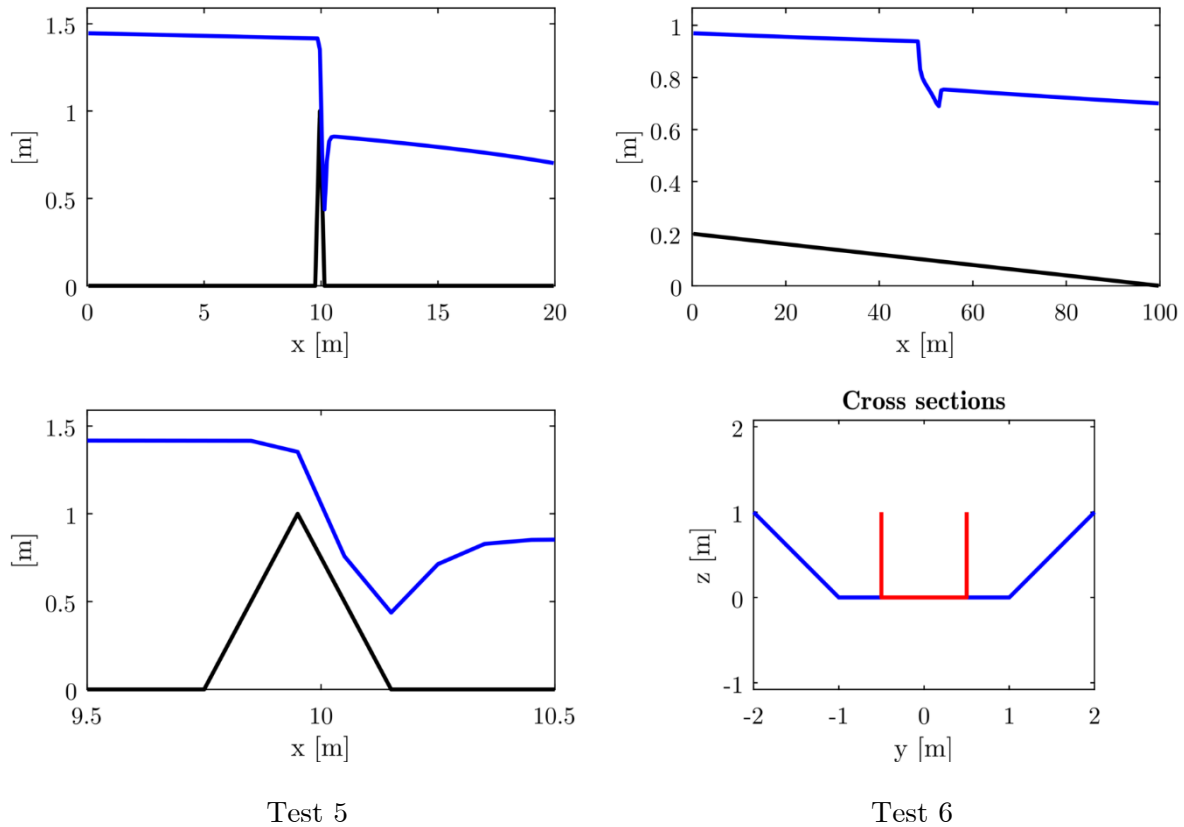


Figure 51: Topography and free surface results for tests 5 and 6

Test	Channel bed	Friction	BC
1	$z(x) = 0.05 \sin(\pi x / 2) + 0.05$ , rectangular cross-section	Manning, $n = 0.04 \text{ s/m}^{1/3}$	$q = 1 \text{ m/s}^2$ , $z_{down} = 1.2 \text{ m}$
2	$z(x) = 0.05 \sin(\pi x / 2) + 0.05$ , rectangular cross-section	Manning, $n = 0.04 \text{ s/m}^{1/3}$	$q = 1 \text{ m/s}^2$ , $z_{down} = 0.55 \text{ m}$
3	$z(x) = 0.05 \sin(\pi x / 2) + 0.05$ , rectangular cross-section	Barr-Bathurst, $k_s = 0.0963 \text{ m}$	$q = 1 \text{ m/s}^2$ , $z_{down} = 0.55 \text{ m}$
4	$z(x) = 0.05 \sin(2\pi x) + 0.05$ , rectangular cross-section	Manning, $n = 0.04 \text{ s/m}^{1/3}$	$q = 1 \text{ m/s}^2$ , $z_{down} = 0.55 \text{ m}$
5	Flat bottom with a weir, rectangular cross-section	Manning, $n = 0.04 \text{ s/m}^{1/3}$	$q = 1 \text{ m/s}^2$ , $z_{down} = 0.7 \text{ m}$
6	0.2 % slope, sudden change in cross-section	Manning, $n = 0.04 \text{ s/m}^{1/3}$	$q = 1 \text{ m/s}^2$ , $z_{down} = 0.7 \text{ m}$

Table 17: Description of the 6 test cases

As stated earlier, various parameters are identified to interact with our model performances. For each parameter, several values are tested. Hereafter, we review each parameter and how we suppose they can have influence of the computation time.

The minimum number of nodes to keep in the computation list is supposed to influence the overall computation time. Indeed, this parameter directly influences the computation time for partial domains. For the tests proposed here, 2 to 40 nodes (with a step of 2 between these two values) are considered as the minimum number of nodes to keep in the computation list.

Then, the coefficient used to relax the accelerator when a sudden change in the cross-section occurs ( $\eta$  in equation (160)) is supposed to have some influence on the computation time, in some situations only. We test this coefficient at values of 0.2, 0.4, 0.6, 0.8 and 1.

The last parameter tested is the temporal scheme. Three explicit schemes are tested: a single-step Euler (with a Courant-Friedrichs-Lewy number (CFL) of 0.2), a two-step Runge-Kutta (with a CFL of 0.4) and a three-step Runge-Kutta (with a CFL of 0.65). The number of sub-steps and the CFL number should influence the computation time when the accelerator is not activated. Otherwise, this parameter should have little influence.

The computation for each test is performed on a desktop computer (CPU: Intel i7, 4 cores at 3.5 GHz). OpenMP is also activated in order to parallelize loops over nodes and borders in the computation core (where equations are solved). The indicator that will guide our conclusions is the CPU time. This means that, since OpenMP is activated, this indicator will be larger than the real execution time. For best precision, the `QueryPerformanceCounter` function (Windows) is used. It provides a precision of the order of 1  $\mu$ s (counter value updated at a frequency of 2.6 MHz) while the intrinsic Fortran procedure `cpu_time` has only a precision of the order of 10 ms (counter value updated at a frequency of 60 Hz).

The assumptions about the outcome on computation time presented here are tested in next subsection. A deep analysis of the results for each test case is developed.

### **3.5.2 Results and analysis**

Since four parameters are tested, a classical 2-D map with computation times cannot be drawn. In order to represent and analyze the behavior of the computation time according to the value of the four identified parameters, boxplots are used. For each parameter, a plot is produced. In this plot, for each value of the parameter tested, a boxplot that depicts the dispersion of the computation times obtained with all values of the other parameters is drawn. Boxplots depicted hereafter can be read in the following way:

- The horizontal red line is the median value.
- The upper and lower limits of the blue box are respectively the 75<sup>th</sup> ( $Q75$ ) and 25<sup>th</sup> ( $Q25$ ) percentiles.
- The upper and lower limits of the black dashed line are the extremes of the data set where the outliers have been removed.
- Outliers are depicted in red “+” and are the values lying further than  $1.5(Q75 - Q25)$  from the limits of the blue box.

These plots will help to discover which parameters have the most influence on the computation time. For each test, the analysis is conducted with and without the Anderson accelerator.

For test 1, results show that the main variations are induced by the minimum number of nodes to keep in the computation list and the partial residual (Figure 52). For the two other parameters (Figure 53), only outliers vary slightly. The median,  $Q25$  and  $Q75$  do not show noticeable variations. From these observations we conclude that the parameters with the most effect on the computation time are the minimum number of nodes to keep in the lists and the partial residual.

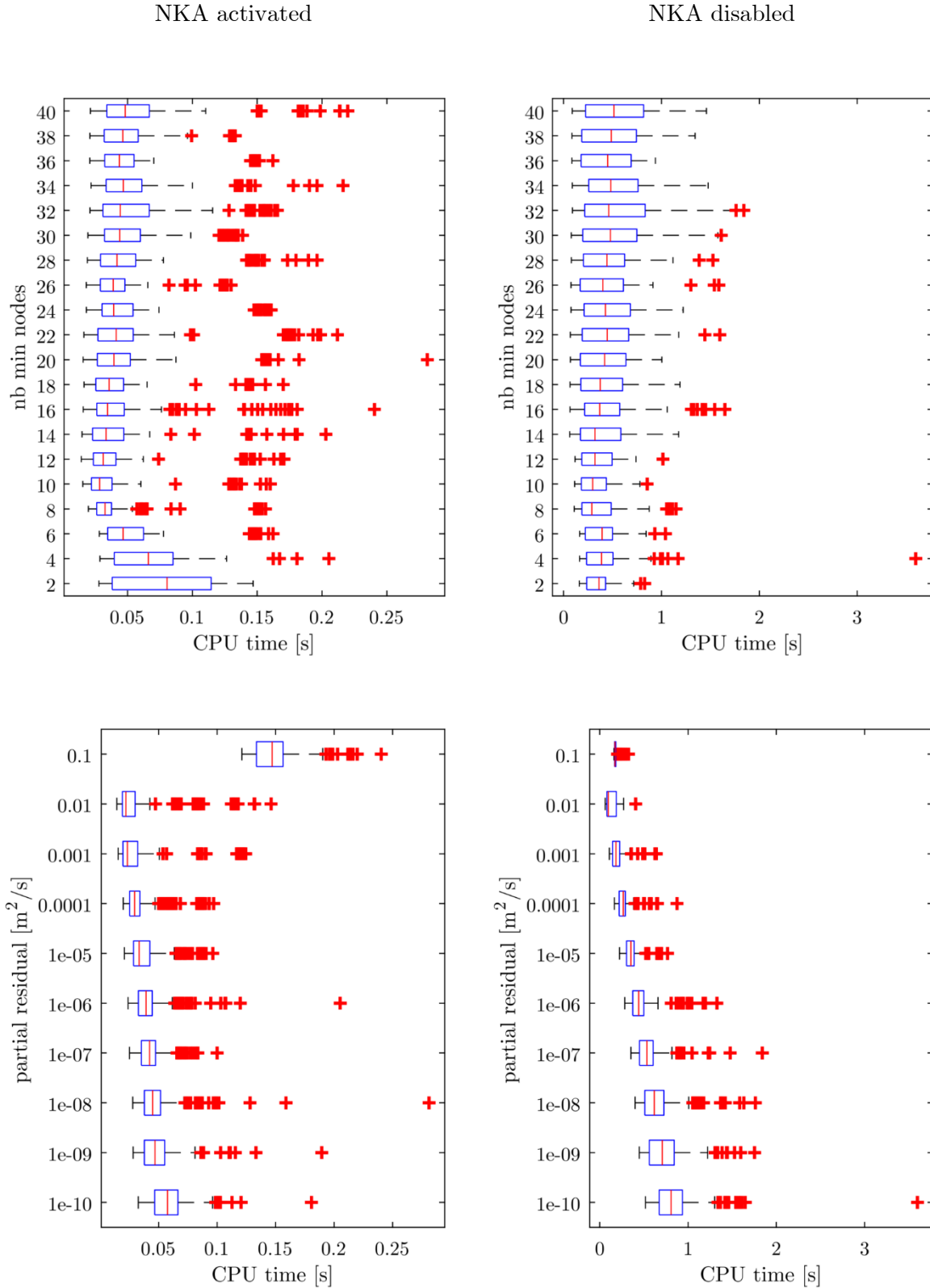


Figure 52: Boxplots according to the minimum number of nodes to keep in computation list and the partial residual for test 1

When looking at the differences when NKA is activated or not, it appears that the behavior is similar for the partial residual effect: higher values lead to lower computation times (except

the lowest value  $0.1 \text{ m}^2/\text{s}$  when NKA is activated). Concerning the minimum number of nodes to keep in the list, the behavior is slightly different. However, an optimal value seems to be around 10 nodes. This will be justified later.

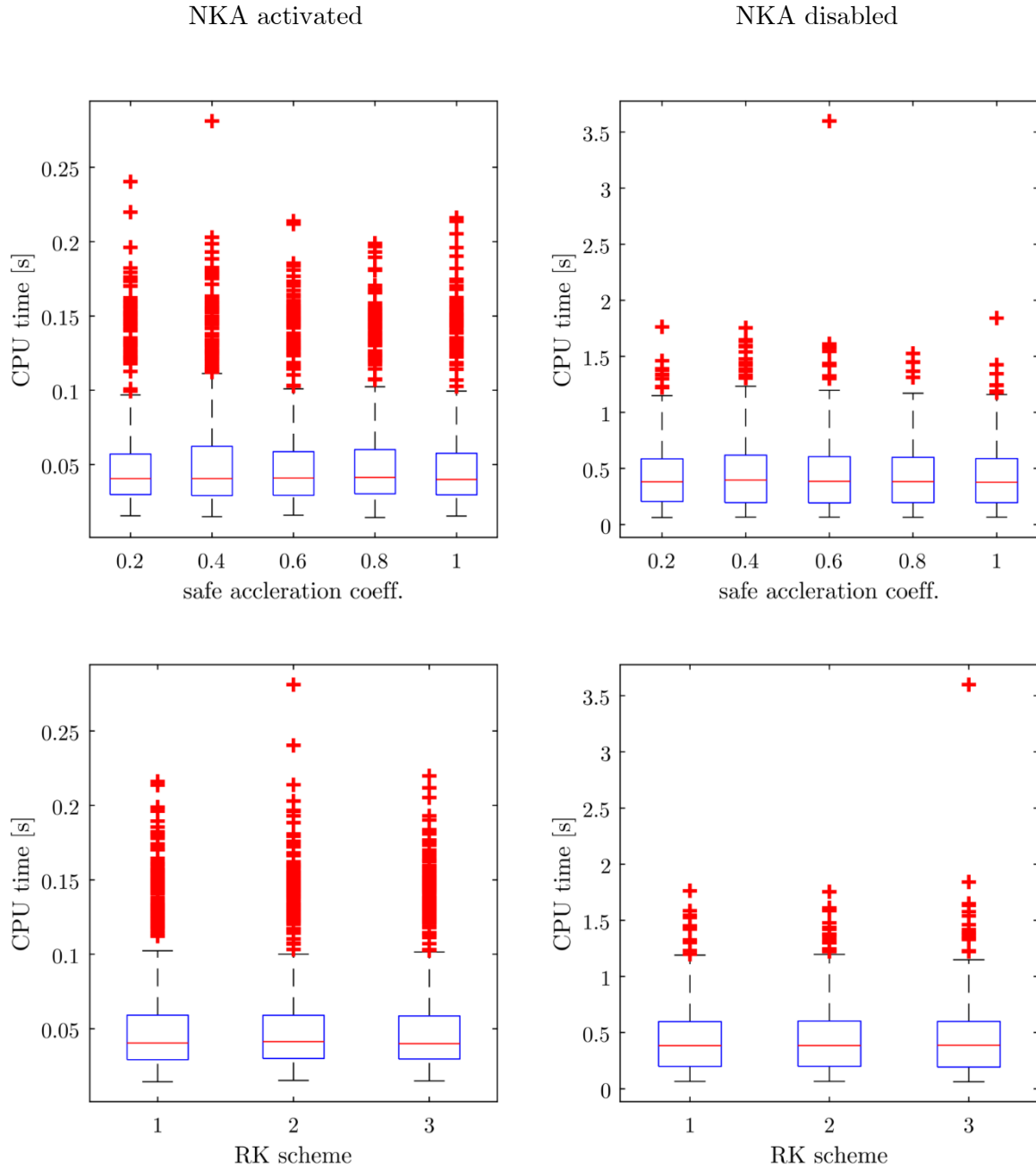


Figure 53: Boxplots according to the value of the safe acceleration coefficient and the temporal scheme for test 1

For test 2, such as for test 1, the last two parameters (Figure 55) have almost no effect on the computation time while the first two parameters (Figure 54) show variation in the computation time when their values change. The activation of NKA however leads to different conclusions concerning optimal values of these two first parameters. A deeper analysis will be conducted later.

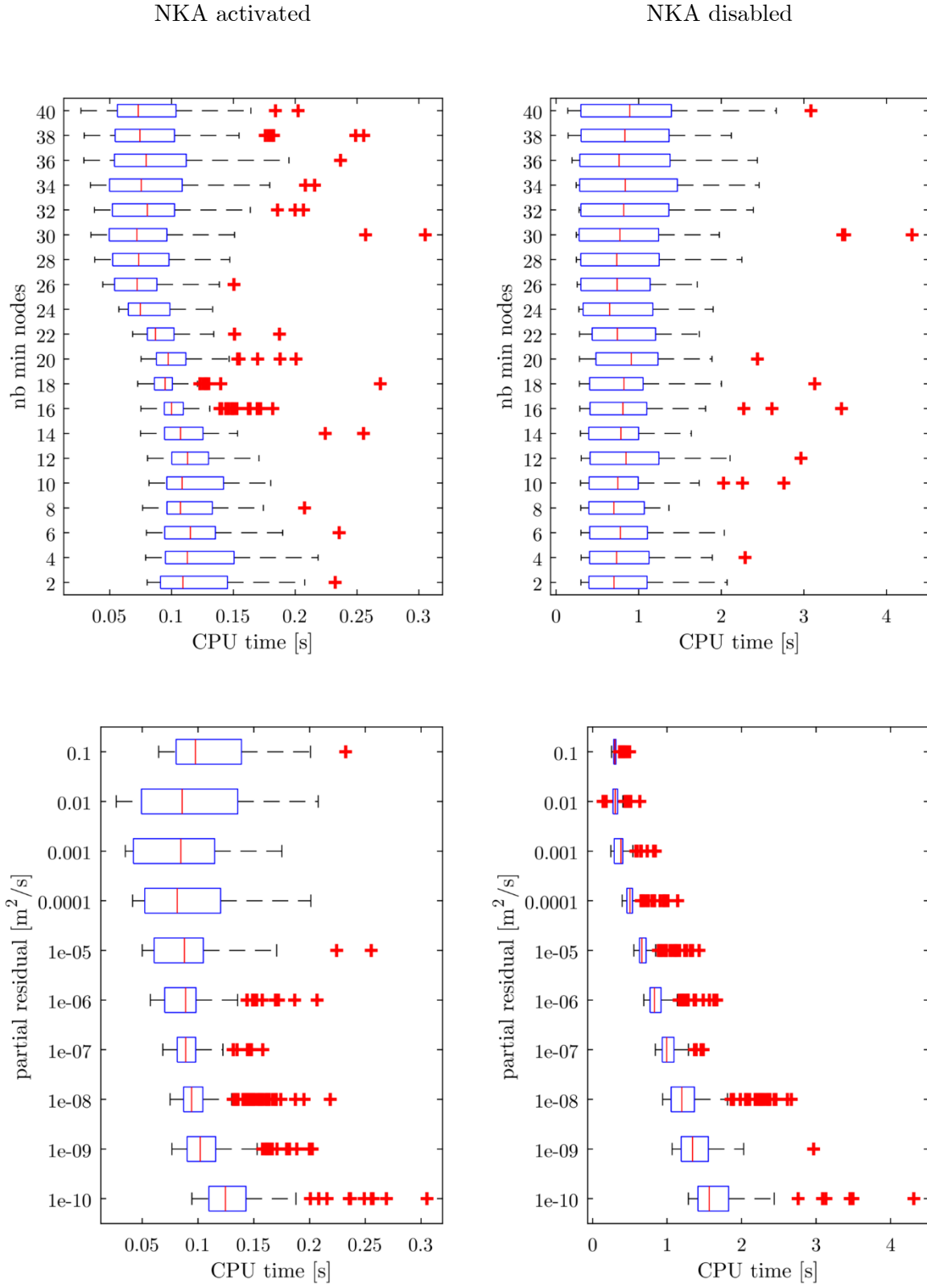


Figure 54: Boxplots according to the minimum number of nodes to keep in computation list and the partial residual for test 2

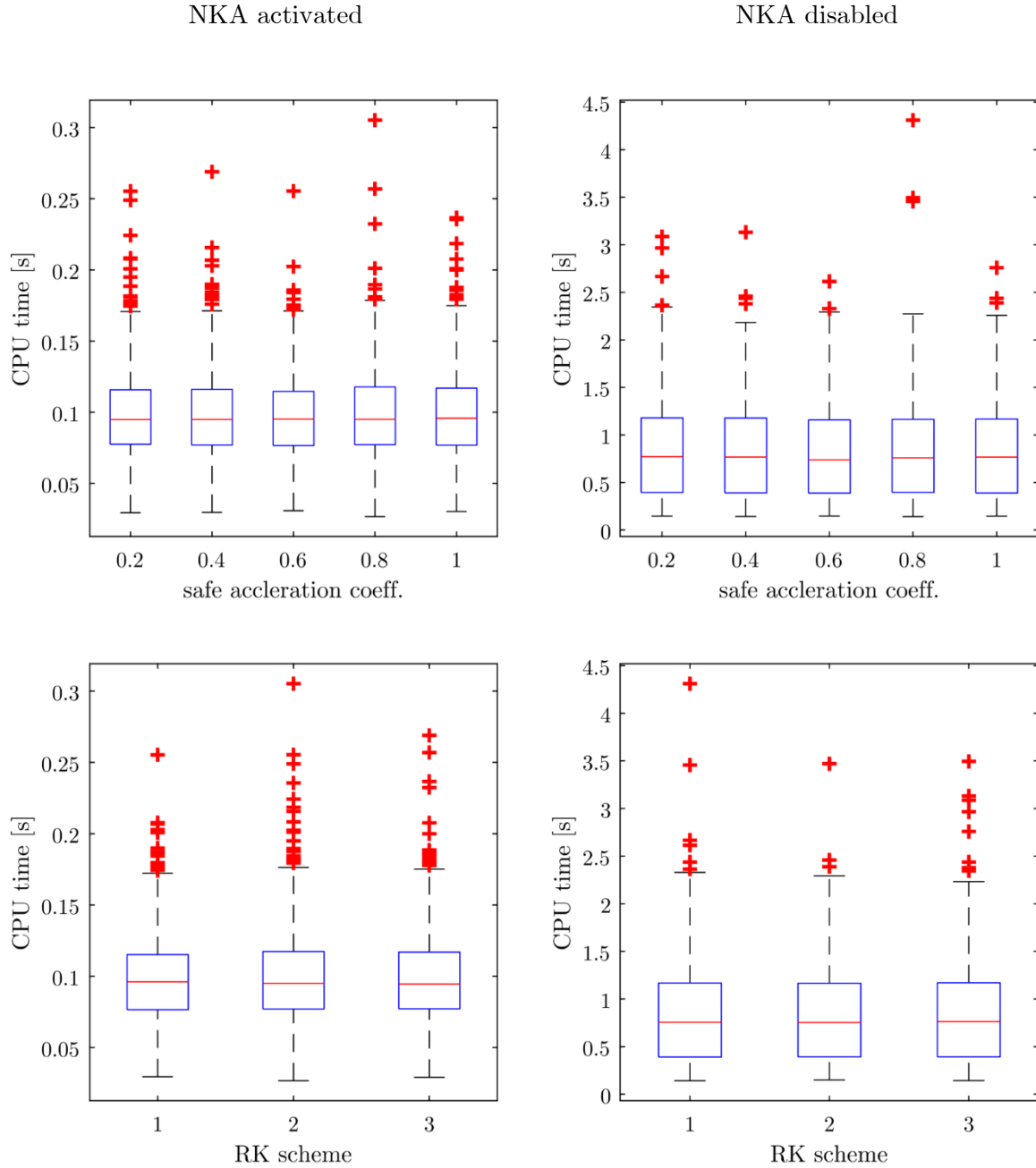


Figure 55: Boxplots according to the value of the safe acceleration coefficient and the temporal scheme for test 2

Test 3 changes from test 2 only in the formulation of the friction law (see Table 17). From the boxplots reproduced in appendix B.1 (Figure 193 and Figure 194), same conclusions as for the previous test can be drawn. From this observation, we are able to conclude that the friction formulation has no influence for the present test case.

For test 4, even if bed oscillations are shorter, conclusions remain similar to test 2 outcomes. Boxplots are reproduced in appendix B.1 at Figure 195 and Figure 196.

From these first four test cases, it appears that the computation time is mainly a function of the minimum number of nodes kept in the computation list and the partial residual. We are

also able to conclude that the activation of the NKA leads generally to lower computation times.

Concerning test 5, results differ slightly from tests 1 and 2 concerning the two first parameters (Figure 56). Indeed, especially when NKA is activated, the computation times do not vary as much in test 5 as in tests 1 and 2. For the value of the safety coefficient (Figure 57), a small variation can be noticed. Indeed, computation times are slightly higher for  $\eta = 0.2$  and  $\eta = 0.4$ . Higher values of  $\eta$  produce lower computation times.

Finally, test 6 results show that, when NKA is activated, the minimum number of nodes to keep in the computation list (Figure 58) should be higher than 10 in order to keep low computation times. Concerning the partial residual, conclusions differ according to the activation status of NKA. If it is activated, one should keep the partial residual lower than  $0.001 \text{ m}^2/\text{s}$ . If NKA is disabled, partial residual should be at or higher than  $0.0001 \text{ m}^2/\text{s}$ . Once more, the RK scheme has no influence on the computation time and the safety coefficient has almost no effects. Only the whiskers at 0.8 and 1 are a little bit lower.

The main outcomes of this boxplots analysis are:

- the minimum number of nodes in the computation list and the partial residual are the two main parameters that guide the computation time,
- enabling NKA allows statistically shorter computation times,
- the temporal scheme has almost no impact on computation times,
- the safety coefficient for the use of the accelerator has only a limited impact and,
- at this point, it is not possible to determine an optimal set of parameters.

Fast convergence of a steady 1-D open-channel flow

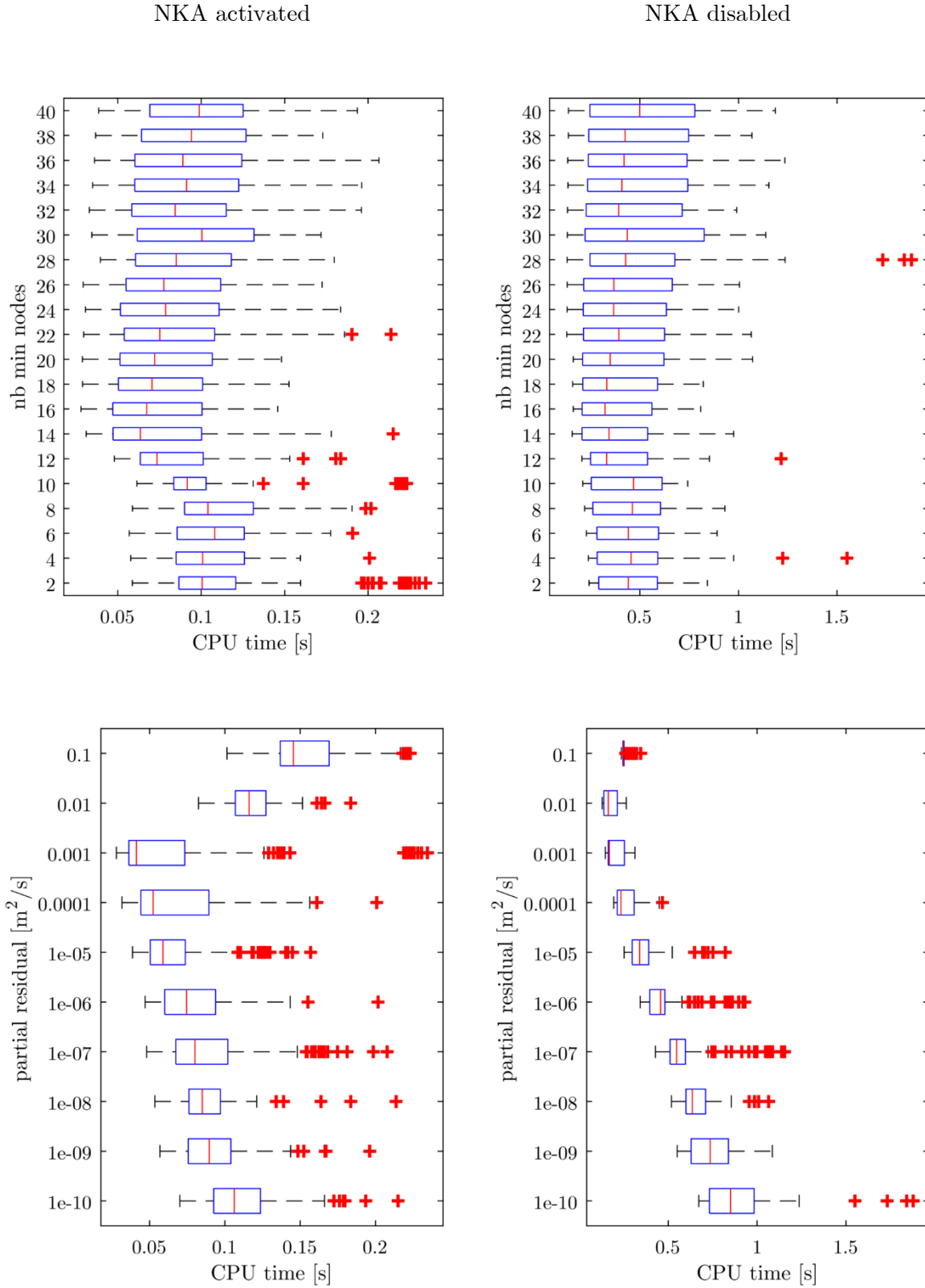


Figure 56: Boxplots according to the minimum number of nodes to keep in computation list and the partial residual for test 5

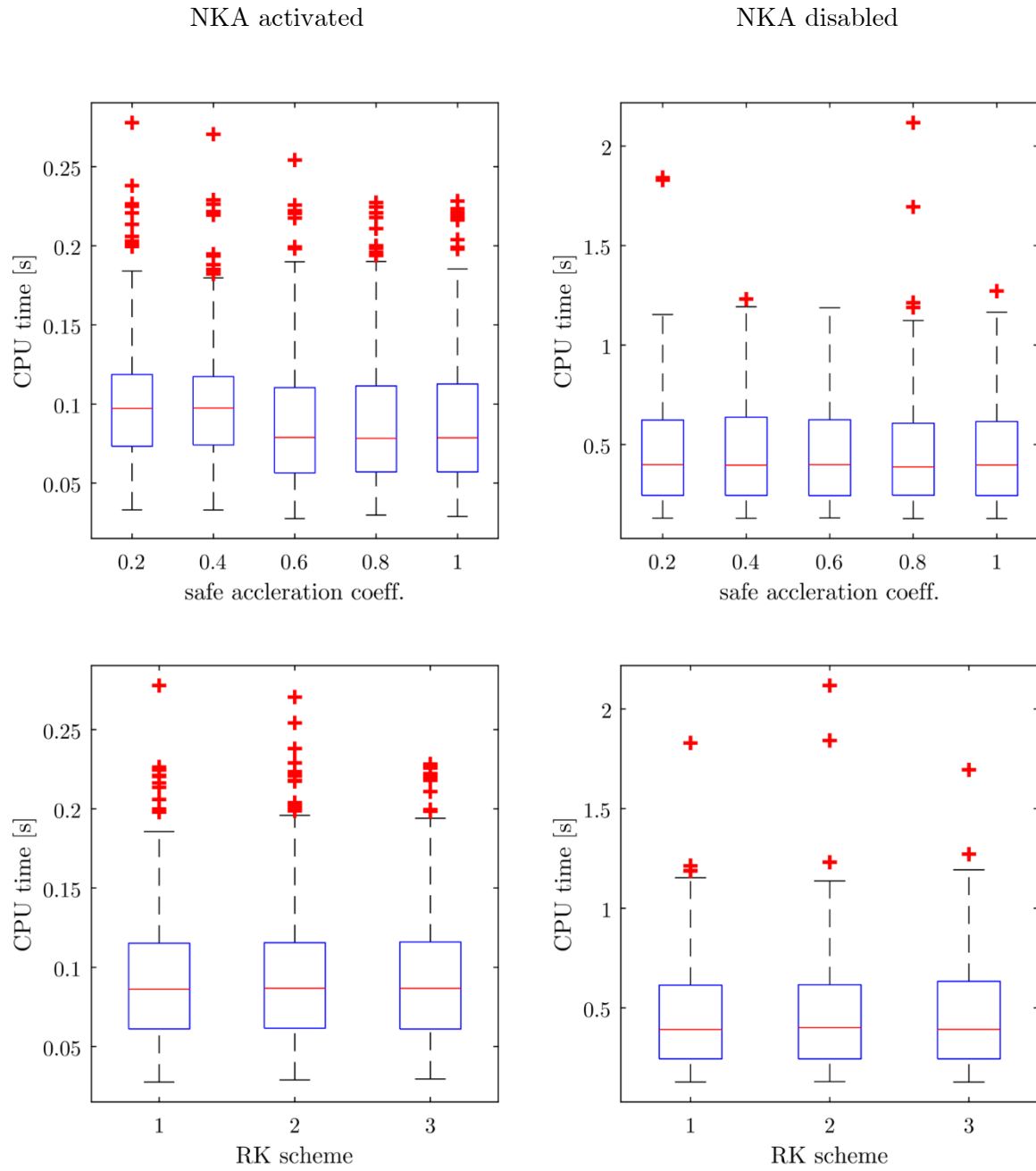


Figure 57: Boxplots according to the value of the safe acceleration coefficient and the temporal scheme for test 5

Fast convergence of a steady 1-D open-channel flow

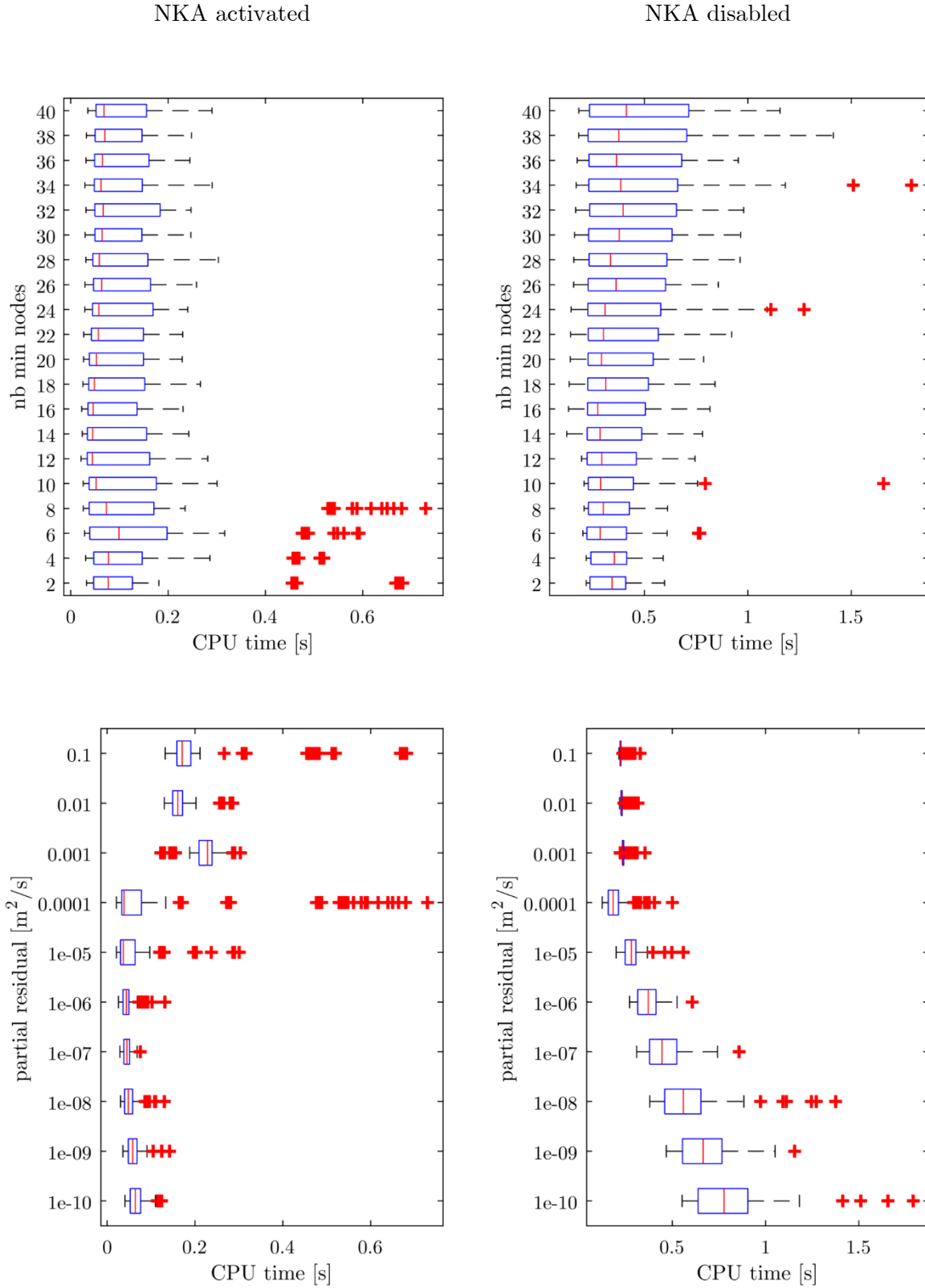


Figure 58: Boxplots according to the minimum number of nodes to keep in computation list and the partial residual for test 6

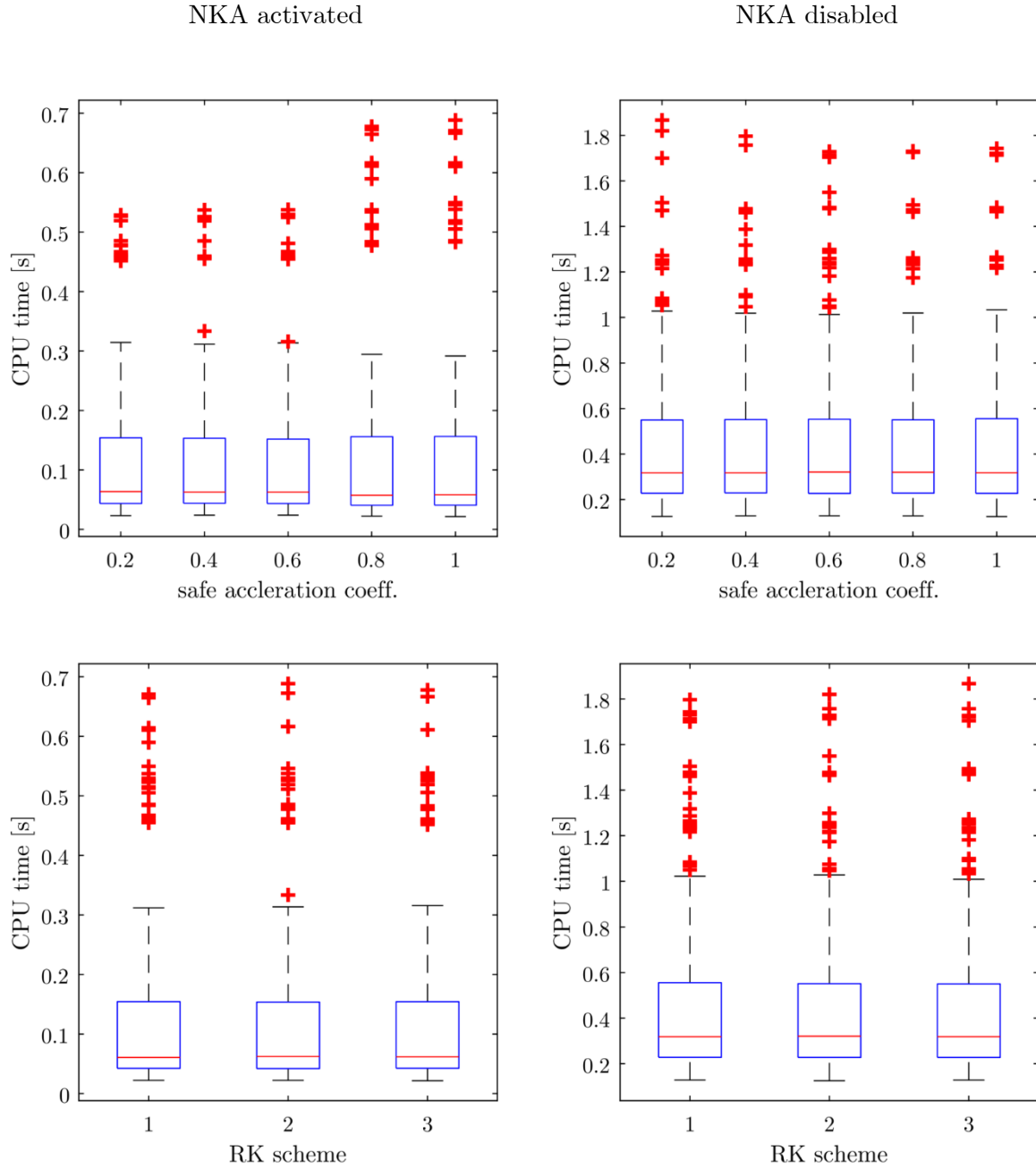


Figure 59: Boxplots according to the value of the safe acceleration coefficient and the temporal scheme for test 6

Having now determined the two main parameters that rule the computation time (the minimum number of nodes in the computation list and the partial residual), 2-D maps will be plotted in order to highlight best combinations. These 2-D maps are presented in Figure 60 and Figure 61. They represent the median computation time for a couple  $(p1, p2)$ ,  $p1$  being the minimum number of nodes to keep in the computation list and  $p2$  the partial residual. The median is computed over the values of computation times obtained at  $(p1, p2)$  and for all values of  $p3$  and  $p4$ ,  $p3$  being the safety coefficient and  $p4$  the temporal scheme. Four points are also

plotted on these graphs. They are not treated immediately but will be useful for further discussion.

At first glance, a general conclusion for a best couple when NKA is activated cannot be drawn immediately. Indeed, test 6 shows best computation times at the left hand side of the map, while best times for test 1 are located to right hand side. However, it appears that it is better to include more nodes in the computation list and keep the partial residual quite low. A good agreement between the 6 tests seems to be around 30 nodes and  $10^{-3}$  m<sup>2</sup>/s.

For each test, best times are obtained with NKA activated. If it is disabled, the behavior of the computation time for the six tests is similar. It should be noticed that higher computation times are obtained at low residual values while they were obtained at high residual values when NKA was activated. This corresponds to the results of the boxplots. A good agreement for all the tests seems to be around 35 nodes and  $10^{-2}$  m<sup>2</sup>/s with NKA disabled.

It is now important to figure out why larger number of nodes and a relatively high partial residual are a good combination. Indeed, a first guess would have given a low number of nodes (for a quick partial computation) and a partial residual close to  $10^{-8}$  m<sup>2</sup>/s (in order to reduce the importance of the last computation all over the domain). In order to understand this counter intuitive conclusion, some more results are analyzed hereafter.

Fast convergence of a steady 1-D open-channel flow

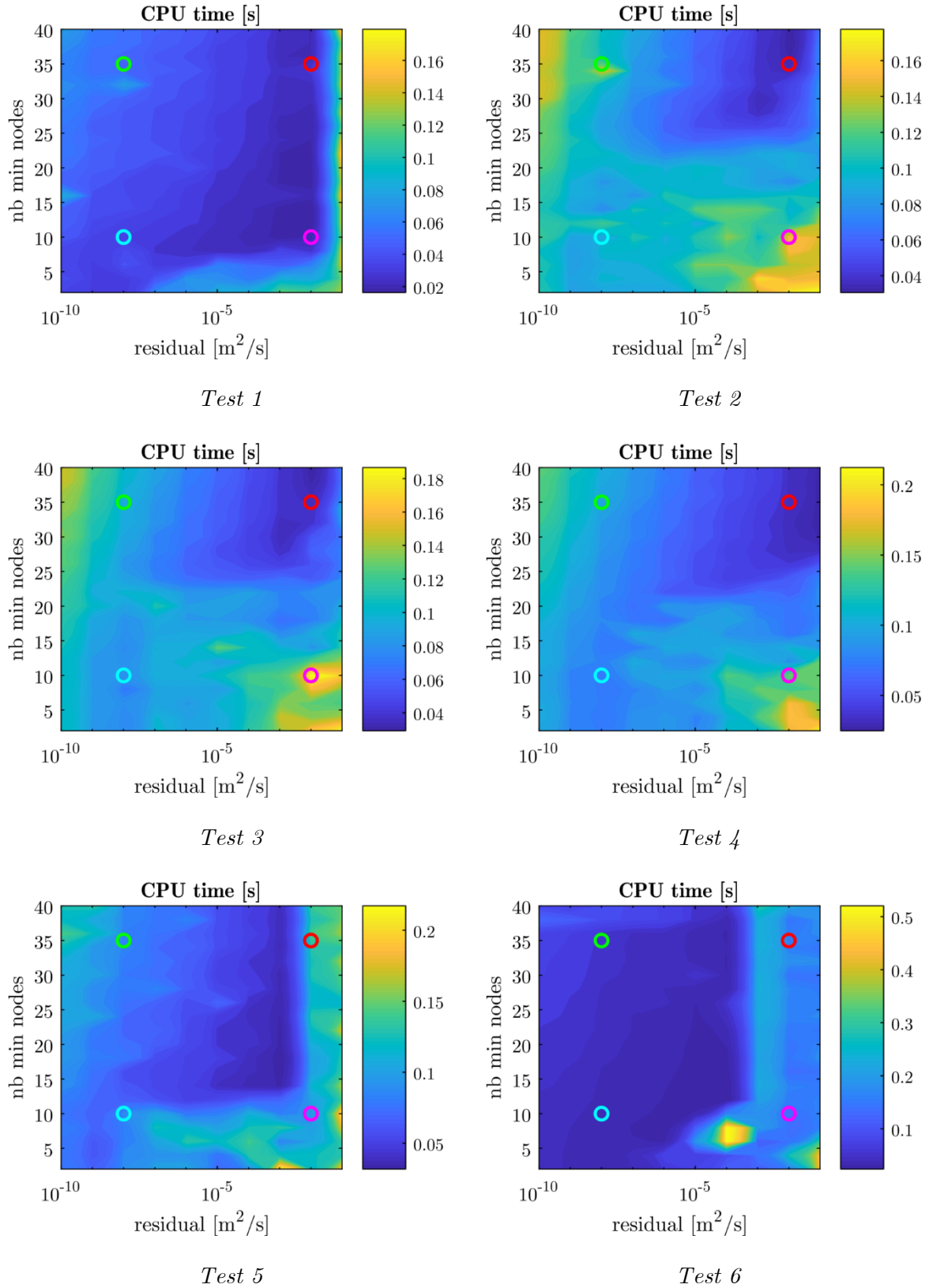


Figure 60: 2-D maps of the median CPU time for tests 1 to 6 with NKA activated

Fast convergence of a steady 1-D open-channel flow

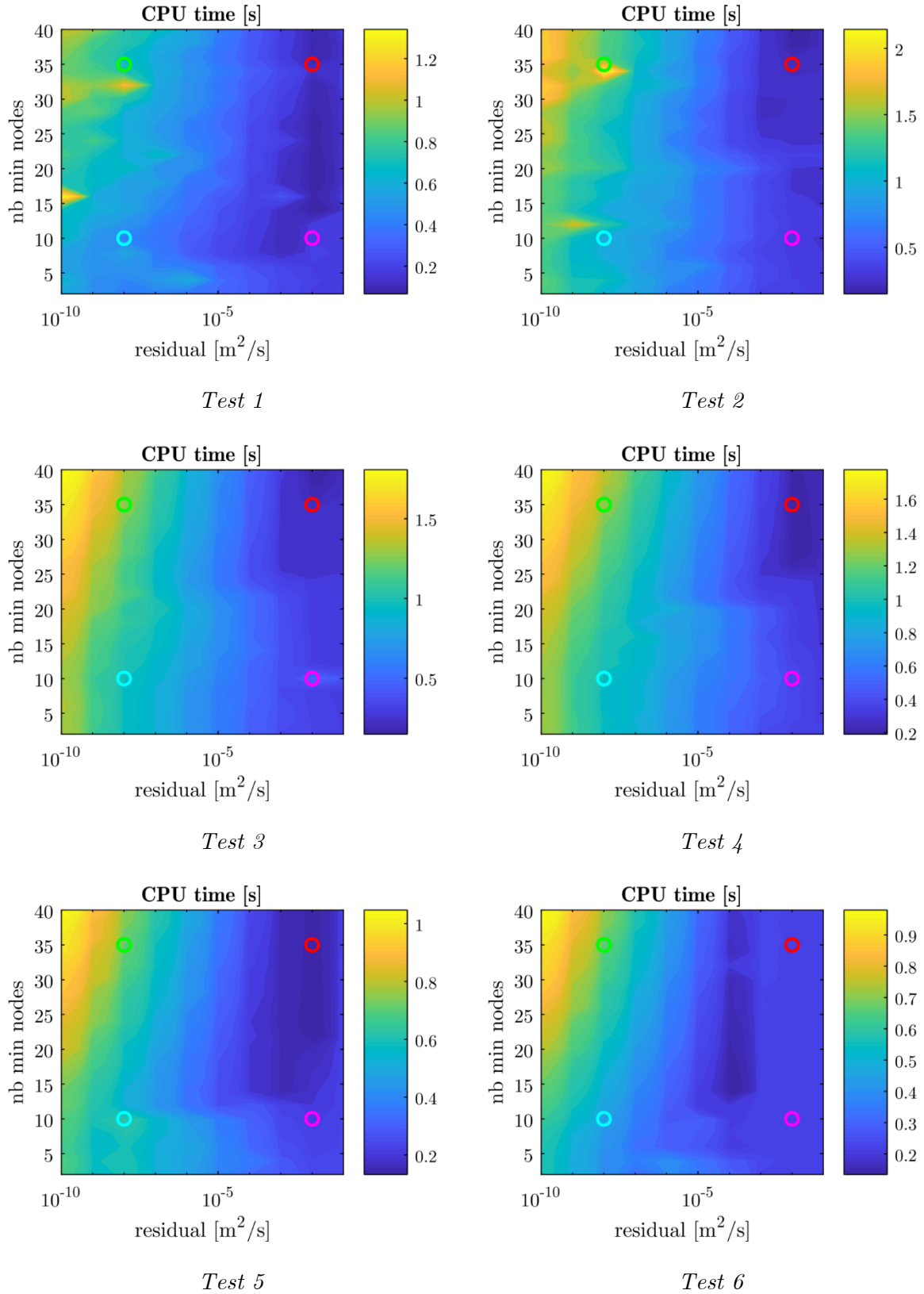


Figure 61: 2-D maps of the median CPU time for tests 1 to 6 with NKA disabled

A first tentative of explanation is to look at the ratio between the time spent when only parts of the domain are computed and when the entire domain is computed at the final iteration. Since the activation of NKA leads to best results, the following analysis is performed with NKA activated. From Figure 62 to Figure 67, one can notice that higher ratios are located at the upper left part of graphics, meaning that the final iteration has a computation time close to 0 for high number of nodes in the computation list and low partial residuals. Having a time ratio close to 1 does not guarantee low overall computation time. Indeed, it was shown earlier that best computation times are located around 30 nodes and  $10^{-3}$  m<sup>2</sup>/s. In this region, the time ratio is higher than 0.8 for the five first tests. For test 6 (Figure 67), the ratio is close to 0.1 for this parameter combination, meaning that 90 % of the time is spent in the final iteration. Having a look at Figure 60 and Figure 67 teaches that best computation times for test 6 are obtained at high ratios.

From these observations, it appears that best computation times are located at high ratios. However a high ratio does not ensure a low computation time.

Before continuing this analysis, it should be noticed that the variations of the ratios are very low (see right parts of Figure 62 to Figure 67). This shows once more that the other parameters have a very little influence of the computation time.

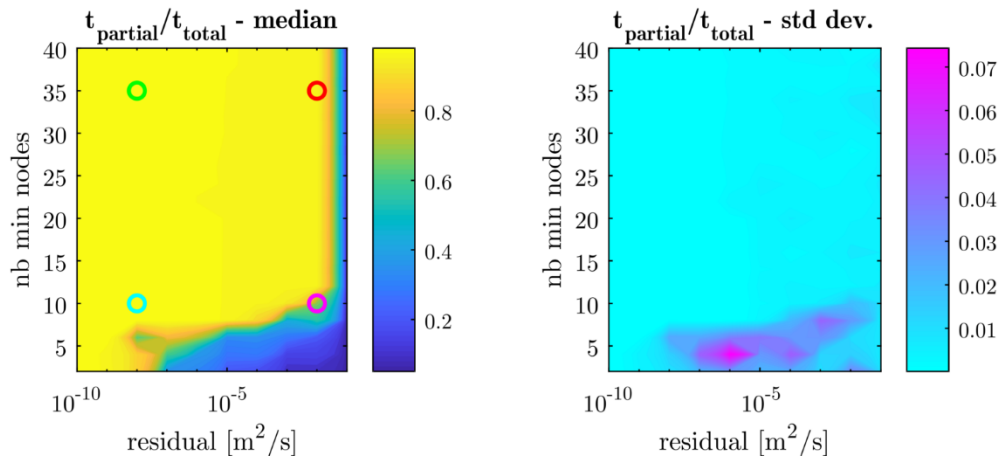


Figure 62: Time ratio for test 1

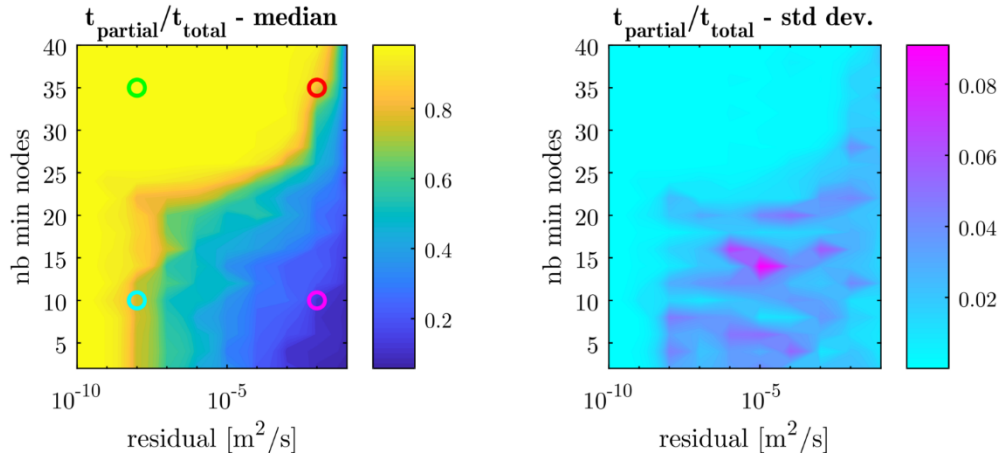


Figure 63: Time ratio for test 2

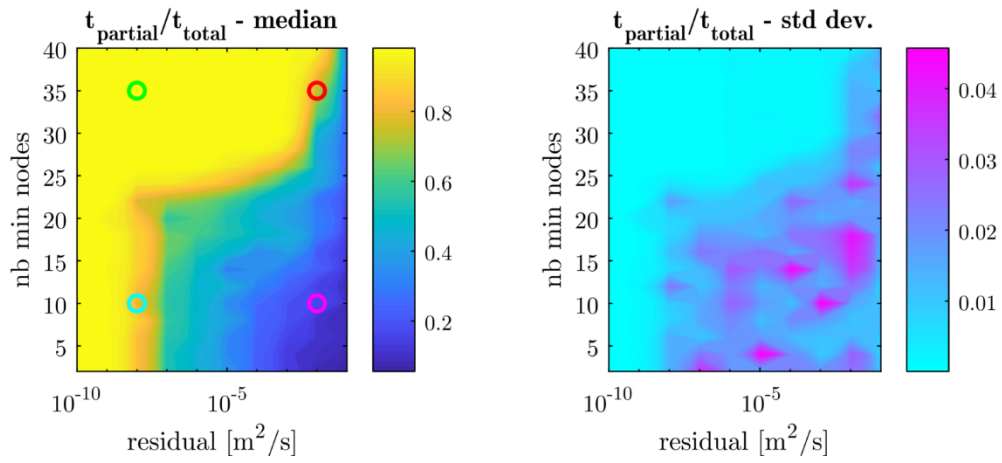


Figure 64: Time ratio for test 3

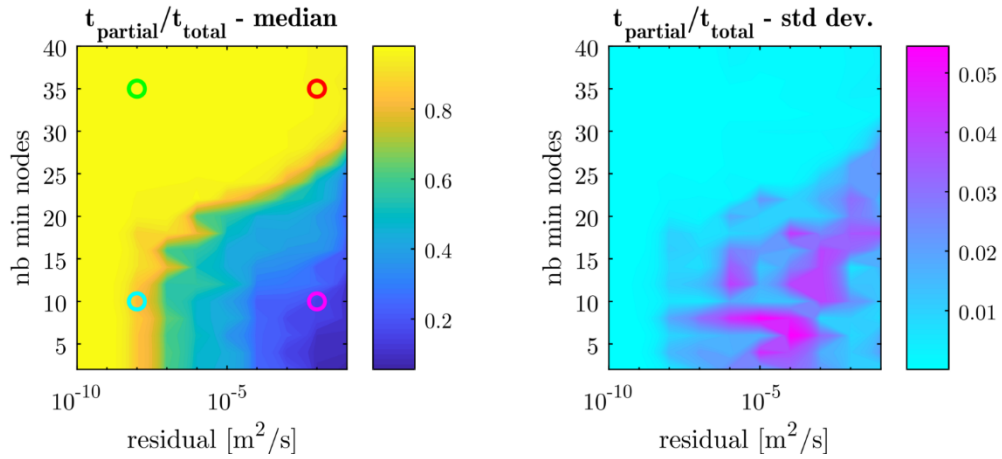


Figure 65: Time ratio for test 4

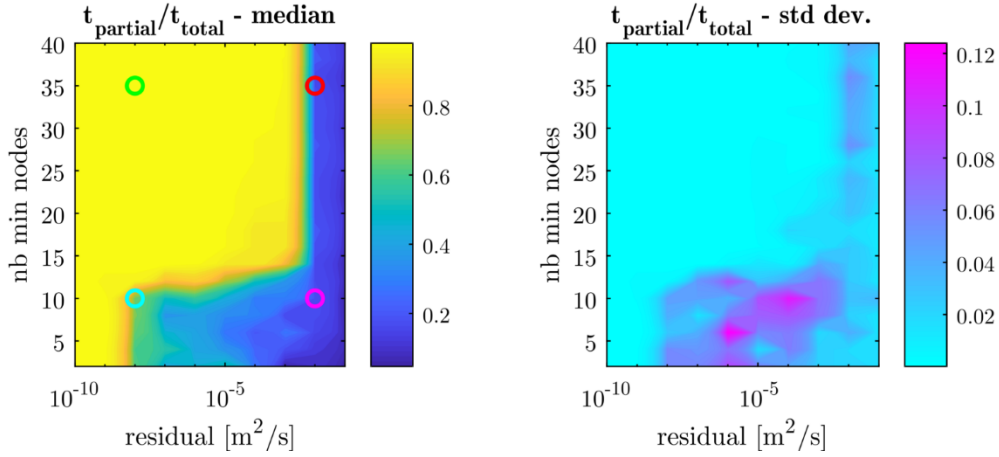


Figure 66: Time ratio for test 5

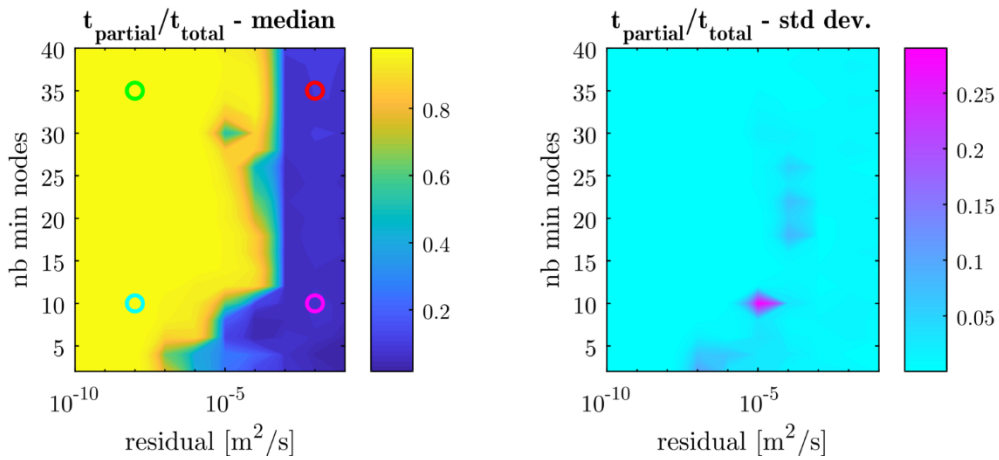


Figure 67: Time ratio for test 6

In order to understand the optimal link between the minimum number of nodes in the list and the partial residual, the convergence path is analyzed for each test and for an arbitrary point (for at least 30 nodes in the computation list and a partial residual of  $10^{-3} \text{ m}^2/\text{s}$ ). For tests 1 to 5, this point is located 5 m from the downstream BC. For test 6, this point is located 25 m from the downstream BC. The convergence path reproduces the residual ( $dA/d\tau$ ) obtained for a given node at each iteration after the first equation solving (blue line) and when all nodes of the computation domain reached the partial residual threshold (red line). For tests 1 to 5 (Figure 68 to Figure 72), it appears that the last residual reached evolves with the number of iterates. When the node is added to the computation list, it reaches at least a residual of  $10^3 \text{ m}^2/\text{s}$  at the end of the first iterate. After this first iterate, this node remains in the computation list for 29 more iterates. All along these new iterates, the values of the cross-section area is recomputed and refined. It appears that the residual decreases under the final residual threshold (dashed black line). It should be noticed here that when a point is missing, it means that its residual reached 0 and it could not be represented in log-scale plots. One can

also notice that for the arbitrary point we chose, the residual was sufficient at the final iteration. For this specific node, it was not necessary to launch a new computation.

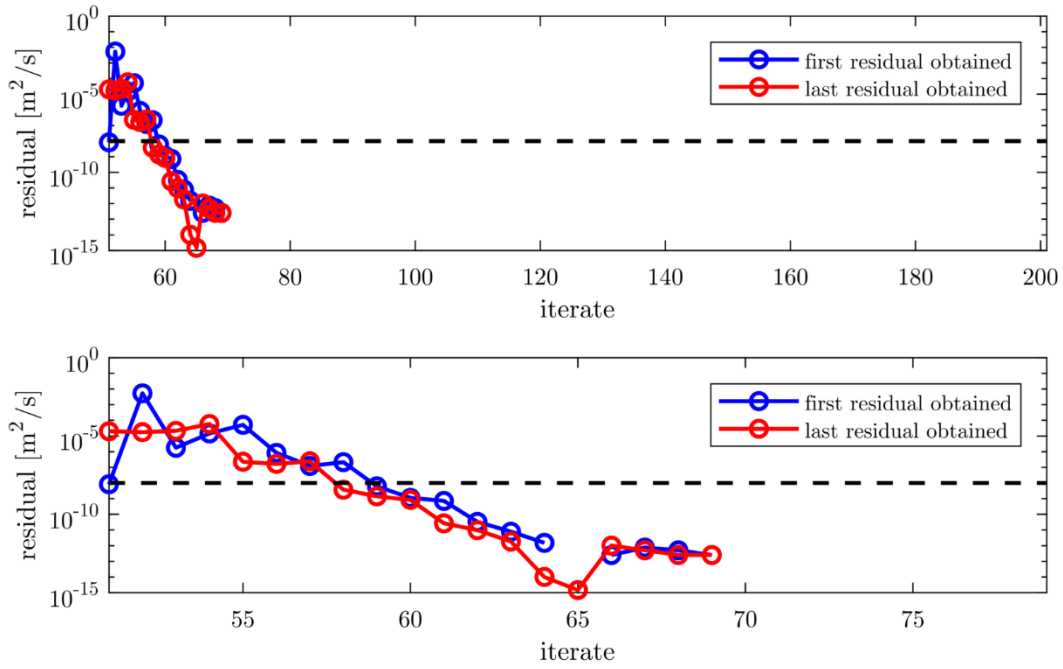


Figure 68: Convergence path of node 150 for test 1 for at least 30 nodes in the computation list and an intermediate residual of  $10^{-3} \text{ m}^2/\text{s}$

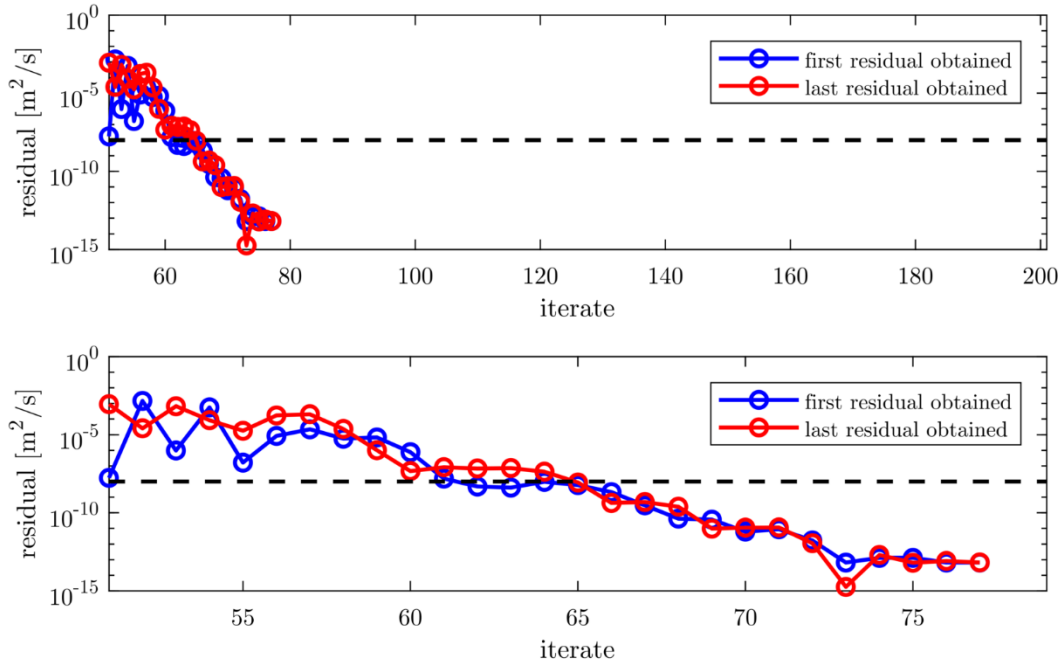


Figure 69: Convergence path of node 150 for test 2 for at least 30 nodes in the computation list and an intermediate residual of  $10^{-3} \text{ m}^2/\text{s}$

Fast convergence of a steady 1-D open-channel flow

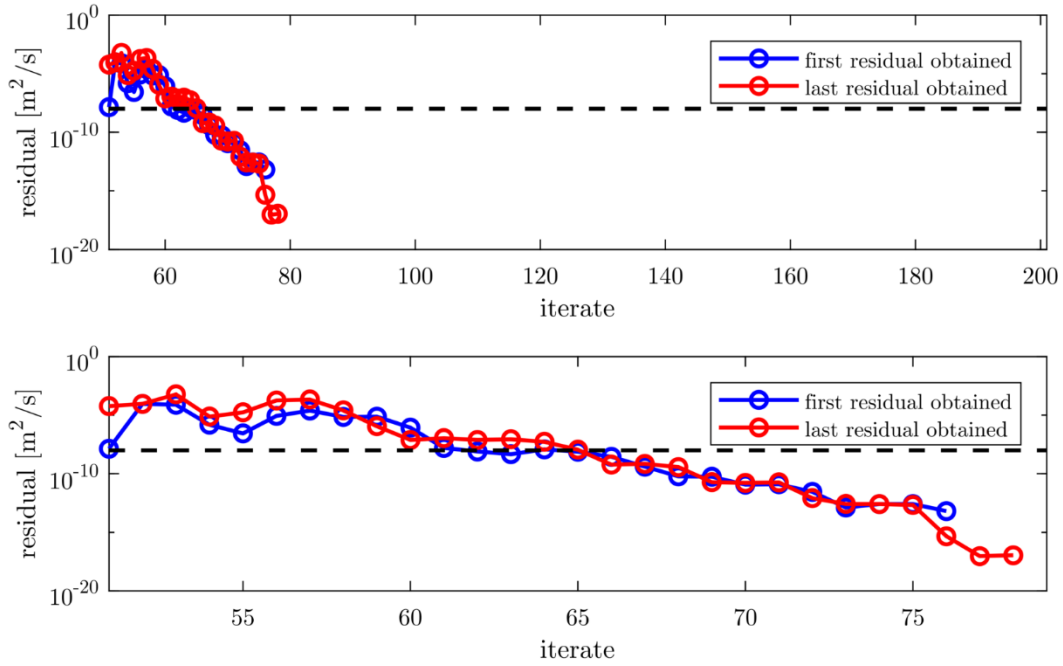


Figure 70: Convergence path of node 150 for test 3 for at least 30 nodes in the computation list and an intermediate residual of  $10^{-3} \text{ m}^2/\text{s}$

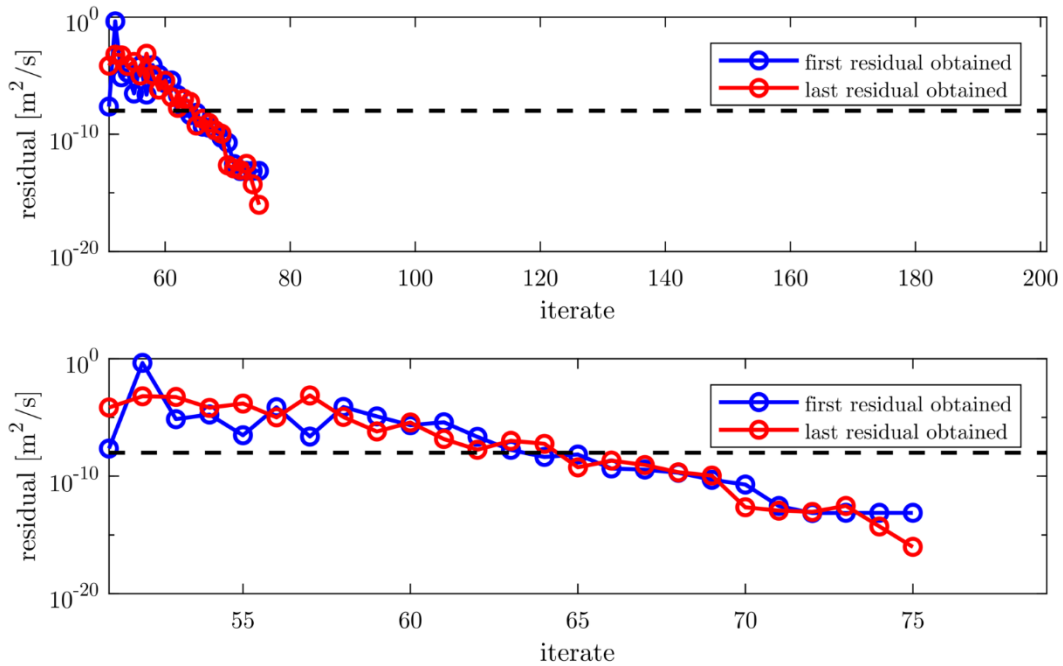


Figure 71: Convergence path of node 150 for test 4 for at least 30 nodes in the computation list and an intermediate residual of  $10^{-3} \text{ m}^2/\text{s}$

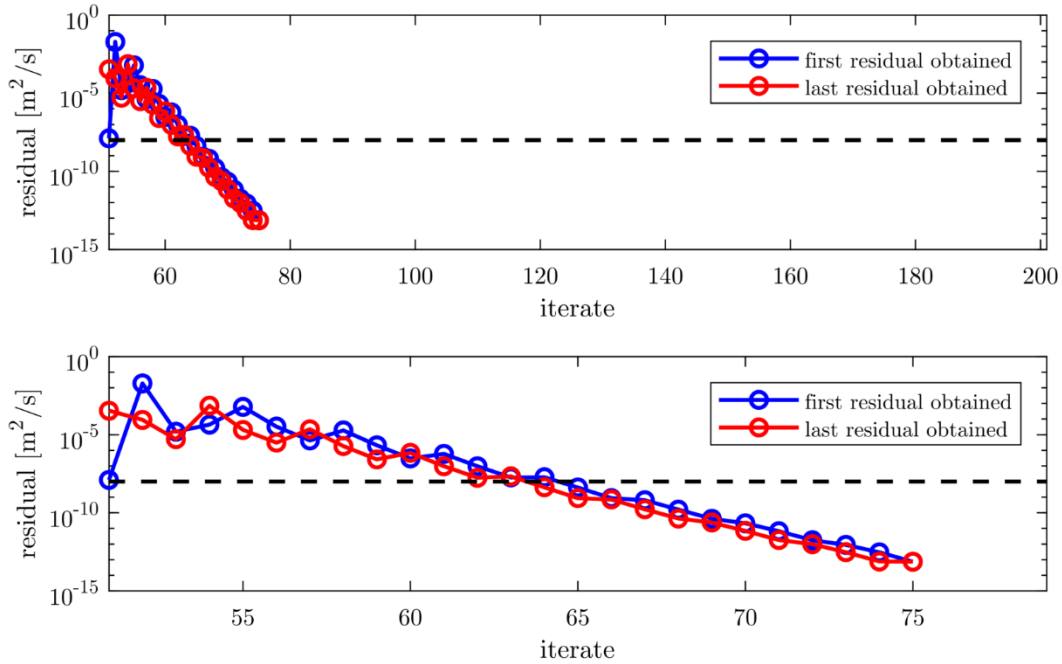


Figure 72: Convergence path of node 150 for test 5 for at least 30 nodes in the computation list and an intermediate residual of  $10^{-3} \text{ m}^2/\text{s}$

For test 6 (Figure 73), the observations and conclusions are different. Indeed, while the residual decreases when iterates increase for tests 1 to 5, for test 6 the residual remains constant during all iterates. The difference in the convergence path between test 5 and test 6 is due to the difference in the evolution of the free surface. For test 5, the narrower cross-section induces higher velocities and higher stresses. Moreover, test 5 has no slope while test 6 has a 0.2 % slope. This means that the free surface slope is steeper for test 5 than for test 6.

When a node is added in the computation list for test 6, its initialization provides an estimate of the cross-section area good enough in such a way that the residual is lower than the threshold. Furthermore, adding a new node with a good estimation of its cross-section area does not influence significantly the residual of the other nodes in the computation list: their residuals remain below the threshold. Since the cross-section area is not challenged when a new node is added and that the residual remains at  $10^{-3} \text{ m}^2/\text{s}$ , the final iteration over the entire domain is required and all nodes are computed in order to reach the desired residual ( $10^{-8} \text{ m}^2/\text{s}$ ).

For test 5, the initial estimation of the cross-section area of the newly added node induces modifications to the other nodes in the list in such a way that several iterations are required in order to reach at least the residual threshold for all nodes. These iterations help to decrease the residual of the nodes already present in the computation list. This means that, for the final

iterate (which includes all the nodes), most nodes have already reached the desired final residual.

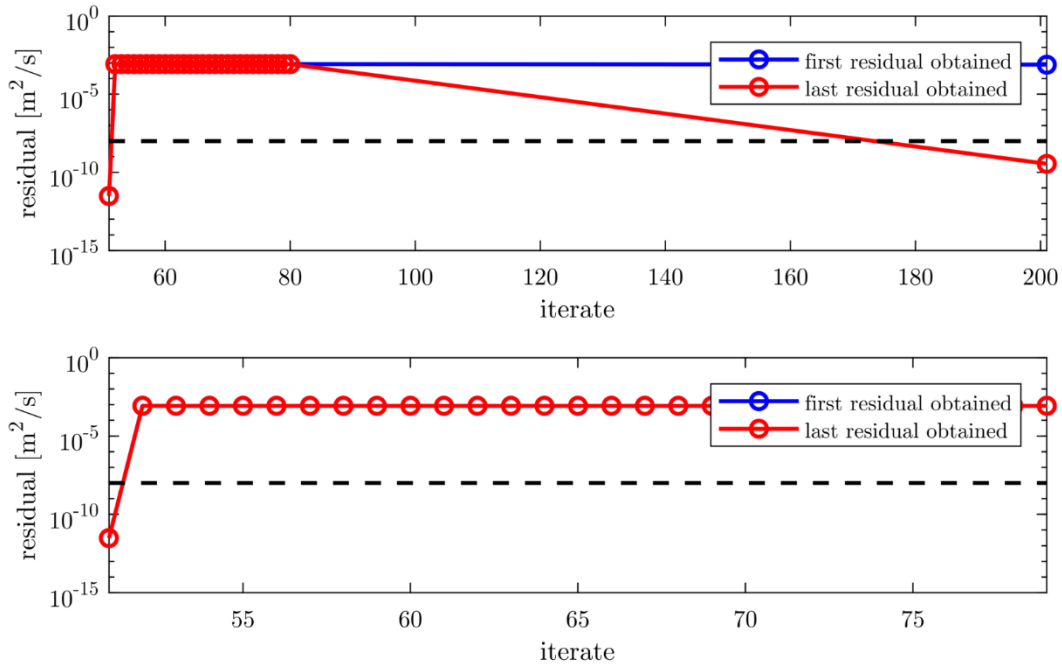


Figure 73: Convergence path of node 150 for test 6 for at least 30 nodes in the computation list and an intermediate residual of  $10^{-3} \text{ m}^2/\text{s}$

The convergence path was analyzed above for a particular set of parameters that we found to be optimal for five of the six tests. In order to perform a more rigorous study, the convergence path of four particular points is analyzed. These points are depicted with color circles in Figure 60 and Figure 61. They are located at the corners of the square lying between 10 and 35 nodes and  $10^{-8} \text{ m}^2/\text{s}$  and  $10^{-2} \text{ m}^2/\text{s}$  for the partial residual. At these points, for each node the values of  $dA / d\tau$  obtained at the end of the first iteration and at the beginning of the final iterate are reported in a plot for each test (Figure 74). In these plots, four black dashed lines give some marks:

- the two vertical lines represent the partial residuals tested ( $10^{-2}$  and  $10^{-8} \text{ m}^2/\text{s}$ )
- the horizontal line represents the final residual that has to be reached
- the bisector helps to figure out which node get a finer residual at the beginning of the last iterate, compared to the result at the end of the first computation (points below the bisector improve their residual)

It should be noticed here that the plots in Figure 74 use log-scales. This implies that nodes with one of the two  $dA / d\tau$  equal to 0 will not be plotted.

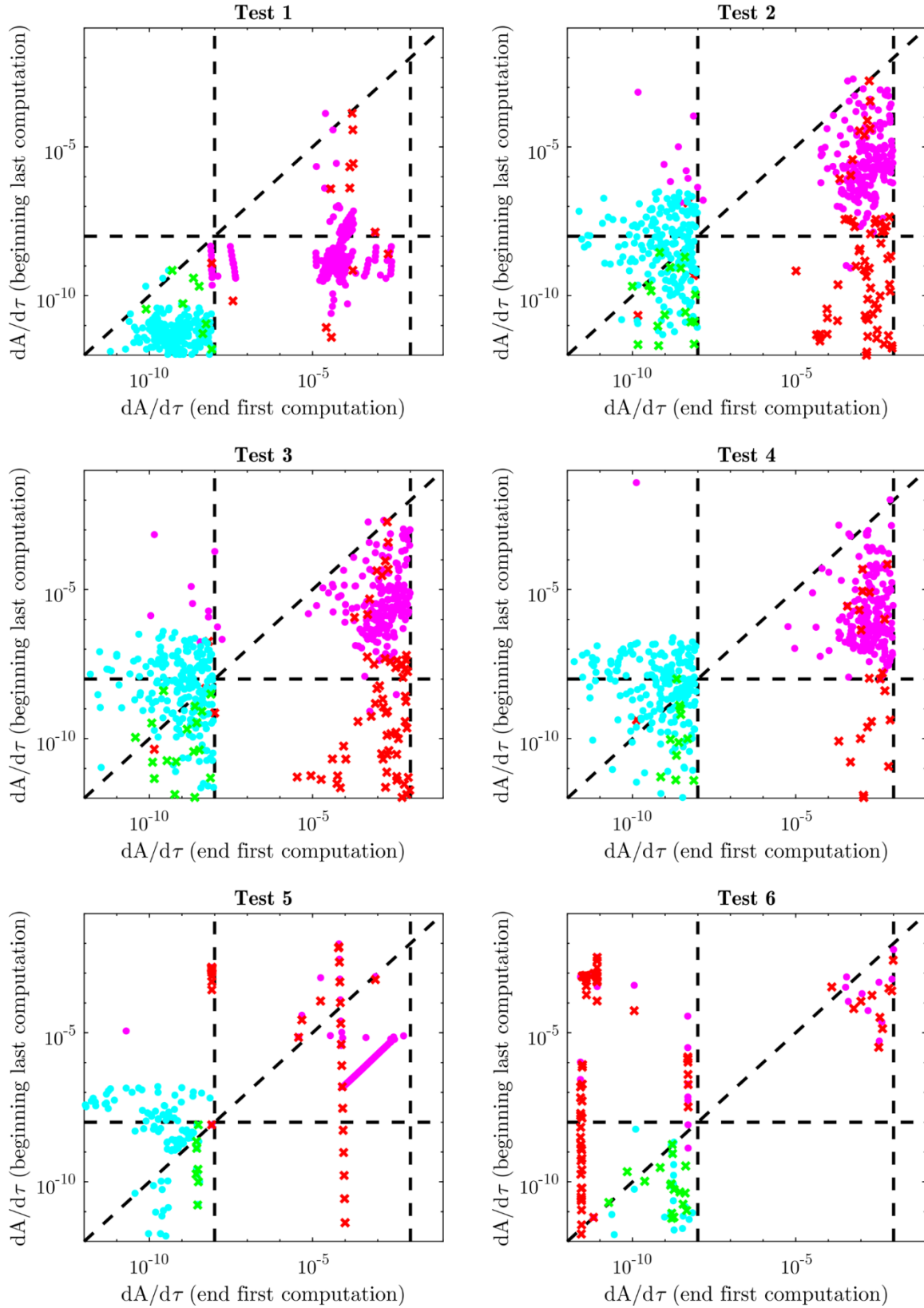


Figure 74: Evolution of the residual between the first iterate and at the beginning of the last computation

Analyzing Figure 74 shows different behaviors according to the tests. First, let us begin with the tests on a sine wave bottom (test 1 to 4). For test 1 and for the four sets of parameters, almost all nodes improve their residual during the iterates. For tests 2 to 4, only the set of parameters associated to the red dot (35 nodes and  $10^{-2}$  m<sup>2</sup>/s) produce an improved residual after all iterates on partial domains. In order to avoid a last computation on the entire domain, crosses and dots in Figure 74 should be under the horizontal dashed line. This is possible only in test 1 when the partial residual is set to  $10^{-8}$  m<sup>2</sup>/s. For tests 2 to 4, this happens only with a low partial residual and with a high number of nodes to keep in the list (green crosses in Figure 74). This combination is not a guarantee of low computation times (see Figure 60) for the specific cases tested here.

For tests 5 and 6, conclusions are different. Indeed, more red crosses are now located above the bisector, indicating that a larger amount of nodes degrade their residual. One can also notice that some points are aligned vertically in Figure 74 for tests 5 and 6. This means that a group of nodes obtain a similar residual at the end of their first computation, but the values of  $dA/d\tau$  at the beginning of the last computation differ. This can be explained by the initialization of the newly added node in the computation list in the case of a uniform channel: all nodes should be initialized similarly.

From these analyses, we have shown that:

1. The main parameters that influence the computation time are the minimum number of nodes to keep in the computation list and the partial residual.
2. Activating NKA provides better computation times.
3. Having a rough precision (residual around  $10^{-3}$  m<sup>2</sup>/s) and a relatively big amount of nodes in the computation list (around 30) leads to shorter computation times.
4. Best computation times are obtained when the time spent in the final computation is almost nil.
5. Using a larger amount of nodes and a rough precision helps to initialize quickly a node and improve its residual up to the final residual threshold all along partial iterations, before reaching it.

### **3.6 Optimized algorithm for the evolution of the domain span**

It was shown earlier that having a large number of nodes in the computation list associated to a partial residual  $\xi_p$  higher than the final residual  $\xi_f$  ( $\xi_f < \xi_p$ , i.e. the partial computation has precision requirements less restrictive than for the final computation) helped to reduce the time needed for the final computation. Analyzing the convergence path of some nodes showed

that the residual reached before the final iteration can be much lower than the desired final residual. This is because some nodes were kept too long in the computation list, which means that the computation time may be reduced with an appropriate strategy.

Other tests showed also that the residual of some nodes at the beginning of the final iteration was much higher than the final residual ( $|\partial A / \partial \tau| \gg \xi_f$ ), leading to a longer final computation. In order to avoid this last computation, the algorithm has to make sure that the residual of all nodes is decreasing under the final residual threshold.

In order to reach these objectives, and consequently target lower computation times, the algorithm used above is redesigned with new features. First, the maximum number of nodes to keep in the list is adapted according to the residual values of the nodes currently present in the computation list. Then, in order to be sure that all nodes improve their residual, the new algorithm will check that the partial residual  $\xi_p$  is low enough in order to force the computation on the partial domain.

### 3.6.1 Algorithm structure

The evolution of the domain is based on a few basic ideas:

1. The computation of a partial domain ends when all the nodes included in this partial domain reach a threshold called “partial residual threshold” and denoted  $\xi_p$ .
2. The last node can be removed from the partial domain once it dropped under the final residual threshold  $\xi_f$ .
3. We have to make sure that the nodes that were removed from the domain are not impacted by the computation domain in such a way that their residual  $\partial A / \partial \tau$  get higher than the final residual threshold  $\xi_f$ .

In order to be able to reach these two objectives, an analytical analysis of the discretized model is performed. Let us consider three nodes and their borders (Figure 75). The discretized formulation of equation (134) at node  $i$  is:

$$\begin{aligned} \left[ \frac{\partial A}{\partial \tau} \right]_i &= \left[ \frac{\partial}{\partial x} \left( \frac{Q^2}{A} \right) + gA \frac{\partial z_s}{\partial x} + gAS_f - u_x q_l \right]_i \\ &\approx \frac{\left( \frac{Q_i^2}{A_i} - \frac{Q_{i-1}^2}{A_{i-1}} \right)}{\Delta x} + g \frac{A_{i+1}^2 - A_i^2}{A_{i+1} - A_i} \left( \frac{z_{s,i+1} - z_{s,i}}{\Delta x} \right) + \left[ gAS_f - u_x q_l \right]_i \end{aligned} \quad (167)$$

The influence of a change in the cross-section area in  $i - 1$  on the value of  $\partial A / \partial \tau$  in  $i$  is given by the derivative:

$$\frac{\partial}{\partial A_{i-1}} \left( \left[ \frac{\partial A}{\partial \tau} \right]_i \right) = \frac{Q_{i-1}^2}{\Delta x} \frac{1}{A_{i-1}^2} \quad (168)$$

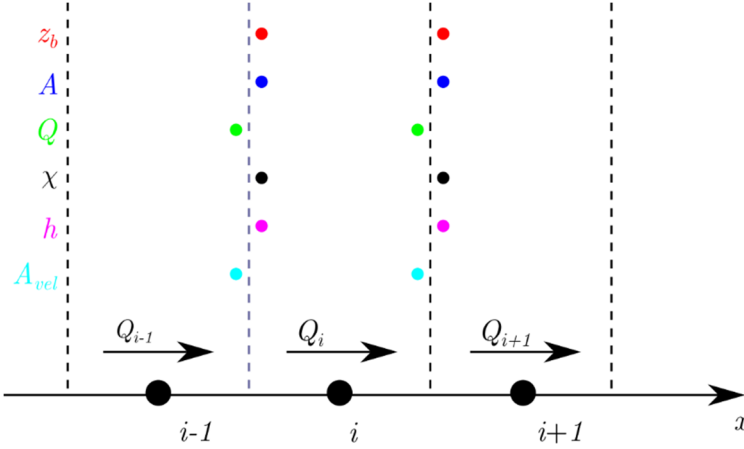


Figure 75: Discretization and upwinding direction of unknowns and properties at borders

From the result in equation (168), one can predict the evolution of the residual  $\partial A / \partial \tau$  of a node that is not in the computation domain anymore. If node  $i$  has been removed from the computation domain, one can check that its  $\partial A / \partial \tau$  remains below the threshold even with an evolution of the cross section area in the node  $i - 1$ , located just upstream of it. In order to do so, the residual of the removed node after the computation is evaluated thanks to its previous value and the evolution of its upstream neighbor, such as described in equation (168) :

$$\left[ \frac{\partial A}{\partial \tau} \right]_{i,next} \approx \left[ \frac{\partial A}{\partial \tau} \right]_{i,prev} + \frac{Q_{i-1}^2}{\Delta x} \frac{1}{A_{i-1}^2} \Delta A_{i-1} \quad (169)$$

where  $\Delta A_{i-1}$  is the evolution of the cross section  $A$  in  $i - 1$  from the last evaluation of  $\left[ \frac{\partial A}{\partial \tau} \right]_{i,prev}$ .

If the evolution of the cross section area in the computation domain ( $i - 1$ ) implies  $\left[ \frac{\partial A}{\partial \tau} \right]_i$  to exceed the threshold, then node  $i$  should be added again in the computation domain in order to make sure it remains below the threshold until the end of the entire computation.

This technique paves the way for a new strategy for the evolution of the computation domain. Moreover, it also guarantees that a final iterate on the entire domain is not required anymore since we verify that  $\partial A / \partial \tau$  of the nodes outside of the computation are not affected significantly.

The principle of the optimized algorithm is summarized in Figure 76. The computation domain starts from the downstream boundary and slides toward the upstream boundary. While it

slides, the domain adapts its size according to various circumstances, including the convergence level of the last node.

The flowchart of the optimized algorithm is given in Figure 77. A first test is performed on the potential evolution of the downstream node, just outside of the domain. If the value  $|\partial A / \partial \tau|$  of this node is supposed to get above the threshold, then the downstream node is added to the computation domain and the upstream limit is frozen. Moreover, the threshold is lowered if the domain did not compute more than once.

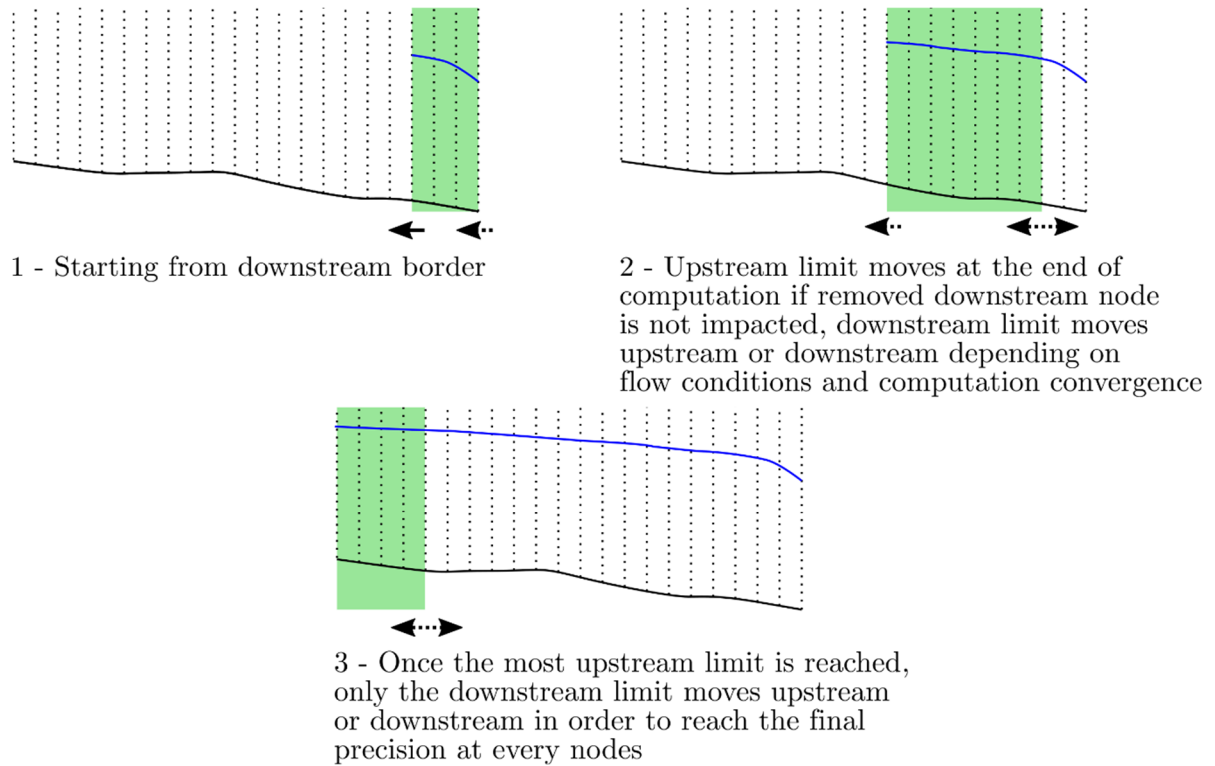


Figure 76: Principle of the sliding domain (green area) with the optimized method. It starts from the downstream border et slides gradually toward the upstream limit while continuously adapting its size.

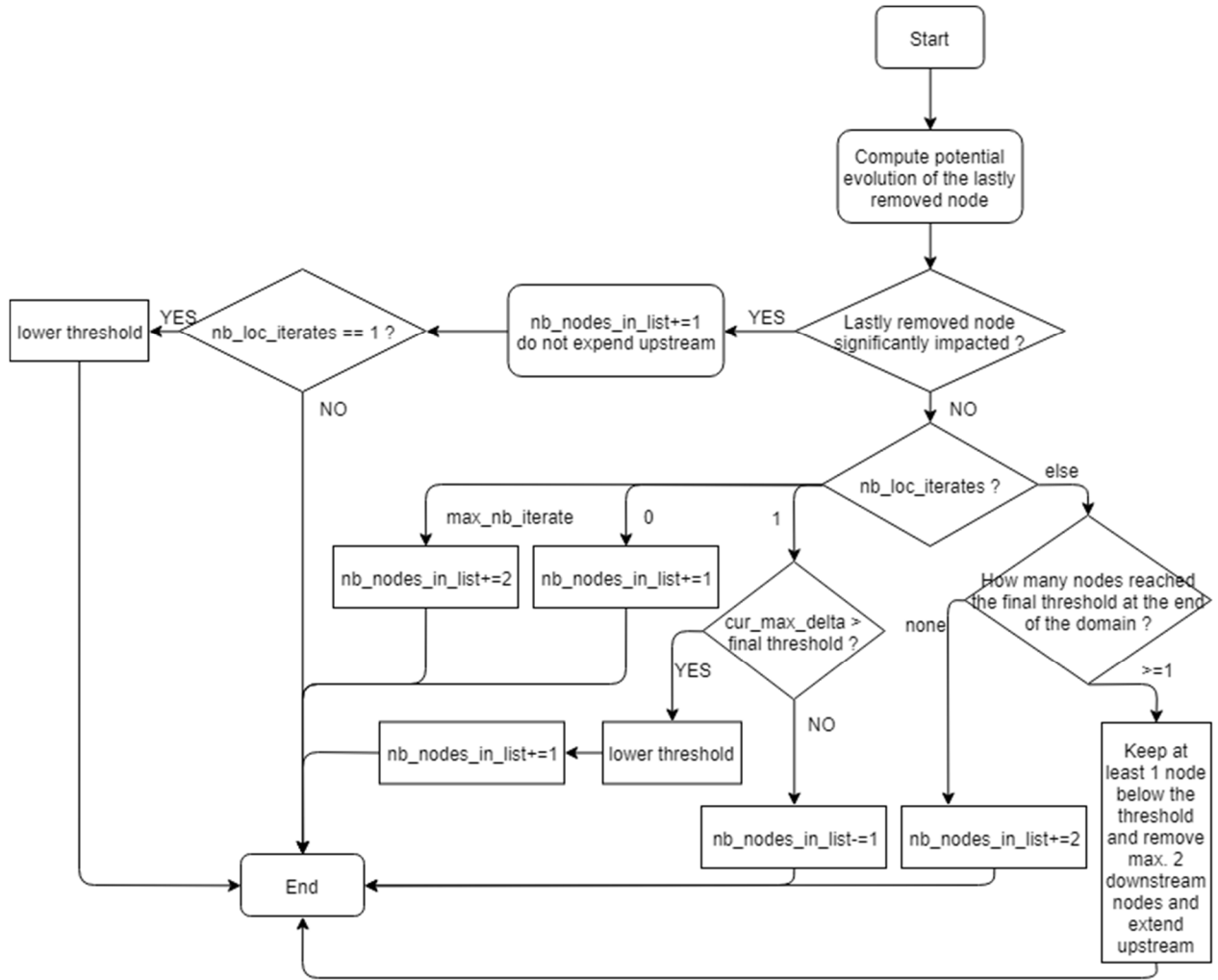


Figure 77: Flowchart of the optimized algorithm for the evolution of the computation domain

If the downstream node outside of the computation domain is not impacted by the evolution of the cross section area of the last inner node, then the evolution of the domain depends on the number of iterates:

- If too many iterates are done without reaching a converged state ( $\text{nb\_loc\_iterates} = \text{max\_nb\_iterate}$ ), then the domain is extended upstream and downstream (+2 nodes).
- If only a single iteration was performed, then it may be suspected that the nodes inside the computation domain could not improve significantly their residual. This is why the largest value of  $|\partial A / \partial \tau|$  is compared to the final threshold. If it is below this threshold, then the number of nodes in the computation domain can be decreased (-1 node). Otherwise, the number of nodes is increased (+1 node) and the intermediate threshold divided by 10.

- If a supercritical flow is met upstream, the domain is not computed (`nb_loc_iterates = 0`) and the domain is simply extended upstream (+1 node)
- When several iterations occurred, the number of nodes in the domain is adjusted according to the number of downstream nodes that reached the final threshold. If none reached that final residual, the domain is extended upstream and downstream (+2 nodes). Otherwise, the number of nodes is set in order to keep at least one node downstream at the final residual. The number of nodes within the computation domain is not decreased by more than 1 node in order to limit brutal changes.

The method can be summarized with the following pseudo-code:

---

**Algorithm**

---

Initialize (computation list is empty)

Add most downstream node to computation list

**While** some nodes still have to be converged ( $|\partial A / \partial \tau| > \xi_f$ ):

    Initialize lastly added upstream node

**While** nodes of computation list not converged ( $|\partial A / \partial \tau| > \xi_p$ ):

        Compute cross section change for each node

**If** NKA activated:

            Adapt cross section change with NKA algorithm

**If** lastly removed downstream node significantly impacted:

    Add it back to the computation list and do not expand upstream

**Else:**

**If** downstream node in computation list fully converged ( $|\partial A / \partial \tau| \leq \xi_f$ ):

        Remove this node from computation list

**If** upstream nodes remain to be added to computation list:

    Add 1 upstream node to the computation list

Finalize

---

### 3.6.2 Comparison to the previous algorithm

The new algorithm is compared in this section to the algorithm used previously. The comparison is performed on the 6 tests presented previously. The original algorithm is used with 30 nodes, the value identified as a good compromise. The new algorithm has no minimum number of nodes in its computation list since it deals itself with this aspect. This means that the computation time of the new algorithm is mainly dependent on the partial residual.

The computation times are compared in Figure 78 for the original algorithm (blue lines) and the new one (red lines). Moreover, the very best computation time obtained with the original algorithm (not necessarily with 30 nodes) is depicted with the black dashed line.

It appears that for most partial residual values, the new algorithm provides best computation times. The new algorithm is also able to reach and even (for tests 2 and 3) get below the best computation time obtained with the original algorithm. Furthermore, the new algorithm shows a clear tendency for an optimal value of the partial residual. Observing the results for the six cases tested, it appears that choosing a high partial residual ( $10^{-1}$  to  $10^{-2}$  m<sup>2</sup>/s) provides lower computation times.

From these observations, one can conclude that the new algorithm provides excellent computation times for a high residual values and without having to worry about the number of nodes to include in the computation list.

Fast convergence of a steady 1-D open-channel flow

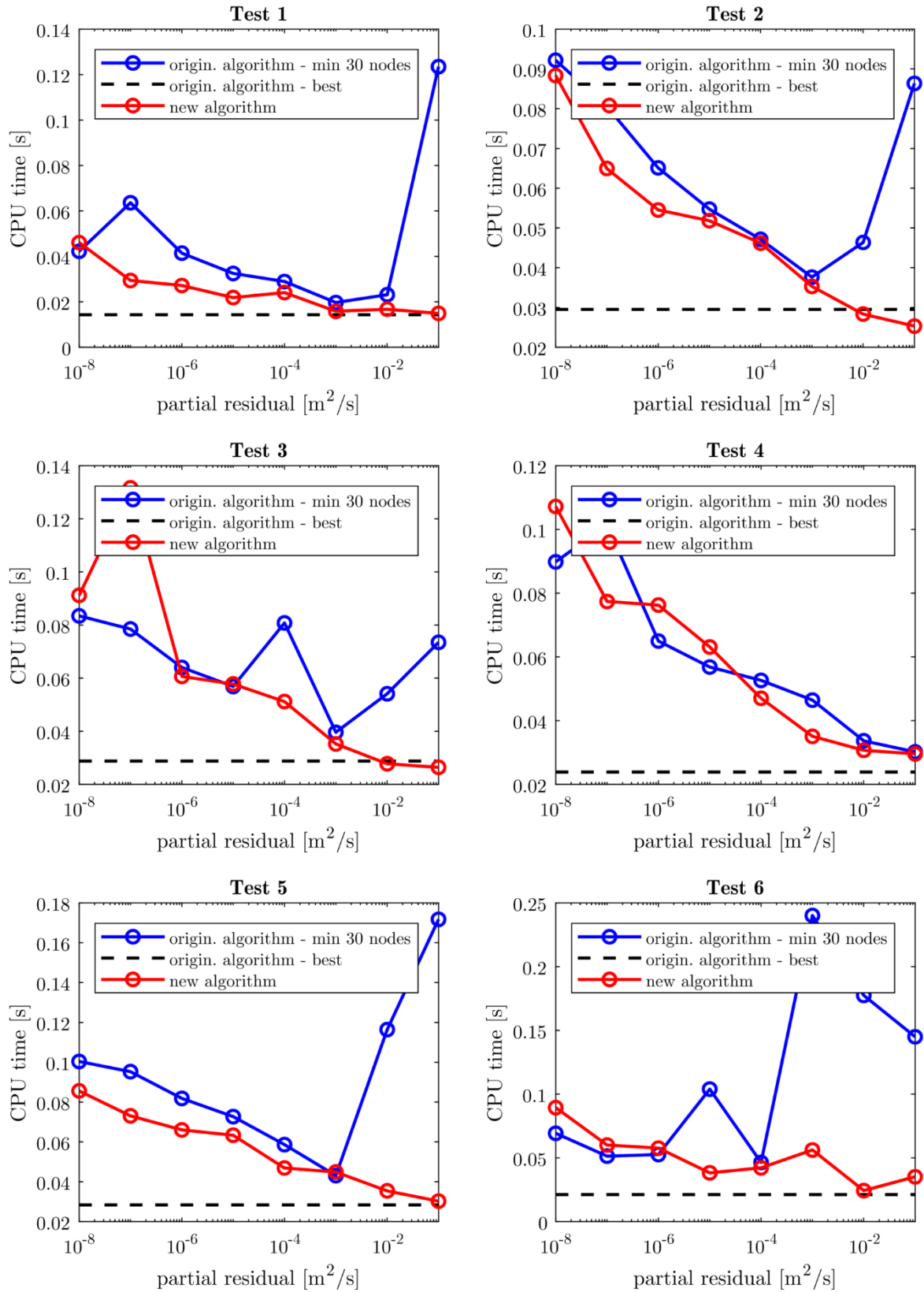


Figure 78: Comparison of computation times between the original algorithm and the new algorithm

### **3.6.3 Scalability tests**

In order to assess the efficiency of this new algorithm, two scalability tests are performed. The first one consists in extending a domain upstream, with a constant spatial discretization. The second test consists in keeping a same span but the number of nodes is increased by a variation of the spatial discretization.

The first test takes place on frictionless sine wave bottom, described by:

$$z(x) = 0.05 \sin(2\pi x) + 0.05 \tag{170}$$

The downstream boundary condition is a water level imposed at 0.65 m. The discharge is constant along the channel stretch and is equal to 1 m<sup>2</sup>/s. Cross sections are rectangular and 1 m wide. Four domain lengths are tested (20 m, 200 m, 2 km and 20 km) with a spatial step of 0.1 m, meaning that these domains include 200, 2,000, 20,000 and 200,000 nodes.

The computation results (Figure 79 and Table 18) show that the computation time per node decreases when the number of nodes increase. Looking at the values in Table 18, one can observe that the increase in computation times does not follow the increase in the number of nodes (factor 10). This can be explained by the fact that when the domain gets longer, the flow conditions upstream are smoother than downstream. Longer domains undergo fewer changes than shorter domains, leading to shorter computation time per node. This example highlights the fact that low partial residual values provide best computation times.

Fast convergence of a steady 1-D open-channel flow

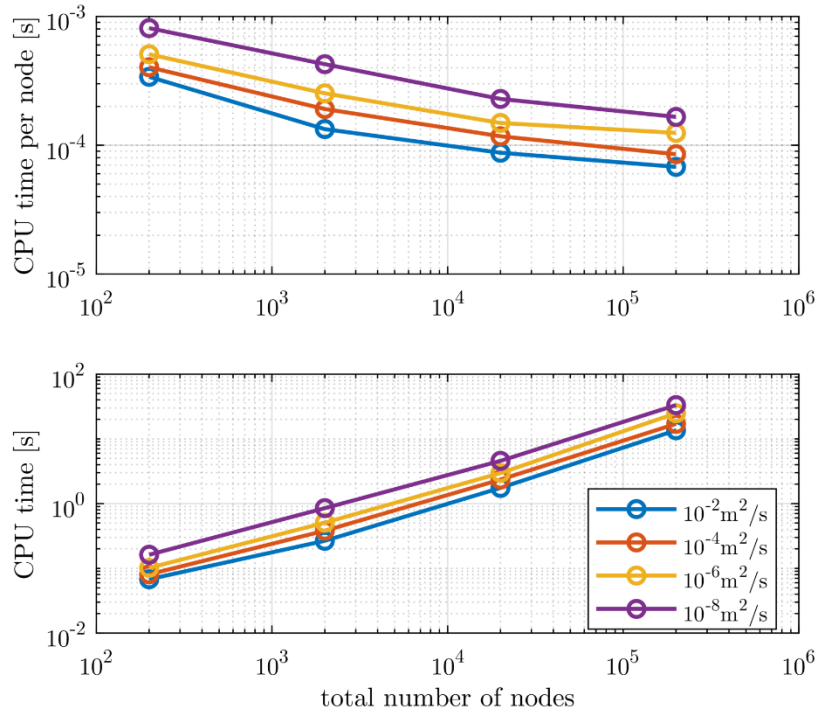


Figure 79: Computation time according to the total number of nodes in the domain and the partial residual for a domain extension

	$10^{-2} \text{ m}^2/\text{s}$	$10^{-4} \text{ m}^2/\text{s}$	$10^{-6} \text{ m}^2/\text{s}$	$10^{-8} \text{ m}^2/\text{s}$
<b>200 nodes</b>	0.068	0.081	0.102	0.162
<b>2000 nodes</b>	0.267	0.382	0.506	0.852
<b>20000 nodes</b>	1.748	2.348	2.974	4.571
<b>200000 nodes</b>	13.580	17.038	24.883	33.186

Table 18: Numerical values of the computation time (s) according to the number of nodes for a domain extension and according to the partial residual

In order to complete this scalability study, it is interesting to have a look at the behavior of the algorithm when the spatial step decreases for a given domain length. In classical explicit schemes, this case leads to a quadratic evolution of the computation time. Indeed, when the spatial step decreases, the number of nodes increases and the time step decreases.

The test chosen to illustrate the behavior of the new algorithm is a 100 km-long channel with a constant 0.025 % slope. Cross-sections are trapezoidal and are described using tabular values (1 m width at the bottom of the section and 5 m width at 1 m above the bottom). Friction is generated using a Manning law with  $n = 0.03 \text{ s/m}^{1/3}$ . The downstream boundary condition is

a water level set at 1 m.  $1 \text{ m}^3/\text{s}$  is injected at the upper node and the injection of  $4 \text{ m}^3/\text{s}$  is shared amongst the other nodes.

The computation times are showed in Figure 80 and Table 19. The behavior is slightly different from that observed in the previous test. Indeed, the evolution of the computation time is linear in regard to the number of nodes (the CPU time per node is globally constant) when the partial residual is set at  $10^{-6}$  and  $10^{-8} \text{ m}^2/\text{s}$ . For partial residual values of  $10^{-2}$  and  $10^{-4} \text{ m}^2/\text{s}$ , the evolution is linear up to 50 000 nodes; however, for the finest discretization, the computation time increases in a nonlinear way.

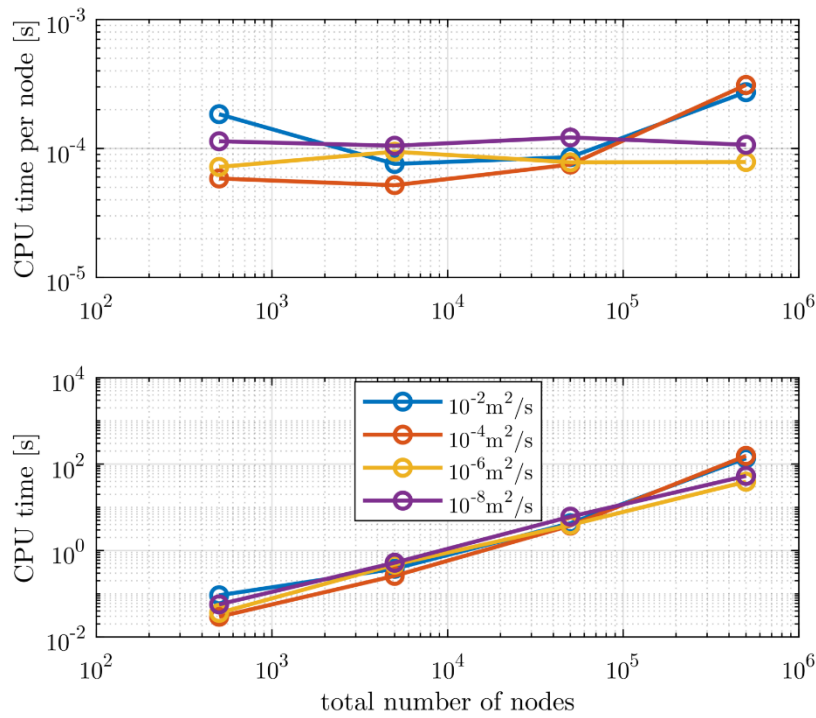


Figure 80: Computation time according to the total number of nodes for a domain refinement and according to the partial residual

	$10^{-2} \text{ m}^2/\text{s}$	$10^{-4} \text{ m}^2/\text{s}$	$10^{-6} \text{ m}^2/\text{s}$	$10^{-8} \text{ m}^2/\text{s}$
<b>500 nodes</b>	0.031	0.039	0.043	0.067
<b>5000 nodes</b>	0.369	0.321	0.445	0.599
<b>50000 nodes</b>	5.314	3.096	4.775	6.056
<b>500000 nodes</b>	132.505	149.814	55.885	66.905

Table 19: Numerical values of the computation time (s) according to the number of nodes for a domain refinement and according to the partial residual

This point was investigated further. It appears that at some moment in the computation, the algorithm needs to increase its computation domain size without being able to reduce it quickly (i.e., upstream nodes are added to the computation list while downstream nodes cannot be removed for residual values reasons). This increase in the number of nodes in the computation list was nonlinear compared to the situation with coarser discretization.

In order to complete the study of this optimized algorithm, it will be challenged in the next section against an implicit non-linear solver. This will highlight the capabilities of this algorithm especially when it is used with a large number of nodes.

### **3.7 Comparison of our optimized algorithm against CasADi**

Various techniques can be used to solve nonlinear equation (134). Up to this point, we have chosen to discretize the equation using a finite volume scheme and solve it with an explicit time scheme, which is consistent with the unified strategy of WOLF (Epicum, Dewals, Archambeau & Piroton 2010). Other techniques can be used, including finite difference schemes and/or implicit time schemes. Another possibility is to use an optimization algorithm for nonlinear systems. One of these is the recently developed CasADi software (Andersson et al. 2018; Baayen et al. 2018).

The code used for this section is available at <https://gitlab.uliege.be/HECE/HydroCasADi>.

#### **3.7.1 CasADi: features and limitations**

CasADi first started as an algorithmic differentiation tool. During its evolution, developers chose to shift the focus toward optimization. From non-linear expressions, CasADi is able to generate all the information needed by a nonlinear solver in order to return a solution to the problem. CasADi provides interfaces to MATLAB or Python for easy use.

Since the equations of the nonlinear system should be provided in an analytical way, some features available in the WOLF software cannot be used with CasADi (or with more difficulty). Indeed, cross-sections described using tabular relations cannot be used directly in CasADi. A Barr-Bathurst friction law would require a relationship written by part which is not straightforward.

The purpose of using CasADi is to show how our algorithm performs compared to a state-of-the-art solver.

### **3.7.2 Implementation for CasADi**

The implementation in CasADi was done through Opti stack, a collection of helper functions used for nonlinear programming problems. It is possible to define variables to optimize, parameters, an objective function and constraints. The solving of a 1-D steady open channel flow can be done thanks to this framework.

The constraints of the problem are the discretized form of equation (134) for each node and a water depth above 0 everywhere. The downstream boundary condition is imposed through equation (137). If no boundary condition is required downstream (supercritical flow through the downstream boundary), then a flow condition can be imposed through a constraint on the Froude number for the downstream node and the flow head is minimized at the upstream node. If the flow presents a critical section, minimizing the head upstream is equivalent to finding the section with the highest critical head.

Another way to solve a flow with a critical section is to prescribe a Froude number transition from  $Fr < 1$  to  $Fr > 1$  at that critical section. This is done by setting a constraint on the Froude number on the nodes upstream and downstream of the critical section. The identification of the critical section should be done prior to the computation on the basis of a critical head analysis. A summary of the objective function and constraints that can be set is given in Table 20.

The implementation of this model is done with the Python interface. An example is given hereafter for a subcritical flow (such as presented in section 3.7.4) and for a rectangular cross-section. First, a nonlinear optimization object is created:

```
opti = Opti()
```

Then, some parameters are defined:

```
Q = opti.parameter()    # Uniform discharge
Z_bc = opti.parameter() # Downstream boundary condition
L = opti.parameter()    # Channel width
dx = opti.parameter()   # Spatial step
n = opti.parameter()    # Roughness coefficient
g = opti.parameter()    # Gravity acceleration
Z = opti.parameter(nb)  # Bed altitude (nb being the number of nodes)
exp = opti.parameter()  # Exponent of the friction law
```

The variables of the problem are the water levels for each node:

```
Z_s = opti.variable(nb)
```

The equations are implemented as constraints of the problem. This means that CasADi will make sure that these equations are verified for each node. Equations are written in their discretized form.

```
for i in range(1,nb-1): #all nodes except upstream and downstream nodes
    opti.subject_to((Q**2/(Z_s[i]-Z[i])/L-Q**2/(Z_s[i-1]-Z[i-1])/L)/dx+ \
        g*(Z_s[i]-Z[i])*L*((Z_s[i+1]-Z_s[i])/dx+ \
            n**2*Q**2/((Z_s[i]-Z[i])*L)**2/ \
                ((Z_s[i]-Z[i])*L/((Z_s[i]-Z[i])*2+L))**exp))==0)

i = 0      # upstream node
opti.subject_to((Q**2/(Z_s[i]-Z[i])/L-Q**2/(Z_s[i]-Z[i])/L)/dx+ \
    g*(Z_s[i]-Z[i])*L*((Z_s[i+1]-Z_s[i])/dx+ \
        n**2*Q**2/((Z_s[i]-Z[i])*L)**2/ \
            ((Z_s[i]-Z[i])*L/((Z_s[i]-Z[i])*2+L))**exp))==0)

i = nb-1   # downstream node
opti.subject_to((Q**2/(Z_s[i]-Z[i])/L-Q**2/(Z_s[i]-Z[i])/L)/dx+ \
    g*(Z_s[i]-Z[i])*L*((Z_bc-Z_s[i])/dx+ \
        n**2*Q**2/((Z_s[i]-Z[i])*L)**2/ \
            ((Z_s[i]-Z[i])*L/((Z_s[i]-Z[i])*2+L))**exp))==0)
```

Next step is to set the solver, initialize the values of the parameters and set initial values of the variables:

```
opti.solver('ipopt')          # set solver
opti.set_value(Z_bc, z_s_bc)  # set parameter values
opti.set_value(Z, z_level)
opti.set_value(Q, 1.0)
opti.set_value(L, 1.0)
opti.set_value(dx,delta_x)
opti.set_value(g, 9.81)
opti.set_value(n, 0.04)
```

```

opti.set_value(exp, 4/3)
for i in range(nb):
    opti.set_initial(Z_s[i],z_s_bc)
    
```

The final step is to call the “solve” routine and retrieve results:

```

sol = opti.solve()
z_s_res = sol.value(Z_s)
    
```

	Objective function	Constraints
Water depth $> 0$ at each node		x
Discretized form the conservation of momentum at each node		x
Supercritical flow at the downstream BC		x
Presence of a critical section (by setting an objective function)	Minimize the upstream head	
Presence of a critical section (by setting constraints)		Fr $> 1$ upstream and Fr $< 1$ downstream of the critical section

Table 20: Objective function and constraints to set in CasADi

### 3.7.3 Validation of CasADi

Using CasADi to solve a steady state 1-D hydrodynamic problem is validated against data collected on a physical model.

#### 3.7.3.1 Case study description: a flow in a tunnel spillway

The case study presented in this section concerns a dam in France. The HECE laboratory studied its spillways under several discharges. For this dam, two spillways are located on the left bank. When water overflows the crests, it is directed inside two distinct tunnels. Downstream, these tunnels connect and water is restituted to the river thanks to a ski jump. The general setup is given in Figure 81. Further details will not be given in this thesis since the identity of the project is confidential.

We focus our numerical study on one of these tunnels. Its geometry is described in an AutoCAD file thanks to several cross sections and a vector that links the middle of the bottom of each

cross section. The longitudinal profile of the studied tunnel is given in Figure 82. This figure gives the position of the bottom as well as the position of the ceiling of the tunnel.

Concerning the cross-sections, we noticed two main shapes. They are both depicted in Figure 83. The non-circular cross section is found in the most upstream part of the tunnel (from  $x = 0$  m to  $x = 0.453$  m). Dimensions  $b_1$ ,  $b_2$ ,  $h_t$  and  $R$  vary along the tunnel axis until some point ( $x = 0.453$  m). At this point, the section begins to transform to a circular cross-section. The circular cross section is the last section of the tunnel ( $x = 0.697$  m).



*Figure 81: General view of the setup of two tunnel spillways*

*Fast convergence of a steady 1-D open-channel flow*

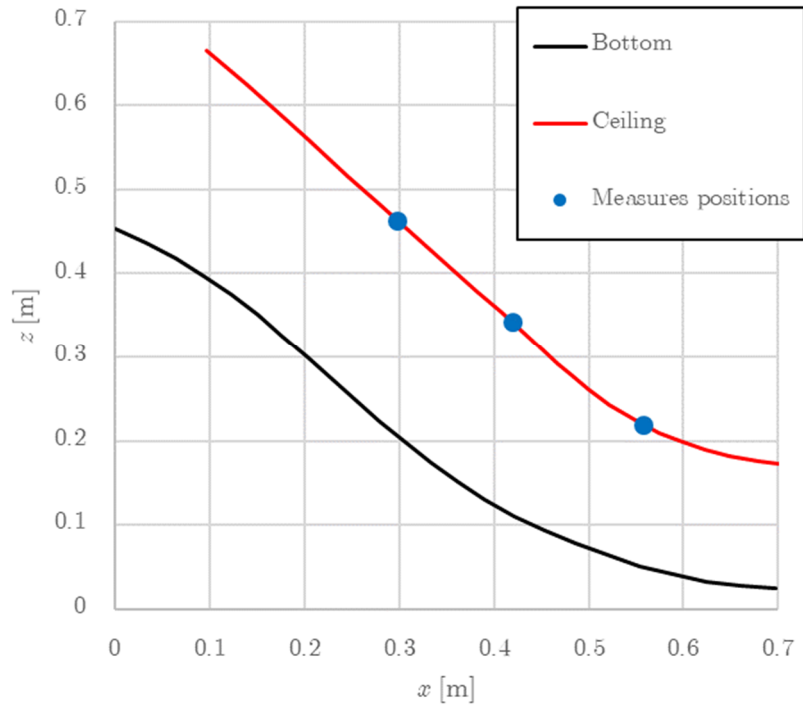


*Figure 82: Longitudinal profile of the tunnel*

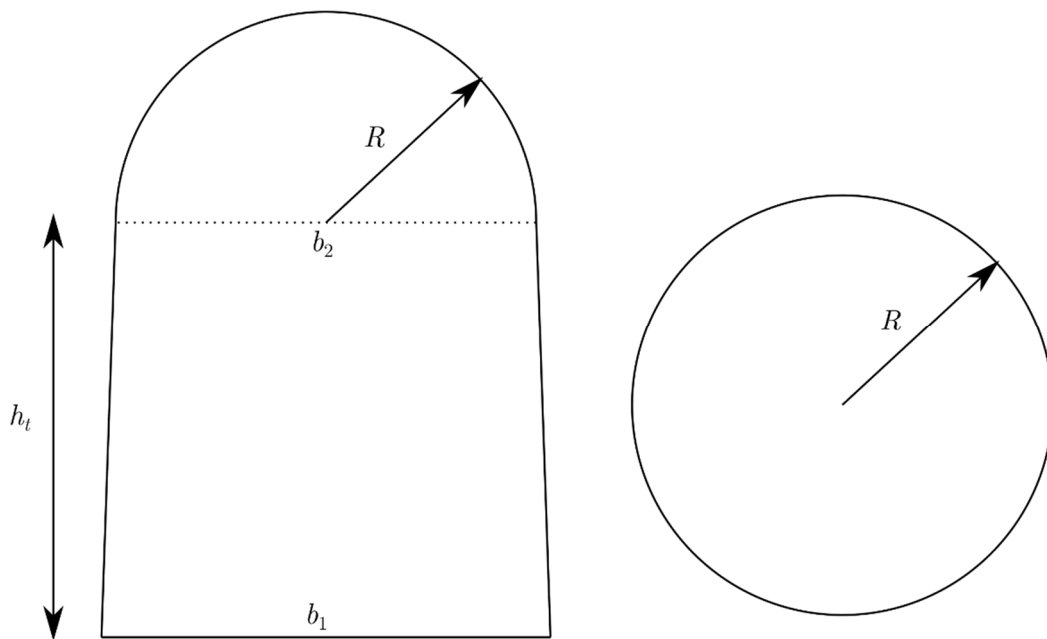


*Figure 83: Two main cross sections that constitutes the tunnel*

Cross-sections tabular relations are extracted from the AutoCAD file thanks to a module available in the WOLF software. After having projected the sections on a plane perpendicular to the bottom vector, tabular values are computed by the software. They represent the link

between the water depth, the cross-section area and the wet perimeter. These information are produced for every cross section of the AutoCAD file.

In order to use CasADi, the cross section – water depth and wet perimeter – water depth relationships should be expressed analytically. For the circular cross-sections the cross-section area  $A_c$ , the wet perimeter  $\chi_c$  and the width at the surface  $L_c$  are expressed in function of the water depth  $h$ :

$$\begin{aligned} b &= 1 - \frac{h}{R} \\ L_c &= 2R\sqrt{1 - b^2} \\ \chi_c &= 2R \arccos(b) \\ A_c &= \frac{R}{2}(\chi_c - L_c b) \end{aligned} \quad (171)$$

The tunnel-like cross-section is divided into two parts: a lower trapezoidal one (denoted with subscript  $t,1$ ) and a upper semi-circular one (denoted with subscript  $t,2$ ). The analytical relationships are:

$$\begin{aligned} \text{if } h \leq h_t : & \begin{cases} b' = L_{t,1} = b_1 + (b_2 - b_1) \frac{h}{h_t} \\ \theta = \arctan \frac{2h}{b_1 - b'} \\ h' = \frac{h}{\sin \theta} \\ A_{t,1} = \frac{b_1 + b'}{2} h \\ \chi_{t,1} = b_1 + 2h' \end{cases} \\ \text{if } h > h_t : & \begin{cases} h'' = h - h_t \\ k = \frac{h''}{R} \\ L_{t,2} = 2R\sqrt{1 - k^2} \\ \chi_{t,2} = \chi_{t,1} + 2R \left( \frac{\pi}{2} - \arccos k \right) \\ A_{t,2} = A_{t,1} + \frac{R}{2} \left( 2R \left( \frac{\pi}{2} - \arccos k \right) + L_{t,2} k \right) \end{cases} \end{aligned} \quad (172)$$

It can be noticed that for the tunnel cross-section,  $R = b_2 / 2$ .

Since the cross-sections are closed, the flow might touch the ceiling of the tunnel. In such a situation, we are in presence of a pressurized flow. In order to take this into account, a Preissman slot (Preissmann 1961) can be added at the top of the cross-sections. This slot is a very thin rectangular section in which the water can enter in order to increase artificially the pressure in

the main flow. The slot should be small enough in order to have a neglectable contribution to the flow. The width of the slot is denoted  $L_p$ .

The cross-sections presented hereabove are made of several parts. In order to ensure a smooth transition between these parts and allow an analytical writing, sigmoid functions  $s$  are used to weight each contribution according to a water depth  $h$  and the position of the transition  $h_0$ :

$$s(h, h_0) = \frac{1}{1 + e^{-B(h-h_0)}} \quad (173)$$

With  $B$  a coefficient that defines the steepness of the transition (for the application presented here,  $B = 100$ ). Notice that sigmoid functions will be used in Chapter 6 as well. The general analytical formulation of the circular cross section is:

$$\begin{aligned} A_{c,tot}(h) &= A_c (1 - s(h, 2R)) + (\pi R^2 + L_p (h - 2R)) s(h, 2R) \\ \chi_{c,tot}(h) &= \chi_c (1 - s(h, 2R)) + (2\pi R + 2(h - 2R)) s(h, 2R) \\ L_{c,tot}(h) &= L_c (1 - s(h, 2R)) + L_p s(h, 2R) \end{aligned} \quad (174)$$

A similar approach is adopted for the tunnel cross section:

$$\begin{aligned} A_{t,tot}(h) &= A_{t,1} (1 - s(h, h_t)) + A_{t,2} s(h, h_t) (1 - s(h, h_t + R)) \\ &\quad + (A_{t,2} (h_t + R) + (h - h_t - R) L_p) s(h, h_t + R) \\ \chi_{t,tot}(h) &= \chi_{t,1} (1 - s(h, h_t)) + \chi_{t,2} s(h, h_t) (1 - s(h, h_t + R)) \\ &\quad + (\chi_{t,2} (h_t + R) + 2(h - h_t - R)) s(h, h_t + R) \\ L_{t,tot}(h) &= L_{t,1} (1 - s(h, h_t)) + L_{t,2} s(h, h_t) (1 - s(h, h_t + R)) + L_p s(h, h_t + R) \end{aligned} \quad (175)$$

As stated earlier, the cross-section evolves along the spillway. This evolution is considered linear. For the tunnel cross-section, parameters  $b_1$ ,  $b_2$  and  $h_t$  are weighted according to their curvilinear position and the values at the extreme sections. Between the tunnel cross-section (at  $x = 0.453$  m) and the circular cross-section (at  $x = 0.697$  m), values  $A$ ,  $\chi$  and  $L$  are directly weighted from the values computed in (174) and (175) according to the curvilinear position.

Parameters of the cross-sections depicted in Figure 83 are measured directly on the AutoCAD file. The resulting values are given in Table 21. The cross section areas and wet perimeter obtained by formulae (174) and (175) with the parameters of Table 21 were compared to the results from the tabular relations given by the WOLF software and good agreement was found.

For the tests performed in this section, three discharges are tested: 10 l/s, 33.2 l/s and 48.9 l/s.

Section	$b_1$ [m]	$b_2$ [m]	$h_t$ [m]	$R$ [m]
$x = 0$ m	0.2066	0.19702	0.1395	$b_2/2$
$x = 0.453$ m	0.146	0.146	0.083	$b_2/2$
$x = 0.697$ m	-	-	-	0.07293

*Table 21: Values that define the cross sections of the tunnel spillway*

### 3.7.3.2 Measurements on the physical model

In order to validate the results produced by CasADi, measurements of the water level were made in HECE laboratory. Since the flow occurs in a closed and relatively small section, a dedicated measurement technique was designed. It consists of tubes glued on top of the tunnel section (Figure 84). These tubes are placed in order to be perpendicular to the bottom slope. Inside each tube, it is possible to insert a pointed shank in order to measure a distance (Figure 85).

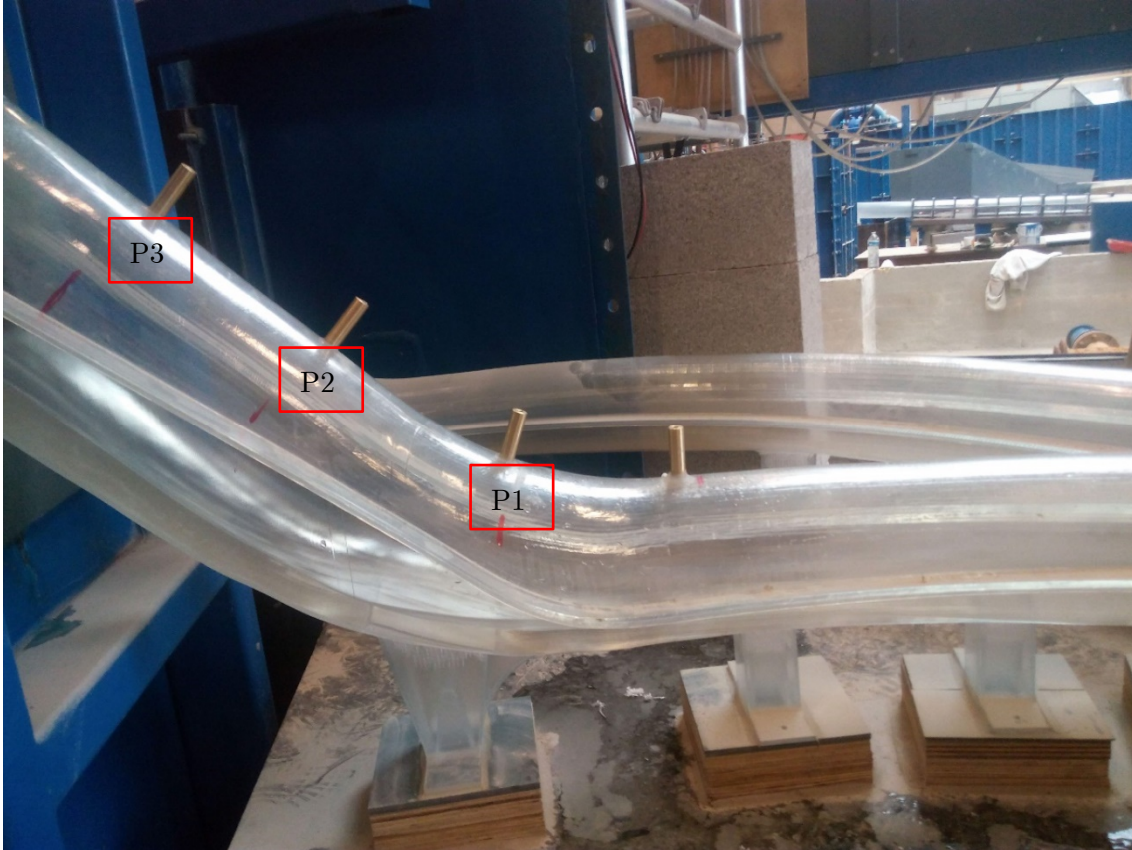


*Figure 84: Tubes positioned on top of the tunnel*



*Figure 85: Measurement of the distance of penetration of the shank*

The shank is used to measure the water depth through a subtraction process. First, the penetration of the shank is measured when it touches the bottom of the tunnel.  $d_b$  is the length of the shank that remains outside of the tube when the point touches the bottom. Then, the penetration of the shank is measured when its tip touches the water surface.  $d_s$  is the length of shank that remains outside of the tube in this situation. The water depth  $h$  is computed as:

$$h = d_s - d_b \quad (176)$$

For each discharge, three recordings of the water depth were performed. They are given in Table 22 with the mean value associated. In order to remain on a straight part of the tunnel (and avoid effects that our shallow water model is unable to represent), only three out of the four tubes were used. They are denoted P1, P2 and P3 and are located in Figure 84.

		<b>P1</b>	<b>P2</b>	<b>P3</b>
$Q = 10$ l/s		28	24	26
	Measures [mm]	28	24	24
	Mean [mm]	28	25	28
$Q = 33.2$ l/s		77	83	81
	Measures [mm]	77	83	81
	Mean [mm]	77	84	81
$Q = 48.9$ l/s		118	123	116
	Measures [mm]	119	124	115
	Mean [mm]	121	123	117
	Mean [mm]	119.3	123.3	116

Table 22: Measured water depth for 3 discharges at 3 gauging points

### 3.7.3.3 Comparison between numerical and physical results

Our CasADi model is used to simulate the flow in the tunnel spillway for three discharges: 10 l/s, 33.2 l/s and 48.9 l/s. The spatial step is set at 1 cm. The bottom is discretized evenly according to the curvilinear coordinate. In order to impulse the passage by a critical section at the crest of the spillway, a flat bottom, positioned 5 cm under the crest is created upstream. This trick allows CasADi to set a subcritical solution upstream of the crest and a supercritical solution downstream. Due to the smooth nature of the sides of the tunnel, no friction is considered. Tests and comparison will be made with the assumption that friction is neglectable compared to other terms.

Since the tunnel presents a slope that varies significantly and that can reach up to  $45^\circ$ , the usual assumption that the bed angle  $\theta$  is neglectable is not valid. In order to take this into account, the water level  $z_s$  is linked to the water depth by:

$$h = \frac{z_s - z_b}{\cos \theta} \quad (177)$$

with  $z_b$  the altitude of the bottom. The constraint that is set in CasADi is the discretized equation (135) for each node with the pseudo-temporal term set at 0. In equation (135),  $z_s$ ,  $A$  and  $S_f$  are functions of the water depth  $h$ . Since the flow is ruled by the critical section, it is not necessary to set water depth boundary conditions. Only the discharge is imposed at every node.

Numerical results computed by CasADi are compared to experimental measurements (Figure 86, Figure 87 and Figure 88). It appears that numerical results and experimental measurements are in very good agreement, especially for the two first discharges. For the third discharge, slightly larger differences appear. These can be explained by the lack of friction term in the equation and also by the possibility to have 3-D effects not represented numerically but present in the physical model.

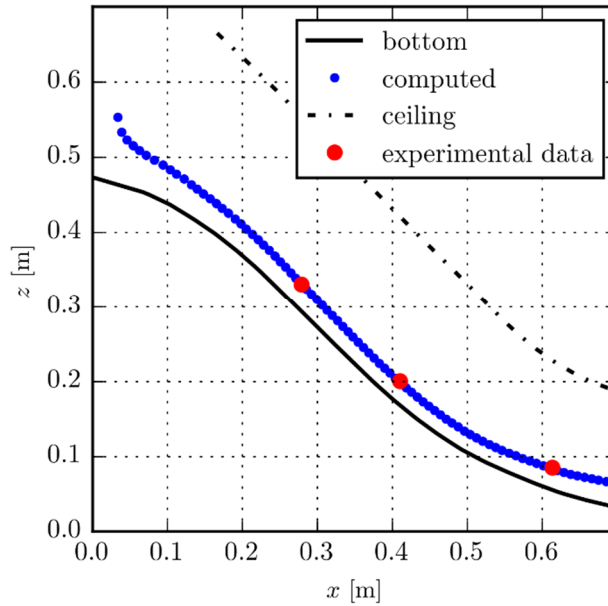


Figure 86: Water level computed by CasADi and measured experimentally for  $Q = 10$  l/s

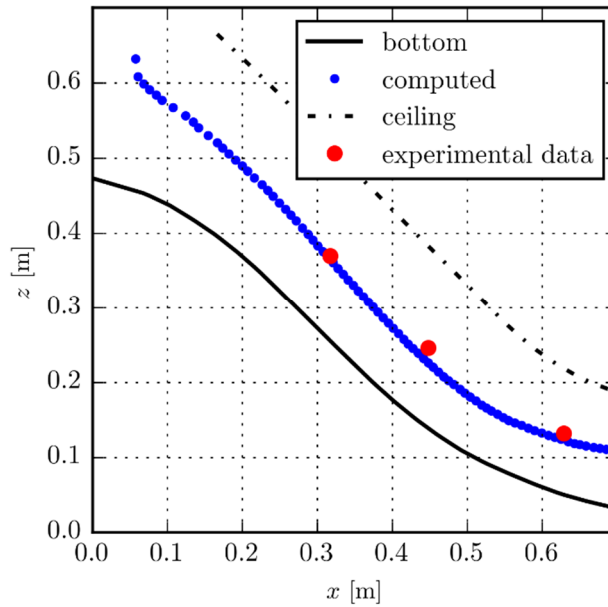


Figure 87: Water level computed by CasADi and measured experimentally for  $Q = 33.2$  l/s

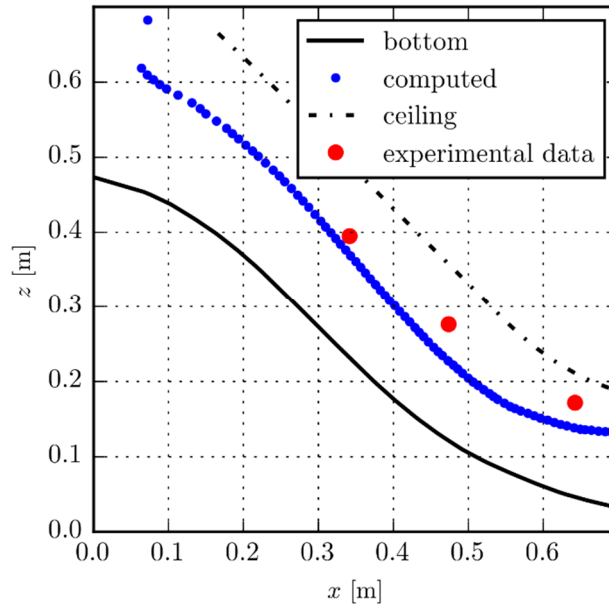


Figure 88: Water level computed by CasADi and measured experimentally for  $Q = 48.9 \text{ l/s}$

This practical example shows that CasADi is able to deal with the computation a transcritical steady 1-D flows.

As a perspective, it would be interesting to modify the CasADi model in order to include the three discharges inside a single optimization problem and set the optimization of the roughness coefficient as the objective function. Testing CasADi for such a comprehensive application would be of great interest for the research and engineering community.

### 3.7.4 CasADi vs. our optimized algorithm

#### 3.7.4.1 Test description

The test case chosen for the comparison between CasADi and our algorithm is a rectangular channel (1 m wide) with a 100 m long sine wave bottom as shown in the following equation:

$$z(x) = 0.05 \sin\left(\frac{\pi}{4} x\right) + 0.05 \quad (178)$$

A Manning friction formula with  $n = 0.04 \text{ s/m}^{1/3}$  was used to estimate friction losses. The downstream boundary condition is a water depth equal to 0.6 m. The unit discharge is uniform and is equal to  $1 \text{ m}^2/\text{s}$ . The residual parameters used with our optimized algorithm are as follows:  $\xi_p = 10^{-6} \text{ m}^2/\text{s}$  and  $\xi_f = 10^{-8} \text{ m}^2/\text{s}$ .

## 3.7.4.2 Performances comparison

We compared the CPU time spent in the solving stages of our new algorithm and CasADi. The goal was to compare the evolution of the computation time with the number of nodes, rather than comparing absolute values. The results are given in Figure 89 and Table 23. They confirm that the computation time evolves almost linearly with the number of nodes when the new algorithm is used. This is not the case with CasADi: the computation time increases following a power law  $N^\alpha$ ,  $\alpha > 1$ . This is due to the matrix operations that CasADi has to perform. Increasing the number of nodes leads to a non-proportional increase in computation time. The speed up factor, which is the ratio between the CPU time spent when using our new algorithm and the CPU time spent with CasADi, ranges from in order of  $10^0$  to in order of  $10^2$  according to the number of nodes considered.

From this example, it appears clearly that our algorithm provides a better behavior when the number of nodes in a domain tends to increase. Moreover, it is much easier to use “non-analytical” friction laws and cross-sections described thanks to tabular values with our algorithm than in CasADi. Indeed, CasADi requires to use some tricks, such as sigmoid functions, in order to be able to include these features in an optimization problem. Even if CasADi presents some weakness on the “computation time” side, it is an elegant and easy to implement solution for many problems.

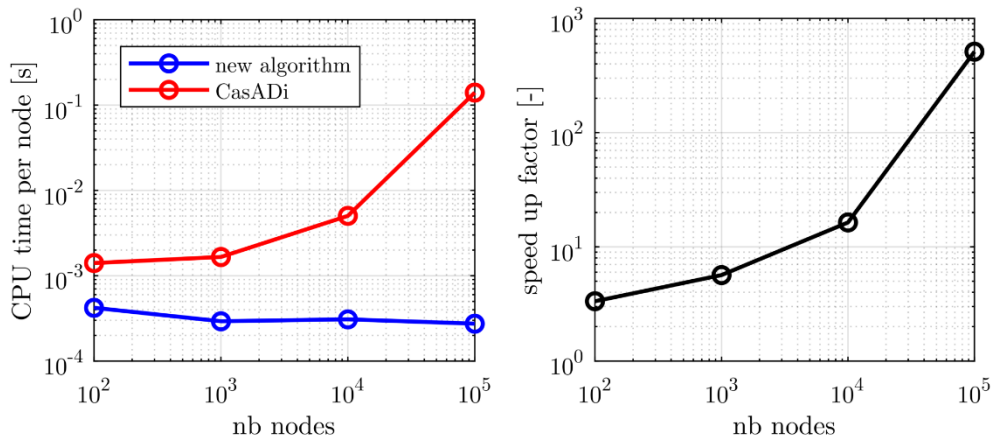


Figure 89: Comparison of the CPU time evolution with the number of nodes between our algorithm and CasADi and the associated speed up factor

	<b>New algorithm</b>	<b>CasADi</b>
<b>100 nodes</b>	0.0421	0.1563
<b>1000 nodes</b>	0.2927	1.6563
<b>10000 nodes</b>	3.0828	50.5625
<b>100000 nodes</b>	27.4295	14039.1406

*Table 23: CPU times [s] for computing the test case using our algorithm or CasADi*

### 3.8 Conclusion

This chapter focused on the implementation of an algorithm for converging quickly a steady solution of a 1-D model. Several innovations are introduced, including the use of the non-linear Krylov accelerator in open-channel flows, an evolutionary domain algorithm and the use of CasADi to solve steady 1-D flows. These improvements lead to an algorithm that is able to quickly solve steady open-channel flows. Therefore, optimization problems and uncertainty analyses that require many evaluations, become more tractable.

Simplified equations from Kerger et al. (2011) are used for this model. They are the result of a simplification of Saint-Venant equations for steady flows. They also keep a similar formulation as the momentum equation of the traditional system of equations. This enables to keep the same upwinding technique as the one used for the unsteady model.

The first algorithm used to solve these equations is optimized with two techniques: an Anderson accelerator and a sliding domain strategy. The accelerator relies on previous estimates in order to converge more quickly toward a solution. The sliding domain method is based on the physical observation of subcritical river flows: a perturbation of the water level at a point affects only upstream domain. In practice, the upwinding technique used in our model affects also downstream nodes. This is why a method that considers only a limited number of nodes was implemented. The computation domain slides upstream according to the convergence status of the nodes.

This model was validated against three test cases on a bump, featuring different flow regimes. The algorithm and the model gave good results, identical to the traditional 1-D model. This step allowed to validate the equation implemented as well as the optimizing techniques included in the algorithm.

We argued that the computation time was mainly a function of two parameters: the minimum number of nodes to keep in the computation list and the partial residual. A systematic analysis on six tests allowed to extract optimal parameters. However, it appeared that these values

were not optimal for each test. Furthermore, the analysis of the evolution of the residual fostered a reflection about an optimized algorithm. Indeed, while some nodes reached a residual much lower than needed, other nodes could obtain worse residual values at the end of the computation of partial domains, requiring a final iteration all over the domain. It also appeared that the residual could remain constant all over the iterations on partial domains, requiring a last iteration all over the domain as well.

These observations lead to the implementation of an optimized algorithm. The computational cost of this algorithm for a given test showed to depend only on the partial residual value. A systematic analysis on the six same tests as previously highlighted the need of relatively high partial residual values. This new algorithm lead at least to equivalent computation times as best computation times obtained previously. This optimized algorithm proved the unnecessary use of a last computation all over the domain. Moreover, scalability tests showed that the algorithm gave a linear evolution of the computation time when the number of nodes increases.

Finally, our algorithm was compared to a state-of-the-art nonlinear optimizing algorithm: CasADi. We showed that CasADi was able to deal with closed complex cross sections and it produced very satisfactory results compared to experimental data. Results of an academic test case showed that our code outperforms CasADi in terms of scalability and flexibility.

The implementation of an algorithm for a fast convergence of steady 1-D flows paves the way for the use of physically based hydraulic models in the frame of intensive uncertainty analysis. Indeed, low computation times that we are now able to reach enables its use in cases where a large number of evaluations is required.

# Chapter 4: Uncertainty analysis applied to 1-D hydraulic models

## 4.1 Introduction

The second chapter of this thesis focused on the fundamentals of uncertainty analysis. It also introduced efficient methods to apply uncertainty analysis to more computationally expensive cases. In order to be able to assess the validity of these methods in the frame of hydraulic models, a fast computing method was implemented and presented in chapter 3. Thanks to this new algorithm, we aim to compare the Monte Carlo method, considered as a reference in term of accuracy, to efficient methods (PEM and PMM) in the frame of open-channel flows.

This task is performed in this chapter for 1-D models. These 1-D models are renown to compute quickly compared to their 2-D and 3-D counterparts, especially when our new algorithm is used. Some computation times are given in chapter 3. A first comparison between uncertainty methods is applied to the academic case of a flow over bump. Various flow regimes and uncertain variables are used. Then, a real world application is presented. It concerns a 7.5 km long river reach for which we wish to determine the potential flooding of a private land. This example is the occasion to present the entire workflow to run an uncertainty analysis. It treats the setting of the model, the definition of uncertainty sources and the interpretation of uncertainty results.

The general method used to apply uncertainty analysis to hydrodynamic cases is briefly described. First, sources of uncertainty should be defined (e.g. downstream boundary condition, discharge, roughness coefficient, rating curve, etc.). Then, based on the uncertainty analysis method chosen, the values picked for the uncertain parameters are used in the hydrodynamic model. Several hydraulic results are obtained (water profiles, velocities, etc.). From these results, we dispose of several hydrodynamic results at a given point of the computation domain. This allows to fit a pdf for that particular point of the domain. From the pdf and the statistical moments, several interesting information can be derived such as the median, the mean, a confidence interval, etc. This process, which is used in the following sections, is schematically illustrated in Figure 90.

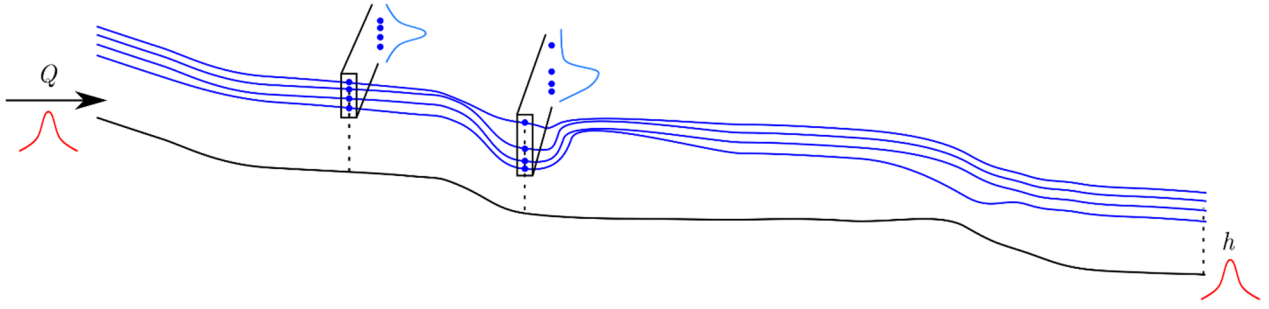


Figure 90: General methodology to apply uncertainty analysis to hydrodynamic cases

## 4.2 First hydraulic application to a flow over a bump

### 4.2.1 Case study description

The first uncertainty analysis on a hydraulic case will be performed on a bump. It is described in (Aureli et al. 2008). The whole domain ranges from 0 to 20 m with the following bed elevation:

$$z_b(x) = \begin{cases} 0.8 \left( 1 - \frac{(x-10)^2}{4} \right) & 8\text{m} \leq x \leq 12\text{m} \\ 0 & \text{otherwise} \end{cases} \quad (179)$$

The channel is considered rectangular (1 m width) and frictionless. This particular geometry was already used in chapter 3 and depicted in Figure 36, Figure 41 and Figure 45. The discretization is chosen at 0.1 m.

In order to test the capabilities of different methods concerning the discontinuous behavior of a flow, various flow regimes will be tested. A first set of tests (tests A) consists in defining two uncertain variables: the upstream discharge and the downstream water depth boundary condition. Their variation are described in Table 24. The variability of these two variables is defined in order to avoid as much as possible flow regime changes. Maximum and minimum values are also defined in order to avoid unphysical values. An analysis of rejected points from the Monte-Carlo simulations will be performed in order to evaluate the bias introduced from a truncated probability distribution. Test A.1 features symmetrical distributions represented by a normal law while test A.2 features Gamma distribution in order to analyze the consequences of the introduction of skewness.

A second set of tests (test B) is defined in order to see how uncertainty analysis methods deal with hydraulic discontinuities. The downstream boundary condition is the only uncertain variable. Its variation range is chosen in order to respect physical limitations. Once again, a

symmetrical distribution is featured in test B.1 while the influence of skewness is introduced in test B.2.

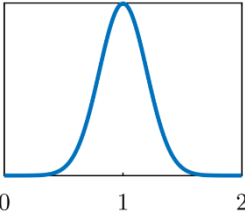
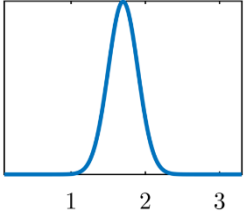
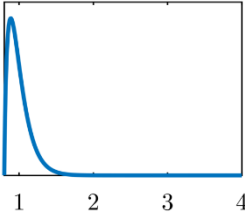
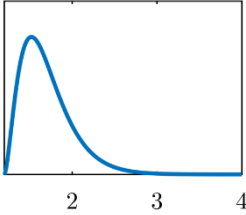
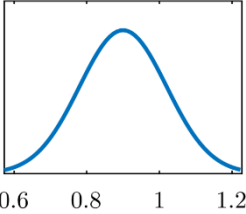
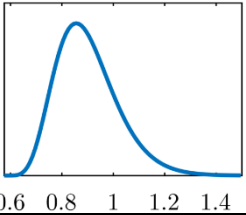
	Upstream discharge $Q$	Downstream water depth $h$
Test A.1	$\bar{Q} = 1 \text{ m}^3/\text{s}$ , $\sigma_Q = 0.2 \text{ m}^3/\text{s}$ , $\gamma_Q = 0$ , Normal distribution, $Q \in [0; 2]$	$\bar{h} = 1.7 \text{ m}$ , $\sigma_h = 0.2 \text{ m}$ , $\gamma_h = 0$ , Normal distribution, $h \in [0.1; 3.3]$
		
Test A.2	$\bar{Q} = 1 \text{ m}^3/\text{s}$ , $\sigma_Q = 0.15 \text{ m}^3/\text{s}$ , $\gamma_Q = 1.5$ , Gamma distribution, $Q \in [0.8; 10]$	$\bar{h} = 1.7 \text{ m}$ , $\sigma_h = 0.3 \text{ m}$ , $\gamma_h = 1.2$ , Gamma distribution, $h \in [1.2; +\infty[$
		
Test B.1	$\bar{Q} = 0.4 \text{ m}^3/\text{s}$ , $\sigma_Q = 0 \text{ m}^3/\text{s}$ , Constant value	$\bar{h} = 0.9 \text{ m}$ , $\sigma_h = 0.12 \text{ m}$ , $\gamma_h = 0$ , Normal distribution, $h \in [0.573; 1.227]$
		
Test B.2	$\bar{Q} = 0.4 \text{ m}^3/\text{s}$ , $\sigma_Q = 0 \text{ m}^3/\text{s}$ , Constant value	$\bar{h} = 0.9 \text{ m}$ , $\sigma_h = 0.12 \text{ m}$ , $\gamma_h = 0.74$ , Gamma distribution, $h \in [0.5756; +\infty[$
		

Table 24: Uncertain variables characteristics for the bump test cases

The purpose of defining symmetrical, skewed and/or bounded distributions comes from practical considerations. Indeed, in real-life cases, some uncertain variables are bounded with physical limitations. For instance, a water depth boundary condition cannot be lower than 0. Distributions can also be skewed due to the nature of random variables. Finally, a flow may require a minimum head to be feasible (in order to deal with a critical section). If the flow cannot exist with some combination of uncertain variables, the hydraulic model should be able to produce and manage an error message. The computation of the output uncertainty should then consider this error for an accurate evaluation.

This principle on feasibility is illustrated with a theoretical study for the bump described earlier for a given discharge  $Q = 0.4 \text{ m}^3/\text{s}$  without any friction loss. Figure 91 shows the evolution of the downstream head  $E$  according to the prescribed downstream water depth  $h_{BC}$  (blue plain line). The maximum critical head is computed and denoted  $E_{cr}$ . In this case, it corresponds to the critical head (head of a flow with  $Fr = 1$ ) at the top of the bump. This value is the minimum head required for a flow to get over the bump. If the head upstream of the bump is lower, then the flow is unable to go over this topographical difficulty. If the head downstream is greater than  $E_{cr}$ , then it is obvious that, without any head loss, a solution can be found.

When the downstream head is lower than  $E_{cr}$ , some solutions are still possible for some values of the downstream water depth. If a hydraulic jump occurs between the critical section and the downstream boundary condition, a head loss occurs. This configuration allows having a higher critical head than the head at the downstream boundary condition. However, the head lost in the hydraulic jump is linked to a water depth ratio  $h_2 / h_1$  (with  $h_1$  the supercritical upstream water depth and  $h_2$  the subcritical downstream water depth) which depends on the application of the continuity and momentum conservation principles. This ratio depends on the Froude number in the supercritical zone  $Fr_1$ :

$$\frac{h_2}{h_1} = \frac{\sqrt{1 + 8Fr_1^2} - 1}{2} \quad (180)$$

In Figure 91, we plot with the yellow dotted line the head upstream of a hydraulic jump for a corresponding  $h_2$  downstream water depth. It appears that the head just upstream of the hydraulic jump remains lower than the critical head for a range of downstream water depth. In this region, since the head is not sufficient, a hydraulic solution cannot be found. When the head gets higher than the critical head, a hydraulic solution becomes feasible with a hydraulic jump (turquoise zone (c) in Figure 91).

When the downstream water depth reaches a value that implies a downstream head at least equal to the critical head, a hydraulic jump is not needed anymore to create a head loss. All the water depths greater than this value allow to find a hydraulic solution.

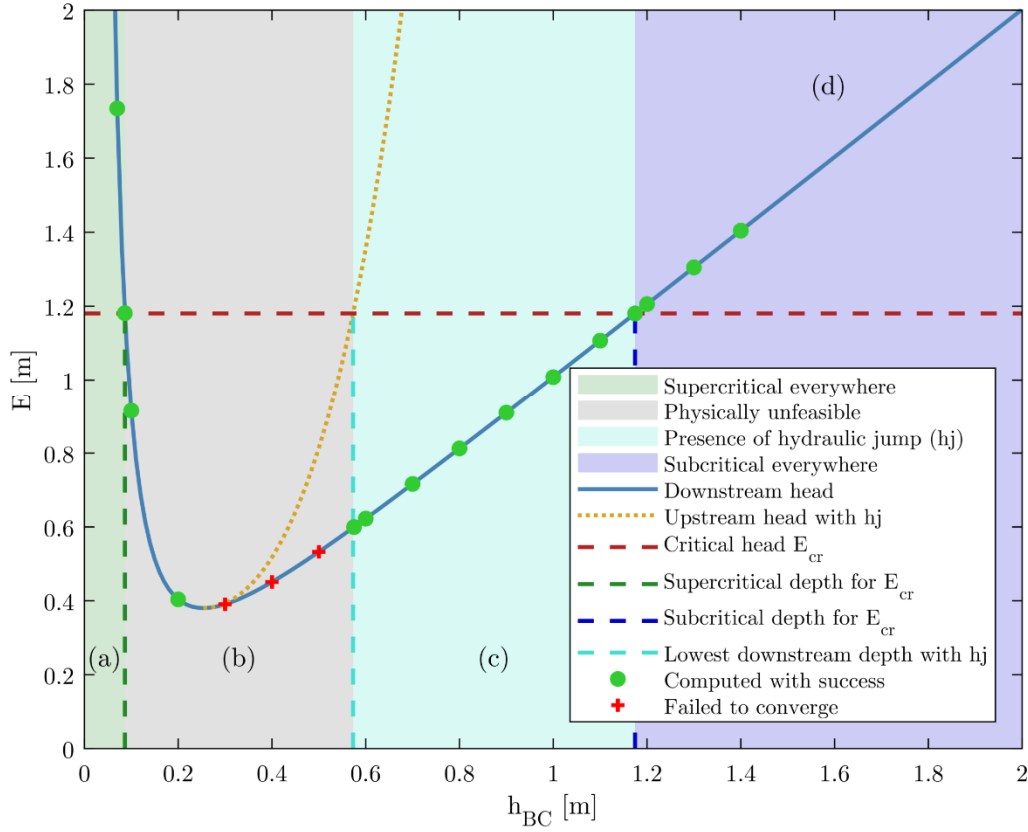


Figure 91: Theoretical analysis the head and of feasible solutions according to the prescribed downstream water depth

Several numerical experiments were performed in order to illustrate this theoretical reasoning. Several values of downstream water depths were tested and are represented by the dots on the blue plain line in Figure 91. Green dots depict computations that successfully converged to a solution while red “+” depict computations unable to converge. Without surprise, the “+” located between the critical water depth and the turquoise line could not converge while the dots located to the right of this turquoise line successfully converged ((c) and (d) zones). The successful convergence of the dots located to the left of the critical water depth can be explained by the fact that the problem is not well-posed. Indeed, for a supercritical downstream regime, no boundary condition is required and the water depth in that part of the flow is deduced from an upstream condition. Since no upstream water depth condition is imposed in this problem, the solution converged by our algorithm takes into account the critical water depth at the

summit of the bump. The water depth at the downstream part of the computation domain does not correspond to the water depths depicted by the green left dots in Figure 91.

## 4.2.2 Results and discussion

### 4.2.2.1 General considerations about computation feasibility

Before discussing in details the results produced by the uncertainty analysis methods, it is important at this point to recall some limitations of some of these methods. First, the PEM and PMM evaluation points are computed using equation (46) for skewed distributions. In order to produce real numbers, the following condition must be met:

$$\kappa_{X_i} - 3 \left( \frac{\gamma_{X_i}}{2} \right)^2 \geq 0 \quad (181)$$

For example, for a kurtosis which is characteristic of a normal distribution ( $\kappa_{X_i} = 3$ ), the skewness should not exceed 2:  $|\gamma_{X_i}| < 2$ . PEM and PMM are not suitable for any combination of skewness and kurtosis coefficients.

Concerning SRSM, the choice of collocation points is performed according to an empirical algorithm that does not take into account the skewness of a random variable. This can result in inconsistent evaluation points. For instance, if a Gamma distribution is considered, it includes a bound. SRSM, which does not take into account this skewness, could pick an evaluation point out of the bounds of the Gamma distribution. It appears then that the direct application of SRSM is not likely to be suitable for skewed (and bounded) distributions. Even if an alternative approach is developed in appendix A.4, we prefer to apply the original method from Isukapalli et al. (1998) in order to avoid any undesired effects of a new technique that is not fully tested and validated.

For each tested configuration, some points could not be computed. This appears in two conditions:

1. If the picked points are out of the bounds defined by the user
2. If the algorithm stopped for the picked points on one of the non-convergence conditions.

The algorithm declares the computation as not convergeable if:

- the decreasing rate of nodes to compute for a fixed upstream node is lower than 1 node per 5 iterations or,

- the convergence process for a fixed partial domain exited 10 times consecutively because of the reaching of the maximum number of iterations (1000).

The points picked out of bounds can be identified prior to the computation of the hydraulic model. They are removed and the weights of the remaining points are adapted in order to keep an overall unit weight. Concerning the unfeasible points, they are listed and the weights of the feasible points are adjusted to reach a sum of 1 for the Monte-Carlo method. For the other methods, a warning message is produced so that the user can deal with this inconsistency.

#### 4.2.2.2 Tests A: avoiding flow regime changes as much as possible

For test A.1 (normal distribution for the discharge and the downstream boundary condition), considering Monte-Carlo with  $10^6$  points as the reference, all methods give good approximation of the mean water level (Figure 92). When looking at the standard deviation, differences are more obvious between the methods. Close to the peak, SRSM at 2<sup>nd</sup> and 3<sup>rd</sup> order are closer to the Monte-Carlo results than PEM and PMM. PEM and PMM methods estimate the standard deviation equally. Out of the peak zone, all methods produce similar results. Finally, the skewness is not very well estimated by any of the “low-computation-time” methods (PEM, PMM and SRSM). It is interesting to notice as a verification procedure that the variation properties of the downstream boundary condition are well reproduced by all the methods.

In order to assess the importance of the number of points that could not be computed, the feasibility is reported in Figure 93 and Table 25. One can observe that only a low number of points could not be computed ( $< 0.03\%$ ). Out of these points, the one located below the turquoise line are physically unfeasible (see section 4.2.1). For the remaining points, the computation was stopped due to a convergence criterion. Relaxing these criteria would lead to an increasing computation time for the points physically unfeasible. We decide to accept to lose a small amount of feasible points in order to keep overall low computation times. It is important to notice that convergence issues may also affect methods with a lower number of computation points (e.g. some points of PMM are close to the blue lines where convergence difficulties were reported). For these ones, the user must make sure that all points were computed successfully. For further details about the convergence process of the 1-D model, the reader can refer to chapter 3.

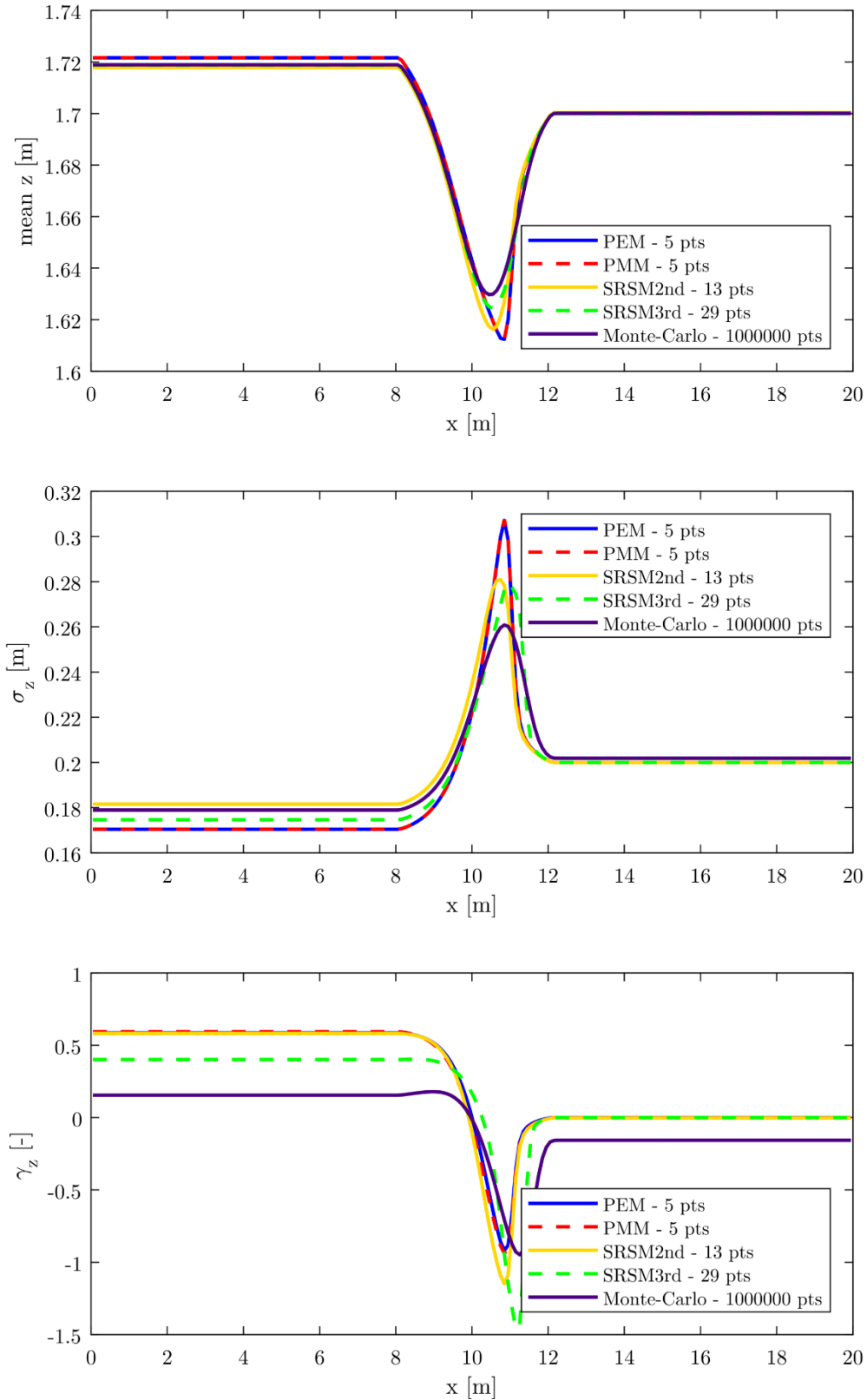


Figure 92: Statistical moments for the free surface level for test A.1

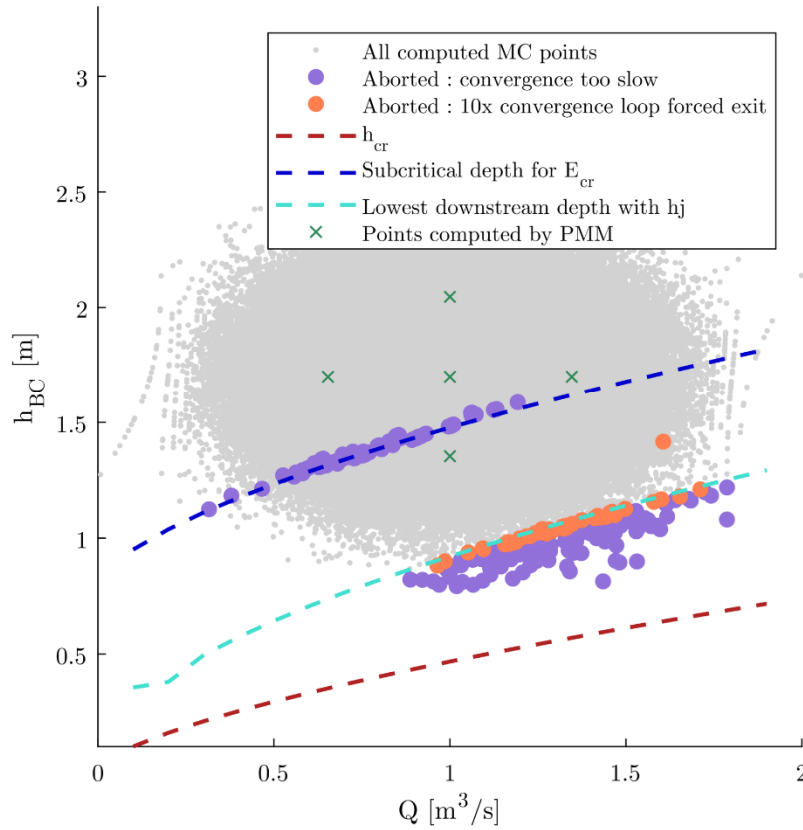


Figure 93: Computed points and unfeasible computation points with remarkable water depths for test A.1

	Out of bounds	Unfeasible	Elapsed time <sup>9</sup>
PEM	0/5	0/5	< 1 s
PMM	0/5	0/5	< 1 s
SRSSM 2nd order	0/13	0/13	21 s
SRSSM 3rd order	0/29	0/29	26 s
MC 10 <sup>6</sup> pts	0/1000000	270/1000000	1 h 47 min

Table 25: Number of unfeasible points and elapsed times for test A.1

Distributed water levels are given in Figure 94 for PMM and Monte-Carlo (10<sup>6</sup> points). These graphs give the median water level and a confidence interval. These values were computed with the assumption that the results are distributed according to a Gamma distribution. It appears that, even if the statistical moments present some differences between PMM and

<sup>9</sup> Elapsed times reported in this chapter are obtained on a Windows machine with an Intel i7-6700K CPU (4 cores @ 4GHz) and 32 Go RAM.

Monte-Carlo, the overall results produced with PMM (5 evaluation points) compete very well with the reference solution.

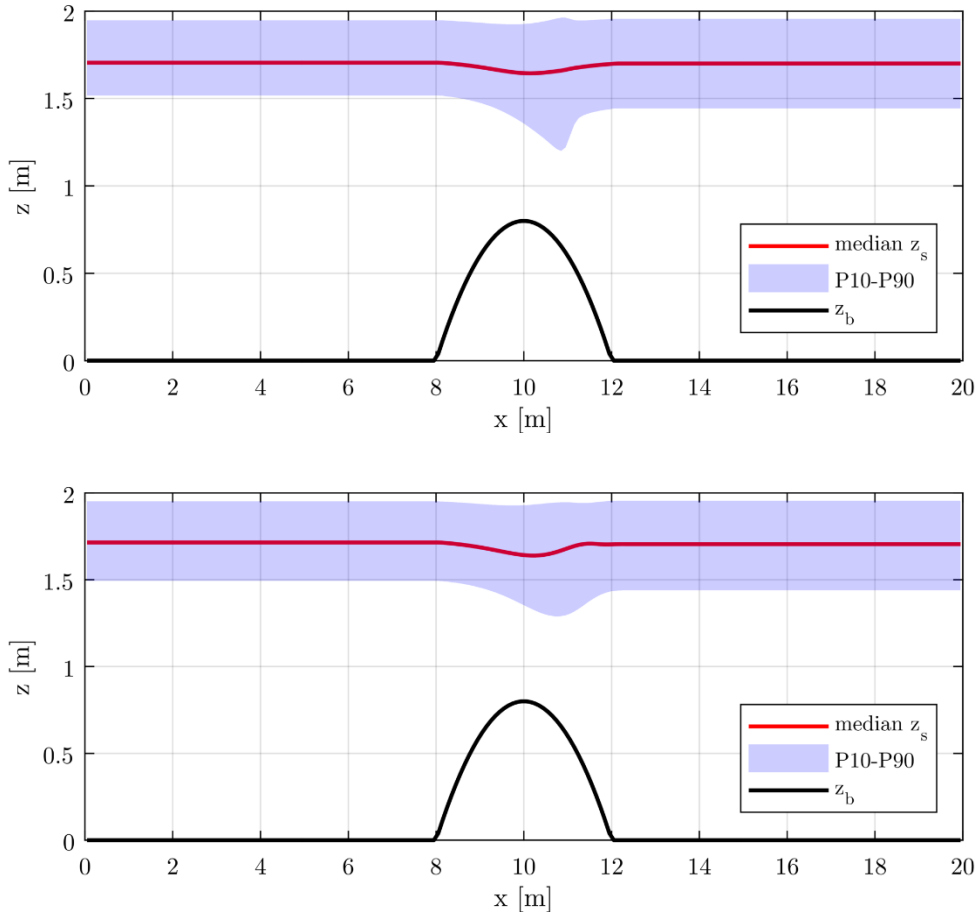


Figure 94: Distributed free surface levels and confidence interval for PMM (upper graph) and Monte-Carlo (1 million points, lower graph) for test A.1

For test A.2, since the distributions of uncertain variables are skewed, only PEM, PMM and Monte Carlo methods are considered. SRSM is not included in the comparison process since the additional steps are required to adapt the method for skewed distributions (see appendix A.4) are not fully tested and validated. Mean values of the free surface (Figure 95) are evaluated in a satisfactory way with PEM and PMM compared to Monte-Carlo. Indeed, maximum differences of the order of 1 cm can be observed. Same observations can be done for the standard deviation. Concerning the skewness coefficient, larger differences appear between the Monte Carlo method with  $10^6$  points and the methods with 5 points. While results were similar or even identical between PEM and PMM for the mean and standard deviation, the skewness coefficient diverges between PEM and PMM around the flow acceleration zone. Better results are obtained with PMM.

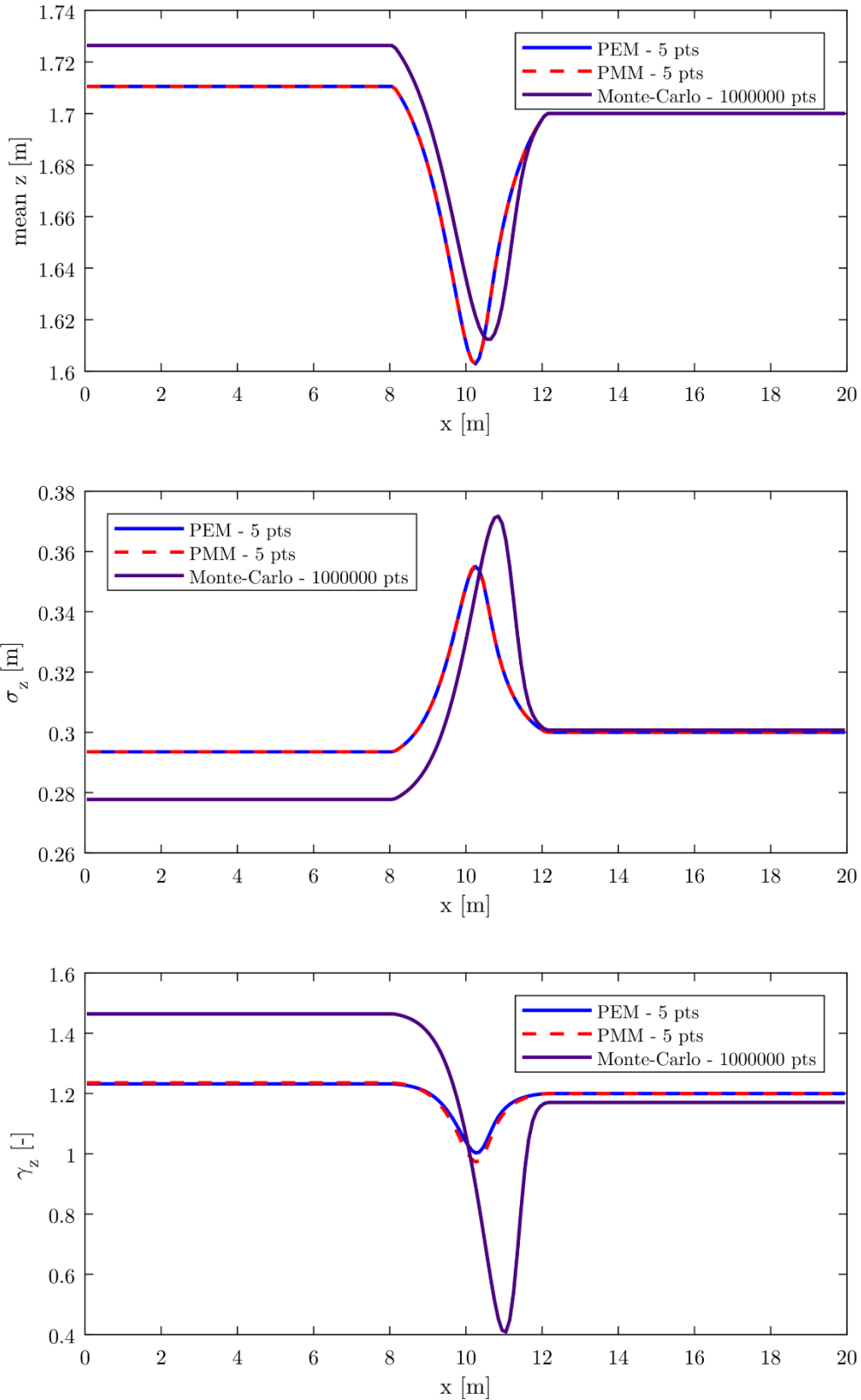


Figure 95: Statistical moments for the free surface level for test A.2

As for test A.1, some points could not be computed (Figure 96) due to a low convergence rate. These points are rare compared to the total number of points computed (Table 26) and some of these lie in a zone of physical unfeasibility. The positions of the points used in the PMM are reported as well. They were all able to converge to a solution.

The distributed values of the median water level and of the P10 and P90 values are reported in Figure 97 for two methods. Even with differences in the statistical moments, both distributed results are close. PMM with its low number of evaluation points is able to draw a satisfactory approximation of the water level distribution compared to the results with a million points for the Monte-Carlo method.

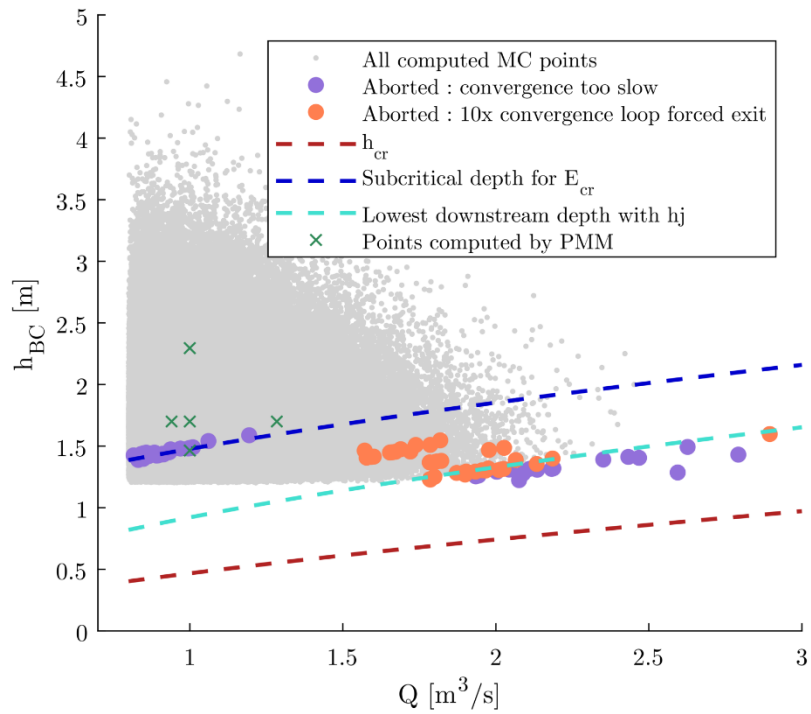


Figure 96: Computed points and unfeasible computation points with remarkable water depths for test A.2

	Out of bounds	Unfeasible	Elapsed time
PEM	0/5	0/5	< 1 s
PMM	0/5	0/5	< 1 s
MC 10 <sup>6</sup> pts	0/1000000	148/1000000	2 h 16 min

Table 26: Number of unfeasible points and elapsed times for test A.2

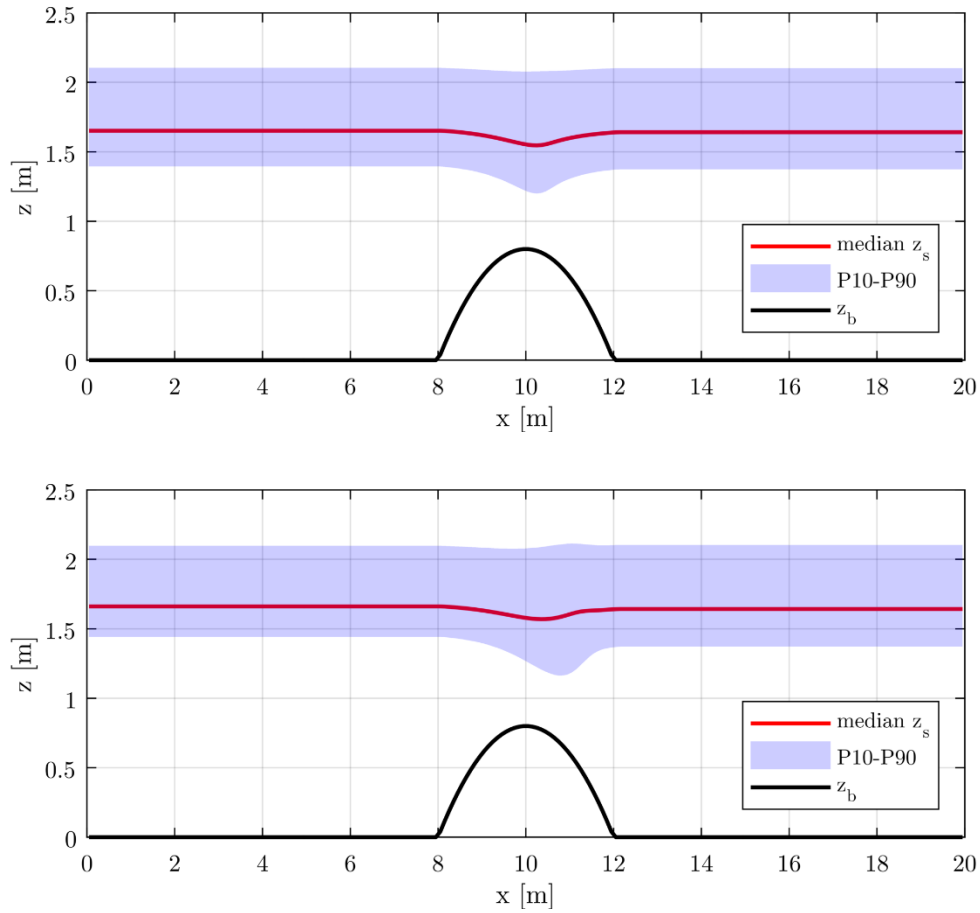


Figure 97: Distributed free surface levels and confidence interval for PMM (upper graph) and Monte-Carlo (1 million points, lower graph) for test A.2

#### 4.2.2.3 Tests B: effect of hydraulic discontinuities

For test B.1, only the downstream boundary condition is uncertain. All methods give similar results concerning the mean value of the water level (Figure 98). Only a small difference can be observed for the lowest levels. Standard deviations are also similar between methods for the entire domain. The Monte-Carlo method exhibits a non-nil standard deviation (but still small) due to the picking of points above the blue line threshold in Figure 99. PEM and PMM do not get over this limit and can only experience a flow where the critical section determines the upstream water level.

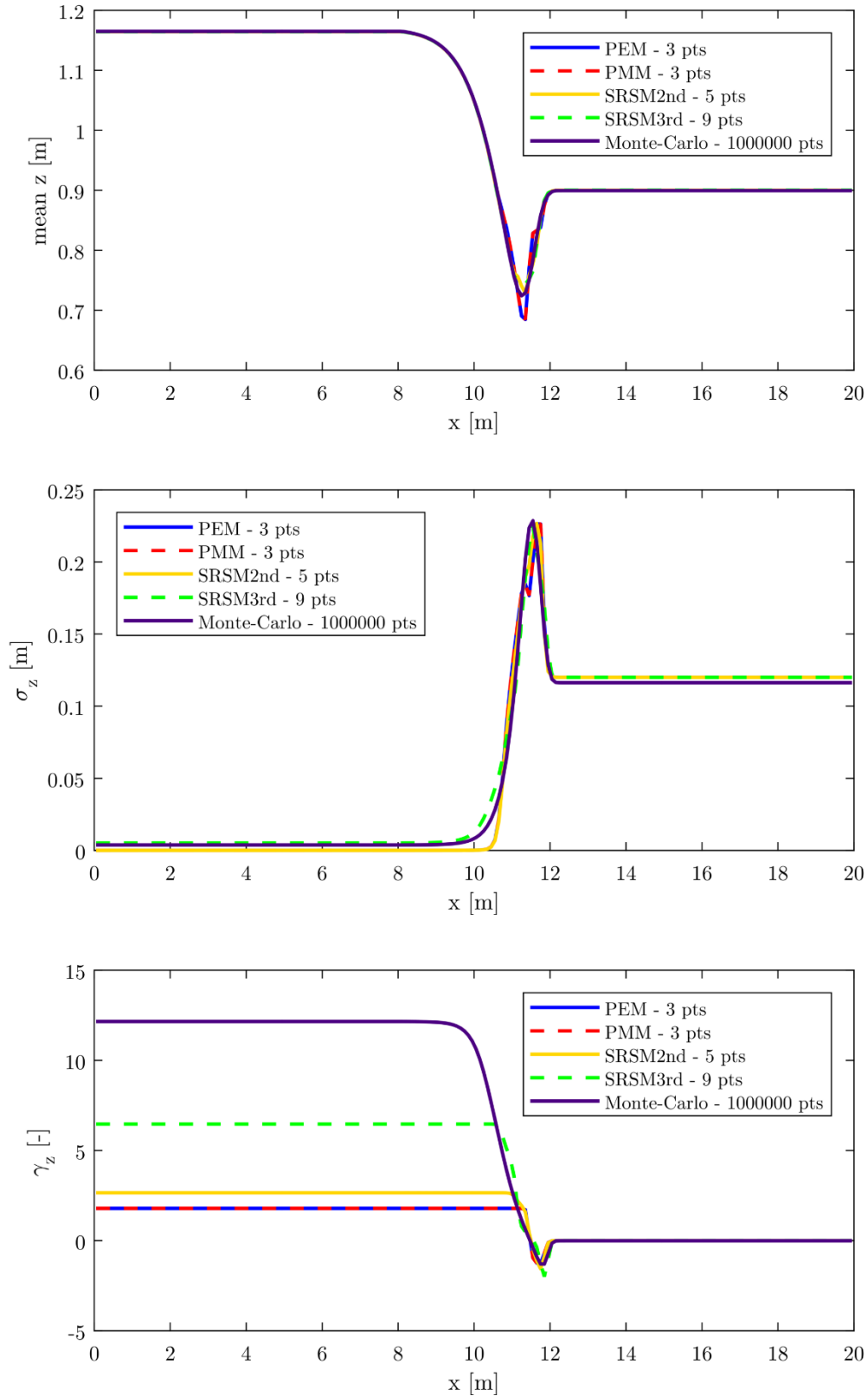


Figure 98: Statistical moments for the free surface level for test B.1

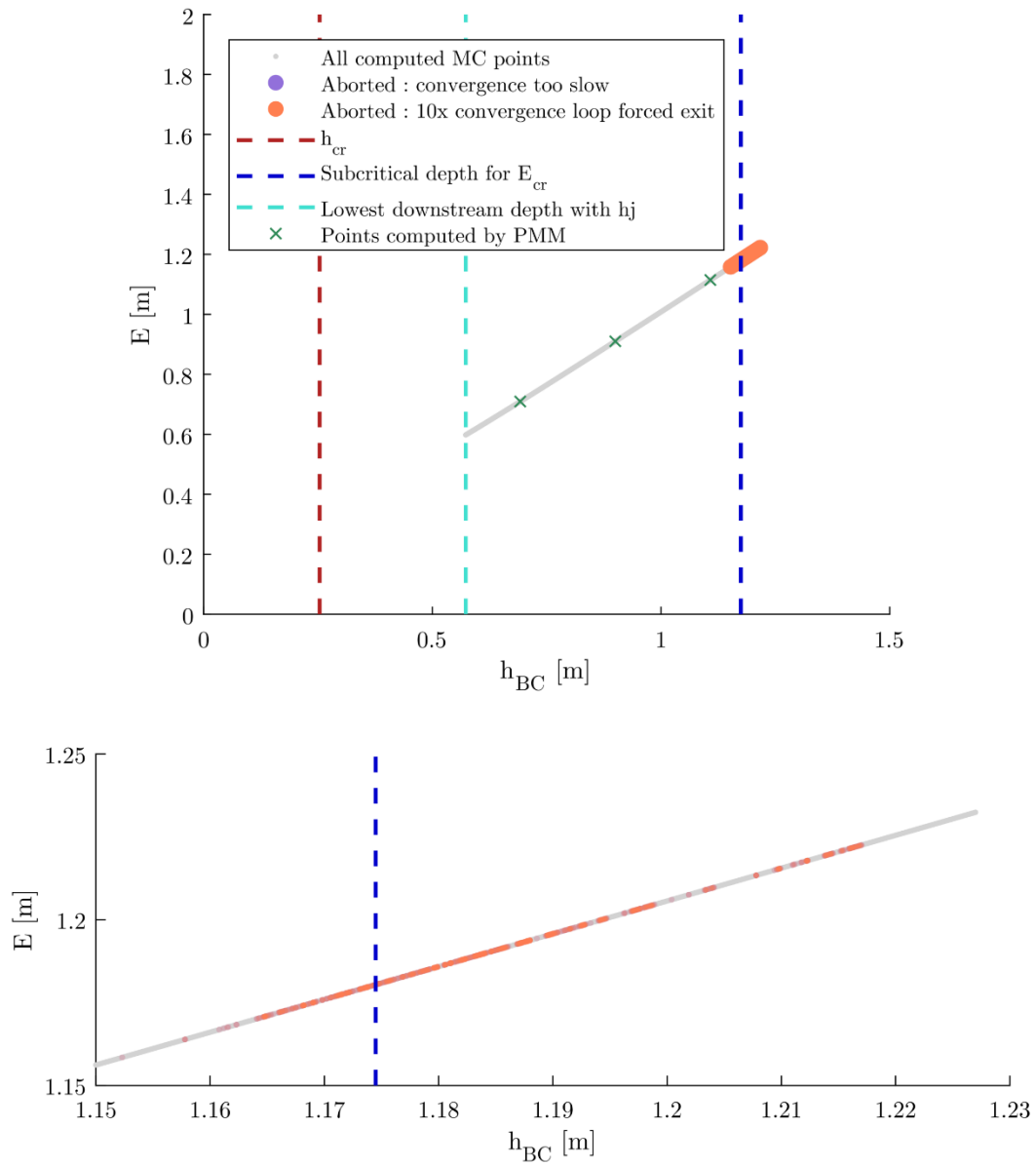


Figure 99: Computed points and unfeasible computation points with remarkable water depths for test B.1

	Out of bounds	Unfeasible	Elapsed time
PEM	0/3	0/3	< 1 s
PMM	0/3	0/3	< 1 s
SRSSM 2nd order	0/5	0/5	21 s
SRSSM 3rd order	0/9	0/9	23 s
MC $10^6$ pts	6395/1000000	1174/1000000	5 h 36 min

Table 27: Number of unfeasible points and elapsed times for test B.1

The skewness coefficient differs between methods in the upstream part. This can be understood by the fact that fast-computing methods result in a null standard deviation. This implies that the skewness coefficient has no meaning in such a situation. Concerning the Monte-Carlo method, a large skewness coefficient is obtained upstream. This can be justified by the statistical distribution of the water depth for the most upstream node of the domain (Figure 100). Most values occur at  $\sim 1.165$  m and some other are larger which leads to a highly skewed distribution. The Gamma distribution corresponding to the computed moments is also depicted in Figure 100 for comparison purposes. It appears that the Gamma distribution represents the actual distribution in a satisfactory way even if the skewness is not so marked on the theoretical distribution.

For test B.1, much more points were out of bounds and unfeasible than for tests A. The unfeasible points are once again located around the subcritical depth for  $E_{cr}$  (Figure 99). Even if the number of points is higher, the proportion of rejected points remain low and all points could be computed for PEM, PMM and SRSM (Table 27).

A comparison between distributed water levels obtained with PMM and Monte-Carlo (Figure 101) show similar characteristics even if slight differences can be noticed around the hydraulic jump.

Results obtained for test B.2 allow drawing the same observations as for test B.1, concerning statistical moments (Figure 102) and distributed hydraulic results (Figure 104). Due to the use of a skewed distribution, no points were rejected due to an out-of-bound criterion (Table 28). A small percentage of points could not be computed neither around the blue line that depicts the limit from a flow with a hydraulic jump and a fully subcritical flow (Figure 99). This problem does not affect PEM and PMM.

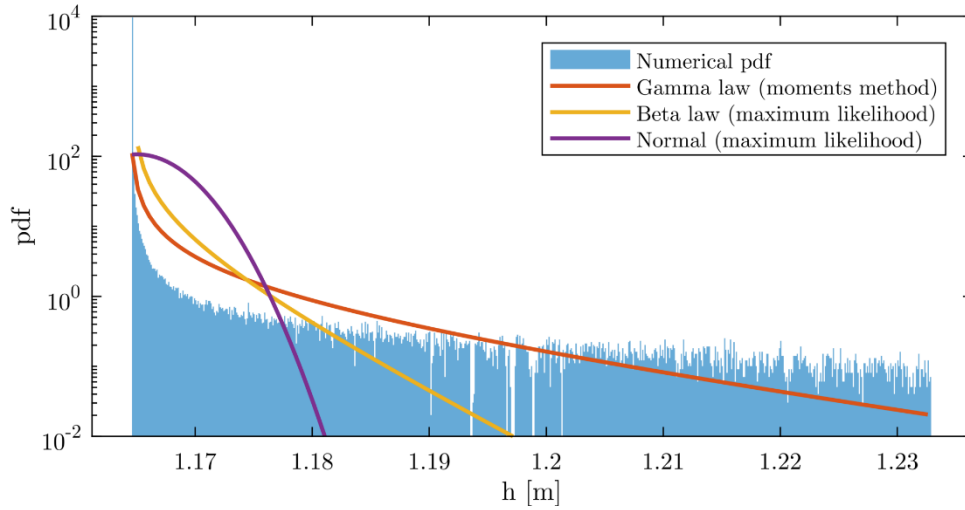


Figure 100: Normalized distribution of upstream water depth compared to the Gamma law fitted with the 3 first statistical moments (test B.1)

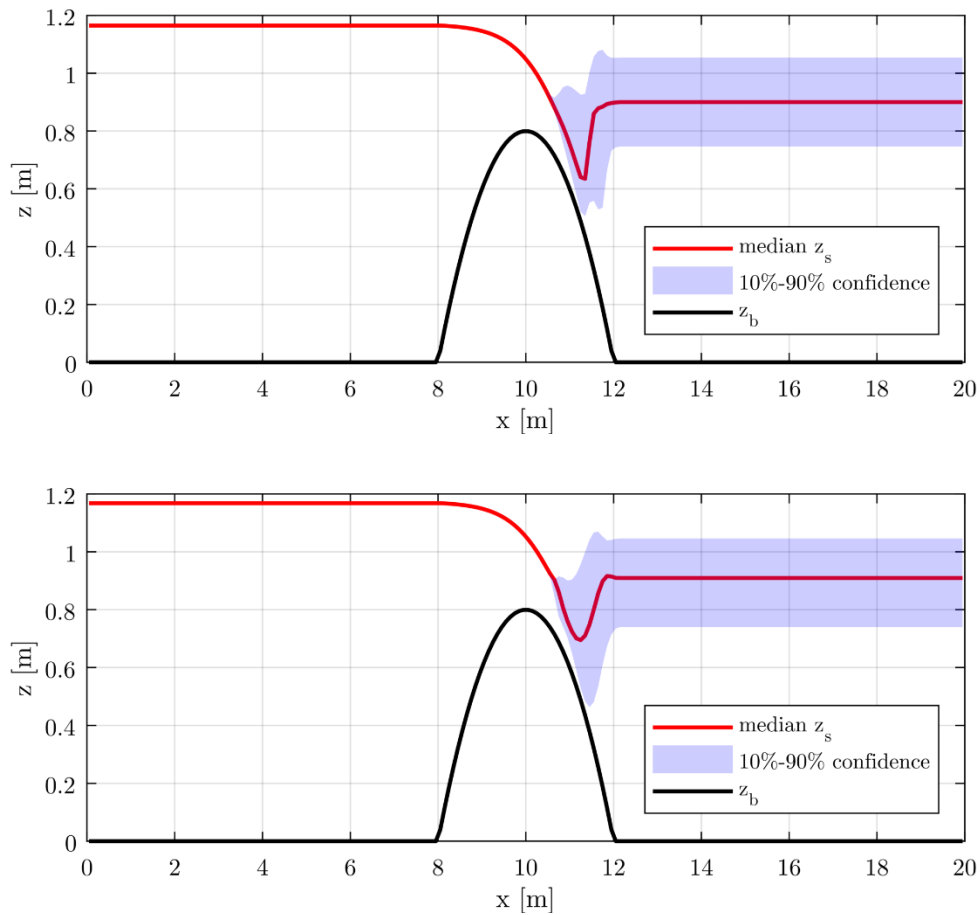


Figure 101: Distributed free surface levels and confidence interval for PMM (upper graph) and Monte-Carlo (1 million points, lower graph) for test B.1

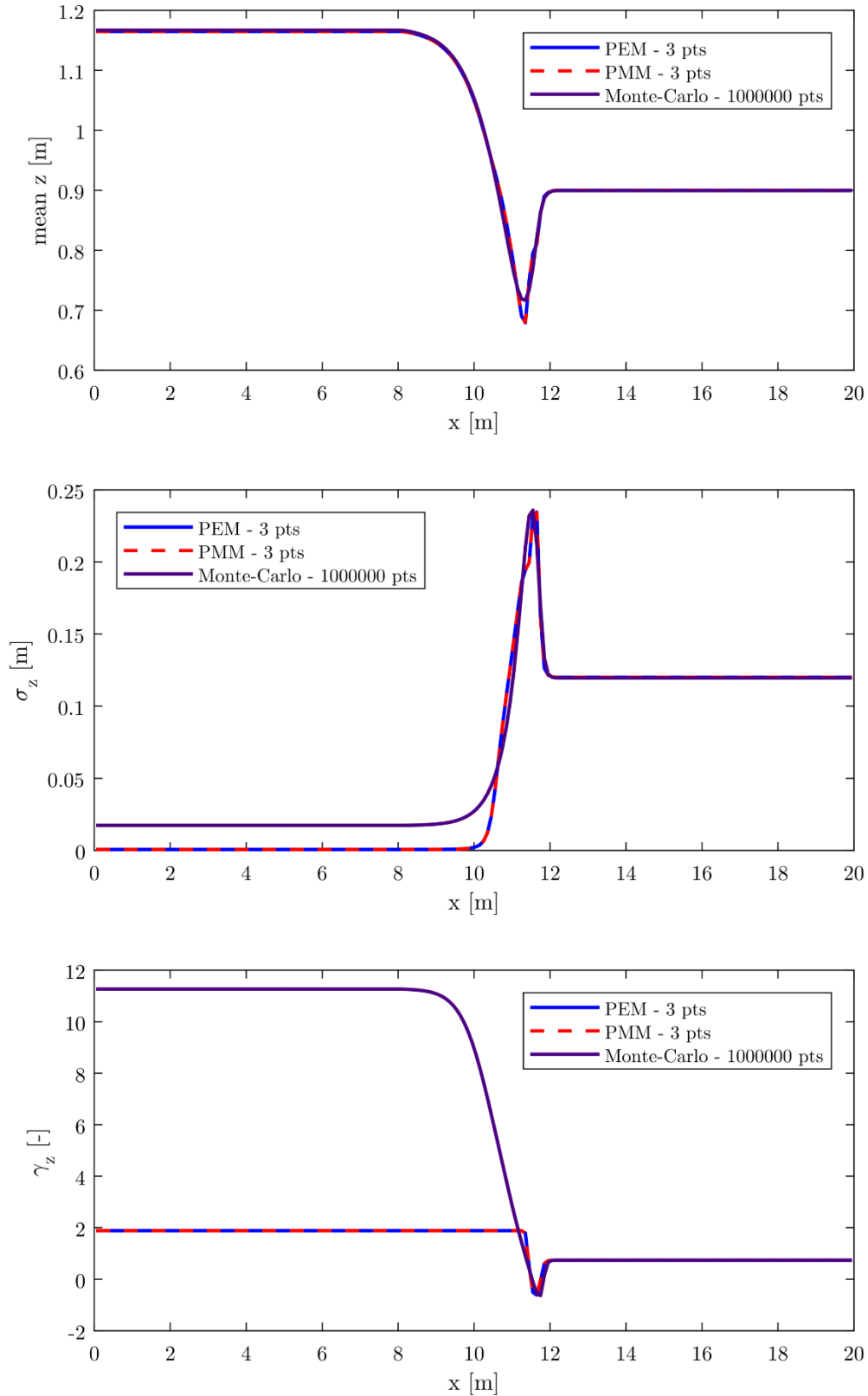


Figure 102: Statistical moments for the free surface level for test B.2

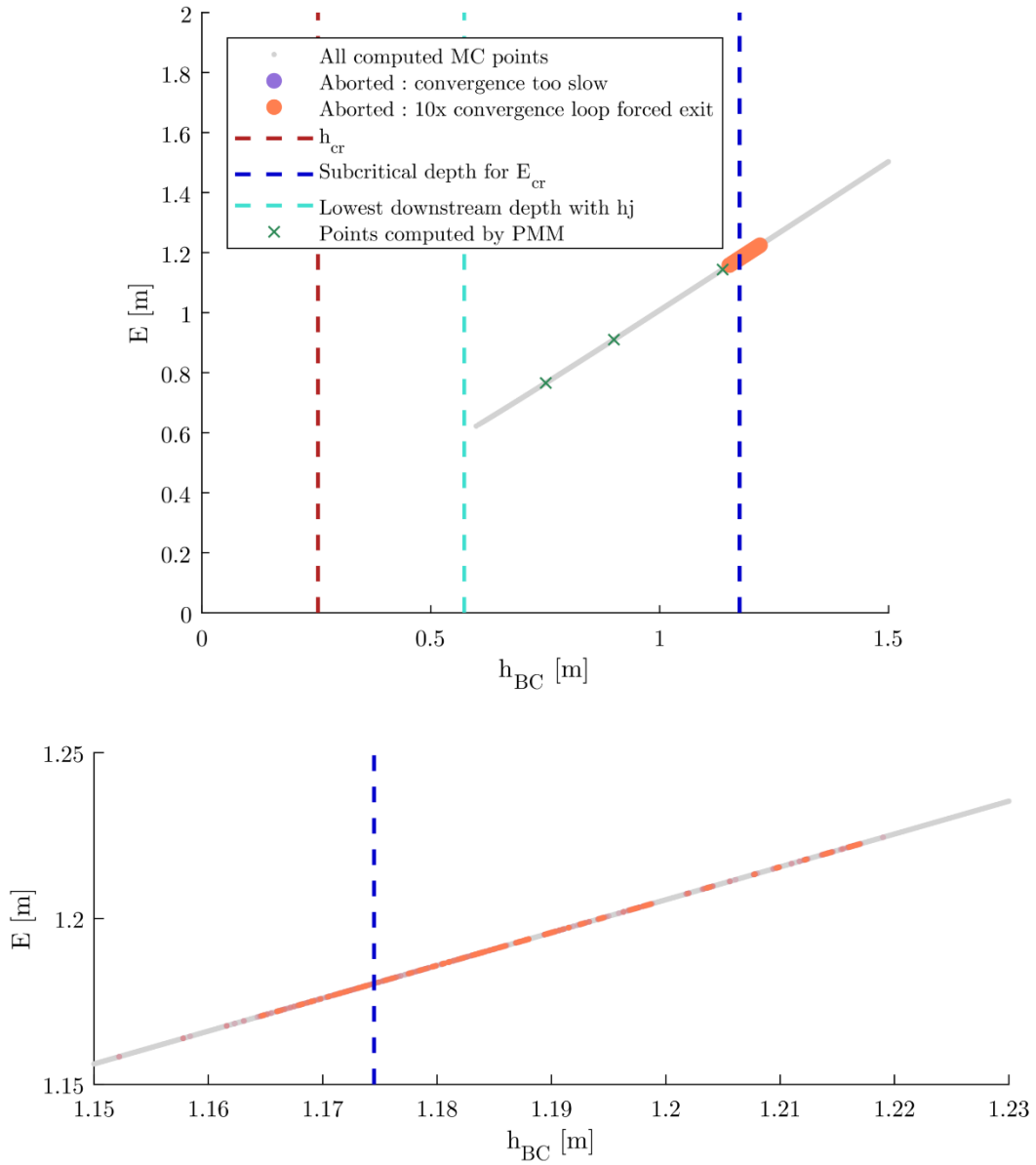


Figure 103: Computed points and unfeasible computation points with remarkable water depths for test B.2

	Out of bounds	Unfeasible	Elapsed time
PEM	0/3	0/3	< 1 s
PMM	0/3	0/3	< 1 s
MC $10^6$ pts	0/1000000	1724/1000000	5 h 12 min

Table 28: Number of unfeasible points and elapsed times for test B.2

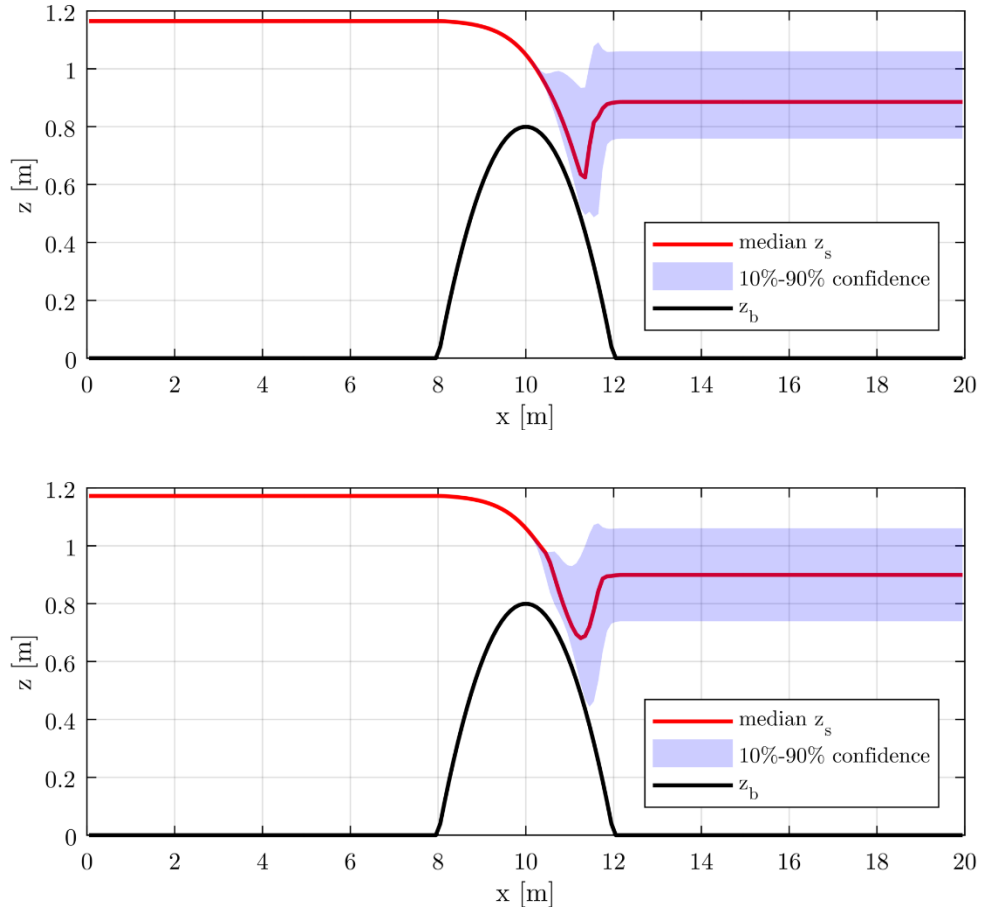


Figure 104: Distributed free surface levels and confidence interval for PMM (upper graph) and Monte-Carlo (1 million points, lower graph) for test B.2

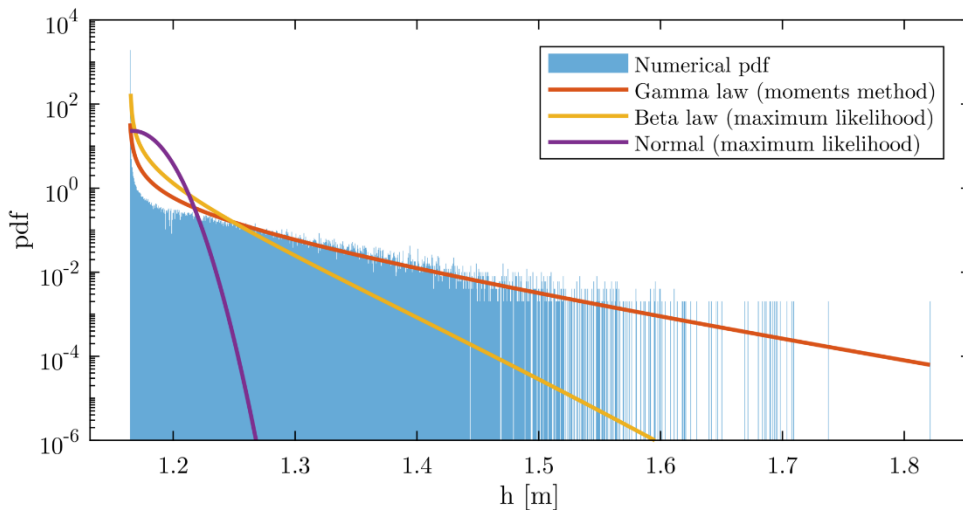


Figure 105: Normalized distribution of upstream water depth compared to the Gamma law fitted with the 3 first statistical moments (test B.2)

#### 4.2.2.4 Summary

After these observations on flows over a bump, it appears that methods with less points (PEM, PMM and SRSM) compete well against the more computing demanding Monte Carlo method. Indeed, even if results diverge slightly in some areas, the overall behavior is well represented with less computationally expensive methods. Since SRSM is the most computationally expensive method amongst time effective methods, PEM and PMM hold our attention for their excellent computation cost/results accuracy ratio. In further developments, PMM is favored against PEM due to its theoretical appealing background and the slightly better results obtained for the skewness coefficient (see test A.2).

### 4.3 Second hydraulic application to a real world example

#### 4.3.1 Case study description

The Haine River is a Scheldt tributary that flows in Belgium and France. A part of it was studied recently in order to precise the flooding hazard of a specific piece of land. This section focuses on the extension of this study for uncertainty characterization.

During the original study (Goffin, Piroton, Dewals, et al. 2016), only a part of the river was studied. It stretches from Boussoit to Obourg, on approximately 7.5 km (Figure 106). The boundaries of the simulation domain are located at gauging stations:

- The upstream boundary is located at Boussoit gauging station (Figure 107) and it is managed by SPW MI (“Service Public de Wallonie Mobilité et Infrastructures”). The gauging station was commissioned in January 1974.
- The downstream boundary condition is located at Obourg gauging station (Figure 108) and it is managed by SPW ARNE (“Service Public de Wallonie Agriculture, Ressources Naturelles et Environnement”). The gauging station was commissioned in august 2012.

These two stations record water depths every hour. From a rating curve established by SPW, it is possible to convert the water depth into discharge data. Given the nature of the flow in the Haine River (subcritical regime), the upstream boundary condition provides a discharge information while the downstream boundary condition imposes a water depth.

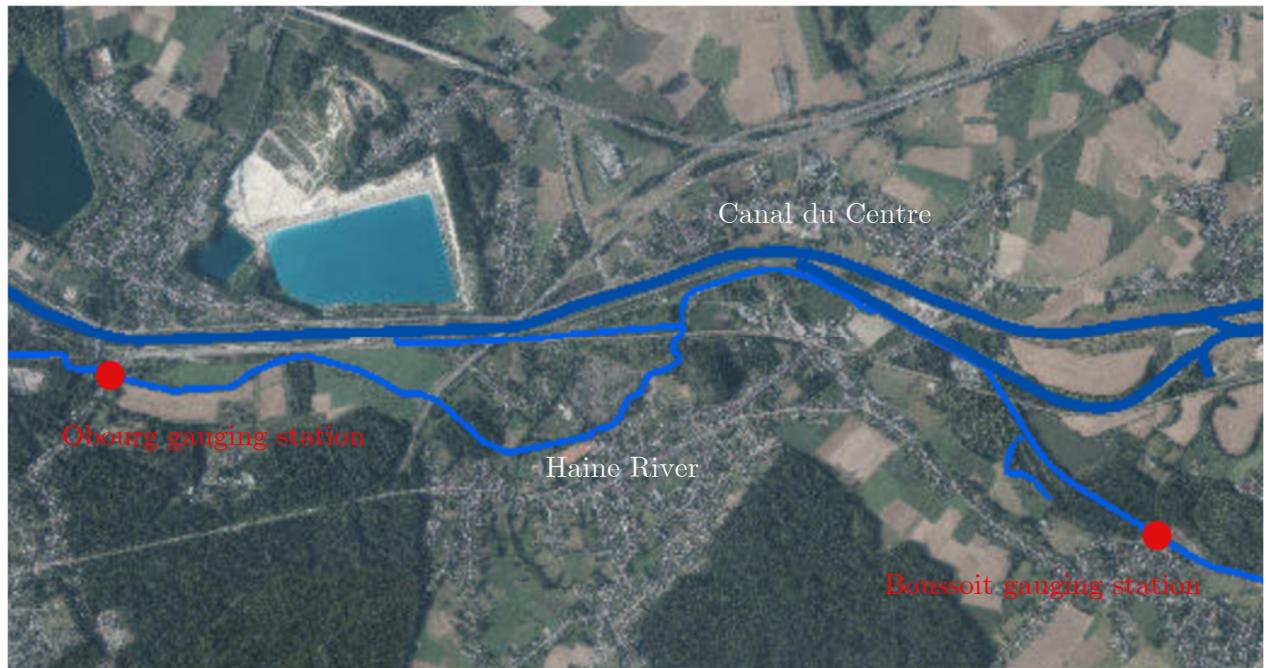


*Figure 106: General view of the Haine River and the location of gauging stations (source: Walonmap)*



*Figure 107: Boussoit gauging station*



Figure 108: Obourg gauging station

The Haine River is modeled using a 1-D approach as developed in chapter 3. The choice of this kind of model can be justified as follows:

- The studied part of the Haine River is highly channelized and the flow occurs mainly in the direction of river axis for the range of discharges in which we are interested.
- The topographic data available does not include distributed elevation data (bathymetry) for the river bed. Instead, we dispose of cross-sections plans from which we are able to deduce  $h - A - \chi$  relationships (water depth – cross-section area – wet perimeter)

The friction losses are modeled using the Manning formula. It links the friction slope  $S_f$  with the velocity of the flow, a friction coefficient (Manning coefficient,  $n$ ) and the hydraulic radius ( $R_h = A / \chi$ ):

$$S_f = \frac{n^2 (Q / A)^2}{R_h^{4/3}} \quad (182)$$

The Manning coefficient is linked to the Strickler coefficient  $K$  as:  $n = 1 / K$ . It is often used to link friction losses to hydraulic properties in a river (Machiels et al. 2011). Since the Manning

coefficient is not based on physical properties of the river bed (e.g. grain sizes), its determination relies only on a fitting process. This is detailed later in this document.

The definition of the topography of the Haine River is based on measured cross sections and planar data. Each of these data were available on paper and were digitalized prior to their use. Cross-sections are processed in order to result in tabular relations which link the water depth to the cross section area and perimeter. The planar information enabled to compute the distance between measured cross sections. Once the topographic data processed, the 1-D discretization of the 7565 m long domain resulted in 1513 nodes (5 m mesh size). This spatial step is chosen according to the structures met along the river: bridges for roads and railways, old structures for weirs, etc. In order to take these structures into account in the computation, a spatial step fine enough is required. Five meters was chosen as a good compromise between representativeness of the cross sections variation and computation cost. Figure 109 illustrates the variation of the cross section at a railway crossing and a weir structure.

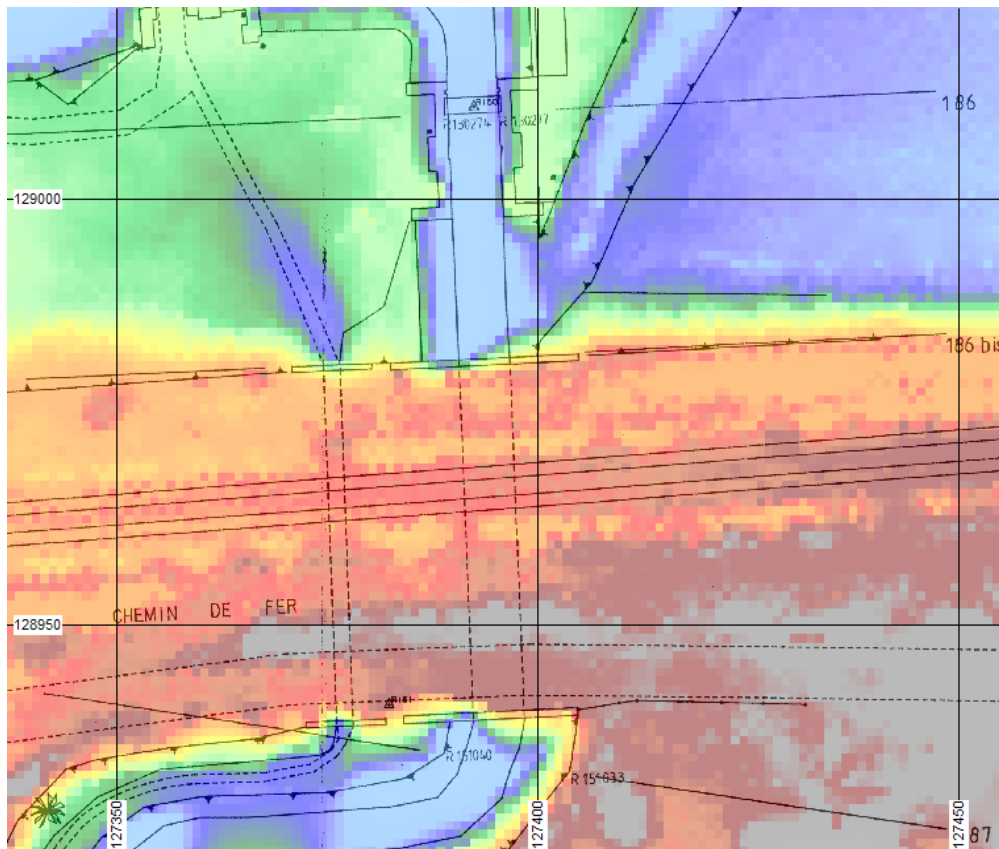


*Figure 109: Illustration of the Haine river cross section variation at an old weir structure and a railway crossing (colors = DEM)*

From common historical data of both gauging stations (02/08/2012 to 31/12/2015), it is possible to extract flood events. These events will be useful to calibrate a roughness coefficient and to assess the additional discharge injected in the river between upstream and downstream

boundary conditions. Four events with a peak discharge higher or equal to  $15 \text{ m}^3/\text{s}$  at the downstream BC were selected (Figure 110).

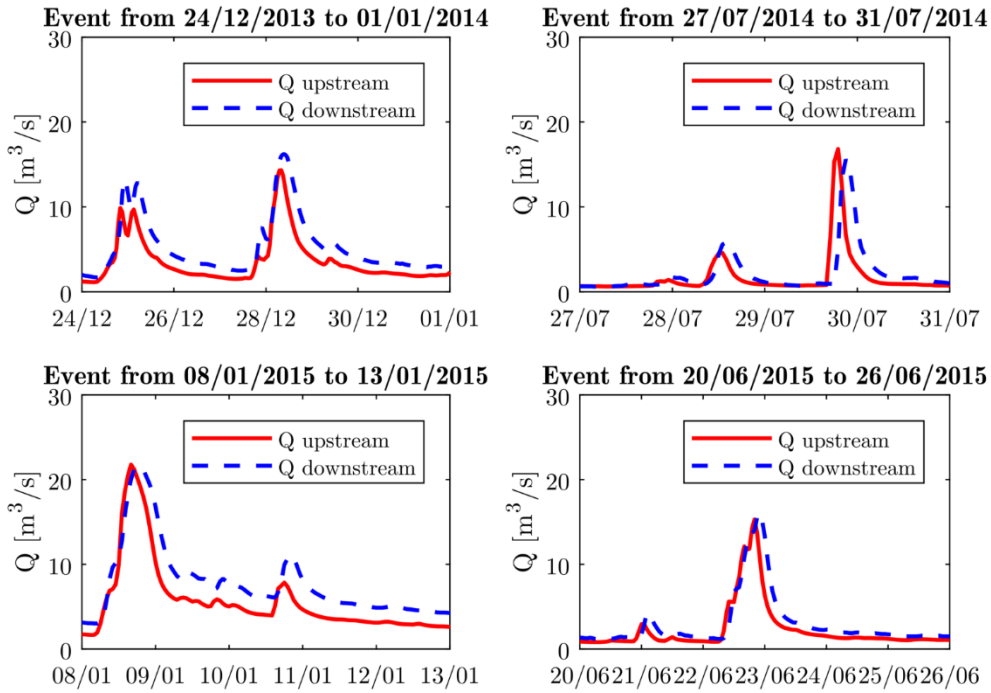


Figure 110: Four selected flood events on the Haine River

A mass balance can be performed on these four events. First, we shift the hydrographs in order to synchronize the peaks. Then we compute the volume of water that flows through the upstream and downstream boundaries. A comparison between these volumes is performed at Figure 111. It appears that some volume is added between the upstream and downstream boundary conditions. The additional discharge ranges between 25 % and 50 % of the upstream discharge for these four events.

In order to refine this approximation, a brief hydrological study was performed. It is based on the Walloon region DEM<sup>10</sup>. First, an in-house HECE algorithm (Archambeau 2006; Bruwier 2017) agglomerates meshes with a spatial discretization of  $100 \times 100 \text{ m}^2$ . Then, this new DEM is corrected in order to ensure the consistency of the slopes (and avoid “holes” in the middle of the DEM). Finally, the area of drained watersheds is computed thanks to a flow accumulation technique. The results are given in Figure 112. Three main intermediate injection points can be identified. These injection points can also be identified in the plans (Table 29).

<sup>10</sup> <http://geoportail.wallonie.be/catalogue/6029e738-f828-438b-b10a-85e67f77af92.html>

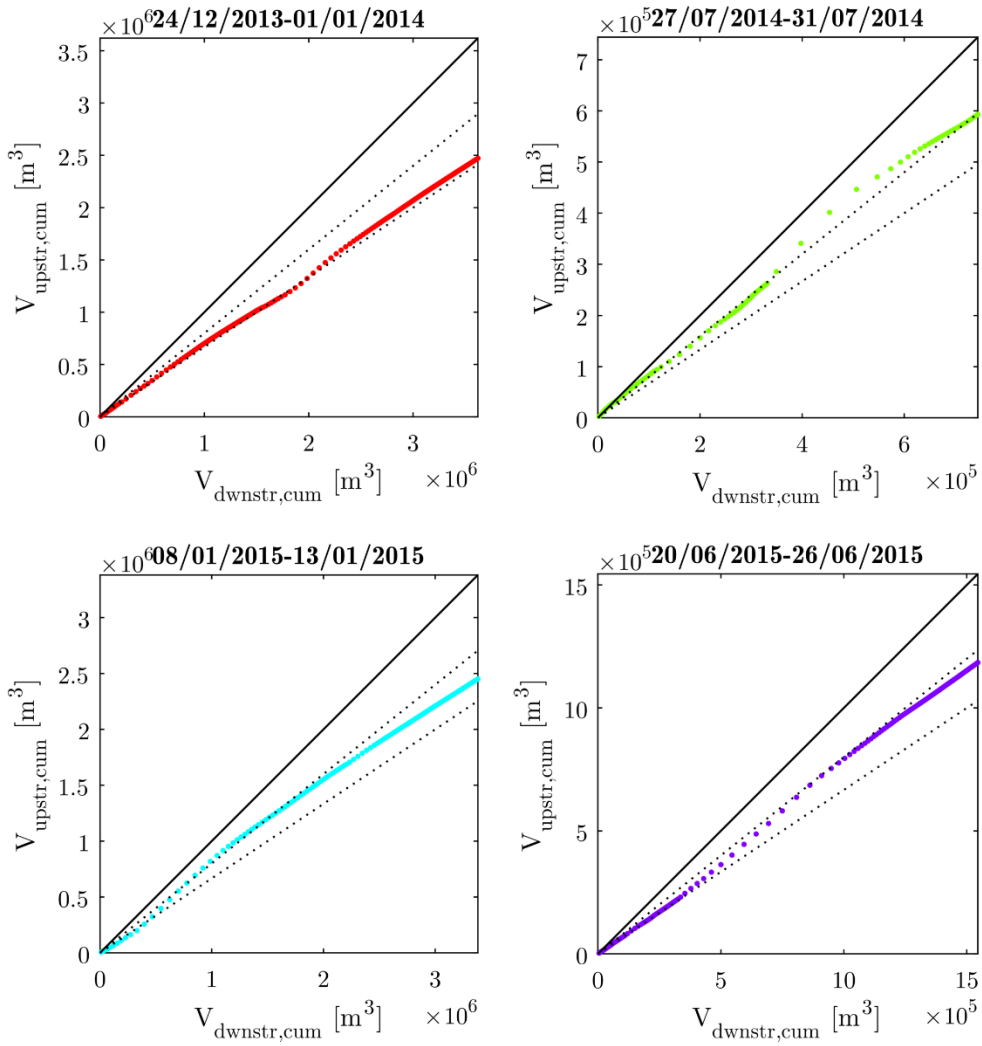


Figure 111: Comparison between upstream and downstream volumes (plain line = 1:1 ratio, dotted lines = 1:1.25 to 1.5 ratios)

Based on the area of the watershed at the upstream and downstream boundary conditions, and considering uniformly distributed rains, the ratio between downstream and upstream discharges should be equal to:

$$\frac{S_{WS,dwnstr}}{S_{WS,upstr}} = \frac{241\text{km}^2}{170\text{km}^2} = 1.42 \quad (183)$$

Since the value computed in (183) relies on two heavy assumptions, uniformly distributed rains and a uniform runoff coefficient, and based on the observations in Figure 111, it is decided to set the additional discharge at 40 % of the upstream discharge. The ratios related to intermediate injection points are given in Table 29.

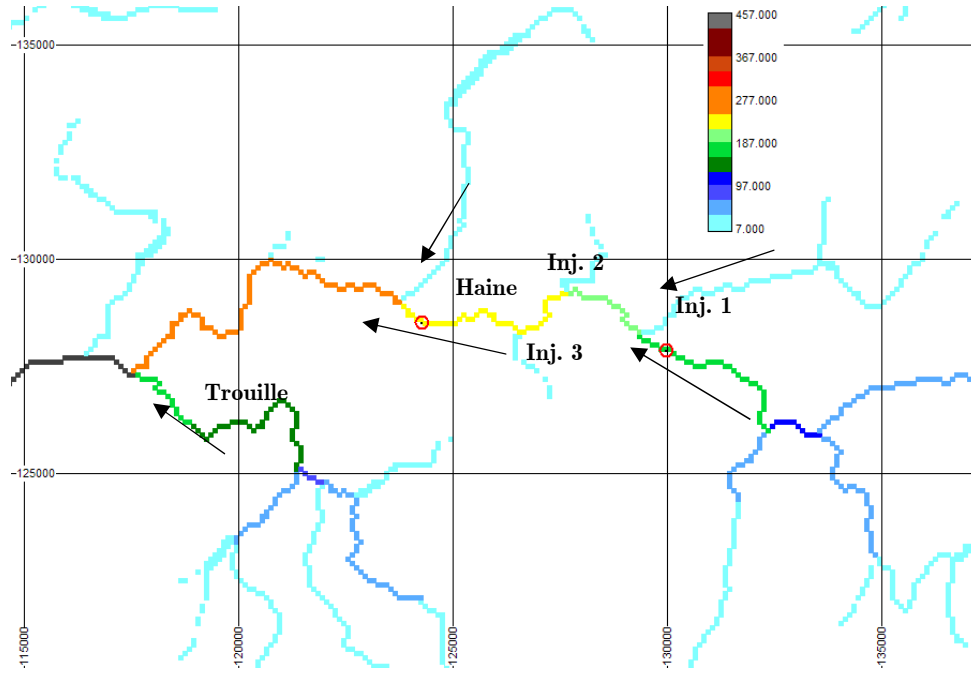


Figure 112: Watershed areas [km<sup>2</sup>] close to the two gauging stations used as boundary conditions (red dots)

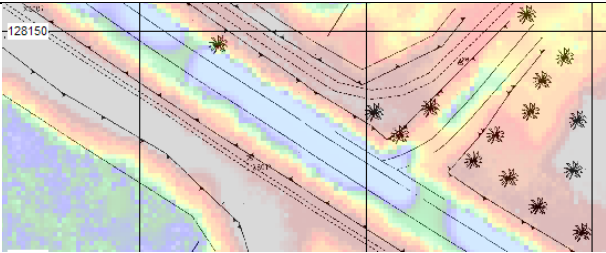
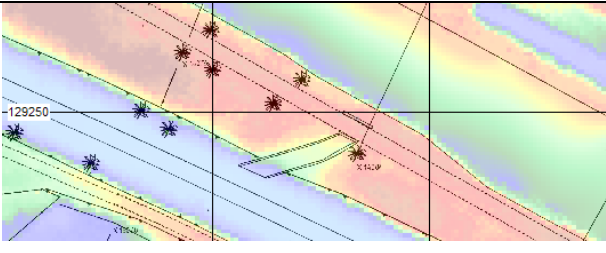
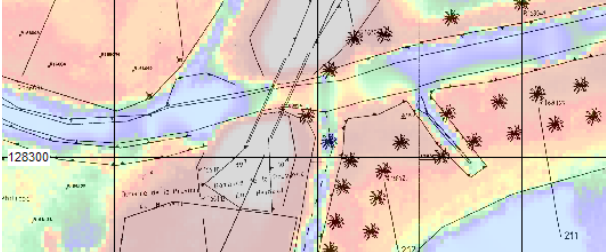
	Position	Add. area	Injection ratio
<b>Injection 1</b>		36.27 km <sup>2</sup>	0.257
<b>Injection 2</b>		11.37 km <sup>2</sup>	0.080
<b>Injection 3</b>		8.88 km <sup>2</sup>	0.063

Table 29: Additional discharge injection points

Given these intermediate discharge injections, a roughness coefficient can be calibrated. As stated later, the roughness coefficient is not considered as uncertain which allows us to calibrate it without taking into account the uncertainty on the discharge and downstream boundary condition for instance.

Due to the lack of distributed historical data along the river reach, the calibration of the roughness coefficient could not be performed on steady state flows. Thus, the roughness coefficient is fitted on the four reference events presented in Figure 110. These events are chosen due to the presence of high discharge values, which are suitable to enhance friction effects. For each of these events, the downstream hydrograph, the upstream water level evolution and the upstream water level – discharge couples are used as a comparison basis for various techniques. The reference data are the measurements at SPW gauging stations.

In order to assess the goodness-of-fit of the computed time evolutions of the downstream discharge and the upstream water level, two indicators are used: the Nash-Sutcliffe efficiency (NSE) coefficient (Jain & Sudheer 2008; Nash & Sutcliffe 1970) and the coefficient of determination  $R^2$  (Legates & McCabe Jr. 1999). Concerning the comparison between reference and computed water level – discharge couples at the upstream gauging station, the Hausdorff distance is used (Birsan & Tiba 2005).

The NSE is expressed as

$$NSE = 1 - \frac{\sum_{i=1}^N (y_{i,c} - y_i)^2}{\sum_{i=1}^N (y_m - y_i)^2} \quad (184)$$

with  $y_i$  the reference value,  $y_{i,c}$  the computed value with the model,  $y_m$  the mean of the reference values and  $N$  the number of discrete points. This factor ranges from  $-\infty$  to 1.  $NSE = 1$  means that computed values fit perfectly the reference.  $NSE = 0$  means that the model can only predict the mean. Equation (184) can be adapted in order to assess the goodness of fit of hydrographs (replace  $y$  with  $Q$ ) and of the time evolution of the water level (replace  $y$  with  $z$ ).

The coefficient of determination  $R^2$  expresses the proportion of the variance that the model is able to represent:

$$R^2 = \frac{\left( \sum_{i=1}^N (y_i - y_m)(y_{i,c} - y_{c,m}) \right)^2}{\sum_{i=1}^N (y_i - y_m)^2 \sum_{i=1}^N (y_{i,c} - y_{c,m})^2} \quad (185)$$

$y_{c,m}$  is the mean of the values computed by the model.  $R^2$  values range from 0 to 1, higher values represent better agreement.

The Hausdorff distance measures the distance between two subsets of points. This method is used mainly in the image-processing domain. For example it allows to recognize a shape in a picture (Huttenlocher et al. 1993). The Hausdorff distance  $d_H$  between two subsets  $X$  and  $Y$  is:

$$d_H(X, Y) = \max \left( \max_{x \in X} \left( \min_{y \in Y} d(x, y) \right), \max_{y \in Y} \left( \min_{x \in X} d(x, y) \right) \right) \quad (186)$$

where  $d(x, y)$  is the Euclidian distance between two points  $x$  and  $y$  from subsets  $X$  and  $Y$  respectively. Formula (186) can be understood as follows:

Let  $X$  and  $Y$  be two subsets of points. For each subset, we compute the minimal distance of each point with the other subset. We take the greatest one. Then, the Hausdorff distance is the maximal value of the two previously computed values. This is illustrated in Figure 113.

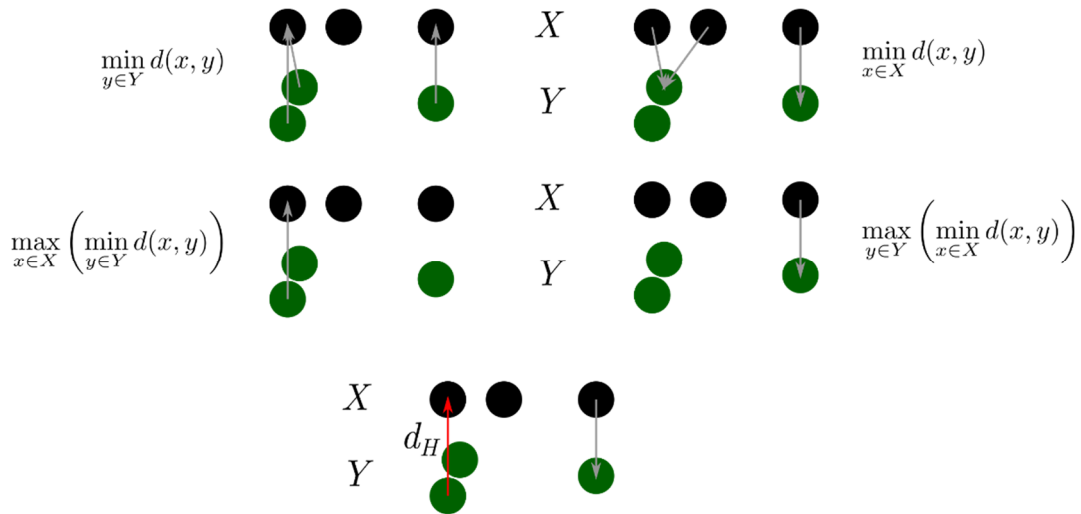


Figure 113: Principle of the Hausdorff distance

Unlike previous indicators, the Hausdorff distance is applied to the comparison of clouds of points. It does not own a maximal limit and its minimal value is 0:  $d_H \in [0; +\infty[$ . Two subsets are considered identical when  $d_H = 0$ . A comparison between the indicators introduced in this section is given in Table 30.

Indicator	Possible values	Perfect fit at	Comments
NSE	$] -\infty; 1]$	1	Initially developed for the comparison of hydrographs
R <sup>2</sup>	$[0; 1]$	1	General purpose indicator
Hausdorff distance	$[0; +\infty[$	0	Compares two sets of points, best suited for scatters

Table 30: Comparison between the three proposed goodness-of-fit indicators

Eleven values of the Strickler coefficient are tested. They range from  $K = 25 \text{ m}^{1/3}\text{s}^{-1}$  to  $K = 35 \text{ m}^{1/3}\text{s}^{-1}$ . These preliminary values are chosen considering the nature of the Haine River which is channelized but shows proofs of lack of cleaning and abundant vegetation on the banks. For this reach of the river, banks are mainly made of concrete and a visual inspection does not reveal large roughness patterns on the bed. For this category of rivers, based on an expert judgment, the Strickler coefficient often varies between 25 and  $35 \text{ m}^{1/3}\text{s}^{-1}$ . These values are tested for the four events presented earlier. The indicators of each event is weighted with 0.25 in order to obtain global indicators.

For each event and each tested value of the Strickler coefficient, the NSE and R<sup>2</sup> indicators are computed for the downstream hydrograph and the time evolution of the upstream water level. Results can be observed in Figure 114. The Hausdorff distance for the discharge – water level points at the upstream station are computed for each of the four selected events. Results are given in Figure 115.

From these figures, it appears that lower values of the Strickler coefficient are better. Overall,  $K = 26 \text{ m}^{1/3}\text{s}^{-1}$  produces best indicators.

Observing the hydraulic results for  $K = 26 \text{ m}^{1/3}\text{s}^{-1}$  allows to strengthen the previous conclusion. For the downstream hydrographs (Figure 116), the computed result is well synchronized on the reference hydrograph. Computed peak values are lower than reference peaks values while base flow discharges are well reproduced. Other tested roughness coefficients could not overcome this difference, which may be due to errors inherent to the downstream rating curve.

The highest upstream water levels computed (Figure 117) match well the reference data. Differences can be observed for lower discharges. This is due to the poor maintenance of the river (Figure 119, abundant vegetation on the river banks, debris in the river bed and observed landslide locally), which is not represented in the numerical model. This poor maintenance creates additional losses that lower Strickler coefficients are able to produce.

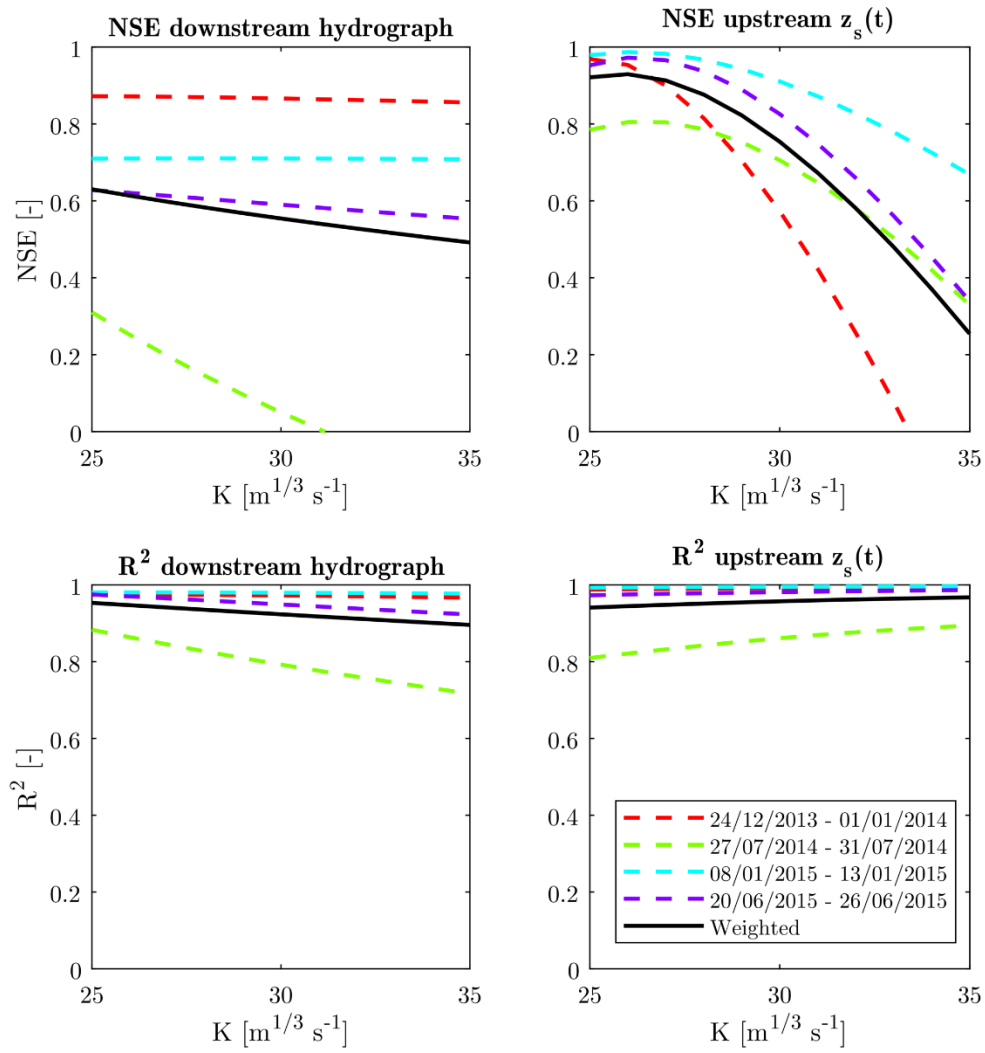


Figure 114: NSE and  $R^2$  indicators for the downstream hydrograph and the upstream evolution of the water level

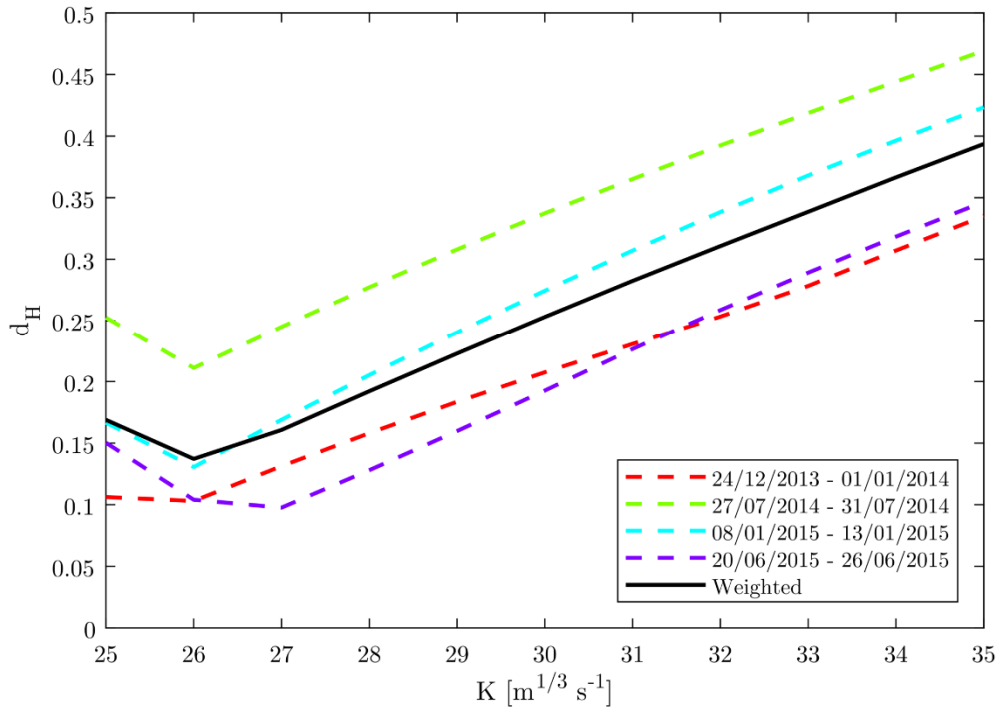


Figure 115: Hausdorff distance for the discharge – water level points at the upstream gauging station

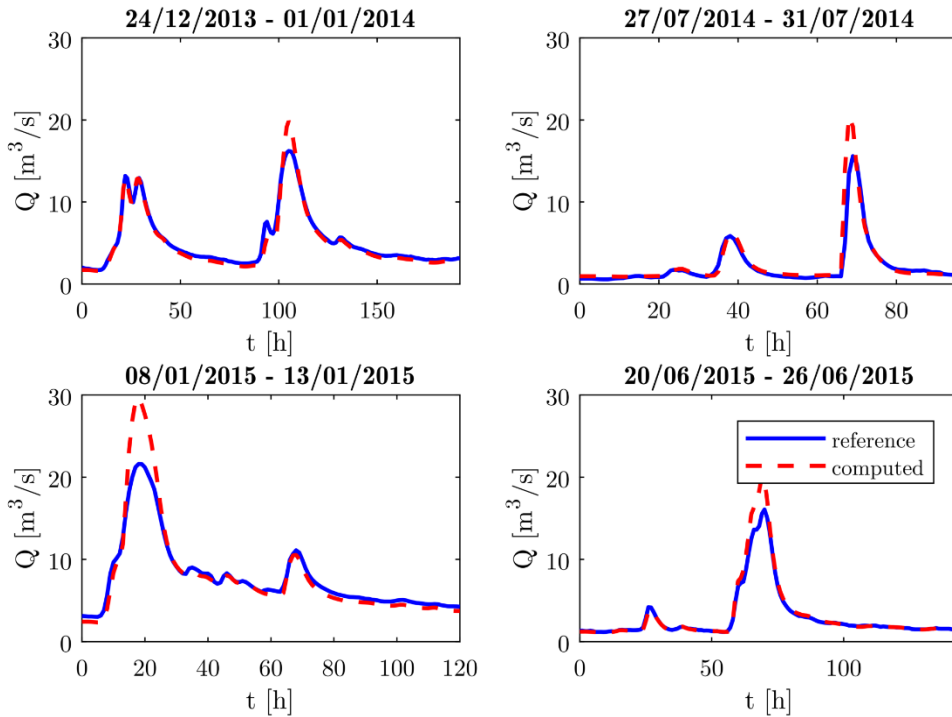


Figure 116: Downstream hydrographs for  $K = 26 \text{ m}^{1/3} \text{ s}^{-1}$

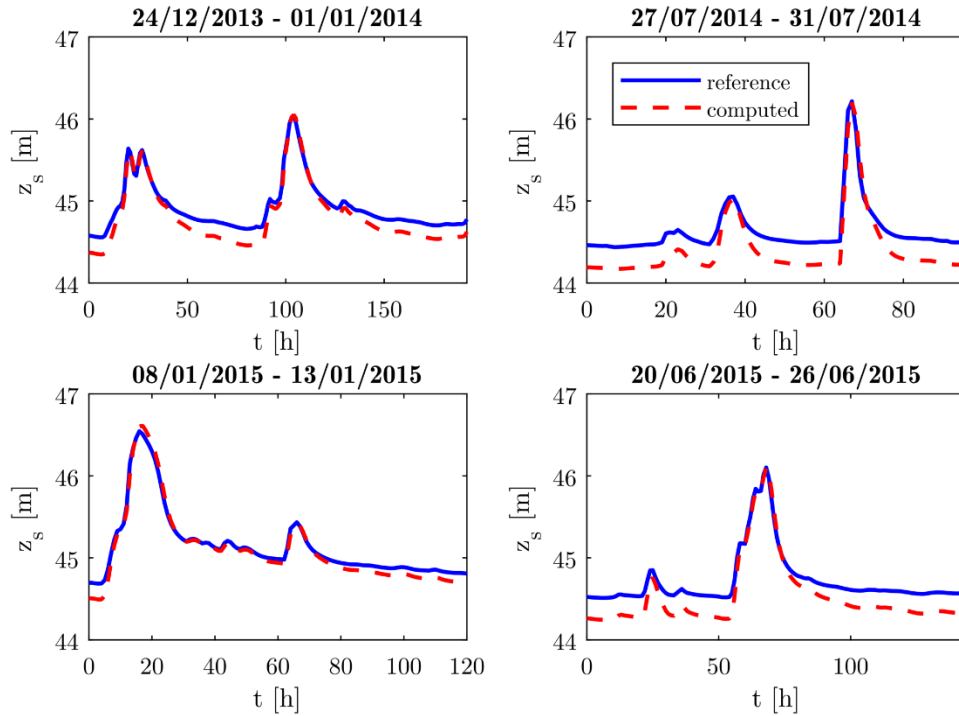


Figure 117: Upstream evolutions of the water level for  $K = 26 \text{ m}^{1/3} \text{ s}^{-1}$

A similar observation can be done for the discharge – water levels points (Figure 118). Values match well for higher discharges but differences are observed for lower discharges. A hysteresis is also present for the results produced by the numerical model. This hysteresis pattern does not appear in the reference data since they are based on a rating curve.

Differences between the model and the reference at lower discharges are not really problematic since the goal of the study is to predict water levels at high discharges. For this study, as explained later, the typical values of the upstream discharge will be higher than  $15 \text{ m}^3/\text{s}$ . For this range of discharges, the maintenance issues are not predominant.

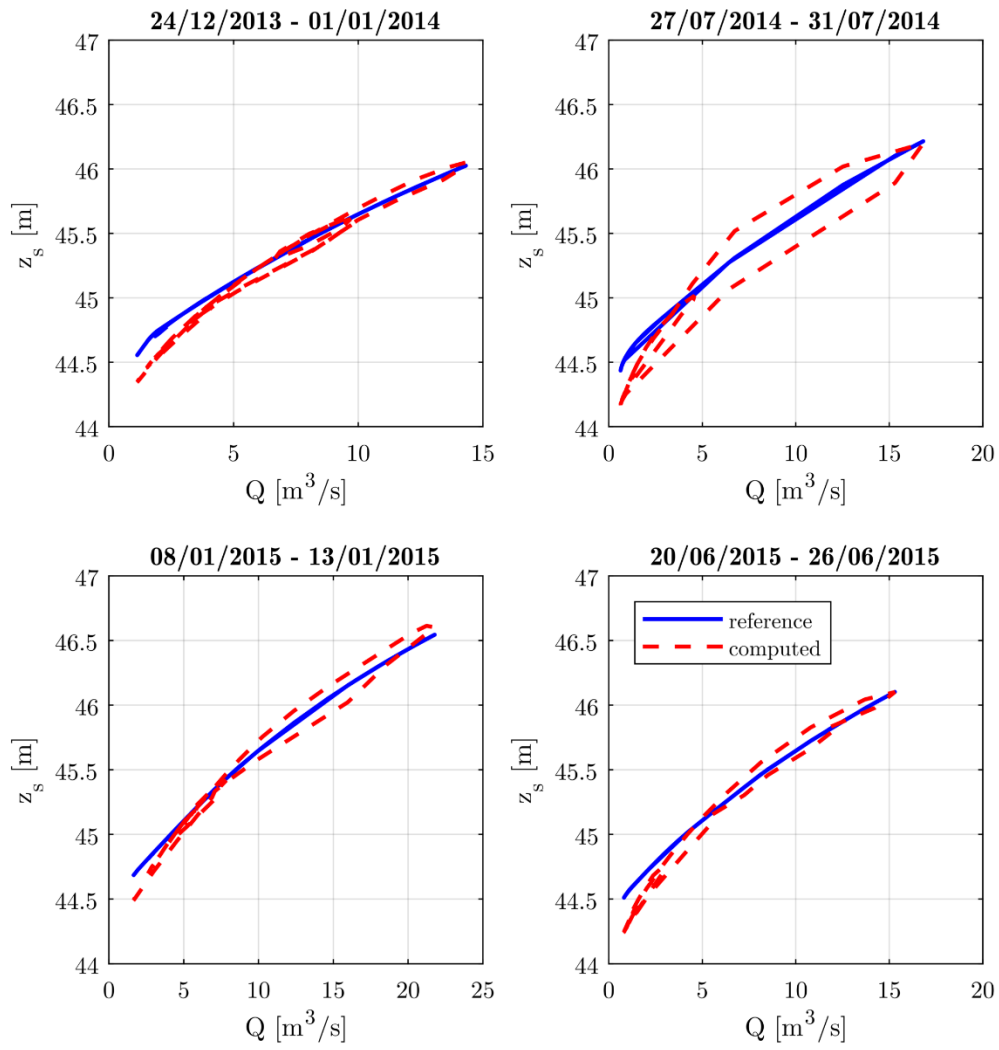


Figure 118: Upstream discharge – water level points for  $K = 26 \text{ m}^{1/3} \text{ s}^{-1}$



Figure 119: Lack of maintenance in the river bed

### 4.3.2 Uncertainty sources

As stated earlier, an uncertainty analysis is performed for some uncertain variables only. The uncertainty outcome should be understood as the uncertainty in the model output related to some given uncertain inputs. For the Haine River, we chose to focus our uncertainty analysis on two epistemic sources: the uncertainty on the discharge value for a given return period and the rating curve calibration. Other variables that could be considered as uncertain are given fixed values in this study. This includes the calibration of the roughness coefficient that is done for the mean value (undisturbed value) of the input discharge and for the mean value of the rating curve. The reader's attention is drawn to the fact that the additional discharge injected in the river is not considered as uncertain in this study. It is also considered as independent from the uncertainty of the upstream discharge. The coefficients in Table 29 are applied for the mean upstream discharge and the resulting injection discharge are kept constant for an upstream discharge at a given return period.

#### 4.3.2.1 Uncertainty on the upstream discharge

The upstream discharge at a given return period is submitted to uncertainty due to the limited number of observations of the discharge. Indeed, the discharge data at the Boussoit gauging station is available from January 1974 to December 2014. Since a hydrological year accounts from October 1 to September 30, 40 annual maximum discharges are available. Thanks to a visual analysis, it appears that a lognormal law, which is the one used by SPW, is relevant to represent the distribution of annual maximum values (Figure 120). From a lognormal law, it is possible to compute a discharge at a given return period. A bootstrap analysis is performed on this basis in order to compute mean values and standard deviations of a discharge at a given return period. For the bootstrap analysis,  $10^6$  draws are performed and the lognormal law is fitted thanks to a maximum-likelihood method provided by the *fitdistr* function in R (R-Core-Team 2019). For instance, we obtain following values for 5-year and 50-year return periods ( $T$ ):

$$\text{For } T = 5 \text{ years: } F = 1 - 1/5 = 0.8 \quad \bar{Q}_5 = 19.48 \text{ m}^3/\text{s} \quad \sigma_{Q_5} = 1.1 \text{ m}^3/\text{s}$$

$$\text{For } T = 50 \text{ years: } F = 1 - 1/50 = 0.98 \quad \bar{Q}_{50} = 28.55 \text{ m}^3/\text{s} \quad \sigma_{Q_{50}} = 2.4 \text{ m}^3/\text{s}$$

The uncertainty on the discharge at a given return period is considered as normally distributed. This was verified visually on the bootstrap result obtained with the R software.

For comparison purposes, the 50-year return period values documented by SPW are the following ones (differences come from the different observation periods (1974-2011 for SPW)):

For  $T = 50$  years:  $F = 1 - 1 / 50 = 0.98$   $\bar{Q}_{50} = 29.8 \text{ m}^3/\text{s}$   $\sigma_{Q_{50}} = 3.06 \text{ m}^3/\text{s}$

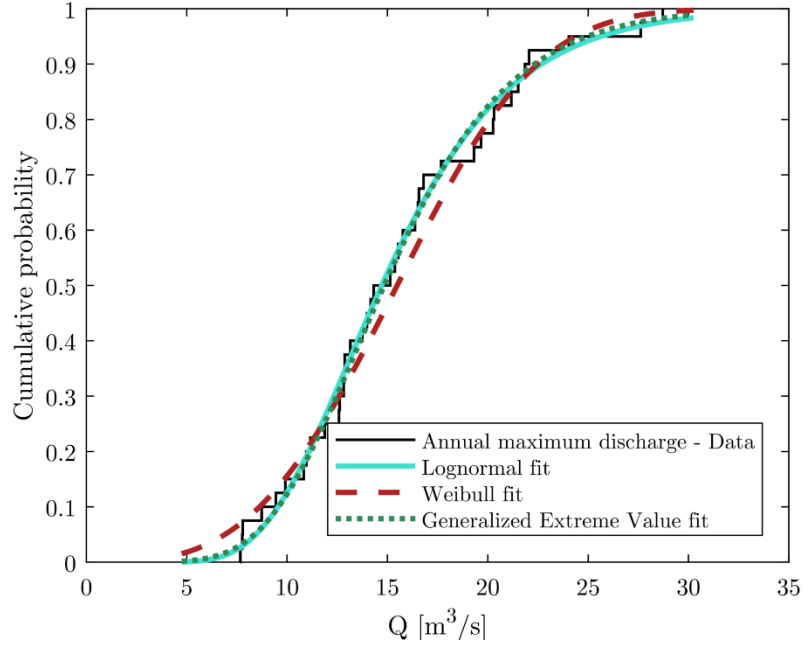


Figure 120: Visual comparison between the empirical cumulative density function for annual maximum discharges and a fit of a lognormal distribution

#### 4.3.2.2 Uncertainty on the downstream rating curve

The downstream boundary condition for this case is a water depth. The water depth to impose for a given discharge is computed from a rating curve. At the downstream gauging station, the SPW calibrated from measurement data a rating curve that is a second order polynomial:

$$Q = ah^2 + bh + c$$

$$\text{with } \begin{cases} a = 0.2911 \\ b = 7.5024 \\ c = -1.5569 \end{cases} \quad (187)$$

The data and the SPW rating curve is depicted in Figure 121 (SPW curve). For the uncertainty analysis and due to the physical reasons explained earlier, power law (120) is used. First, this law is calibrated against field measurements using a least-square fitting:

$$Q = \alpha(h + \gamma)^\beta$$

$$\text{with } \begin{cases} \alpha = 8.622 \\ \beta = 1.1255 \\ \gamma = -0.1889 \end{cases} \quad (188)$$

It is depicted in Figure 121 (Goffin curve). In order to compare SPW rating curve (187) and our curve (188), the root mean squared error (RMSE) is computed for each:

- For SPW curve:  $RMSE = 4.4275 \cdot 10^{-2} \text{ m}^3/\text{s}$
- For Goffin curve:  $RMSE = 3.1105 \cdot 10^{-2} \text{ m}^3/\text{s}$ .

From these numbers and Figure 121, it appears clearly that the rating curve is subject to epistemic uncertainties.

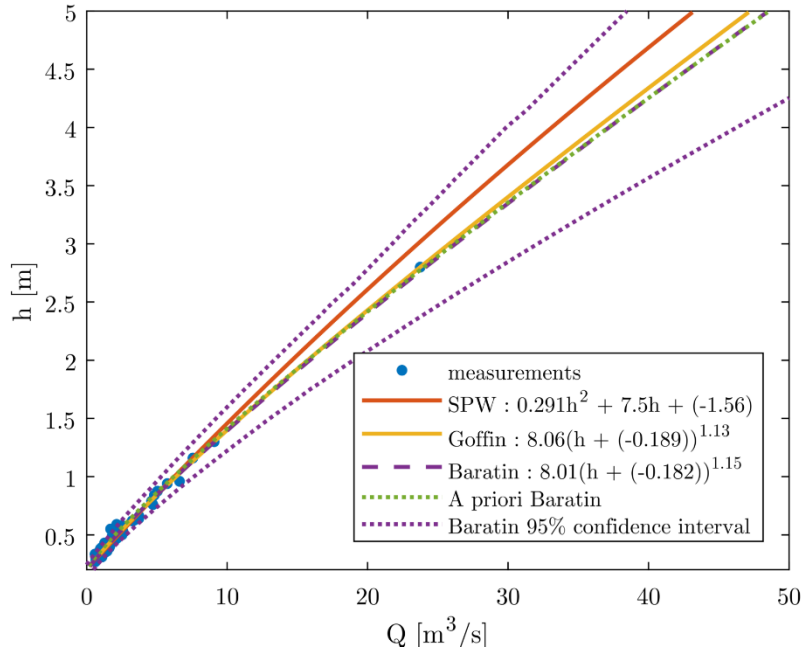


Figure 121: Gauging points and rating curves from the SPW, a power law least square fitting (Goffin) and Baratin

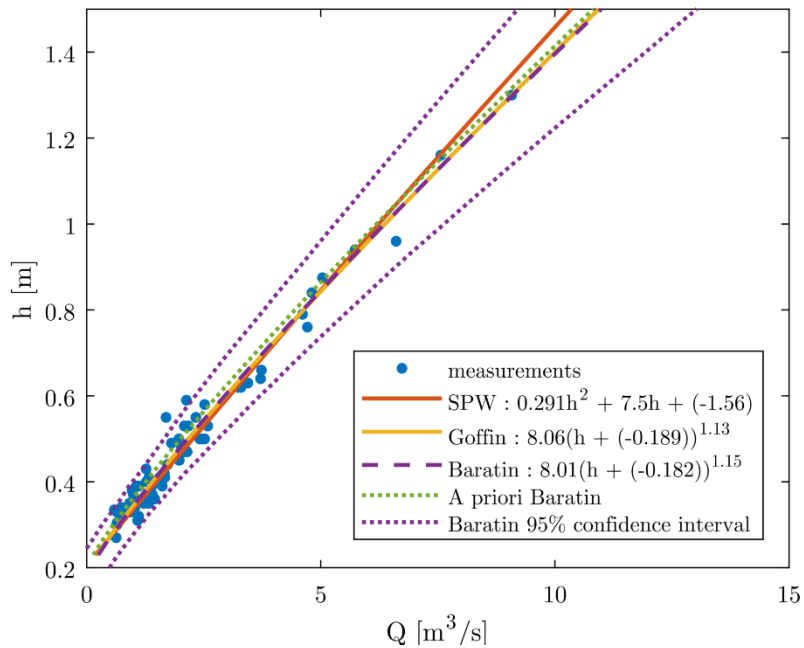


Figure 122: Zoom on lower discharges for fitted rating curves and measurement points

In order to characterize the uncertainty on the rating curve, the Baratin method and the Baratinage software are used. They are introduced in section 2.6.

Due to the lack of information about the control section that drives the behavior a the rating curve at the downstream boundary condition, it is decided to give a priori values for the coefficients of the power law close to the one fitted in (188). We also specify large uncertainties in order to allow Baratin to test other possibilities. We are aware that this method is not optimal and that Baratin authors recommend to use physically based a priori values (Le Coz et al. 2014; Le Coz et al. 2013). A priori coefficients and their associated extended uncertainty (1.96 times the standard deviation) provided to Baratin are:

$$\begin{cases} \bar{\alpha}_{ap} = 8 & u_{\alpha_{ap}} = 10 \\ \bar{\beta}_{ap} = 1.15 & u_{\beta_{ap}} = 5 \\ \bar{\gamma}_{ap} = -0.2 & u_{\gamma_{ap}} = 1 \end{cases} \quad (189)$$

The rating curve that corresponds to these coefficients is given in Figure 121.

The gauging points are imported into Baratinage without defining any measurement error since this is unknown. The remaining error is considered linear as suggested by Mansanarez et al. (2016). After computation in Baratinage, we can extract a set of rating curves from the result files. From this, we can compute mean values of the coefficients:

$$\begin{pmatrix} \bar{\alpha} \\ \bar{\beta} \\ \bar{\gamma} \end{pmatrix} = \begin{pmatrix} 8,005 \\ 1,146 \\ -0,182 \end{pmatrix} \quad (190)$$

and a covariance matrix:

$$\Sigma = \begin{pmatrix} 0.080107 & -0.0055129 & -0.0036295 \\ -0.0055129 & 0.0035531 & 0.001122 \\ -0.0036295 & 0.001122 & 0.00041913 \end{pmatrix} \quad (191)$$

The curve resulting from the mean values of the coefficient is given in Figure 121. The 95% confidence interval provided by Baratin is also plotted in this figure. It appears that this confidence interval encloses almost all measurement points.

The coefficients of the power law appear to be correlated since non-diagonal terms of the covariance matrix (191) are not nil. This can be noticed as well in Figure 123 where the dependence between these uncertain variables is reported. The dependency is particularly marked between  $\alpha$  and  $\gamma$ .

In the uncertainty analysis performed later, the uncertainty on the coefficients is considered normally distributed. A visual inspection of the distributions of the coefficients legitimates this assumption (Figure 124).

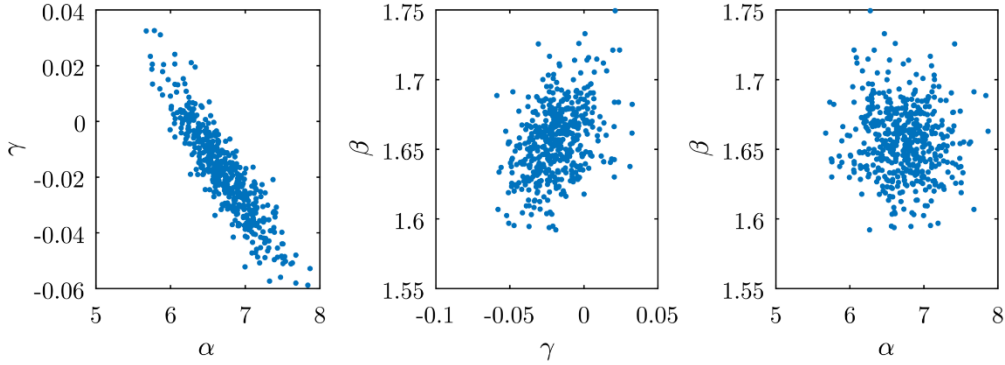


Figure 123: Dependence between the coefficients of the power law

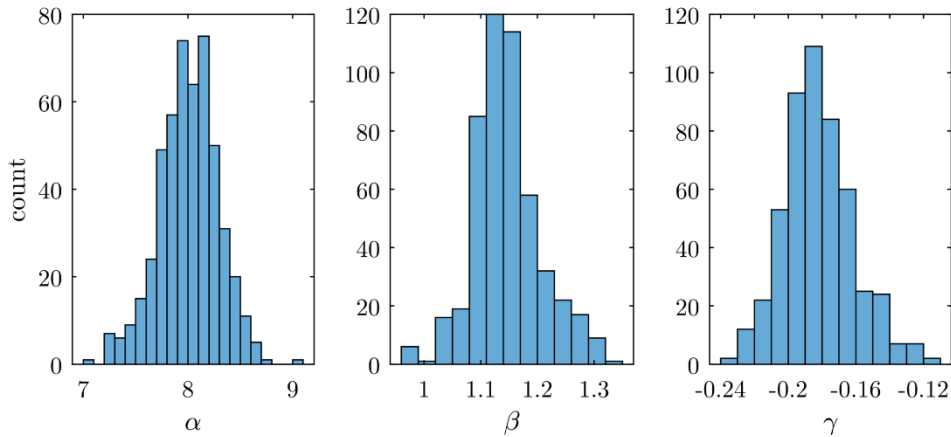


Figure 124: Distribution of the rating curve coefficients that result from Baratin

In order to check if the order of magnitude of uncertainty linked to the rating curve fitting is relevant, a bootstrap method is used. This method is inspired from the computation of a confidence interval for a return period discharge. This method can be interpreted as follows: “what would be the rating curve if some gauging points were not measured or some with a higher occurrence frequency?”

The bootstrap method consists in picking randomly  $N$  measurement points from the  $N$  available points. In this case, 500 picking processes are performed. For each of the 500 sets of measurement points, a power law (120) is fitted using a least squares method. Then, statistical moments can be computed for  $\alpha$ ,  $\beta$  and  $\gamma$ .

Moreover, for discrete values of the water depth  $h$ , the corresponding 500 discharges are computed from the power law. From these 500 discharges, a gamma law is fitted using a

maximum likelihood method<sup>11</sup>. A 95 % confidence interval is computed based on the analytical distribution fitted. The 500 rating curves computed with the bootstrap method, the Baratin results and the bootstrap 95 % confidence interval is plotted in Figure 125.

From Figure 125, we can notice that the results obtained from Baratin and the bootstrap method produce similar values. The confidence interval also have similar spans. From this observation, we conclude that the uncertainty on the rating curve provided by the alternative bootstrap method (which is easily scriptable) is relevant compared to the results obtained with Baratin.

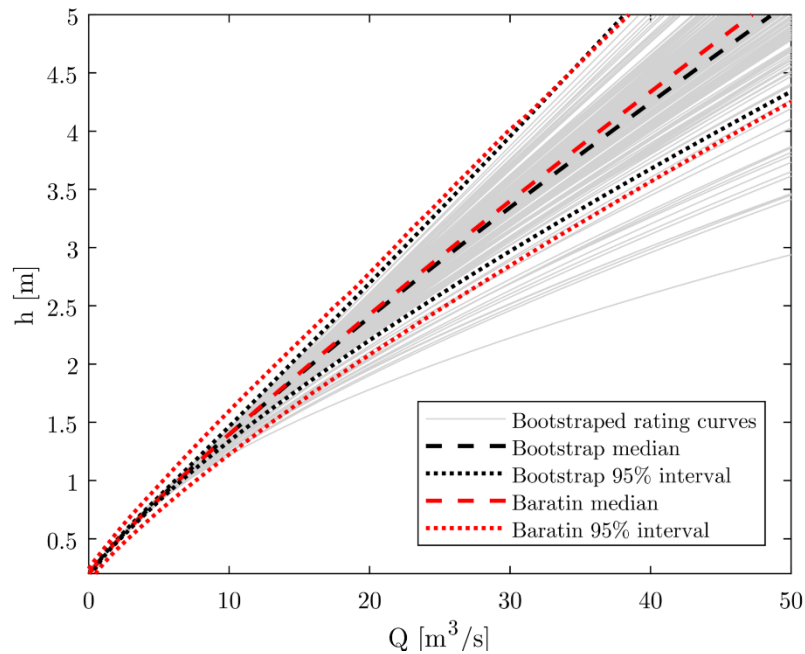


Figure 125: Comparison between Baratin and bootstrap results

To sum up, the uncertainty analysis on the Haine River is lead for two sources of uncertainty, each located at a boundary condition defined by a gauging station (Figure 126):

- the uncertainty on the value of the upstream discharge for a given return period and,
- the uncertainty on the shape of the rating curve at the downstream boundary condition.

---

<sup>11</sup> This approach is used for generality and the use of a systematic method. Indeed, it is impossible to check the shape of the distribution of  $Q$  for every discrete water depth.

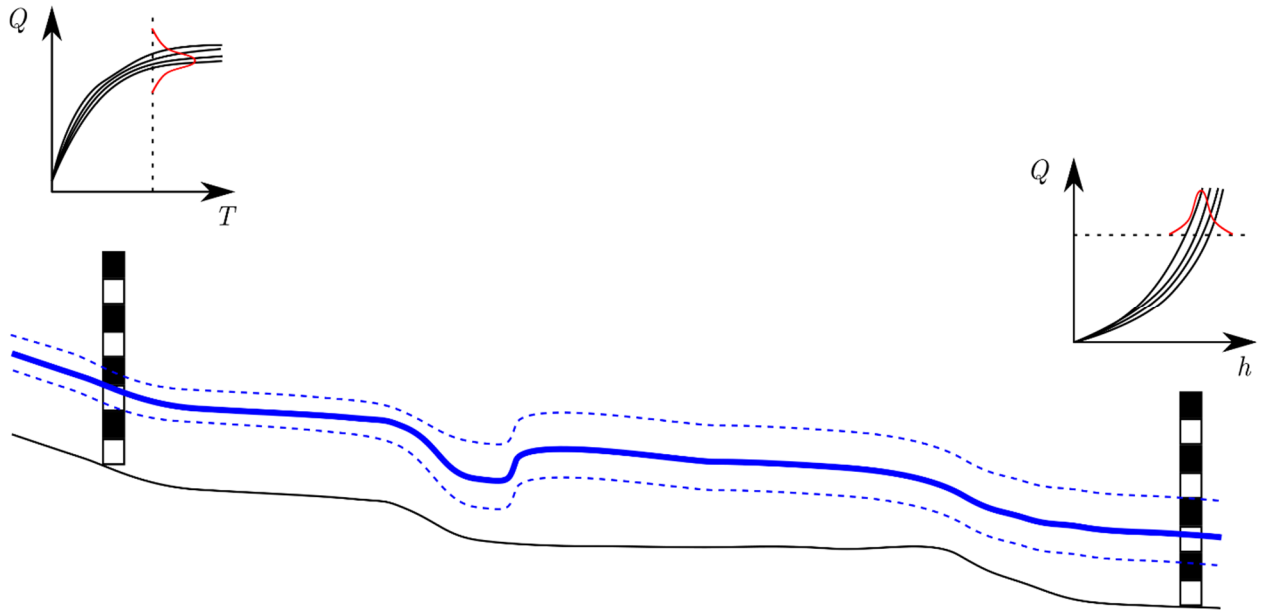


Figure 126: Principle of the uncertainty analysis on the Haine River (NB: axes of the right plot are tilted compared to previous plots)

### 4.3.3 Results and discussion

Two methods are tested for this test case. The Monte Carlo method is tested with 1000 and 10000 points. Then, PMM is tested and compared to Monte Carlo results. This choice of methods results from the conclusions drawn for the bump test case. PMM appeared to be a method which needed few points and proved to produce qualitatively good results. The purpose of this section is to demonstrate the ability of PMM to perform an uncertainty analysis on a real case and to compare it to a more computationally expensive method: Monte Carlo.

As shown in the previous section, the coefficients of the rating curve are correlated. This should be taken into account in order to create appropriate samples to use in the tested methods. In chapter 2, we showed that a decorrelation could be performed on the basis of the covariance matrix. In Figure 127, we represent the points drawn for the Monte Carlo method<sup>12</sup> for 1000 points and the points used for PMM. When compared to Figure 123, it appears that they both present similar patterns in the dependency between coefficients. Moreover, points selected for PMM are located in highest probability regions and dispersed according to main directions, according to the method explained by Bolle (1988). For informative purposes, we plot in Figure 128 the rating curves that correspond to the coefficients sampled by PMM.

---

<sup>12</sup> First, points are drawn like all random variables are uncorrelated. Then, axes are rotated in order to take into account the covariance matrix. The procedure is the inverse process of decorrelation explained in chapter 2.

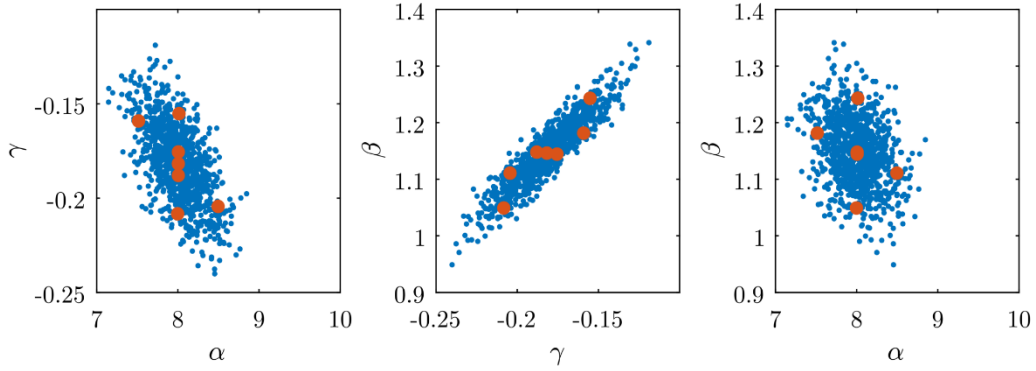


Figure 127: Rating curve coefficients sampled by PMM (orange) and by Monte Carlo (1000 points, blue)

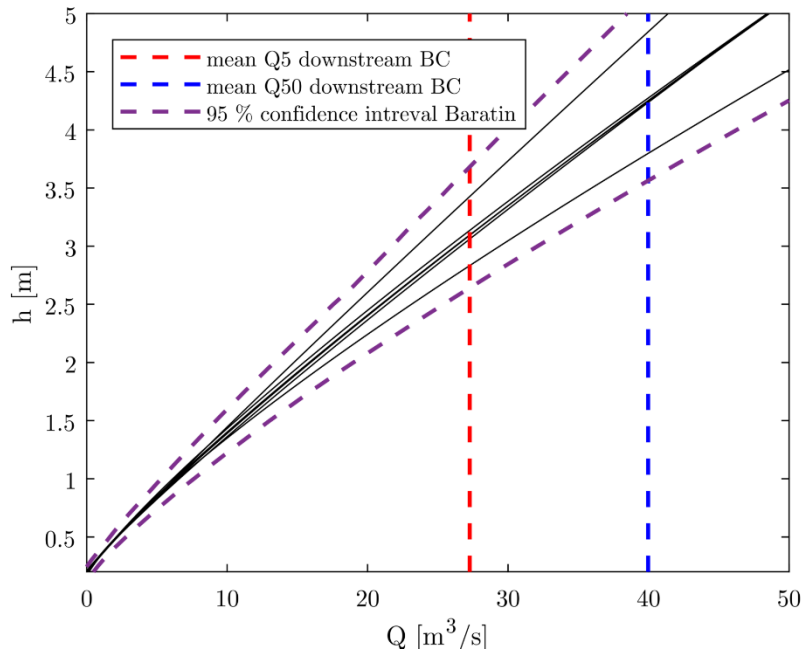


Figure 128: Rating curves for the coefficients sampled by PMM and mean discharges at the downstream BC for the chosen return periods

5-year and 50-year return periods are tested. Results are presented in parallel in order to compare uncertainty order of magnitudes. First, the mean values of the water level computed by different methods (Figure 129) are almost identical. Concerning the standard deviation (Figure 130), values are very close. Monte Carlo results differ slightly according to the number of points used. The larger the number of points, the better should be the result. Taking this into account shows that PMM provides better results than a Monte Carlo method with 1000 points since the red line lies close to the Monte-Carlo with 10000 points line. A similar observation can be made at the upstream part of the domain for the skewness coefficient (Figure 131). At the downstream part of the domain, PMM adopts a similar evolution for the skewness but values differ with Monte Carlo methods.

According to the return period considered, different variabilities can be observed when looking at standard deviation values (Figure 130). This is due to the fact that larger deviations of the uncertain variables at the upstream and downstream boundary conditions (Figure 128) can be observed when the return period is increased.

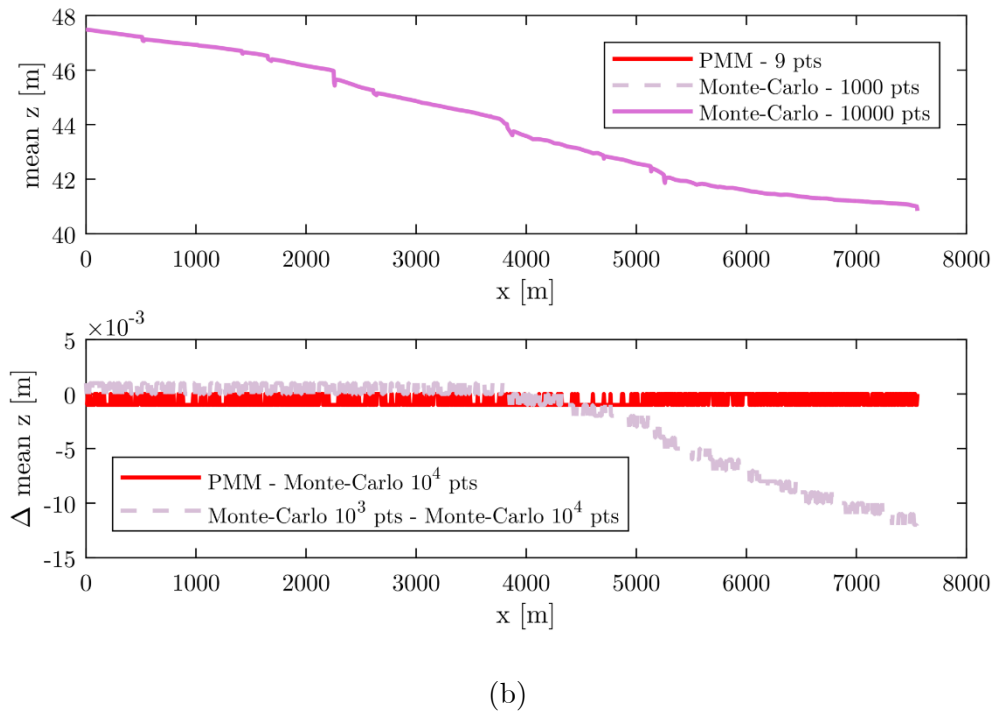
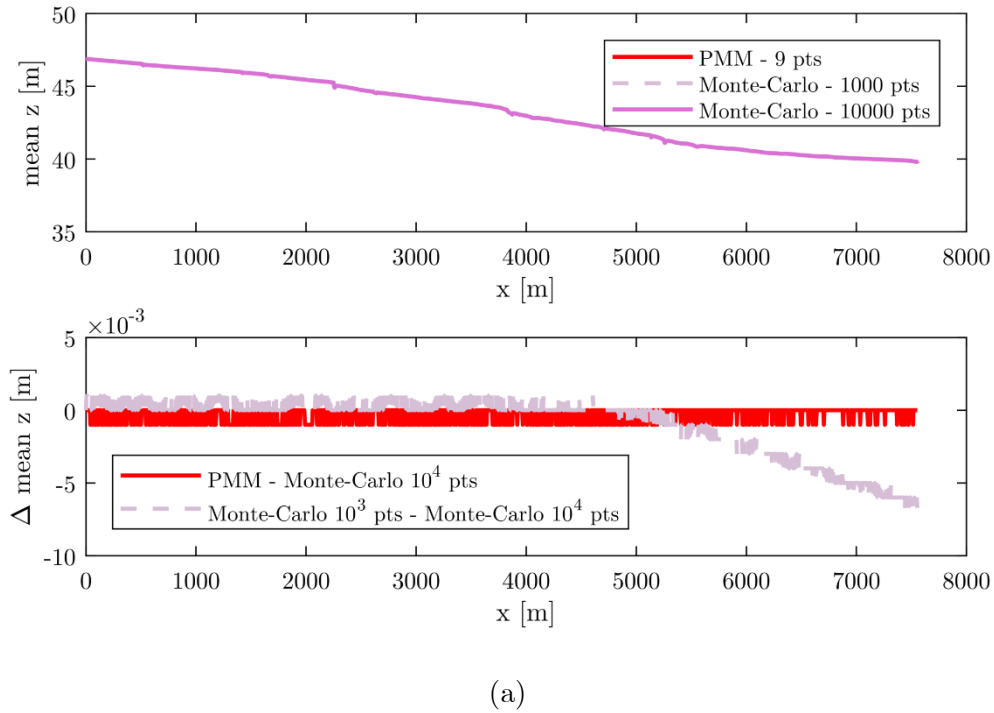


Figure 129: Mean values of the water level for 5-year (a) and 50-year (b) return periods

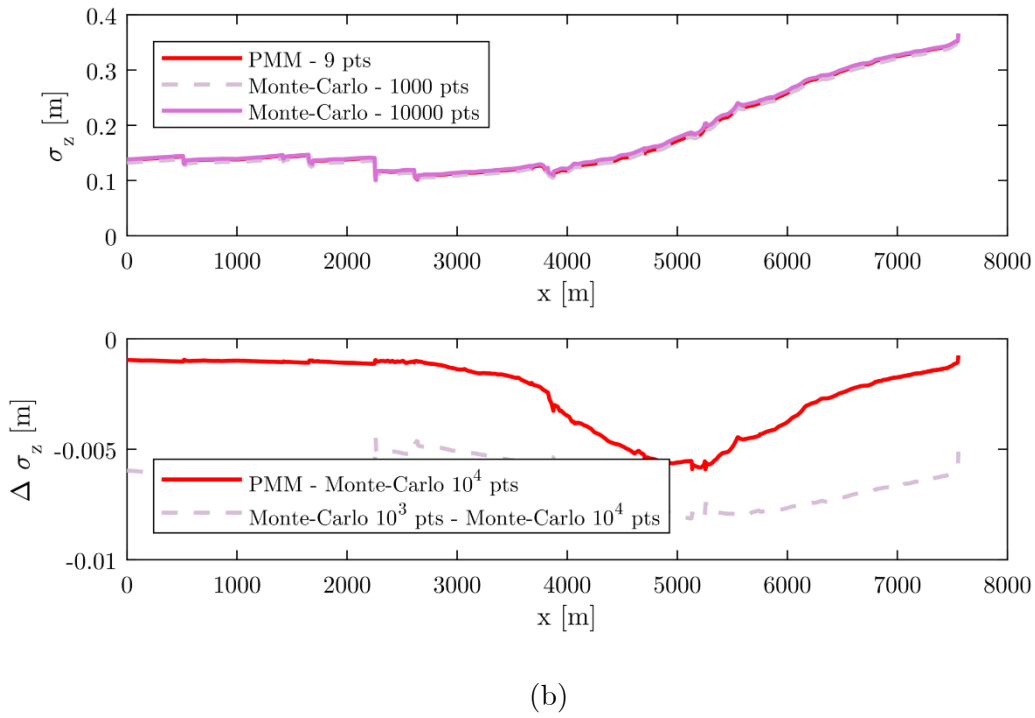
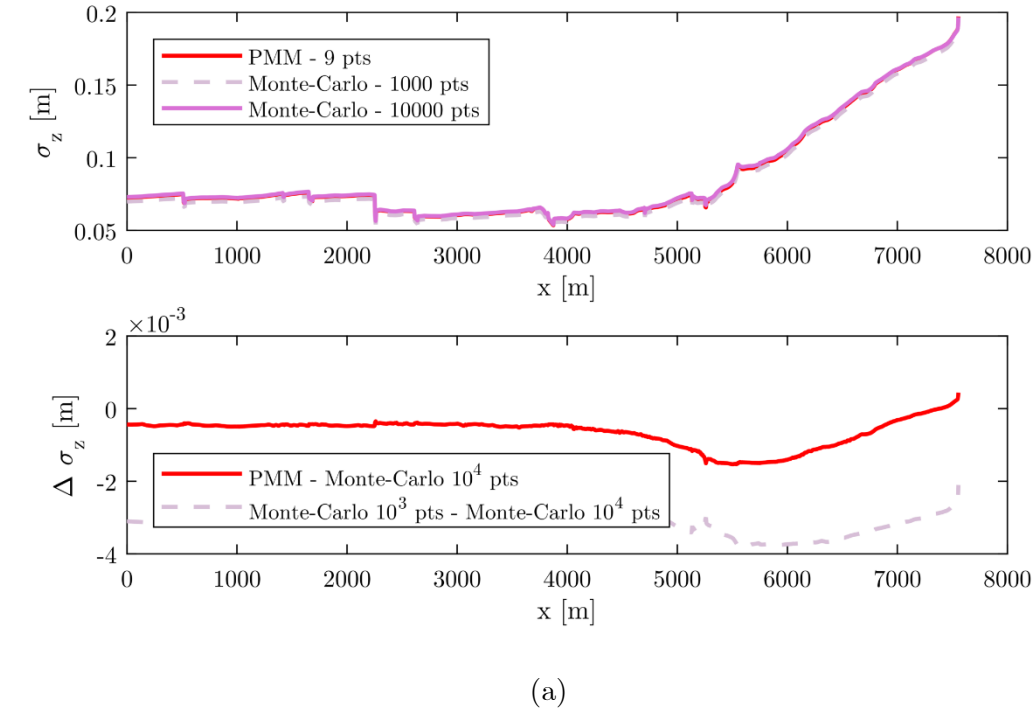
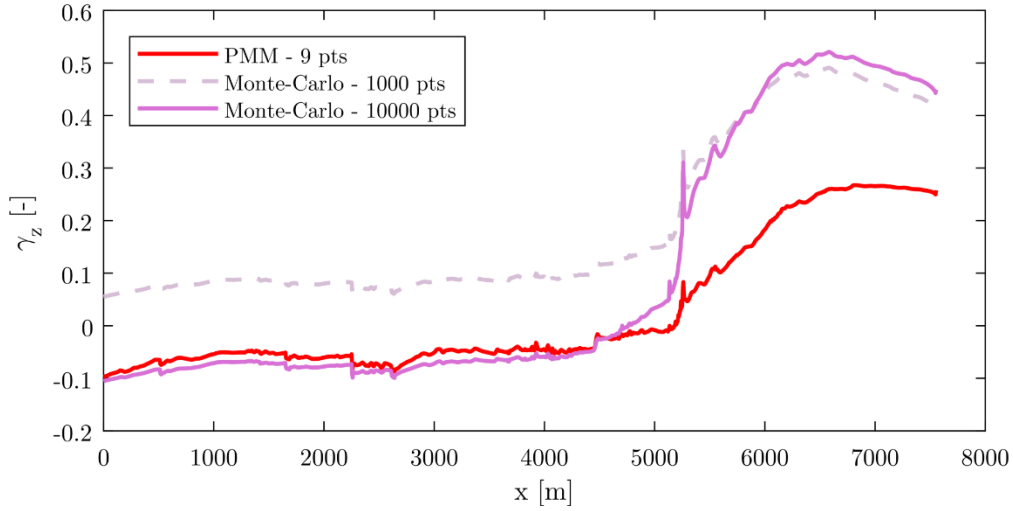
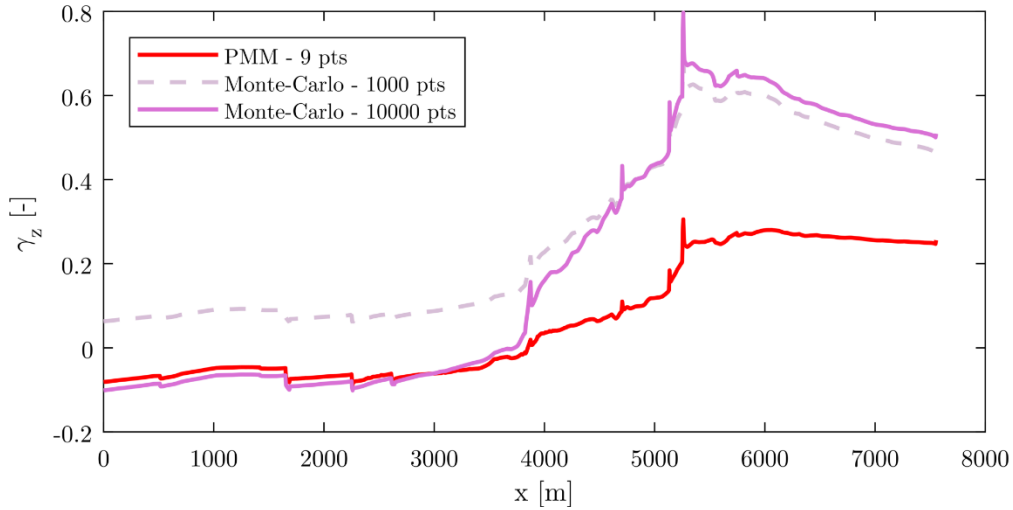


Figure 130: Standard deviation of the water level for 5-year (a) and 50-year (b) return periods



(a)



(b)

Figure 131: Skewness coefficient of the water level for 5-year (a) and 50-year (b) return periods

In Figure 130 and Figure 131, the behavior of the curves seem to change around 5000 m and 4000 m for the 5-year and 50-year return periods respectively. This change of behavior and its location is supposed to be linked to the vanishing point of the influence of the downstream boundary condition. This is verified in Figure 132 where the water levels are represented for both return periods and two boundary conditions. Vanishing points around 5000 m and 4000 m appear clearly.

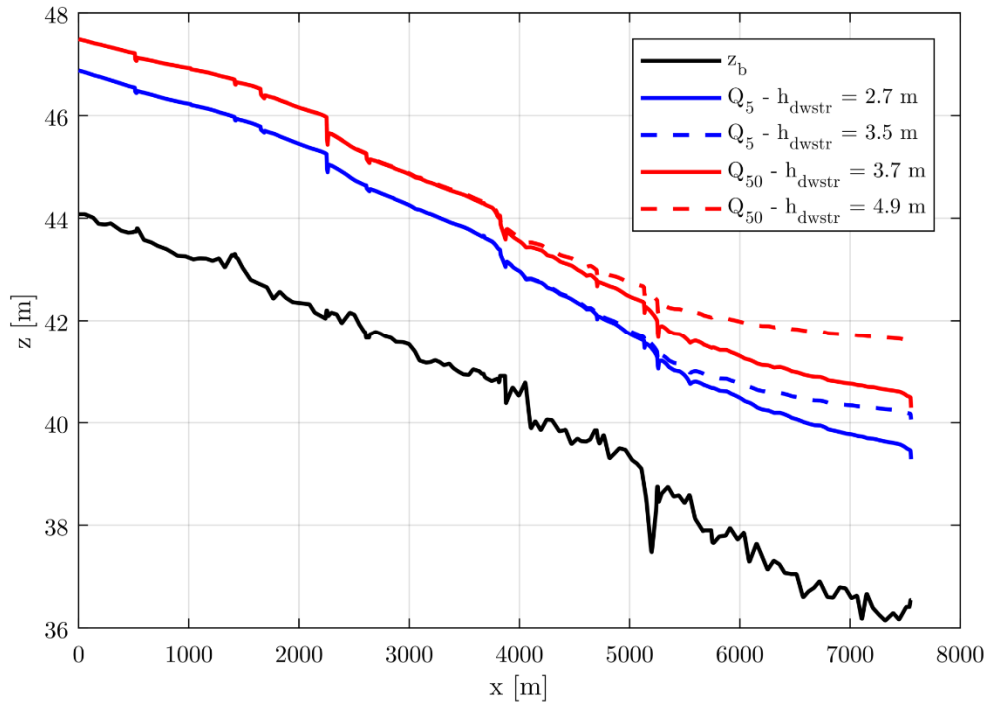


Figure 132: Influence of the downstream boundary condition on the water level for two discharges

A 95 % confidence interval is plotted in Figure 133 and Figure 134 for 5-year and 50-year return periods respectively. For the 5-year return period, the interval size is quite small but not neglectable compared to the water depth. In the downstream part, it is of the order of 50 cm while it is only of the order of 20 cm upstream. For the 50-year return period, the range of the 95 % confidence interval is of the order of 95 cm downstream and 35 cm upstream. Compared to a water depth of the order of 3.5 m, the confidence interval appears to be quite significant. This information can be used in comparison to banks altitude in order to determine the overflow hazard.

PMM results are very close to the more computationally expensive Monte Carlo method. Given its low computation cost (9 points computed vs. 1000-10000 for Monte Carlo, see elapsed times in Table 31) and its good quality of results provided in this case, we can conclude that PMM gives an interesting quality-time ratio for an uncertainty analysis applied to a real case open channel steady flow.

	PMM	Monte-Carlo $10^3$ pts	Monte-Carlo $10^4$ pts
$T = 5$ years	5,8 s	46,3 s	9 min 47 s
$T = 50$ years	7,1 s	1 min 12 s	14 min 48 s

Table 31: Elapsed times for the entire uncertainty analysis process

Uncertainty analysis applied to 1-D hydraulic models

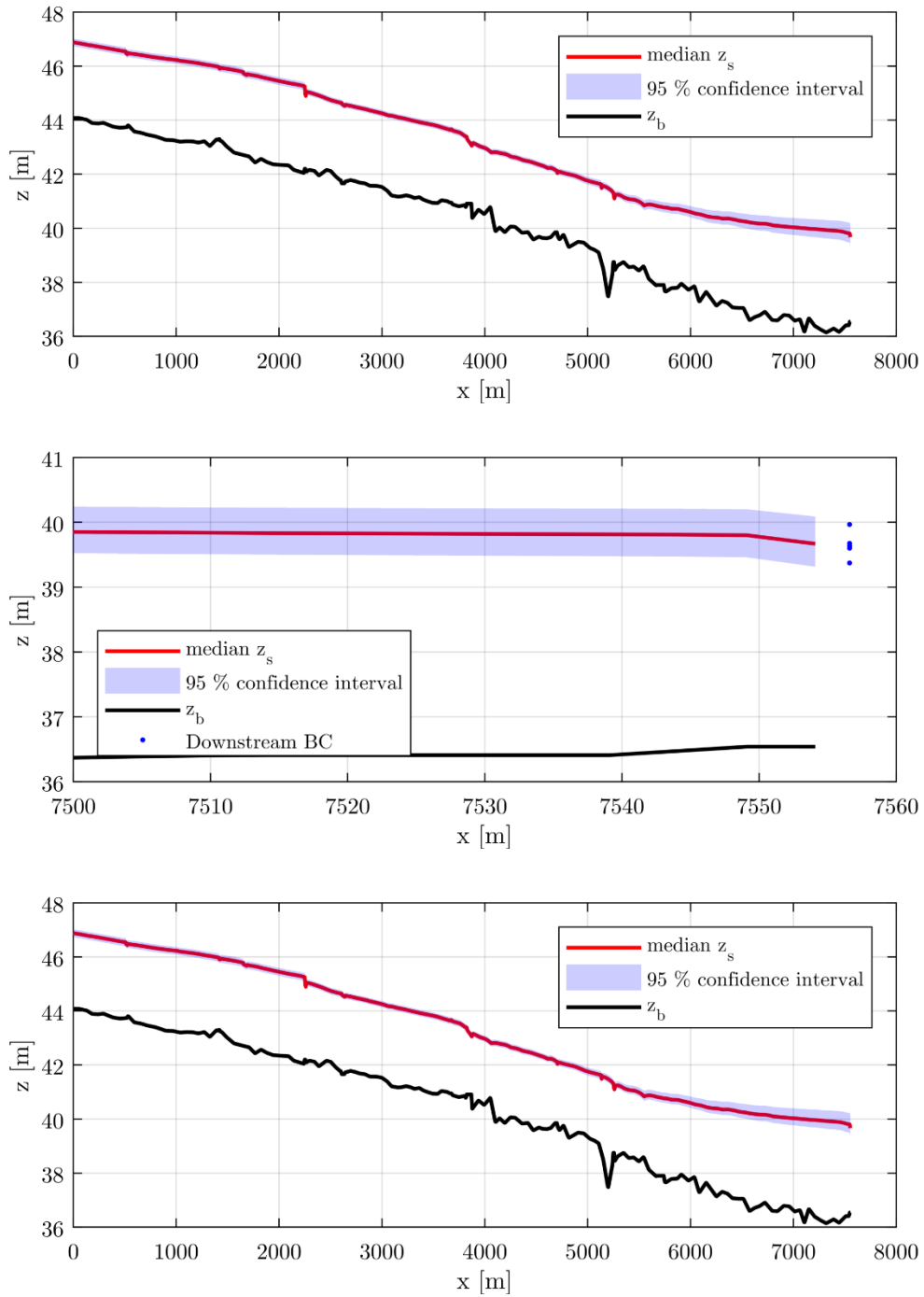


Figure 133: 95 % confidence interval of the water level for 5-year return period computed with PMM (first and second plot) and with a Monte Carlo method (10000 points, lower)

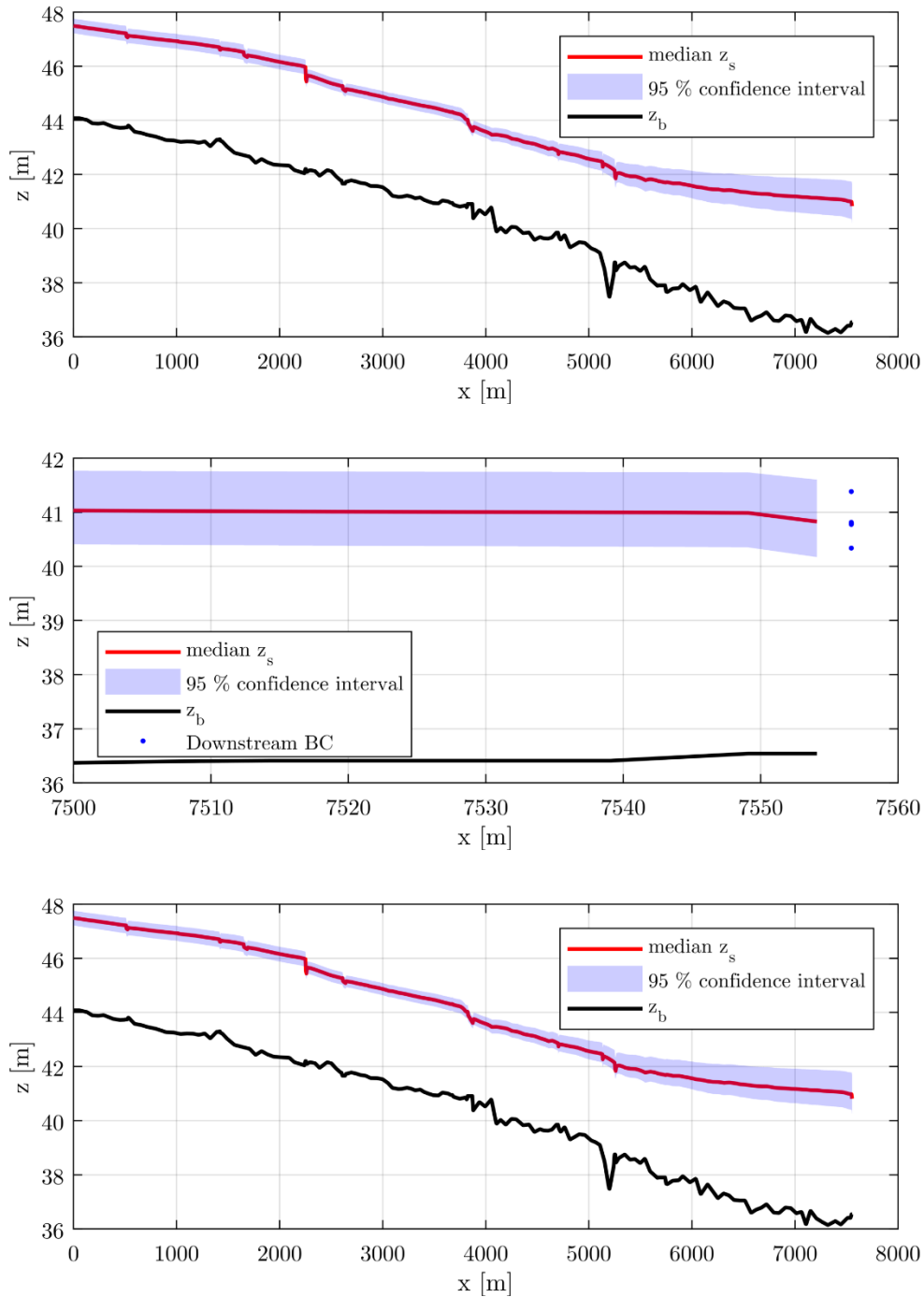


Figure 134: 95 % confidence interval of the water level for 50-year return period computed with PMM (first and second plot) and with a Monte Carlo method (10000 points, lower)

An uncertainty analysis can be useful to justify the validity of conclusions. For example, the uncertainty analysis performed in this chapter can help to strengthen conclusions about the risk of flooding of a field in which we are interested. Comparing the water level and its associated 95 % confidence interval to the altitude of the banks adds confidence to the fact that the field is only subject to a very low risk of flooding for 5-year and 50-year return periods (Figure 135). Indeed, since the top of the banks is much higher than the median water surface

and since the size of the 95 % confidence interval is not significant compared to the distance between the banks and the median water surface, the uncertainty analysis results strengthen the conclusion that the field is not prone to flooding for 5-year and 50-year return periods.

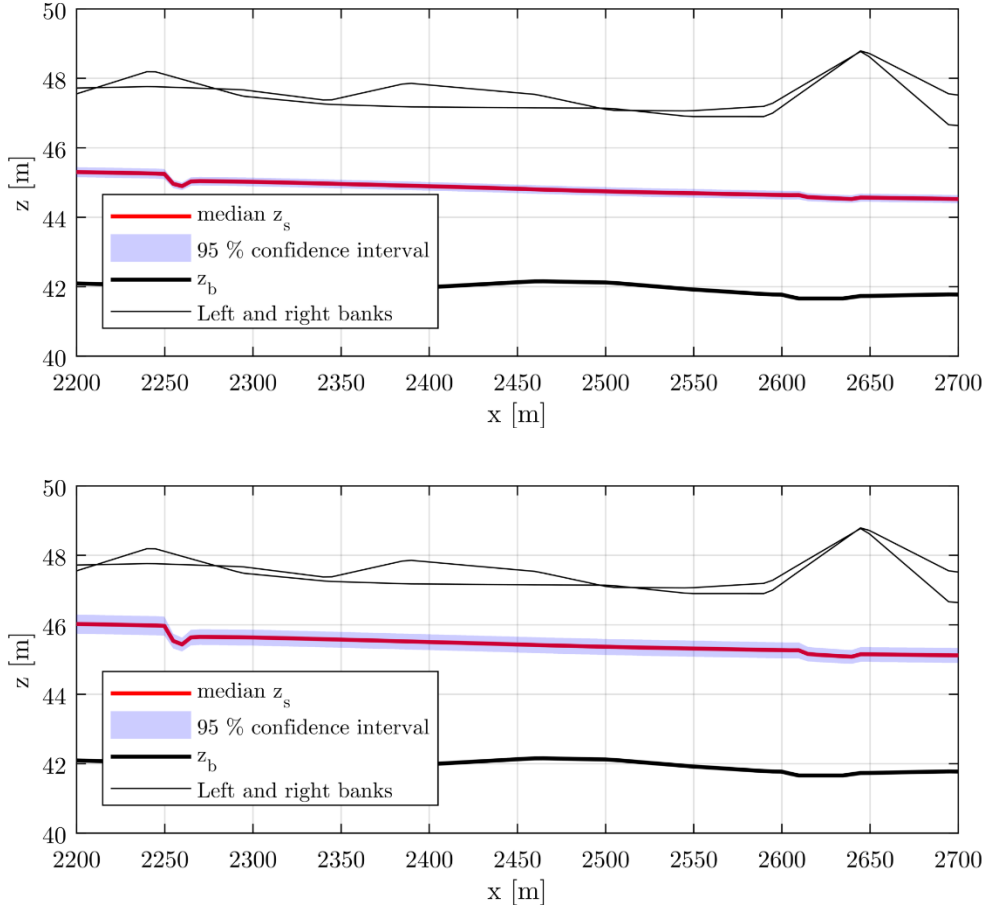


Figure 135: Comparison of uncertainty results against the altitude of the banks at an interest site, using PMM, for 5-year (upper plot) and 50-year (lower plot) return period discharges

However, it should be noticed that not all sources of uncertainty were taken into account but only those that we found to be the more significant. Adding up all sources of uncertainty would tend to increase the size of the confidence interval. Given the fact that a comfortable margin is available between the top of the banks and the upper limit of the actual confidence interval, the flooding of the studied field is very unlikely for a 50-year return period.

It is also interesting to notice that the confidence interval gets larger when the return period increases. This suggests that an uncertainty analysis is particularly relevant for high return periods. Depending on the nature of the goods submitted to a flooding risk, return periods of the order of 500 years or more can be used. For instance, critical infrastructures such as hospitals, power plants or data centers may require a protection to flooding for return periods of the order of 500 years. Even more critical structures, such as nuclear power plants, require

a design for flooding protection with return periods of the order of 10 000 years. In such situations, an uncertainty analysis takes all its sense.

## **4.4 Conclusion**

In this chapter, we applied successfully several uncertainty analysis methods to 1-D open channel flows. Thanks to the fast computing 1-D algorithm presented in chapter 3, comparison between the Monte-Carlo method, PEM and PMM was made more tractable.

After having tested uncertainty analysis methods on generic cases (chapter 2), this chapter focused on the application of uncertainty analysis methods to hydrodynamic cases. Since the computational cost of such applications can reach several hours when applied with 2-D or 3-D meshes, it was chosen to apply uncertainty analysis methods first to 1-D meshes. The algorithm developed in chapter 3 is used to decrease even more the computation time in order to be able to compare the Monte Carlo method to PEM, PMM and SRSM. The cases tested in this chapter are classified into two categories: an academic application (a flow over a bump) and a real-world case (steady state simulation of a 7-km reach of the Haine river in Belgium).

For the flow over a bump, several uncertainty sources were defined. This concerned the upstream discharge and the downstream water depth. Symmetrical and skewed distributions were tested. The boundary conditions were chosen in order to induce several flow regimes. We showed that methods with less points (PEM, PMM and SRSM) competed well against the more computing demanding Monte Carlo method even if results diverge slightly in some areas.

The real-world example intended to apply uncertainty analysis (Monte Carlo method and PMM) to a case that engineers could face in their everyday life. Two sources of uncertainty were chosen: the uncertainty on the upstream discharge for a given return period and the uncertainty on the downstream rating curve. Results on a 7-km reach of the Haine river showed that PMM provided very good results compared to the more expensive Monte-Carlo method. Moreover, on an engineering point of view, applying uncertainty analysis to flood risk analysis allows to settle firmly conclusions. Indeed, comparing a confidence interval with the remaining height before flooding allows to assess the strength of the conclusions that are based on a median water level.

The excellent results provided by PMM allow to conclude that this method is suitable to perform a cost effective uncertainty analysis of hydraulic problems. This paves the way for uncertainty analysis applied to more computationally expensive hydrodynamic modeling. The following chapter will take advantage of these conclusions.

# Chapter 5: Uncertainty analysis applied to 2-D hydraulic simulations

## 5.1 Introduction

In previous chapters, uncertainty analysis was introduced and applied to simple models (polynomials and a bungee jump example) and 1-D hydrodynamic models (academic cases and a real-world 1-D application). We showed that PMM provided excellent results in a short period of time, compared to more computationally expensive methods. The objective of this chapter is to apply uncertainty analysis to a 2-D real-world case.

### 5.1.1 2-D hydrodynamic modelling

When the flow is channelized and that flow patterns are mainly directed according to the channel longitudinal axis, a 1-D hydrodynamic model is relevant for the computation of water depths and velocities. Things might become more complex in more natural streams where a direction is not clearly given to the flow by the bed geometry. In that case, the modeler can use a 2-D horizontal hydrodynamic model. These 2-D horizontal models (also known as quasi 3-D models) average the vertical flow velocity profile and neglect any vertical velocity component (see section 5.1.2 for justification). The unknowns in a 2-D horizontal model are the water depth and two horizontal velocity components.

Using a 2-D horizontal hydrodynamic model is of main interest for some applications such as flood mapping (Epicum, Dewals, Archambeau, Detrembleur, et al. 2010), dam break flows (Epicum, Dewals, Archambeau & Pirotton 2010), urban flooding (Arrault et al. 2016; Bruwier et al. 2017; Bruwier et al. 2018), etc.

Since this kind of models relies on more unknowns, more equations and more discretization points<sup>13</sup>, the computation cost is much higher than for 1-D models. This is the reason why, in this chapter, only PMM is used for uncertainty analysis.

### 5.1.2 WOLF 2-D model

Numerical hydraulic computations performed in this chapter rely on the quasi 3-D WOLF 2-D model (Epicum, Dewals, Archambeau & Pirotton 2010; Epicum, Dewals, Archambeau,

---

<sup>13</sup>Since a 2-D model discretizes the river in the longitudinal and transversal directions while a 1-D model discretizes the river only in the longitudinal direction, more discretization points are required for a 2-D model for a constant spatial step.

Detrembleur, et al. 2010). In this particular context, WOLF 2-D uses square cells of constant size across the domain. This model computes the depth-averaged Navier-Stokes equations at each cell: the mass conservation equation and the momentum conservation equations according to  $x$  and  $y$ . These three equations describe the evolution of the water depth  $h$  and the velocities  $u$  and  $v$  at each cell:

$$\begin{aligned} \frac{\partial h}{\partial t} + \frac{\partial uh}{\partial x} + \frac{\partial vh}{\partial y} &= S \\ \frac{\partial uh}{\partial t} + \frac{\partial u^2 h}{\partial x} + \frac{\partial uvh}{\partial y} + \frac{g}{2} \frac{\partial h^2}{\partial x} &= -gh \frac{\partial z_b}{\partial x} + gh J_x \Delta \Sigma + S_u \\ \frac{\partial vh}{\partial t} + \frac{\partial v^2 h}{\partial y} + \frac{\partial uvh}{\partial x} + \frac{g}{2} \frac{\partial h^2}{\partial y} &= -gh \frac{\partial z_b}{\partial y} + gh J_y \Delta \Sigma + S_v \end{aligned} \quad (192)$$

$z_b$  is the bottom elevation,  $g$  the gravity acceleration,  $J_{x,y}$  the components of the friction slope in the  $x,y$  plan and  $\Delta \Sigma$  is the increase of the surface on which the shear stress acts due bottom irregularities:

$$\Delta \Sigma = \sqrt{1 + \left( \frac{\partial z_b}{\partial x} \right)^2 + \left( \frac{\partial z_b}{\partial y} \right)^2} \quad (193)$$

The main assumption of the shallow-water model consists in assuming (Piroton 1994):

- a low ratio between velocity components perpendicular to the main flow and those parallel to the main flow, and
- a neglectable squared ratio between velocity components perpendicular to the main flow and those parallel to the main flow.

Most of the time, these assumptions are licit, except close to hydraulic structures.

WOLF 2-D solves equations (192) using a finite volume scheme and an original flux splitting method. The algorithm is capable of dealing with mobile boundaries and with wetting and drying cells. Concerning the present case, the domain is discretized using 1 m<sup>2</sup> square cells.

The friction law used for this chapter is the Barr-Bathurst law (Machiels et al. 2011). It is valid for a wide range of relative roughness sizes. The friction slopes in both directions of the plan are:

$$J_x = \frac{\lambda}{4h} \frac{uU}{2g} \quad (194)$$

$$J_y = \frac{\lambda}{4h} \frac{vU}{2g} \quad (195)$$

where  $U$  is the norm of the velocity and  $\lambda$  the friction coefficient, which is defined by the equation (123).

### **5.1.3 A 2-D application**

In order to apply uncertainty analysis to 2-D hydrodynamic modelling, we chose a real-world case that focusses on a dam removal study in the French Alps.

Dam removal may lead to long-term ecological benefits including improved fish passage, increased biodiversity and recovery of sediment continuity (Bednarek 2001). However, removing a dam may trigger substantial geomorphic evolutions (Konrad 2009), which in turn may endanger buildings and infrastructures located on the riverbanks. Therefore, the dam removal works must be carefully designed so that river incision and bank instabilities are avoided at critical locations, and that appropriate mitigation measures are implemented to control the extent of bed and bank erosion.

After several decades, sediment deposition can occur upstream of the dam. After the removal, these deposited sediments can be set in movement. While this phenomenon can trigger destabilization problems for neighboring structures in some cases, in other, it can be useful (e.g. too many sediments deposited in an area).

In principle, morphodynamic modelling could be used to inform the design of the dam removal works (Poepl et al. 2019). Nonetheless, in many situations, this is hardly feasible due to multiple reasons, such as the lack of data on sediment supply upstream, the absence of validation data (e.g. historical riverbed profiles) and the complexity of the process involved (e.g. role of large boulders, which cannot be described as a continuous medium).

Here, we present an original method which is based on 2-D hydraulic simulations to extract valuable information for assessing the post-dam-removal stability of riverbed.

A remarkable case study is used to illustrate the application of our method. Carried out by Electricité de France (EDF), it consists in the replacement of five one-century-old hydropower schemes by a single one, more powerful and more environmentally friendly. Public authorities request that EDF considers the (partial) removal of five existing dams, which will not be used anymore in the new project (Goffin et al. 2015; Goffin, Piroton, Archambeau, et al. 2016; Goffin et al. 2017; Rulot et al. 2012).

While the removal of 5 dams and the local and global consequences is treated in (Goffin et al. 2018), the focus of this chapter is on the effect of the removal of the upper dam on the dynamic of finer sediments in the upstream part of the river.

## **5.2 Case study description**

The Romanche River is located in the French Alps. The overall study area lies between the confluence with the Eau d’Olle and Gavet. Five century-old dams are planned to be (partially) removed by Electricité de France (EDF) between Livet and Gavet (Figure 136). A few hundred meters downstream of the new dam, the “Prise d’eau de l’Infernet” (where the dam is also known as “Seuil Keller”) is planned to be completely removed. The current situation is depicted in Figure 138. At this location, the river slope changes from approximately 0.1 % to 2.7 %.

Further, in the high slope part, two other dams at “Prise d’eau des Roberts” and “Prise d’eau de Rioupéroux” (Figure 138) are planned to be completely removed. The dam at “Prise d’eau des Clavaux” presents a bigger chute than previous ones. Removing it without any mitigation technique would lead to much higher stresses on the riverbed and destabilization problems. Moreover, houses are located upstream of the dam. In order to limit the effects the dam removal and ensure fish passage, EDF plans to build a 8 % slope ramp made of rocks.

The most downstream dam planned to be removed is located at “Prise d’eau de Pierre-Eybesse”. According to EDF, no particular structures are located close to this dam and a complete removal is planned.

The characteristics of the river change drastically at the Keller dam. Indeed, the slope modification induces changes in the flow regimes and in the size of particles that can be observed. While upstream of the “seuil Keller” the maximum grain size is of the order of 10 cm, much larger rocks are present downstream (Figure 139).

It is interesting to notice in the view from the “seuil Keller” in Figure 139, the presence of a large amount of rocks. This alluvial fan constitutes an important sediment source for the river. Without any relevant quantitative data, a full morphodynamic computation cannot be lead and cannot take into account this input. However, in practice, it can supply in sediments zones that are being eroded.

Figure 139 justifies also why we rely on 2-D simulations for this chapter. Indeed, the area close to the dams present structures that are prone to induce flow direction changes and speed-up zones. Such characteristics cannot be accurately represented in a 1-D model. For satisfactory results, in particular for producing sediment movement indicators, a 2-D model is required for this application.

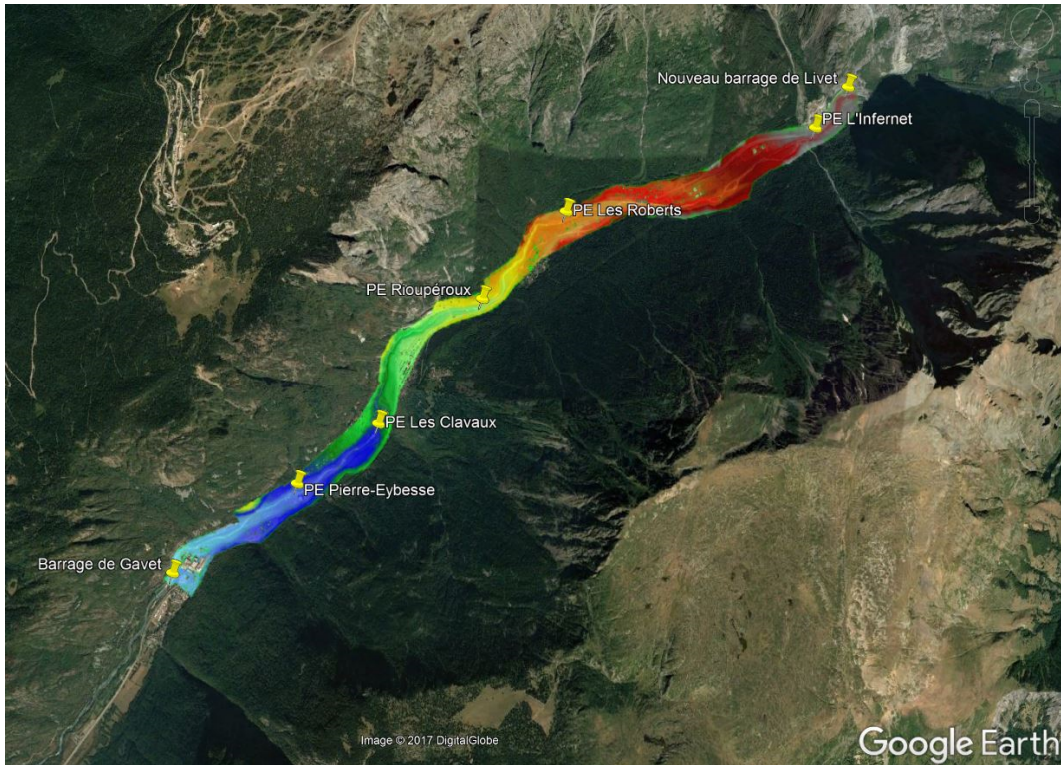


Figure 136: Locations of the five (partially) removed dams (referenced by PE)



Figure 137: Upstream section of the River ("Seuil Keller" = dam at PE L'Infernet)

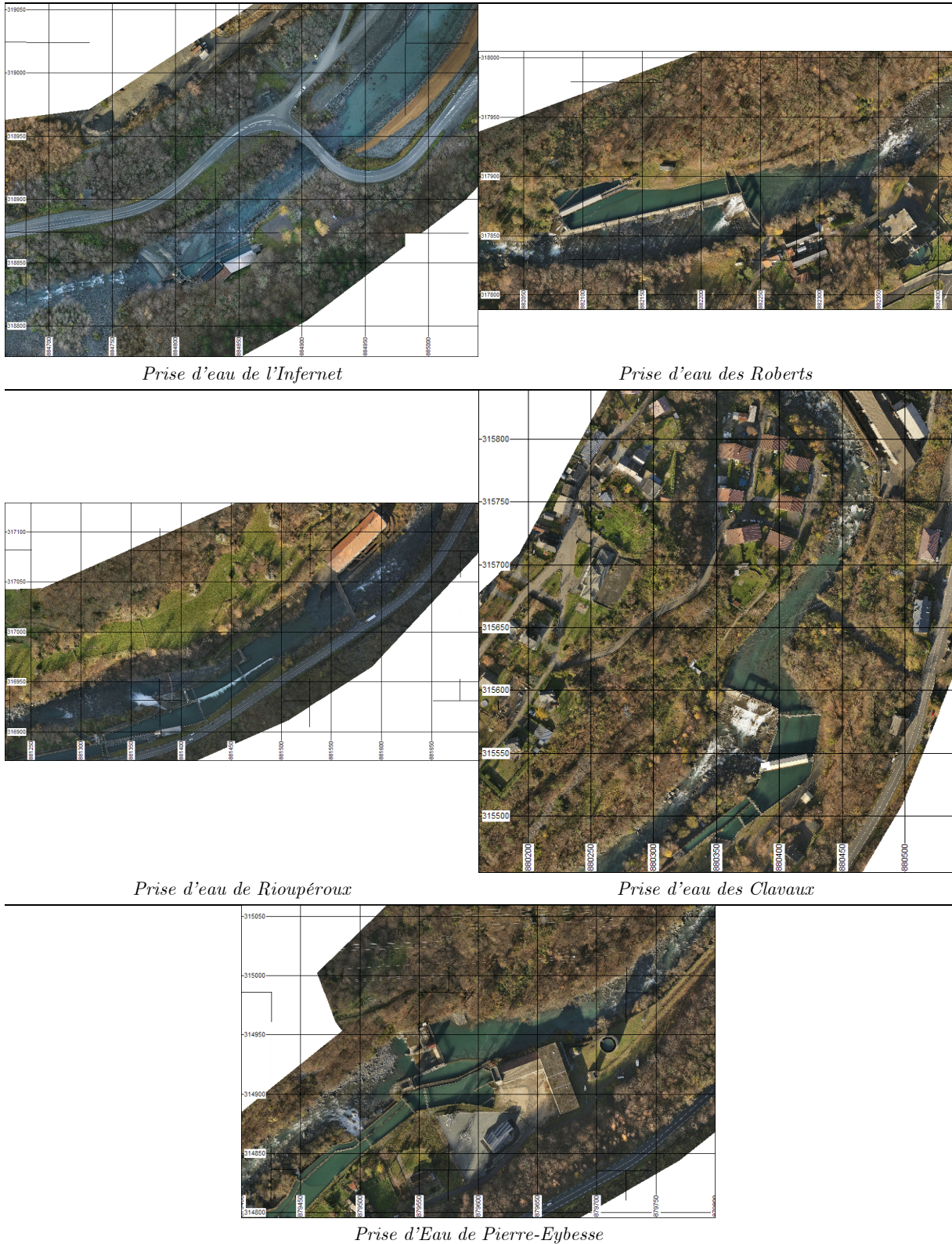
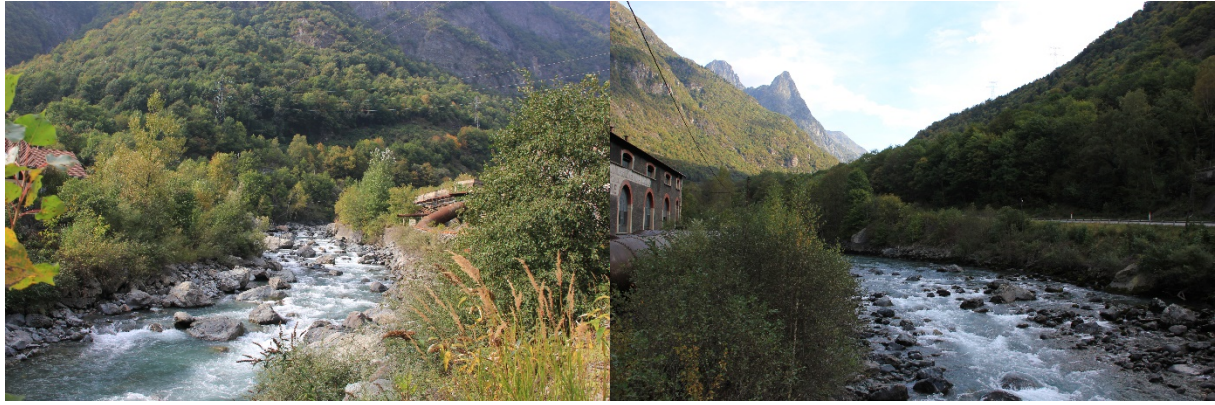


Figure 138: Aerial views of the 5 hydropower schemes planned to be removed by EDF



*Upstream of “Rioupéroux” hydropower plant*

*Along “Les Roberts” hydropower plant*



*Downstream of “Prise d’eau des Roberts”*

*View from “Seuil Keller” toward downstream*

*Figure 139: The Romanche River downstream of the Keller dam*

The section of interest for this thesis chapter has the Keller dam (which is planned to be removed) in its downstream part (Figure 137) and goes up to the confluence with the Eau d’Olle at the upstream boundary condition.

During the works for the new hydropower facility, EDF noticed the deposition of sediments in the area close to the new Livet dam. In order to evaluate the potential of mobilization of these sediments following the removal of the Keller dam, they ordered a study based on hydraulic simulations and on the computation of a morphodynamic indicator (see section 5.3). As stated earlier, morphodynamic simulations were not possible due to the lack of relevant information about bed and wash loads for boundary conditions and validation.

In order to assess the influence of the removal of the downstream dam (“Seuil Keller”), on recent sediments depositions, two digital elevation models (DEM) are used. The first one, named

“current” depicts the current situation, with the “Prise d’eau de l’Infernet” that is still present. It is mainly made of LiDAR and bathymetry data acquired in 2016 by EDF. The second DEM, named “planned”, relies on the first one except from the “seuil Keller” to 200 m upstream. In this zone, removal plans designed by EDF for the “seuil Keller” and the water intake are considered. A calibration of the river from the Keller dam to 200 m upstream is also considered. EDF plans consist in a lower riverbed and reshaped banks.

In order to assess the evolution of the riverbed elevation and water levels, an extraction vector is defined from the upstream limit of the computation domain to its downstream limit. A full view is provided in appendix C.1 (Figure 197) and a zoom on the most interesting part is given in Figure 140. In next pages, only zoomed views are provided. Full views are available in appendix C.

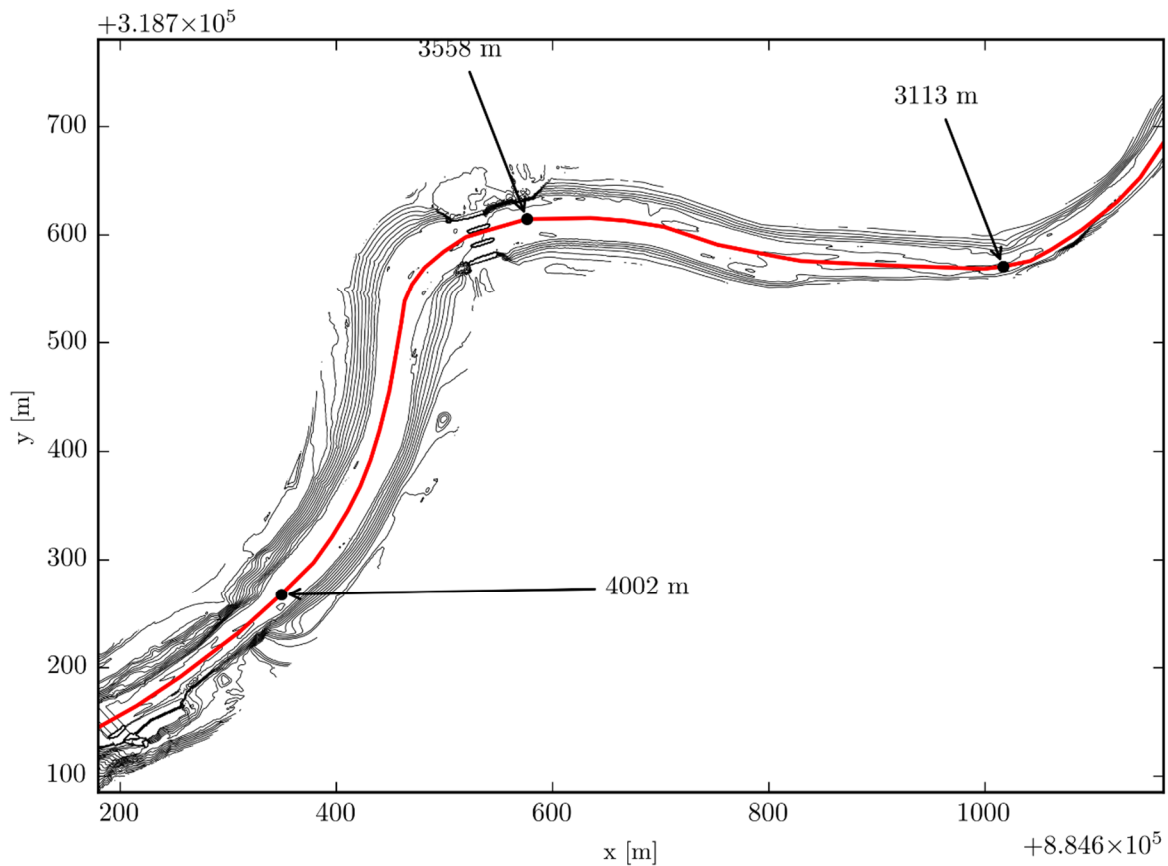


Figure 140: Vector used for extracting bed elevations and water levels. It is represented in the zone of interest with some curvilinear coordinates for better interpretation. The origin of the vector is located at the confluence of the Eau d’Olle with the Romanche.

A comparison between current and planned DEMs is given in Figure 141. As stated earlier, these models are equivalent except at the neighborhood of the Keller dam. The removal of the dam and the deepening of the river will have tendency to decrease water depths and increase velocities upstream. This expectation is checked later in this document.

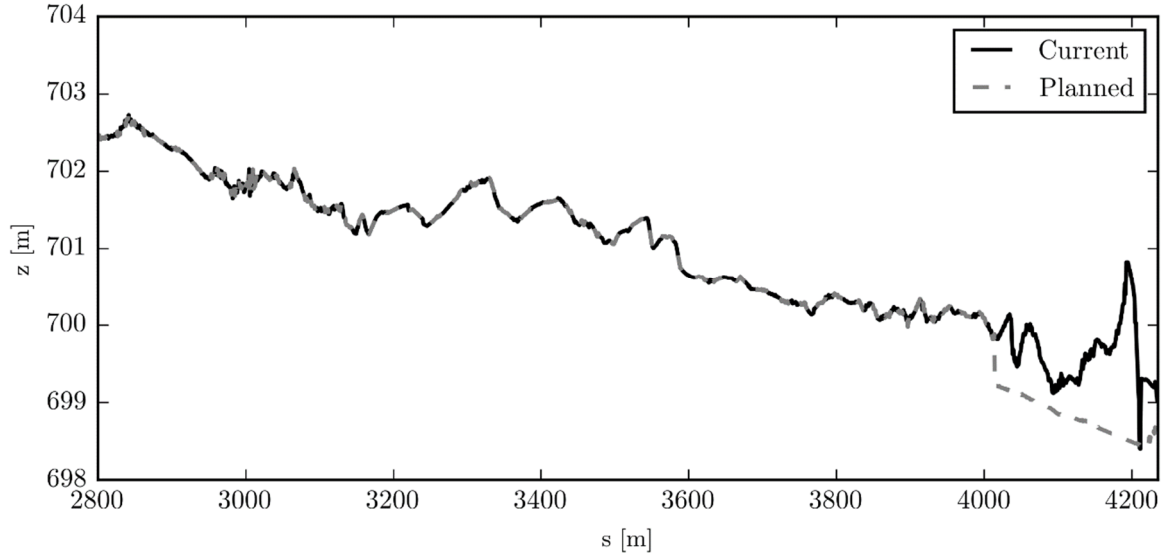


Figure 141: Bed profile in the current and planned situations

The upstream boundary condition is a discharge injected as a source term in the continuity equation for the nodes located across the river at the upstream boundary. The momentum equations are also corrected according to the injected discharge. This technique, which is different from imposing a discharge at a border of a finite volume, avoids imposing a predefined direction to the flow. A constant discharge in time is imposed in order to reach a steady flow condition. For this thesis chapter, a single discharge is tested. It is taken at  $150 \text{ m}^3/\text{s}$ , which is the one-year return period discharge. In the frame of a full study on the removal of the dams, several discharges should be tested in order to assess the potential of sediments mobility.

For the downstream boundary condition, no data are available about the water levels downstream of the Keller dam. However, we know that the slope increases sharply at this location. The increase in the slope is such that a critical section exists at some location downstream of the dam for a wide range of discharges. A critical section is a section that prescribes naturally a water depth at its location for a given discharge. However, due to the irregular nature of the topography, there are no warranty that the critical section will be unique and that it will coincide with the downstream border. In order to ensure numerical stability for the model, it is decided to increase artificially the slope at the end of the domain. The downstream borders are set as “free borders”. Since critical sections are present between this

artificial slope and the dam, the water depths computed upstream are not affected by the presence of the artificial slope.

Concretely, the DEM is maintained in its “natural” state for 100 m downstream of the dam, then an artificial slope of 30 % is imposed on 20 m in order to have a supercritical flow at the downstream boundary.

Previous studies on this stretch of the river fitted a roughness size  $k_s = 0.15$  m. This value corresponds in order of magnitude to the typical roughness size that can be met in this part of the river. No further calibration of this coefficient is made in this chapter. As explained later, it will be considered as uncertain.

This stretch of the Romanche River is modelled using the 2-D shallow water model WOLF that is described in section 5.1.2. The choice for a 2-D model is based on the desire to have an information distributed across the river section, which is not possible with a 1-D model. Moreover, as described earlier in this section, 2-D simulations allow to take into account horizontal flow patterns that result from the presence of hydraulic structures. This choice for a 2-D model brings a number of computation nodes of the order of 170 000 (1 m x 1 m cells). The computation time for stabilizing a steady flow with such a number of nodes is of the order of 3 hours. This withdraws the use of uncertainty techniques that require too many evaluation points. Monte-Carlo will not be considered and PMM is the only technique that is used in this chapter. In previous tests, PMM showed to perform well compared to other methods such as PEM and SRSM.

This study aims at determining the potential of sediment movement following a dam removal. The objective is to know if recently deposited sediments will be put in movement after the dam removal. Based on two DEMs (one before dam removal and one after), hydraulic simulations are lead in order to obtain water depths and velocity fields in the river. From these hydraulic data, a maximum particle diameter set in movement is computed for each wet node (see section 5.3). Using a granulometry curve and the computed diameter, we are able to compute the percentage of the soil of the riverbed that is supposed to be set in movement. If we assume that sediment supplies remain constant between the current and planned situations, the evolution of the percentage of soil is a good indicator of the possibility to have more solid transport. A schematic view of this framework is given in Figure 142. It is important to recall that this non-morphodynamic computation has limitations: the riverbed is supposed fixed and no sediment load is considered.

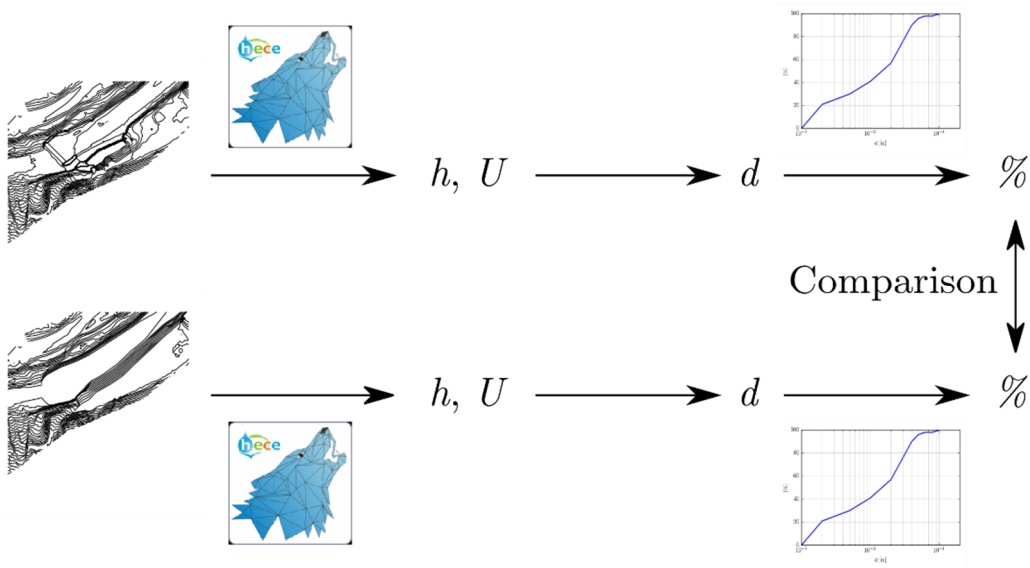


Figure 142: Workflow for the discussion of the stability of the riverbed after the removal of a dam

### 5.3 Riverbed stability

A flow in a river is subject to friction losses. In this chapter, we chose to model the friction by a Barr-Bathurst law that uses a roughness size  $k_s$  as a calibration factor. These friction losses come from the irregular shape of the riverbed at the particle scale but also at a larger scale (e.g. presence of dunes). While the flow is submitted to friction losses, it produces a shear stress on the riverbed. According to its magnitude and the size of the particles in direct contact with the flow, this stress might be capable to initiate particles motion.

Two extreme cases of particles position can be described. First (Figure 143), fine particles, whose sizes are compatible with sediment transport, are located under grosser and more stable particles. In this case, fine particles are protected from the flow shear stress and are not available for sediment transport. The second case (Figure 144) is representative of channels where deposition occurred. The particles which make the structure of the riverbed (grosser particles) are located under finer particles. These finer particles are not protected from the shear stress generated by the flow and are available for sediment transport.

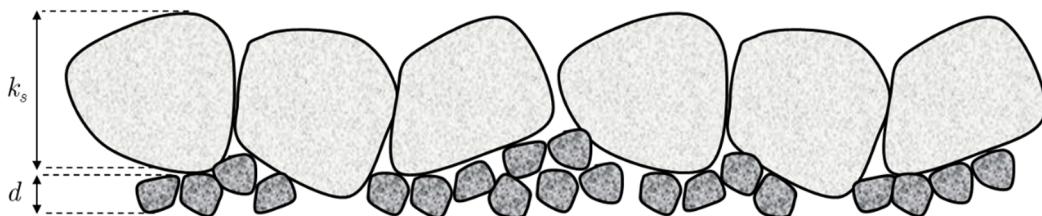


Figure 143: Schematic representation of particles positions where finer particles (dark gray, characteristic size  $d$ ) are located under grosser particles (light gray, characteristic size  $k_s$ ) that make up the structure of the riverbed

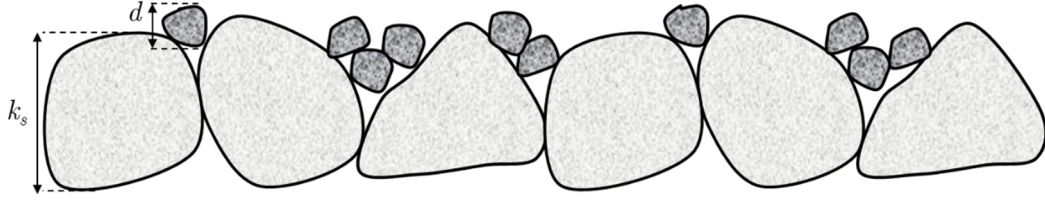


Figure 144: Schematic representation of particles positions where finer particles (dark gray, characteristic size  $d$ ) are located above grosser particles (light gray, characteristic size  $k_s$ ) that make up the structure of the riverbed

The stretch of the Romanche River studied in this chapter is representative of the second case. Indeed, following recent works, the dam operators and local authorities noticed the deposition of fine sediments. These newly deposited sediments are located above the grosser particles and are available for sediment transport.

In the second configuration (Figure 144), smaller particles (diameter  $d$ ) will probably be available for sediment transport. However, the friction shear (which is a function of  $k_s$ ) may not be totally available to put small particles in motion. Indeed, the shear stress computed by the friction law is representative of all momentum losses of the flow. Only a part of these losses is effectively used to put particles in motion, the rest is dissipated in other processes (e.g. turbulence at the scale of bigger size particles).

In details, we distinguish:

- the global shear stress  $\tau_b$ , linked to the roughness size  $k_s$ , that is responsible for the flow friction losses, and
- the effective shear stress  $\tau'_b$ , linked to the grain size  $d$ , that is responsible for the sediment motion.

This distinction is similar to the one used in the presence of waves at the riverbed level. These waves, which have a larger characteristic size than the particles, participate in the momentum loss process, sometimes in larger proportion than the friction generated at the grain size level.

Based on the general Darcy-Weisbach approach, the bed shear stress  $\tau_b$  is written in 2-D:

$$\tau_b = \rho \frac{\lambda}{8} U^2 \quad (196)$$

where  $\rho$  is the density of the fluid,  $U$  the norm of the velocity and  $\lambda$  the Darcy-Weisbach friction coefficient. The Darcy-Weisbach coefficient  $\lambda$  is evaluated thanks to the Barr-Bathurst formula (123). The following developments are first done with the Manning coefficient, according to what can be found in literature. Then, developments are generalized for Barr-Bathurst friction approach.

In the presence of waves at the riverbed level (e.g. dunes), the following correction coefficient is usually applied to distinguish the global shear stress  $\tau_b$  from the effective shear stress  $\tau'_b$  (Degoutte 2006; Graf & Altinakar 1998):

$$\tau'_b = \left( \frac{n'}{n} \right)^{3/2} \tau_b \quad (197)$$

where  $n$  is the global Manning friction coefficient, obtained for example after a calibration phase of the hydraulic model, and  $n'$  is the Manning friction coefficient relative to the friction losses due to the particle sizes. Typically,  $n'$  is evaluated as follows (Chaudhry 2007; Degoutte 2006; Graf & Altinakar 1998):

$$n' = \frac{d^{1/6}}{21} \quad (198)$$

The standard formulation (197) is based on Manning coefficients while we are using the more general friction formula of Barr-Bathurst.

The Manning coefficient can be linked to the Darcy-Weisbach coefficient through the bed shear stress formula (196):

$$\frac{\tau_b}{\rho} = \frac{\lambda}{8} U^2 = gh \frac{n^2 U^2}{h^{4/3}} \Rightarrow n = \sqrt{\lambda \frac{h^{1/3}}{8g}} \text{ and } n' = \sqrt{\lambda' \frac{h^{1/3}}{8g}} \quad (199)$$

Injecting the results of (199) and (196) in (197) yields:

$$\tau'_b = \left( \frac{\lambda'}{\lambda} \right)^{3/4} \tau_b = \rho \left( \frac{\lambda'}{\lambda} \right)^{3/4} \frac{\lambda}{8} U^2 = \rho \frac{\lambda'^{3/4} \lambda^{1/4}}{8} U^2 \quad (200)$$

$\lambda$  and  $\lambda'$  are evaluated with the Barr-Bathurst formula (123) on the basis of hydraulic results (water depth and velocity fields). For  $\lambda$ , the roughness size is  $k_s$ , responsible for global losses. For  $\lambda'$ , the roughness size is  $\min(d, k_s)$ , which is linked to the losses at the grain size level.

The Shields parameter  $\theta$  represents the ratio between destabilizing forces (bed shear stress) and stabilizing forces (particles apparent weight):

$$\theta = \frac{\tau'_b}{\rho(s-1)gd} \quad (201)$$

with  $s$  the ratio between the particles density and the fluid density  $\rho_s / \rho$ . The particle diameter set in motion is deduced from (201):

$$d = \frac{\lambda'(d)^{3/4} \lambda^{1/4} U^2}{8(s-1)g\theta_{cr}} \quad (202)$$

where  $\theta_{cr}$  is the critical shields parameter. This parameter depicts the limit above which particles of diameter  $d$  are set in motion. Its value will be discussed later.

It is interesting to notice the nonlinear and implicit form of formula (202). For given hydraulic results,  $\lambda$  and  $U$  are known. In order to compute  $d$ , a nonlinear solver should be used. We tested a classical Newton-Raphson implementation to solve equation (202). However, we experienced convergence issues due to the nonlinear nature of this equation (the expression of  $\lambda'$  is also nonlinear, by part and continuously derivable as explained by Machiels et al. (2011)) and the bad choice of an initial guess of  $d$ . In order to overcome this issue, we decided to solve equation

$$d = \frac{\lambda'(d)^m \lambda^{1-m} U^2}{8(s-1)g\theta_{cr}} \quad (203)$$

where  $m$  gradually varies from 0 to  $3/4$ <sup>14</sup>. For each value of  $m$ , equation (203) is solved thanks to a Newton-Raphson algorithm (the derivative is computed numerically). The solution of  $d$  for  $m_i$  is used as initial condition for  $m_{i+1}$ . Another solution would have been to use a the nonlinear Krylov Accelerator presented in chapter 3. This is not tested in this thesis.

The progressive method used to solve equation (203) is known as homotopy. It consists in transforming gradually an equation from a form that allows to find easily a solution (typically a linear equation) to the complete form. Further details about this method are given in chapter 6.

For the application on the Romanche River, the relative density  $s$  is considered as a known data. Field surveys performed by local actors gave a value  $s = 2.65$ .

Once  $d$  is computed, it is interesting to compare its value to the granulometry curve. This process allows figuring out which proportion of soil is susceptible to be set in motion by the flow. For the Romanche River, a field survey performed by BURGEAP (a local engineering office) in 2016 allowed to build mass granulometry curves at several locations in the River. For the section of interest we retained one of these curves. It is depicted in Figure 145. The grain

---

<sup>14</sup> First,  $m$  varies from 0 to 0.4 by 0.1 increments. Then, from 0.4 to 0.7 by 0.02 increments. Finally, from 0.7 to 0.75 by 0.01 increments. This empirical approach was found to work robustly.

sizes range from 1 mm to 10 cm. 90 % of the particles (in mass) have a diameter smaller or equal to 4 cm.

Dealing with the percentage of the granulometry curve rather than the diameter set in motion allows to visualize more clearly the effect of the flow on the riverbed. For instance, between a diameter of 2 mm and a diameter of 1 cm (+ 400 % in diameter), the difference in mass (Figure 145) is only of approximately 20 %. The increase in diameter might appear as very significant, while its translation in mass proportion relativizes this increase.

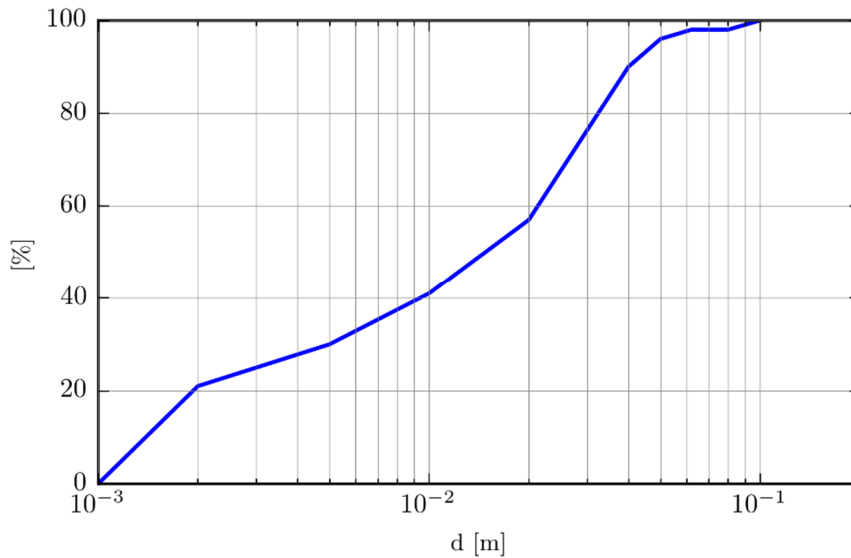


Figure 145: Granulometry in the section of interest as measured by BURGEAP in 2016

## 5.4 Uncertainty sources

As shown in previous sections and especially in Figure 142, the computation of the percentage of soil possibly set in motion relies on a relatively complex chain of computations. Many uncertainty sources could be taken into account, but we chose to focus our analysis on two particular uncertain variables: the roughness size  $k_s$  and the critical Shields number  $\theta_{cr}$ . These two sources of uncertainty are considered as epistemic since they come from our “poor” understanding of the processes that takes place.

The roughness size was fitted at 15 cm during previous studies (Goffin et al. 2015; Goffin, Piroton, Archambeau, et al. 2016; Goffin et al. 2017; Rulot et al. 2012). However, this value is likely to be inexact. Indeed, since the last calibration process, the river may have changed and a new roughness coefficient is maybe more appropriate. The analysis of the granulometry shows values of diameter of the order of magnitude of the roughness  $k_s$  but 2 to 3 times lower. This might be due to friction losses generated at a larger scale than the particle scale. Even if

it appears quite clearly that this value is uncertain, it is difficult, given the data available, to define strictly a standard deviation, even less a skewness coefficient.

In order to take into account this uncertainty, we will base our study on the way of proceeding that is used for instance in (Van Bijnen et al. 2012) where the distribution shape is chosen according to an expert judgement. In our case, we stick to a normal law, we fix the mean at 0.15 m (the value fitted during previous studies) and the standard deviation at 0.05 m. The choice for the mean value is relevant with previous studies and previous fittings. The choice for a standard deviation at 5 cm allows to reach the typical grain sizes at  $\bar{k}_s - 2\sigma_{k_s}$  (approximately at a percentile 2.5 %). We based our choice for a normal law on Bolle's justification to maximize the entropy (Bolle 1988).

The critical Shields parameter is a value that characterizes the beginning of sediments motion. Several authors proposed values according to the particle diameters and the nature of the transport (initiation of motion or suspension). These values are summarized in Figure 146, which is taken from (Van Rijn 1993). The curves presented in Figure 146 present a plateau that begins at diameters of 5 mm-10 mm (when the water is considered to have a temperature of 15 °C). Looking at the granulometry curve (Figure 145) confirms that most grains (60 to 70 % in mass) have a diameter larger than this threshold. The values of the plateau for various authors are reported in Figure 147. We decide to characterize the uncertainty on the critical Shields parameter by a normal law centered at 0.2. This value is the central value defined by van Rijn for the beginning of suspension, which can be understood as the limit for significant transport. Bagnold defined higher values which are not represented in Figure 147 due to axis limits. The standard deviation is chosen at 0.07 in order to encompass with a reasonable probability the lower values defined by Shields and Engelund.

Once more, the definition of the uncertainty on the critical Shields value has a part of subjectivity. It is important to notice that, in practice, this kind of choices should be made in agreement with stake holders and that the results might depend largely on these choices. Moreover, other uncertainties can affect the results and are not taken into account here. The main goal, here, is to prove the applicability of the uncertainty method on a real-world case. Results should not be understood as absolute. It is rather the comparison between the current and planned situations that is of main interest.

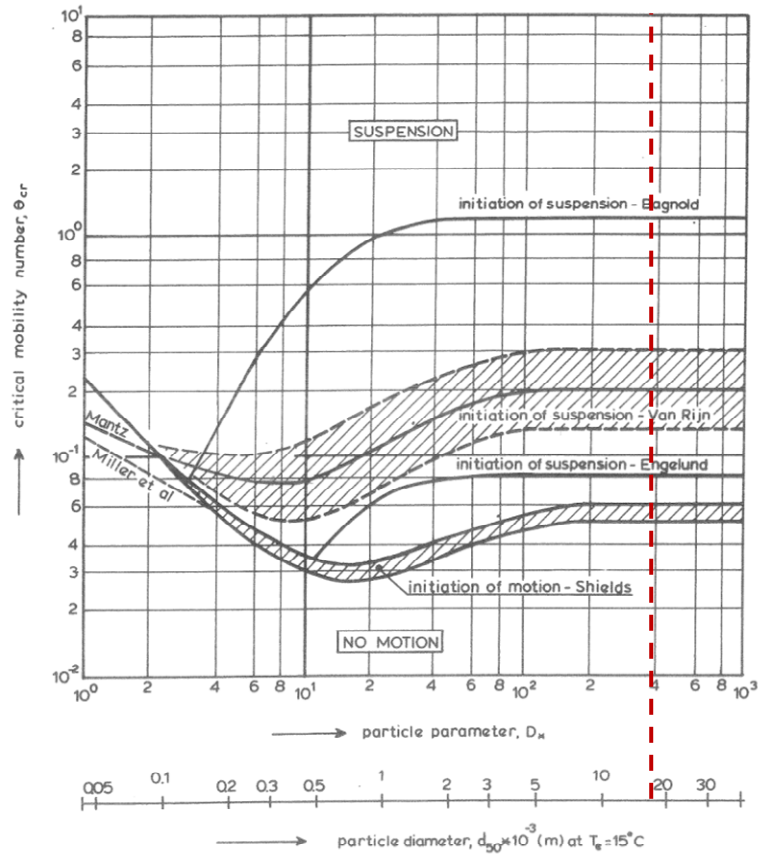


Figure 146: Critical Shields parameters according to various authors (reproduced from (Van Rijn 1993)). Red dashed line reports the particle  $d_{50}$  for the Romanche case study.

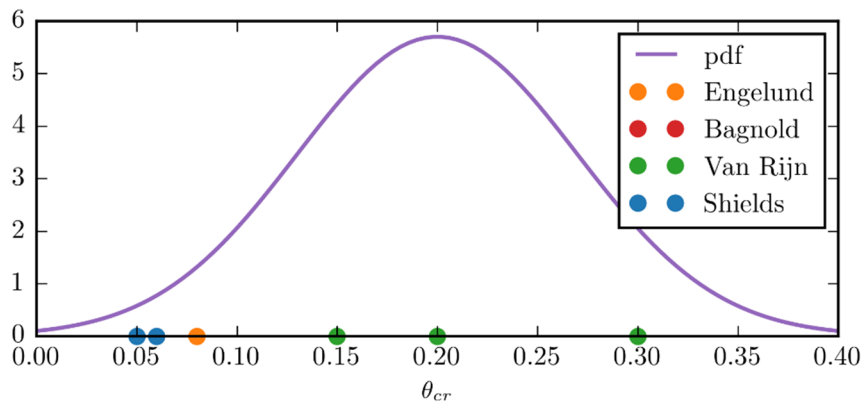


Figure 147: Critical Shields parameters according to various authors and chosen normal law

Only PMM method is used for this case due the computational cost of these 2-D simulations. The points used by PMM are depicted in Figure 148. Only the points along the  $k_s$  axis require a full hydraulic computation. The two other points can rely on the hydraulic results computed for  $k_s = 0.15$  m. For these two points, only the post-processing of hydraulic results into a diameter and a granulometry percentage is required. The uncertainty analysis algorithm is adapted in order to avoid unnecessary hydraulic computations.

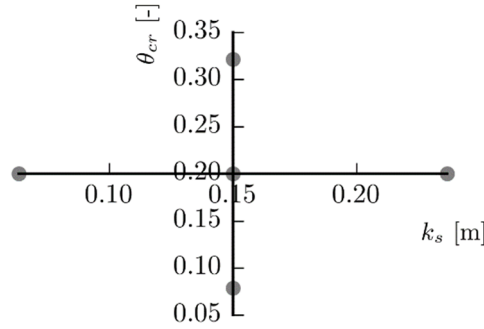


Figure 148: Points used in the uncertainty analysis (PMM)

## 5.5 Results and discussion

This results section is split into two parts. A first part presents hydraulic results and the effect of undamming on the hydraulic fields (water depth and velocity). The second part is about the uncertainty analysis results on the indicator for the bed stability.

The graphs produced in this section focus on the zone on influence of the undamming works. Some larger maps of the entire domain are given in appendices C.2 and C.3.

### 5.5.1 Hydraulic results

As shown in Figure 148, five points are required for the uncertainty analysis. However, only three different hydraulic computations are needed. The difference between each hydraulic computation is the roughness size  $k_s$ . We compute the model with  $k_s = 0.0634$  m,  $k_s = 0.15$  m and  $k_s = 0.237$  m. The computation time required for the hydraulic model is approximately 3 hours for each roughness size.

First, we focus our analysis on the water levels. A longitudinal profile is given in Figure 149. Current and planned situations are represented with the water levels corresponding to the three  $k_s$  used in the uncertainty analysis. Several comments can be formulated on the basis of Figure 149.

First, the effect of the roughness size is clearly visible. Logically, lower  $k_s$  values produce smaller water depths since friction losses are lower. Then, removing the Keller dam and deepening the river upstream of this dam produces naturally a decrease in water levels. The decrease is effective up to a natural control section located around  $x = 3050$  m. Upstream of this natural control section, undamming the river has no more significant effect. This first observation suggests that the undamming works will only have potential effects on the sediments transport over approximately 1.1 km.

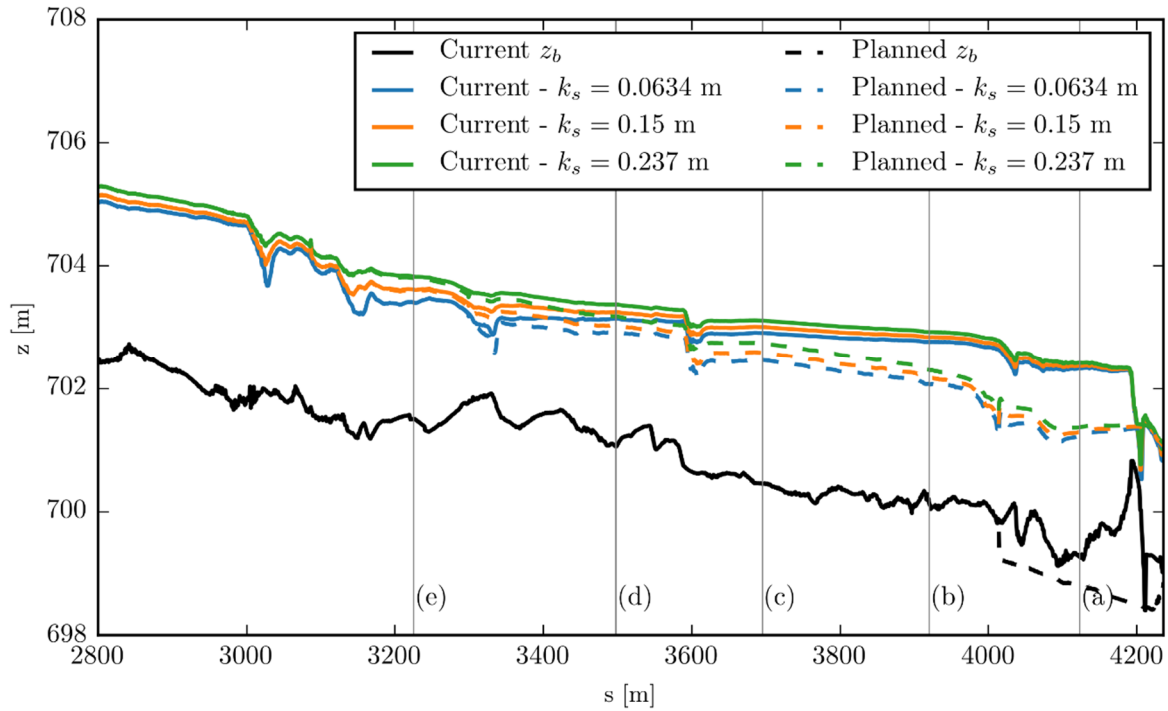


Figure 149: Bed elevation and water levels for the current and planned situations, considering the three roughness sizes used for the hydraulic computations

For the sake of completeness, 2-D maps of the water levels are provided in Figure 150, Figure 151 and Figure 152 for each roughness size and each situation (current and planned). These maps do not provide any additional information about the evolution of the water levels, which is well summarized in Figure 149. However, the reader is able to figure out the area occupied by the river and that the steep banks avoid a large expansion of it.

2-D maps of the norm of the velocity field are given in Figure 153, Figure 154 and Figure 155. Most obvious differences are present downstream of the new dam. Indeed, in that region, velocities tend to increase.

Confirmations for the increase of the velocity and a decrease in the water depths are given in Figure 156, Figure 157 and Figure 158 where a differential in the water depth and the norm of the velocity between the current and the planned situations are given. Negative values mean that there is a decrease in the water depth/velocity after the dam removal. These maps show that the largest differences are present from the dam up to 200 m upstream of the new dam. In this area, the water depth mainly decreases while the velocity increases. These conditions are favorable for higher sediment transport after dam removal. This will be confirmed and quantified in next section.

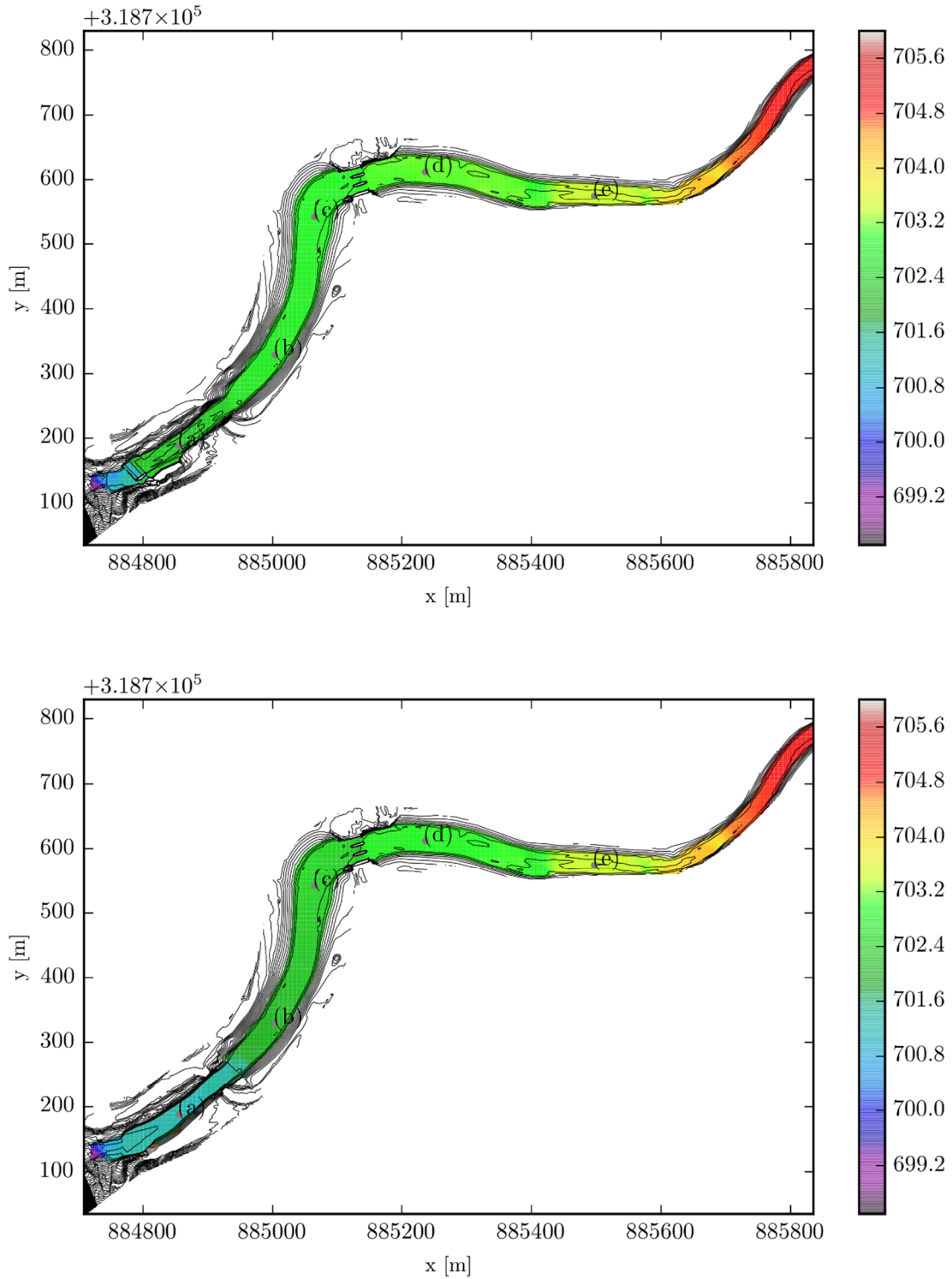


Figure 150: Water levels [m] for  $k_s = 0.0634$  m in the current situation (upper) and considering removal plans (lower)

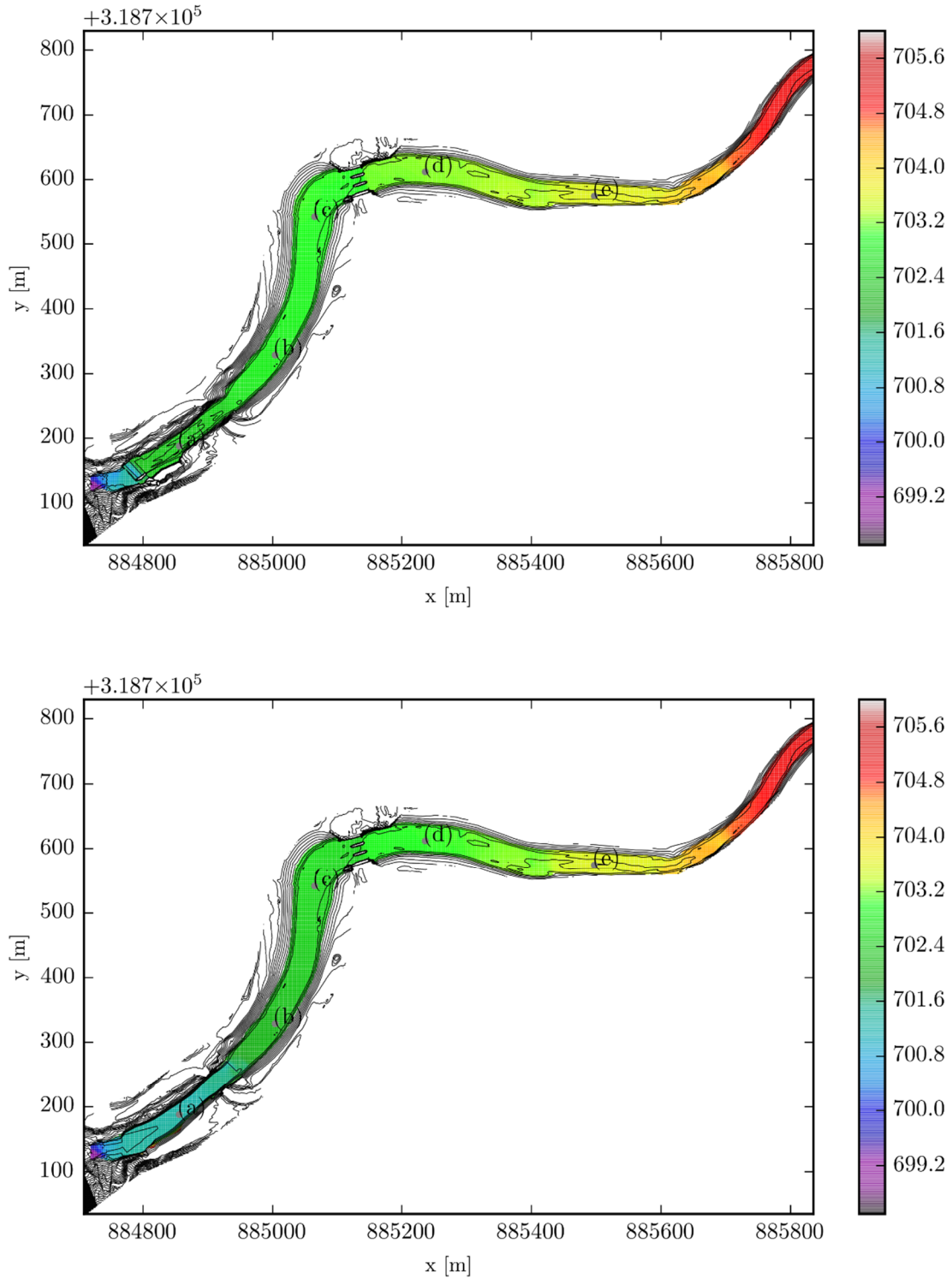


Figure 151: Water levels [m] for  $k_s = 0.15$  m in the current situation (upper) and considering removal plans (lower)

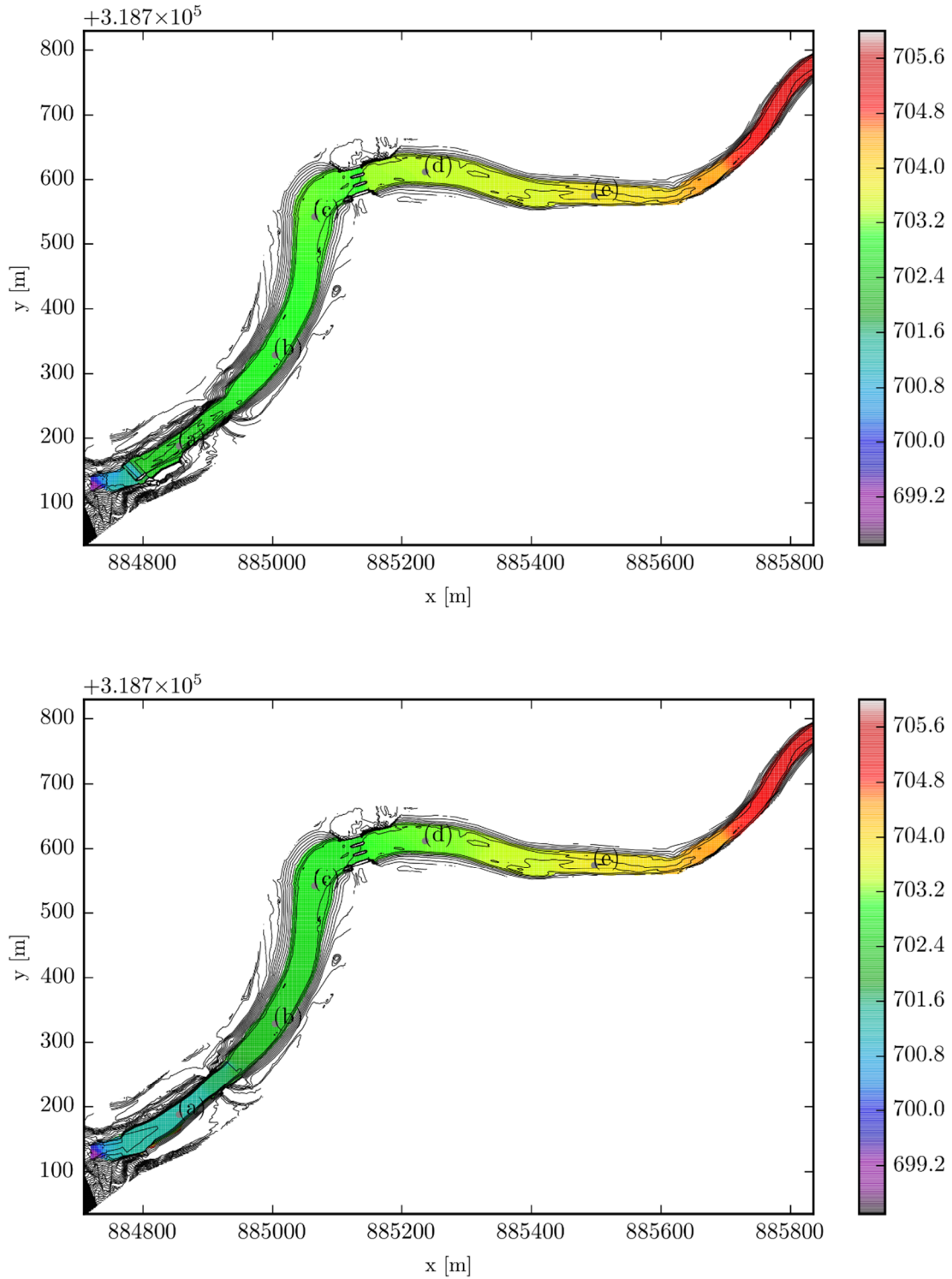


Figure 152: Water levels [m] for  $k_s = 0.237$  m in the current situation (upper) and considering removal plans (lower)

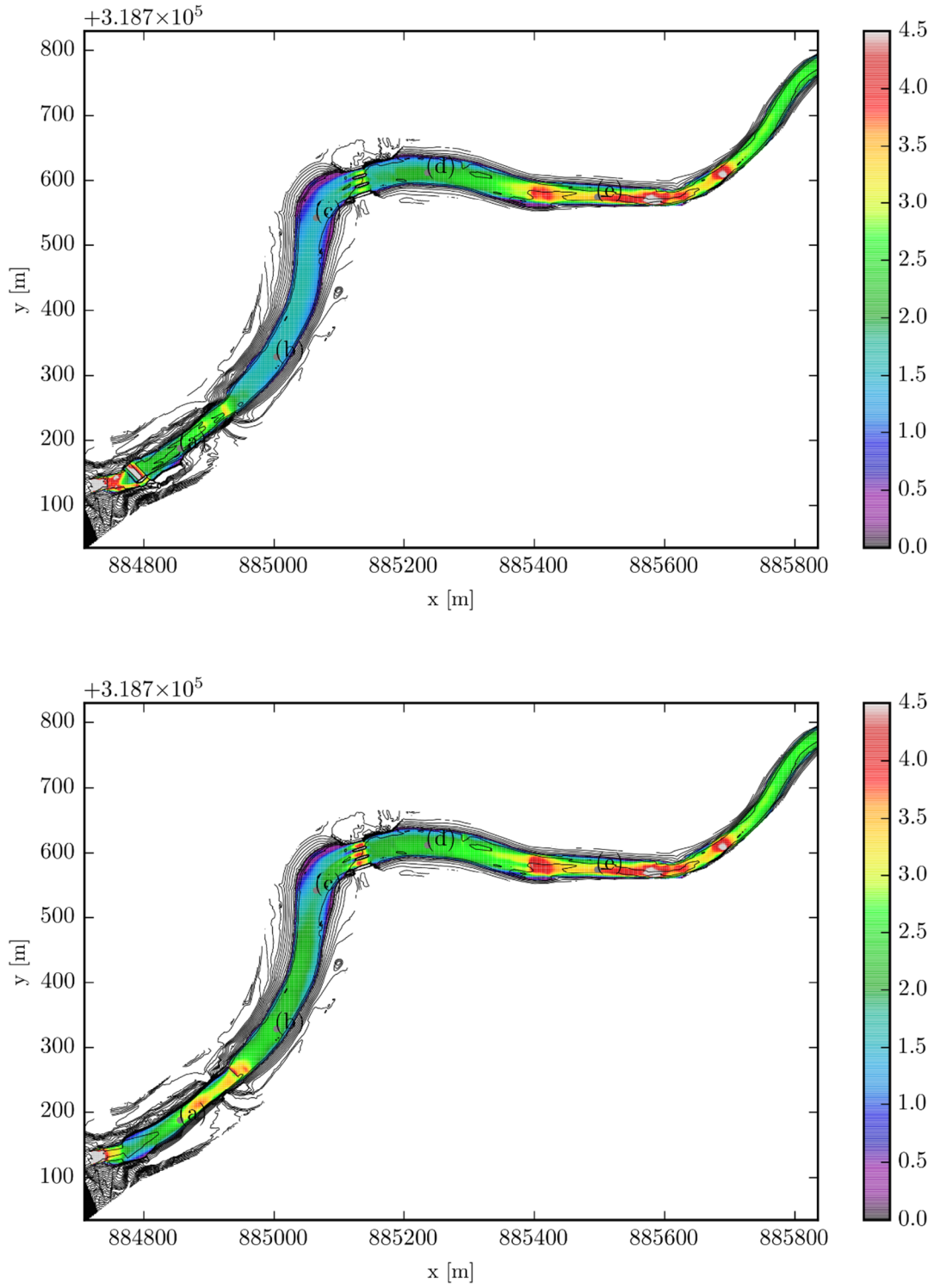


Figure 153: Velocity [m/s] for  $k_s = 0.0634$  m in the current situation (upper) and considering removal plans (lower)

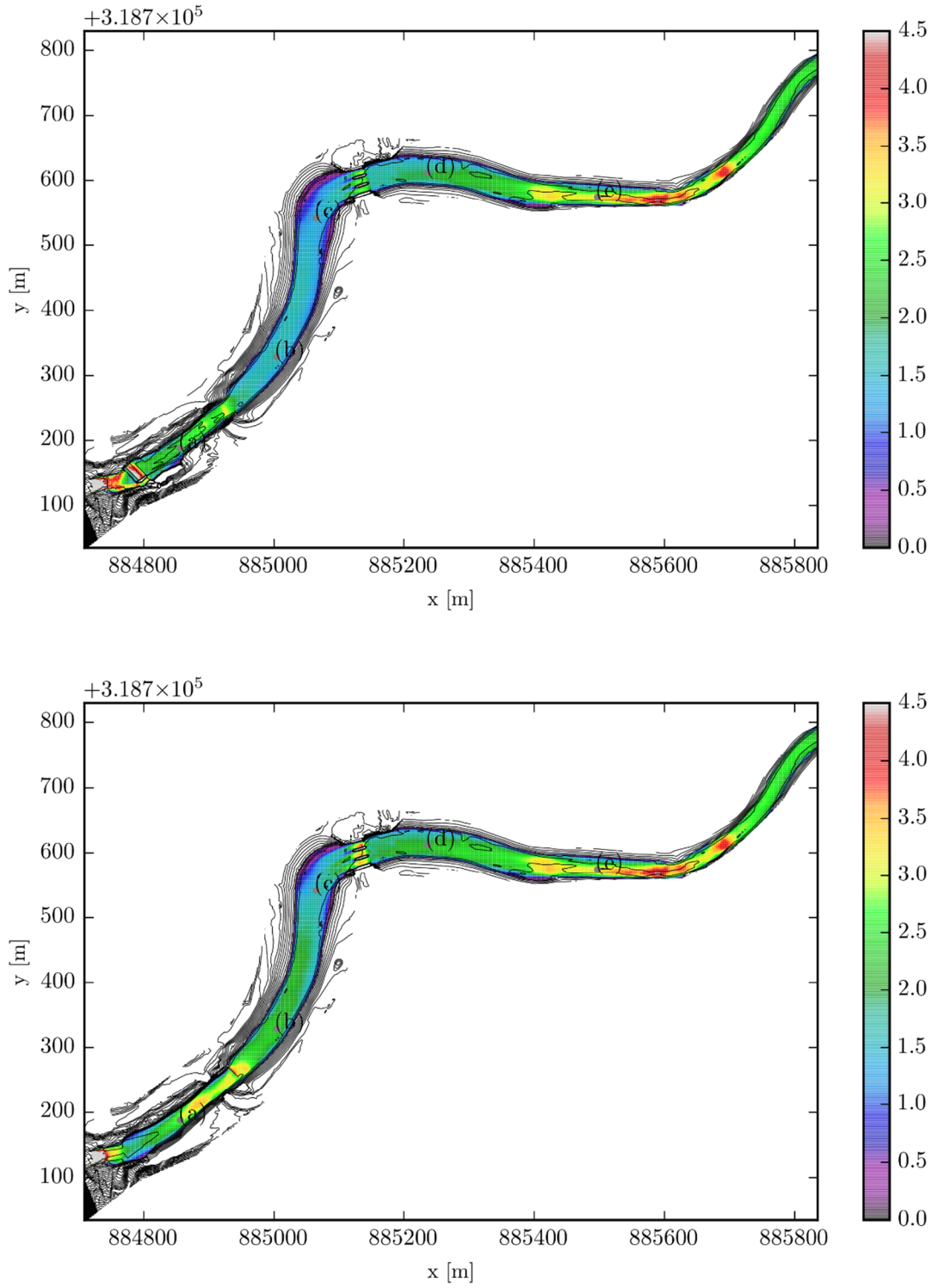


Figure 154: Velocity [m/s] for  $k_s = 0.15$  m in the current situation (upper) and considering removal plans (lower)

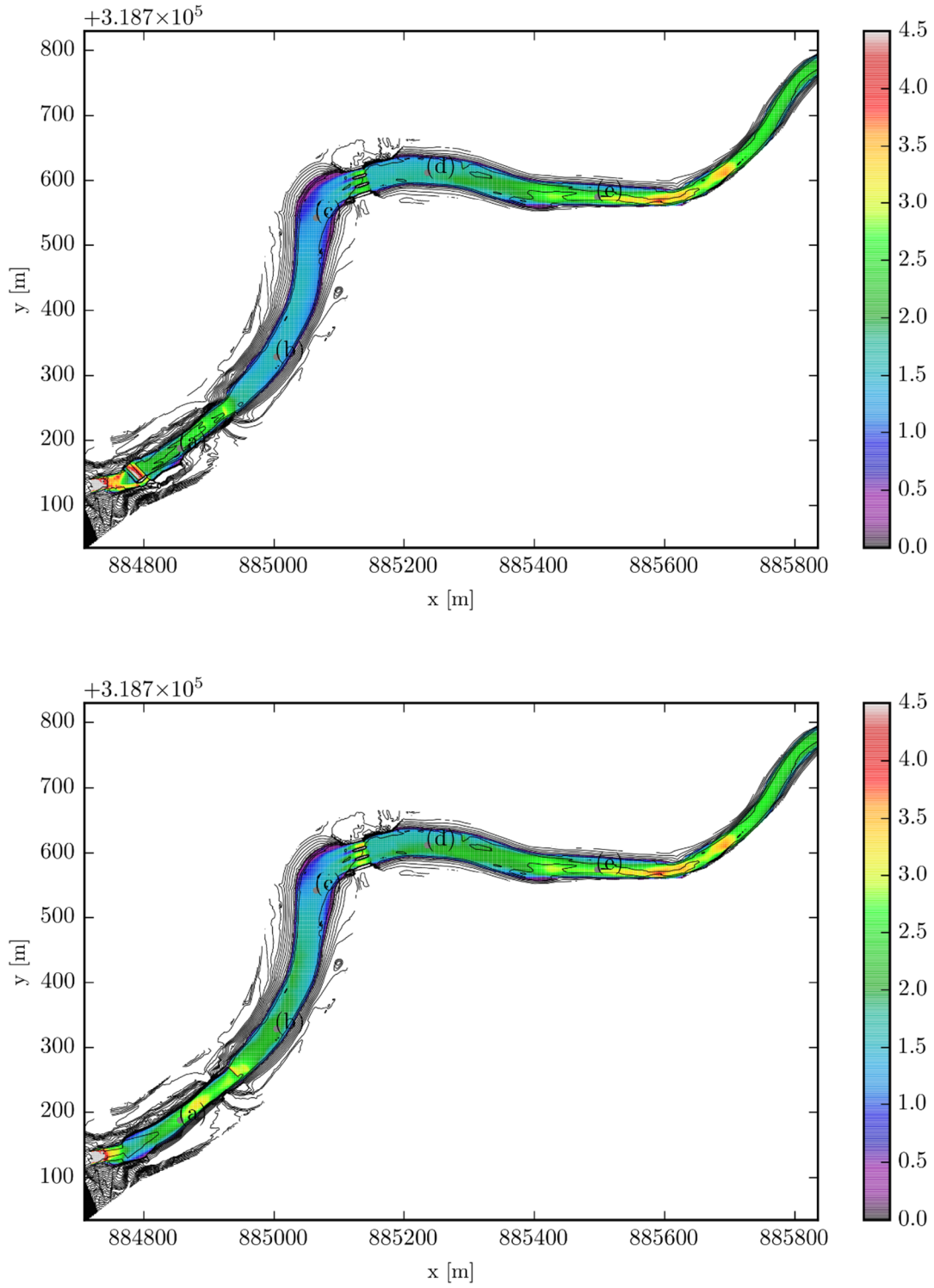


Figure 155: Velocity [m/s] for  $k_s = 0.237$  m in the current situation (upper) and considering removal plans (lower)

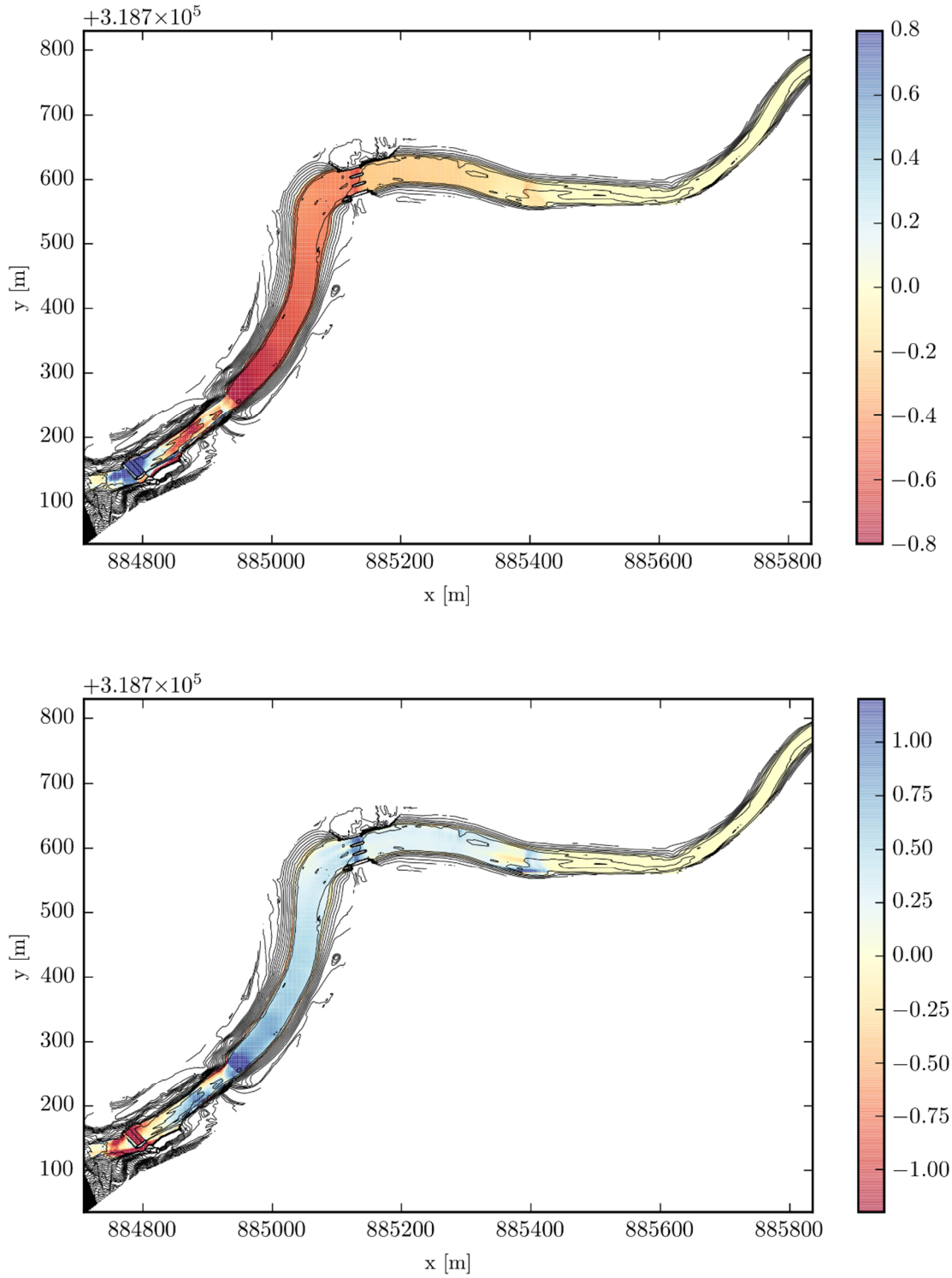


Figure 156: Differential of water depth (upper plot, [m]) et velocity (lower plot, [m/s]) between the current (c) and the planned (p) situations ( $p - c$ ) for a discharge of  $150 \text{ m}^3/\text{s}$  and  $k_s = 0.0634 \text{ m}$

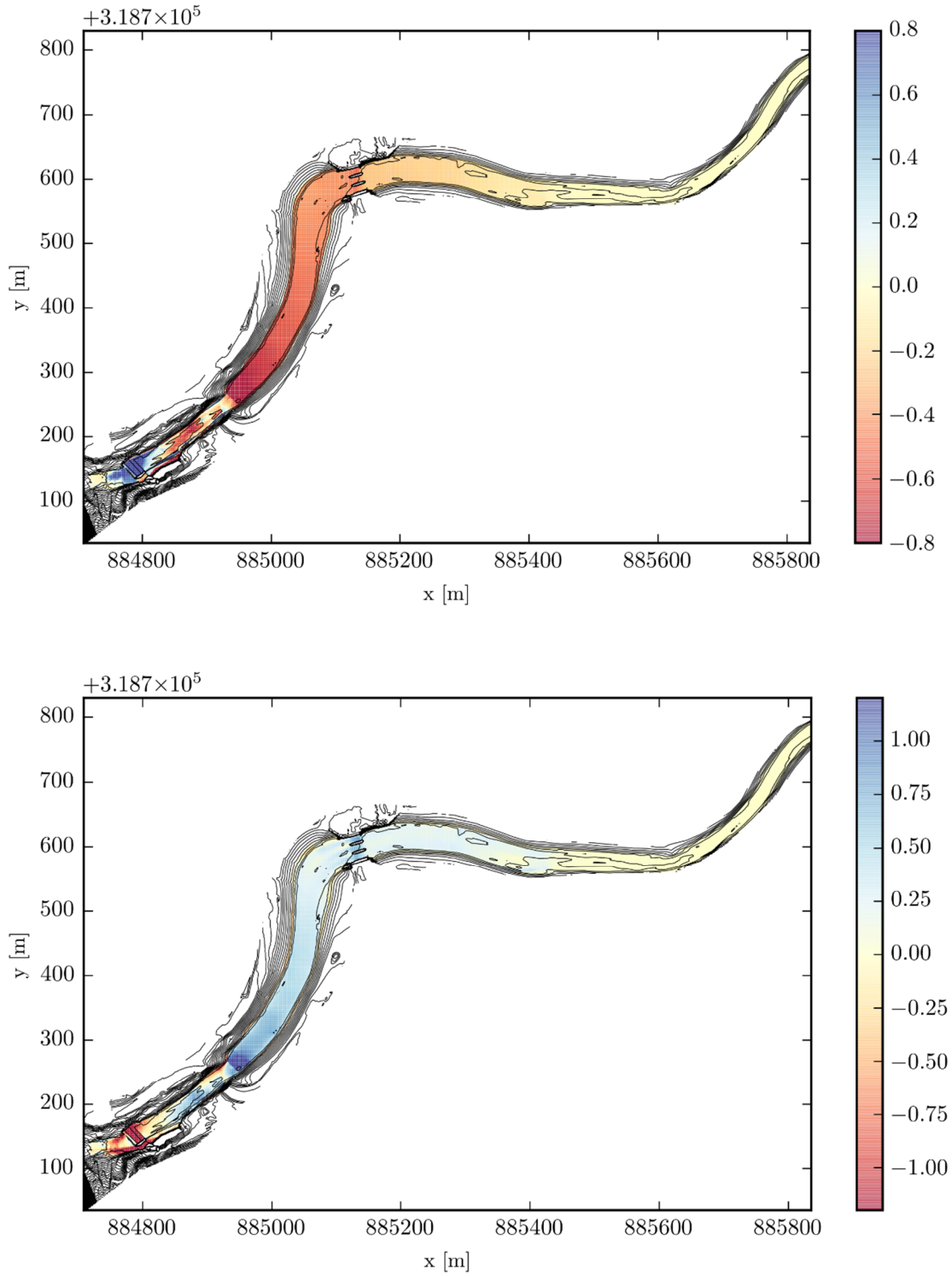


Figure 157: Differential of water depth (upper plot, [m]) et velocity (lower plot, [m/s]) between the current (c) and the planned (p) situations ( $p - c$ ) for a discharge of  $150 \text{ m}^3/\text{s}$  and  $k_s = 0.15 \text{ m}$

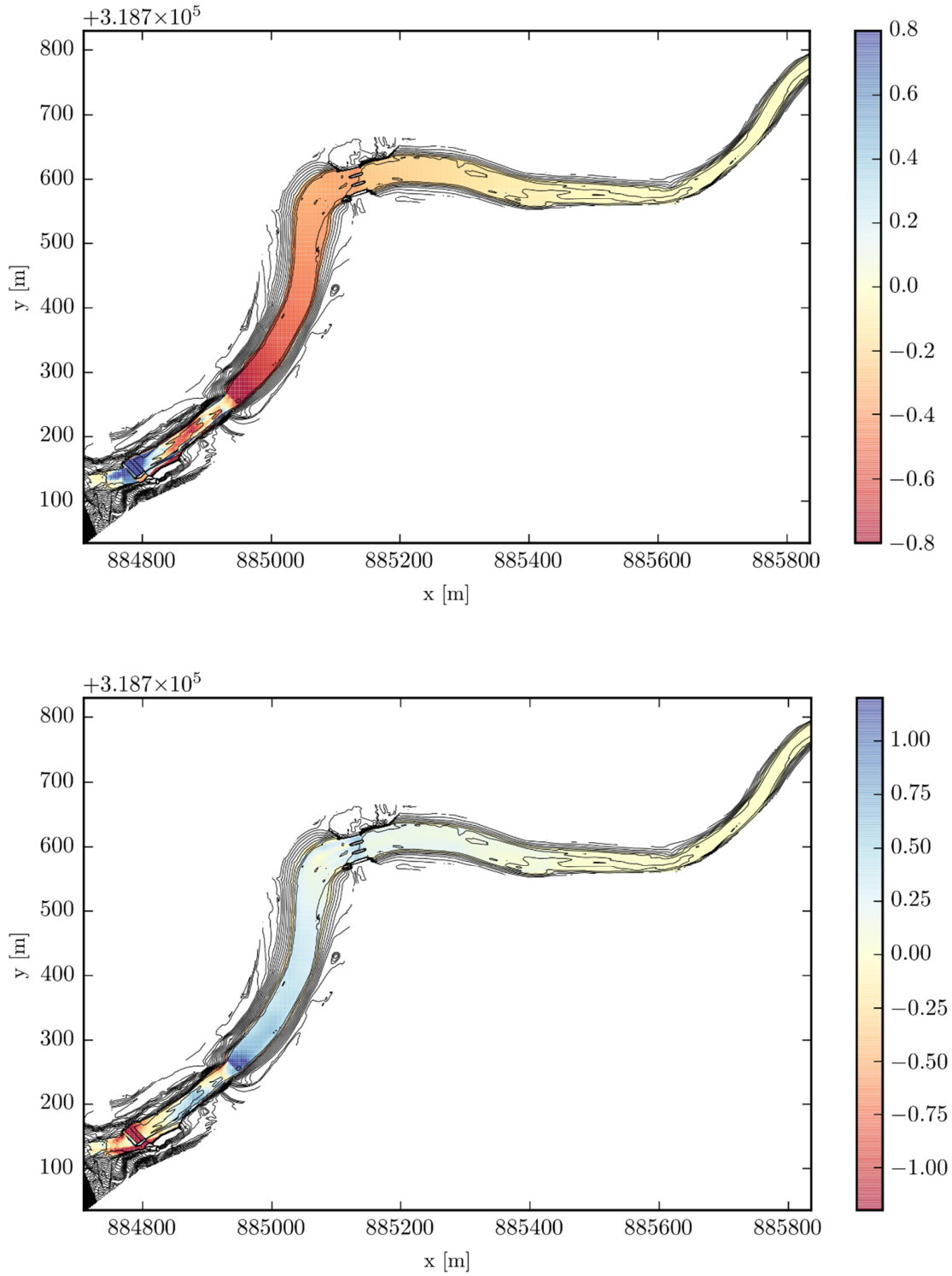


Figure 158: Differential of water depth (upper plot, [m]) et velocity (lower plot, [m/s]) between the current (c) and the planned (p) situations ( $p - c$ ) for a discharge of  $150 \text{ m}^3/\text{s}$  and  $k_s = 0.237 \text{ m}$

### **5.5.2 Indicator on the river bed stability**

The results presented in this section take into account the 5 points depicted in Figure 148 (and not only the 3 points necessary for the hydraulic computations). PMM is used to compute the uncertainty on the indicator for riverbed stability. This indicator is the percentage of soil that is set in motion by the flow. It is computed thanks to a granulometry curve and the diameter computed from equation (202). The comparison between the indicators before and after dam removal as well as the magnitude of the indicator can help to figure out the effect of dam removal on the evolution of sediment transport. The results shown in this section are valid for a 150 m<sup>3</sup>/s discharge. For a comprehensive study on the effect of the removal of the Keller dam, several other discharges should be tested.

The mean, standard deviation and skewness coefficients are given in Figure 159, Figure 160 and Figure 161. Differences between the mean values in the current and planned situations can be observed from the removed dam to upstream of the new dam. This is consistent with hydraulic observations made in previous section.

The standard deviation does not seem to be significantly affected by the presence of the “seuil Keller”. This can be understood by the fact that the width of the distribution is mainly due to the variability of the roughness size and of the critical Shields. The presence or absence of the dam affects hydraulic conditions, but these differences do not seem to infer significantly on the width of the distribution of the uncertain output. On the other hand, these different hydraulic conditions influence the value of the skewness coefficient as it can be observed in Figure 161. At some locations, the skewness coefficient changes its sign. This will be highlighted later.

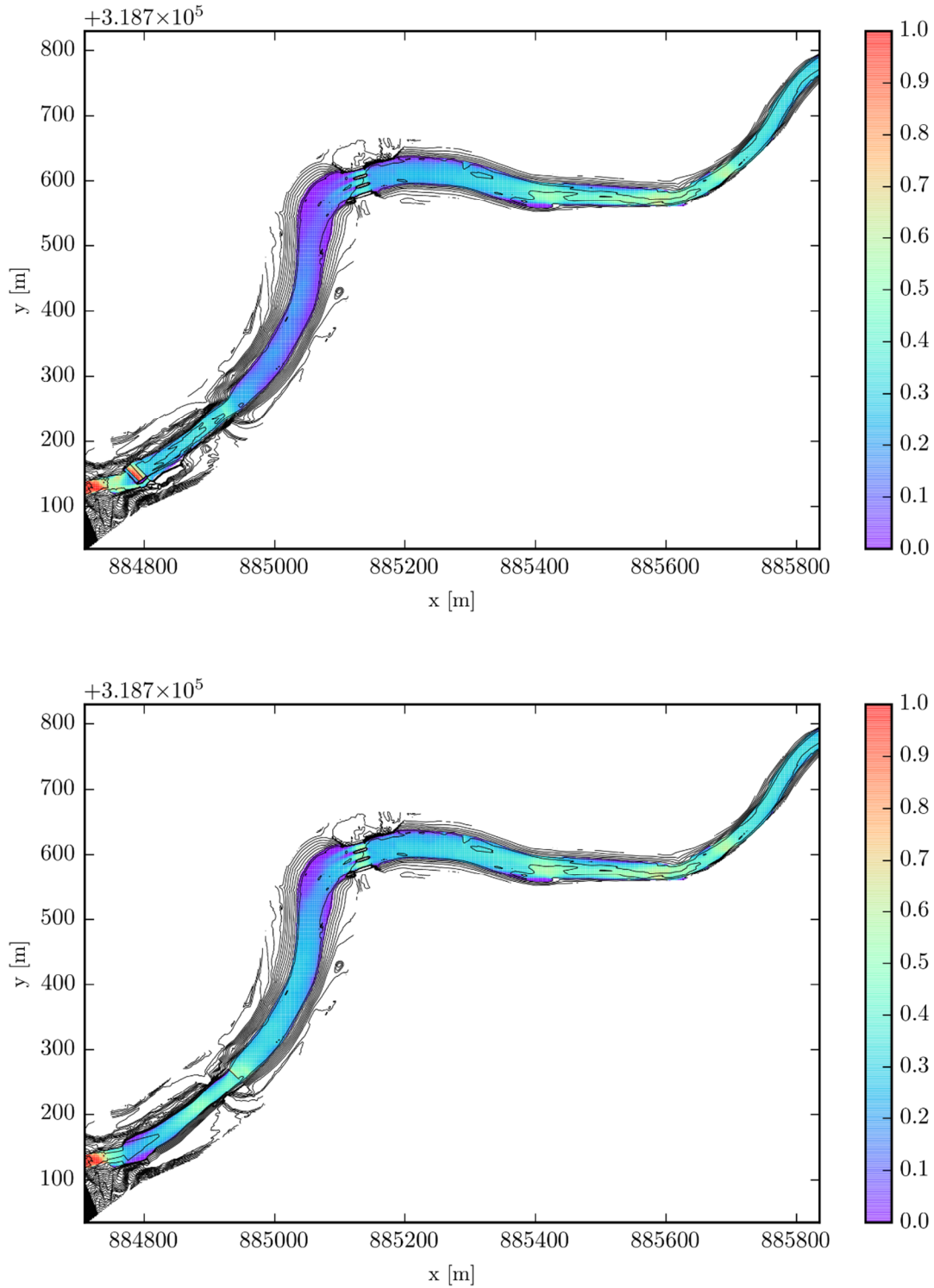


Figure 159: Mean proportion of bed soil that is set in movement by a  $150 \text{ m}^3/\text{s}$  discharge in the current (upper plot) and planned (lower plot) situations

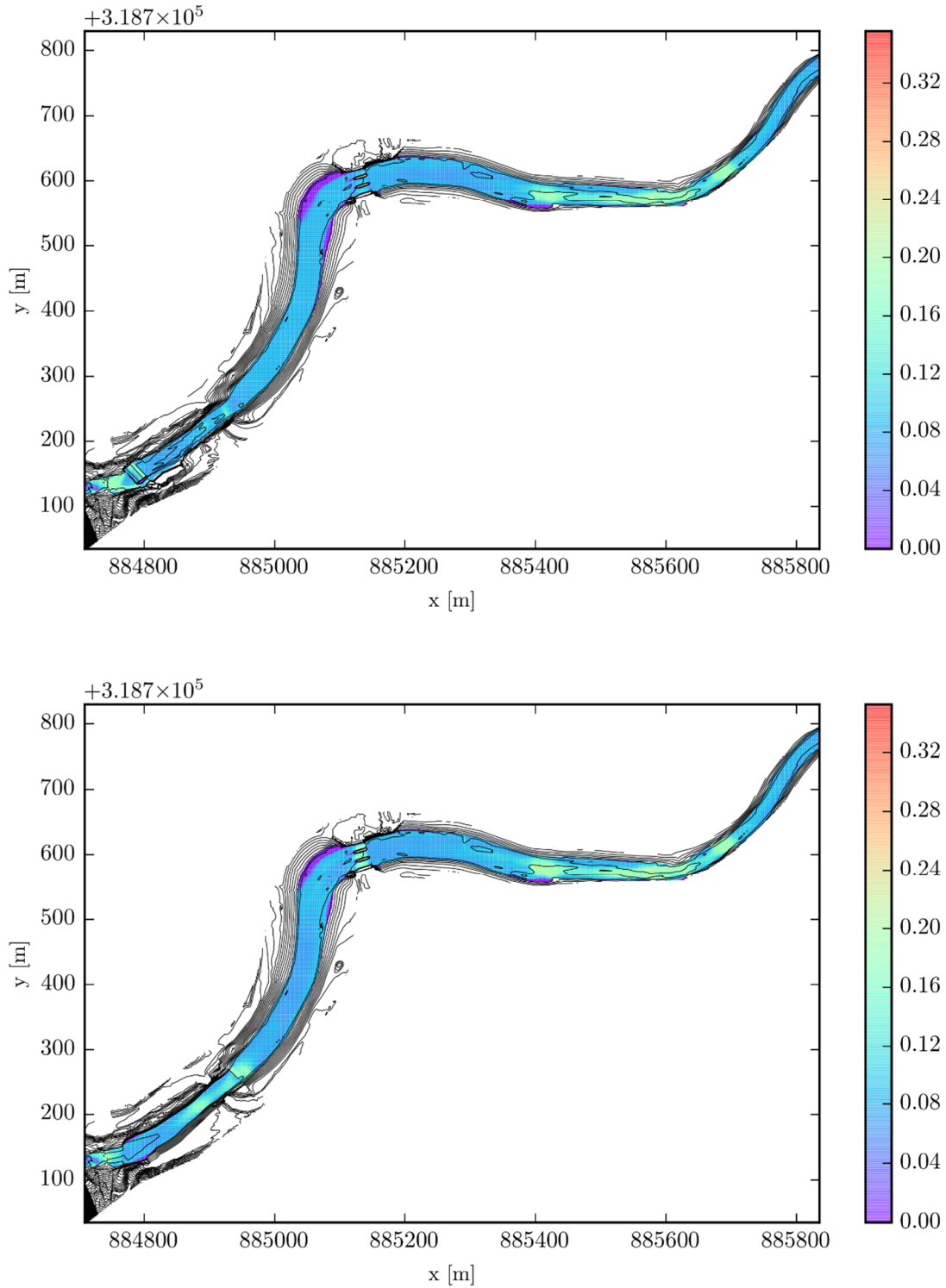


Figure 160: Standard deviation of the proportion of bed soil that is set in movement by a  $150 \text{ m}^3/\text{s}$  discharge in the current (upper plot) and planned (lower plot) situations

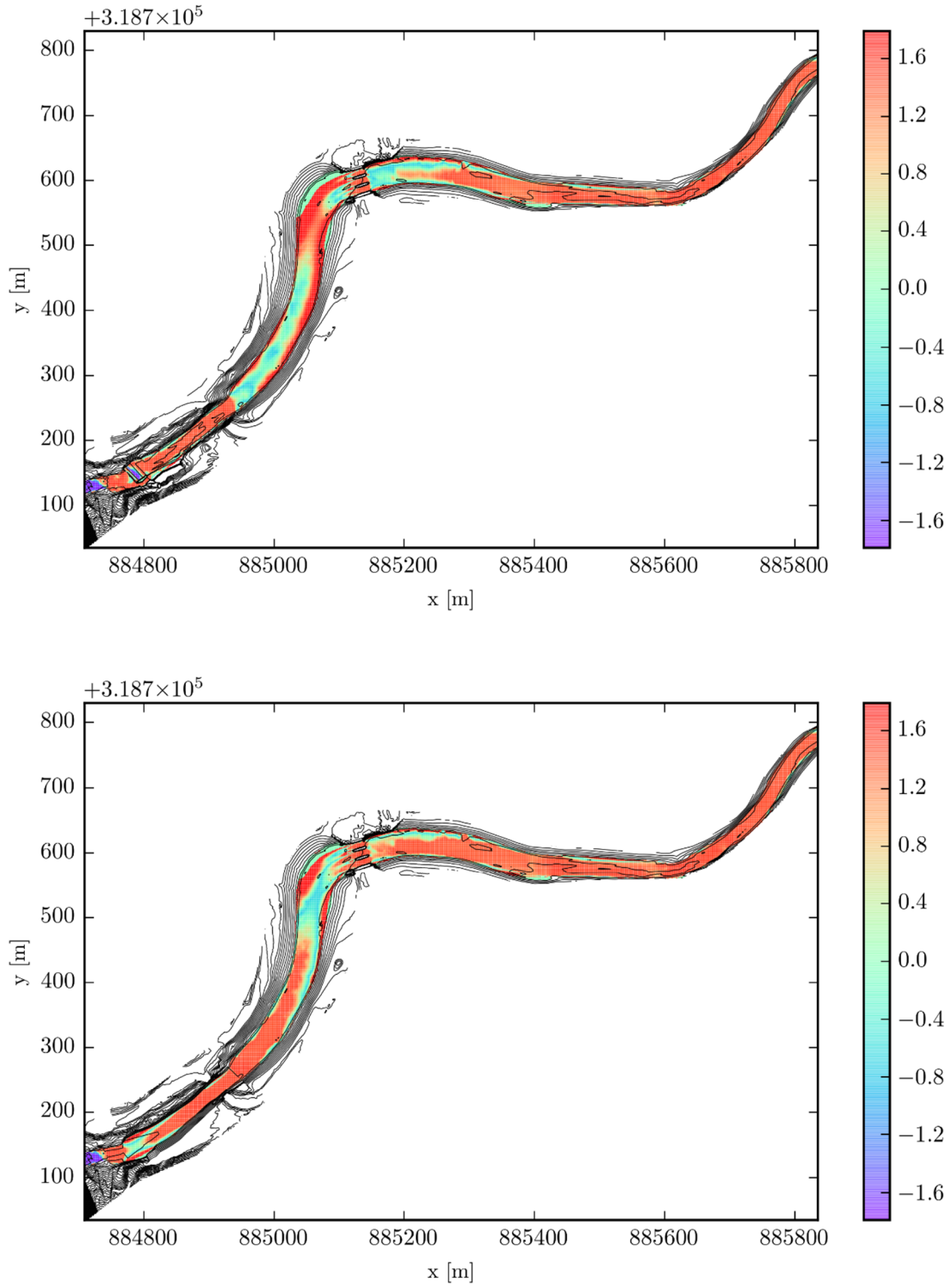


Figure 161: Skewness coefficient of the proportion of bed soil that is set in movement by a  $150 \text{ m}^3/\text{s}$  discharge in the current (upper plot) and planned (lower plot) situations

In order to compare the distributions before and after the dam removal, two maps of ratios are plotted: the mean and the standard deviation. The first ratio is representative of the shift of the distribution while the second one is representative of the widening of the distribution.

The first map (Figure 162) is the ratio between the means of the percentage of soil set in motion by the flow in the planned and current situations. The color scale used allows to visualize easily the effect of undamming:

- dark green is used when the mean is lower after removing the Keller dam
- light green is used when almost no change is observed
- yellow is used when the mean is larger after dam removal (from + 20 % to + 100 %)
- orange and red are used when the increase in the mean is the most significant (more than + 100 %)

As expected from previous results, the bigger differences appear from the removed dam up to the new dam. The magnitude of the effect is slightly different downstream of the “Pont de la Vena” and upstream of it. Between the removed dam and the bridge, the increase is not significant. This is due to the deepening of the river in the planned situation. Upstream of the bridge, the increase is at least of 100 % and can reach even values higher than + 200 % close to the banks. This region is the most impacted by the dam removal. Further comments will be provided later.

The second map (Figure 163) is the ratio between the standard deviations before and after the dam removal. The color scale used is slightly different from the previous one:

- dark green is used when the extent of the distribution is much lower after removing the Keller dam
- light green is used when the extent of the distribution is slightly lower after removing the Keller dam
- yellow is used when the extent of the distribution is slightly higher after removing the Keller dam
- orange and red are used when the extent of the distribution becomes significantly higher

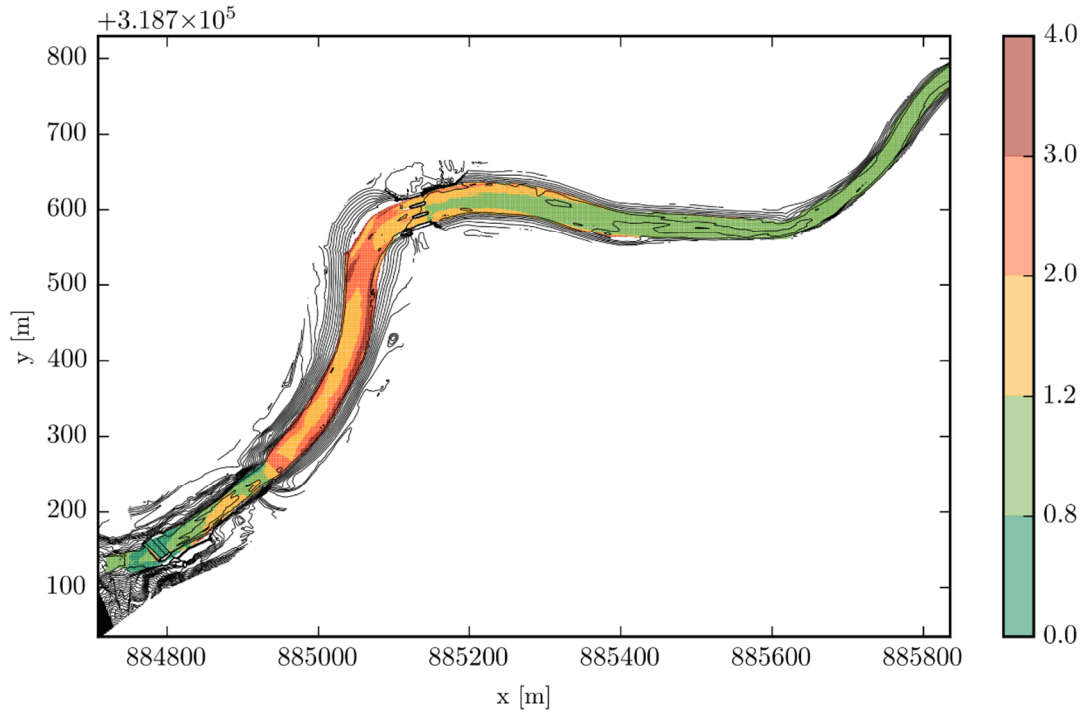


Figure 162: Ratio between the mean proportions of bed soil that is set in movement in the planned situation and in the current situation for a  $150 \text{ m}^3/\text{s}$  discharge

Once more, the region impacted by the dam removal can be divided in two parts:

- the section where the river is deepened in the planned situation and,
- upstream of the “Pont de la Vena” up to the new dam.

In the deepened region, blueish colors can be observed, meaning that the extent of the distribution is mainly increased. Upstream of this deepened region, this is mainly greenish colors that are visible, meaning that the extent of the distribution is tightened. Exceptions are at the new dam, where a large increase of the standard deviation is noticed, and on a few meters downstream of the new dam where the extent of the distribution is slightly increased at some nodes.

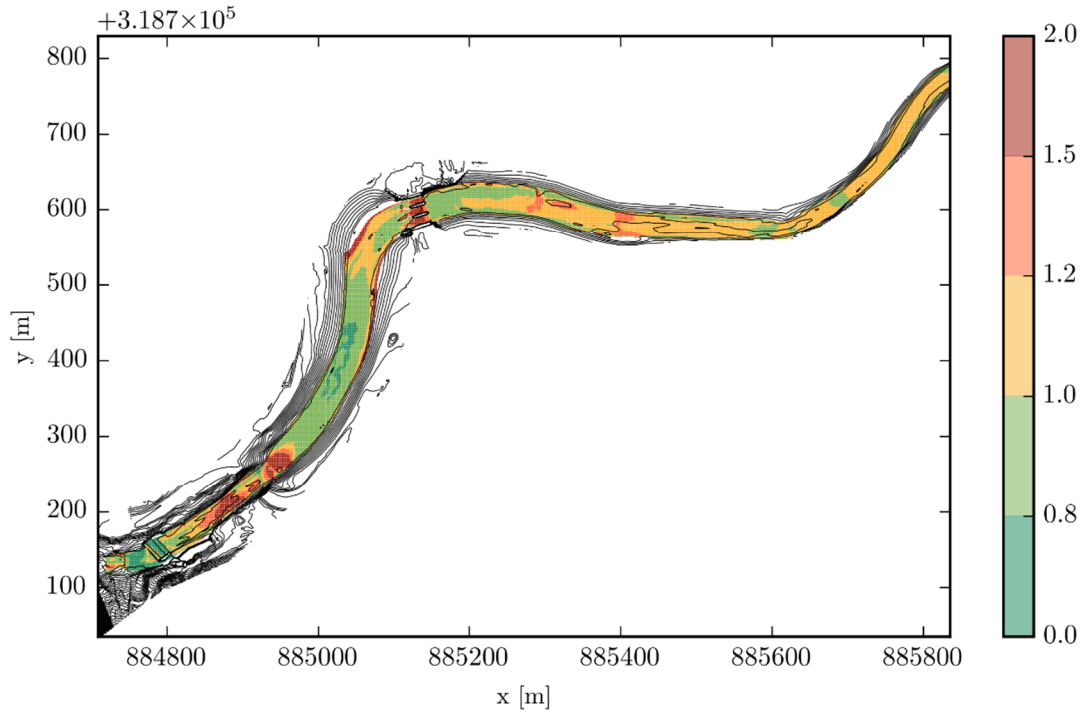


Figure 163: Ratio between the standard deviations of the proportions of bed soil that is set in movement in the planned situation and in the current situation for a  $150 \text{ m}^3/\text{s}$  discharge

A finer analysis of the distributions can be made based on Figure 164 and Figure 165. For five points chosen in this figure (the values of the moments for these points are given in Table 32), the distributions of the percentage of soil set in motion is plotted in the current (blue) and planned situations (red). The normal (Figure 164) and gamma (Figure 165) distributions respect the moments provided by PMM. This does not guarantee to have the distributions included between 0 and 1, the physical bounds. This is why some distributions in Figure 164 and Figure 165 might appear unphysical with tails out of physical bounds. Such a situation may come from a poor choice of a theoretical law or errors arising from the use of PMM. However, due to relatively large values of the skewness coefficient (see Table 32), the gamma law appears to be more suited to this case, compared to a normal distribution. This gamma law will be used for the following discussion.

First, we will focus on the physical interpretation for a fixed situation. In the current situation, it appears that the distribution of the percentage of soil set in motion moves from higher values to lower values when moving from downstream to upstream ((a), then (b), then (c)). After ((d), then (e)), the distribution moves toward higher values. The behavior from (a) to (c) can be defined as counter intuitive at first sight. Indeed, in the presence of a dam, velocities tend to decrease and water depths to increase at the approach the structure. These conditions are less favorable to sediment transport. This is not what is observed in Figure 165.

The behavior in Figure 165 can be understood by an analysis of Figure 149 and Figure 154 ((a), (b), (c), (d) and (e) points are reported in these figures). In Figure 149, we can see that the water depths around points (a), (b) and (c) are not significantly different. Moreover, the velocity depicted in Figure 154 shows that higher values can be observed downstream such that  $U_{(a)} > U_{(b)} > U_{(c)}$ . This difference in velocities is due to a narrower channel downstream of the “Pont de la Vena”. For a constant water depth and an increasing velocity, the shear stress increases. This explains the behavior of distributions in Figure 165.

	Current situation			Planned situation		
	mean	$\sigma$	$\gamma$	mean	$\sigma$	$\gamma$
(a)	0.306	0.077	1.453	0.380	0.109	1.502
(b)	0.157	0.088	-0.098	0.302	0.077	1.467
(c)	0.077	0.086	1.481	0.181	0.092	-0.563
(d)	0.246	0.073	0.696	0.288	0.073	1.477
(e)	0.461	0.154	1.483	0.467	0.158	1.501

Table 32: Statistical moments obtained by PMM for the proportion of the bed soil that is set in movement at 5 locations

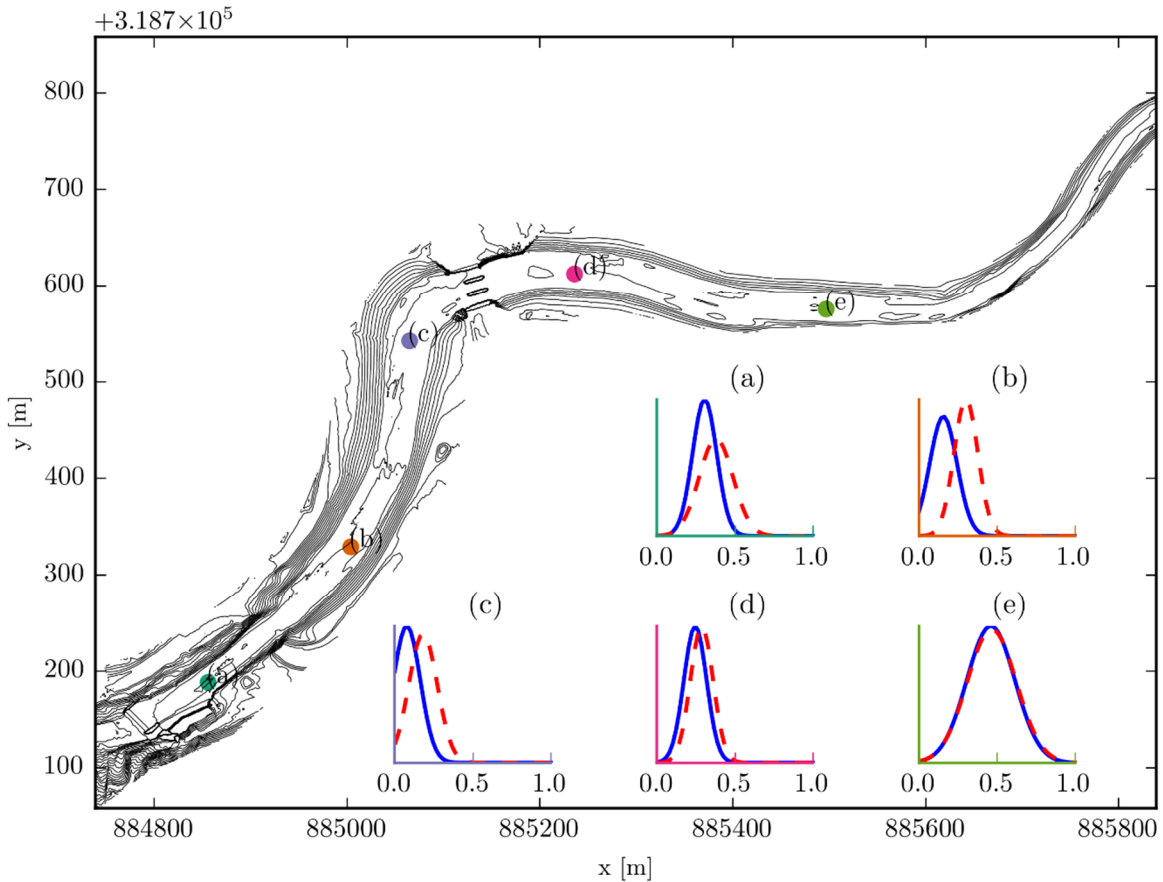


Figure 164: Distributions (normal law) of the proportion of the bed soil that is set in movement at 5 locations (plain blue line = current situation, dashed red line = planned situation)

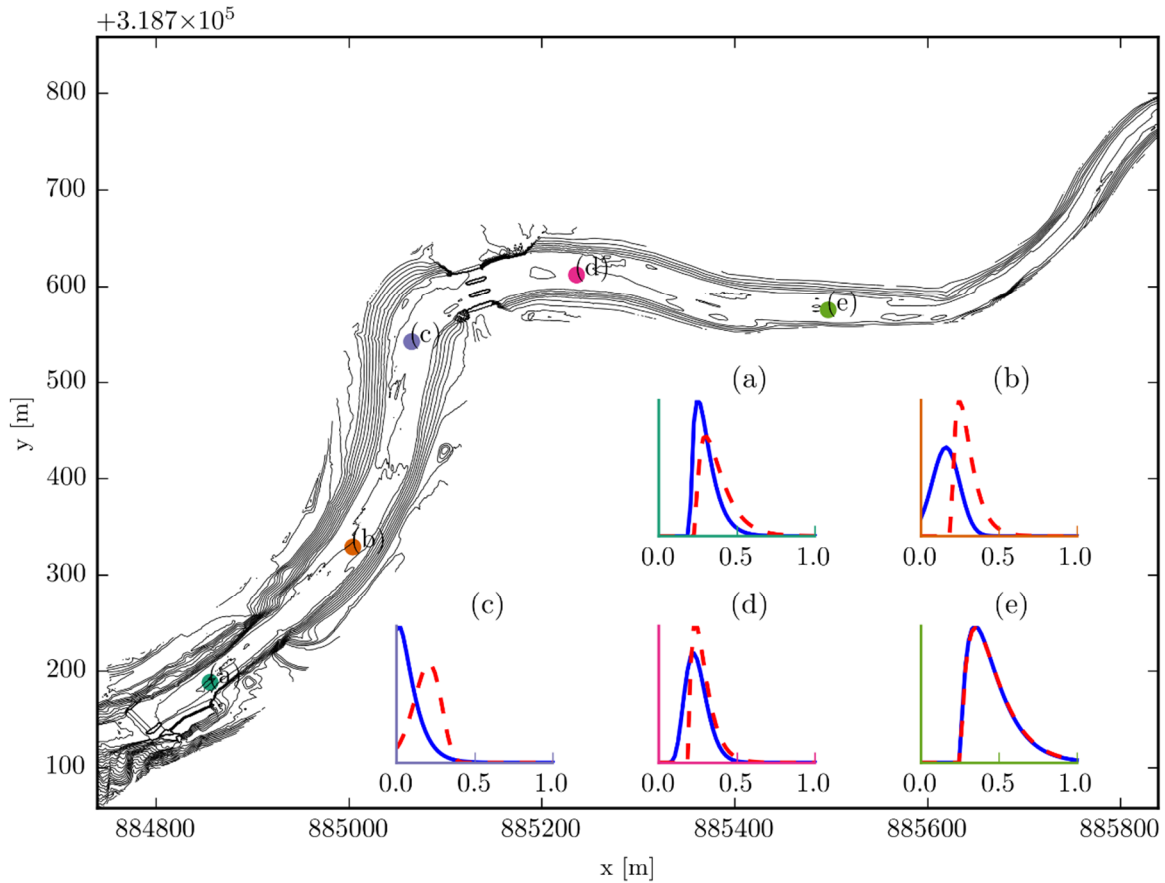


Figure 165: Distributions (gamma law) of the proportion of the bed soil that is set in movement at 5 locations (plain blue line = current situation, dashed red line = planned situation)

Concerning the comparison between the current and planned situations, a first comment concerns the most upstream point (e). It shows that removing the Keller dam does not have any effect at this location. This is in line with previous observations where we showed that hydraulic results were not impacted upstream of a natural control section. Concerning the other points, as stated earlier, distributions are shifted to the right after removing the Keller dam. Biggest changes appear to be at (b) and (c) points. This corresponds to the area identified earlier where biggest impacts were noticed.

From these observations, we are able to conclude that the effect of removing the Keller dam for a  $150 \text{ m}^3/\text{s}$  is mainly felt from the dam up to the new dam. Moreover, an increase in the percentage of soil set in motion is noticed. Even by taking into account uncertainties on the roughness coefficient and on the critical Shields, percentages set in motion do not reach 100 %. This can have different meanings according to the structure of the riverbed:

- If the grains are randomly mixed and that fine sediments are available for transport then, only finer grains of the soil will be set in movement and that the structure of the riverbed will mostly remain as it is currently.
- If finer grains are located under bigger particles (such as illustrated in Figure 143), these are protected from flow and will not be available for sediments transport.

Given the observations made by EDF that fine sediments deposited recently in the riverbed, the second bullet point is unlikely to happen.

Moreover, the distributions before and after dam removal overlap. This means that there is some probability that the percentage of soil set in motion after dam removal is lower than in the current situation. However, the most likely outcome of the removal works is that more sediments will be put in motion, especially around (b) and (c). Indeed the uncertainty considered for this study (roughness size and critical Shields coefficient) are identical between the two situations (current and planned). This means that even if we consider that we do not know exactly the roughness size and the critical Shields coefficient, there are no clue that their exact values would significantly change between the current and planned situations. In other words, the “real” amount of soil set in motion in the current and planned situations should be located in the same area of their respective distribution (e.g. if the real amount of soil set in motion in the current situation is located to the left part of the current distribution, then the real amount of soil set in motion in the planned situation should also be located in the left part of the planned distribution).

For a final illustration of the extent of the distributions, the bounds of the 95 % confidence interval are plotted in Figure 166 and Figure 167. A gamma law is used for these figures. Values lower than 0 are limited to 0. The large variability of the distributions appear once more clearly as well as the differences between the current and planned situations.

As a final and practical conclusion on this case study, we are able to write that:

- Removal works, as designed in the planned DEM, affect the amount of soil set in motion only between the Keller dam and the new dam.
- For this area, a shift in the distributions is noticed, meaning that more soil would be set in motion after removal works.
- However, given the 97.5 % percentile maps for a 150 m<sup>3</sup>/s flood event, only finer grains will move (except in some areas where grosser sediments are likely to be set in motion) for this event. An approximation of the larger diameter likely to be set in motion in such a case is  $d_{50}$ , or sediments with a diameter up to 1.5 cm according to Figure 145.

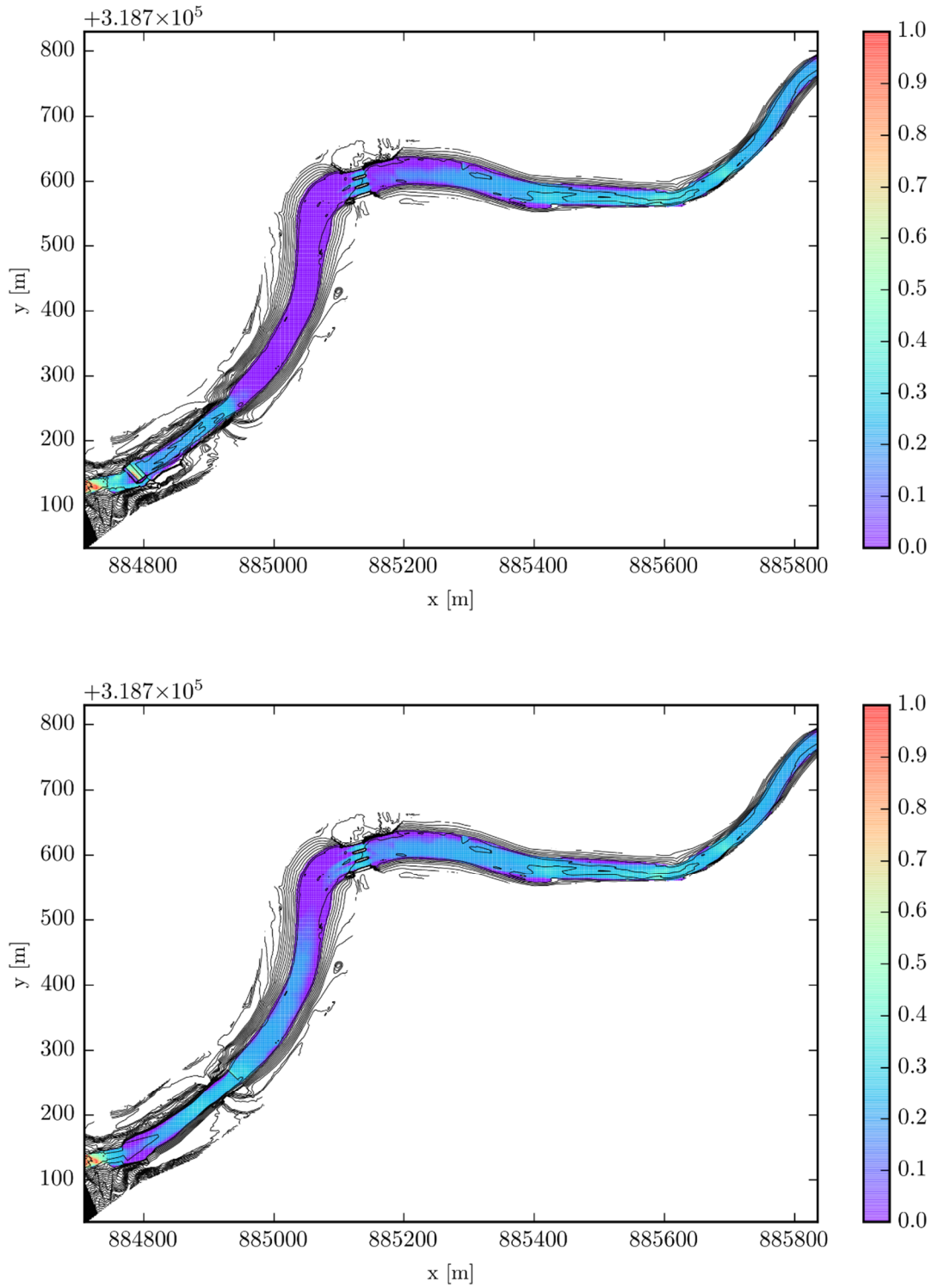


Figure 166: 2.5 % percentile of the proportion of soil set in motion in the current (upper plot) and planned (lower plot) situations for  $150 \text{ m}^3/\text{s}$

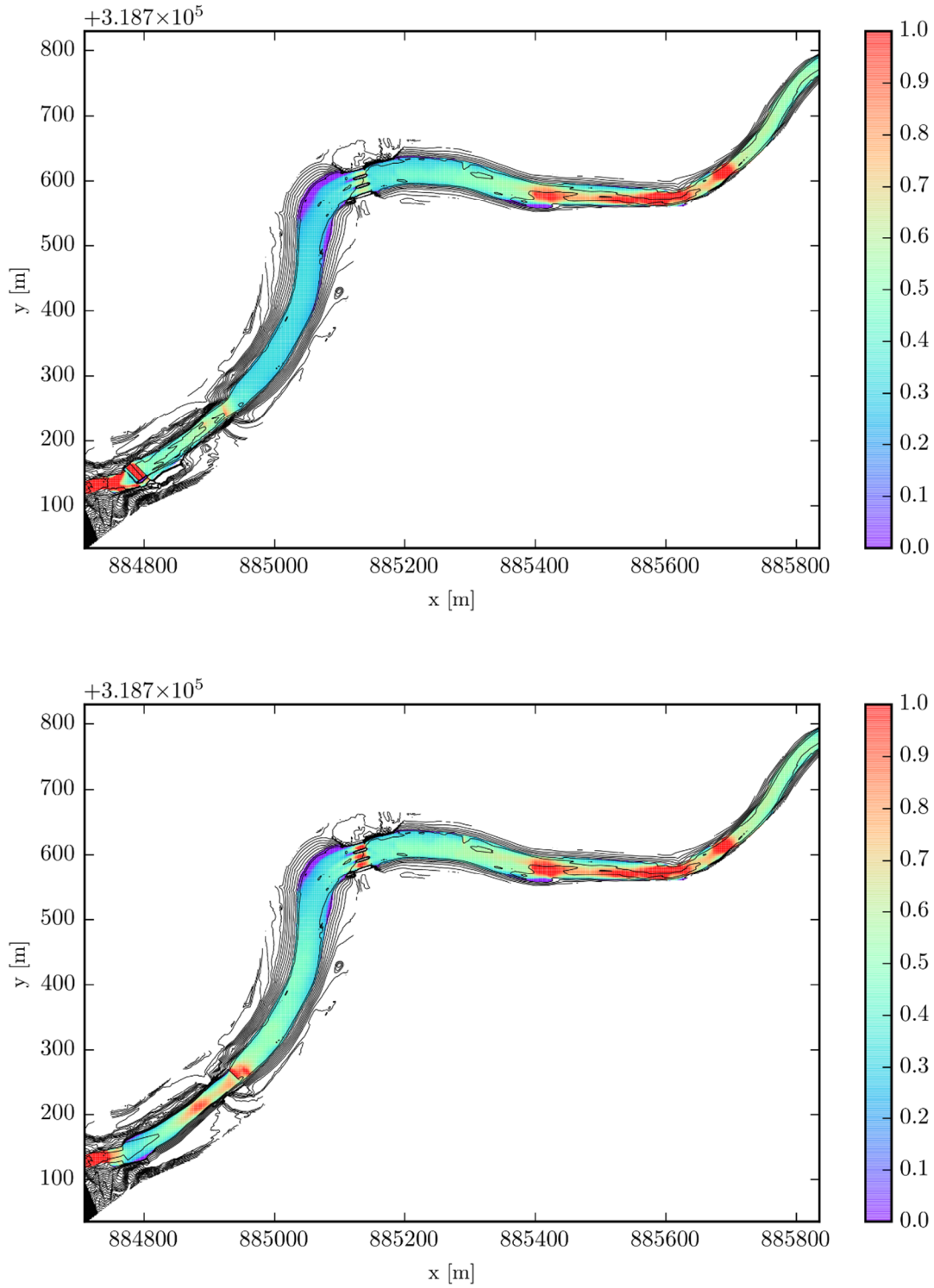


Figure 167: 97.5 % percentile of the proportion of soil set in motion in the current (upper plot) and planned (lower plot) situations for  $150 \text{ m}^3/\text{s}$

## **5.6 Conclusion**

This chapter presented a real-world application on the Romanche River in France. The dam operator is planning to remove several dams and wants to study the risk of bed destabilization following these operations. We presented an original approach to compute bed stability indicators without needing to implement a full morphodynamic model. The uncertainty analysis was made on the resulting stability indicator.

Since 2-D hydrodynamic simulations require computation times of the order of several hours, applying uncertainty analysis to these models can be considered only with simplified methods. Indeed, the Monte Carlo method is not suited due to its need for a large number of evaluation points. Based on the conclusions from previous chapters, PMM was chosen to apply uncertainty analysis to a 2-D hydrodynamic example.

We showed in this chapter the applicability of PMM to 2-D hydraulic simulations. In our example, the number of full hydraulic simulations was limited to 3, leading to a limited total computation time. The uncertainty method allowed to show that a large variability of the stability indicators could be noticed. Moreover, removing the studied dam leads to an increase of the risk of bed destabilization on a limited portion of the river for the considered discharge.

More specific and practical conclusions could also be drawn. The main question that this study had to answer was “Are recent sediment deposits going to be washed after the dam removal?”. Based on current and planned situations DEMs and a 150 m<sup>3</sup>/s flood event (1-year return period discharge), the main outcome is that more sediments should be set in motion after dam removal. The size of sediment set in motion after dam removal should not exceed 1.5 cm and this effect is limited on an extent of approximately 500 m upstream of the removed dam.

For conciseness reasons, we chose to limit the study presented in this chapter to a single discharge. However, for a better view of the possibilities to set sediments in motion, several discharges should be studied (Goffin, Piroton, Archambeau, et al. 2016).

Moreover, we chose to limit the uncertainty analysis to two uncertain parameters (the roughness size and the critical Shields coefficient) although other aspects of this study are uncertain. For instance, the DEM of the planned situation after the dam removal could be defined with some uncertain parameters such as the depth and extent of the channel reshaping (see Figure 141). The roughness size is distributed uniformly on the computation domain. This aspect can also be discussed and improved by linking the roughness size to a soil occupation data.

As stated earlier, we did not consider the Monte Carlo method in this chapter due to the high number of evaluations to perform on a computationally expensive model (it takes approximately 3 hours to perform the evaluation of a single point). However, during the last decade, more and more hydraulic models are based on the use of GPU (graphics processing unit, (Brodtkorb et al. 2012)) which allows to lower the time required for computation. Even if the WOLF software implements parallelization through OpenMP, further developments are still required to allow a 2-D GPU model in this computing suite. This new feature would be a great advantage in order to envisage an uncertainty analysis based on the Monte Carlo method for 2-D horizontal hydrodynamic problems.

This successful application of uncertainty analysis to a 2-D horizontal hydrodynamic example paves the way for other applications. One of these is the construction of risk maps for dam break emergency plans. For such application, a typical uncertainty source that can be considered is the roughness coefficient according to the land use. At each cell of the computation domain, distributions of the maximum water depth and maximum velocity can be computed thanks to an uncertainty analysis method. This kind of output helps public authorities to design emergency plans for the companies and people living close to a river concerned by dam brake hazards.

# Chapter 6: Investigations for better convergence of the 1-D Richards equation

## 6.1 Introduction

In order to apply uncertainty analysis to computationally expensive hydrodynamic cases, a fast 1-D algorithm was developed in chapter 3 and applied in chapter 4. Based on the results and conclusions of chapters 2, 3 and 4, chapter 5 applied uncertainty analysis to a 2-D hydrodynamic real-world case. Moreover, another condition for an efficient and automatic application of uncertainty analysis is to rely on robust models. Indeed, a large number of evaluations can be launched with various values of the uncertain parameters. One should be confident in the ability of a model to process all these values of uncertain parameters without convergence issues. As shown later in this chapter, unsaturated groundwater flows can present such issues, making them poorly suitable for uncertainty analysis. This chapter suggests methods to overcome these difficulties.

This chapter focusses on the production of a robust and efficient code able to interface with other components of the WOLF software. As stated in the general introduction (chapter 1), WOLF contains several modules that are able to model a variety of flows in hydraulics using different kind of meshes. It includes, among others, a module able to model hydrological processes on a watershed using only physically based equations. This model is further developed in (Paulus et al. 2013).

Paulus et al. couple several independent models in order to represent these processes. For underground flows, three types of models are used:

- a fully saturated finite difference 3-D model at the lowest end of the domain,
- several finite volume vertical 1-D columns to represent the partially saturated part of soil and,
- a 2-D plane depth integrated diffusion model to exchange mass between vertical columns.

1-D and 2-D shallow water models are used to take surface processes into account. All these models communicate with each other in order to exchange mass at their boundaries.

This chapter focusses only on the 1-D column model. Indeed, this part of the software, where partially saturated processes occur, can be difficult to converge. These convergence difficulties were recently reported in (Farthing & Ogden 2017). They review the literature about Richards

equation and conclude that, at the time of publishing their paper, no method is able to deal reliably with the whole variety of practical cases.

This chapter starts from the observation that converging a numerical solution of Richards equation may be difficult in order to propose possible improvements. First, the equation, soil laws and the numerical model are introduced. For the numerical model, various techniques that are recognized to improve the convergence process are presented and some are implemented in our software. Then, from 6 scenarios that aim to represent the variety of underground flows that can be met in reality, numerical tests are performed. Their goal is to find best parameters to foster convergence and to identify cases that are difficult (or even impossible) to converge. Finally, homotopy is introduced as a possible way to improve convergence problems and improve the robustness of the groundwater model. This method is tested on the most problematic scenarios.

## **6.2 Richards equation**

The flow in a porous media can be modelled through the use of the mass and momentum conservation principles. Since we focus our study on vertical 1-D columns, the only spatial coordinate is written  $z$  [m] and increases when going up. The time variable is  $t$  [s].

### **6.2.1 Conservation equations**

In a vertical column, the mass conservation writes:

$$\frac{\partial \theta}{\partial t} + \frac{\partial q_z}{\partial z} = S \quad (204)$$

$\theta$  [-] is the water content in an elementary volume of soil. It represents the ratio between the volume occupied by the fluid and the total volume of the control element. The variable  $q_z$  [m/s] is the specific discharge, also referred as Darcy velocity. It is the total discharge of fluid divided by the exchange surface of the elementary volume. It does not represent the real velocity of the fluid in the porous medium. Finally,  $S$  [s<sup>-1</sup>] is a source term that represents an addition or removal of mass.

The application of the momentum conservation principle for porous media considers low velocities in order to neglect inertial terms. The resulting equation is known as Darcy's law:

$$q_z = -K_z(\psi) \frac{\partial}{\partial z}(\psi + z) \quad (205)$$

$\psi$  [m] is the pressure in the fluid divided by the fluid specific weight. The saturation of the porous media depends on  $\psi$ :

- Positive pressures mean that the porous medium is in a saturated state
- Negative pressures mean that the porous medium is unsaturated or partially saturated.

Combining  $\psi$  with the altitude  $z$  gives the potential [m]:  $\phi = \psi + z$ .

The hydraulic conductivity in the  $z$  direction is  $K_z$  [m/s]. It will be denoted  $K$  further in this thesis.

Combining equation (204) with equation (205) gives Richard's equation:

$$\frac{\partial \theta}{\partial t} = \frac{\partial}{\partial z} \left( K_z \frac{\partial \phi}{\partial z} \right) + S \quad (206)$$

It contains two unknowns,  $\theta$  and  $\phi$ , which define the state of the soil. The hydraulic conductivity is a property of the soil which depends on the pressure state. Constitutive laws are required in order to solve equation (206).

## 6.2.2 Constitutive soil laws

The hydraulic conductivity  $K$  and the water content  $\theta$  can be linked to the potential  $\phi$  (or the pressure  $\psi$ ) through mathematical relationships. Several authors such as Brooks-Corey (Brooks & Corey 1964), van Genuchten-Mualem (Mualem 1976; Van Genuchten 1980) or Vauclin-Vachaud (Haverkamp et al. 1977; Vauclin et al. 1979; Vauclin et al. 1975) proposed constitutive soil laws. In the following pages, only the van Genuchten-Mualem soil law is presented and the behavior of the nonlinear relationship is further studied. The ability of this law to represent the full range of saturation of a soil is one of the reasons of its popularity among the scientific community. A proposition of a linear relationship based on the van Genuchten-Mualem law is also given in appendix D.1.

The van Genuchten law links the water content  $\theta$  to the pressure  $\psi$  thanks to three parameters  $\alpha$ ,  $m$  and  $n$ :

$$\begin{aligned} \psi \geq 0 &\Leftrightarrow \theta(\psi) = \theta_s \\ \psi < 0 &\Leftrightarrow \theta(\psi) = \theta_r + (\theta_s - \theta_r) \left[ 1 + (\alpha |\psi|)^n \right]^{-m} \end{aligned} \quad (207)$$

Parameters of relationship (207) are related to the soil nature. Mualem law allows to reduce the number of parameters to two by linking  $m$  and  $n$ :

$$m = 1 - \frac{1}{n} \quad (208)$$

Combining (207) and (208) gives the van Genuchten-Mualem law:

$$\begin{aligned}\psi \geq 0 &\Leftrightarrow \theta(\psi) = \theta_s \\ \psi < 0 &\Leftrightarrow \theta(\psi) = \theta_r + (\theta_s - \theta_r) \left[ 1 + (\alpha |\psi|)^n \right]^{\frac{1}{n}-1}\end{aligned}\quad (209)$$

with  $\theta_s$  [-] the water content when the soil is saturated and  $\theta_r$  [-] the residual water content.

The hydraulic conductivity  $K$  is also linked to the pressure  $\psi$  through the Mualem law:

$$\begin{aligned}\psi \geq 0 &\Rightarrow K(\psi) = K_s \\ \psi < 0 &\Rightarrow K(\psi) = K_s \frac{1}{\left[ 1 + (\alpha |\psi|)^n \right]^{\frac{1}{2} - \frac{1}{2n}}} \left\{ 1 - (\alpha |\psi|)^{n-1} \left[ 1 + (\alpha |\psi|)^n \right]^{\frac{1}{n}-1} \right\}^2\end{aligned}\quad (210)$$

where  $K_s$  is the hydraulic conductivity when the soil is saturated.

As it will be explained later, a third relationship is required for the solver. It links the pressure to the water holding capacity denoted  $\eta$  [ $\text{m}^{-1}$ ], which is the derivative of the water content according to the pressure. The derivation of (209) gives:

$$\begin{aligned}\psi \geq 0 &\Rightarrow \eta(\psi) = \frac{\partial \theta}{\partial \psi} = 0 \\ \psi < 0 &\Rightarrow \eta(\psi) = \frac{\partial \theta}{\partial \psi} = \alpha (n-1) (\theta_s - \theta_r) (\alpha |\psi|)^{n-1} \left[ 1 + (\alpha |\psi|)^n \right]^{\frac{1}{n}-2}\end{aligned}\quad (211)$$

Equations (209), (210) and (211) need to be supplied with parameter values relative to the soil one wishes to simulate. The United States Department of Agriculture (USDA) provides the parameters required by the van Gneuchten – Mualem law for eleven typical soils (Table 33). At this point, it is interesting to notice the orders of magnitude and range of variations of the parameters, especially for  $\alpha$  and  $n$ .  $\alpha$  lies typically between  $0.5 \text{ m}^{-1}$  and  $15 \text{ m}^{-1}$  while typical values of  $n$  lies between 1.1 and 2.8.

Type of soils	$\theta_s$ [-]	$\theta_r$ [-]	$K_s$ [m/s]	$\alpha$ [m <sup>-1</sup> ]	$n$ [-]	$\psi_0$ [m]
Sand	0.43	0.045	$8.25 \cdot 10^{-5}$	14.5	2.68	-0.0579
Loamy sand	0.43	0.057	$4.05 \cdot 10^{-5}$	12.4	2.78	-0.0687
Sandy loam	0.41	0.065	$1.23 \cdot 10^{-5}$	7.5	1.89	-0.0895
Loam	0.43	0.078	$2.89 \cdot 10^{-6}$	3.6	1.56	-0.1440
Silt loam	0.45	0.067	$1.25 \cdot 10^{-6}$	2.0	1.41	-0.2082
Sandy clay loam	0.39	0.100	$3.63 \cdot 10^{-6}$	5.9	1.48	-0.0792
Clay loam	0.41	0.098	$7.18 \cdot 10^{-7}$	1.9	1.31	-0.1752
Silty clay loam	0.43	0.089	$1.97 \cdot 10^{-7}$	1.0	1.23	-0.2559
Sandy clay	0.38	0.100	$3.37 \cdot 10^{-7}$	2.7	1.23	-0.0948
Silty clay	0.36	0.070	$5.78 \cdot 10^{-8}$	0.5	1.09	-0.2029
Clay	0.38	0.068	$5.67 \cdot 10^{-7}$	0.8	1.09	-0.1268

Table 33: Parameters for the van Genuchten-Mualem law for 11 soils defined by the USDA (Carsel & Parrish 1988; Shao & Irannejad 1999)

It is also interesting to compare the van Genuchten – Mualem law to a generalized logistic function in order to better understand its behavior. A generalized logistic function writes:

$$y(x) = A + \frac{C - A}{\left(1 + e^{-B(x-x_0)}\right)^{\frac{1}{\nu}}} \quad (212)$$

$$\frac{y(x) - A}{C - A} = \frac{1}{\left(1 + e^{-B(x-x_0)}\right)^{\frac{1}{\nu}}}$$

with :

- $A$  the ordinate of the lower horizontal asymptote
- $C$  the ordinate of the upper horizontal asymptote
- $B$  the rate of growth
- $\nu > 0$  the steepness of the transition
- $x_0$  the position of the inflection point on the abscissa (only when  $B = 1$  and  $\nu = 1$  )

The family of functions (212) was first introduced by Richards (1959) in order to represent the growth of populations. More generally, a generalized logistic function allows to represent a S-shape curve. It allows to link smoothly two values (upper and lower bounds). These values, the position of the transition and the steepness of the transition are ruled by the parameters of the logistic function. An illustration of a generalized logistic function with some particular parameter values is given in Figure 168.

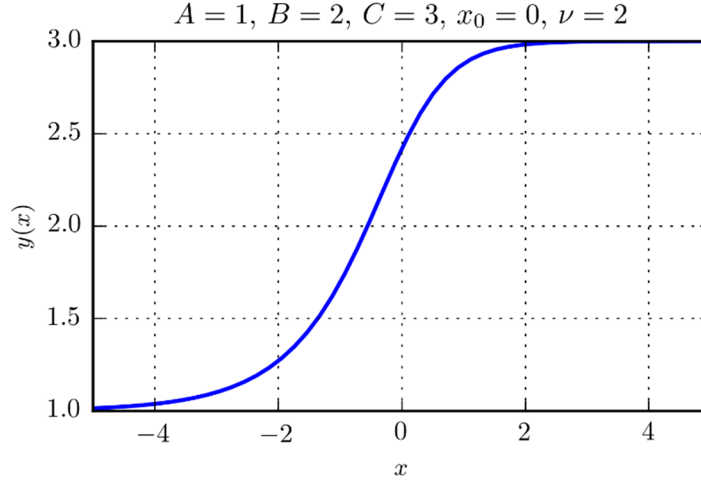


Figure 168: Graphical representation of a generalized logistic function

The van Genuchten – Mualem law (209) can be compared to a generalized logistic function (212) . Comparing (209) and (212) yields:

$$\begin{aligned}
 A &= \theta_r \\
 C &= \theta_s \\
 e^{-B(x-x_0)} &= (\alpha |\psi|)^n \\
 \nu &= \frac{n}{n-1}
 \end{aligned} \tag{213}$$

By developing the third equality in (213), we get :

$$\begin{aligned}
 e^{-B(x-x_0)} &= (\alpha |\psi|)^n = e^{n \ln(\alpha |\psi|)} = e^{n(\ln \alpha + \ln |\psi|)} \\
 \Leftrightarrow -B(x-x_0) &= n(\ln \alpha + \ln |\psi|) \\
 \Rightarrow \begin{cases} B = n \\ x = -\ln |\psi| \\ x_0 = \ln \alpha \end{cases}
 \end{aligned} \tag{214}$$

As expected,  $\theta_r$  and  $\theta_s$  are the lower and upper asymptotes of the van Genuchten – Mualem law. The coefficient  $n$  rules the steepness of the transition. Finally, a difference in the sign of  $x_0$  might appear according to the type soil. When  $\alpha < 1$  (which is the case for the last two soils in Table 33),  $x_0$  becomes lower than 0, which is different from the other soils. However, it is difficult to interpret this with respect to the position of an inflection point since  $n$  varies according to the kind of soil. The shape of the van Genuchten – Mualem law expressed in a logistic function way (with  $x = -\ln |\psi|$ ) for the soils in Table 33 can be observed in Figure 169.

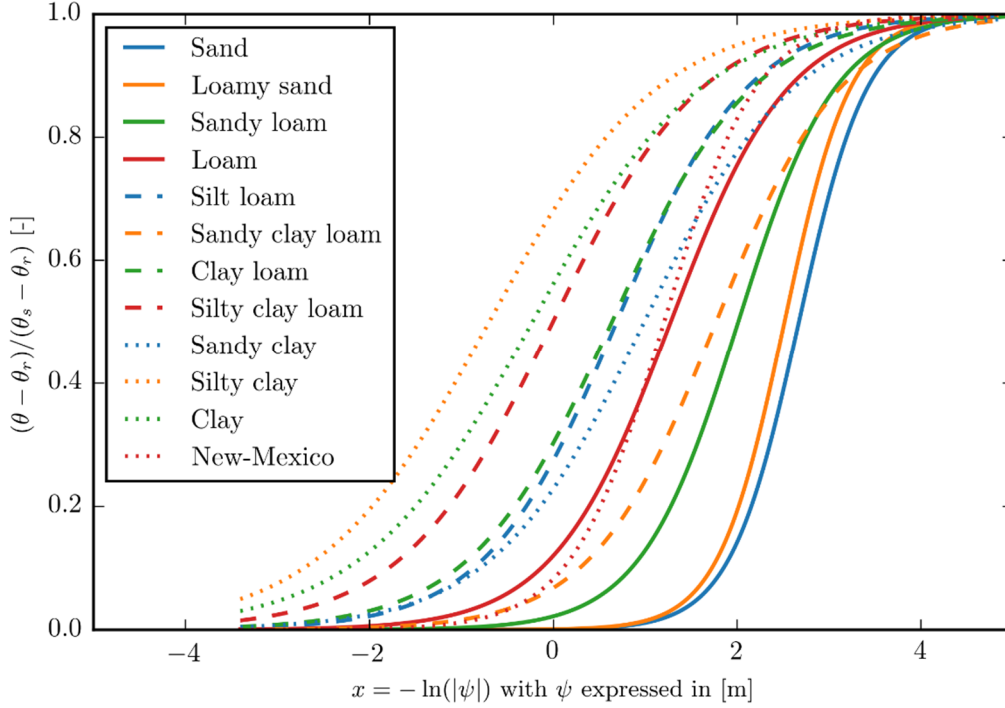


Figure 169: van Genuchten - Mualem law for 11 representative soils and New-Mexico soil

The laws for sand, loam and clay are represented in Figure 170, Figure 171 and Figure 172 respectively, in a  $\psi$  scale for the abscissa. These figures intend to demonstrate the position of the inflection point for different type of soils and how the curves connect to the saturation threshold. The inflection point is found at  $\partial^2\theta / \partial\psi^2 = 0$ . Considering the van Genuchten - Mualem law (209) and  $\psi < 0$ :

$$\frac{\partial^2\theta}{\partial\psi^2} = (\theta_s - \theta_r) \frac{(-1+n)(-\alpha\psi)^n \left(1 + (-\alpha\psi)^n\right)^{-3+\frac{1}{n}} \left(1 + n \left(-1 + (-\alpha\psi)^n\right)\right)}{\psi^2} = 0 \quad (215)$$

A root  $\psi_0$  of  $\partial^2\theta / \partial\psi^2$  is:

$$\begin{aligned} \left(1 + n \left(-1 + (-\alpha\psi)^n\right)\right) &= 0 \\ \Leftrightarrow \psi_0 &= \frac{-1}{\alpha} \sqrt[n]{\frac{n-1}{n}} \end{aligned} \quad (216)$$

Values of the inflection points are given in Table 33. It appears that all inflection points are located at least at  $-5$  cm of pressure from the saturation threshold.

While this inflection point is clearly positioned in the unsaturated zone of the graphs for the three types of soils, the connection might not appear as smooth as expected, at least at the chosen observation scale. However, we demonstrated earlier that the logistic function, which

corresponds to the van Genuchten – Mualem law, tends asymptotically to the saturation water content for  $x \rightarrow \infty$ , i.e.  $|\psi| \rightarrow 0$ . This same conclusion is drawn further when analyzing the dimensionless van Genuchten – Mualem relationships.

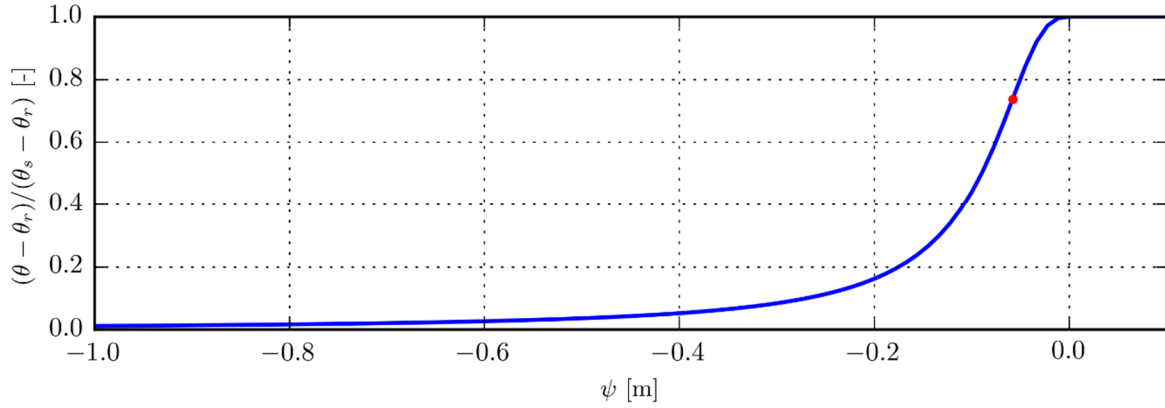


*Figure 170: van Genuchten – Mualem law for sand*

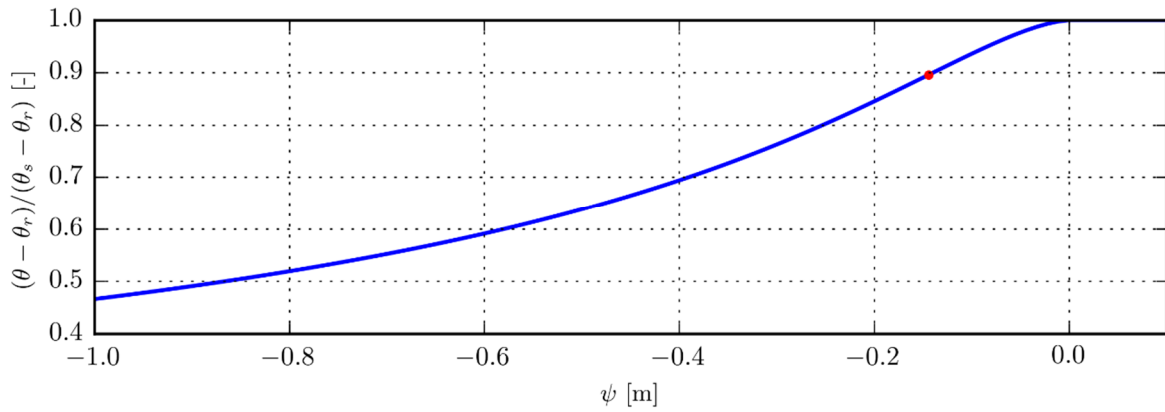


*Figure 171: van Genuchten – Mualem law for loam*

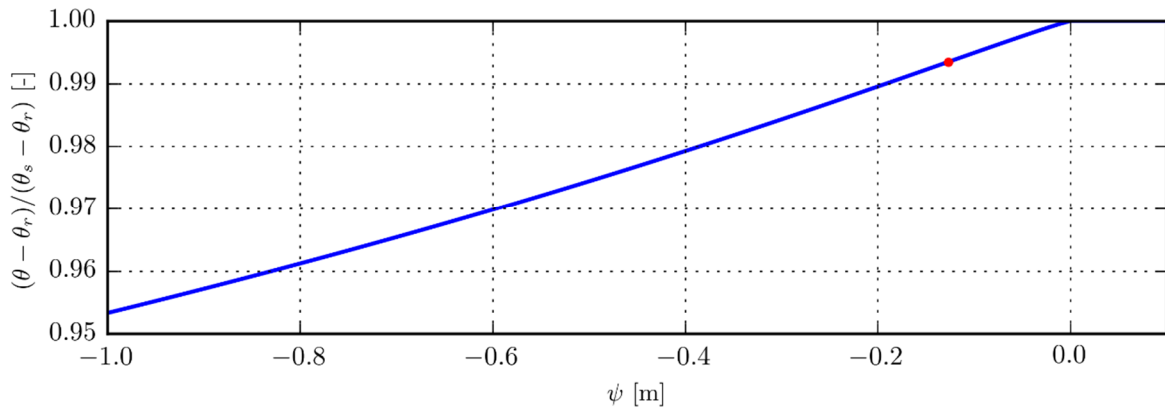


*Figure 172: van Genuchten – Mualem law for clay*

The hydraulic conductivity is represented according to  $\ln|\psi|$  in Figure 173. It appears that silty clay and clay tend to reach their  $K_s$  only for values of the pressure very close to 0. This is due to their low  $n$  value.

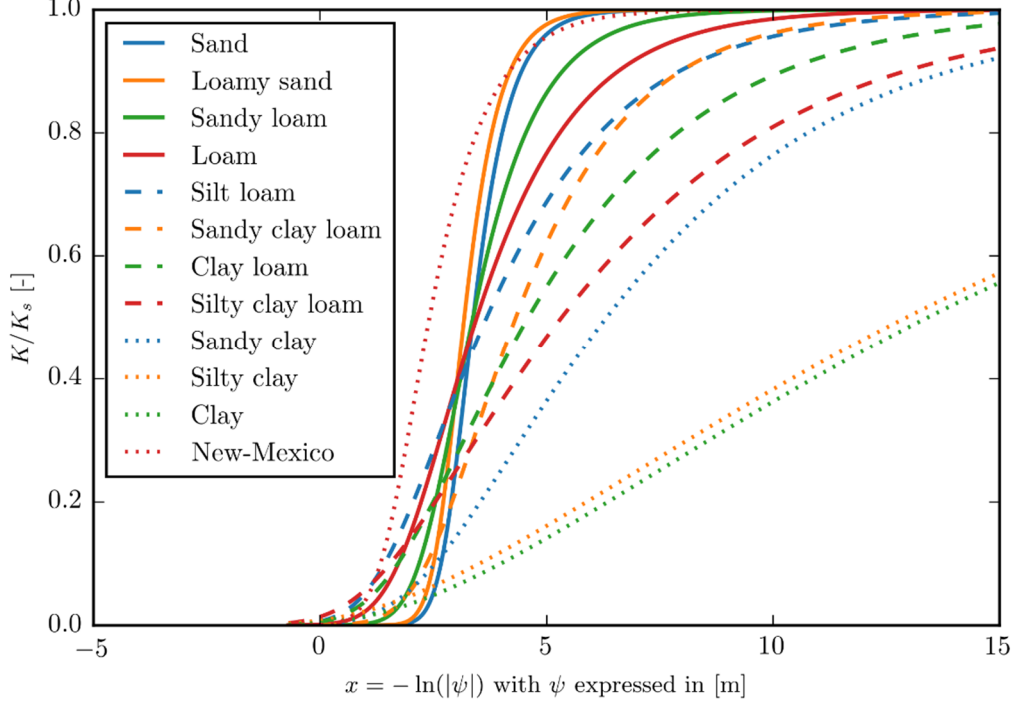


Figure 173: Hydraulic conductivity according to van Genuchten – Mualem model for 11 representative soils and New-Mexico soil

In order to better understand the behavior of the soils under the van Genuchten – Mualem law, dimensionless relationships can be written for the water content, hydraulic conductivity and water holding capacity. The following dimensionless variables are introduced:

$$\begin{aligned}
 \tilde{\psi} &= \alpha\psi \\
 \tilde{\theta} &= \frac{\theta - \theta_r}{\theta_s - \theta_r} \\
 \tilde{K} &= \frac{K}{K_s} \\
 \tilde{\eta} &= \frac{\eta}{\alpha(\theta_s - \theta_r)}
 \end{aligned} \tag{217}$$

Equation (209) becomes:

$$\begin{aligned}
 \tilde{\psi} \geq 0 &\Leftrightarrow \tilde{\theta}(\tilde{\psi}) = 1 \\
 \tilde{\psi} < 0 &\Leftrightarrow \tilde{\theta}(\tilde{\psi}) = \left[1 + |\tilde{\psi}|^n\right]^{\frac{1}{n}-1}
 \end{aligned} \tag{218}$$

Equation (210) becomes:

$$\begin{aligned}\tilde{\psi} \geq 0 &\Rightarrow \tilde{K}(\tilde{\psi}) = 1 \\ \tilde{\psi} < 0 &\Rightarrow \tilde{K}(\tilde{\psi}) = \frac{1}{\left[1 + |\tilde{\psi}|^n\right]^{\frac{1}{2} \frac{1}{2n}}} \left\{ 1 - |\tilde{\psi}|^{n-1} \left[1 + |\tilde{\psi}|^n\right]^{\frac{1}{n}-1} \right\}^2\end{aligned}\quad (219)$$

Finally, the water holding capacity (211) can be written in the following dimensionless form:

$$\begin{aligned}\tilde{\psi} \geq 0 &\Rightarrow \tilde{\eta}(\tilde{\psi}) = \frac{\partial \tilde{\theta}}{\partial \tilde{\psi}} = 0 \\ \tilde{\psi} < 0 &\Rightarrow \tilde{\eta}(\tilde{\psi}) = \frac{\partial \tilde{\theta}}{\partial \tilde{\psi}} = (n-1) |\tilde{\psi}|^{n-1} \left[1 + |\tilde{\psi}|^n\right]^{\frac{1}{n}-2}\end{aligned}\quad (220)$$

Equations (218), (219) and (220) are represented graphically in Figure 174, Figure 175 and Figure 176 respectively. In Figure 174, it appears that all depicted curves evolve smoothly. Steeper changes can be noticed in Figure 175 and Figure 176 for lower values of  $n$ . Moreover, some curves do not seem to connect asymptotically to the steady values for  $\tilde{\psi} > 0$ . This discontinuous behavior may lead to convergence issues when the soil is approaching its saturation state.

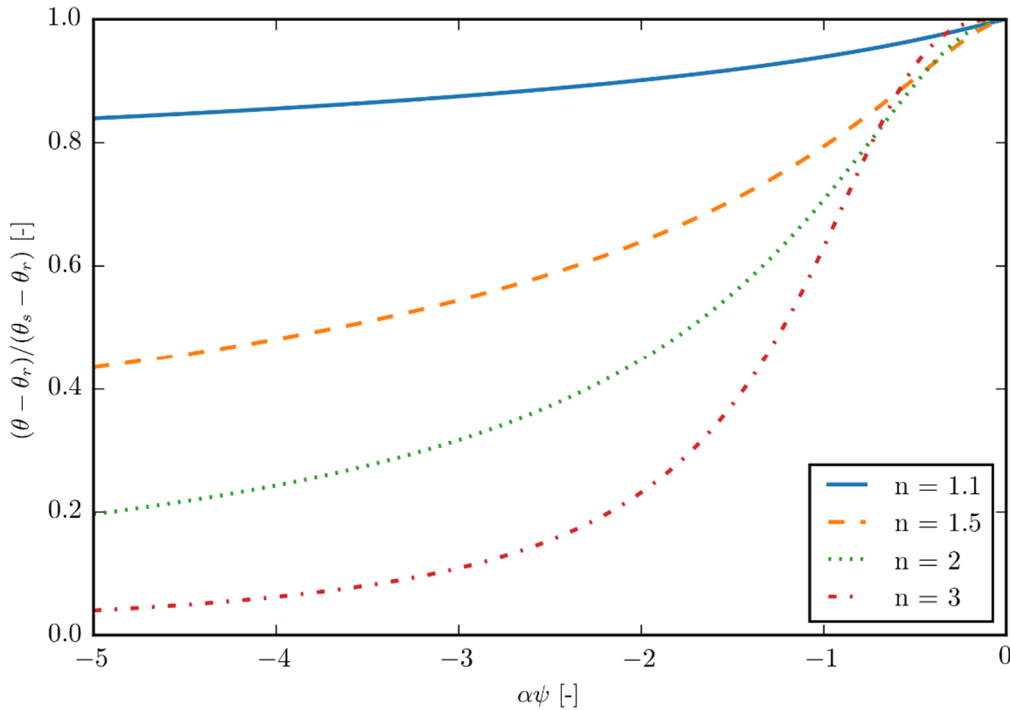


Figure 174: Influence of the  $n$  parameter on the water content relationship

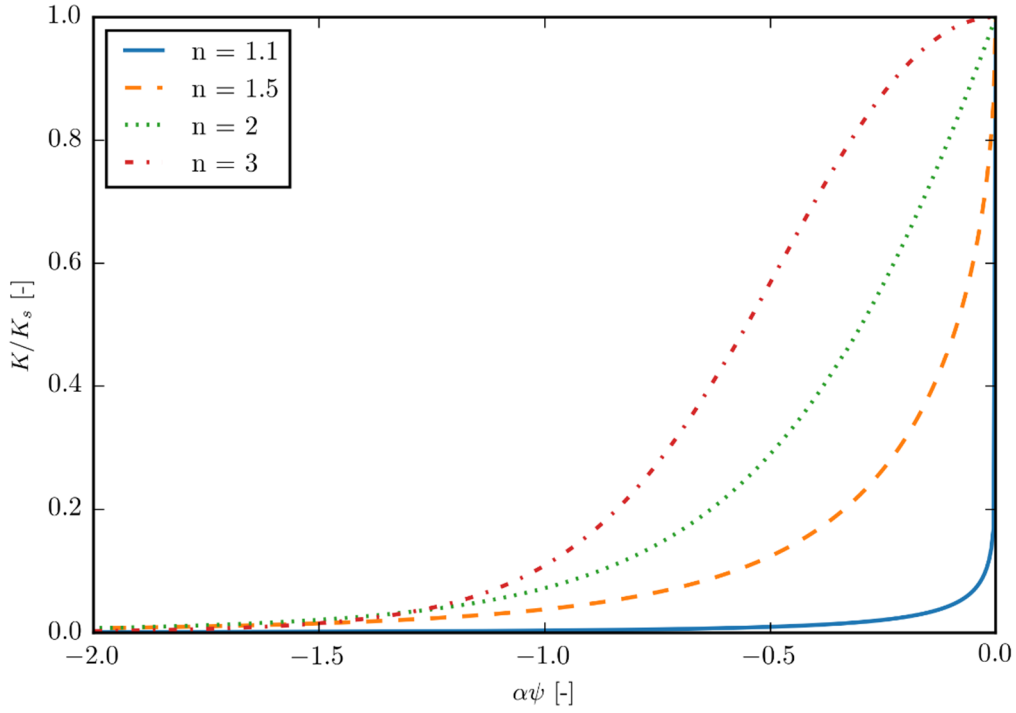


Figure 175: Influence of the  $n$  parameter on the hydraulic conductivity relationship

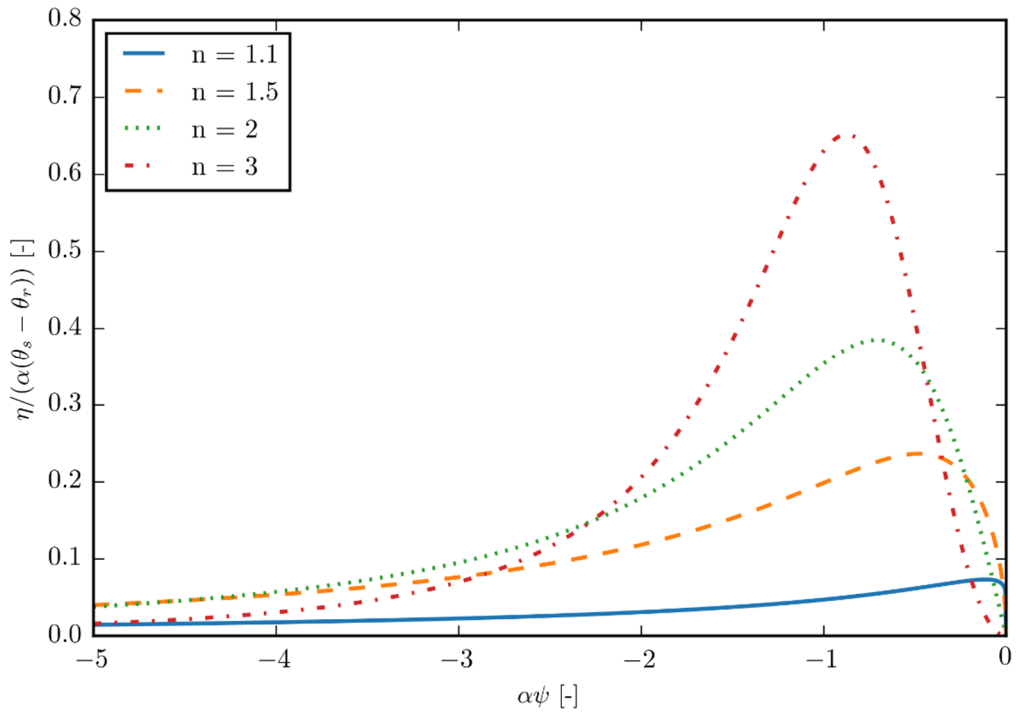


Figure 176: Influence of the  $n$  parameter on the water holding capacity relationship

Having a close look to the hydraulic conductivity evolution (Figure 175) shows that, for the greatest values of  $n$ , the hydraulic conductivity varies suddenly at the neighborhood of saturation. This characteristic leads to the sharpness of an infiltration front. Indeed, for a given

gradient of potential, zones with a low water content can only have a very low Darcy velocity while zones completely saturated have a much larger Darcy velocity. The infiltration process features almost binary water content values ( $\theta_r$  or  $\theta_s$ ). This (almost) discontinuous behavior can be a source of convergence issues.

## 6.3 Numerical model

### 6.3.1 Discretized equations

The spatial discretization of the equations is based on a finite volume scheme as depicted in Figure 177. The mesh is considered regular in the following developments. The potential  $\phi$  is the unknown that is stored at the gravity center of a cell. The mass conservation equation (204) is discretized in this finite volume perspective for the spatial derivative while the time derivative is written in an Euler scheme:

$$\frac{\theta_i^{t+\Delta t} - \theta_i^t}{\Delta t} + \frac{q_{i+1/2}^{t+\Delta t} - q_{i-1/2}^{t+\Delta t}}{\Delta z} = S_i^{t+\Delta t} \quad (221)$$

where the subscripts relate to the spatial discretization and the superscripts to the time discretization. The variables out of the time derivative in (221) are expressed in  $t + \Delta t$  in order to obtain an implicit time scheme, well-known for its unconditional stability regarding the time step.

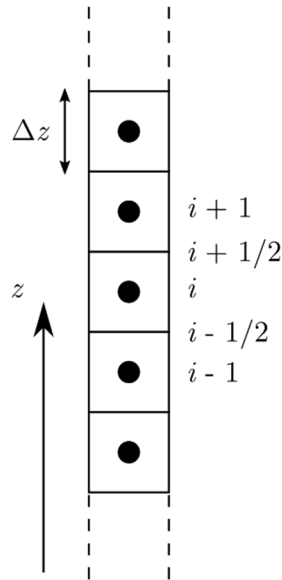


*Figure 177: Spatial discretization of a 1-D column*

The velocities at the borders are computed using the momentum equation discretized as a centered finite difference:

$$\begin{aligned} q_{i-1/2}^{t+\Delta t} &= -\frac{1}{\Delta z} K_{i-1/2}^{t+\Delta t} \left( \phi_i^{t+\Delta t} - \phi_{i-1}^{t+\Delta t} \right) \\ q_{i+1/2}^{t+\Delta t} &= -\frac{1}{\Delta z} K_{i+1/2}^{t+\Delta t} \left( \phi_{i+1}^{t+\Delta t} - \phi_i^{t+\Delta t} \right) \end{aligned} \quad (222)$$

Combining (221) and (222) yields the equation to solve at each regular node (boundary conditions are introduced below):

$$0 = -\frac{\theta_i^{t+\Delta t} - \theta_i^t}{\Delta t} + \frac{K_{i+1/2}^{t+\Delta t}}{\Delta z^2} \left( \phi_{i+1}^{t+\Delta t} - \phi_i^{t+\Delta t} \right) - \frac{K_{i-1/2}^{t+\Delta t}}{\Delta z^2} \left( \phi_i^{t+\Delta t} - \phi_{i-1}^{t+\Delta t} \right) + S_i^{t+\Delta t} \quad (223)$$

As stated earlier, the potential  $\phi$  is the main unknown while  $\theta$  and  $K$  are computed from constitutive laws. Equation (223) is known as a mixed form of Richards' equation (Farthing & Ogden 2017).

### 6.3.2 Boundary conditions

Due to the parabolic form of Richards' equation, an upper and a lower boundary conditions (BC) are required. At least one of these BC must a Dirichlet condition, meaning that a value  $\phi_{CL}$  must be imposed at a border ( $1/2$  for the lower border and  $N + 1/2$  for the upper border). Then, the flux is not computed as a centered finite difference but as:

$$\begin{aligned} q_{1/2}^{t+\Delta t} &= -\frac{2}{\Delta z} K_{1/2}^{t+\Delta t} \left( \phi_1^{t+\Delta t} - \phi_{CL}^{t+\Delta t} \right) \\ q_{N+1/2}^{t+\Delta t} &= -\frac{2}{\Delta z} K_{N+1/2}^{t+\Delta t} \left( \phi_{CL}^{t+\Delta t} - \phi_N^{t+\Delta t} \right) \end{aligned} \quad (224)$$

A Neumann condition can be imposed on one of the boundary borders. It consists in imposing directly a value  $q_{CL}$  for the flux at the border.

### 6.3.3 Hydraulic conductivity at the borders

In equation (223), hydraulic conductivity values are required at the borders of the finite volumes. However, unknowns ( $\phi$ ) and derived values ( $\psi, \theta, K, \eta$ ) are located at the center of the volumes. In order to reconstruct the  $K$  values at the border, several techniques exist (Szymkiewicz 2012).

A first approach consists in averaging the hydraulic conductivity from the two neighboring nodes. This mean can be arithmetic, geometric or harmonic. As explained by Szymkiewicz (2012), the harmonic and geometric means suffer from more severe instability problems than the arithmetic mean. This might be the reason why the arithmetic mean is well-established in the scientific community. For this reason, the arithmetic mean is part of the methods that will be used further:

$$K_{i+1/2} = \frac{1}{2}(K_i + K_{i+1}) \quad (225)$$

Another technique consists in reconstructing the hydraulic conductivity by taking into account a propagation direction. In the case of advection equations (which equation (206) is a kind of), an upstream upwinding direction is the preferred method to reconstruct values at the borders. We develop here two methods of reconstruction based on an upstream upwinding. The first method is a constant reconstruction from the upstream node:

$$K_{i+1/2} = \begin{cases} K_i & \text{if } \frac{\partial\phi}{\partial z} < 0 \\ K_{i+1} & \text{if } \frac{\partial\phi}{\partial z} > 0 \\ \frac{K_i + K_{i+1}}{2} & \text{if } \frac{\partial\phi}{\partial z} = 0 \end{cases} \quad (226)$$

Szymkiewicz (2012) states that this upwinding technique produces good results for advective flows (e.g. gravity driven flows) while large errors can be observed when it is used for diffusive flows (e.g. capillary driven flows).

The second method is a linear upstream reconstruction:

$$K_{i+1/2} = \begin{cases} K_i + \frac{\partial K}{\partial z} \Big|_i \frac{\Delta z}{2} & \text{if } \frac{\partial\phi}{\partial z} < 0 \\ K_{i+1} - \frac{\partial K}{\partial z} \Big|_{i+1} \frac{\Delta z}{2} & \text{if } \frac{\partial\phi}{\partial z} > 0 \\ \frac{K_i + K_{i+1}}{2} + \frac{\Delta z}{4} \left( \frac{\partial K}{\partial z} \Big|_i - \frac{\partial K}{\partial z} \Big|_{i+1} \right) & \text{if } \frac{\partial\phi}{\partial z} = 0 \end{cases} \quad (227)$$

The derivatives  $\partial K / \partial z$  are evaluated according to a finite difference derivative and their values can be limited in order to avoid local extrema.

## 6.3.4 Iterative solving

### 6.3.4.1 Matrix formulation

The system (223) being implicit a system must be solved. Each equation must be solved at each node of the domain. This means that we have to find the root of a function  $f$  at each node. This function  $f$  takes a general form for the nodes located inside the domain

$$f_{i \in [2; N-1]} = -\frac{\theta_i^{t+\Delta t} - \theta_i^t}{\Delta t} + \frac{K_{i+1/2}^{t+\Delta t}}{\Delta z^2} (\phi_{i+1}^{t+\Delta t} - \phi_i^{t+\Delta t}) - \frac{K_{i-1/2}^{t+\Delta t}}{\Delta z^2} (\phi_i^{t+\Delta t} - \phi_{i-1}^{t+\Delta t}) + S_i^{t+\Delta t} \quad (228)$$

and a particular form for the nodes next to the boundary condition. For these nodes, the formulation depends on the type of BC imposed. For Dirichlet BC:

$$\begin{aligned} f_1 &= -\frac{\theta_1^{t+\Delta t} - \theta_1^t}{\Delta t} + \frac{K_{3/2}^{t+\Delta t}}{\Delta z^2} (\phi_2^{t+\Delta t} - \phi_1^{t+\Delta t}) - \frac{2K_{1/2}^{t+\Delta t}}{\Delta z^2} \phi_1^{t+\Delta t} + S_1^{t+\Delta t} + \frac{2K_{1/2}^{t+\Delta t}}{\Delta z^2} \phi_{CL,1}^{t+\Delta t} \\ f_N &= -\frac{\theta_N^{t+\Delta t} - \theta_N^t}{\Delta t} - \frac{2K_{N+1/2}^{t+\Delta t}}{\Delta z^2} \phi_N^{t+\Delta t} - \frac{K_{N-1/2}^{t+\Delta t}}{\Delta z^2} (\phi_N^{t+\Delta t} - \phi_{N-1}^{t+\Delta t}) + S_N^{t+\Delta t} + \frac{2K_{N+1/2}^{t+\Delta t}}{\Delta z^2} \phi_{CL,N}^{t+\Delta t} \end{aligned} \quad (229)$$

For Neumann BC:

$$\begin{aligned} f_1 &= -\frac{\theta_1^{t+\Delta t} - \theta_1^t}{\Delta t} + \frac{K_{3/2}^{t+\Delta t}}{\Delta z^2} (\phi_2^{t+\Delta t} - \phi_1^{t+\Delta t}) + S_1^{t+\Delta t} - \frac{1}{\Delta z} q_1^{t+\Delta t} \\ f_N &= -\frac{\theta_N^{t+\Delta t} - \theta_N^t}{\Delta t} - \frac{K_{N-1/2}^{t+\Delta t}}{\Delta z^2} (\phi_N^{t+\Delta t} - \phi_{N-1}^{t+\Delta t}) + S_N^{t+\Delta t} + \frac{1}{\Delta z} q_N^{t+\Delta t} \end{aligned} \quad (230)$$

Equations (228), (229) and (230) can be written in a matrix form, such as:

$$f = -\Theta + A\phi + s \quad (231)$$

with  $A$  a matrix that contains the hydraulic conductivity terms,  $\Theta$  a column matrix with the time derivatives of the water content and  $s$  the constant terms (source terms and boundary conditions). For matrix  $A$ , the lines for an inner node  $i$  is:

$$A_{i,j} = \frac{K_{i-1/2}^{t+\Delta t}}{\Delta z^2} \phi_{i-1}^{t+\Delta t} \delta_{i,j+1} - \frac{K_{i-1/2}^{t+\Delta t} + K_{i+1/2}^{t+\Delta t}}{\Delta z^2} \delta_{i,j} + \frac{K_{i+1/2}^{t+\Delta t}}{\Delta z^2} \delta_{i,j-1} \quad (232)$$

where  $\delta$  is the Kronecker delta. (232) shows the tridiagonal pattern of matrix  $A$ . Moreover, since the hydraulic conductivity is unique on a border,  $A$  is symmetrical. This property will be useful later for the choice of an efficient solver algorithm.

#### 6.3.4.2 Modified Picard iteration scheme

Since the equations presented in previous section are nonlinear due to the constitutive laws, they should be solved iteratively. To do so, a modified Picard iteration scheme can be used (Celia et al. 1990). This method consists in expressing the variables at the next time step according to a guess value denoted  $*$ , and an increment of the variable:

$$\begin{aligned} \phi_i^{t+\Delta t} &= \phi_i^* + \Delta\phi_i \\ \theta_i^{t+\Delta t} &= \theta_i^* + \Delta\theta_i \\ &= \theta_i^* + \eta_i \Delta\phi_i \end{aligned} \quad (233)$$

with  $\eta_i = \left( \frac{\partial \theta}{\partial \psi} \right)_i$  which can be computed from constitutive laws.

Considering (233), the system to solve (231) becomes:

$$\left( A - \frac{1}{\Delta t} H \right) \Delta \phi = \frac{1}{\Delta t} (I \theta^* - I \theta^t) - A \phi^* - s \quad (234)$$

where  $I$  is the identity matrix and  $H$  the diagonal matrix that contains the water holding capacities  $\eta_i$ .

System (234) is solved in order to update the guesses until the residual vector  $\Delta \phi$  reaches some convergence threshold. In the case of the algorithm used in this thesis the convergence criterium is

$$\max(|\Delta \phi|) \leq 10^{-8} \text{ m} \quad (235)$$

Since  $(A - 1 / \Delta t H)$  is a tridiagonal matrix, specific algorithms can be used. In the frame of this thesis, we chose to use the tridiagonal matrix algorithm (TDMA). Moreover, when the hydraulic conductivity at a border is determined in a unique way,  $(A - 1 / \Delta t H)$  is symmetric which can lead to further simplifications in the solving process.

#### 6.3.4.3 Anderson accelerator

As explained in chapter 3 (section 3.3.2.1), an Anderson accelerator can be used in order to improve the convergence of a nonlinear problem. It relies on the results of successive iterations (subspaces) in order to go more quickly to the solution. The nonlinear Krylov acceleration method (NKA) (Carlson & Miller 1998a; Carlson & Miller 1998b) is the algorithm used for this part. Further details about this method can be obtained in section 3.3.2.1. Several number of subspaces are tested in following pages.

Concretely, at each step,  $\Delta \phi$  is computed from (234). Then, this vector is passed to the NKA algorithm which returns it modified (let us denote this modified vector  $\Delta \phi'$ ). The new guess for the modified Picard iteration becomes:

$$\phi_i^{t+\Delta t} = \phi_i^* + \Delta \phi_i' \quad (236)$$

#### 6.3.4.4 Evolution limiter

The evolutions of the potential and of the water content are linearized for numerical reasons. However, the soil behavior, modelled by the van Genuchten – Mualem law, is highly nonlinear as shown in section 6.2.2. In order to avoid evolutions that are too large and that could present local heavy discontinuities, two limiter techniques are designed. They are both based on the van Genuchten – Mualem soil law properties.

The position of the inflection point of the  $\psi - \theta$  curve is located at the position computed by (216). From this pressure (which is negative) until the null pressure, the slope of the law can change quickly. In order to ensure somehow a smooth journey in this area, the amplitude of the evolution of the potential for a node is limited to  $\Delta\phi_{max,i} = -\psi_{0,i} / 4$ . Since the soil might not be homogenous over the column, the value  $\Delta\phi_{max,i}$  might be different for each node.

For the first designed technique, all the amplitudes of the values of  $\Delta\phi$  (or  $\Delta\phi'$  if NKA is enabled) are compared to their corresponding  $\Delta\phi_{max,i}$  and are limited if they exceed this value.

The second designed technique is very similar to the first one, except that changes are broadcasted over all the nodes. A unique relaxation coefficient  $\lambda$  is defined. Its value should lie between 0 and 1. It multiplies the vector  $\Delta\phi$  in order to lower the amplitude of the values at least at the threshold  $\Delta\phi_{max}$ . For the application proposed in this thesis,  $\lambda \in ]0;0.7]$ . This allows to relax naturally all nodes.

When NKA is used and that more than one value is limited, the accelerator is disabled for next iterations in order to avoid a disruption of the NKA algorithm. Indeed, applying a correction lower than the one saved in NKA may lead to irrelevant overflows.

#### 6.3.4.5 Other techniques facilitating convergence

As summarized by Farthing & Ogden (2017), solving the Richards' equation can present difficulties due to the non-linearity nature of the problem coming from various sources. In order to overcome such issues, many techniques have been designed but none of them seem universal, such as stated by Farthing & Ogden (2017):

*“A universally robust and accurate solution methodology has not yet been identified that is applicable across the range of soils, initial and boundary conditions found in practice.”*

We give here three other techniques (other than the ones developed earlier) and their state of implementation in the WOLF software.

1. Time step refinement (Paniconi & Putti 1994). If the code is unable to converge a time step, the time step can be divided by 2 (several times if needed). This technique gives an initial condition for the new time step closer to its solution. However, it increases the importance of the H matrix in (234) which may be a source of high nonlinearity. This technique is implemented in the WOLF software but disabled for the computations performed in this chapter, in order to keep the focus on the effects of the time steps.

2. Local spatial refinement at the wetting front or close to the surface. This feature is not implemented in our code. This choice is based on the wish to keep a simple spatial discretization scheme that does not require front tracking techniques and remeshing at every time step (which may increase computational burden).
3. Using a preconditioning strategy such as developed in (Lipnikov et al. 2016). As stated by the authors, this method, combined or not with other strategies, can improve significantly the convergences path for solving Richards' equation. This preconditioning strategy is currently not implemented in the WOLF software.

## 6.4 Validation

The validity of the model is checked against the “New-Mexico” test (Manzini & Ferraris 2004). It consists in a 1-D vertical column of a soil named “New-Mexico”. The constitutive law used for this soil is the van Genuchten – Mualem law with the parameters given in Table 34. The boundary conditions are:

- a constant pressure of  $-0.75$  m at the upper boundary condition ( $z = 0$  m) and,
- a constant pressure of  $-10$  m at the lower boundary condition ( $z = -1$  m).

The initial condition is a constant pressure of  $-10$  m for all the nodes. The simulation is ran for 48 h and results are extracted every 12 h.

The initial and boundary conditions can be compared to the soil law curve depicted in Figure 179. It appears that the initial condition is close to the residual water content state. Moreover, the boundary conditions do not imply a saturation of the soil.

Type of soil	$\theta_s$ [-]	$\theta_r$ [-]	$K_s$ [m/s]	$\alpha$ [ $\text{m}^{-1}$ ]	$n$ [-]	$\psi_0$ [m]
New-Mexico	0.368	0.102	$9.22 \cdot 10^{-5}$	3.35	2	-0.2111

*Table 34: van Genuchten – Mualem parameters for the “New-Mexico” soil*

The computation is lead with several different parameters. We vary the number of nodes, the times step, the upwinding method and the number of Krylov subspaces. The number of iterations needed to converge the 48 h simulated as well as the success to converge or not a solution are recorded. These data allow to understand which set of parameters are more favorable for fast and/or reliable computations. Results are given in Figure 178.

In this figure, the number of iterations is represented as boxplots. Indeed, for a given value represented in Figure 178, the other parameters take all their possible values. This lead to a set of number of iterations for which it is possible to represent boxplots. Looking at the trend between boxplots allow to understand which values favor faster computation.

In Figure 178, it appears that some parameters guaranty 100 % success rate while others do not. In particular, higher number of nodes and the use of the Anderson accelerator favor high success rates. Concerning the upwinding method, the arithmetic mean as well as the constant reconstruction are the most successful methods.

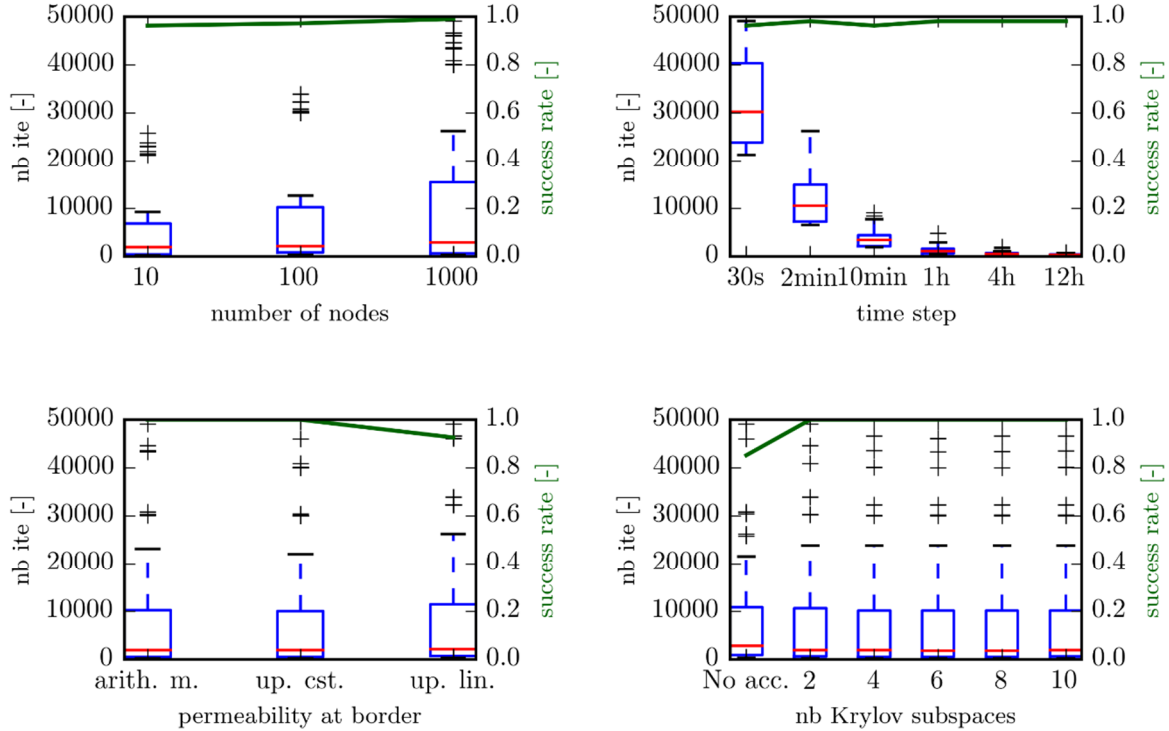


Figure 178: Number of iterations required for the computation of the validation test and associated success rates

Concerning the number of iterations, fewer nodes and larger time steps seem to yield less iterations. While this observation appears natural for the time step, it is less obvious for the spatial discretization. We attribute this trend to the fact that with a higher number of nodes the wetting front is better represented. This zone of high nonlinearity requires more iterations to be converged. With less nodes, the wetting front is badly captured and highly nonlinear phenomenon are hidden. The other parameters do not have effects on the number of iterations as significantly as the previous ones.

Numerical results obtained with the three upwinding methods, 100 nodes, a 2 minute time step and 10 Krylov subspaces are compared to Manzini & Ferraris' results (plain lines) in Figure 180. While Manzini & Ferraris' results are obtained with 1000 nodes, our results are obtained with less nodes but produce satisfactory agreement, especially when the linear reconstruction is used. Using the arithmetic mean to compute the hydraulic conductivity at the borders produce slightly inferior results compared to the linear reconstruction. Finally, the constant

reconstruction is the “worst” upwinding method and it does not produce a higher success rate than the arithmetic mean.

This observation can be justified by the rapid changes in the hydraulic conductivity. Indeed, considering a constant upstream reconstruction takes the hydraulic conductivity at the node ( $\Delta z / 2$  away from the border), where the wet soil has a higher hydraulic conductivity. On the other hand, the arithmetic mean and the linear reconstruction consider the downstream node where hydraulic conductivity is much lower. This leads to a more balanced evaluation of the hydraulic conductivity at the border.

Having a look at the range of the van Genuchten – Mualem law explored by this validation test is interesting. Indeed, as Figure 179 shows, only the lower part of the curve, where low level of nonlinearity exists, is explored. This is the situation that is the less critical for the convergence of a solution.

The influence of the spatial and time steps on this validation test is discussed in appendix D.2.

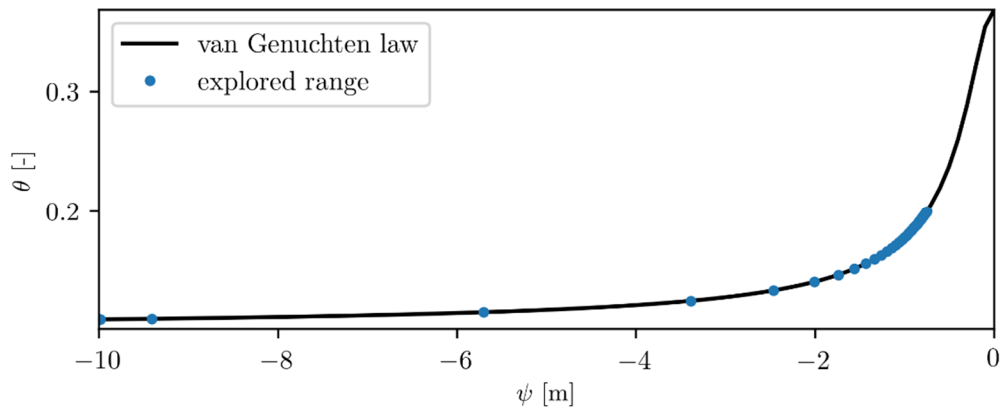


*Figure 179: Range of the van Genuchten law explored by the validation test*

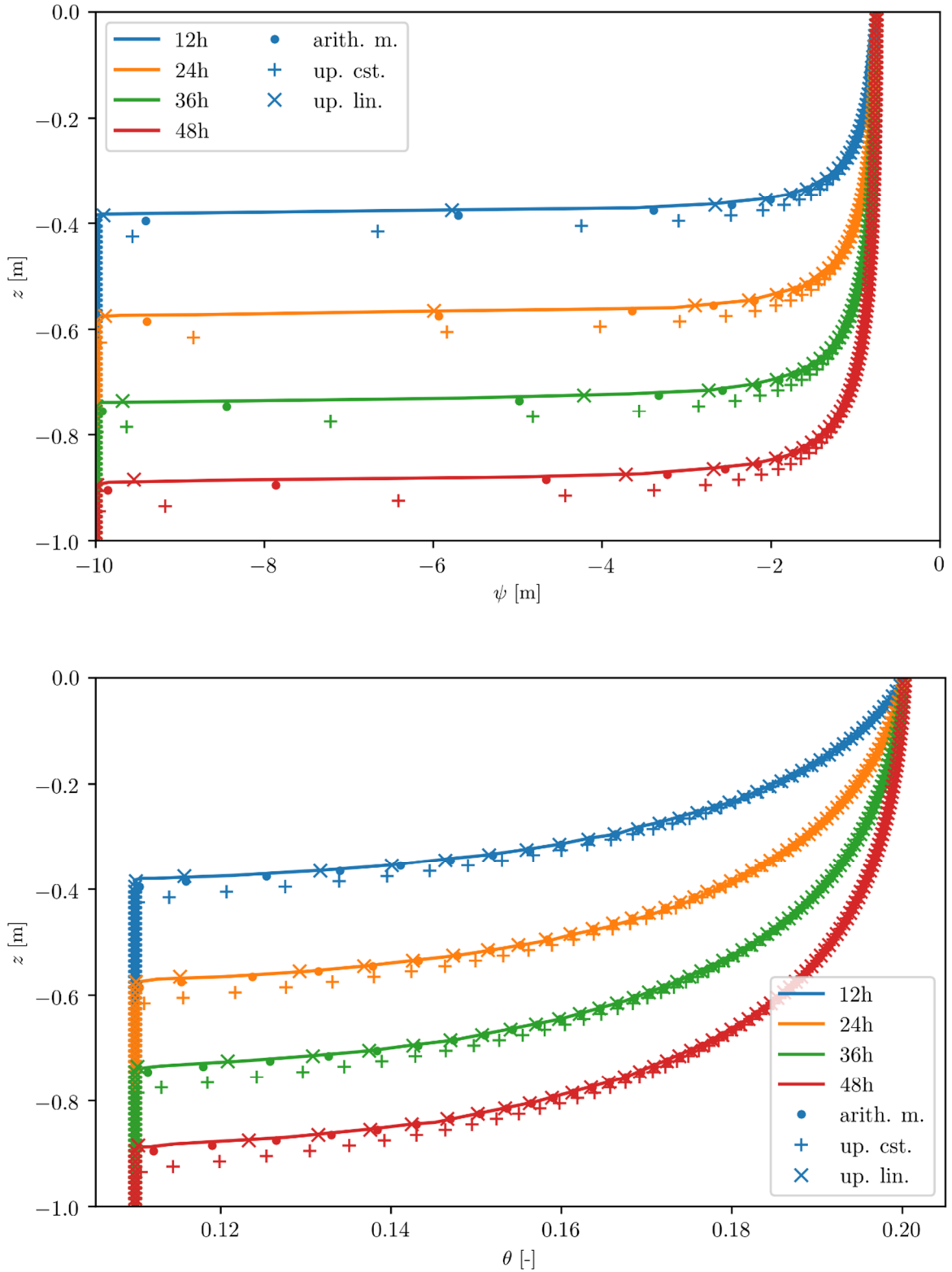


Figure 180: Results obtained with 100 nodes, a 120 s time step and no Anderson acceleration (markers) compared to (Manzani et al., 2004) (plain lines)

## **6.5 Scenarios**

In order to evaluate the ability and the speed of our model to converge an unsteady solution 6 scenarios are defined. They are meant to reproduce a wide range of different physical situations.

### **6.5.1 Description of the scenarios**

All the cases are briefly described in Table 35 where initial conditions (IC) and boundary conditions (BC) are given. All cases represent a 10 m deep column. The altimetric reference ( $z = 0$  m) is placed at the top of the column. Simulations are all performed over 14 days.

The first scenario consists in an emptying process of a vertical column. The initial condition gives a hydrostatic pressure on the entire column. All the column is saturated. Decreasing the lower BC leads to the emptying of the column. The final value of the lower BC is chosen in order to keep some soil saturated at the bottom.

The second scenario is very similar to the first one except that the initial condition is chosen in order to have the presence of a vadose zone initially.

For the four other scenarios, the filling of a column is represented in various ways: the column is filled from the bottom (scenario 3), from the top (scenario 4) or from both limits (scenario 5). Scenario 6 is typical from a water input from the surface limited in time (e.g. rain falling on the surface). As explained in (Ogden et al. 2015), this is one of the phenomenon that should be reproduced by a model.

For all the scenarios tested, the lower part of the column is always kept saturated. This was chosen in order to correspond to the practical situation where these 1-D columns will be used in the WOLF software. Indeed, these 1-D columns are designed to interact with surface input and fully saturated water tables at the bottom. The lower positions of the columns are chosen in order to be always saturated, ensuring the compatibility with the saturated model below.

	Scenario 1	Scenario 2	Scenario 3	Scenario 4	Scenario 5	Scenario 6
	<i>Emptying a saturated column</i>	<i>Emptying a partially saturated column</i>	<i>Filling a column by the bottom</i>	<i>Filling a column by the surface</i>	<i>Filling a column by both limits</i>	<i>Falling slug</i>
						
<b>Column depth</b>	10 m	10 m				
<b>Duration</b>	14 days	14 days				
<b>IC</b>	$\phi = 0$ m	$\phi = -5$ m	$\phi = -9$ m	$\phi = -9$ m	$\phi = -9$ m	$\phi = -9$ m
<b>Upper BC</b>	Impervious	Impervious	Impervious	$\phi$ varies linearly from -9 m to 0.5 m in 24 h	$\phi$ varies linearly from -9 m to 0.5 m in 24 h	$\phi$ varies linearly from -9 m to 0.5 m in 12 h and then from 0.5 m to -9 m in 12 h
<b>Lower BC</b>	$\phi$ varies linearly from 0 m to 8 m in 24 h	$\phi$ varies linearly from -5 m to -9 m in 24 h	$\phi$ varies linearly from -9 m to 0.5 m in 24 h	Impervious	$\phi$ varies linearly from -9 m to 0.5 m in 24 h	Impervious

Table 35: Description of 6 scenarios

For a better understanding of the phenomenon represented in the 6 scenarios, practical results are shown below. A sandy loam soil is chosen with a fine spatial discretization of 1 cm (1000 nodes) and a fine time step (1 minute). In order to improve the convergence process, 10 Krylov subspaces are used. The hydraulic conductivity at the borders is computed with an arithmetic mean.

For scenario 1 (Figure 181), the emptying of a fully saturated water column, the drying front evolves quickly at the beginning (first 72 h) and then the process slows down. The emptying is first driven by the evolution of the lower boundary condition and then by capillary flow. It can be noticed that the front becomes sharper with time, leading to more abrupt changes in the hydraulic conductivity values. Figure 187 shows that, for the upper node of the soil column, only the most saturated part of the van Genuchten law is explored for a sandy loam.

Scenario 2 (Figure 182) is very similar to scenario 1 except that it begins from a partially saturated column. For a node located close to the initial capillary fringe (around -6 m), the explored range of the van Genuchten law is similar to what was observed for scenario 1 (see Figure 187).

For scenario 3 (Figure 183), the filling of the column from the bottom boundary induces a sharp front in terms of pressure, water content and hydraulic conductivity. Filling the column from the upper boundary (Figure 184) leads to similar observations. When both boundaries are used to fill the column (Figure 185), different apparent propagation velocities of the front can be observed. This is due to the values of the boundary condition used. Since the BC evolves with time and that infiltration can only begin when the pressure gets closer to 0, the upper BC begins to infiltrate water only during the last hours of the 24 h of BC changes, while the lower BC infiltrates from the beginning of the simulation. These 3 scenarios explore a wide range of the van Genuchten law, from a water content very low to full saturation.

The final scenario tested is a falling slug (Figure 186). It represents the infiltration of water for an input at the surface limited in time. The soil parameters and the input parameters used to produce this figure lead to a non-saturation state and  $K$  remained relatively low in the region of the slug. This lead to a slow advance of the wetting and drying front. We can also notice the diffusive effect of the phenomenon. Moreover, the explored range of the van Genuchten law is limited and does not include the zone of high nonlinearity close to the saturation point.

Compared to the validation case (section 6.4), the explored range of the van Genuchten law includes the saturation point (at  $\psi = 0$  m) for scenarios 1 to 5 which is a zone of high nonlinearity. Differences in the convergence success rate that are observed later may be linked to this observation.

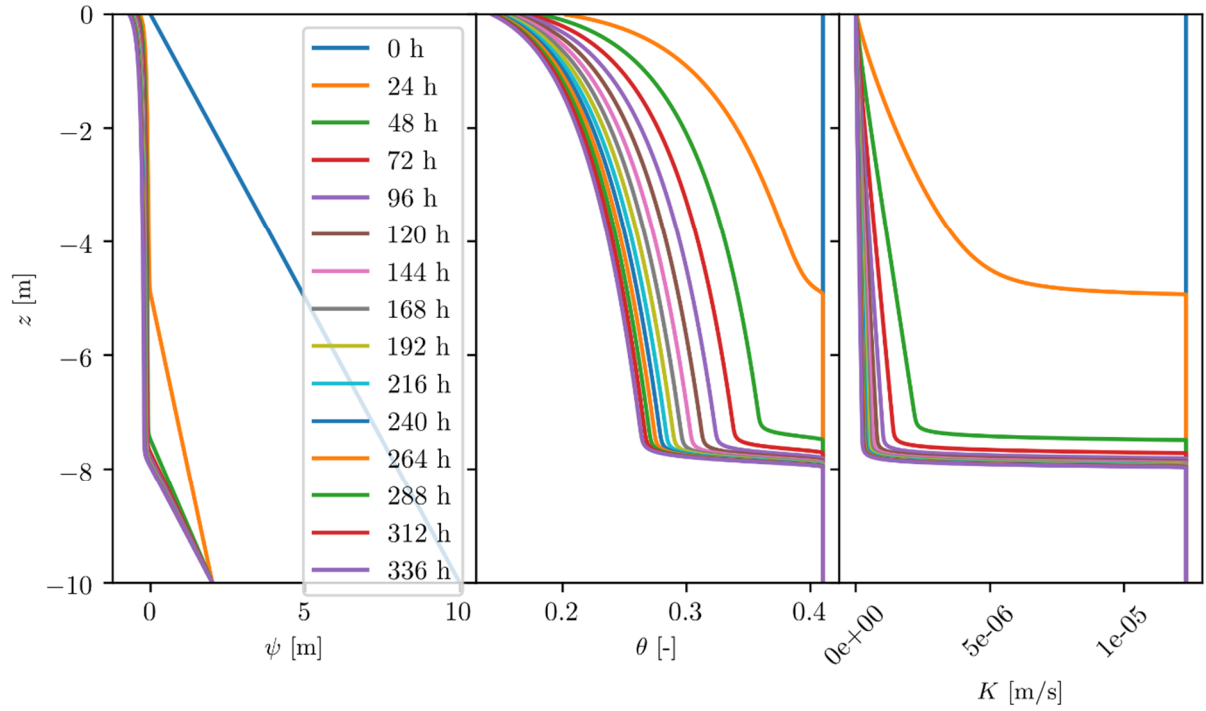


Figure 181: Pressure, water content and hydraulic conductivity for scenario 1 with sandy loam

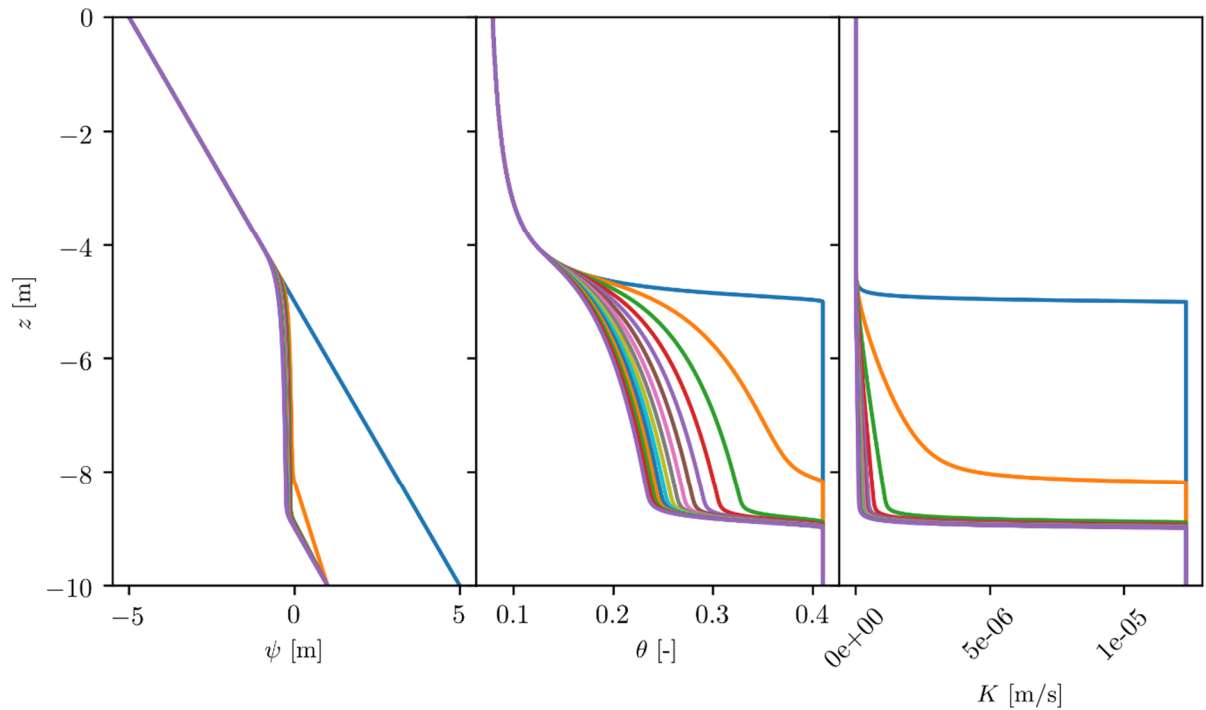


Figure 182: Pressure, water content and hydraulic conductivity for scenario 2 with sandy loam

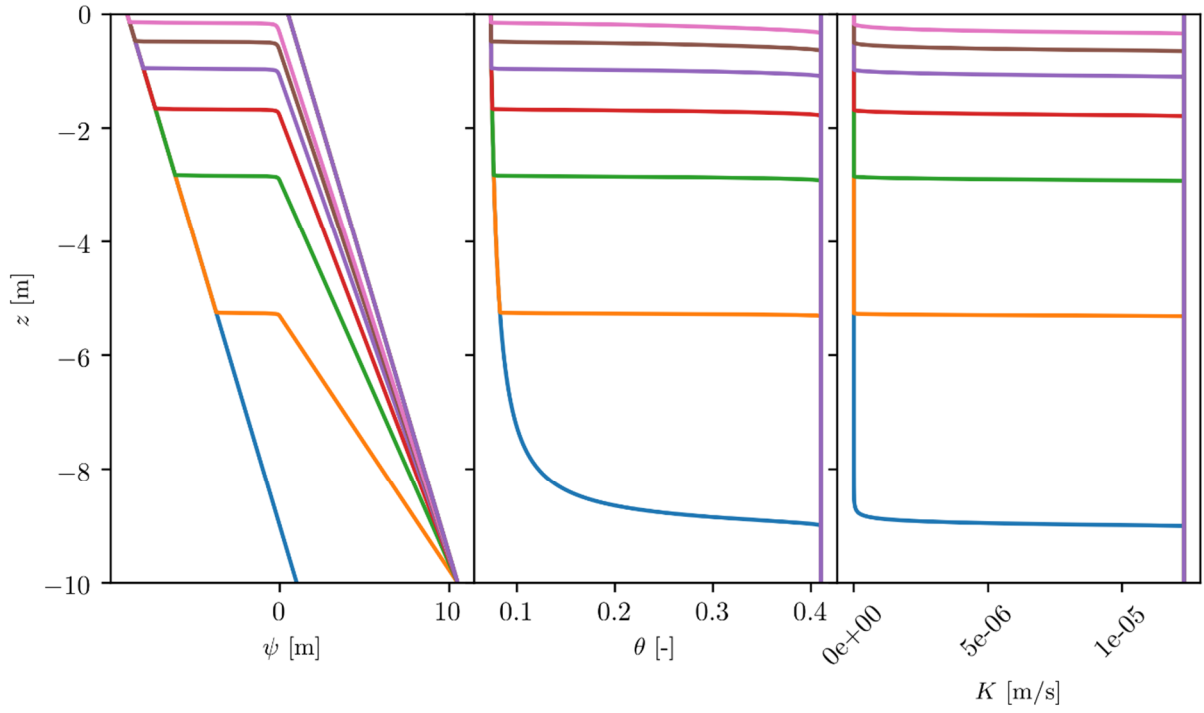


Figure 183: Pressure, water content and hydraulic conductivity for scenario 3 with sandy loam

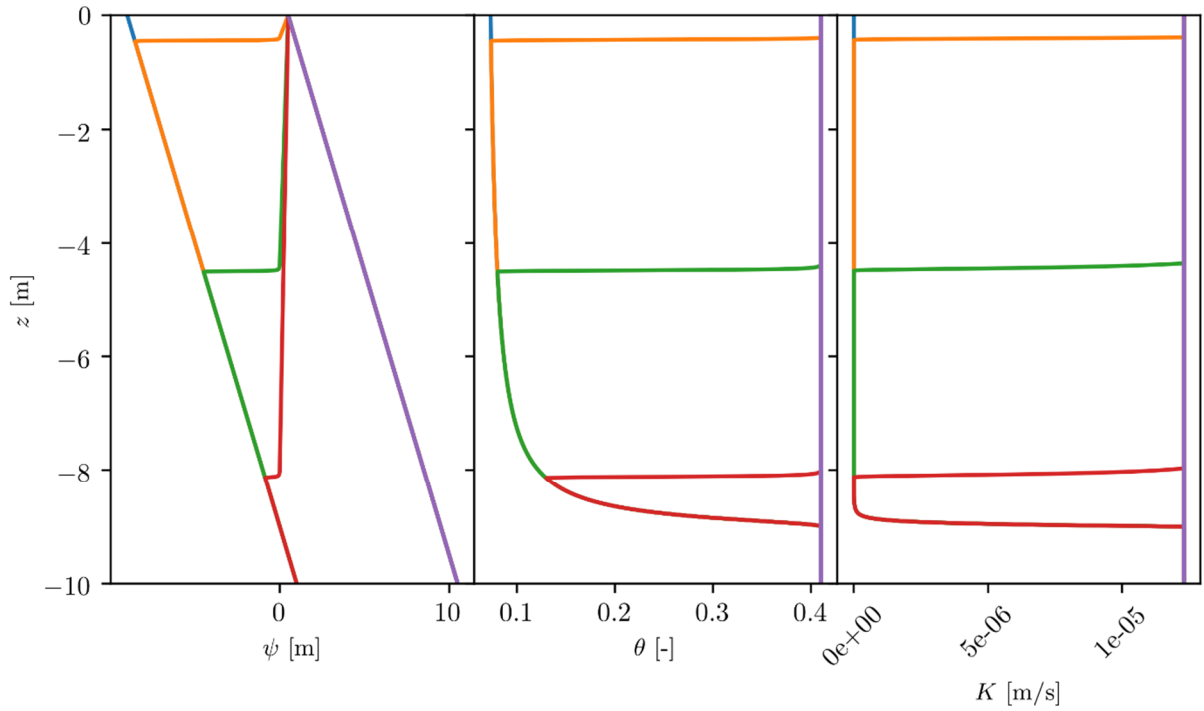


Figure 184: Pressure, water content and hydraulic conductivity for scenario 4 with sandy loam

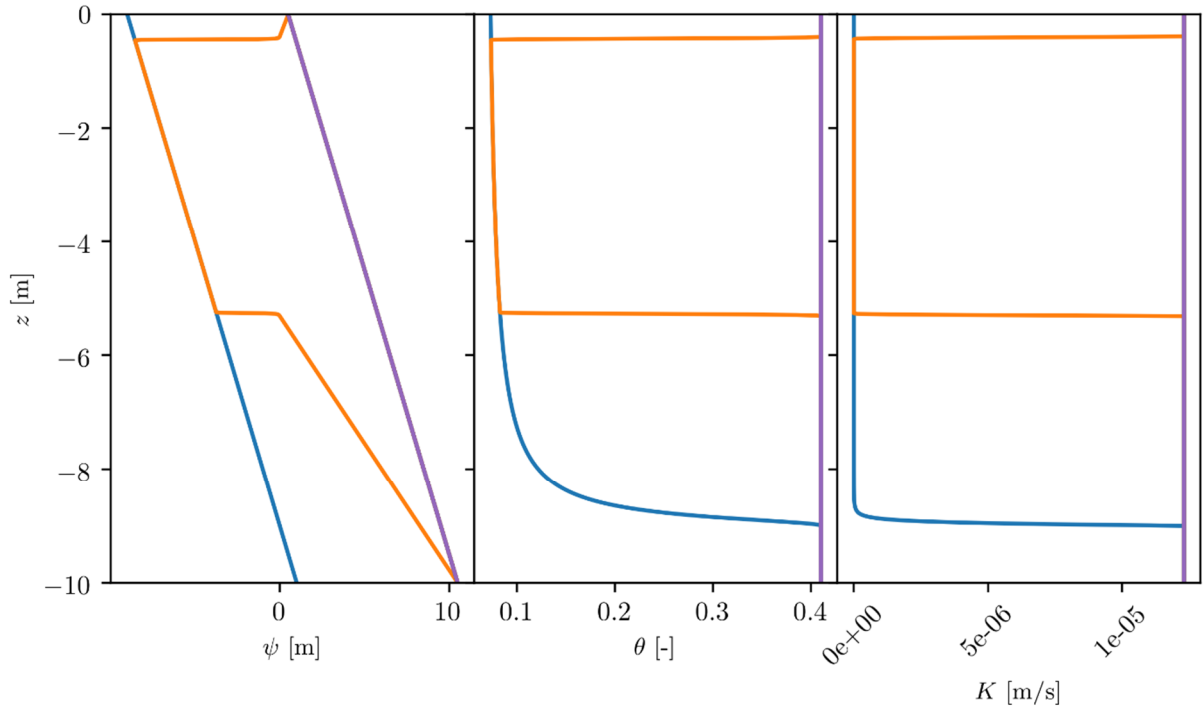


Figure 185: Pressure, water content and hydraulic conductivity for scenario 5 with sandy loam

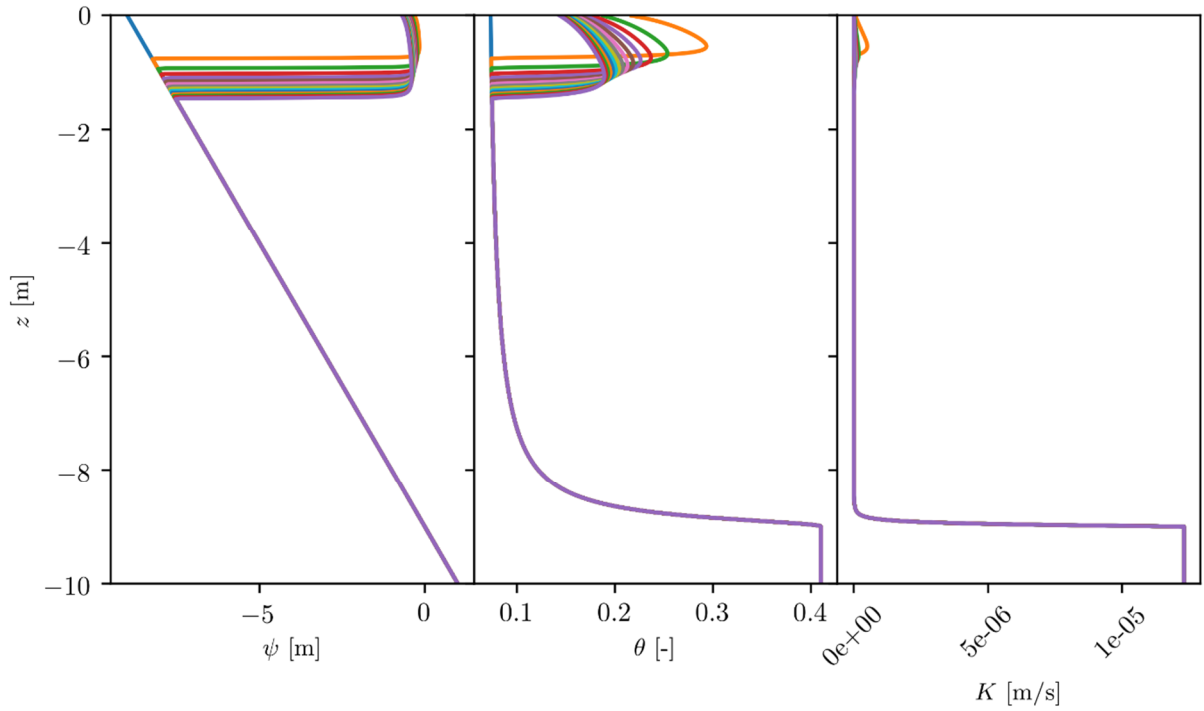


Figure 186: Pressure, water content and hydraulic conductivity for scenario 6 with sandy loam

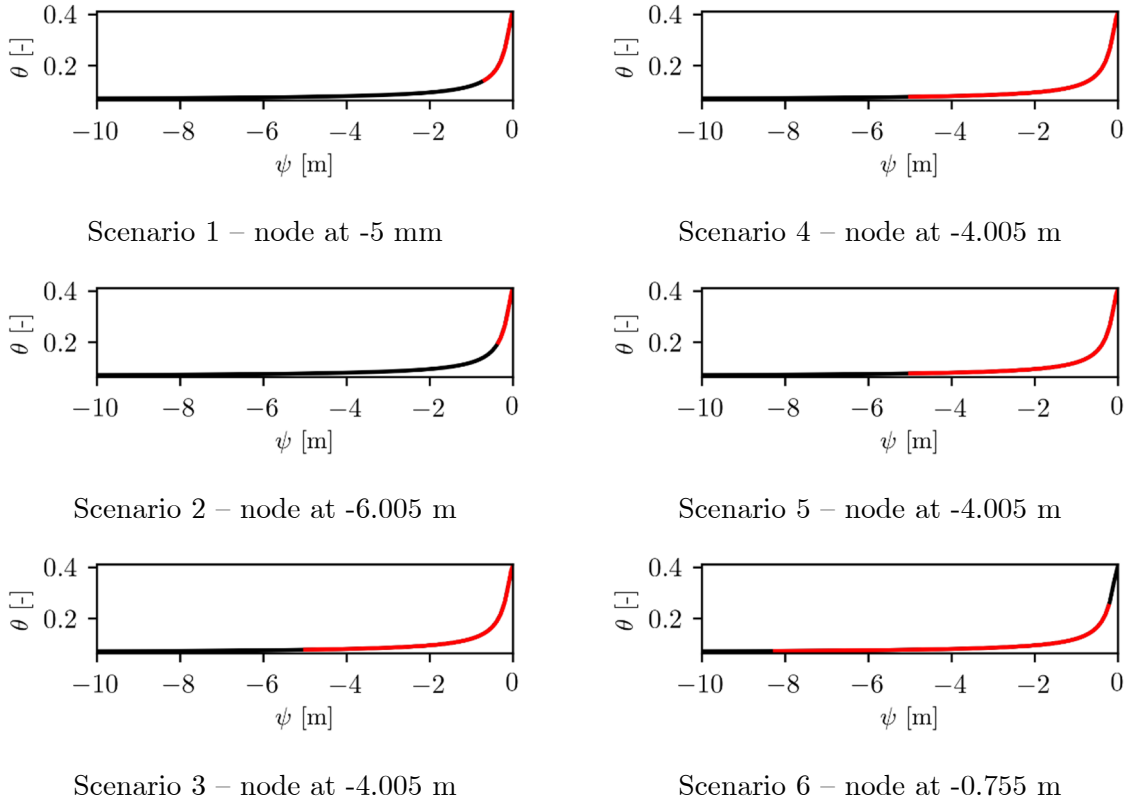


Figure 187: Range of the van Genuchten law explored with a sandy loam for a node specific for each scenario

### 6.5.2 Convergence success with the van Genuchten – Mualem law

The goal of this section is to assess the convergence success of the 6 scenarios for different soils (modelled by the van Genuchten – Mualem law) using different computation parameters. The parameters tested are:

- The number of nodes: 10, 100 and 1000 nodes
- The time step: 1 minute, 1 hour, 12 hours and 1 day
- The method to compute the hydraulic conductivity at the borders: using an arithmetic mean or a linear upstream reconstruction
- The setting of the Anderson accelerator: 3, 5, 7 and 10 Krylov subspaces and without any accelerator
- The type of limiter used: no limiter, limiter based on the soil law and a relaxation coefficient based on the soil law

The computation of the scenarios described hereabove for a whole range of parameters is handled automatically in the WOLF software.

In order to get a first idea of the best parameters for best convergence, a preliminary analysis is performed (graphical results are available in appendix D.3). This analysis consists in taking all results and focusing only on particular values of a studied parameter, the other parameters

can take any other value. The resulting indicator is the success rate. It is defined as the ratio between the number of computation that succeeded to converge all time steps and the total number of computations.

For the method to compute the hydraulic conductivity at borders (Figure 210), the arithmetic mean seems to lead to higher convergence rate than the linear reconstruction. Indeed, the lines in Figure 210 are either flat or decreasing, meaning that the arithmetic mean has better convergence rates.

The second parameter tested under the same conditions is the type of limiter. Results are given in Figure 211. It appears that higher success rates are always obtained without a limiter.

Taking for granted that the arithmetic mean to compute the hydraulic conductivity at borders and not using a limiter are the best way to foster convergence, these two parameters are now considered as fixed. A last analysis is performed for the number of subspaces to use for the Anderson accelerator. Graphical results (Figure 212) show that disabling the accelerator is not encouraging convergence (in a vast majority of cases). Concluding about the best number of Krylov subspaces to use is not an easy task. Indeed, the convergence rate increases slightly almost monotonously with the number of subspace for scenarios 1 and 2 while it remains somehow constant with the number of subspaces for scenarios 3 to 6. Some of the cases show an optimum around 5 Krylov subspaces. This value is held for the next steps of the discussion.

Figure 188 is produced considering these preferred values. It shows the number of iterations required to converge all the time steps, according to the time discretization (abscissa) and the number of nodes (line color). Several observations and comments can be made on the basis of this figure.

First, as it could be expected, the number of iterations generally decreases with an increasing time step. Larger time steps mean less time steps to compute for a given total time. If the number of iterations required to converge a time step is kept constant, then the total number of iterations decreases. Exceptions can be found, for example, for the second scenario with sand. In such a case, the number of iterations increases slightly between  $\Delta t = 12$  h and  $\Delta t = 24$  h (with 10 nodes). This means that the number of iterations to converge a time step can be increased by about a factor 2. It can also be noticed that, in general, for a given time discretization, the number of iterations increases with the number of nodes used. This may be explained by the fact that a finer discretization capture the front well enough and that nonlinearity effects should be handled correctly.

A general look at Figure 188 shows that we were not able to converge some cases with the chosen parameters. These cases concern scenarios 3 to 5 for the less permeable soils (from clay loam to clay). These cases are representative of problems with very sharp fronts. Only larger time steps and coarser grids favorize the convergence of some cases. A tentative of solution is proposed in next section.

For all other cases, some combinations of time step and spatial discretization work and others do not. In general, coarser grids provide better chances to converge a solution. But, as seen in appendix D.2, coarser grids lead to poorer results. Concerning the two first scenarios, low time steps allow to converge almost all spatial steps. For the other scenarios, a general conclusion seems difficult to draw.

Moreover, scenario 6, which can be understood as a more complex case as scenario 5, shows a better convergence success rate than scenario 5. This can be explained by the explored range of the van Genuchten law, as shown in previous subsection. Indeed, scenario 5 explores the constitutive soil law up to saturation while scenario 6 operates only a limited part of the law.

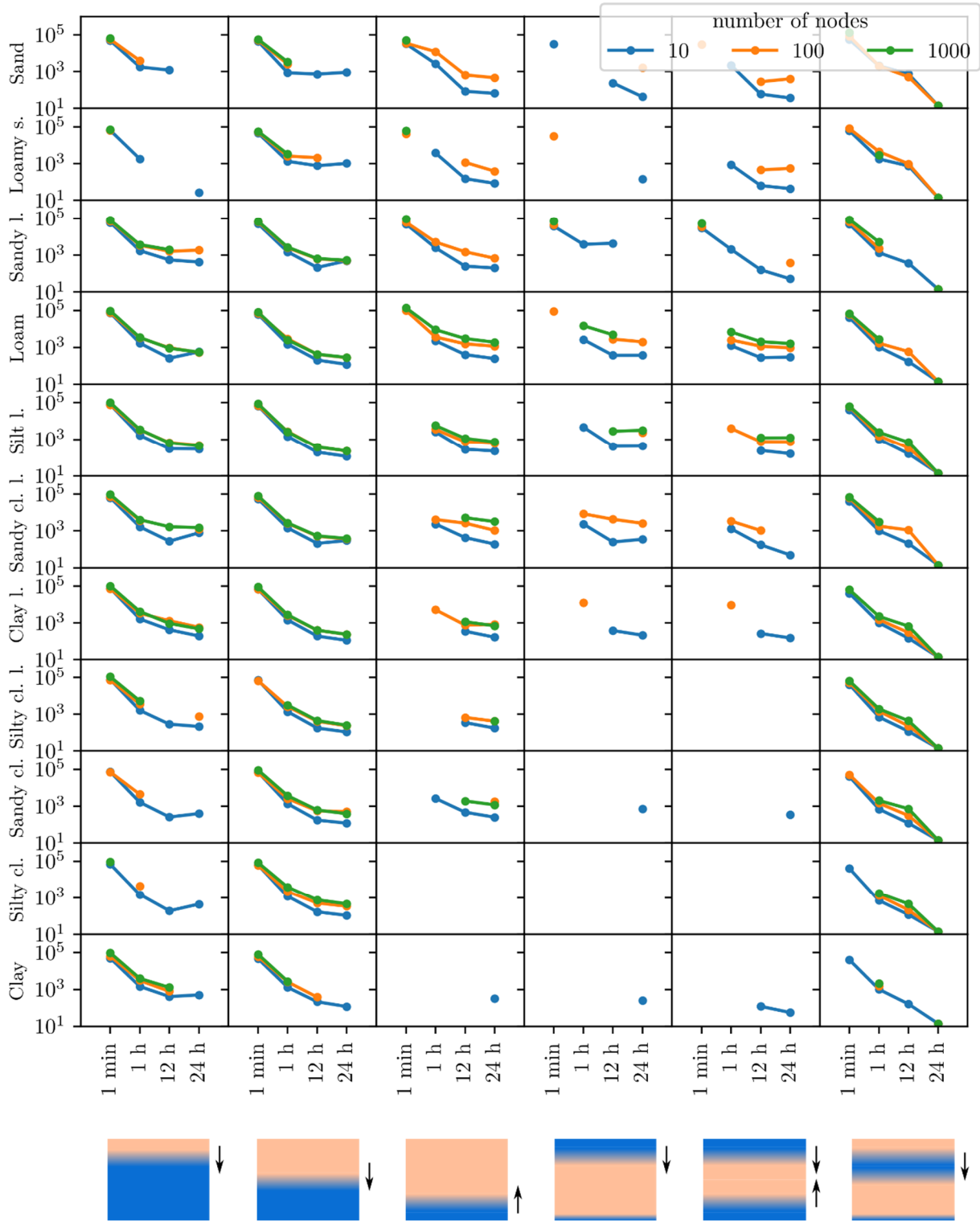


Figure 188: Number of iterations required to converge each scenario for 11 different soils (hydraulic conductivity at borders computed using an arithmetic mean, no limiter used and 5 Krylov subspaces)

## 6.6 Homotopy to improve the convergence

As seen in previous section, the convergence of some cases with some soils was not possible. In order to overcome this issue, the use of homotopy is tested. First, the concept of homotopy is explained, then we apply it to the soil law and show how it performs on the problematic cases.

### 6.6.1 Introduction to homotopy

Functions  $f$  and  $g$  are said to be homotopic if  $f$  can be transformed continuously to  $g$  and vice versa. This principle is illustrated in a  $(x,y)$  plane in Figure 189. This mathematical concept can be used to solve polynomial systems (Bates et al. 2013). For instance, Baayen et al. (2018) use the concept of homotopy in the frame of the optimization problem of hydraulic controls on river networks.

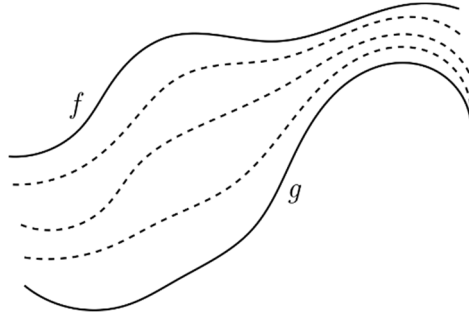


*Figure 189: Concept of homotopy illustrated on a random example*

The basic idea that enables to use homotopy as a strategy to solve nonlinear system lies in the concept of deforming the system that should be solved to another system that ensures to find a solution. From this deformed system, the solution found, even if it is far from the real solution, constitutes a starting point for the deformation process of the system. Let us define  $S_0$  as the initial deformed system and  $S_N$  as the final system (not deformed) that should be solved. Each system  $S_i$  is a continuous deformation of system  $S_0$  to system  $S_N$ . The solution found for system  $S_i$  is used as the initial guess to solved system  $S_{i+1}$ .

### 6.6.2 Homotopy applied to the soil law

As shown previously, the van Genuchten – Mualem soil law is highly nonlinear. In order to encourage better convergence, the homotopy concept is applied to the pressure – water content law. The initial deformed function is the constant relationship

$$\theta(\psi) = \theta_0 \quad (237)$$

with  $\theta_0$  a constant value chosen as  $\theta_0 = \theta^t$ . Then, the intermediate laws are a continuous deformation from equation (237) to equation (209). To do so, the following generic law is used:

$$\begin{aligned}\psi \geq 0 &\Leftrightarrow \theta(\psi) = \theta_0 - \beta(\theta_0 - \theta_s) \\ \psi < 0 &\Leftrightarrow \theta(\psi) = \theta_0 - \beta(\theta_0 - \theta_r) + \beta(\theta_s - \theta_r) \left[ 1 + (\alpha |\psi|)^n \right]^{\frac{1}{n}-1}\end{aligned}\quad (238)$$

Where  $\beta$  is a value that varies between 0 and 1. When  $\beta = 0$ , equation (238) is equivalent to equation (237). When  $\beta = 1$ , equation (238) is equivalent to equation (209). Coefficient  $\beta$  can be seen as a squeezing coefficient. It allows to modify the van Genuchten – Mualem law from its full range (from  $\theta_r$  to  $\theta_s$ , when  $\beta = 1$ ) to a flat law (when  $\beta = 0$ ).

The water holding capacity is computed by taking into account the squeezing of the  $\theta(\psi)$  law.

It becomes:

$$\begin{aligned}\psi \geq 0 &\Rightarrow \eta(\psi) = 0 \\ \psi < 0 &\Rightarrow \eta(\psi) = \alpha(n-1)\beta(\theta_s - \theta_r)(\alpha |\psi|)^{n-1} \left[ 1 + (\alpha |\psi|)^n \right]^{\frac{1}{n}-2}\end{aligned}\quad (239)$$

For the hydraulic conductivity, the homotropy principle is also applied but indirectly. Indeed, in order to limit the possible values that can be taken by  $K$ , it was chosen not to squeeze the law in the same way as it is done for equation (238). The law is rather expressed in a way that only a range of the law is explored and its nonlinear nature is kept. To do so, rather than expressing  $K$  as a function of the pressure, we express it as a function of the water content:

$$\begin{aligned}\theta = \theta_s &\Rightarrow K(\theta) = K_s \\ \theta_r \leq \theta < \theta_s &\Rightarrow K(\theta) = K_s \sqrt{\frac{\theta - \theta_r}{\theta_s - \theta_r}} \left\{ 1 - \left[ 1 - \left( \frac{\theta - \theta_r}{\theta_s - \theta_r} \right)^{1/m} \right]^m \right\}^2\end{aligned}\quad (240)$$

with  $m$  linked to  $n$  as expressed in (208). Since the possible values of the water content are limited by the squeezing coefficient  $\beta$ , the possible values of  $K$  are also limited, but the range extends as  $\beta$  grows. In the frame of homotopy, computing  $K$  as a function of the pressure is not relevant. Indeed, since the water content is a constant at the beginning, pressures might not be estimated accurately which would lead to incorrect values of the permeability parameter. The proposed technique aims to estimate  $K$  as accurately as possible since the beginning homotopy.

At the beginning of the homotopy process, the use of  $\beta = 0$  implies that  $\theta = \theta_0$ ,  $\eta = 0$  and  $K = K(\theta_0)$ , all values being constants. System to solve (234) becomes:

$$A\Delta\phi = -A\phi^* - s \quad (241)$$

with the terms in  $A$  remaining constant since the hydraulic conductivity is a constant. This system is linear and does not require iterations. Finding a solution is certain provided a good conditioning of the system.

The choice of values to give to  $\beta$  defines how fast the soil law transforms itself. In our code, the values of  $\beta$  can be distributed according to two methods:

- values of  $\beta$  can be evenly spaced from 0 to 1 or,
- they can be picked according to a geometric progression.

The number of values to pick is an input parameter. The second implementation would have larger steps when the law does not present large non linearities but smaller steps when the law approaches its final form. A geometrical progression takes values

$$(0) \quad a \quad a + aq \quad a + aq + aq^2 \quad a + aq + aq^2 + aq^3 \quad \dots \quad a + aq + aq^2 + \dots + aq^n \quad (242)$$

The last value  $\beta$  must be equal to 1:

$$a + \sum_{i=0}^n aq^i = a \frac{1 - q^{n+1}}{1 - q} = 1 \quad (243)$$

Parameters  $a$  and  $q$  of the geometric progression are linked by (243).

As shown hereabove, choosing  $\beta = 0$  is equivalent to a steady state computation. This approximation might be valid for the first time step. For further time steps,  $\beta = 0$  can move the solution away from its final state compared to the solution found at the previous time step. For this reason, when  $t > 0$ , the initial value of the squeezing coefficient is not taken at 0.

### 6.6.3 Homotopy method applied to scenarios

As shown previously (Figure 188), we were unable to converge some scenarios with some soils. These cases are tested here with the use of the homotopy method presented hereabove. Several numbers of homotopy steps are tested.

A first test is done with an even distribution of coefficients  $\beta$ . The number of iterations needed to converge the cases are given in Figure 190. The absence of point means that the computation failed to converge.

The efficiency of the homotopy method such as implemented here is limited but allows some cases to converge. These cases can be recognized by the absence of a point at the “no hom.” (no homotopy) tick and the presence of a point further. This is the case for example for the 12

hour time step with 100 nodes for scenario 4 with silty clay loam. For that case, homotopy with 1000 steps allows to converge a solution while it was not feasible without homotopy. This situation can be found for other scenarios and other soils.

Increasing the number of homotopy steps increases the total number of iterations, meaning that, for a given number of nodes, the total computation time increases. It is also worth noting that the silty clay soil is still unable to converge for any of the time and spatial steps.

A second test is done with a geometric distribution of  $\beta$ . We take  $q = 0.93$  (in order to begin with a relatively low  $\beta$  value) and  $n$  is set according the corresponding number of homotopy steps to compute. Results are given in Figure 191. No particular improvements in term of convergence can be noticed compared to Figure 190. Silty clay is still impossible to converge for scenarios 3 to 5.

Based on the results presented in Figure 190 and Figure 191, homotopy seems to be a promising technique to improve the chances to converge difficult cases. However, homotopy does not solve all convergence issues and further research and developments should be made in order to improve this technique and test all its capabilities.

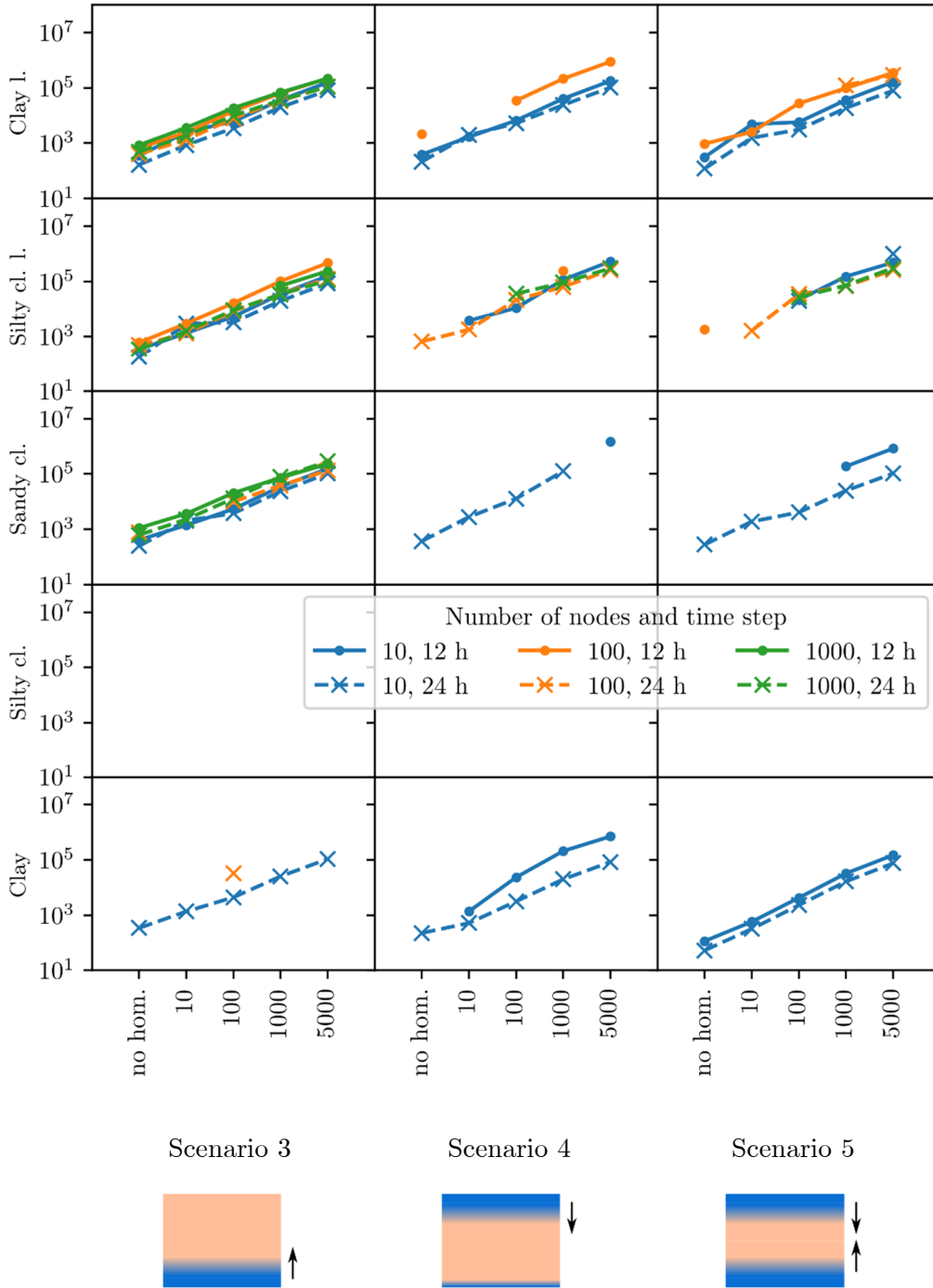


Figure 190: Number of iterations required to converge 3 of the scenarios for 5 selected soils according to the number of steps used in the homotopy process (hydraulic conductivity at borders computed using an arithmetic mean, no limiter used and 5 Krylov subspaces) – linear distribution of  $\beta$

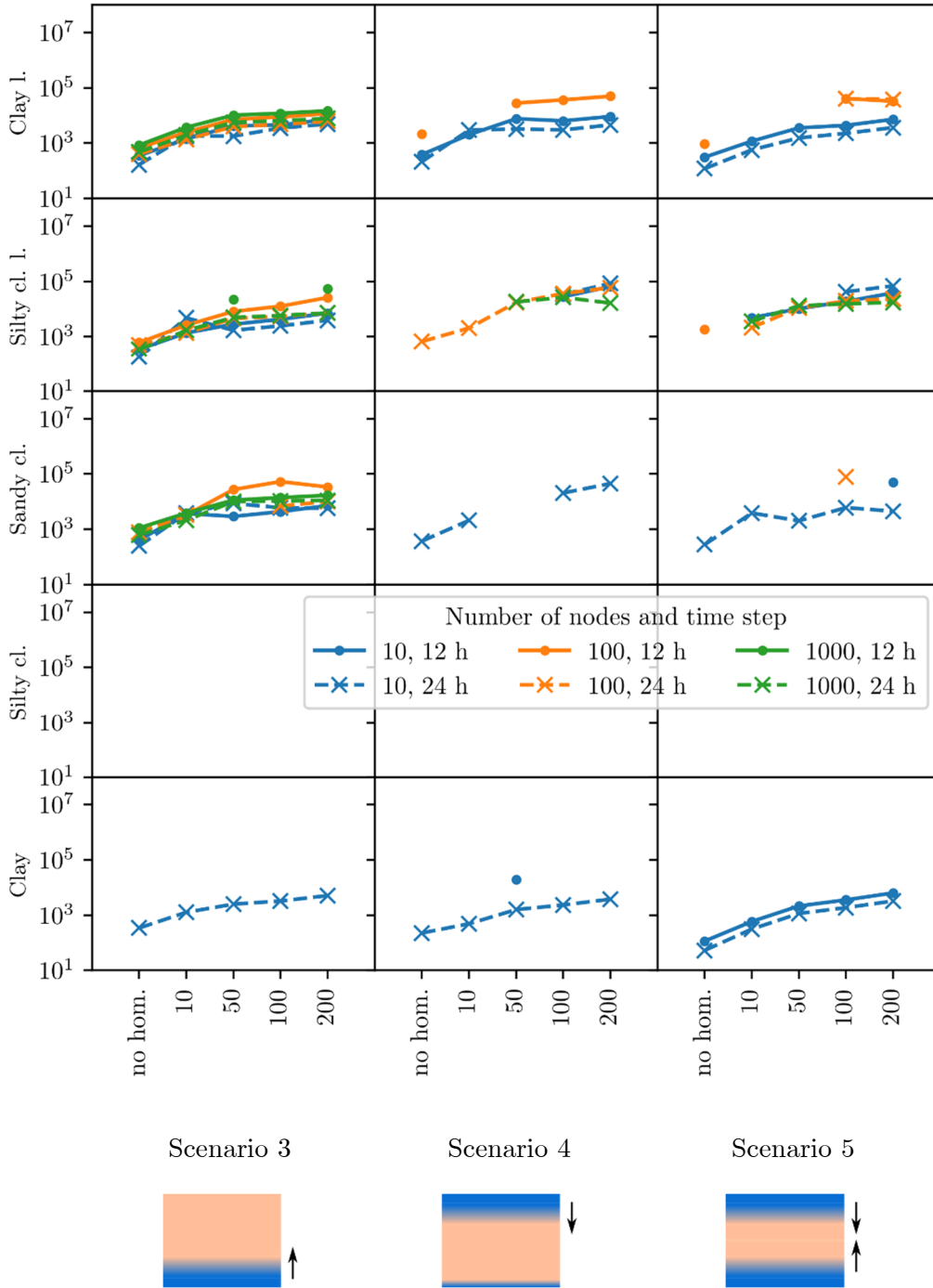


Figure 191: Number of iterations required to converge 3 of the scenarios for 5 selected soils according to the number of steps used in the homotopy process (hydraulic conductivity at borders computed using an arithmetic mean, no limiter used and 5 Krylov subspaces) – geometric distribution of  $\beta$

## **6.7 Conclusions and perspectives**

In this chapter we investigated convergence problems that may occur when we solve Richards' equation. First, we showed that for 6 scenarios and 11 typical soils, the convergence may be impossible for some parameters (spatial discretization, time step, etc.). Filling a column was especially difficult for less permeable soils.

We investigated the use of homotopy in order to facilitate the convergence of most difficult cases. Homotopy is applied on the van Genuchten – Mualem  $\theta - \psi$  law. It squeezes initially the law to reach a constant value of water content and then progressively extends it to reach the real range of the soil law. A linear and a geometric evolutions were tested. Both methods improve the convergence under some parameters. However, in this state of implementation, they do not allow a universal improvement of non-converging cases. Especially, one out of the eleven soils was not able to converge with any parameter set.

These first encouraging results with homotopy make us believe that further research and developments should be carried out. For instance, the homotopy method could be tested over other parameters of the soil law (e.g.  $\alpha$  or  $n$ ). The evolution of the  $\beta$  coefficient should be further investigated in order to find a better path. Also, other strategies exist in order to improve the convergence of Richards' equation. Testing extensively the combination of these techniques would be of great interest.

# Chapter 7: General conclusions

## 7.1 Contributions

Applying uncertainty analysis to hydraulic models is a real challenge. Indeed, hydrodynamic and physically-based hydrological models are computationally expensive and require special strategies to be integrated in an uncertainty analysis framework. In order to tackle this challenge, this thesis focused on two main topics:

- implementing efficient uncertainty analysis methods in the WOLF suite and,
- developing fast and robust numerical models for hydrodynamics and physically-based hydrology

We began with a general overview of the uncertainty analysis methods that exist. A special focus was made on efficient methods that require less evaluation points than the traditional Monte Carlo method. A rigorous theoretical literature review of these methods was performed. In order to compare these methods, we designed polynomial tests and a more playful bungee jump test. We found that methods that use less evaluation points produce satisfactory results when compared to Monte Carlo method. In order to apply all reviewed methods to hydraulic cases, a software was designed and implemented in the WOLF suite. It was able to launch several hydraulic simulations in parallel and to process the results in the chosen uncertainty analysis method. The implementation is general and allows to apply uncertainty analysis to any model available in the WOLF software. Our literature review continued with a selection of uncertainty sources that concerns hydraulic applications.

Then, concerning the development of fast and robust numerical models, two models were implemented and improved. The first one is a fast steady 1-D open-channel flow solver. In addition to uncertainty analysis, this fast solving algorithm can be used, for instance, for the computation of a steady initial condition or hydraulic optimization. Our algorithm uses several original techniques to lower the computation time: a pseudo-temporal version of Saint-Venant equations, a sliding domain and an Anderson accelerator. These techniques allow to decrease the computation time but also to have excellent scalability characteristics. We found that our algorithm has a computation time linearly dependent on the number of nodes.

CasADi, an optimization tool, was introduced for comparison purpose with our fast solving algorithm. We began by setting the tool in order to use it with a formulation of the pseudo temporal equation. Thanks to a validation test based on experimental measurements in the HECE laboratory, we proved that CasADi is able to simulate steady 1-D flows. We also found

that our algorithm produced better computation times. Besides lower computation times, our algorithm scales linearly while it is not the case for CasADi.

However, CasADi is an elegant, original and easy-to-implement solution to solve steady 1-D problems. Moreover, we found that, thanks to the tricky use of sigmoid functions, CasADi is able to deal with complex closed cross sections that can be expressed analytically by parts.

After the implementation of 1-D models for open-channel and pressurized flows, the second numerical kind of model developed and improved in this thesis is the unsaturated component of physically-based hydrological model. The vertical 1-D unsaturated soil column model is enhanced with many state-of-the-art computation techniques known to improve the converge of Richards' equation solving. However, as pointed by the hydrogeology community, some cases are difficult to compute due to the high non linearity nature of the equation and constitutive laws. We highlighted this thanks to six scenarios, eleven soils and the combination of several time steps, spatial discretization, etc. Systematic tests were automatically launched on this basis in order to identify the sources of non-convergence. In order to overcome these convergence difficulties, homotopy (never applied in this context to our best knowledge) was applied to the most difficult cases. Encouraging results showed that this technique was prone to improve the convergence success rate. However, at this level of development, homotopy did not prove to be a universal technique to ensure convergence.

Based on the developments explained hereabove, the final goal of this thesis was to apply uncertainty analysis methods to hydraulic models. Due to the level of robustness and the computational speed of hydrodynamic and hydrological models, uncertainty analysis could be applied only under certain conditions.

First, applying extensively uncertainty analysis to a physically-based hydrological model was not yet possible. Even if some components of this model are robust enough to handle an uncertainty analysis (i.e., the surface hydrodynamic model and the fully saturated underground 3-D model), the unsaturated 1-D columns still suffer from a lack of robustness. However, developments in this thesis improved promisingly the convergence rate of this model.

Then, all uncertainty analysis methods introduced in this thesis were applied to hydrodynamic 1-D cases thanks to our fast 1-D solver. Academic 1-D cases allowed to highlight that methods with less points (PEM, PMM and SRSM) represent well the general behavior of the uncertain result compared to the more computing demanding Monte Carlo method. Over the three methods that require less evaluation points, we found that PMM produced best results and provided the most appealing theoretical background.

An original real world 1-D case was presented. This 7.5 km long river stretch allowed to test uncertainty methods in order to identify flooding risks of a field. We found that an uncertainty analysis is valuable to emphasize the validity of the conclusions that can be drawn from hydraulic results. Moreover, PMM showed to be an excellent alternative to Monte Carlo method.

After the 1-D application, we presented another original application, in 2-D this time. In order to assess the amount of sediments put in motion following a dam removal, we developed an original method that does not rely on full morphodynamic simulations. These morphodynamic models require sediments load data at boundaries and validation data that are rarely available. Moreover, morphodynamic simulations are often realized with unsteady boundary conditions, which increase the computational burden. Our bed stability indicator is a good alternative to full morphodynamic models when they cannot be applied. However, the modeler should pay special attention when s-he uses this technique. Indeed, the sediment load of the flow is not taken into account. It is the comparison between indicators obtained before and after dam removal that should lead the conclusions. Due to the computation time required for these 2-D hydrodynamic simulations, uncertainty analysis could be applied through PMM. Using uncertainty analysis was very valuable to discuss the confidence that one can have in the conclusions drawn.

## **7.2 Perspectives**

Uncertainty analysis brings valuable insight on the validity of conclusions. The validated computationally-cheap techniques that were tested on real world cases are available for engineering applications. In order to apply this kind of analysis in the best way, relevant information about the sources of uncertainty should be available. One who wishes to apply them should pay attention to this aspect and plan the acquisition of valuable data prior to the study. We found also that few uncertainty sources were well documented. Contributions to create a database of uncertainty sources in hydraulics and how one should evaluate them would be of great interest for the scientific and engineering community.

Topography is especially a source of uncertainty for which we could not find information in the scientific literature. It is however well-known that the topography of a hydrodynamic model is prone to uncertainty due to measurement errors or river bed morphological changes. Being able to quantify this uncertainty and introduce it in an uncertainty analysis framework would be very valuable.

For the application of uncertainty analysis, we developed fast computing techniques for 1-D shallow water models. They pave the way for an extended usage of hydrodynamic models in every-day engineering practice. Indeed, practitioners need easy to use and fast models to design, optimize and validate solutions to be implemented in the frame of civil and environmental engineering. Our fast 1-D steady open channel flow algorithm and the use of CasADi as a 1-D steady flow solver are in perfect adequation with this aim.

When applying uncertainty analysis to the 2-D hydrodynamic case presented in this thesis, a pragmatic approach to assess riverbed stability was chosen since a full morphodynamic model could not be used due to the lack of sediment transport data. Removing dams to restore river continuity is currently a major trend in many areas in the World. For a significant part of removal projects, having enough data related to sediment transport is a real challenge. To overcome this issue, practitioners can take advantage of the proposed pragmatic approach and/or use uncertainty analysis on a full morphodynamic model. The developments in this thesis bring valuable opportunities for recent river engineering projects.

Testing Richards' equation on vertical 1-D columns showed convergence issues. We were able to converge some difficult cases thanks to homotopy. However, it did not appear as a universal method. Further research and developments on this promising technique would be of great interest for the scientific and engineering community. Among other improvements and tests, we think that testing the homotopy on other parameters of the van Genuchten law could be interesting. Testing also other evolution laws for the homotopy parameters could also lead to some benefits. Improvements in the 1-D unsaturated model would pave the way for an extensive use of the full physically-based hydrological model.

Over the use of homotopy, this thesis brought other innovative approaches (to our best knowledge) in the field of hydraulics. In particular, CasADi and the nonlinear Krylov accelerator were used in the frame of 1-D shallow water modelling. Extending their usage to 2-D hydrodynamic modelling would be interesting in order to reduce the computational cost. This would pave the way for the application of the Monte Carlo method to 2-D hydrodynamic models.

We only applied uncertainty analysis methods in hydrodynamics to steady state examples. An interesting perspective would be to extend the approach to unsteady cases. However, the challenges linked to the computational burden are even more present for these cases. Efficient uncertainty analysis methods, such as PMM and PEM, are probably an elegant way to

### *General conclusions*

overcome this difficulty. Nevertheless, these efficient methods should be validated in this context, by comparing them to the Monte Carlo method.

This thesis brought several novelties and solved some issues encountered by the engineers but also leaves some questions partially unsolved for unsaturated flows. Uncertainty analysis appears to be a real added value for engineering studies and we believe that further developments in this field should be undertaken. Having access to fast solving algorithms (whether based on hardware acceleration or on software architecture) is an advantage in many applications. Developments in this area should be maintained and included in the WOLF suite for best availability for further research.



# Bibliography

- Altarejos Garcia, L. et al., 2012. Assessing the impact of uncertainty on flood risk estimates with reliability analysis using 1-D and 2-D hydraulic models. *Hydrology and Earth System Sciences and Discussions*, 16(7), pp.1985–1994.
- Anderson, D.G., 1965. Iterative Procedures for Nonlinear Integral Equations. *J. ACM*, 12(4), pp.547–560.
- Anderson, T.V. & Mattson, C.A., 2012. Propagating skewness and kurtosis through engineering models for low-cost, meaningful, nondeterministic design. *Journal of Mechanical Design*, 134(10), p.100911.
- Andersson, J.A.E. et al., 2018. CasADi – A software framework for nonlinear optimization and optimal control. *Mathematical Programming Computation*.
- Apel, H. et al., 2004. Flood risk assessment and associated uncertainty. *Natural Hazards and Earth System Science*, 4(2), pp.295–308.
- Archambeau, P., 2006. *Contribution à la modélisation de la genèse et de la propagation des crues et inondations*. University of Liège.
- Arrault, A. et al., 2016. Hydrodynamics of long-duration urban floods: experiments and numerical modelling. *Nat. Hazards Earth Syst. Sci.*, 16(6), pp.1413–1429.
- Aureli, F. et al., 2008. A weighted surface-depth gradient method for the numerical integration of the 2D shallow water equations with topography. *Advances in Water Resources*, 31(7), pp.962–974.
- Baayen, J., Piovesan, T. & VanderWees, J., 2018. Continuation method for PDE-constrained global optimization: Analysis and application to the shallow water equations.
- Di Baldassarre, G., 2012. Flood trends and population dynamics. In *EGU General Assembly Conference Abstracts*. p. 1152.
- Di Baldassarre, G. et al., 2010. Flood-plain mapping: a critical discussion of deterministic and probabilistic approaches. *Hydrological Sciences Journal–Journal des Sciences Hydrologiques*, 55(3), pp.364–376.
- Di Baldassarre, G. & Montanari, A., 2009. Uncertainty in river discharge observations: a quantitative analysis. *Hydrology and Earth System Sciences*, 13(6), p.913.

## Bibliography

- Bates, D.J. et al., 2013. *Numerically solving polynomial systems with Bertini*, SIAM.
- Bednarek, A.T., 2001. Undamming rivers: A review of the ecological impacts of dam removal. *Environmental Management*, 27(6), pp.803–814.
- Bessar, M.A., Matte, P. & Anctil, F., 2020. Uncertainty Analysis of a 1D River Hydraulic Model with Adaptive Calibration. *Water*, 12(2), p.561.
- Biancamaria, S. et al., 2009. Large-scale coupled hydrologic and hydraulic modelling of the Ob river in Siberia. *Journal of Hydrology*, 379(1-2), pp.136–150.
- Van Bijnen, M., Korving, H. & Clemens, F., 2012. Impact of sewer condition on urban flooding: an uncertainty analysis based on field observations and Monte Carlo simulations on full hydrodynamic models. *Water Science and Technology*, 65(12), pp.2219–2227.
- Birsan, T. & Tiba, D., 2005. One hundred years since the introduction of the set distance by Dimitrie Pompeiu. In *IFIP Conference on System Modeling and Optimization*. Springer, pp. 35–39.
- Bolle, A., 1988. *Approche probabiliste en mécanique des sols avec prise en compte de la variabilité spatiale*. E.P.F. Lausanne.
- Bolle, A., 1994. How to manage the spatial variability of natural soils. In D. Breyesse, ed. *Probabilities and Materials*. Kluwer Academic, pp. 505–516.
- Bolstad, W.M., 2007. *Introduction to Bayesian Statistics*, John Wiley & Sons.
- Bourdarias, C., Gerbi, S. & Gisclon, M., 2008. A kinetic formulation for a model coupling free surface and pressurised flows in closed pipes. *Journal of Computational and Applied Mathematics*, 218(2), pp.522–531.
- Brodtkorb, A.R., Sætra, M.L. & Altinakar, M., 2012. Efficient shallow water simulations on GPUs: Implementation, visualization, verification, and validation. *Computers & Fluids*, 55, pp.1–12.
- Brooks, R.H. & Corey, A.T., 1964. Hydraulic properties of porous media. *Hydrol. Pap. Colorado State Univ.*, 3, pp.1–27.
- Broyden, C.G., 1965. A class of methods for solving nonlinear simultaneous equations. *Mathematics of computation*, pp.577–593.

## Bibliography

- Bruwier, M., 2017. *Advanced porosity-based models to assess the influence of urban layouts on inundation flows and impact of urban evolution on flood damage*. University of Liege.
- Bruwier, M. et al., 2016. Discretization of the divergence formulation of the bed slope term in the shallow-water equations and consequences in terms of energy balance. *Applied Mathematical Modelling*, 40(17), pp.7532–7544.
- Bruwier, M. et al., 2018. Influence of urban pattern on inundation flow in floodplains of lowland rivers. *Science of The Total Environment*, 622-623, pp.446–458.
- Bruwier, M. et al., 2017. Shallow-water models with anisotropic porosity and merging for flood modelling on Cartesian grids. *Journal of Hydrology*, 554, pp.693–709.
- Calef, M.T. et al., 2013. Nonlinear Krylov acceleration applied to a discrete ordinates formulation of the k-eigenvalue problem. *Journal of Computational Physics*, 238, pp.188–209.
- Camacho, R.A. & Martin, J.L., 2013. Bayesian Monte Carlo for evaluation of uncertainty in hydrodynamic models of coastal systems. *Journal of Coastal Research*, 65(sp1), pp.886–891.
- Carlson, N.N. & Miller, K., 1998a. Design and application of a gradient-weighted moving finite element code I: in one dimension. *SIAM Journal on Scientific Computing*, 19(3), pp.728–765.
- Carlson, N.N. & Miller, K., 1998b. Design and Application of a Gradient-Weighted Moving Finite Element Code II: In Two Dimensions. *SIAM J. Sci. Comput.*, 19(3), pp.766–798.
- Carsel, R.F. & Parrish, R.S., 1988. Developing joint probability distributions of soil water retention characteristics. *Water resources research*, 24(5), pp.755–769.
- Celia, M.A., Bouloutas, E.T. & Zarba, R.L., 1990. A general mass-conservative numerical solution for the unsaturated flow equation. *Water resources research*, 26(7), pp.1483–1496.
- Chaudhry, M.H., 2007. *Open-channel flow*, Springer Science & Business Media.
- Christian, J.T. & Baecher, G.B., 2002. The point-estimate method with large numbers of variables. *International Journal for Numerical and analytical methods in geomechanics*, 26(15), pp.1515–1529.

## Bibliography

- Clarke, R.T., 1999. Uncertainty in the estimation of mean annual flood due to rating-curve indefiniton. *Journal of Hydrology*, 222(1-4), pp.185–190.
- Cook, A. & Merwade, V., 2009. Effect of topographic data, geometric configuration and modeling approach on flood inundation mapping. *Journal of Hydrology*, 377(1), pp.131–142.
- Le Coz, J. et al., 2013. Bayesian analysis of rating curves and their uncertainties: The BaRatin method [Analyse bayésienne des courbes de tarage et de leurs incertitudes: la méthode BaRatin]. *Houille Blanche*, (6), pp.31–41.
- Le Coz, J. et al., 2014. Combining hydraulic knowledge and uncertain gaugings in the estimation of hydrometric rating curves: A Bayesian approach. *Journal of Hydrology*, 509, pp.573–587.
- Degoutte, G., 2006. *Diagnostic, aménagement et gestion des rivières T. & DOC*, ed., Paris: Lavoisier.
- Devroye, L., 1986. *Non-Uniform Random Variate Generation*, Springer, New-York.
- Dewals, B. et al., 2014. Dam break flow modelling with uncertainty analysis. In P. Gourbesville, J. Cunge, & G. Caignaert, eds. *Advances in Hydroinformatics*. Springer, pp. 107–116.
- Dewals, B., 2006. *Une approche unifiée pour la modélisation d'écoulements à surface libre, de leur effet érosif sur une structure et de leur interaction avec divers constituants*. University of Liege.
- Dimitriadis, P. et al., 2016. Comparative evaluation of 1D and quasi-2D hydraulic models based on benchmark and real-world applications for uncertainty assessment in flood mapping. *Journal of Hydrology*, 534, pp.478–492.
- Domeneghetti, A. et al., 2013. Probabilistic flood hazard mapping: effects of uncertain boundary conditions. *Hydrology and Earth System Sciences*, 17(8), pp.3127–3140.
- Domeneghetti, A., Castellarin, A. & Brath, A., 2012. Assessing rating-curve uncertainty and its effects on hydraulic model calibration. *Hydrology and Earth System Sciences*, 16(4), p.1191.
- Drab, A. & Riha, J., 2010. An approach to the implementation of European Directive 2007/60/EC on flood risk management in the Czech Republic. *Natural Hazards and Earth System Science*, 10(9), pp.1977–1987.

## Bibliography

- Ercicum, S., Dewals, B., Archambeau, P. & Piroton, M., 2010. Dam break flow computation based on an efficient flux vector splitting. *Journal of Computational and Applied Mathematics*, 234(7), pp.2143–2151.
- Ercicum, S., Dewals, B., Archambeau, P., Detrembleur, S., et al., 2010. Detailed Inundation Modelling Using High Resolution DEMs. *Engineering Applications of Computational Fluid Mechanics*, 4(2), pp.196–208.
- Ercicum, S., 2006. *Optimisation objective de paramètres en écoulements turbulents à surface libre sur maillage multibloc*. University of Liege.
- Farthing, M.W. & Ogden, F.L., 2017. Numerical solution of Richards' Equation: a review of advances and challenges. *Soil Science Society of America Journal*, 81(6), pp.1257–1269.
- Franceschini, S., Marani, M., et al., 2012. A Perturbance Moment Point Estimate Method for uncertainty analysis of the hydrologic response. *Advances in water resources*, 40, pp.46–53.
- Franceschini, S., Tsai, C. & Marani, M., 2012. Point estimate methods based on Taylor Series Expansion – The perturbation moments method—A more coherent derivation of the second order statistical moment. *Applied Mathematical Modelling*, 36(11), pp.5445–5454.
- Franzini, F. & Soares-Frazão, S., 2016. Efficiency and accuracy of Lateralized HLL, HLLS and Augmented Roe's scheme with energy balance for river flows in irregular channels. *Applied Mathematical Modelling*, 40(17), pp.7427–7446.
- Gentle, J.E., 2003. *Random Number Generation and Monte Carlo Methods*, Springer-Verlag New York.
- Van Genuchten, M.T., 1980. A closed-form equation for predicting the hydraulic conductivity of unsaturated soils. *Soil science society of America journal*, 44(5), pp.892–898.
- Glynn, P.W. & Iglehart, D.L., 1989. Importance sampling for stochastic simulations. *Management Science*, 35(11), pp.1367–1392.
- Goffin, L. et al., 2020. An Optimized and Scalable Algorithm for the Fast Convergence of Steady 1-D Open-Channel Flows. *Water*.
- Goffin, L., Piroton, M., Archambeau, P., et al., 2016. *Etude hydraulique de l'engravement de la Romanche à Livet*, University of Liege.

## Bibliography

- Goffin, L. et al., 2017. *Etude hydraulique de l'impact du démantèlement des prises d'eau de moyenne Romanche*, University of Liege.
- Goffin, L. et al., 2015. *Etude hydraulique de l'impact du démantèlement des prises d'eau de moyenne Romanche: Analyse complémentaire relative à la prise d'eau de Livet*, University of Liege.
- Goffin, L., Piroton, M., Dewals, B., et al., 2016. *Etude hydrodynamique de la Haine entre Boussoit et Obourg afin de définir l'inondabilité du terrain de la SPAQUE situé sur ce tronçon*, University of Liege.
- Goffin, L., Dewals, B.J., et al., 2016. Non-linear optimization of a 1-D shallow water model and integration into Simulink for operational use. In *Sustainable Hydraulics in the Era of Global Change - Proceedings of the 4th European Congress of the International Association of Hydroenvironment engineering and Research, IAHR 2016*. CRC Press/Balkema, pp. 445–451.
- Goffin, L. et al., 2018. Operational method for assessing riverbed stability after (partial) dam removal on threshold channels: a case study in the Alps. In *5th IAHR Europe Congress : New challenges in hydraulic research and engineering*.
- Graf, W.H. & Altinakar, M.S., 1998. *Fluvial hydraulics: Flow and transport processes in channels of simple geometry*, New York: Wiley.
- Graham, C. & Talay, D., 2013. *Stochastic simulation and Monte Carlo methods: mathematical foundations of stochastic simulation* Springer, ed., Springer Science & Business Media.
- Hahn, G.J. & Shapiro, S.S., 1967. *Statistical Models in Engineering*, John Wiley & Sons.
- Han, S.S., Biron, P.M. & Ramamurthy, A.S., 2011. Three-dimensional modelling of flow in sharp open-channel bends with vanes. *Journal of Hydraulic Research*, 49(1), pp.64–72.
- Harr, M.E., 1989. Probabilistic estimates for multivariate analyses. *Applied Mathematical Modelling*, 13(5), pp.313–318.
- Haverkamp, R. et al., 1977. A comparison of numerical simulation models for one-dimensional infiltration 1. *Soil Science Society of America Journal*, 41(2), pp.285–294.
- Hong, H.P., 1998. An efficient point estimate method for probabilistic analysis. *Reliability Engineering & System Safety*, 59(3), pp.261–267.

## Bibliography

- Hong, H.P., 1996. Point-estimate moment-based reliability analysis. *Civil Engineering Systems*, 13(4), pp.281–294.
- Horritt, M.S. & Bates, P.D., 2002. Evaluation of 1D and 2D numerical models for predicting river flood inundation. *Journal of Hydrology*, 268(1), pp.87–99.
- Huttenlocher, D.P., Klanderman, G.A. & Rucklidge, W.J., 1993. Comparing images using the Hausdorff distance. *IEEE Transactions on Pattern Analysis and Machine Intelligence*, 15(9), pp.850–863.
- ISO1100-2:2010, 2010. *Hydrometry – Measurement of liquid flow in open channels – Part 2: Determination of the stage-discharge relationship*, Geneva, Switzerland: International Organization for Standardization.
- ISO748:2007, 2007. *Hydrometry – Measurement of liquid flow in open channels using current-meters or floats*, Geneva, Switzerland: International Organization for Standardization.
- Isukapalli, S.S., Roy, A. & Georgopoulos, P.G., 2000. Efficient sensitivity/uncertainty analysis using the combined stochastic response surface method and automated differentiation: application to environmental and biological systems. *Risk Analysis*, 20(5), pp.591–602.
- Isukapalli, S.S., Roy, A. & Georgopoulos, P.G., 1998. Stochastic response surface methods (SRSMs) for uncertainty propagation: application to environmental and biological systems. *Risk analysis*, 18(3), pp.351–363.
- Jain, S.K. & Sudheer, K.P., 2008. Fitting of hydrologic models: a close look at the Nash–Sutcliffe index. *Journal of hydrologic engineering*, 13(10), pp.981–986.
- Kelley, C.T., 1995. *Iterative Methods for Linear and Nonlinear Equations*, SIAM.
- Kerger, F. et al., 2011. A fast universal solver for 1D continuous and discontinuous steady flows in rivers and pipes. *International Journal for Numerical Methods in Fluids*, 66(1), pp.38–48.
- Kirkpatrick, S., Gelatt, C.D. & Vecchi, M.P., 1983. Optimization by simulated annealing. *Science*, 220(4598), pp.671–680.
- Knoll, D.A. & Keyes, D.E., 2004. Jacobian-free Newton–Krylov methods: a survey of approaches and applications. *Journal of Computational Physics*, 193(2), pp.357–397.

## Bibliography

- Konrad, C.P., 2009. Simulating the recovery of suspended sediment transport and river-bed stability in response to dam removal on the Elwha River, Washington. *Ecological Engineering*, 35(7), pp.1104–1115.
- Kottegoda, N.T., Natale, L. & Raiteri, E., 2014. Monte Carlo Simulation of rainfall hyetographs for analysis and design. *Journal of hydrology*, 519, pp.1–11.
- Kreyszig, E., 2006. *Advanced engineering mathematics*, John Wiley & Sons.
- Kroese, D.P. et al., 2014. Why the Monte Carlo method is so important today. *WIREs Computational Statistics*, 6(6), pp.386–392.
- Kyabu, S., 2011. *Analyse d'incertitudes et de sensibilité : application à une rupture de barrage*. University of Liège.
- Lacasta, A. et al., 2013. Preprocess static subdomain decomposition in practical cases of 2D unsteady hydraulic simulation. *Computers & Fluids*, 80, pp.225–232.
- Lai, X. et al., 2013. Large-scale hydrodynamic modeling of the middle Yangtze River Basin with complex river-lake interactions. *Journal of Hydrology*, 492, pp.228–243.
- Legates, D.R. & McCabe Jr., G.J., 1999. Evaluating the use of “goodness-of-fit” measures in hydrologic and hydroclimatic model validation. *Water resources research*, 35(1), pp.233–241.
- Lipnikov, K., Moulton, D. & Svyatskiy, D., 2016. New preconditioning strategy for Jacobian-free solvers for variably saturated flows with Richards’ equation. *Advances in water resources*, 94, pp.11–22.
- Machiels, O. et al., 2011. Theoretical and numerical analysis of the influence of the bottom friction formulation in free surface flow modelling. *Water SA*, 37(2), pp.221–228.
- Mansanarez, V. et al., 2016. Bayesian analysis of stage-fall-discharge rating curves and their uncertainties. *Water Resources Research*, 52, pp.7424–7443.
- Manzini, G. & Ferraris, S., 2004. Mass-conservative finite volume methods on 2-D unstructured grids for the Richards’ equation. *Advances in Water Resources*, 27(12), pp.1199–1215.
- McKay, M.D., Beckman, R.J. & Conover, W.J., 1979. Comparison of three methods for selecting values of input variables in the analysis of output from a computer code. *Technometrics*, 21(2), pp.239–245.

## Bibliography

- Merz, B. & Thielen, A.H., 2005. Separating natural and epistemic uncertainty in flood frequency analysis. *Journal of Hydrology*, 309(1-4), pp.114–132.
- Metropolis, N. & Ulam, S., 1949. The Monte Carlo Method. *Journal of the American statistical association*, 44(247), pp.335–341.
- Montanari, A., 2007. What do we mean by “uncertainty”? The need for a consistent wording about uncertainty assessment in hydrology. *Hydrological Processes*, 21(6), pp.841–845.
- Mualem, Y., 1976. A new model for predicting the hydraulic conductivity of unsaturated porous media. *Water resources research*, 12(3), pp.513–522.
- Nash, J.E. & Sutcliffe, J.V., 1970. River flow forecasting through conceptual models part I—A discussion of principles. *Journal of hydrology*, 10(3), pp.282–290.
- Neal, J.C. et al., 2010. A comparison of three parallelisation methods for 2D flood inundation models. *Environmental Modelling & Software*, 25(4), pp.398–411.
- Ogden, F.L. et al., 2015. A new general 1-D vadose zone flow solution method. *Water Resources Research*, 51(6).
- Paiva, R.C.D., Collischonn, W. & Tucci, C.E.M., 2011. Large scale hydrologic and hydrodynamic modeling using limited data and a GIS based approach. *Journal of Hydrology*, 406(3), pp.170–181.
- Paniconi, C. & Putti, M., 1994. A comparison of Picard and Newton iteration in the numerical solution of multidimensional variably saturated flow problems. *Water Resources Research*, 30(12), pp.3357–3374.
- Papaioannou, G. et al., 2017. Probabilistic flood inundation mapping at ungauged streams due to roughness coefficient uncertainty in hydraulic modelling. *Advances in Geosciences*, 44, p.23.
- Pappenberger, F. et al., 2005. Uncertainty in the calibration of effective roughness parameters in HEC-RAS using inundation and downstream level observations. *Journal of Hydrology*, 302(1-4), pp.46–69.
- Paulus, R. et al., 2013. Innovative modelling of 3D unsaturated flow in porous media by coupling independent models for vertical and lateral flows. *Journal of Computational and Applied Mathematics*, 246, pp.38–51.

## Bibliography

- Paz, A.R. et al., 2010. Large-scale hydrodynamic modeling of a complex river network and floodplains. *Journal of Hydrologic Engineering*, 15(2), pp.152–165.
- Pearson, K., 1895. Notes on Regression and Inheritance in the Case of Two Parents. In *Proceedings of the Royal Society of London*.
- Petaccia, G., Leporati, F. & Torti, E., 2016. OpenMP and CUDA simulations of Sella Zerbino Dam break on unstructured grids. *Computational Geosciences*, 20(5), pp.1123–1132.
- Petersen-Overleir, A., 2004. Accounting for heteroscedasticity in rating curve estimates. *Journal of Hydrology*, 292(1-4), pp.173–181.
- Piroton, M., 1994. *Modélisation des discontinuités en écoulement instationnaire à surface libre. Du ruissellement hydrologique en fine lame à la propagation d'ondes consécutives aux ruptures oe barrages*. University of Liege.
- Poepl, R.E. et al., 2019. Modeling the impact of dam removal on channel evolution and sediment delivery in a multiple dam setting. *International journal of sediment research*, 34(6), pp.537–549.
- Preissmann, A., 1961. Propagation des intumescences dans les canaux et rivières. In *First Congress of French Association for Computation*. Grenoble.
- Proust, S. et al., 2016. Predicting the flow in the floodplains with evolving land occupations during extreme flood events (FlowRes ANR project). In *E3S Web of Conferences*.
- Rantz, S.E., 1982. *Measurement and computation of streamflow: volume 2, computation of discharge*, USGS.
- R-Core-Team, 2019. *R: A Language and Environment for Statistical Computing*, Vienna, Austria: R Foundation for Statistical Computing.
- Refsgaard, J.C. et al., 2012. Review of strategies for handling geological uncertainty in groundwater flow and transport modeling. *Advances in Water Resources*, 36, pp.36–50.
- Remo, J.W.F. & Pinter, N., 2007. Retro-modeling the Middle Mississippi River. *Journal of Hydrology*, 337(3-4), pp.421–435.
- Richards, F.J., 1959. A Flexible Growth Function for Empirical Use. *Journal of Experimental Botany*, 10, pp.290–301.

## Bibliography

- Van Rijn, L.C., 1993. *Principles of sediment transport in rivers, estuaries and coastal seas* L. C. Van Rijn, ed., Amsterdam: Aqua Publications.
- Rosenblueth, E., 1975. Point estimates for probability moments. *Proceedings of the National Academy of Sciences*, 72(10), pp.3812–3814.
- Rosenblueth, E., 1981. Two-point estimates in probabilities. *Applied Mathematical Modelling*, 5(5), pp.329–335.
- Rulot, F. et al., 2012. *Etude hydraulique de l'impact de la déconstruction des ouvrages hydroélectriques de moyenne Normandie*, University of Liege.
- Saad, Y. & Schultz, M.H., 1986. GMRES: A generalized minimal residual algorithm for solving nonsymmetric linear systems. *SIAM Journal on scientific and statistical computing*, 7(3), pp.856–869.
- Saltelli, A. et al., 2008. *Global Sensitivity Analysis. The Primer*, John Wiley & Sons.
- Saltelli, A. et al., 2004. *Sensitivity analysis in practice: a guide to assessing scientific models*, John Wiley & Sons.
- Sandric, I. et al., 2019. Using CUDA to accelerate uncertainty propagation modelling for landslide susceptibility assessment. *Environmental Modelling & Software*, 115, pp.176–186.
- Schmidt, A.R. & Yen, B.C., 2008. Theoretical development of stage-discharge ratings for subcritical open-channel flows. *Journal of Hydraulic Engineering*, 134(9), pp.1245–1256.
- Schwanenberg, D., Becker, B.P.J. & Xu, M., 2015. The open real-time control (RTC)-Tools software framework for modeling RTC in water resources systems. *Journal of Hydroinformatics*, 17(1), pp.130–148.
- Shao, Y. & Irannejad, P., 1999. On the choice of soil hydraulic models in land-surface schemes. *Boundary-Layer Meteorology*, 90(1), pp.83–115.
- Singh, V.P., Jain, S.K. & Tyagi, A., 2007. *Risk and reliability analysis: a handbook for civil and environmental engineers* V. P. Singh, ed., ASCE Press.
- Smith, L.S. & Liang, Q., 2013. Towards a generalised GPU/CPU shallow-flow modelling tool. *Computers and Fluids*, 88, pp.334–343.

## Bibliography

- Spearman, C., 1904. The Proof and Measurement of Association Between Two Things. *American Journal of Psychology*.
- Stilmant, F. et al., 2017. Hydraulic determination of dam releases to generate warning waves in a mountain stream: performance of an analytical kinematic wave model. *Journal of Hydraulic Engineering*.
- Szymkiewicz, A., 2012. *Modelling water flow in unsaturated porous media: accounting for nonlinear permeability and material heterogeneity*, Springer Science & Business Media.
- Tayefi, V. et al., 2007. A comparison of one- and two-dimensional approaches to modelling flood inundation over complex upland floodplains. *Hydrological Processes*, 21(23), pp.3190–3202.
- Teng, J. et al., 2017. Flood inundation modelling: A review of methods, recent advances and uncertainty analysis. *Environmental Modelling & Software*, 90, pp.201–216.
- Toro, F.E., 2000. *Shock-Capturing Methods for Free-Surface Shallow Flows*, John Wiley and Sons Ltd.
- Tran, Q.Q., De Niel, J. & Willems, P., 2018. Spatially distributed conceptual hydrological model building: A generic top-down approach starting from lumped models. *Water Resources Research*, 54(10), pp.8064–8085.
- Tsai, C.W. & Li, M., 2014. Uncertainty analysis and risk assessment of DO concentrations in the Buffalo River using the perturbation moments method. *Journal of Hydrologic Engineering*, 19(12).
- Tung, Y.-K., 2017. Effect of Uncertainties on Probabilistic-based Design Capacity of Hydrosystems. *Journal of Hydrology*.
- Vauclin, M., Khanji, D. & Vachaud, G., 1979. Experimental and numerical study of a transient, two-dimensional unsaturated-saturated water table recharge problem. *Water Resources Research*, 15(5), pp.1089–1101.
- Vauclin, M., Vachaud, G. & Khanji, J., 1975. Two dimensional numerical analysis of transient water transfer in saturated-unsaturated soils. *Modeling and simulation of water resources systems*, pp.299–321.
- Walker, H.F. & Ni, P., 2011. Anderson acceleration for fixed-point iterations. *SIAM Journal on Numerical Analysis*.

## Bibliography

- Wang, C. et al., 2018. Application of nonlinear Krylov acceleration to a reconstructed discontinuous Galerkin method for compressible flows. *Computers & Fluids*, 163, pp.32–49.
- Wilson, M.D. et al., 2007. Modeling large-scale inundation of Amazonian seasonally flooded wetlands. *Geophysical Research Letters*, 34(15).
- Xiao, Y. et al., 2017. Performance of Three-Dimensional Modeling for Flow Structures in Channel Bends. *Journal of Waterway, Port, Coastal, and Ocean Engineering*, 143(6), p.06017004.
- Zhong, H. et al., 2016. The Influence of Statistical Uncertainty in the Hydraulic Boundary Conditions on the Probabilistically Computed High Water Level Frequency Curve in the Rhine Delta. *Water*, 8(4), p.147.
- Zhong, H., Overloop, P.-J. van & Van Gelder, P., 2013. A joint probability approach using a 1-D hydrodynamic model for estimating high water level frequencies in the Lower Rhine Delta. *Natural Hazards and Earth System Sciences*, 13(7), p.1841.



## A Uncertainty analysis appendix

### A.1 Coskewness and cokurtosis for normally distributed and independent random variables

For  $N$  independent random variables gathered in vector  $\mathbf{X}$ , the joint probability density function is the product of the marginal probability density function of each variable:

$$p_{\mathbf{X}}(x_1, \dots, x_N) = \prod_{i=1}^N p_{X_i}(x_i) \quad (244)$$

Three combinations of the coskewness can be written and developed in the frame of normally distributed and independent random variables:

$$\begin{aligned} S(X_1, X_1, X_1) &= \gamma_{X_1} = 0 \\ S(X_1, X_1, X_2) &= \frac{1}{\sigma_{X_1}^2 \sigma_{X_2}} \int_{-\infty}^{+\infty} (x_1 - \bar{X}_1)^2 (x_2 - \bar{X}_2) p_{\mathbf{X}}(\mathbf{x}) d\mathbf{x} \\ &= \frac{1}{\sigma_{X_1}^2 \sigma_{X_2}} \int_{-\infty}^{+\infty} (x_1 - \bar{X}_1)^2 (x_2 - \bar{X}_2) p_{X_1}(x_1) p_{X_2}(x_2) d\mathbf{x} \\ &= \frac{1}{\sigma_{X_1}^2 \sigma_{X_2}} (\sigma_{X_1}^2 \cdot 0) = 0 \\ S(X_1, X_2, X_3) &= \frac{1}{\sigma_{X_1} \sigma_{X_2} \sigma_{X_3}} \int_{-\infty}^{+\infty} (x_1 - \bar{X}_1)(x_2 - \bar{X}_2)(x_3 - \bar{X}_3) p_{\mathbf{X}}(\mathbf{x}) d\mathbf{x} \\ &= \frac{1}{\sigma_{X_1} \sigma_{X_2} \sigma_{X_3}} \int_{-\infty}^{+\infty} (x_1 - \bar{X}_1)(x_2 - \bar{X}_2)(x_3 - \bar{X}_3) p_{X_1}(x_1) p_{X_2}(x_2) p_{X_3}(x_3) d\mathbf{x} \\ &= \frac{1}{\sigma_{X_1} \sigma_{X_2} \sigma_{X_3}} (0 \cdot 0 \cdot 0) = 0 \end{aligned} \quad (245)$$

Under these assumptions, all coskewness coefficients are nil. For the cokurtosis, five main different combinations can be written and the results are as follow:

$$\begin{aligned}
K(X_1, X_1, X_1, X_1) &= \kappa_{X_1} = 3 \\
K(X_1, X_1, X_2, X_3) &= \frac{1}{\sigma_{X_1}^2 \sigma_{X_2} \sigma_{X_3}} \int_{-\infty}^{+\infty} (x_1 - \bar{X}_1)^2 (x_2 - \bar{X}_2) (x_3 - \bar{X}_3) p_{\mathbf{x}}(\mathbf{x}) d\mathbf{x} \\
&= \frac{1}{\sigma_{X_1}^2 \sigma_{X_2} \sigma_{X_3}} \int_{-\infty}^{+\infty} (x_1 - \bar{X}_1)^2 (x_2 - \bar{X}_2) (x_3 - \bar{X}_3) p_{X_1}(x_1) p_{X_2}(x_2) p_{X_3}(x_3) dx \\
&= \frac{1}{\sigma_{X_1}^2 \sigma_{X_2} \sigma_{X_3}} (\sigma_{X_1}^2 \cdot 0 \cdot 0) = 0 \\
K(X_1, X_1, X_2, X_2) &= \frac{1}{\sigma_{X_1}^2 \sigma_{X_2}^2} \int_{-\infty}^{+\infty} (x_1 - \bar{X}_1)^2 (x_2 - \bar{X}_2)^2 p_{\mathbf{x}}(\mathbf{x}) d\mathbf{x} \\
&= \frac{1}{\sigma_{X_1}^2 \sigma_{X_2}^2} \int_{-\infty}^{+\infty} (x_1 - \bar{X}_1)^2 (x_2 - \bar{X}_2)^2 p_{X_1}(x_1) p_{X_2}(x_2) dx \\
&= \frac{1}{\sigma_{X_1}^2 \sigma_{X_2}^2} (\sigma_{X_1}^2 \sigma_{X_2}^2) = 1 \\
K(X_1, X_1, X_1, X_2) &= \frac{1}{\sigma_{X_1}^3 \sigma_{X_2}} \int_{-\infty}^{+\infty} (x_1 - \bar{X}_1)^3 (x_2 - \bar{X}_2) p_{\mathbf{x}}(\mathbf{x}) d\mathbf{x} \\
&= \frac{1}{\sigma_{X_1}^3 \sigma_{X_2}} \int_{-\infty}^{+\infty} (x_1 - \bar{X}_1)^3 (x_2 - \bar{X}_2) p_{X_1}(x_1) p_{X_2}(x_2) dx \\
&= \frac{1}{\sigma_{X_1}^3 \sigma_{X_2}} (E[d_1^3] \cdot 0) = 0 \\
K(X_1, X_2, X_3, X_4) &= \frac{1}{\sigma_{X_1} \sigma_{X_2} \sigma_{X_3} \sigma_{X_4}} \int_{-\infty}^{+\infty} (x_1 - \bar{X}_1) (x_2 - \bar{X}_2) (x_3 - \bar{X}_3) (x_4 - \bar{X}_4) p_{\mathbf{x}}(\mathbf{x}) d\mathbf{x} \\
&= \frac{1}{\sigma_{X_1} \sigma_{X_2} \sigma_{X_3} \sigma_{X_4}} \int_{-\infty}^{+\infty} (x_1 - \bar{X}_1) \dots (x_4 - \bar{X}_4) p_{X_1}(x_1) \dots p_{X_4}(x_4) dx \\
&= \frac{1}{\sigma_{X_1} \sigma_{X_2} \sigma_{X_3} \sigma_{X_4}} (0 \cdot 0 \cdot 0 \cdot 0) = 0
\end{aligned}
\tag{246}$$

It appears that only two combinations give non-zero results: the kurtosis of a single variable and the cokurtosis of two variables taken twice.

## A.2 Mathematical developments of Taylor series expansion of statistical moments

The mean of  $Y$  is evaluated with a second-order Taylor series expansion:

$$\begin{aligned}
\bar{Y} &= E[Y] \\
&\approx E\left[f(\mathbf{X}_c) + \nabla f(\mathbf{X}_c)(\mathbf{X} - \mathbf{X}_c) + \frac{1}{2}(\mathbf{X} - \mathbf{X}_c)^T \mathbf{H}f(\mathbf{X}_c)(\mathbf{X} - \mathbf{X}_c)\right] \\
&\approx \int_{-\infty}^{+\infty} \left[f(\mathbf{X}_c) + \nabla f(\mathbf{X}_c)(\mathbf{X} - \mathbf{X}_c) + \frac{1}{2}(\mathbf{X} - \mathbf{X}_c)^T \mathbf{H}f(\mathbf{X}_c)(\mathbf{X} - \mathbf{X}_c)\right] p_{\mathbf{X}}(\mathbf{x}) d\mathbf{x} \\
&\approx f(\mathbf{X}_c) + \int_{-\infty}^{+\infty} \nabla f(\mathbf{X}_c)(\mathbf{X} - \mathbf{X}_c) p_{\mathbf{X}}(\mathbf{x}) d\mathbf{x} \\
&\quad + \int_{-\infty}^{+\infty} \frac{1}{2}(\mathbf{X} - \mathbf{X}_c)^T \mathbf{H}f(\mathbf{X}_c)(\mathbf{X} - \mathbf{X}_c) p_{\mathbf{X}}(\mathbf{x}) d\mathbf{x} \\
&\approx Y_c + \nabla f(\mathbf{X}_c) \left[ \int_{-\infty}^{+\infty} \mathbf{X} p_{\mathbf{X}}(\mathbf{x}) d\mathbf{x} - \int_{-\infty}^{+\infty} \mathbf{X}_c p_{\mathbf{X}}(\mathbf{x}) d\mathbf{x} \right] + \frac{1}{2} \text{Tr}(\Sigma \mathbf{H}f(\mathbf{X}_c)) \\
&\approx Y_c + \nabla f(\mathbf{X}_c) [\mathbf{X}_c - \mathbf{X}_c] + \frac{1}{2} \text{Tr}(\Sigma \mathbf{H}f(\mathbf{X}_c)) \\
&\approx Y_c + \frac{1}{2} \text{Tr}(\Sigma \mathbf{H}f(\mathbf{X}_c))
\end{aligned} \tag{247}$$

where  $\text{Tr}$  is the trace operator (sum over the diagonal elements) and  $\Sigma$  the covariance matrix (14). The development of the second-order term in (247) comes from the fact that derivative terms are constant about  $\mathbf{X}$ . In the frame of uncorrelated random variables, non-diagonal terms in  $\Sigma$  are nil and (247) can be transformed into a more convenient indicial notation:

$$\begin{aligned}
\bar{Y} &= E[Y] \\
&\approx Y_c + \frac{1}{2} \sum_{i=1}^N \frac{\partial^2 f}{\partial x_i^2} \Big|_{X_c} \sigma_{X_i}^2
\end{aligned} \tag{248}$$

The first-order approximation of the mean can be deduced from (248):  $\bar{Y} = Y_c$ .

For the variance of  $Y$ , the first-order Taylor series expansion is used:

$$\begin{aligned}
\sigma_Y^2 &= E\left[(Y - \bar{Y})^2\right] \\
&\approx E\left[\left(Y_c + \sum_{i=1}^N \left(\frac{\partial f}{\partial x_i} \Big|_{X_c} (x_i - x_{i,c})\right) - Y_c\right)^2\right] \\
&\approx E\left[\left(\sum_{i=1}^N \left(\frac{\partial f}{\partial x_i} \Big|_{X_c} (x_i - x_{i,c})\right)\right)^2\right] \\
&\approx \int_{-\infty}^{+\infty} \sum_{i=1}^N \left[ \left(\frac{\partial f}{\partial x_i} \Big|_{X_c}\right)^2 (x_i - x_{i,c})^2 + \sum_{j=i+1}^N \frac{\partial f}{\partial x_i} \Big|_{X_c} \frac{\partial f}{\partial x_j} \Big|_{X_c} (x_i - x_{i,c})(x_j - x_{j,c}) \right] p_{\mathbf{X}}(\mathbf{x}) d\mathbf{x} \\
&\approx \sum_{i=1}^N \left[ \left(\frac{\partial f}{\partial x_i} \Big|_{X_c}\right)^2 \sigma_{X_i}^2 + \sum_{j=i+1}^N \frac{\partial f}{\partial x_i} \Big|_{X_c} \frac{\partial f}{\partial x_j} \Big|_{X_c} \sigma_{X_i X_j} \right]
\end{aligned} \tag{249}$$

For uncorrelated random variables, equation (249) becomes:

$$\sigma_Y^2 = \sum_{i=1}^N \left( \frac{\partial f(x_{i,c})}{\partial x_i} \right)^2 \sigma_{X_i}^2 \quad (250)$$

The variance can also be developed with a second-order Taylor series expansion of  $Y$  and  $\bar{Y}$ . The first step considers a general development for  $Y$  but it will be simplified further for uncorrelated variables.

$$\begin{aligned} \sigma_Y^2 &= E \left[ (Y - \bar{Y})^2 \right] \\ &\approx E \left[ \left( Y_c + \sum_{i=1}^N \frac{\partial f}{\partial x_i} \Big|_{X_c} (x_i - x_{i,c}) + \frac{1}{2} \sum_{i=1}^N \sum_{j=1}^N \frac{\partial^2 f}{\partial x_i \partial x_j} \Big|_{X_c} (x_i - x_{i,c})(x_j - x_{j,c}) - Y_c - \frac{1}{2} \sum_{i=1}^N \frac{\partial^2 f}{\partial x_i^2} \Big|_{X_c} \sigma_{X_i}^2 \right)^2 \right] \\ &\approx E \left[ \left( \sum_{i=1}^N \frac{\partial f}{\partial x_i} \Big|_{X_c} (x_i - x_{i,c}) + \frac{1}{2} \sum_{i=1}^N \sum_{j=1}^N \frac{\partial^2 f}{\partial x_i \partial x_j} \Big|_{X_c} (x_i - x_{i,c})(x_j - x_{j,c}) - \frac{1}{2} \sum_{i=1}^N \frac{\partial^2 f}{\partial x_i^2} \Big|_{X_c} \sigma_{X_i}^2 \right)^2 \right] \\ &\approx E \left[ \underbrace{\left( \sum_{i=1}^N \frac{\partial f}{\partial x_i} \Big|_{X_c} (x_i - x_{i,c}) \right)^2}_{A_1} + \underbrace{\left( \frac{1}{2} \sum_{i=1}^N \sum_{j=1}^N \frac{\partial^2 f}{\partial x_i \partial x_j} \Big|_{X_c} (x_i - x_{i,c})(x_j - x_{j,c}) \right)^2}_{A_2} + \underbrace{\left( \frac{1}{2} \sum_{i=1}^N \frac{\partial^2 f}{\partial x_i^2} \Big|_{X_c} \sigma_{X_i}^2 \right)^2}_{A_3} \right. \\ &\quad \left. + \underbrace{\left( \sum_{i=1}^N \frac{\partial f}{\partial x_i} \Big|_{X_c} (x_i - x_{i,c}) \right) \left( \sum_{i=1}^N \sum_{j=1}^N \frac{\partial^2 f}{\partial x_i \partial x_j} \Big|_{X_c} (x_i - x_{i,c})(x_j - x_{j,c}) \right)}_{A_4} \right] \\ &\approx E \left[ \underbrace{-\frac{1}{2} \left( \sum_{i=1}^N \sum_{j=1}^N \frac{\partial^2 f}{\partial x_i \partial x_j} \Big|_{X_c} (x_i - x_{i,c})(x_j - x_{j,c}) \right) \left( \sum_{i=1}^N \frac{\partial^2 f}{\partial x_i^2} \Big|_{X_c} \sigma_{X_i}^2 \right)}_{A_5} \right. \\ &\quad \left. - \underbrace{\left( \sum_{i=1}^N \frac{\partial f}{\partial x_i} \Big|_{X_c} (x_i - x_{i,c}) \right) \left( \sum_{i=1}^N \frac{\partial^2 f}{\partial x_i^2} \Big|_{X_c} \sigma_{X_i}^2 \right)}_{A_6} \right] \end{aligned} \quad (251)$$

Equation (251) can be split and simplified for uncorrelated random variables:

$$\begin{aligned}
A_1 &= E \left[ \left( \sum_{i=1}^N \frac{\partial f}{\partial x_i} \Big|_{X_c} (x_i - x_{i,c}) \right)^2 \right] \\
&= E \left[ \sum_{i=1}^N \left( \frac{\partial f}{\partial x_i} \Big|_{X_c} \right)^2 (x_i - x_{i,c})^2 + \sum_{i \neq j} \frac{\partial f}{\partial x_i} \Big|_{X_c} \frac{\partial f}{\partial x_j} \Big|_{X_c} (x_i - x_{i,c})(x_j - x_{j,c}) \right] \\
&= \sum_{i=1}^N \left( \frac{\partial f}{\partial x_i} \Big|_{X_c} \right)^2 \sigma_{X_i}^2 + \sum_{i \neq j} \frac{\partial f}{\partial x_i} \Big|_{X_c} \frac{\partial f}{\partial x_j} \Big|_{X_c} \sigma_{X_i X_j} \\
&= \sum_{i=1}^N \left( \frac{\partial f}{\partial x_i} \Big|_{X_c} \right)^2 \sigma_{X_i}^2
\end{aligned} \tag{252}$$

$$A_2 = E \left[ \left( \frac{1}{2} \sum_{i=1}^N \sum_{j=1}^N \frac{\partial^2 f}{\partial x_i \partial x_j} \Big|_{X_c} (x_i - x_{i,c})(x_j - x_{j,c}) \right)^2 \right] \tag{253}$$

$$\begin{aligned}
A_3 &= E \left[ \left( \frac{1}{2} \sum_{i=1}^N \frac{\partial^2 f}{\partial x_i^2} \Big|_{X_c} \sigma_{X_i}^2 \right)^2 \right] \\
&= \frac{1}{4} \left( \sum_{i=1}^N \frac{\partial^2 f}{\partial x_i^2} \Big|_{X_c} \sigma_{X_i}^2 \right)^2 \\
&= \frac{1}{4} \left( \sum_{i=1}^N \left( \frac{\partial^2 f}{\partial x_i^2} \Big|_{X_c} \right)^2 \sigma_{X_i}^4 + \sum_{i \neq j} \frac{\partial^2 f}{\partial x_i^2} \Big|_{X_c} \frac{\partial^2 f}{\partial x_j^2} \Big|_{X_c} \sigma_{X_i}^2 \sigma_{X_j}^2 \right)
\end{aligned} \tag{254}$$

$$A_4 = E \left[ \left( \sum_{i=1}^N \frac{\partial f}{\partial x_i} \Big|_{X_c} (x_i - x_{i,c}) \right) \left( \sum_{i=1}^N \sum_{j=1}^N \frac{\partial^2 f}{\partial x_i \partial x_j} \Big|_{X_c} (x_i - x_{i,c})(x_j - x_{j,c}) \right) \right] \tag{255}$$

$$\begin{aligned}
A_5 &= E \left[ \frac{1}{2} \left( \sum_{i=1}^N \sum_{j=1}^N \frac{\partial^2 f}{\partial x_i \partial x_j} \Big|_{X_c} (x_i - x_{i,c})(x_j - x_{j,c}) \right) \left( \sum_{i=1}^N \frac{\partial^2 f}{\partial x_i^2} \Big|_{X_c} \sigma_{X_i}^2 \right) \right] \\
&= \frac{1}{2} \sum_{i=1}^N \frac{\partial^2 f}{\partial x_i^2} \Big|_{X_c} \sigma_{X_i}^2 E \left[ \sum_{i=1}^N \sum_{j=1}^N \frac{\partial^2 f}{\partial x_i \partial x_j} \Big|_{X_c} (x_i - x_{i,c})(x_j - x_{j,c}) \right] \\
&= \frac{1}{2} \left( \sum_{i=1}^N \frac{\partial^2 f}{\partial x_i^2} \Big|_{X_c} \sigma_{X_i}^2 \right)^2
\end{aligned} \tag{256}$$

$$\begin{aligned}
 A_6 &= E \left[ \left( \sum_{i=1}^N \frac{\partial f}{\partial x_i} \Big|_{X_c} (x_i - x_{i,c}) \right) \left( \sum_{i=1}^N \frac{\partial^2 f}{\partial x_i^2} \Big|_{X_c} \sigma_{X_i}^2 \right) \right] \\
 &= \left( \sum_{i=1}^N \frac{\partial^2 f}{\partial x_i^2} \Big|_{X_c} \sigma_{X_i}^2 \right) E \left[ \sum_{i=1}^N \frac{\partial f}{\partial x_i} \Big|_{X_c} (x_i - x_{i,c}) \right] \\
 &= 0
 \end{aligned} \tag{257}$$

Equations (253) and (255) are not developed further due to lengthy developments. Indeed, no hypothesis can be made at this stage on coskewness and cokurtosis which prevents from simplifying these formulae. Substituting (252)-(257) into (251) yields:

$$\begin{aligned}
 \sigma_Y^2 &= \overbrace{\sum_{i=1}^N \left( \frac{\partial f}{\partial x_i} \Big|_{X_c} \right)^2}^{A_1} \sigma_{X_i}^2 + A_2 + \frac{1}{4} \overbrace{\left( \sum_{i=1}^N \left( \frac{\partial^2 f}{\partial x_i^2} \Big|_{X_c} \right)^2 \sigma_{X_i}^4 + \sum_{i \neq j} \frac{\partial^2 f}{\partial x_i^2} \Big|_{X_c} \frac{\partial^2 f}{\partial x_j^2} \Big|_{X_c} \sigma_{X_i}^2 \sigma_{X_j}^2 \right)}^{A_3} \\
 &+ A_4 - \frac{1}{2} \underbrace{\left( \sum_{i=1}^N \frac{\partial^2 f}{\partial x_i^2} \Big|_{X_c} \sigma_{X_i}^2 \right)^2}_{A_5}
 \end{aligned} \tag{258}$$

If normally distributed and uncorrelated random variables are considered, then equations (253) and (255) can be simplified using special values taken by (25) and (26) under such assumptions:

$$\begin{aligned}
 A_2 &= E \left[ \left( \frac{1}{2} \sum_{i=1}^N \sum_{j=1}^N \frac{\partial^2 f}{\partial x_i \partial x_j} \Big|_{X_c} (x_i - x_{i,c})(x_j - x_{j,c}) \right)^2 \right] \\
 &= \frac{1}{4} \sum_{i=1}^N \sum_{j=1}^N \left( \frac{\partial^2 f}{\partial x_i \partial x_j} \Big|_{X_c} \right)^2 (x_i - x_{i,c})^2 (x_j - x_{j,c})^2 \\
 &+ \frac{1}{2} \sum_{i=1}^N \sum_{j=i+1}^N \frac{\partial^2 f}{\partial x_i^2} \Big|_{X_c} \frac{\partial^2 f}{\partial x_j^2} \Big|_{X_c} (x_i - x_{i,c})^2 (x_j - x_{j,c})^2 \\
 &+ \frac{1}{2} \sum_{i=1}^N \sum_{j=i+1}^N \frac{\partial^2 f}{\partial x_i \partial x_j} \Big|_{X_c} \frac{\partial^2 f}{\partial x_j \partial x_i} \Big|_{X_c} (x_i - x_{i,c})^2 (x_j - x_{j,c})^2
 \end{aligned} \tag{259}$$

$$\begin{aligned}
 A_4 &= E \left[ \left( \sum_{i=1}^N \frac{\partial f}{\partial x_i} \Big|_{X_c} (x_i - x_{i,c}) \right) \left( \sum_{i=1}^N \sum_{j=1}^N \frac{\partial^2 f}{\partial x_i \partial x_j} \Big|_{X_c} (x_i - x_{i,c})(x_j - x_{j,c}) \right) \right] \\
 &= E \left[ \sum_{i=1}^N \frac{\partial f}{\partial x_i} \Big|_{X_c} \frac{\partial^2 f}{\partial x_i^2} \Big|_{X_c} (x_i - x_{i,c})^3 \right] \\
 &= \sum_{i=1}^N \frac{\partial f}{\partial x_i} \Big|_{X_c} \frac{\partial^2 f}{\partial x_i^2} \Big|_{X_c} E [d_i^3] = 0
 \end{aligned} \tag{260}$$

For a single random variable problem, equation (258) becomes:

$$\begin{aligned}
 \sigma_Y^2 &\approx \overbrace{\left(\frac{\partial f}{\partial x}\right)^2}^{A_1} \sigma_X^2 + \overbrace{\frac{1}{4}\left(\frac{\partial^2 f}{\partial x^2}\right)^2}^{A_2} E[d^4] + \overbrace{\frac{1}{4}\left(\frac{\partial^2 f}{\partial x^2}\right)^2}^{A_3} \sigma_X^4 + \overbrace{\frac{\partial f}{\partial x}\left(\frac{\partial^2 f}{\partial x^2}\right)}^{A_4} E[d^3] - \overbrace{\frac{1}{2}\left(\frac{\partial^2 f}{\partial x^2}\right)^2}^{A_5} \sigma_X^4 \\
 &\approx \left(\frac{\partial f}{\partial x}\right)^2 \sigma_X^2 + \frac{1}{4}\left(\frac{\partial^2 f}{\partial x^2}\right)^2 E[d^4] - \frac{1}{4}\left(\frac{\partial^2 f}{\partial x^2}\right)^2 \sigma_X^4 + \frac{\partial f}{\partial x}\left(\frac{\partial^2 f}{\partial x^2}\right) E[d^3] \\
 &\approx \left(\frac{\partial f}{\partial x}\right)^2 \sigma_X^2 + \frac{\partial f}{\partial x}\left(\frac{\partial^2 f}{\partial x^2}\right) E[d^3] + \frac{1}{4}\left(\frac{\partial^2 f}{\partial x^2}\right)^2 (E[d^4] - \sigma_X^4)
 \end{aligned} \tag{261}$$

For higher order moments, the developments are made with first-order Taylor series expansion.

For the third centered moment, this yields:

$$\begin{aligned}
 \gamma_Y \sigma_Y^3 &= E\left[(Y - \bar{Y})^3\right] \\
 &\approx E\left[\left(Y_c + \sum_{i=1}^N \left(\frac{\partial f}{\partial x_i}\right) (x_i - x_{i,c}) - Y_c\right)^3\right] \\
 &\approx \sum_{i=1}^N \left(\frac{\partial f}{\partial x_i}\right)^3 E\left[(X_i - \bar{X})^3\right]
 \end{aligned} \tag{262}$$

Cross terms in (262) do not appear in the final line because they yield nil values under the assumption of uncorrelated random variables. For the fourth centered moment, some of the cross terms remain:

$$\begin{aligned}
 \kappa_Y \sigma_Y^4 &= E\left[(Y - \bar{Y})^4\right] \\
 &\approx E\left[\left(Y_c + \sum_{i=1}^N \left(\frac{\partial f}{\partial x_i}\right) (x_i - x_{i,c}) - Y_c\right)^4\right] \\
 &\approx \sum_{i=1}^N \left(\frac{\partial f}{\partial x_i}\right)^4 E\left[(X_i - \bar{X})^4\right] \\
 &\quad + 6 \sum_{i=1}^N \sum_{j=1}^N \left(\frac{\partial f}{\partial x_i}\right) \left(\frac{\partial f}{\partial x_j}\right) E\left[(X_i - \bar{X})^2\right] E\left[(X_j - \bar{X})^2\right]
 \end{aligned} \tag{263}$$

### A.3 Comparison of Franceschini's approach to the generalized Bolle's approach

Franceschini's formula (corrected) :

$$\begin{aligned}\sigma_Y^2 &= \sum_{i=1}^N E[d\mu_i^2] \\ &= \sum_{i=1}^N P_{i,1} (y_{i,1} - Y_c)^2 + P_{i,2} (y_{i,2} - Y_c)^2 - (P_c + P_{i,1} + P_{i,2}) e_i^2\end{aligned}\quad (264)$$

Where  $e_i$  is the distance between the central point  $Y_c$  et the local mean  $\bar{y}_i$  :

$$e_i = \bar{y}_i - Y_c = (P_{i,1} y_{i,1} + P_{i,2} y_{i,2} + P_c Y_c) - Y_c \quad (265)$$

Generalization of Bolle's formula to skewed distributions:

$$\sigma_Y^2 = \sum_{i=1}^N P_{i,1} (y_{i,1} - \bar{y}_i)^2 + P_{i,2} (y_{i,2} - \bar{y}_i)^2 + P_c (Y_c - \bar{y}_i)^2 \quad (266)$$

Equation (264) is developed:

$$\begin{aligned}\sigma_Y^2 &= \sum_{i=1}^N P_{i,1} (y_{i,1} - Y_c)^2 + P_{i,2} (y_{i,2} - Y_c)^2 - (P_c + P_{i,1} + P_{i,2}) e_i^2 \\ &= \sum_{i=1}^N P_{i,1} (y_{i,1}^2 - 2y_{i,1} Y_c + Y_c^2) + P_{i,2} (y_{i,2}^2 - 2y_{i,2} Y_c + Y_c^2) - (\bar{y}_i^2 - 2\bar{y}_i Y_c + Y_c^2) \\ &= \sum_{i=1}^N P_{i,1} (y_{i,1}^2 - 2y_{i,1} Y_c) + P_{i,2} (y_{i,2}^2 - 2y_{i,2} Y_c) + (1 - P_c) Y_c^2 - (\bar{y}_i^2 - 2\bar{y}_i Y_c + Y_c^2) \\ &= \sum_{i=1}^N P_{i,1} (y_{i,1}^2 - 2y_{i,1} Y_c) + P_{i,2} (y_{i,2}^2 - 2y_{i,2} Y_c) + (1 - P_c) Y_c^2 - (\bar{y}_i^2 - 2\bar{y}_i Y_c + Y_c^2) \\ &= \sum_{i=1}^N P_{i,1} y_{i,1}^2 + P_{i,2} y_{i,2}^2 - P_c Y_c^2 - \bar{y}_i^2 + 2Y_c (\bar{y}_i - y_{i,1} P_{i,1} - y_{i,2} P_{i,2}) \\ &= \sum_{i=1}^N P_{i,1} y_{i,1}^2 + P_{i,2} y_{i,2}^2 - P_c Y_c^2 - (P_c + P_{i,1} + P_{i,2}) \bar{y}_i^2 + 2Y_c (\bar{y}_i - y_{i,1} P_{i,1} - y_{i,2} P_{i,2}) \\ &= \sum_{i=1}^N P_{i,1} (y_{i,1}^2 - \bar{y}_i^2) + P_{i,2} (y_{i,2}^2 - \bar{y}_i^2) + P_c (-Y_c^2 - \bar{y}_i^2) + 2Y_c (\bar{y}_i - y_{i,1} P_{i,1} - y_{i,2} P_{i,2})\end{aligned}\quad (267)$$

The last line in (267) is getting closer to (266). To continue, terms will be added and removed in order to reach the desired form:

$$\begin{aligned}
\sigma_Y^2 &= \sum_{i=1}^N P_{i,1} (y_{i,1}^2 - \bar{y}_i^2) + P_{i,2} (y_{i,2}^2 - \bar{y}_i^2) + P_c (-Y_c^2 - \bar{y}_i^2) + 2Y_c (\bar{y}_i - y_{i,1}P_{i,1} - y_{i,2}P_{i,2}) \\
&= \sum_{i=1}^N P_{i,1} (y_{i,1}^2 + \bar{y}_i^2 - 2\bar{y}_i y_{i,1}) + P_{i,2} (y_{i,2}^2 + \bar{y}_i^2 - 2\bar{y}_i y_{i,2}) + P_c (Y_c^2 + \bar{y}_i^2 - 2Y_c \bar{y}_i) \\
&\quad - \sum_{i=1}^N P_{i,1} (2\bar{y}_i^2 - 2\bar{y}_i y_{i,1}) + P_{i,2} (2\bar{y}_i^2 - 2\bar{y}_i y_{i,2}) + P_c (2Y_c^2 + 2\bar{y}_i^2 - 2Y_c \bar{y}_i) - 2Y_c (\bar{y}_i - y_{i,1}P_{i,1} - y_{i,2}P_{i,2}) \\
&= \sum_{i=1}^N P_{i,1} (y_{i,1} - \bar{y}_i)^2 + P_{i,2} (y_{i,2} - \bar{y}_i)^2 + P_c (Y_c - \bar{y}_i)^2 \\
&\quad - \underbrace{\sum_{i=1}^N P_{i,1} (2\bar{y}_i^2 - 2\bar{y}_i y_{i,1}) + P_{i,2} (2\bar{y}_i^2 - 2\bar{y}_i y_{i,2}) + P_c (2Y_c^2 + 2\bar{y}_i^2 - 2Y_c \bar{y}_i) - 2Y_c (\bar{y}_i - y_{i,1}P_{i,1} - y_{i,2}P_{i,2})}_A
\end{aligned} \tag{268}$$

In the last equality of (268), the first sum is the same as (266). If  $A$  is proven to be nil, then (268) and (266) are equivalent.

$$\begin{aligned}
A &= \sum_{i=1}^N P_{i,1} (2\bar{y}_i^2 - 2\bar{y}_i y_{i,1}) + P_{i,2} (2\bar{y}_i^2 - 2\bar{y}_i y_{i,2}) + P_c (2Y_c^2 + 2\bar{y}_i^2 - 2Y_c \bar{y}_i) - 2Y_c (\bar{y}_i - y_{i,1}P_{i,1} - y_{i,2}P_{i,2}) \\
&= \sum_{i=1}^N 2Y_c \left( \underbrace{\bar{y}_i - y_{i,1}P_{i,1} - y_{i,2}P_{i,2} - Y_c P_c}_{-\bar{y}_i} \right) - 2\bar{y}_i^2 \left( \underbrace{P_{i,1} + P_{i,2} + P_c}_1 \right) + 2\bar{y}_i \left( \underbrace{P_{i,1} y_{i,1} + P_{i,2} y_{i,2} + P_c Y_c}_{\bar{y}_i} \right) \\
&= \sum_{i=1}^N 0 - 2\bar{y}_i^2 + 2\bar{y}_i^2 \\
&= 0
\end{aligned} \tag{269}$$

Since  $A = 0$ , Franceschini's and the generalized Bolle's approaches are equivalent for the computations of the variance.

#### A.4 Proposal for the extension of SRSM to skewed distributions

The Stochastic Response Surface Method (SRSM) chooses points in the uncertain space according to a heuristic approach described in section 2.3.3. This approach leads to a symmetrical disposal of evaluation points. While this characteristic is not a problem for symmetrical uncertain variables, issues may be encountered when the user deals with skewed and/or bounded distributions. A theoretically appealing alternative approach is proposed in this appendix. However, it should be noticed that it was not extensively tested in the frame of this thesis.

The main assumption to allow an extension to skewed and/or bounded distributions is that the empirical method developed by Isukapalli et al. (1998) was made for normally distributed random variables. From this assumption, for each collocation point chosen by the original method, it is possible to compute a cumulative probability. Then, this cumulative probability is used in the invert cdf that corresponds to the desired distribution. One gets a new position for the collocation points. After the evaluation of the model at these points, a polynomial can be fitted such as described in the original method.

An example is provided for a better understanding. The left plot in Figure 192 shows the points that would be used by the original SRSM method for an uncertain variable defined by a gamma distribution with following statistical moment:

- Mean: 1.7
- Standard deviation: 0.3
- Skewness coefficient: 1.2

It appears that one of these points lies beyond the left bound of the gamma distribution. The new approach proposes a transformation of the points based on an assumed normal cumulative density function. The transformation process is summarized in Table 36. Results are given in the right plot in Figure 192. Now, it appears that all points lies in the support domain of the gamma law. Moreover, points are distributed according to the skewed property of the gamma pdf.

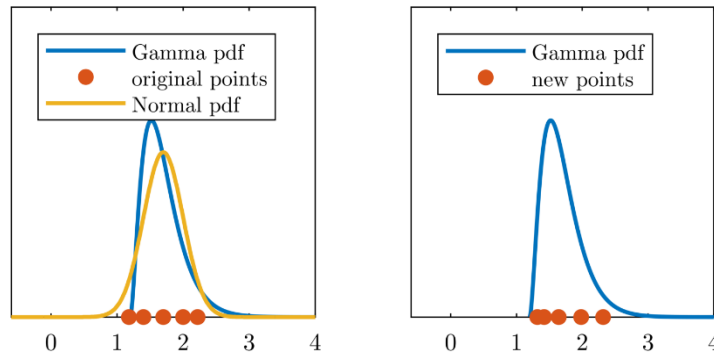


Figure 192: Comparison of the points used by the SRSM method according to the original approach the new one proposed in this appendix

*Appendices*

<b>Point</b>	<b>Original position</b>		<b>Cumulative probability</b>		<b>New position</b>
1	1.1804	→	0.0416	→	1.3173
2	1.4	→	0.1587	→	1.4186
3	1.7	Normal cdf	0.5	Gamma icdf	1.6414
4	2.0	→	0.8413	→	1.9824
5	2.2196	→	0.9584	→	2.3168

*Table 36: From the original position to the new position proposed in this new approach (icdf = inverse cumulative density function)*

## B Fast 1-D convergence of a 1-D steady flow

### B.1 Boxplots for parameters optimization tests 3 and 4

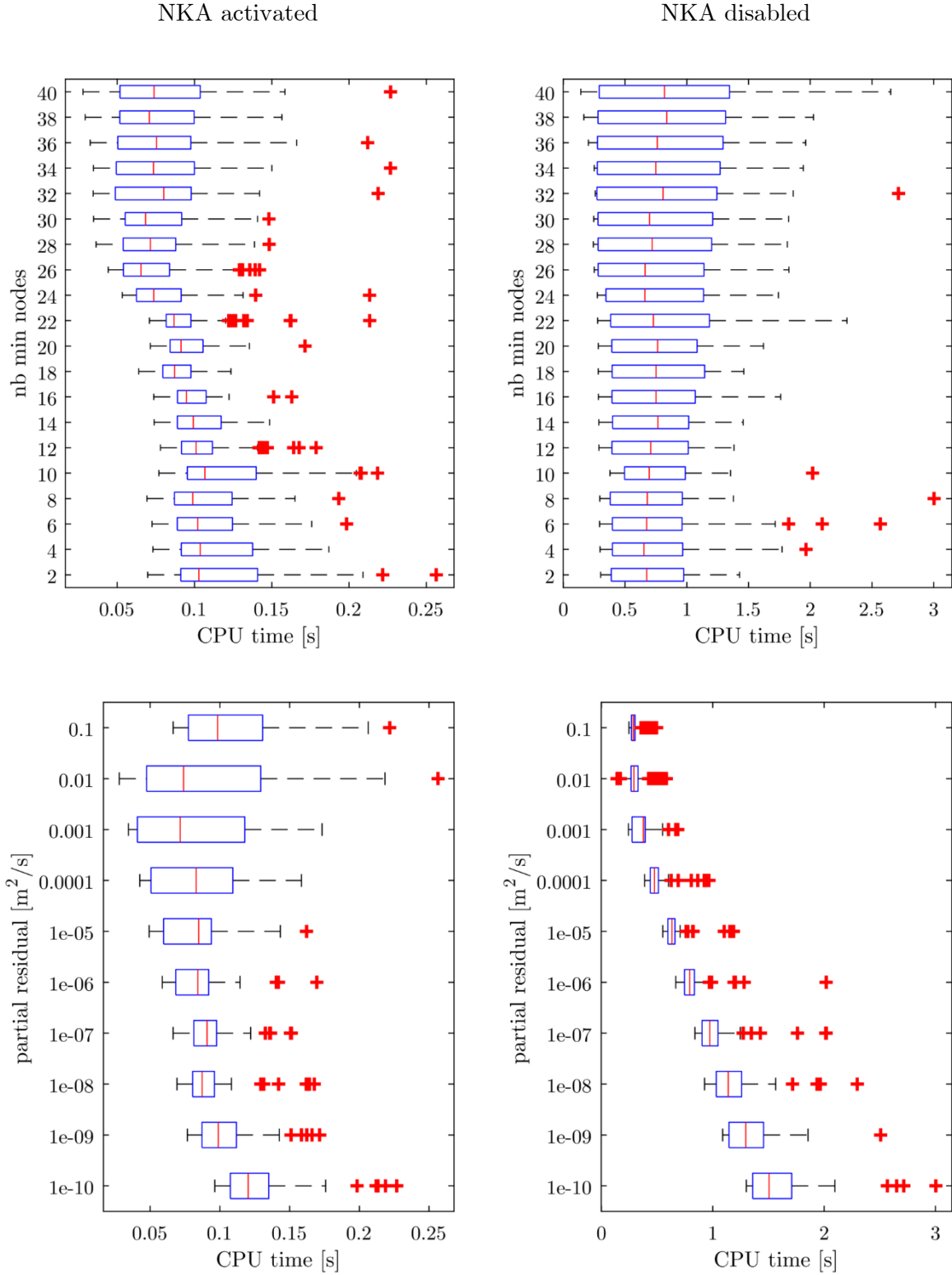


Figure 193: Boxplots according to the minimum number of nodes to keep in computation list and the partial residual for test 3

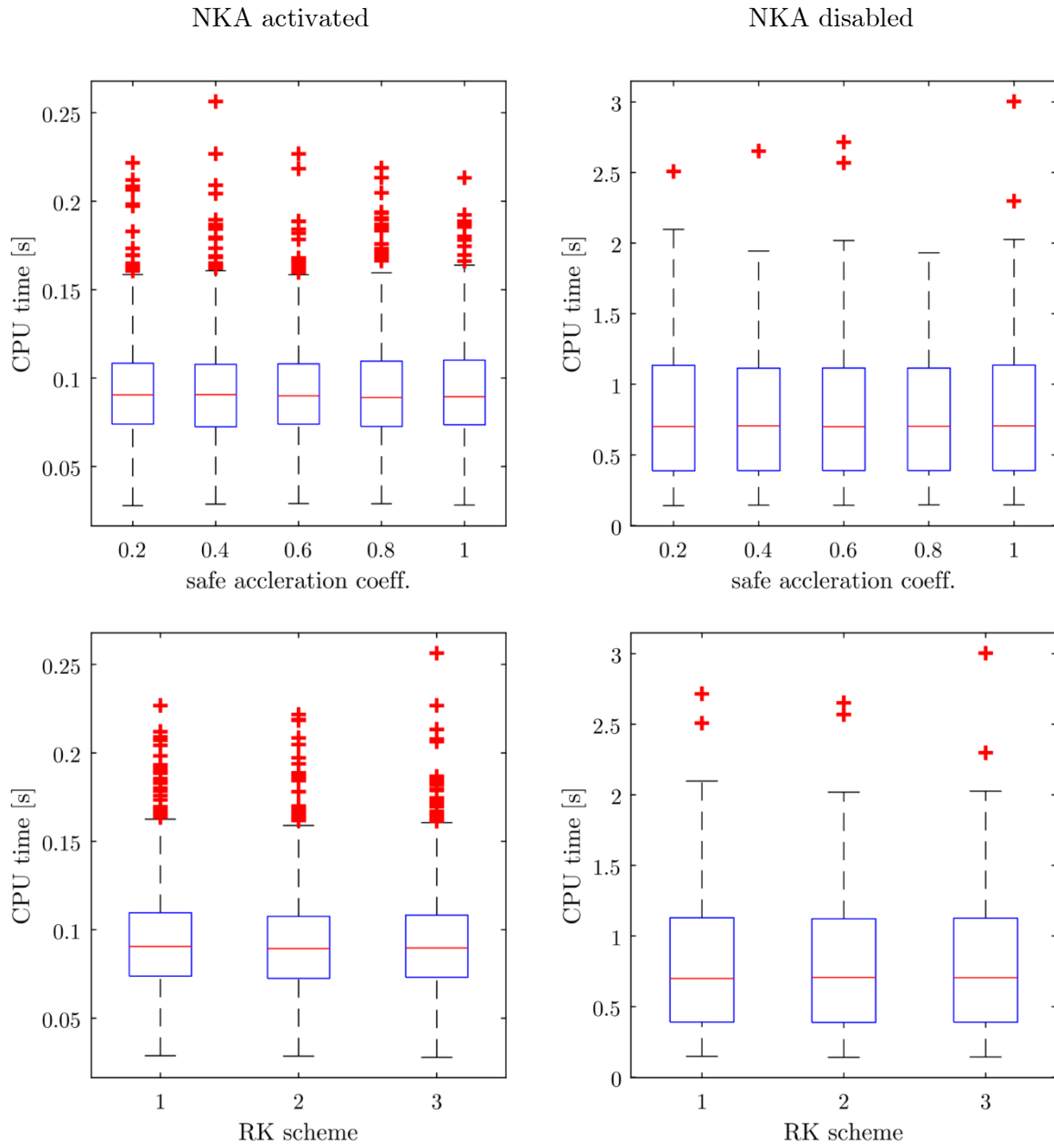


Figure 194: Boxplots according to the value of the safe acceleration coefficient and the temporal scheme for test 3

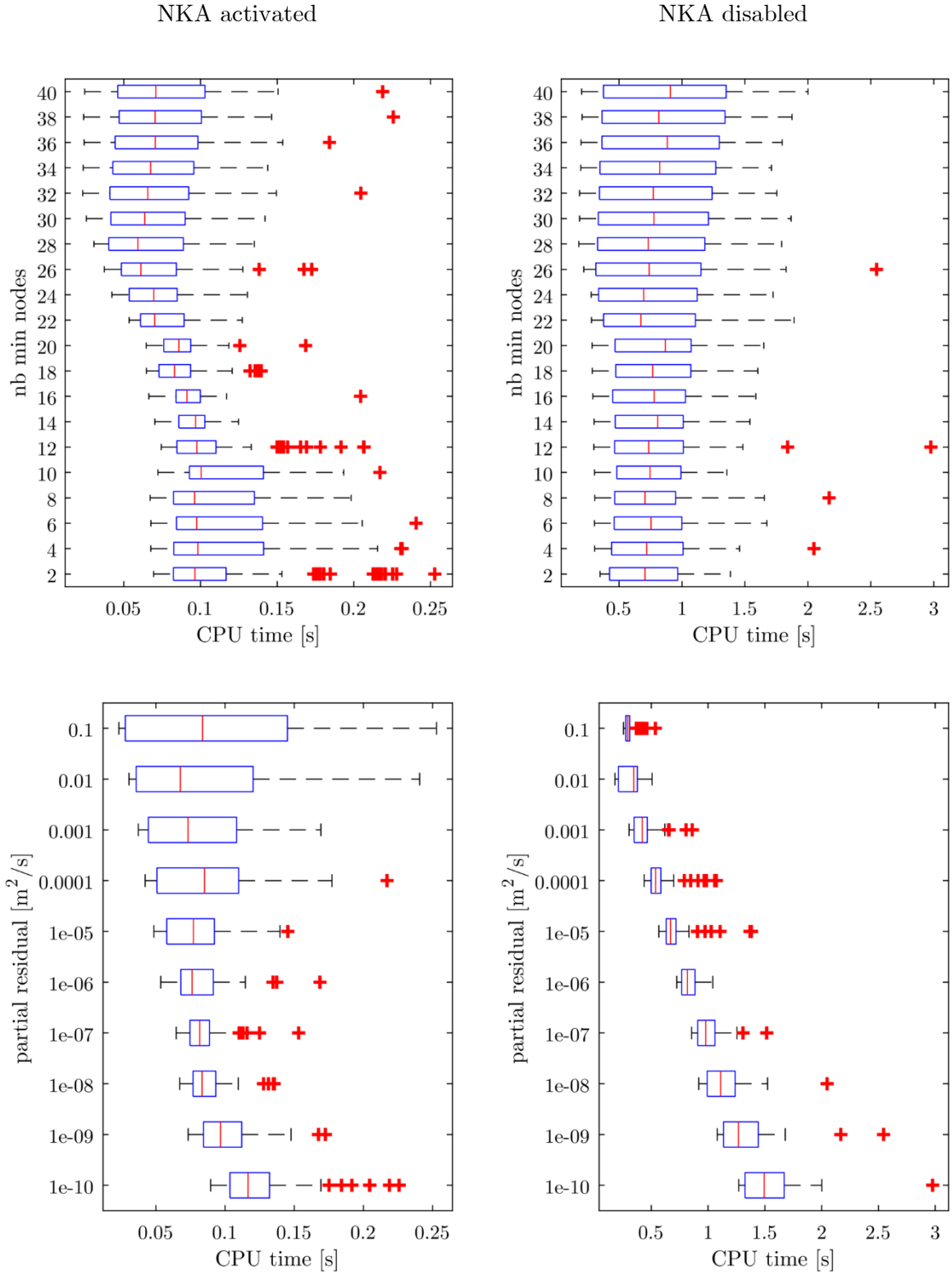


Figure 195: Boxplots according to the minimum number of nodes to keep in computation list and the partial residual for test 4

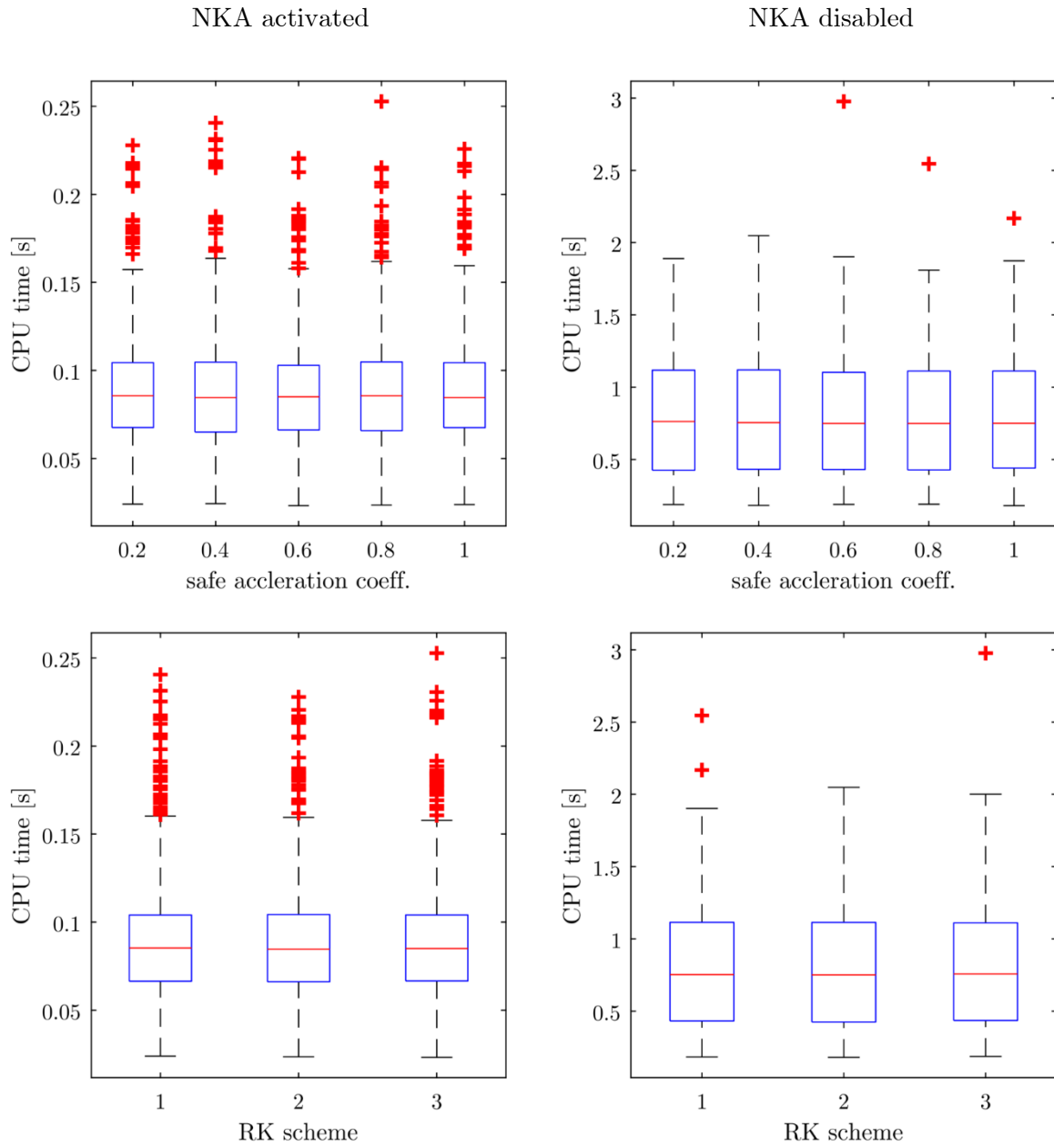


Figure 196: Boxplots according to the value of the safe acceleration coefficient and the temporal scheme for test 4

# C 2-D uncertainty analysis appendix

## C.1 Full view of the extraction vector

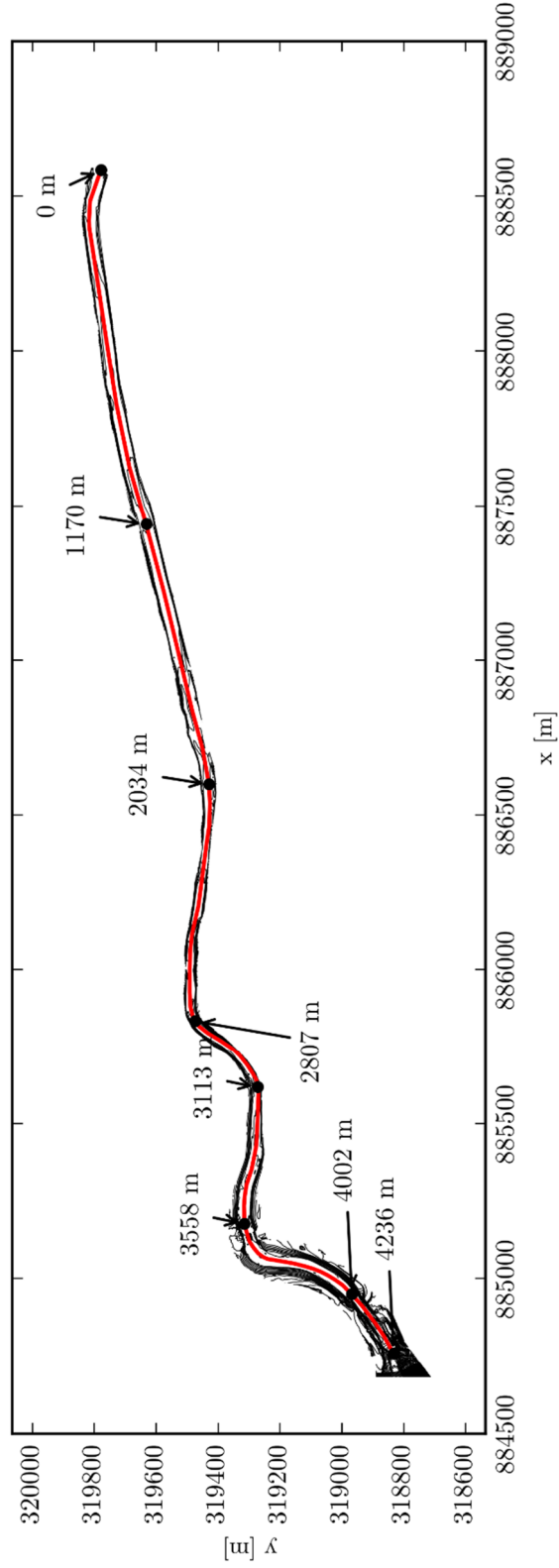


Figure 197: Vector used for extracting bed elevations and water levels – full view

## C.2 Supplementary maps for hydraulic variables

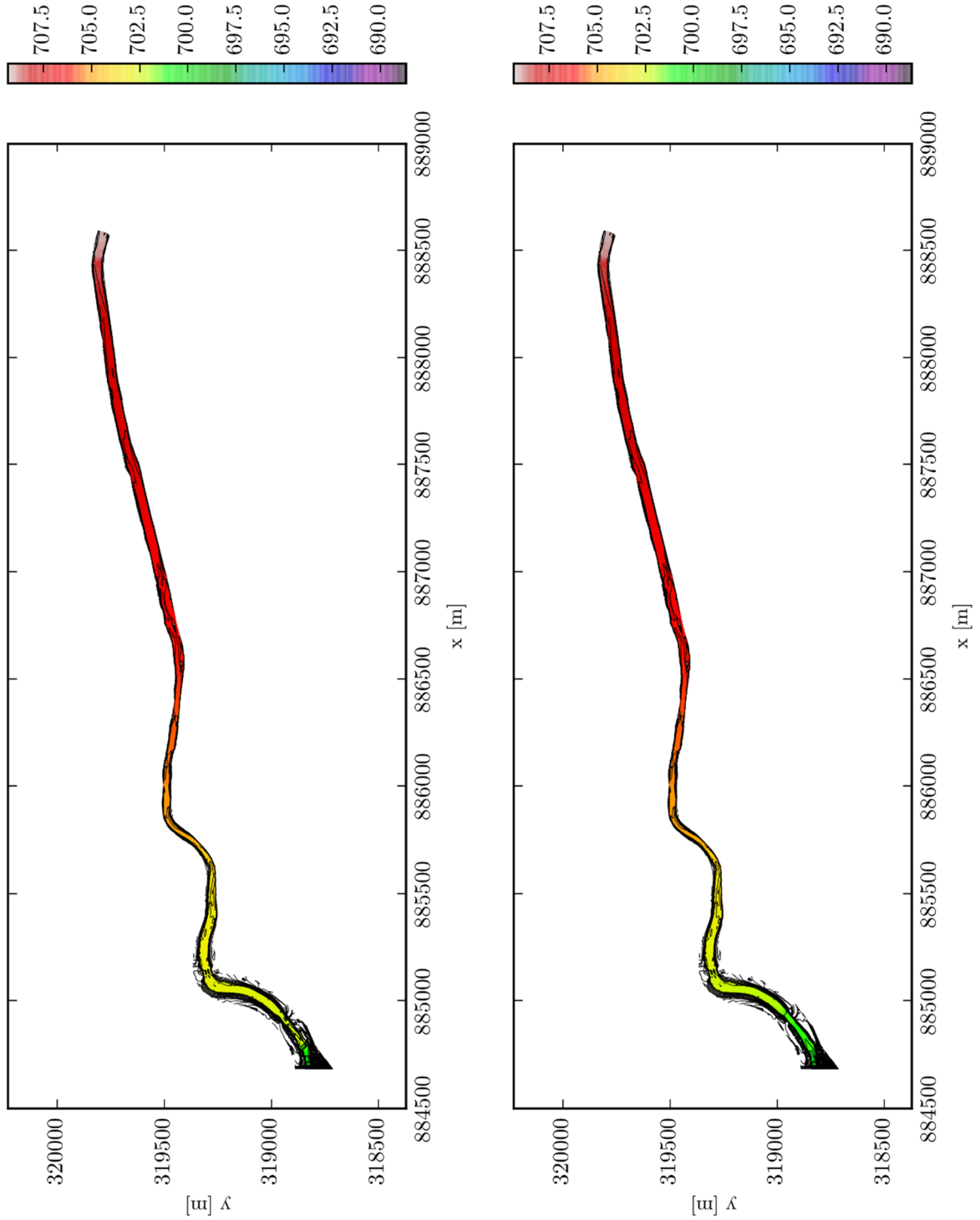


Figure 198: Water levels [m] for  $k_s = 0.0634$  m in the current situation (left) and considering removal plans (right)

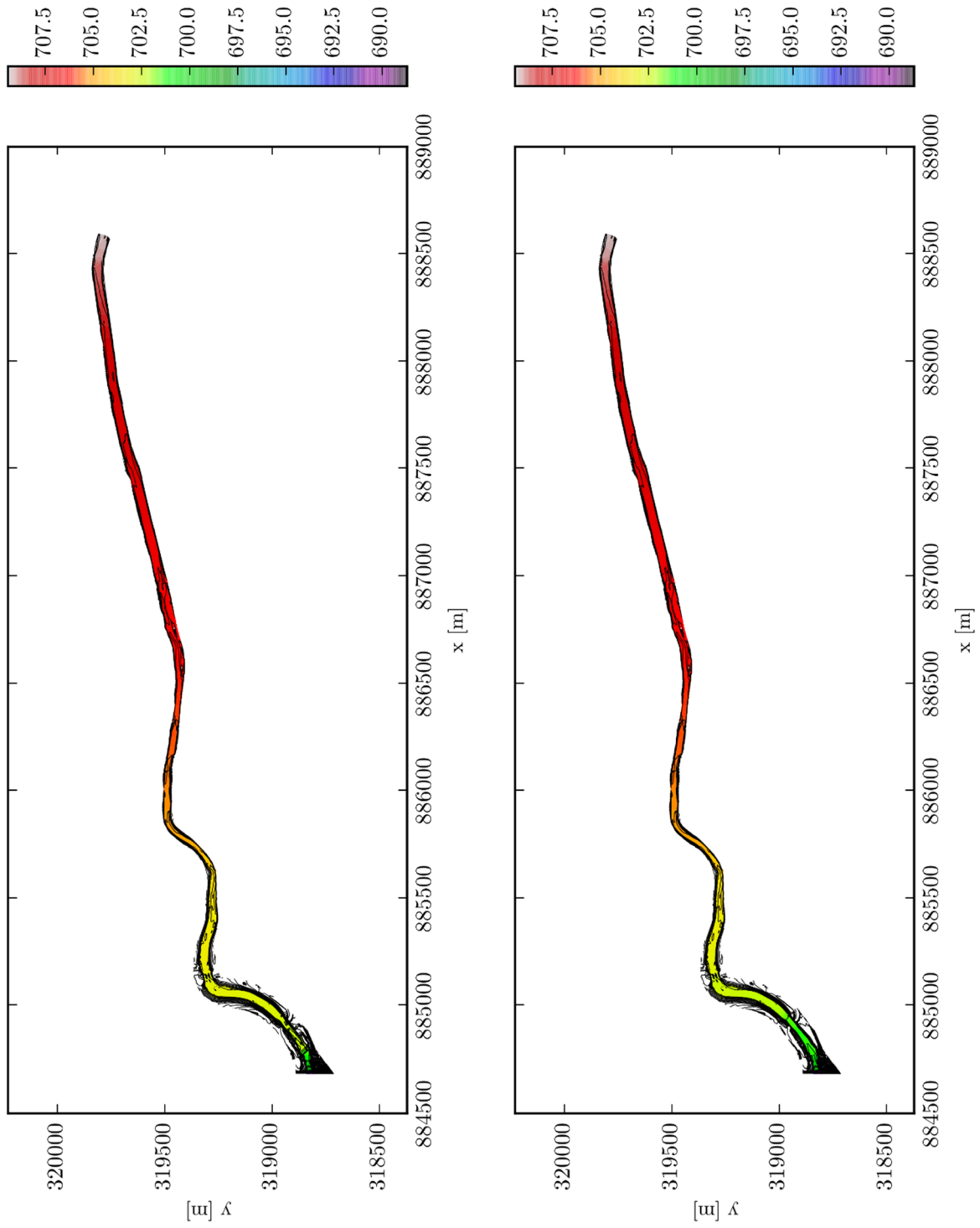


Figure 199: Water levels [m] for  $k_s = 0.15$  m in the current situation (left) and considering removal plans (right)

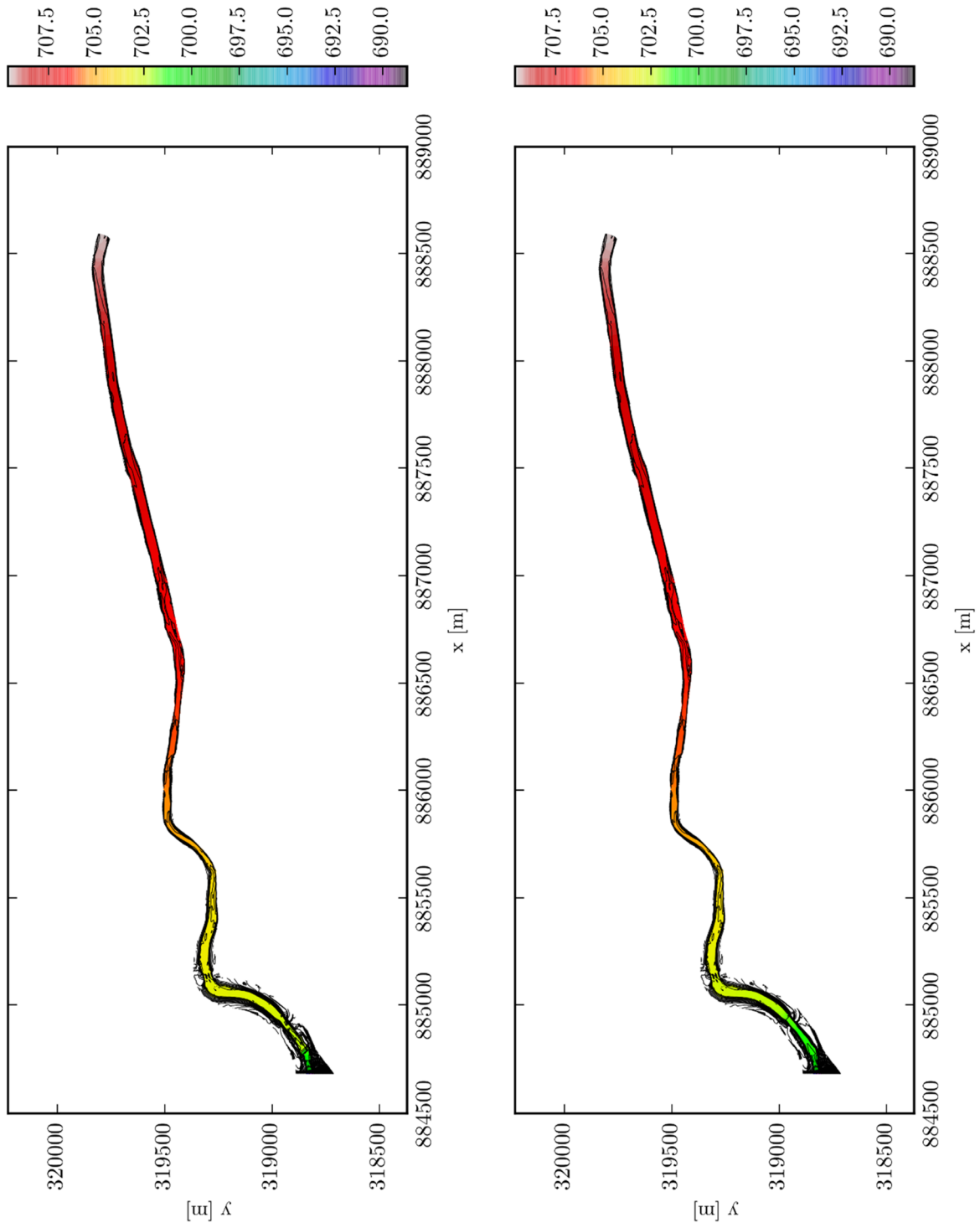


Figure 200: Water levels [m] for  $k_s = 0.237$  m in the current situation (left) and considering removal plans (right)

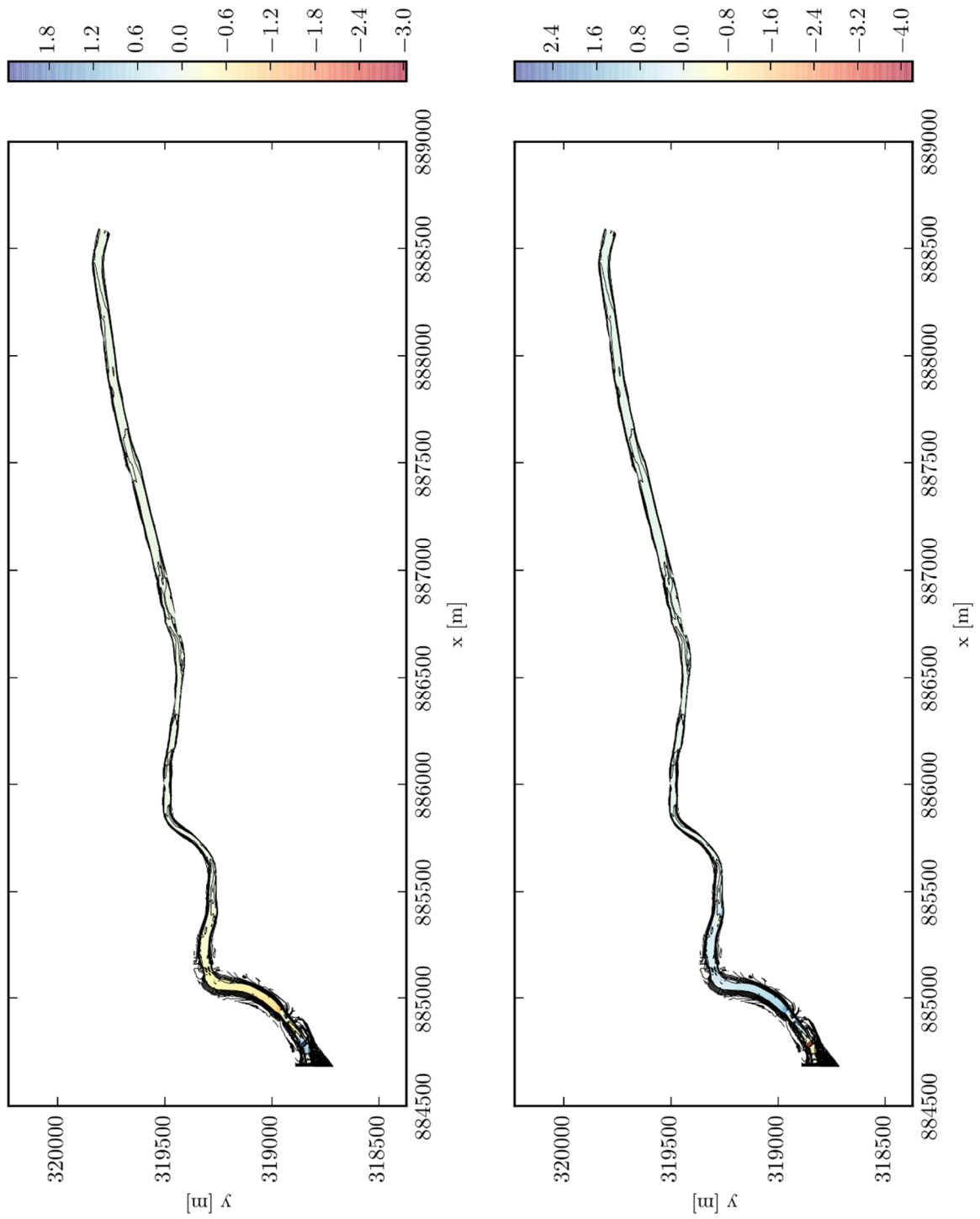


Figure 201: Differential of water depth (left, [m]) et velocity (right, [m/s]) between the current (c) and the planned (p) situations ( $p - c$ ) for a discharge of  $150 \text{ m}^3/\text{s}$  and  $k_s = 0.0634 \text{ m}$

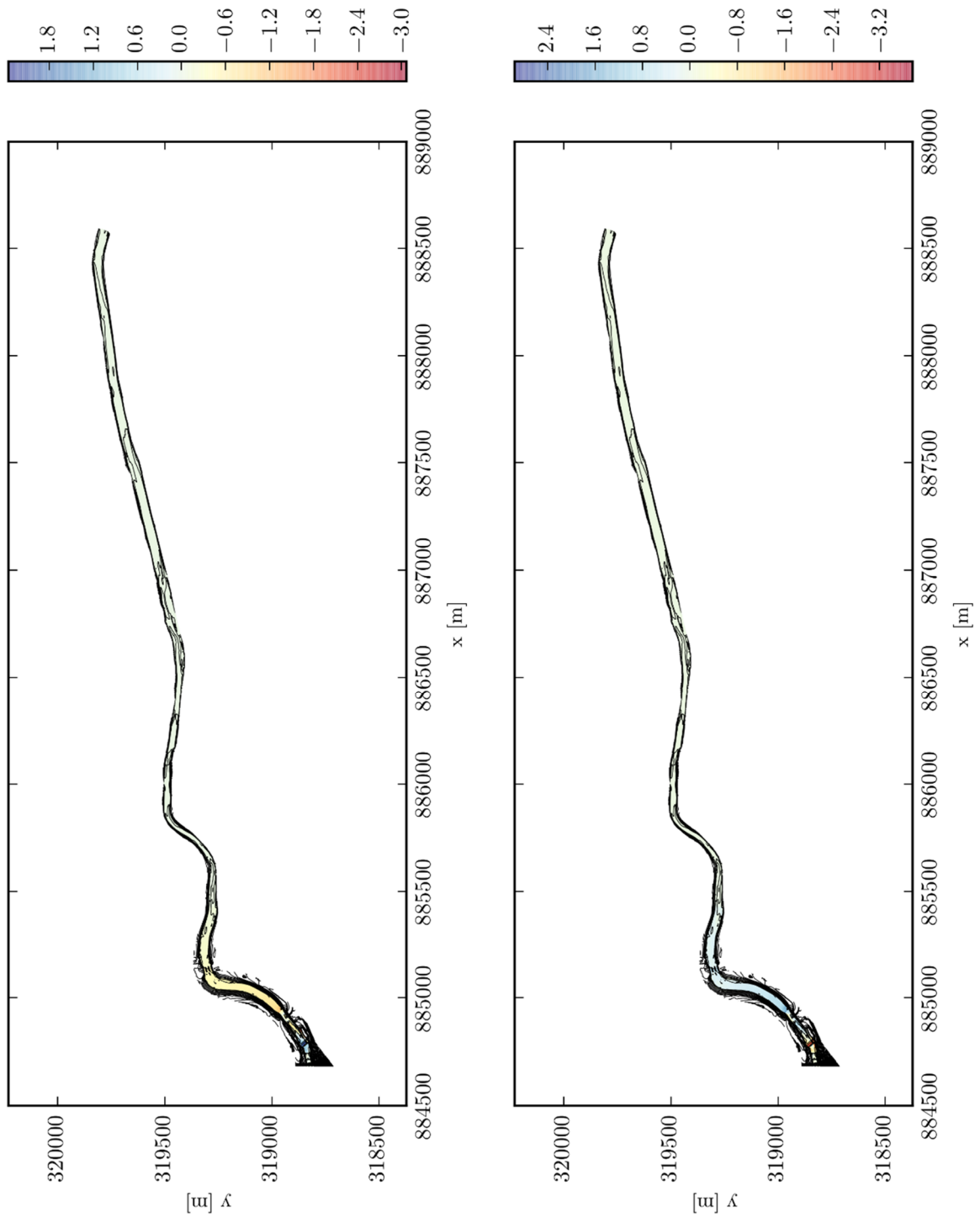


Figure 202: Differential of water depth (left, [m]) et velocity (right, [m/s]) between the current (c) and the planned (p) situations (p - c) for a discharge of  $150 \text{ m}^3/\text{s}$  and  $k_s = 0.15 \text{ m}$

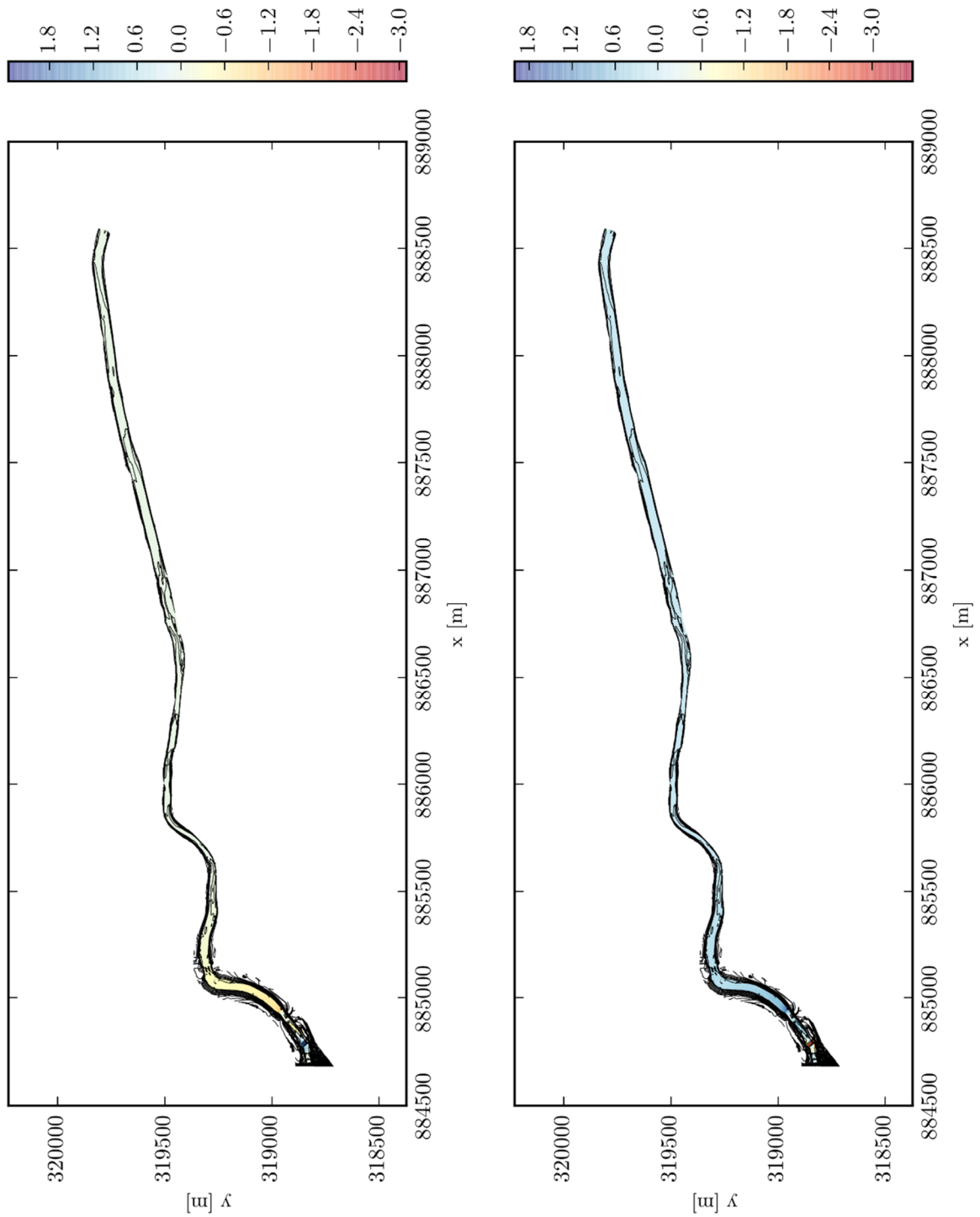


Figure 203: Differential of water depth (left, [m]) et velocity (right, [m/s]) between the current ( $c$ ) and the planned ( $p$ ) situations ( $p - c$ ) for a discharge of  $150 \text{ m}^3/\text{s}$  and  $k_s = 0.237 \text{ m}$

### C.3 Supplementary maps for uncertainty characterization

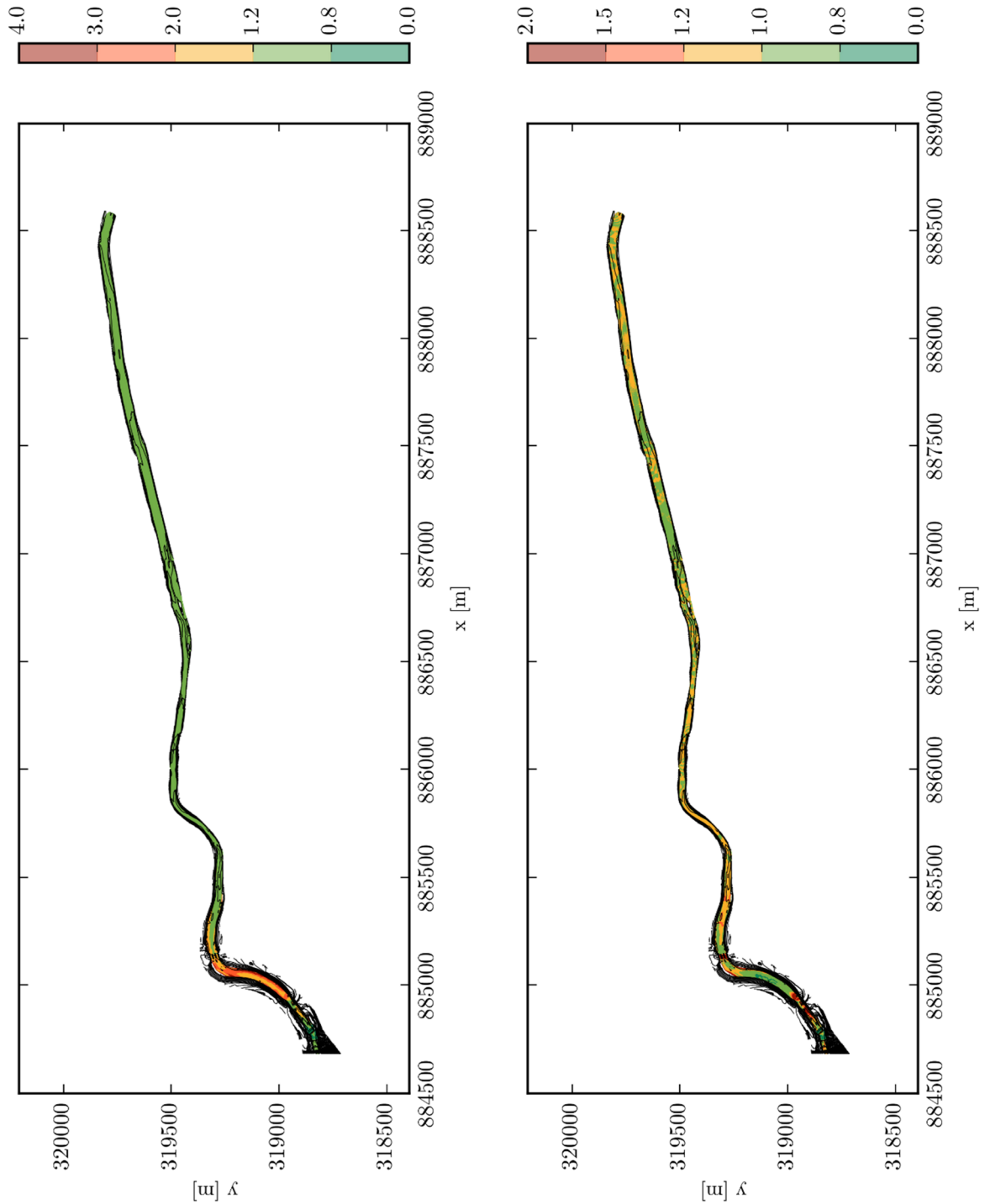


Figure 204: Ratio between the mean (left) and standard deviation (right) of the proportion of bed soil that is set in movement in the planned situation and in the current situation for a  $150 \text{ m}^3/\text{s}$  discharge

## D Porous media flow appendix

### D.1 Linear soil law

The van Gneuchten – Mualem law presents a high level of non-linearity. This might be an issue for the convergence of a numerical solution. In order to overcome such difficulties, we propose here a linear formulation for soil constitutive laws. It should be immediately noticed that the proposed law do not fit experimental observations.

We chose a linear law by parts such as depicted in Figure 205. It consists in four lines:

- a) A horizontal line for the saturation domain
- b) A steep part that takes the slope at the inflection point of the van Genuchten – Mualem law and that passes by this point
- c) A line that join the residual domain to the 20 % wetting front
- d) A horizontal line for the residual domain

For lines (a) and (d), the  $\theta$  function is constant:

$$\begin{aligned}\theta_a(\psi) &= \theta_s \\ \theta_d(\psi) &= \theta_r\end{aligned}\tag{270}$$

Line (b) passes by the inflection point  $(\psi_0, \theta_0)$  of the van Genuchten – Mualem law and takes the slope at this point. The slope is limited in order to ensure that saturation is reached before  $\psi = 0$ . The equation of line (b) is:

$$\theta_b = m_b \psi + p_b\tag{271}$$

With the slope  $m_b$  computed from the inflection point:

$$\begin{aligned}\psi_0 &= \frac{-1}{\alpha} \left( \frac{n-1}{n} \right)^{1/n} \\ \theta_0 &= \theta_{vG}(\psi_0) \\ m_b &= \max \left( \eta_{vG}(\psi_0), \frac{\theta_0 - \theta_s}{\psi_0} \right)\end{aligned}\tag{272}$$

And the constant term  $p_b = \theta_0 - m_b \psi_0$ . The junction with line (a) is performed at  $\psi_1 = (\theta_r - p_b) / m_b$ .

Line (c) starts from the 20 % wetting front  $\theta_2 = \theta_r + (\theta_s - \theta_r)0.2$  and goes until the constant value  $\theta_r$ . The junction is performed at  $\psi_2 = (\theta_2 - p_b) / m_b$  with line (b) and at  $\psi_3 = 5\psi_2$  with line (d). The equation of line (c) is:

$$\theta_c = \frac{\theta_2 - \theta_r}{\psi_2 - \psi_3} \psi + p_c \quad (273)$$

with  $p_c = \theta_r - m_c \psi_2$ .

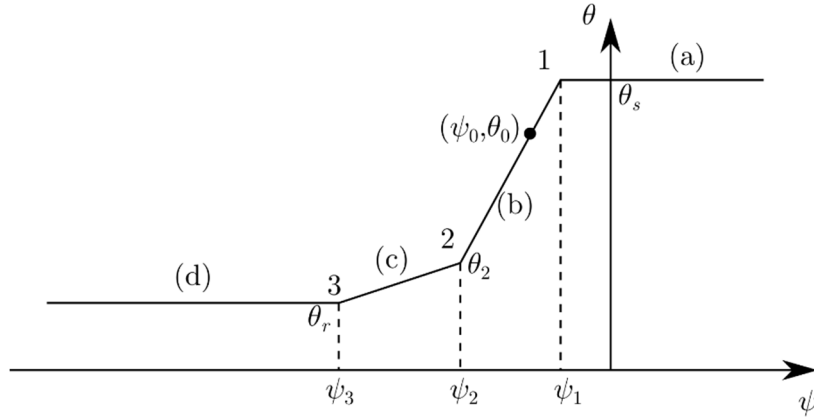


Figure 205: Schematic representation of the linear by parts soil law

The water holding capacity is simply the slopes of the different lines. The hydraulic conductivity is linearly linked to the water content:

$$K(\psi) = K_s \frac{\theta - \theta_r}{\theta_s - \theta_r} \quad (274)$$

In order, to ensure a smooth transition between the different lines, sigmoid curves are used. A simplified form of equation (212) is chosen for this purpose:

$$S(\psi) = \frac{1}{1 + e^{-B(\psi - \psi_0)}} \quad (275)$$

We define the water content as a linear function of the pressure:

$$\theta(\psi) = m(\psi)\psi + p(\psi) \quad (276)$$

$m$  and  $p$  are functions of  $\psi$  because several lines are used to define the water content. Let us consider a simplified case with a transition between two lines (with slopes  $m_1$  and  $m_2$ ). We want the slope to evolve according to a defined sigmoid:

*Appendices*

$$\begin{aligned}
 m(\psi) &= m_1(1 - S(\psi)) + m_2 S(\psi) \\
 &= m_1 + \frac{m_2 - m_1}{1 + e^{-B(\psi - \psi_0)}}
 \end{aligned} \tag{277}$$

The derivative of (276) is

$$\frac{\partial \theta}{\partial \psi} = m(\psi) + \psi \frac{\partial m}{\partial \psi} + \frac{\partial p}{\partial \psi} \tag{278}$$

Two other terms appear and the evolution of the slope wished in (277) can only be met when these two terms neutralize:

$$\begin{aligned}
 \psi \frac{\partial m}{\partial \psi} + \frac{\partial p}{\partial \psi} &= 0 \\
 \Leftrightarrow p &= - \int \psi \frac{\partial m}{\partial \psi} d\psi \\
 \Leftrightarrow p &= -\psi m(\psi) + \int m d\psi \\
 \Leftrightarrow p &= -\psi m(\psi) + \int [m_1(1 - S(\psi)) + m_2 S(\psi)] d\psi
 \end{aligned} \tag{279}$$

The integral of (275) is:

$$\int \frac{1}{1 + e^{-B(\psi - \psi_0)}} d\psi = \psi + \frac{\ln(1 + e^{-B(\psi - \psi_0)})}{B} \tag{280}$$

In the specific case of  $\psi_0 = 0$  and  $B = 1$ , (280) is named the softplus function (it is mainly used in the frame of neural networks) and it is a ramp function with a smooth transition. Using the result of (280) in (279) yields

$$\begin{aligned}
 p &= -\psi m(\psi) + m_1 \psi - m_1 \left( \psi + \frac{\ln(1 + e^{-B(\psi - \psi_0)})}{B} \right) + m_2 \left( \psi + \frac{\ln(1 + e^{-B(\psi - \psi_0)})}{B} \right) + C \\
 &= -\psi m(\psi) + m_2 \psi + (m_2 - m_1) \frac{\ln(1 + e^{-B(\psi - \psi_0)})}{B} + C
 \end{aligned} \tag{281}$$

The integration constant  $C$  can be fixed for  $\psi \rightarrow +\infty$ :

$$\lim_{\psi \rightarrow +\infty} p = C = p_2 \tag{282}$$

Combining (276) and (281) yields:

$$\theta(\psi) = m_2 \psi + p_2 + (m_2 - m_1) \frac{\ln(1 + e^{-B(\psi - \psi_0)})}{B} \tag{283}$$

The transition is illustrated for a random example in Figure 206.

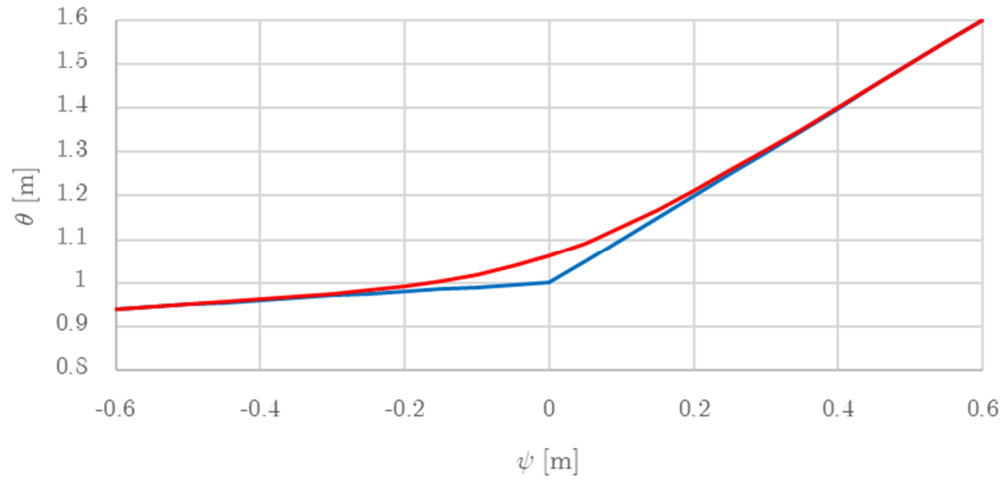
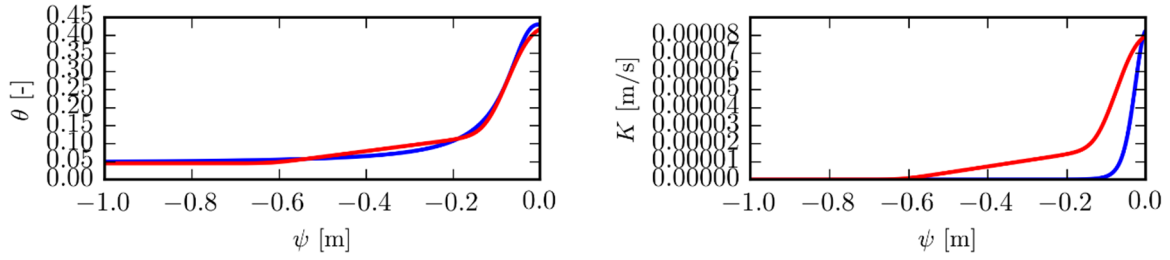


Figure 206: Smooth transition between two lines

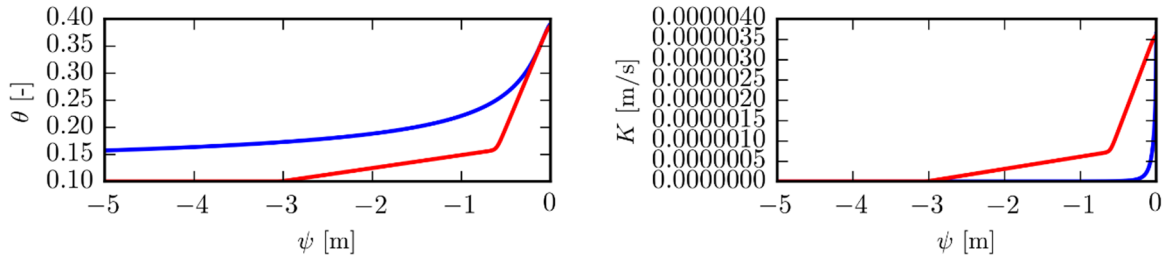
The transitions between the different parts of the linear law are smoothed by sigmoid functions. Using  $B = 50$  in (277) produced the graphs presented in Figure 207. They compare the van Genuchten - Mualem law (blue line) to the linear law by parts (red line). Large differences can appear, especially for the less permeable soils. However, the purpose to use a linear law is to test its ability to improve convergence, even if the physical results are far from reality.

After several tests, it appeared that the linear law by parts does not improve convergence. Globally, this implementation is even worse than the van Genuchten - Mualem law. We attribute this to the changes in the slope of the law. Even if smoothing is implemented, the slope can vary its value suddenly while the van Genuchten - Mualem law is much smoother in the majority of its domain.

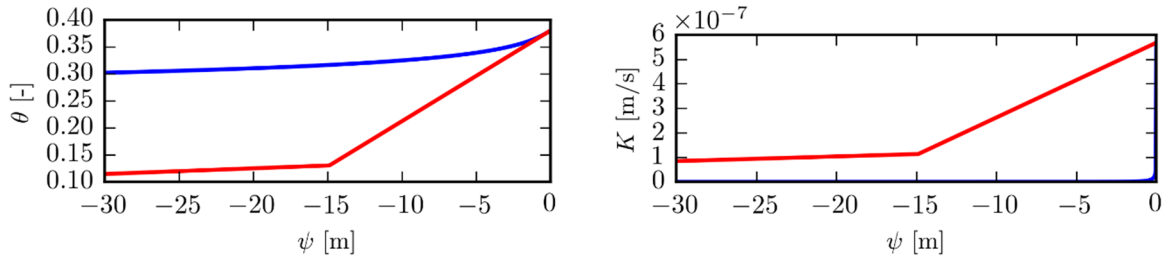
Appendices



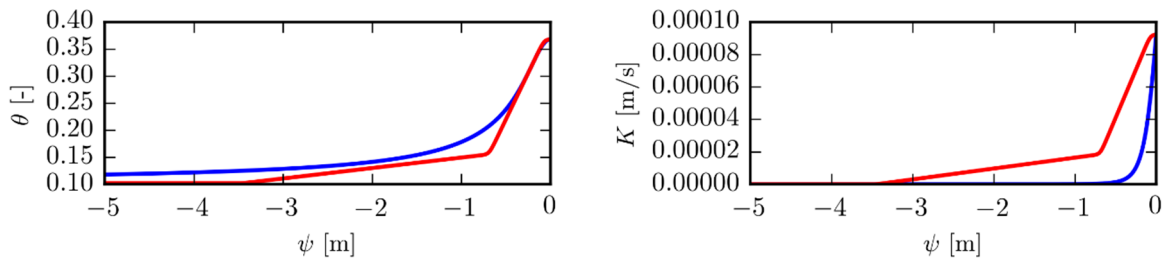
Sand



Sandy clay loam



Clay



New Mexico

Figure 207: Comparison between the van Genuchten – Mualem law and the linear by parts law for 4 soils

## **D.2 Influence of the spatial and time steps on the validation test**

The influence of the time step and of the spatial discretization is studied in this section on the “New-Mexico” validation test. For both cases, 10 Krylov subspaces and an upstream linear reconstruction of the hydraulic conductivity are used.

For the influence of the spatial discretization (Figure 208), a time step of 2 minutes is used. It appears that finer spatial steps (1 mm and 1 cm) produce excellent results compared to the reference solution (Manzini & Ferraris 2004). The coarser mesh (10 cm cells) produces significantly worse results where diffusive effects are more prominent. The linear reconstruction of the hydraulic conductivity leads to larger values of  $K$  at the borders, meaning that the Darcy velocity is larger for a same potential gradient.

The same analysis is done for the influence of the time step (Figure 209). The results produced with 2 minutes and 1 hour time steps are in good agreement with the reference results. The 12 hours time step produces worse results. The position of the tip of the wetting front is almost 12 hours in advance of the expected result. The stability of an implicit time scheme is independent of the time step. However, as shown here, the quality of the results is highly dependent of this parameter.

This short analysis of the influence of the time step and of spatial discretization shows that these values should be chosen carefully in the frame of a practical use.

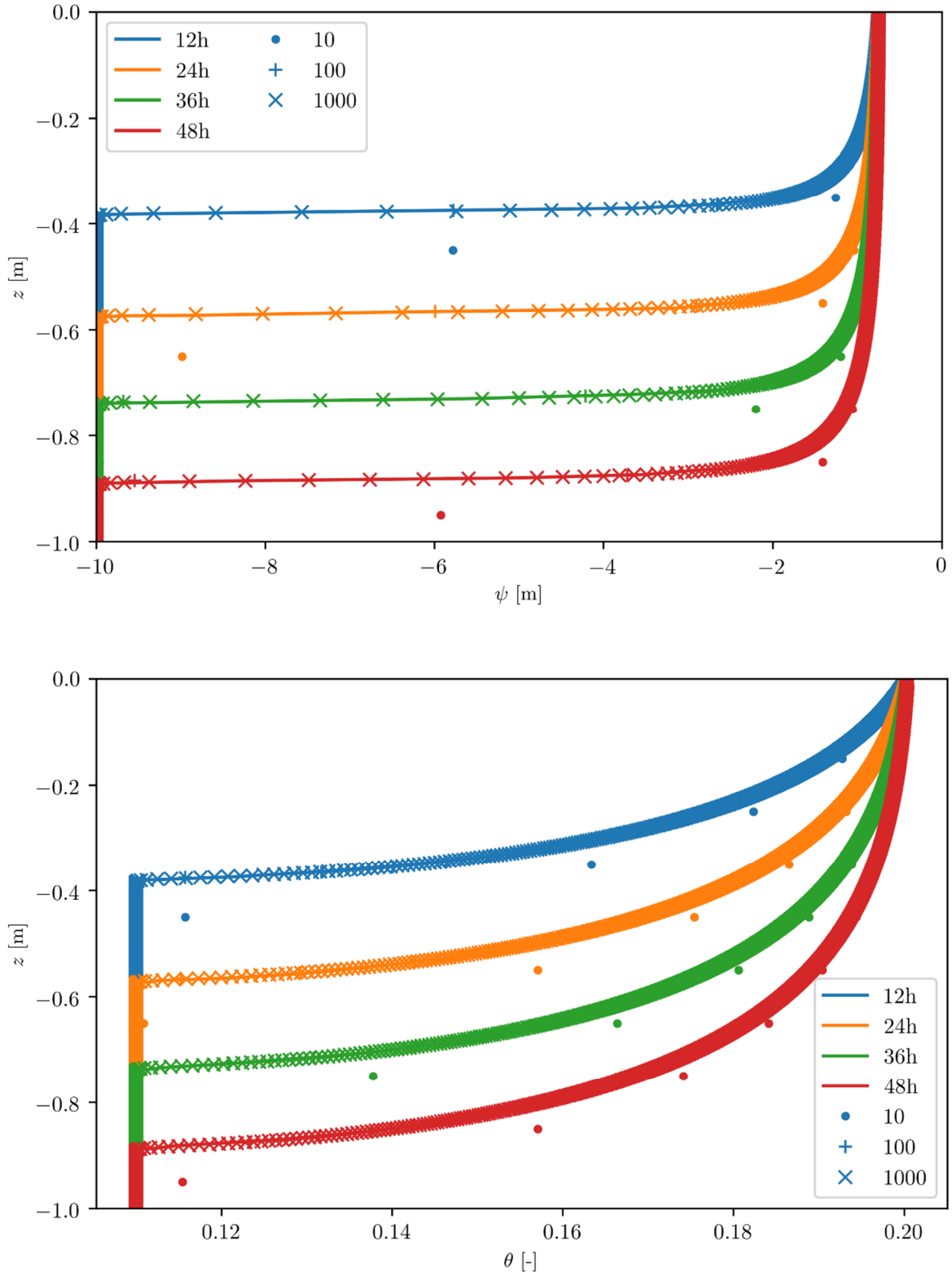


Figure 208: Influence of the number of nodes (120 s time step and 10 Krylov subspaces) (markers) compared to (Manzani et al., 2004) (plain lines)

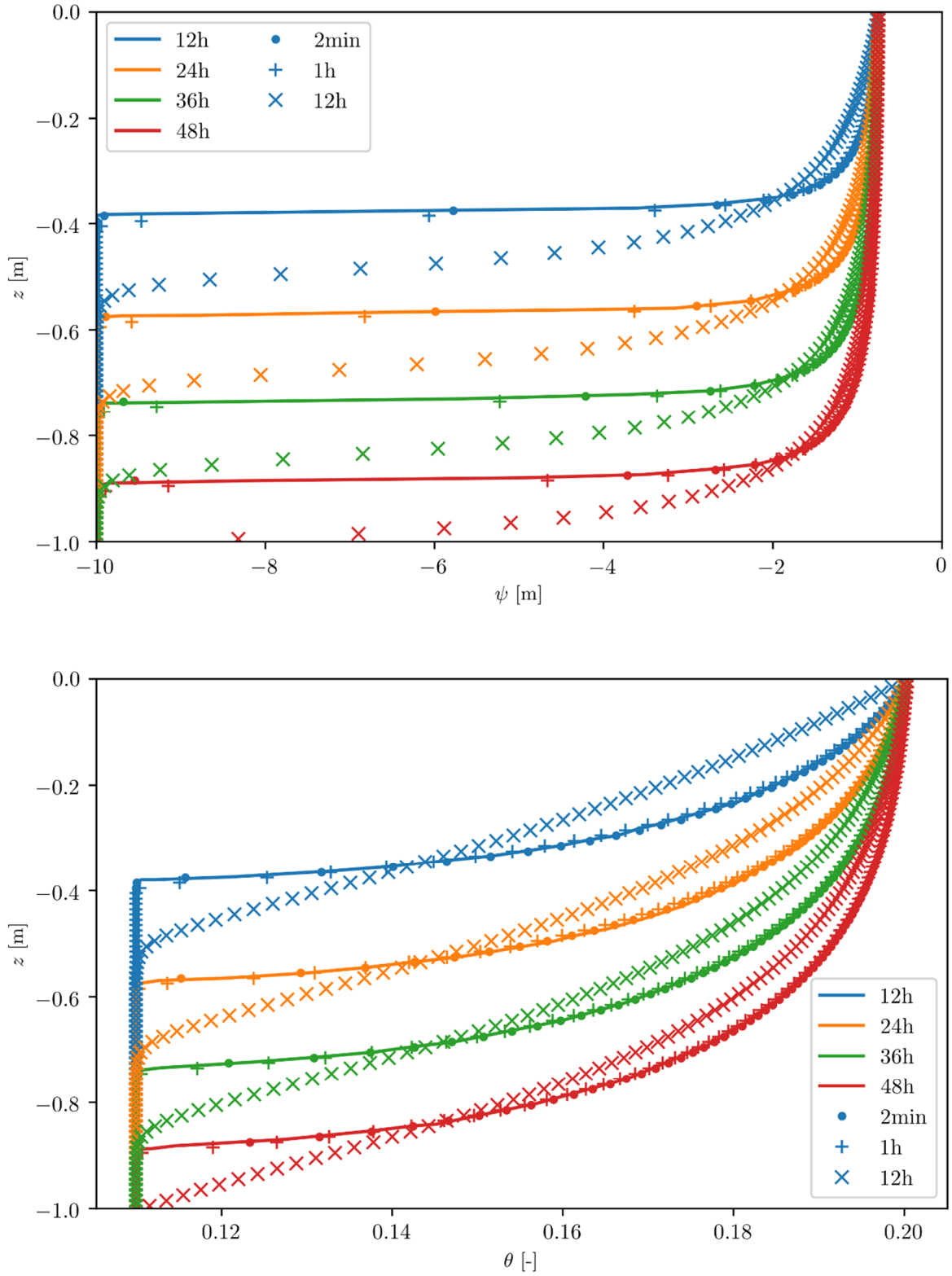


Figure 209: Influence of the time step (100 nodes and 10 Krylov subspaces) (markers) compared to (Manzani et al., 2004) (plain lines)

### D.3 Most favorable parameters for convergence

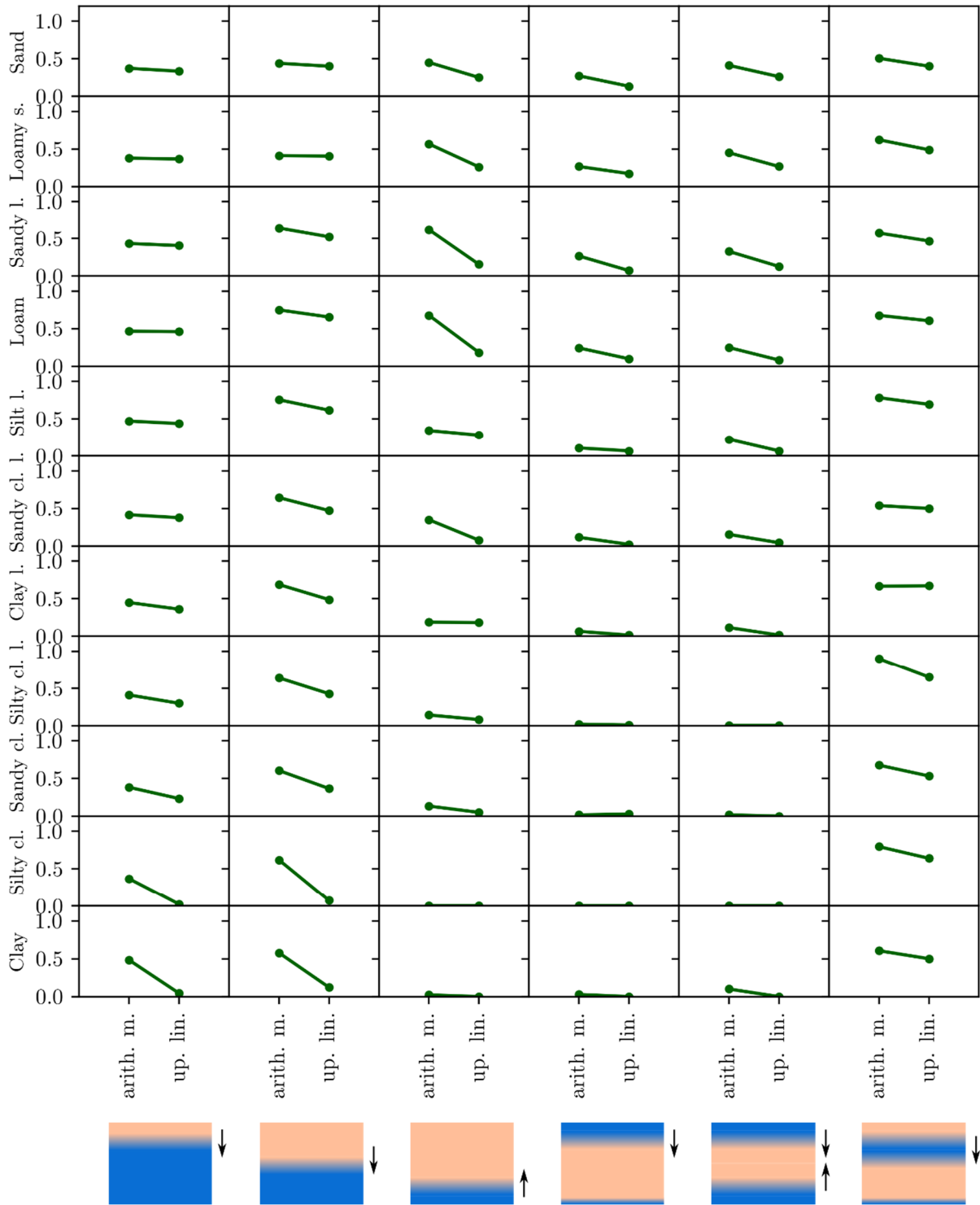


Figure 210: Convergence success rate for 6 scenarios and 11 soils according to the methods used to compute the hydraulic conductivity at borders, considering all other parameters such as defined in section 6.5.2

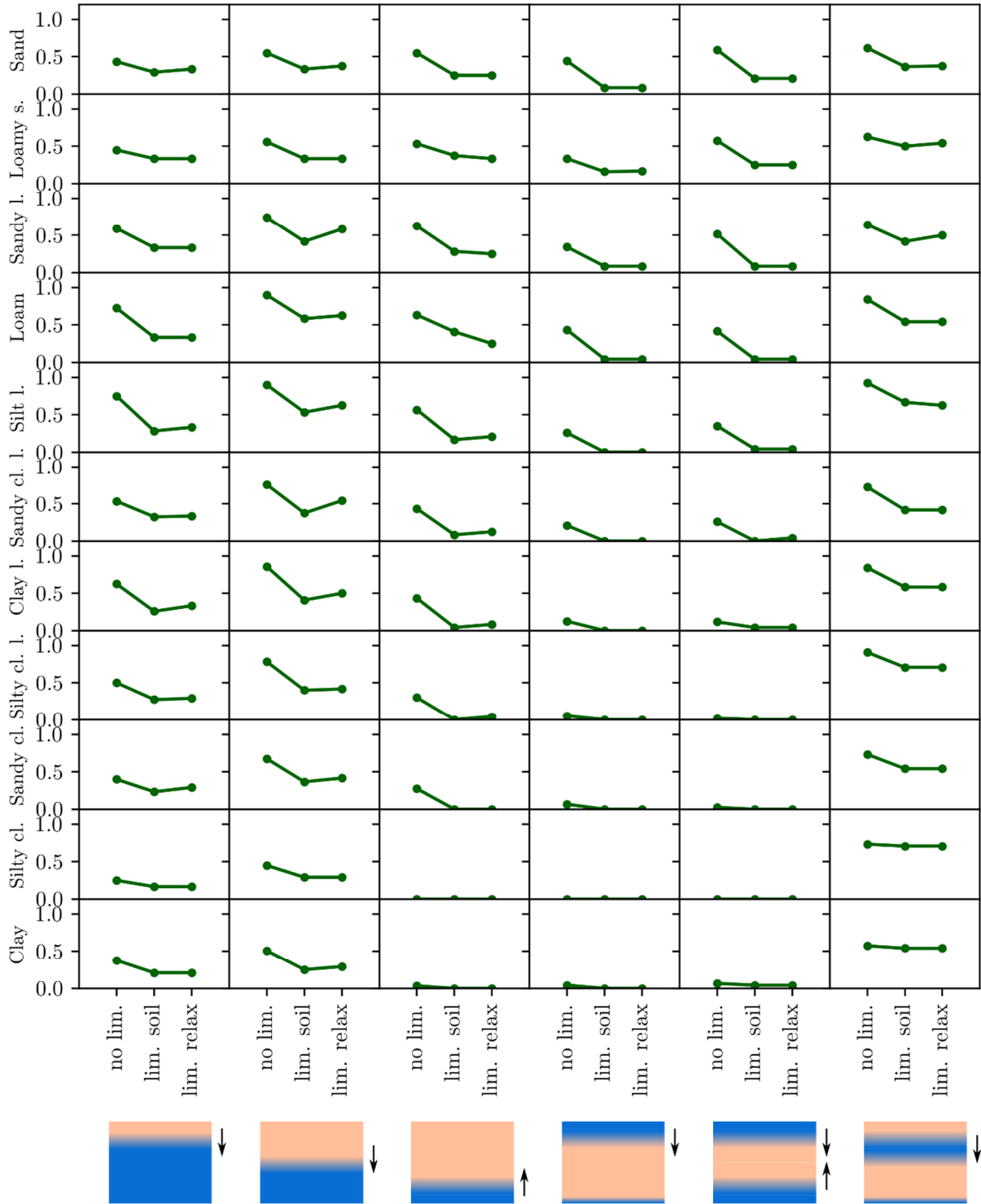


Figure 211: Convergence success rate for 6 scenarios and 11 soils according to the type of limiter, considering all other parameters such as defined in section 6.5.2

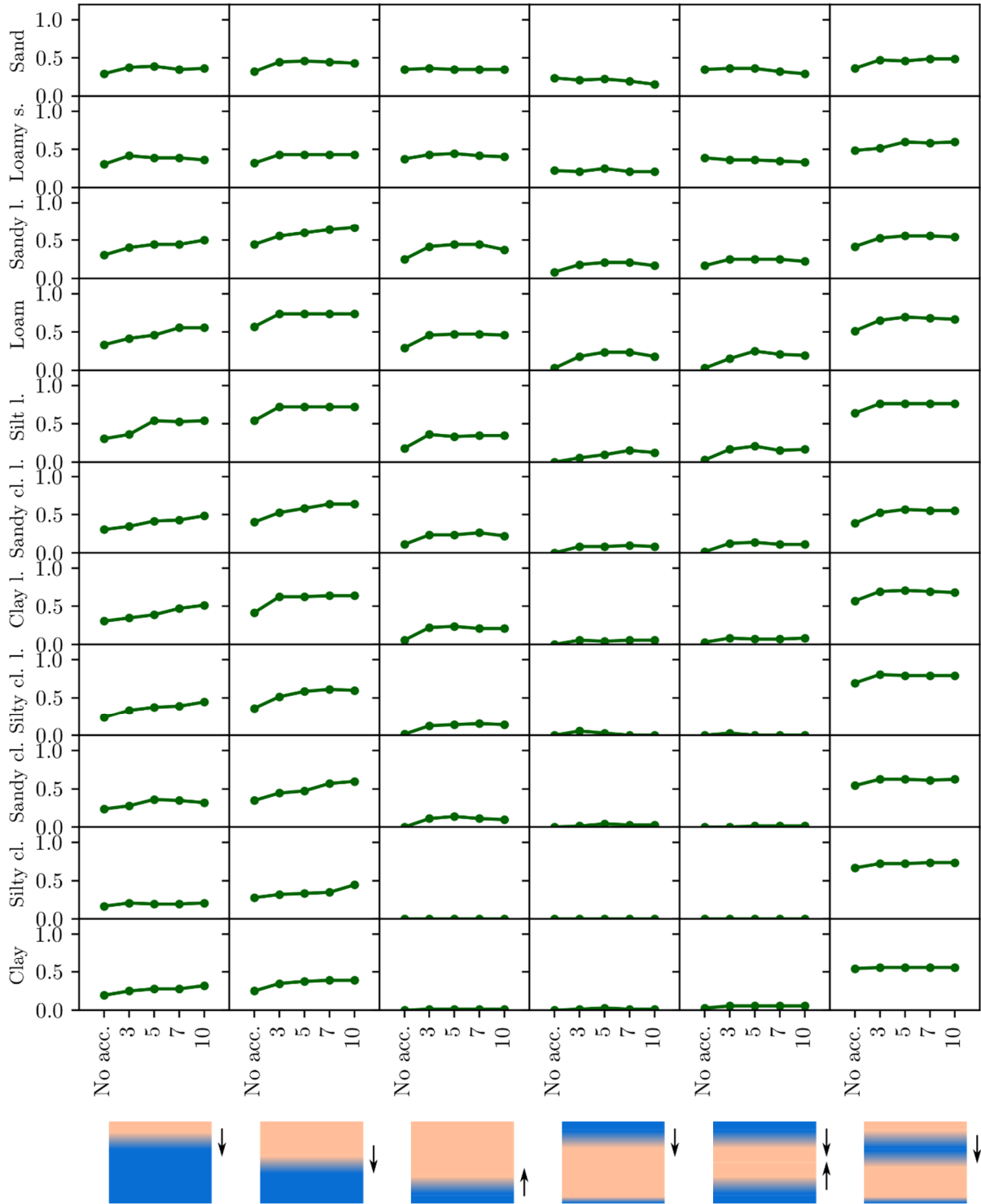


Figure 212: Convergence success rate for 6 scenarios and 11 soils according to the number of Krylov subspaces used in the Anderson accelerator, considering no limiter and an arithmetic mean for the hydraulic conductivity at borders